NATIONAL AERONAUTICS AND SPACE ADMINISTRATION

Technical Report No. 32-800

Ranger VIII and IX

Part II. Experimenters' Analyses
and Interpretations

jpl

JET PROPULSION LABORATORY
CALIFORNIA INSTITUTE OF TECHNOLOGY
PASADENA, CALIFORNIA

March 15, 1966

NATIONAL AERONAUTICS AND SPACE ADMINISTRATION

Technical Report No. 32-800

Ranger VIII and IX

Part II. Experimenters' Analyses and Interpretations

R. L. Heacock
G. P. Kuiper
E. M. Shoemaker
H. C. Urey
E. A. Whitaker

H. M. Schurmeier
Ranger Project Manager

JET PROPULSION LABORATORY
CALIFORNIA INSTITUTE OF TECHNOLOGY
PASADENA, CALIFORNIA

March 15, 1966

CONTENTS

CONTENTS (Cont'd)

I. INTRODUCTION*

Raymond L. Heacock

Jet Propulsion Laboratory
Pasadena, California

The *Ranger* Block III program, consisting of *Rangers VI, VII, VIII,* and *IX,* has been successfully completed. *Ranger VI* impacted within 32 km of its target in Mare Tranquillitatis but failed to provide lunar photographs. *Ranger VII* provided 4308 photographs of the lunar surface and impacted within 16 km of its target in the area subsequently named Mare Cognitum.**

The *Ranger VIII* and *IX* missions culminated in impact in their preselected target areas on February 20, 1965, and March 24, 1965, and returned to Earth 7137 and 5814 photographs of the lunar surface, respectively. Together with the 4308 *Ranger VII* photographs, a total of 17,259 photographs of the Moon were provided by the *Ranger* Block III program. Both *Rangers VIII* and *IX* performed as well as, or better than, *Ranger VII.*

This Report presents the preliminary results of the analyses of the *Ranger VIII* and *IX* lunar photographs by

the team of experimenters appointed by the National Aeronautics and Space Administration, with emphasis on the qualitative interpretations of the photographs. The longer-term quantitative study of the *Ranger VII* photographs is underway, and the *Ranger VIII* and *IX* mission photographs are being added to that effort.

A. Experimenter Team

The National Aeronautics and Space Administration initiated the *Ranger* Block III program in mid-1961 as a follow-on to the earlier *Ranger* Block II program. The primary objective of Block III was to obtain close-up photographs of the lunar surface with significantly better resolution than could be obtained from Earth. Such photographs were expected to provide information about the small-scale topographic features of the Moon's surface needed for Projects *Surveyor* and *Apollo.* NASA appointed an experimenter group made up of a technical team and a scientific team to aid in the planning of the photographic mission. These teams worked with the Jet Propulsion Laboratory to ensure that the photographs obtained from successful *Ranger* flights would provide

---

*Final manuscript received July 30, 1965.

**See JPL Technical Report No. 32-700, *Ranger VII: Part I, Mission Report* (December 15, 1965) and *Part II, Experimenters' Analyses and Interpretations* (February 10, 1965).

significant new information about the Moon, and they were responsible for reporting the scientific results. The original experimenter group for the *Ranger* Block II photographic experiment was:

Scientific team

Dr. G. P. Kuiper, University of Arizona

Dr. E. M. Shoemaker, U. S. Geological Survey

Dr. H. C. Urey, University of California, San Diego

Technical Team

Mr. E. F. Dobies, Jet Propulsion Laboratory

Mr. R. L. Heacock, Jet Propulsion Laboratory

Dr. A. R. Hibbs, Jet Propulsion Laboratory

This group also had the responsibility for the early phase of the *Ranger* Block III photographic experiment. The present appointments were formalized in July of 1963. Dr. A. R. Hibbs and Mr. E. F. Dobies had accepted other positions and were no longer associated with the *Ranger* project. Dr. G. P. Kuiper was appointed as the Principal Investigator, and Mr. E. A. Whitaker, University of Arizona, was added to the group to further strengthen the scientific team.

B. Television Description

There were no physical changes made in the *Ranger* VII television subsystem configuration for *Rangers VIII* and *IX*. However, certain camera electrical gain adjustments were made to increase the sensitivity of the F_B, P_1 and P_2 cameras, which used f/2 optics. This gain change lowered the peak white from 2700 to approximately 1500 ft-L. The television subsystem is described in detail in Part I of Technical Report No. 32-700.

C. Impact-Area Selection

The lunar maria have become categorized on the basis of the slight shift of their reflected solar spectra toward the red or blue. *Ranger VII* impacted the "red" mare area now called Mare Cognitum. Since further classification of lunar maria was scientifically significant and important to the manned landing program, it was decided that *Ranger VIII* should sample a representative "blue" mare. The launch window for *Ranger VIII* permitted the

selection of the "blue" Mare Tranquillitatis as a target. The specific site was also constrained to the *Apollo* landing zone for classification of the small-scale topography of a specific landing area. The target for the February 17, 1965, launch day was 24°E and 3°N selenographic coordinates.

The *Ranger VIII* flight was successfully carried out, with impact occurring at 24.8°E and 2.6°N on February 20, 1965, at 1:58 PST. The spacecraft-trajectory geometry permitted a camera trace across the lunar surface which covered a wide area and provided the potential of good stereo through spatially separated, overlapping views of the surface. It was, therefore, decided that a terminal orientation maneuever was not desired. The composite coverage obtained by *Ranger VIII* is shown in Fig. 1. The lack of a terminal orientation maneuver limited the achieved resolution to approximately 1.5 m, as compared to the 0.5 m achieved with *Ranger VII*.

Since "red" and "blue" maria had been sampled by *Rangers VII* and *VIII*, the prime alternatives for *Ranger IX* were highland terrain and targets of specific scientific interest. It was decided that the latter would be given priority, and the crater Alphonsus was selected as the prime target for *Ranger IX*. The choice of Alphonsus was based on the suspected internal activity, as evidenced by observation and Kozyrev's spectra of an apparent gaseous discharge near the central peak, the dark-haloed craters, and the extensive system of rilles*. In addition, the crater walls and portions of the crater floor were expected to provide data on typical highland terrain types. The specific target was 2.5°W and 13°S selenographic coordinates and represented a compromise between seeing the central peak and the eastern dark-haloed craters and rilles. In order to accommodate the constraints of this target, the first 2 days of the launch window were eliminated.

The *Ranger IX* impact point at 2.4°W and 12.9°S was within 5 km of the preselected target site. The desired coverage of the central peak and the eastern dark-haloed craters and rilles required a nominal terminal orientation maneuver to align the camera central axis and the velocity vector. This maneuver was successfully performed; Fig. 2 shows the composite coverage obtained. A terminal resolution of approximately 0.3 m was achieved.

---

*Kozyrev, N. A., *The Moon*, ed. by Z. Kopal and Z. Mikhailov, New York: Academic Press (1959).

The aiming points, the computer-predicted impact points, and the final impact points for *Rangers VI, VII, VIII,* and *IX* are shown in Fig. 3. The launch-vehicle and spacecraft systems accomplished four successful missions in Ranger Block III. The television subsystems of *Rangers VII, VIII,* and *IX* provided lunar-surface photographs during the terminal sequences of these missions. *Ranger IX* represented an unusual first in space exploration, with real-time coverage of the lunar photographs on nationwide commercial television. This was accomplished through the use of a scan-conversion device which stored the pictures as they were received and converted them for transmission over commercial television.

D. Publication of Data

The quality of the *Ranger* photographs prompted their release as a series of photographic atlases. The *Ranger VII* photographic atlases were published in three separate volumes: *Ranger VII Photographs of the Moon, Part I:*
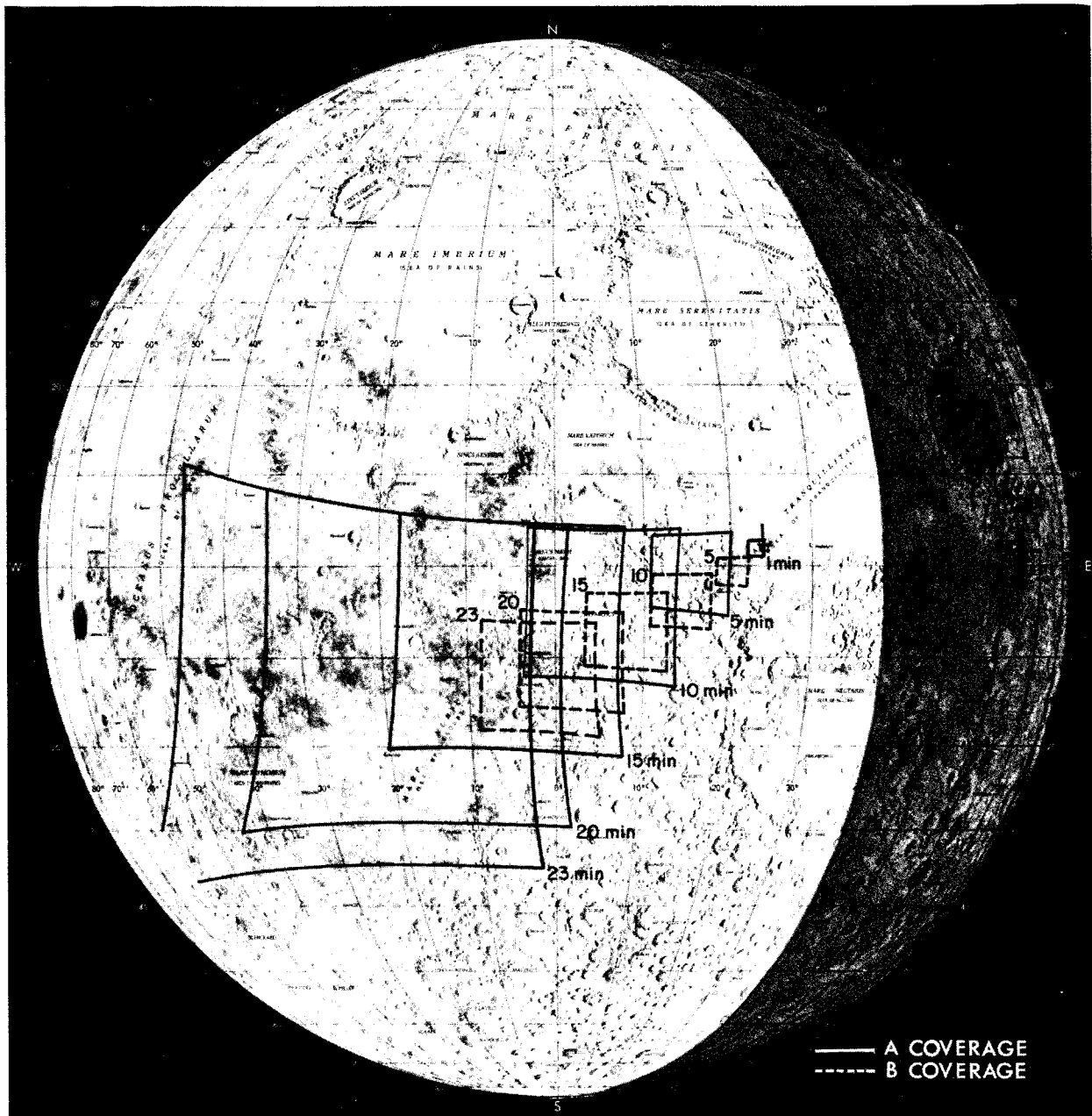
Fig. 1. Area coverage provided by *Ranger VIII.*

Camera A Series, August 27, 1964 (NASA SP-61); *Part II: Camera B Series,* December 15, 1964 (NASA SP-62); and *Part III: Camera P Series,* February 10, 1965 (NASA SP-63).

The atlases were produced in the form of a limited scientific edition consisting of high-quality photographic prints and as a halftone edition by the Government Printing Office.
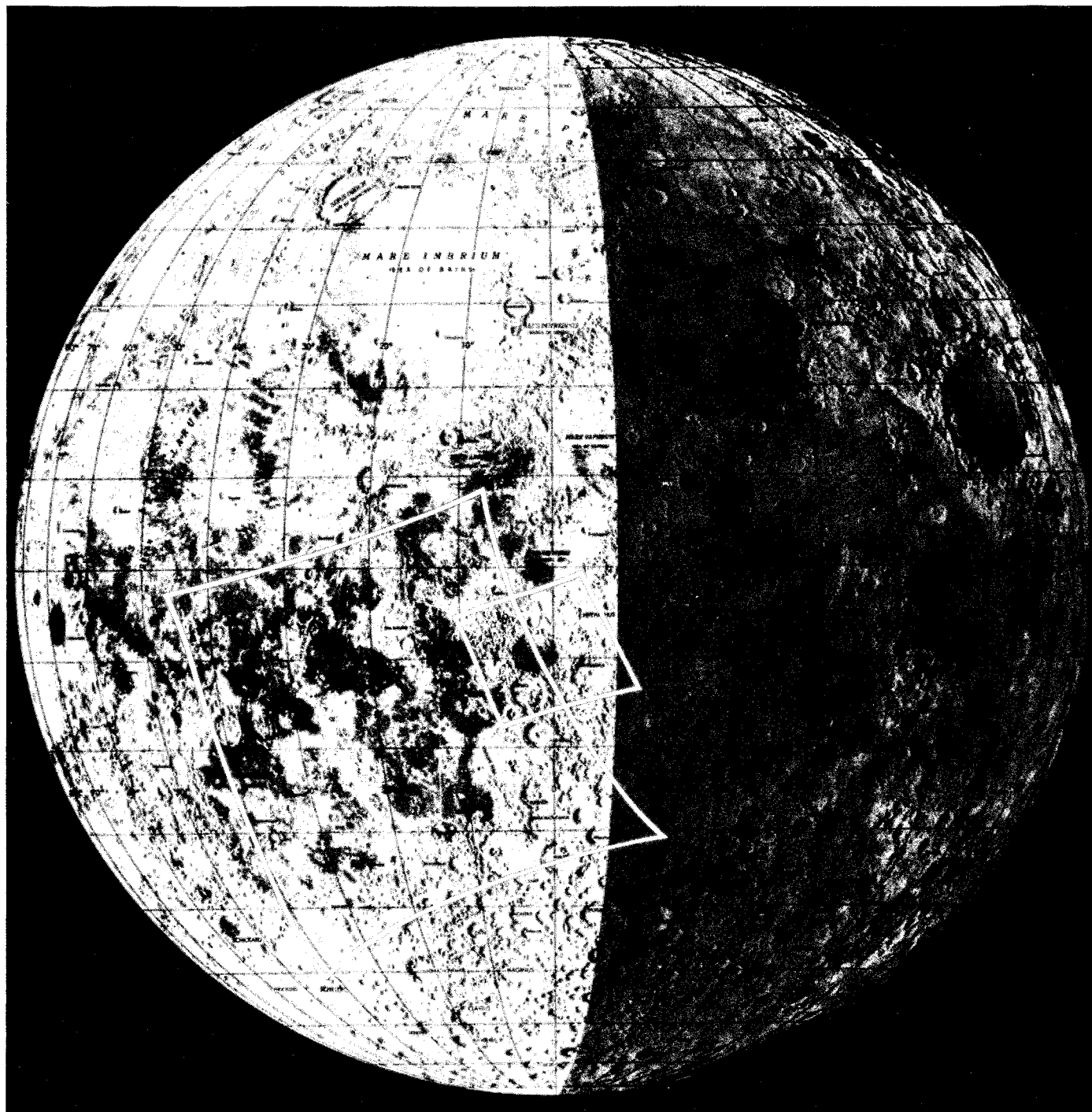
Fig. 2. Area coverage provided by *Ranger IX.*

Ranger VIII and *Ranger IX* each provided more photographs than *Ranger VII*. However, because many of the *Ranger VIII* and *IX* photographs have poorer than Earth-based resolution and considerable redundancy, it was decided to publish a single volume for each mission, containing selected photographs from all cameras. The atlases entitled *Ranger VIII Photographs of the Moon* and *Ranger IX Photographs of the Moon* will be released

in the scientific edition and the halftone printed edition in the near future.

The atlas photographs were dodged to adjust for the variations in sensitivity of the vidicons and to reduce the surface brightness change with longitude in the early pictures. The dodging helps bring the data content of
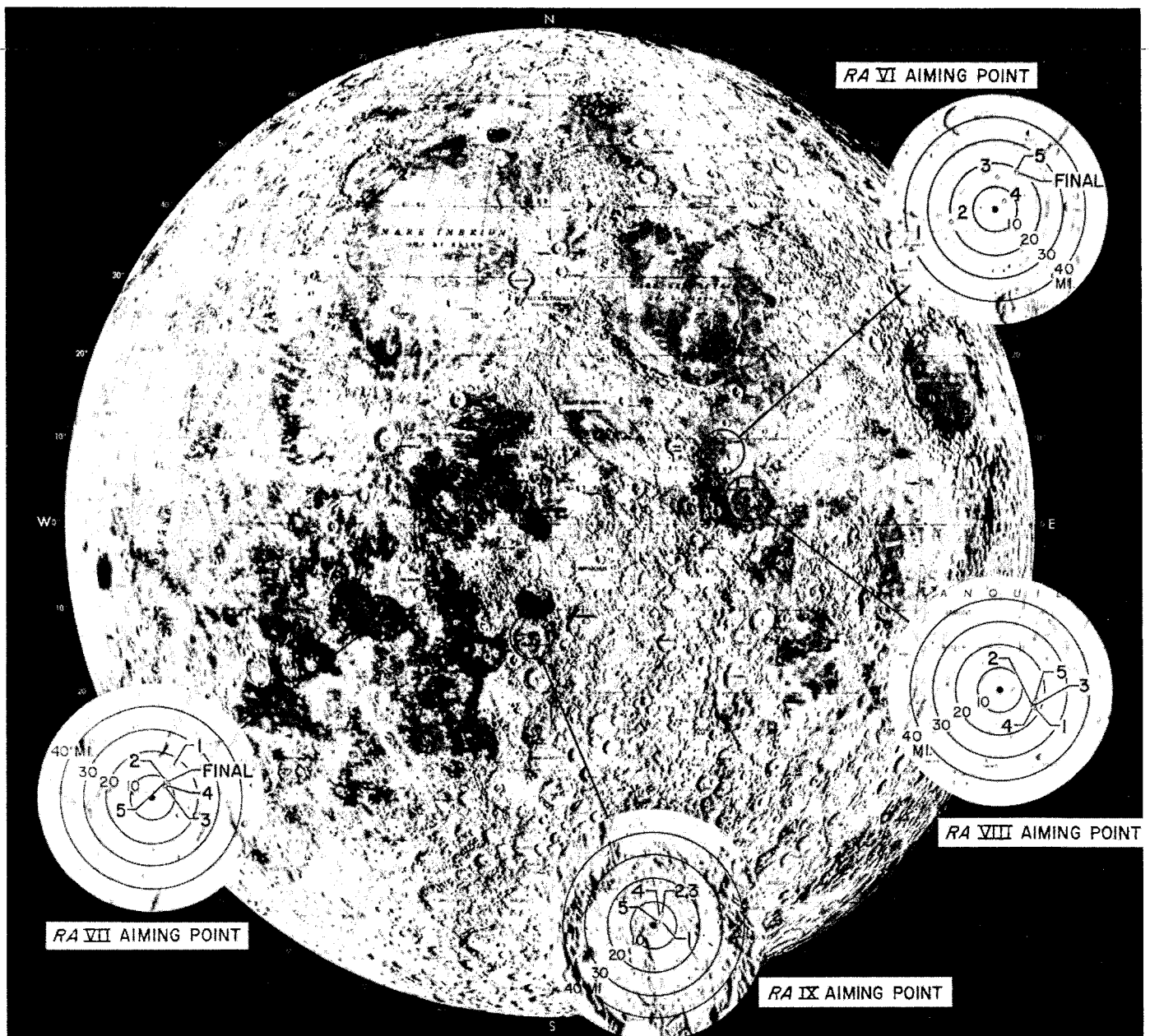
Fig. 3. *Ranger* Block III aiming points, with computer trajectory,
predictions, and final impact points.

the film within the dynamic range of the photographic prints. In addition to vidicon sensitivity variations, residual images, erase-cycle interference, and shutter microphonic noise are present in the pictures. These forms of photometric anomaly and noise are easily interpreted and can be removed by computer processing of the magnetic tape data. (See JPL Technical Report No. 32-700, *Ranger VII: Part I, Mission Report*, December 15, 1964.) Several frames of computer-processed photographs are included in the *Ranger VII* P-camera atlas. The improvement in the photographic data can be readily observed.

The United States Air Force, Aeronautical Chart and Information Center (USAF ACIC), has used the *Ranger*

photographs to refine its shaded relief maps of the Moon. Their LAC 76 map at a scale of 1:1,000,000 was the largest-scale map previously available for the impact area of *Ranger VII*. The USAF ACIC has now published a new series of maps for this area, based upon the *Ranger VII* photographs, at scales of 1:1,000,000, 1:500,000, 1:100,000, 1:10,000, and 1:1000 (*ACIC Ranger VII Lunar Charts RLC 1–5*). Figure 4 shows the shaded relief drawing of the area covered by RLC 3 at a scale of 1:100,000. The *Ranger VIII* and *Ranger IX* photographic data will be utilized to update some of the other ACIC lunar maps. These maps provide in a condensed, but qualitative, form much of the new topographic data acquired by the *Ranger* Block III missions.

Fig. 4. Shaded relief drawing of USAF–ACIC lunar chart RLC 3. (Scale 1:100,000.)

II. RANGER BLOCK III*

Raymond L. Heacock
Jet Propulsion Laboratory
Pasadena, California

The National Aeronautics and Space Administration is committed to landing a man on the Moon before 1970. In order to accomplish this objective with a minimum of risk to the astronauts, it is necessary that the surface of the Moon be known in terms of its hazards to such missions. The study of the Moon by Earth-based observation with supporting laboratory investigations has been intensified during the past few years in preparation for a manned landing. In addition, a series of unmanned lunar space missions were initiated to obtain more direct information. The *Ranger* spacecraft system was the first in the unmanned series. The soft-landed *Surveyor* and the *Lunar Orbiter* missions will follow before the manned *Apollo* landings are attempted.

In addition to the scientific interests to be served by the *Ranger* Block III missions, it was important that the lunar topography be categorized on a scale compatible with the unmanned and manned landing requirements. The *Ranger* photographs have provided a wealth of new visual information about the Moon. Sufficient resolution was achieved in the three impact areas to make adequate

mapping of their small-scale topography possible. The *Ranger VII* mission has been reported upon and its photographs given worldwide distribution and acclaim (Refs. 1–4). This Report attempts to integrate the findings of *Rangers VIII* and *IX* into our developing understanding of the Moon.

A. Background

Before discussing the *Ranger* photographs, it will be useful to review information about the Moon obtained by direct and indirect observations and through supporting laboratory studies. Such information is invaluable for the interpretation of the *Ranger* photographs.**

Under the best of seeing conditions, the lunar surface may be photographed from the Earth with resolutions approaching 400 m. Utilization of shadows cast near the terminator permits the detection of relief on a scale of

---

*Final manuscript received July 30, 1965.

**For an excellent summary of pre-*Ranger* knowledge of the nature and characteristics of the lunar surface, see *The Lunar Surface Layer, Materials and Characteristics*, ed. by J. W. Salisbury and P. E. Glaser, New York: Academic Press (1964).

0.1 to 0.01 the direct resolution. A variety of lunar features has been observed, including craters, maria, mountains, rilles, valleys, and several types of highland terrain. The resolution from the Earth is not sufficient to answer many of the questions associated with these features and their formation. The lunar surface is generally observed to be smooth, with gentle slopes of only a few degrees over the baseline of a kilometer or so which can be measured from Earth. These gentle slopes seem to exist in the "mountainous" regions as well as in the maria, but steeper slopes over shorter baselines are not ruled out.

The color and albedo of the Moon provide unique information about the surface and the effects of at least one of the external agents acting upon the surface materials. The Moon appears to have very little color, as evidenced by the slight shifts of the reflected solar spectra. Ewen Whitaker (Ref. 2, Pt. III-B) has shown that these color shifts separate mare from highland terrain, categorize mare types, and, in some cases, isolate boundaries within a particular mare. Such color differences and their associated boundaries are used as evidence that maria and highlands are composed of different types of material and that the maria were probably formed by the flow of molten material. The albedo of the Moon is generally very low, ranging from 0.05 to 0.18, and appears to be related to the slight color differences.

Consideration of the exposure of the lunar surface to solar radiation prompted laboratory investigations into the effects of such radiation on Earth soils and rock samples. It has been demonstrated that solar radiation will darken material and cause it to lose its color. The conclusion must be reached that the Moon is dark and relatively colorless because of solar radiation, and not because of some unusual compositional makeup.

Below the limits of visual observations, indirect measurement techniques must be used to study the lunar surface. The light-polarization, light-reflection, infrared thermal, radiofrequency thermal, and radiofrequency-reflection (radar) characteristics of the lunar surface can be used to determine its average small-scale structure. The scattered moonlight is polarized by several percent, with the maximum occurring at approximately 90 deg phase. The plane of the polarization rotates with diminishing albedo, and the maximum polarization of dark maria exceeds 15%. The light-polarization properties have been simulated with finely divided opaque particles in laboratory polarization experiments (Ref. 5). It is, therefore, assumed that the surface is either covered by,

or composed of, solar-radiation-darkened, opaque particles of much less than 1-mm average grain size.

The light-reflection or photometric characteristics of the lunar surface provide valuable information on the nature of the lunar-surface microstructure. The intensity of the scattered light changes so drastically as a function of the phase angle that the microstructure must be very open and complex. The Moon is approximately eleven times brighter in its full phase than during the first and last quarter. This reflection characteristic holds not only for the integral disk but for individual surface elements in maria, mountains, highlands, craters, and even the bright crater rays. Hapke (Ref. 5) has shown that finely divided rock dust in a very loose state of compaction simulates the lunar photometric characteristics. In fact, his work has shown that with solar-radiation darkening, a finely divided opaque dust in a very loose state of compaction satisfies the color, the albedo, the light polarization, and the photometric function of the lunar surface.

The *Ranger* television subsystem was adjusted and calibrated against a lunar photometric function derived from the data of Fedorets, Sytinskaya, and Sharonov. The photometric function was derived by D. E. Willingham of the Jet Propulsion Laboratory (Ref. 6) with assistance from Ewen Whitaker in the selection of the best data points. The photometric function shown in Fig. 1 appeared to hold, considering albedo changes and system accuracies, down to the limits of the spatial resolution achieved by *Ranger*.

The color, albedo, light-polarization, and photometric-function measurements relate to the visible surface. Infrared and radiofrequency (microwave) thermal measurements have provided some information on the lunar subsurface properties. Infrared measurements in the 8–12 μ region show distinct limb darkening and a phase variation indicative of a very low thermal inertia. The local temperature of the lunar surface depends essentially upon the angle of incidence of the illuminating sunlight rather than on phase. Microwave measurements in the 1–1000 mm region and their variation with phase reveal that the diurnal heat wave penetrates the lunar surface to a depth of barely ½ m. The change in phase lag with depth of penetration corresponds to a much lower coefficient of heat conduction than for any known solid material. Such a result is consistent with the assumption that an extremely porous surface layer of loosely compacted dust exists on the Moon. The dust-particle grain size undoubtedly increases with increasing material depth.
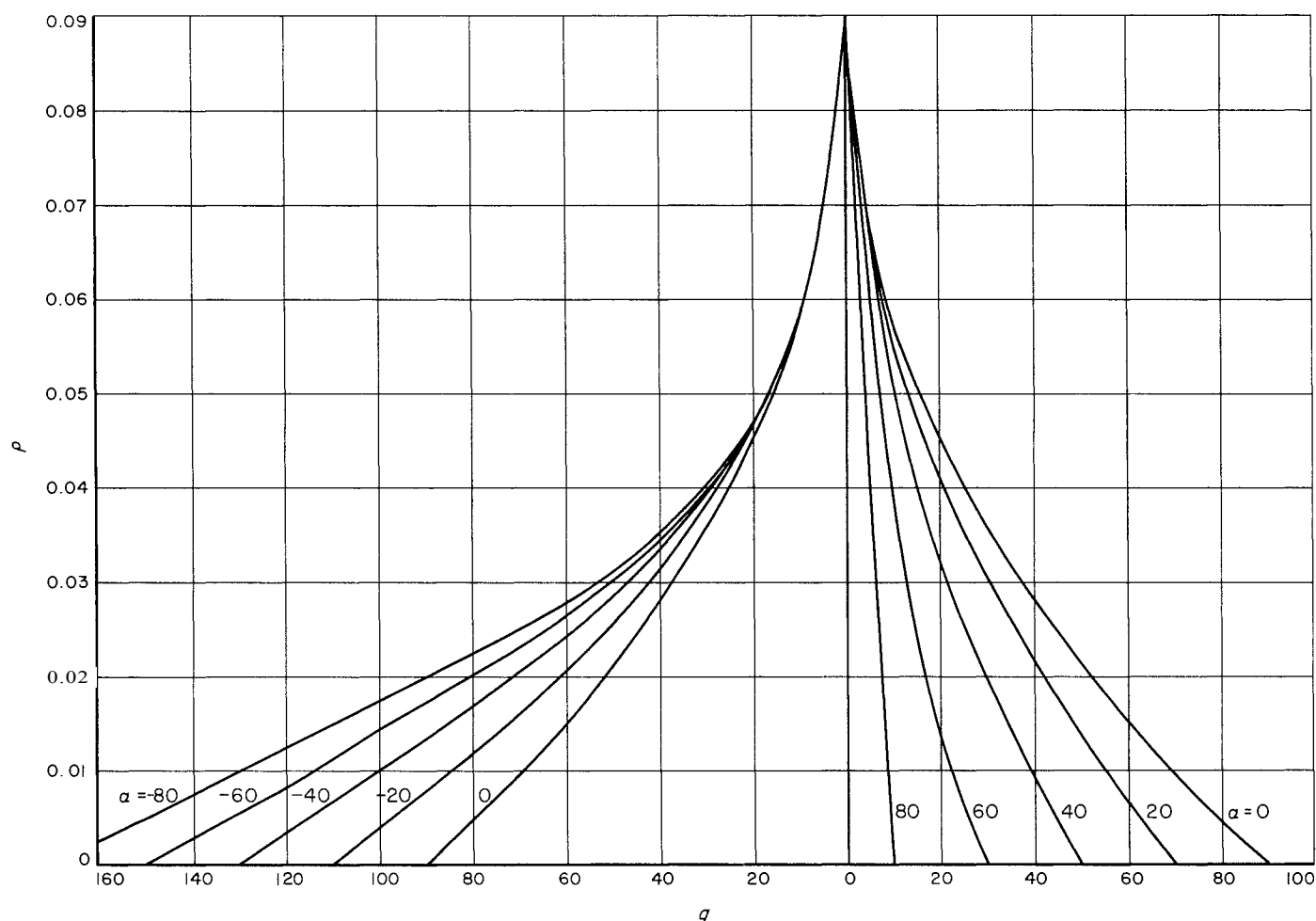
Fig. 1. *Ranger* Block III lunar reflectivity function.

The radiofrequency-reflection measurements generally agree with the visual observations on the smoothness of the surface. These measurements also show that the surface is generally composed of low-density material for the depths sampled by the radar signals. The average slope gradient changes from 1 in 10 to about 1 in 3 as the slope length is decreased from about 1 m to 10 cm.

Recent infrared and radar measurements, with their improved spatial resolution, show that variations do exist in the characteristics of the lunar-surface materials. Dr. Richard Shorthill and his associates at the Boeing Scientific Research Laboratories in Seattle, Washington, took a series of infrared-sensitive line-scan photographs of the Moon during the eclipse of December 19, 1964, from a site in northeastern Egypt (Ref. 7). These photographs indicated that certain craters and some mare areas of the Moon have higher thermal inertias than the general lunar terrain and many other craters. The thermal inertias are still very low, but the differences are significant. Similarly, recent radar data indicate that certain craters exhibit reflection characteristics more representative of a solid material such as rock.

B. Pre-Ranger Lunar-Surface Model

In order to explain the general lunar color–brightness characteristics, it has been postulated that an external agent, the Sun, has acted upon the surface materials. It is also necessary to postulate an external agent to satisfy the general lunar light-polarization and photometric characteristics. The polarization characteristics indicate that a general layer of dust must exist, but such dust must be formed out of local material, or a mixture of external and local material, in order to explain the color

9

differences which can be observed. Surface bombardment by meteorites, micrometeorites, and their secondary ejecta is the most probable external agent for producing the required pulverized material. Even if some other mechanism was responsible, the effects of surface bombardment must be accounted for in the surface processes.

The mechanism by which the open and complex structure required for the photometric function is formed is not known. The vacuum and low lunar gravity suggest the possibility of a loosely compacted dust structure, but the explosive bombardment from meteorites, micrometeorites, and their secondary ejecta would seem to preclude such a simple construction. Certainly, the gentle sifting of very fine dust particles in a vacuum in the laboratory to obtain a loosely compacted, open structure for simulation of the lunar-surface characteristics is not representative of such an explosive bombardment process. Perhaps the mechanism involves the microprocesses associated with the interaction of the more infinitesimal particles from space with the lunar surface, even though such interactions would be explosive in nature. The formation process must include the effects of, and may be dominated by, the secondary ejecta from such micro-explosions. It is important to remember that the polarization and photometric characteristics do not seem to depend upon the type but rather upon the behavior of the materials with respect to the environment and surface processes.

The minimum depth of the pulverized material need only be a few millimeters to satisfy the infrared thermal observations. The microwave thermal measurements extend this minimum depth to about ½ m. The infrared and microwave thermal measurements are limited in spatial resolution and provide only average or integrated indications of surface properties. The local depth of the rubble on the surface will depend upon the local history of meteoric impacts and secondary ejecta. Determination of crater size–frequency distributions to the limits of Earth-based resolution provided pre-*Ranger* estimates of surface rubble depth over and above those required to satisfy the thermal observations. J. W. Salisbury and V. G. Smalley (Ref. 8) provided estimates of average rubble depth which varied from approximately 0.6 to over 80 m, depending on the location on the maria and highlands. It was also judged that the surface roughness on a meter scale would be reduced by the fine dust of varying depth which blankets the surface. It would appear that a fairly reasonable, but unproven, picture of the lunar surface existed in 1963.

C. The Ranger Contribution

The *Ranger VII* mission and preliminary mission results have been reported earlier (Refs. 1–4). *Ranger VII* impacted a "red" mare, since named Mare Cognitum. Several new pieces of information and confirmation of several assumptions about the surface were obtained. The photographs revealed the structure of several crater rays and gave rise to some new interpretations as to their origin (Ref. 2, Pt. VI). The new crater coverage permitted the extension of crater size–frequency distributions (Ref. 2, Pt. IV) down to a crater size of approximately 1 m. Based on the crater size–frequency distributions, Shoemaker provided estimates of surface debris thickness. When the formation of new craters obliterates older craters in such a way that steady-state conditions are achieved, the largest crater size lost provides a means of estimating the surface debris depth. Shoemaker estimated that the surface revealed by *Ranger VII* varied in debris depth from a fraction of a meter to a few tens of meters.

The last *Ranger VII* photograph (Fig. 2) was contoured using photometric techniques (Ref. 2, Pt. IV). This early
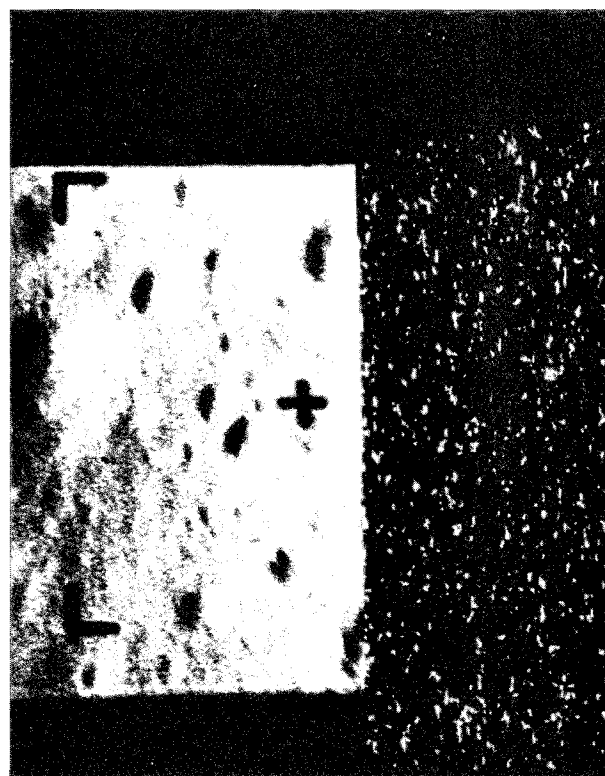
Fig. 2. Last *Ranger VII* photograph. (Covers an area approximately 30 × 50 m; craters of 0.5-m diameter can be detected. Sun angle 23.2 deg.)

work indicated that the surface had slopes over 10% of its area of less than 1 deg (measured over 1-m slope lengths), slopes over 50% of its area of less than 5 deg, and slopes over 90% of its area of less than 15 deg. More accurate computer contouring, which will be discussed later, indicates that the surface is slightly smoother. The Sun elevation angle for the impact area in the *Ranger VII* photographs was 23.2 deg. The area shown in Fig. 2 does not present serious topographic hazards to the unmanned and manned landing systems.

Rangers VIII and *IX* were equally successful in categorizing the lunar small-scale topography at different locations. *Ranger VIII* impacted an area in the "blue"

Mare Tranquillitatis. The specific target was selected within the *Apollo* landing zone so that, in addition to the small-scale topography of a blue mare, the topography of a potential manned landing site could be investigated. In order to obtain stereo coverage of the lunar surface, no terminal pointing maneuver was performed. The photograph shown in Fig. 3 is the next-to-last full picture taken by *Ranger VIII*. The image motion, which resulted without the terminal orientation, is noticeable in this picture. Image motion made the last full picture and a partial one unusable. The resolution in the Fig. 3 photograph permits detection of craters as small as 1.5 m (craters of 0.6 m were resolved by *Ranger VII*). The Sun elevation angle in the Fig. 3 photograph was 14.7 deg.


Fig. 3.   Next-to-last complete *Ranger VIII* photograph. (Covers an area approximately 100 ×
130 m; craters of 1.5-m diameter can be detected. Sun angle 14.7 deg.)

The area shown certainly has no more severe contours than the *Ranger VII* area shown in Fig. 2. *Ranger VIII* demonstrated that the small-scale topography of red and blue maria is very similar. A comparison of Figs. 4, 5, 6, and 7 will make this very evident. Figures 4 and 5 are the last A and B photographs from *Ranger VII*, and Figs. 6 and 7 are the last A and B photographs from *Ranger VIII*. If one considers the difference in Sun elevation angles, the surfaces show a great deal of similarity. The surfaces shown in these photographs must be considered the result

of bombardment by meteorites and micrometeorites and their associated secondary ejecta. The small-scale degradation from such bombardment seems rather extensive, as evidenced by the small number of positive-relief features. Those which can be seen are very low, broad mounds.

Since *Rangers VII* and *VIII* had categorized the topography of red and blue mare, the emphasis in *Ranger IX* was on scientific interest. The crater Alphonsus was
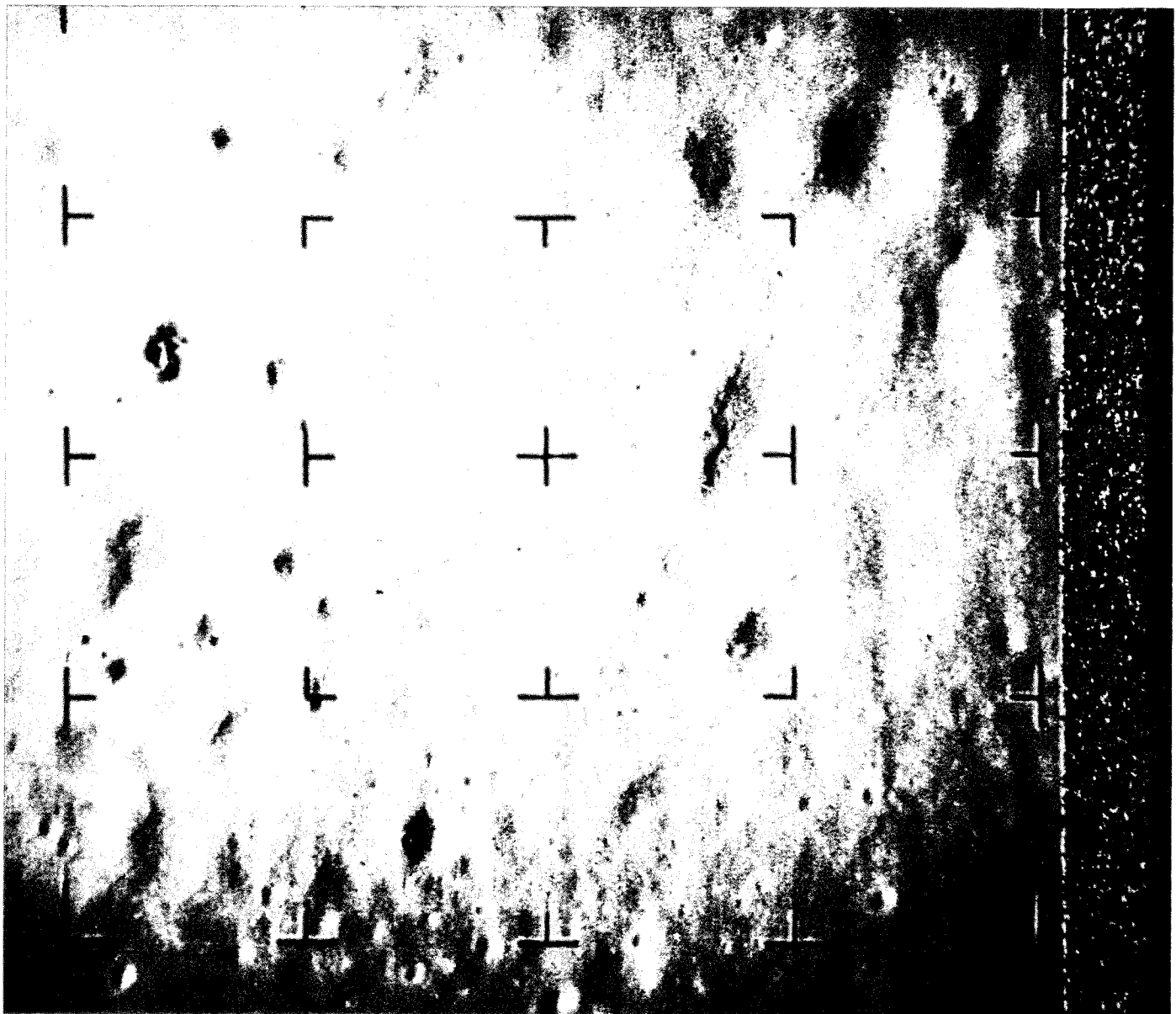
Fig. 4. Last *Ranger VII* A-camera photograph. (Covers an area approximately 2.7 km wide; craters smaller than 10 m in diameter can be detected. Area is relatively rough and appears to be part of a weak Tycho ray.)

selected because of the indications of internal activity that had been noted, such as the dark-haloed craters, the extensive system of rilles, and observation—and Kozyrev's spectra—of an apparent gaseous discharge near the central peak. The target size was selected to optimize the coverage of the central peak and the eastern dark-haloed craters and rilles. The near-perfect execution of

the mission (impact within 5 km of the selected target), including a nominal terminal orientation maneuver, provided the desired photographic coverage. The A-camera-system coverage moved in from Mare Nubium, over the central peak of Alphonsus, to the impact point. The B camera covered an area from Albategnius and Ptolemaeus, over the dark-haloed craters and rilles, to the impact point.
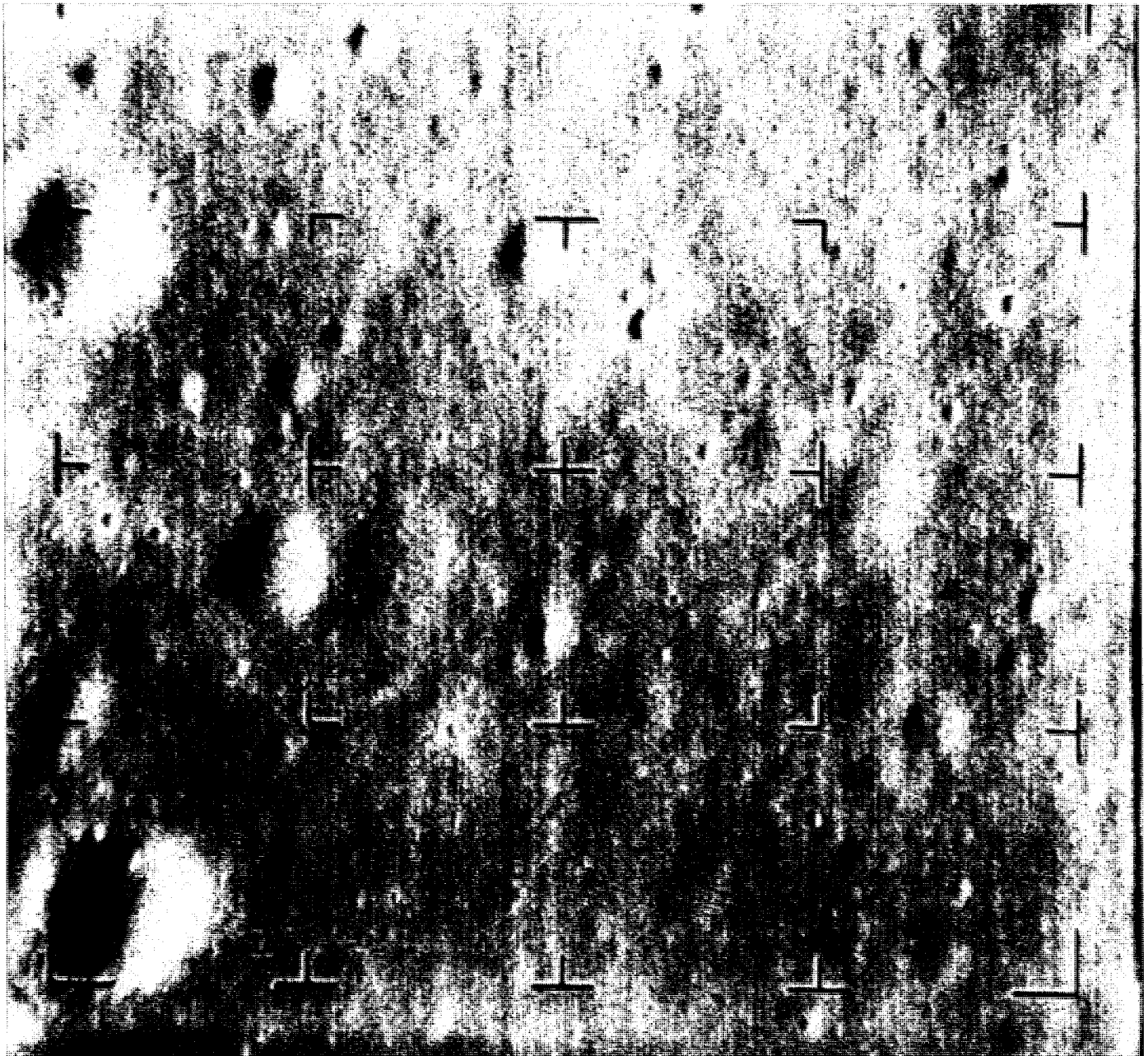
Fig. 5. Last *Ranger VII* B-camera photograph. (Covers an area approximately 2.5 km wide; craters of 10-m diameter can be detected. Area is directly E of last *Ranger VII* A-camera photograph and shows smoother terrain outside boundaries of weak Tycho ray.)
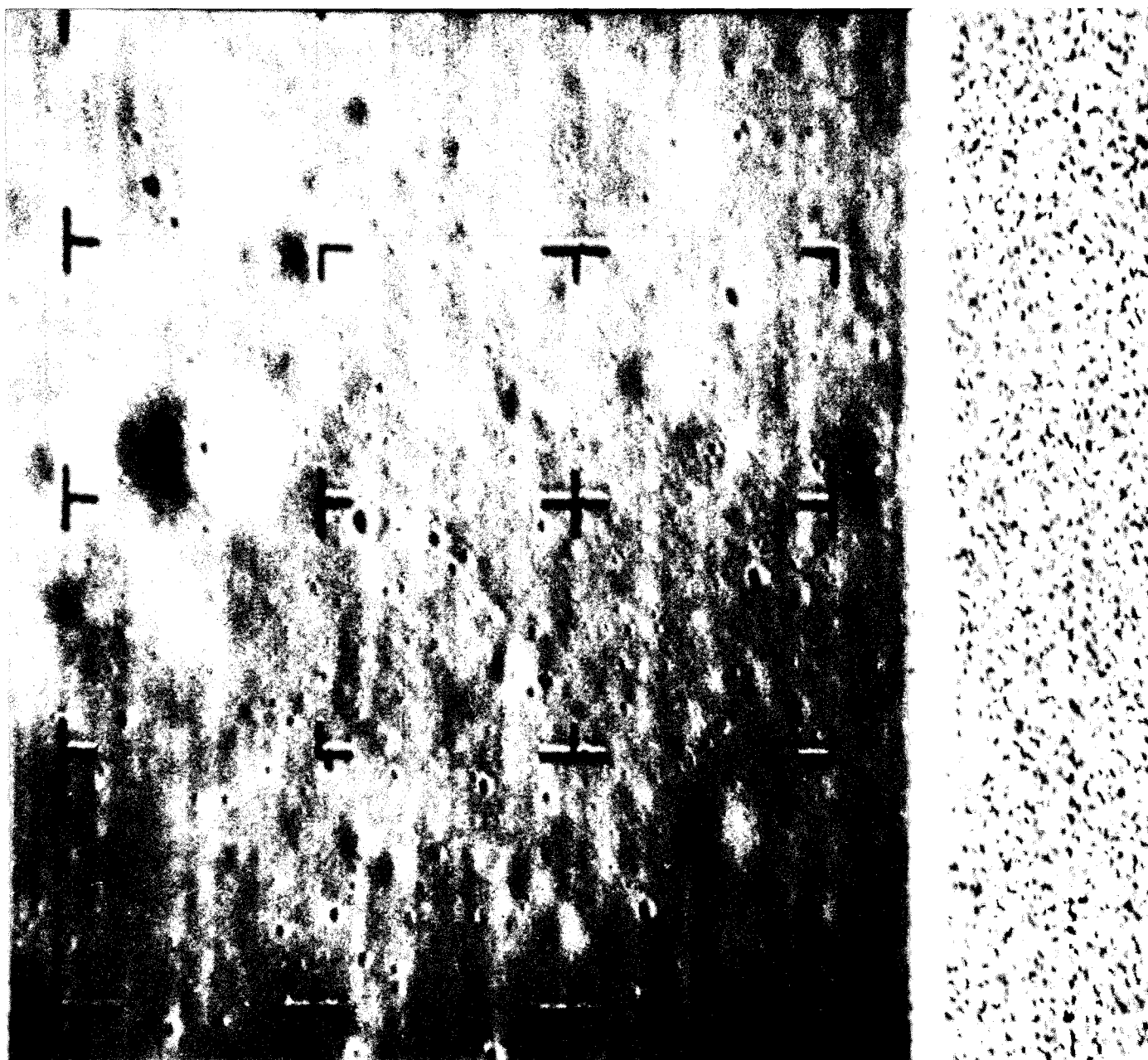
Fig. 6. Last *Ranger VIII* A-camera photograph. (Covers an area in Mare Tranquillitatis approximately 1.5 km wide. Note difference in detail between this and overlapping B-camera photograph shown in Fig. 7, which results from difference in camera sensitivities and, hence, in picture contrast.)

Fig. 7. Last *Ranger VIII* B-camera photograph. (Covers an area slightly over 2 km in width; region of overlap with last A-camera picture shown in Fig. 6 is outlined. Note portion of large crater in lower right-hand corner with several positive-relief features in the wall.)

⟶

The highest-resolution *Ranger IX* photographs are shown in Figs. 8, 9, and 10. The Sun elevation angle for these photographs was 10.4 deg. The surface shown is generally smooth and gently contoured. The only slopes in excess of 10.4 deg, best represented by full shadow, can be seen in craters and perhaps on some of the positive-relief features. The simple geometry shown in Fig. 11 illustrates the shallowness of the craters. The depth-to-diameter ratio generally varies from less than 0.1 to slightly over 0.2, depending upon the assumptions made about the crater shapes and crater-rim anomalies. The few positive-relief features seen are broad, gentle mounds less than 0.3 m in height.

The three successful *Ranger* missions adequately categorized the small-scale topography of a red mare (Mare Cognitum), a blue mare (Mare Tranquillitatis), and high-land crater-floor terrain (crater Alphonsus). Such a small sample of the lunar surface could leave many questions about the Moon's small-scale topography in general unanswered, except for the similarity of the observed surfaces. Considering the differences in lighting and the effects of image motion, the three different types of terrains are surprisingly similar. Certainly, the topography observed at the higher resolutions is dominated by the results of primary and secondary particle bombardment. Craters formed by such bombardment can be detected to the limits of the achieved resolution, and it must be assumed that even smaller craters exist down to a size where some other factor begins to dominate, such as surface particle interactions.

The physical characteristics of the surface material are difficult, if not impossible, to determine from the *Ranger*
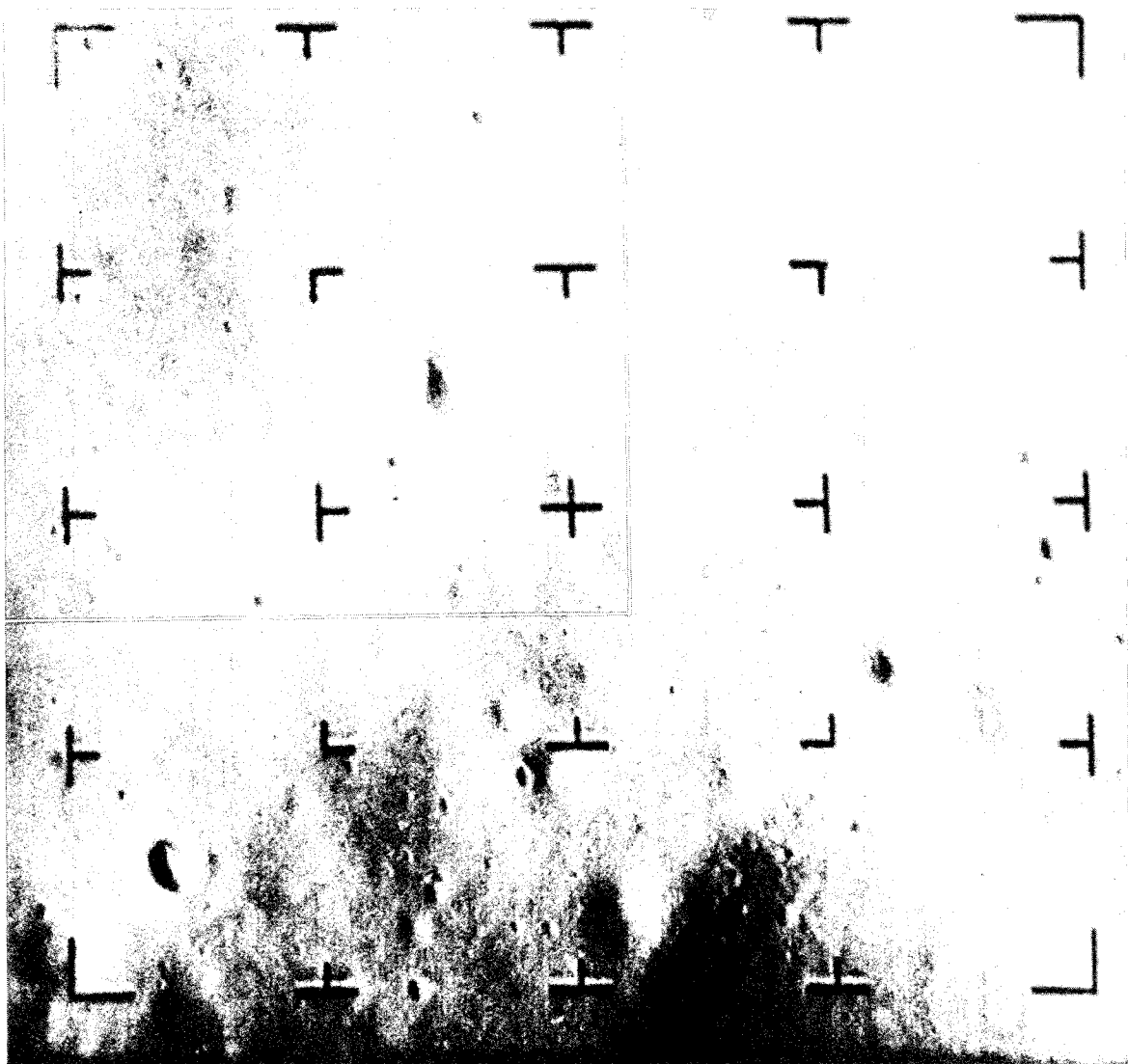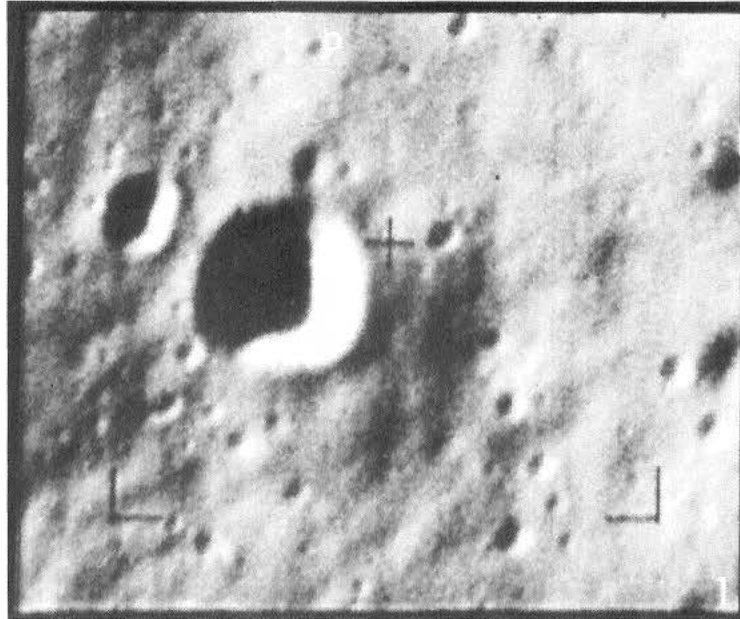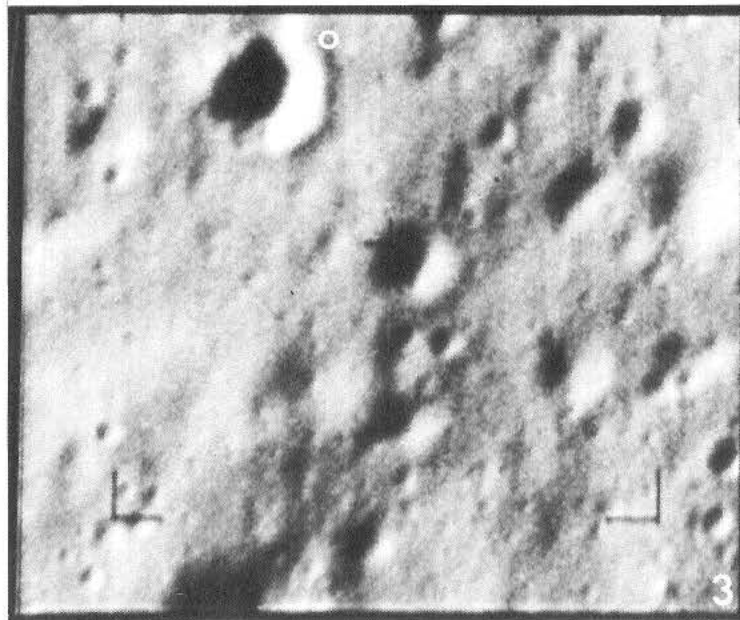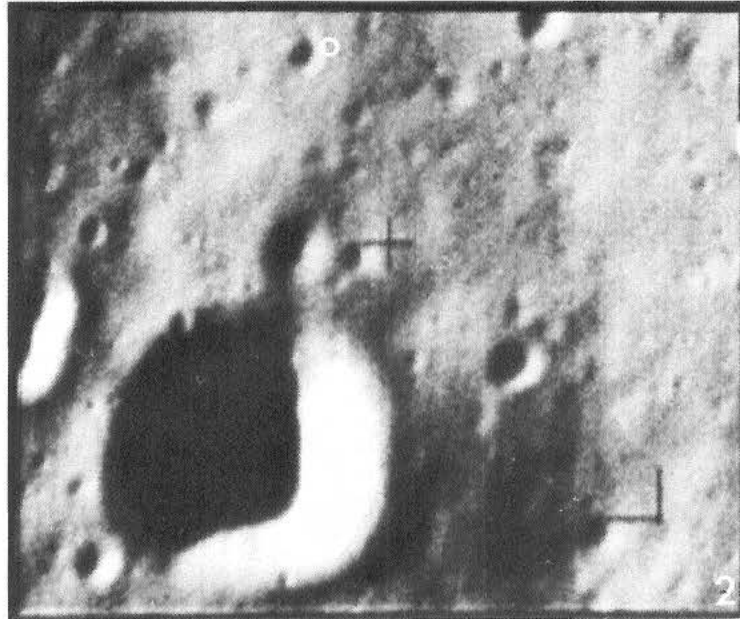
Fig. 8. Last three *Ranger IX* P₁-camera photographs. (White circle marks stationary impact point. Crater near which impact occurred is approximately 8 m in diameter; mound in lower right corner is about 1.5 m across and less than 0.3 m high.)
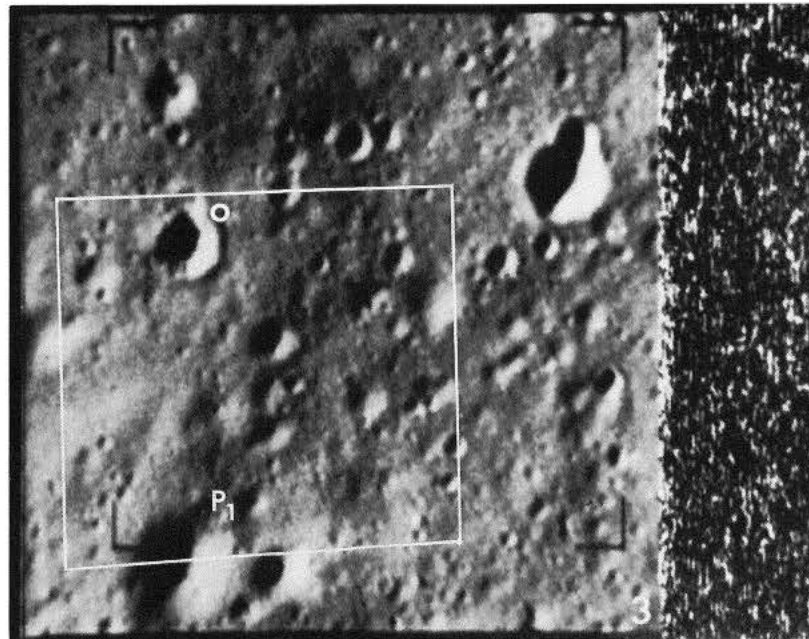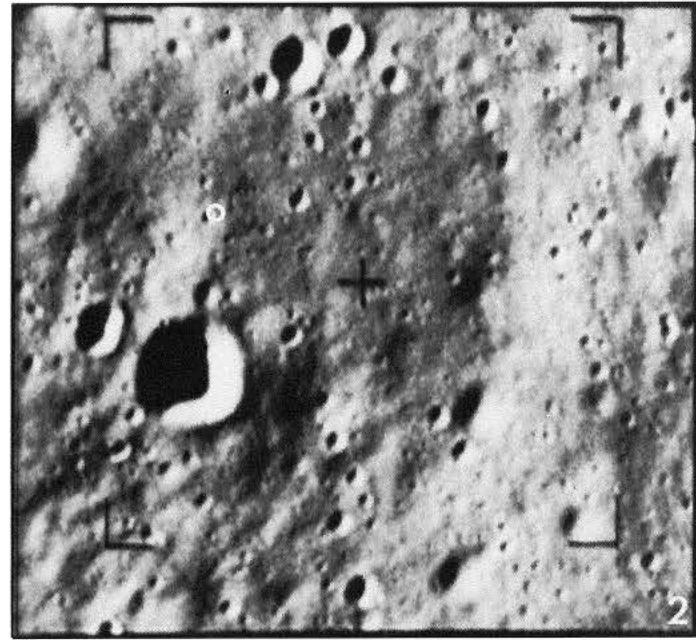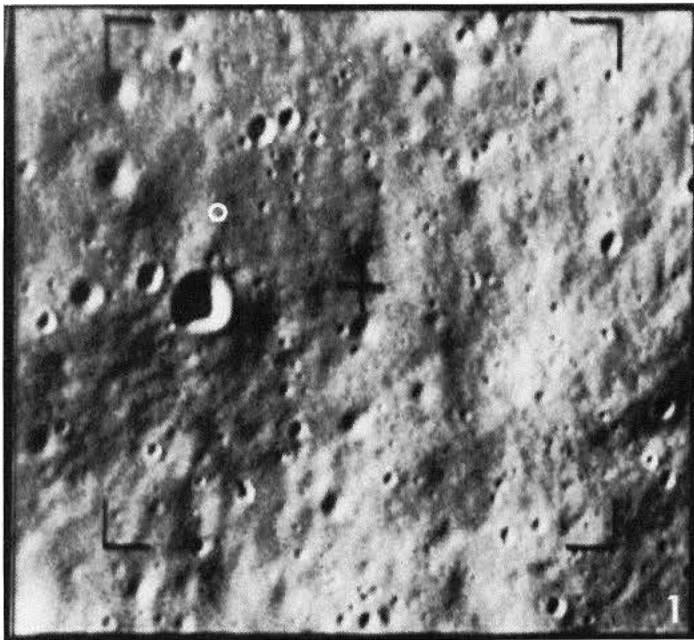
Fig. 9. Last three *Ranger IX* P₃-camera photographs.
(Overlap between last P₁ and last P₃ pictures is
outlined. Note that comparable detail is also
visible in smaller-scale P₃ photograph
because of greater P₃-camera
sensitivity.)
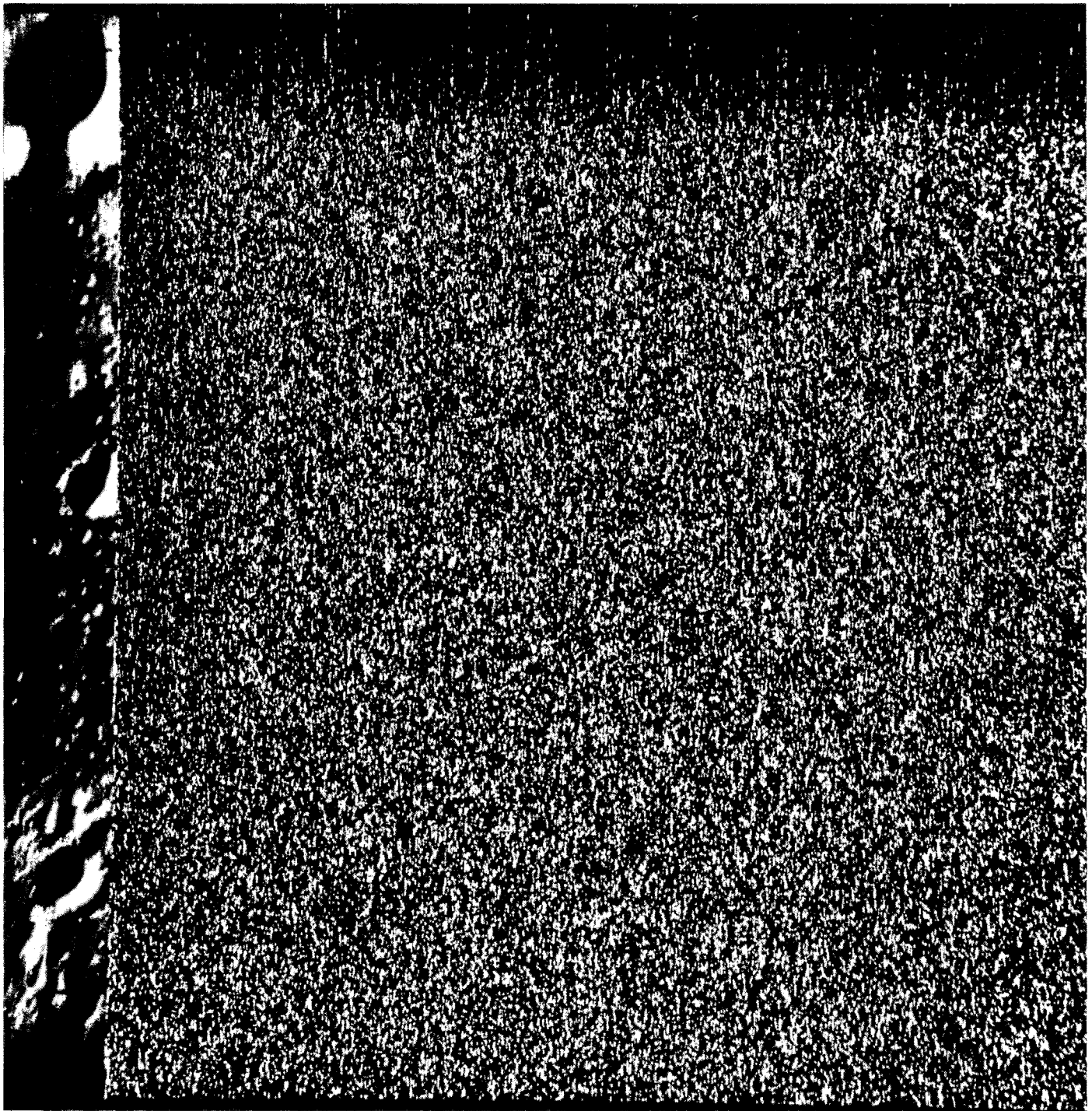
Fig. 10. Last *Ranger IX* B-camera photograph, only partially transmitted before impact, showing several broad, gentle mounds. (Surface resolution better than 0.3 m.)
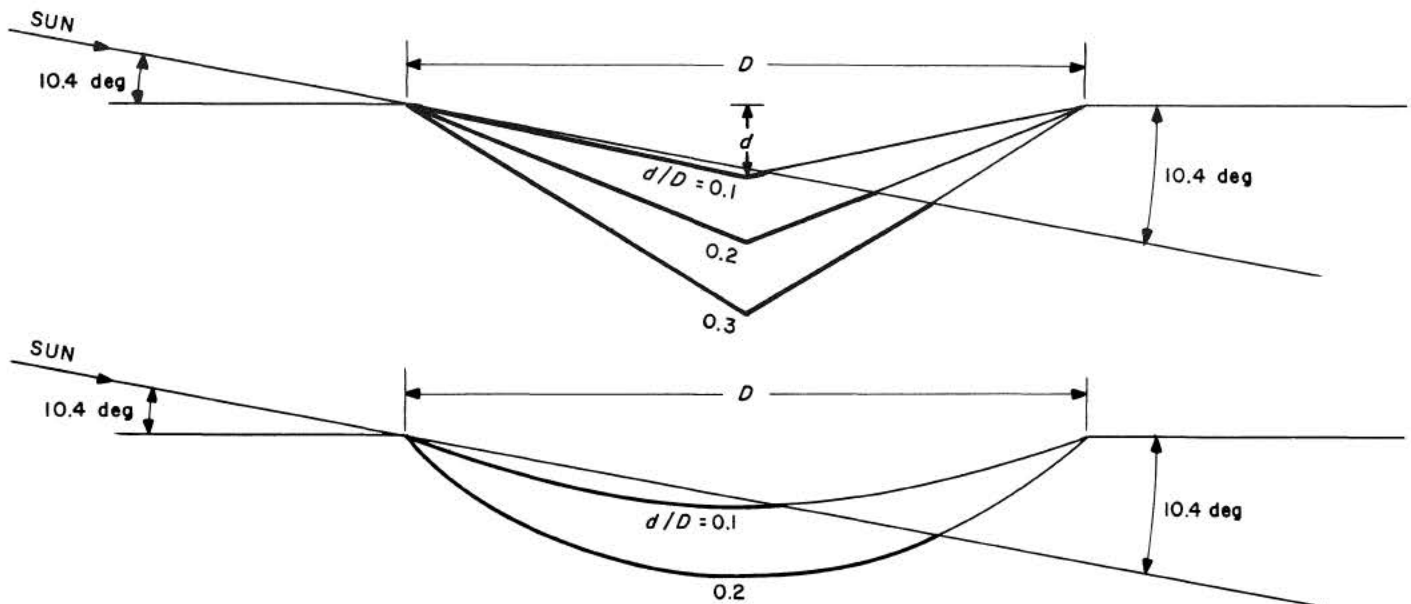
Fig. 11. Crater shadows plotted as a function of shape and depth.

photographs. Impact studies performed by D. Gault at the Ames Research Laboratories (Ref. 9) suggest that the shapes of secondary craters can provide information on the physical properties of the impacted surface. The smoothness of the geometry of suspected secondary craters would imply that the surface is composed of loose or very low-cohesive-strength material with thicknesses measured in meters or tens of meters. However, it must be remembered that the smooth, circular *Ranger* craters may be the result of the physical smoothing of smaller-scale surface degradation by both primary and secondary particles, and of the camera-system resolution limitations.

An artificial softening and smoothing of the observed craters is caused by the sine-wave response limitations of the *Ranger* camera system. The full-scan photographs are constructed with 1150 television scan lines, but the actual resolution is limited to between 700 and 800 effective scan lines by a variety of factors, including system frequency response, scanning spot size, kell factor, etc. The system response or contrast at the limit of 700 or 800 effective scan lines is only a few percent of the flat field dynamic range; at 350 to 400 lines, the response increases to about 50%.

The digital computer can be used to compensate for the loss of contrast as a function of resolution. The actual system calibration data are used in the process*. Figure 12

*Dr. R. Nathan of the Jet Propulsion Laboratory has pioneered digital-computer processing of the Ranger photographs and is responsible for the contrast-correction program.

shows the result of the computer processing of the last usable *Ranger VIII* photograph. This photograph was taken with a partial-scan camera using 300 scan lines, with a resolution cutoff at about 200 effective scan lines. The effects of the loss in contrast in the normally processed photographs must be taken into account in interpreting the *Ranger* photographs. Considering that the correction in Fig. 12 falls short of full compensation, the surface must be assumed to be considerably rougher in its fine-scale structure at the resolutions obtained by *Ranger* than was initially thought. The compensated photograph only begins to reveal the enormous numbers of very small craters which exist on the lunar surface as a result of small primary and secondary particle impacts.

The full potential of the digital computer in processing the *Ranger* photographs has not yet been realized. Two more examples of computer processing are provided in Figs. 13 and 14. Figure 13 shows the same photograph as Fig. 12, but in rectified form. The rectification was accomplished with a computer program using the trajectory-surface-viewing geometry. Figure 14 shows a contour map of the same area generated by the computer using the system calibration data, the mission trajectory, the spacecraft viewing geometry, and a derived photometric function (Ref. 10).

The coverage obtained by the *Ranger IX* A-camera sequence is sampled in Figs. 15 through 19, and that of the B camera in Figs. 20 through 24. Figure 15 provides a good view of Alphonsus and the eastern edge of Mare
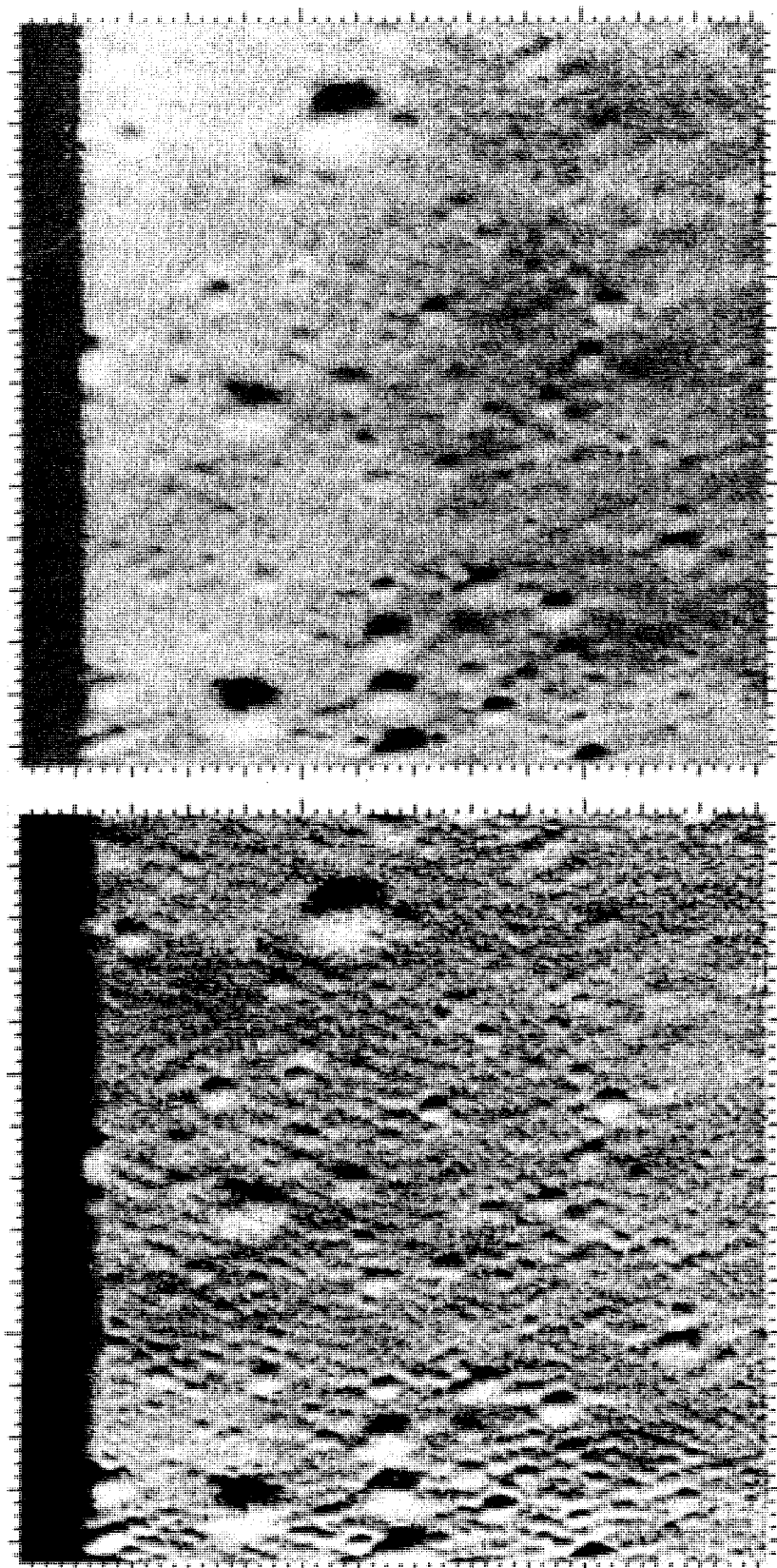
Fig. 12. Contrast enhancement of last usable *Ranger VIII* photograph. (Top, computer-processed version of Fig. 3 without compensation; bottom, result of partial compensation for loss of contrast at higher frequencies. Reticle marks have been removed by insertion of average densities.)

Nubium. Note the marked difference in crater densities at this scale between Mare Nubium and the floor of Alphonsus, whereas the floors of Ptolemaeus and Alphonsus have comparable crater densities, as shown in Fig. 20. Such data support the assumption that the maria are the younger of these lunar features. Figure 16 shows the crater at considerably better than Earth-based resolution. The most striking aspect of this photograph is the smoothness of the central peak, the elevated central spine, and the crater walls. The central peak is shown in greater detail in Fig. 17. The Figure shows no obvious source for the gaseous discharge which has been observed. Perhaps the rille, which runs through the shadow of the central peak, would be a more reasonable source of such a discharge.

Figures 18 and 19 are the last two pictures taken by the A camera. The large crater in Fig. 18 is approximately 2.4 km across. Figure 19 covers an area of over 10 km², and craters smaller than 20 m in diameter can be detected in the prime film. The impact point is approximately halfway between the two left-of-center reticle marks. It should be noted that not all of the circular negative-relief features are impact craters. In Figs. 17 and 18, it may be seen that the rille terminates in a chain of craters which must be slump features. The rille and the slump features are highly degraded by the bombardment process. Such slump features are not sufficient evidence to suggest extensive random slumping on the crater floor.

Figure 21 provides an excellent view of the crater-wall topography on the northeast edge of Alphonsus. Figures 21 and 22 show even more dramatically than Fig. 17 the smoothness of the highland terrain. It is consistent with the meteoric degradation concept to assume that these surfaces are smoothed by the stripping action of the small-scale primary and secondary particles. Where a debris cache basin exists (such as that shown to the left of center in Fig. 22), it takes on the same appearance as the crater floor.

Figure 23 provides an excellent view of the dark-haloed craters along the northeast rille system. These craters do not appear to be of impact origin, in that the dark material surrounding them appears to be a surface deposit. The depth of the deposit is thicker in the proximity of the crater, as can be seen by the filling of the rille. The dark-haloed area has a lower crater count than the floor of Alphonsus because of the covering of older craters. The adjacent wall of Alphonsus, shown in the lower right corner of Fig. 23, has been stripped of any deposit, which conforms with the postulate of the highland stripping process.

The last full B-camera photograph, shown in Fig. 24, covers an area of almost 6 km². Craters as small as 10 m can be detected in the prime film. The "tree-bark" structure resolved in the *Ranger VII* photographs (Ref. 2) can be observed on a more general basis. It appears that this structure exists or becomes visible only on the slopes and may be the result of slumping induced by small-scale bombardment. This is an area in which enhancement to compensate for the system response could aid the interpretation. The tree-bark structure is not visible on the flatter terrain shown in Figs. 8, 9, or 10, even though a much higher resolution is provided. If this structure can be interpreted as slumping, it would support the assumption of a loose or very low-cohesive-strength material which Gault (Ref. 9) made, based on consideration of secondary crater shapes.

D. Conclusions and Summary

The Moon as revealed by Earth-based observations is a complex body. Its present surfaces are primarily the result of external agents, such as the radiation of the Sun and impacts of bodies ranging from planetesimals to micrometeorites. The available data are insufficient to unravel much of the Moon's history. The highland terrain appears to be considerably older than the lunar maria. The age differences cannot be determined very accurately because of inadequate information about the Moon's thermal history and the time history for impacting bodies. Certainly, the thermal history and the impact of planetesimals are interdependent in the formation of many of the observed maria. Many of the planetesimal impacts could have occurred much earlier than the general flooding, which must have been the result of internal melting at some point in the Moon's thermal history.

The development and extension of crater size–frequency distributions from Earth-based observations permitted reasonable estimates to be made of the degree of surface modification to be expected. The multitude of indirect observations provided information on the small-scale structure, and some insight into the processes at work and their effects on the lunar surface.

The *Ranger* missions were only the first step in a series of unmanned and manned missions designed to answer major remaining questions about the Moon. The *Ranger* system was designed to take close-up photographs of the lunar surface in order to provide direct information on the lunar topography at a scale compatible with the unmanned and manned landing requirements. The missions were completely successful in this respect, and it is
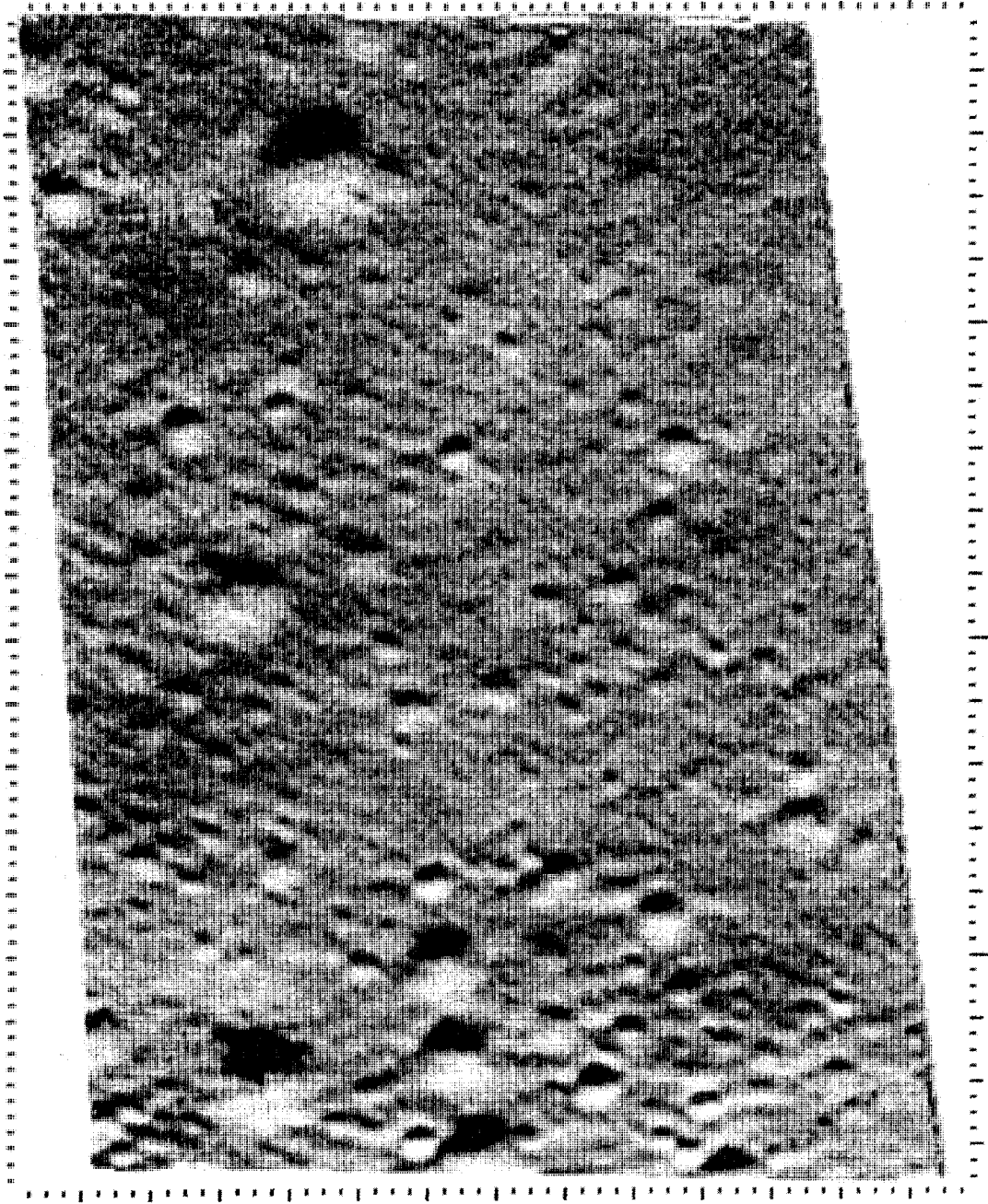
Fig. 13. *Ranger IX* photograph with computer rectification.
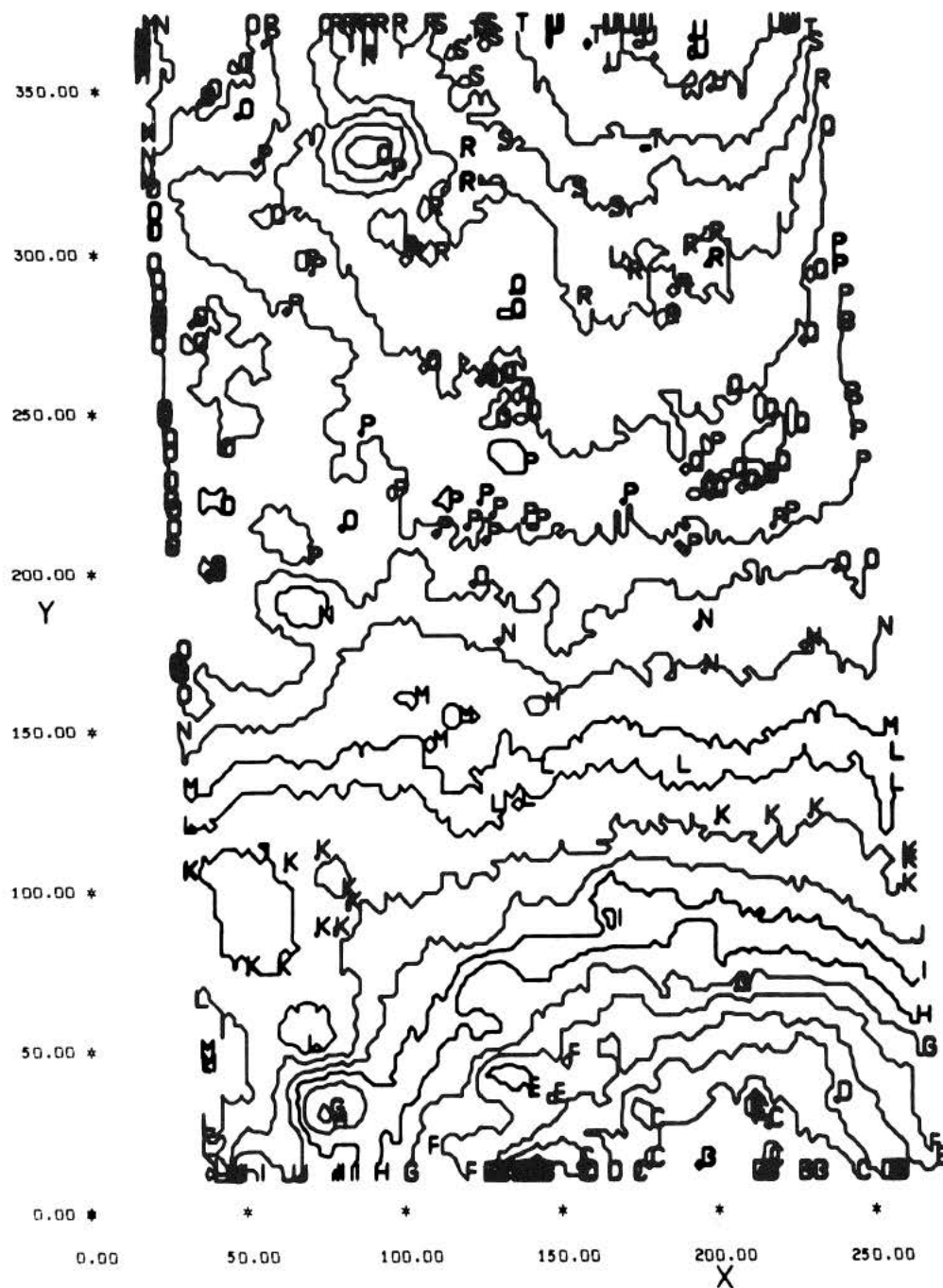
ARC LABEL	CONTOUR VALUE (CM)
A	22.50
B	45.00
C	67.50
D	90.00
E	112.50
F	135.00
G	157.50
H	180.00
I	202.50
J	225.00
K	247.50
L	270.00
M	292.50
N	315.00
O	337.50
P	360.00
Q	382.50
R	405.00
S	427.50
T	450.00
U	472.50

Fig. 14. Contour map of last usable _Ranger VIII_ photograph. (Prepared from computer-stored, rectified camera-system calibration data and an assumed photometric function with constant albedo.)

now known that the topography holds no serious hazards for unmanned or manned landings.

The *Ranger* missions sampled two widely separated maria and a highland crater floor. All three targets were found to have similar small-scale topography. The observed topography is obviously the result of primary meteorite and secondary ejecta bombardments. The surface degradation seems to fit the expectations closely, except for the low incidence of positive-relief rubble. It must be assumed that the surface material is loose enough and has been modified to such a depth that no positive-relief rubble is formed, or that the small-scale degradation from micrometeorites wears down and buries

Fig. 15. *Ranger IX* A-camera photograph, showing craters Alphonsus and Alpetragius and E edge of Mare Nubium. (Resolution is better than can be achieved from Earth. Note difference in crater density between Nubium and Alphonsus areas.)

such rubble, or that a combination of the two situations exists.

The original surface structure of the maria was obliterated by the surface modification processes. It is apparent that the highland terrain has been more extensively modified, and the depths of the debris in the highland basins and craters may prove to be hundreds or even thousands of meters thick. The flattening of the highland topography has been extensive, as evidenced by the slopes of the crater walls, the central peaks, and the flattened crater floors and highland basins. It would appear that highland crater floors and basins are filled with debris and flattened by the statistical distribution of
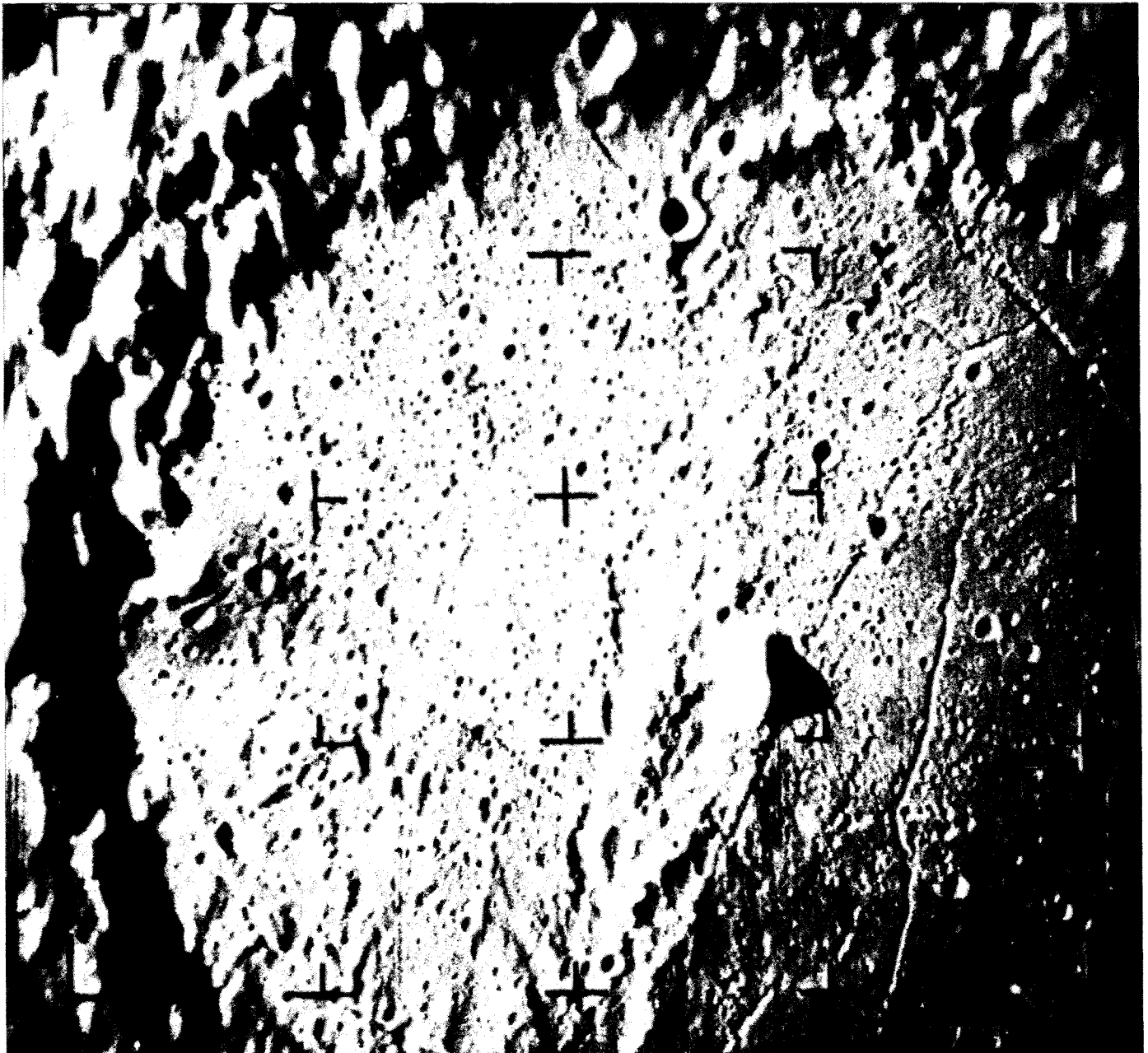
Fig. 16. *Ranger IX* A-camera photograph, showing Alphonsus in detail. (Note difference in crater densities between crater floor and central highland spine, and between central peak and crater rim.)

material through a continuous range of impact particle sizes which increase exponentially in number with decreasing size. The exposed highland terrain is still in the process of being stripped, but the slopes have become so gentle that a debris layer has built up, probably varying in depth from a fraction of a meter to a few meters, except in cache basins and craters, where it will be much deeper.

The evidence for relatively recent or presently existing internal activity is increasing. The extensive rille system in Alphonsus and the dark-haloed craters were assumed to be a part of this evidence. The dark-haloed craters are certainly more recent features than the rilles, since their deposits fill the rilles locally. As several impact craters of reasonable size exist in the dark deposit, it would appear that either the blanketing process proceeds at a very low
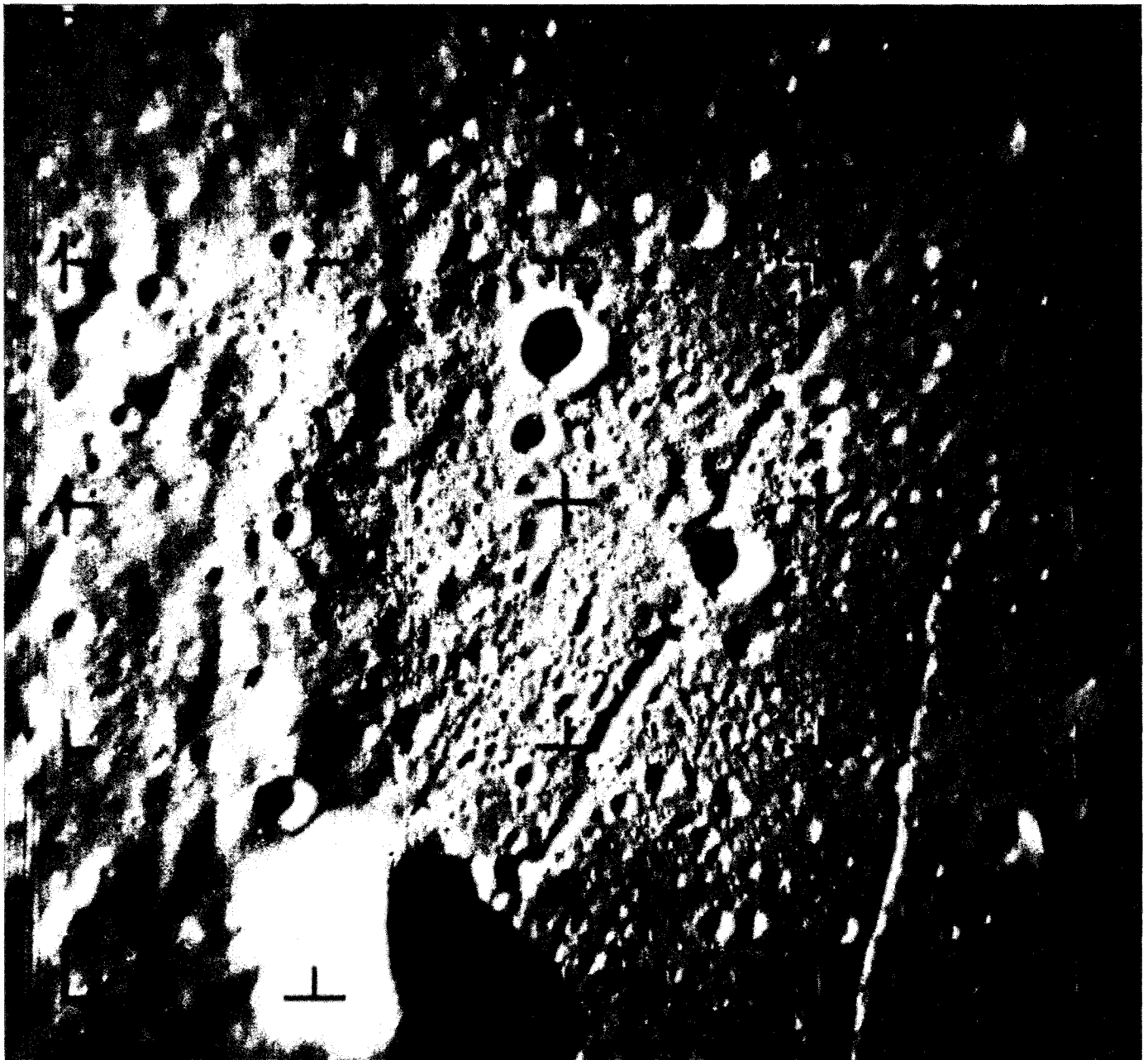
Fig. 17. *Ranger IX* A-camera photograph, showing central peak and central highland spine of Alphonsus. (Two large craters near central reticle are slightly over 2.5 km in diameter.)

rate, or there has been no activity for a considerable period of time. The shallow lighting angle does not permit viewing of the bottom of the crater to determine whether the vent has been filled and the crater floor smoothed by small-scale bombardment. The highlights in the dark-haloed crater wall shown in the lower right corner of Fig. 23 suggest that a vent may still exist.

Many questions about the Moon have been answered through Earth-based observations and by the *Ranger* missions. The capability of providing new information from the Earth is obviously limited. The *Ranger* missions have increased our confidence in being able to land, first unmanned and then manned, vehicles safely on the surface of the Moon. The unmanned *Surveyor* spacecraft

Fig. 18. Next-to-last *Ranger IX* A-camera photograph. (Large crater is 2.5 km in E–W dimension. Majority of craters and rille depressions are very shallow. Sun angle 10.4 deg.)

represents the next critical step in the series of lunar exploratory missions. *Surveyor* will determine the surface hardness by landing and through scientific instruments, and it will obtain information on seismic activity, elemental makeup, secondary microejecta environment, soil properties, and the small-scale surface structure. If the *Surveyor* landings are successful, the last major step may safely be taken. With the landing of trained men on the lunar surface, the way will be open to obtaining the answers to most of the remaining questions about the Moon.

Fig. 19. Last *Ranger IX* A-camera photograph. (Covers an area approximately 3.3 km wide; craters of 15-m diameter can be detected. Impact point is halfway between the two reticles left of center cross.)
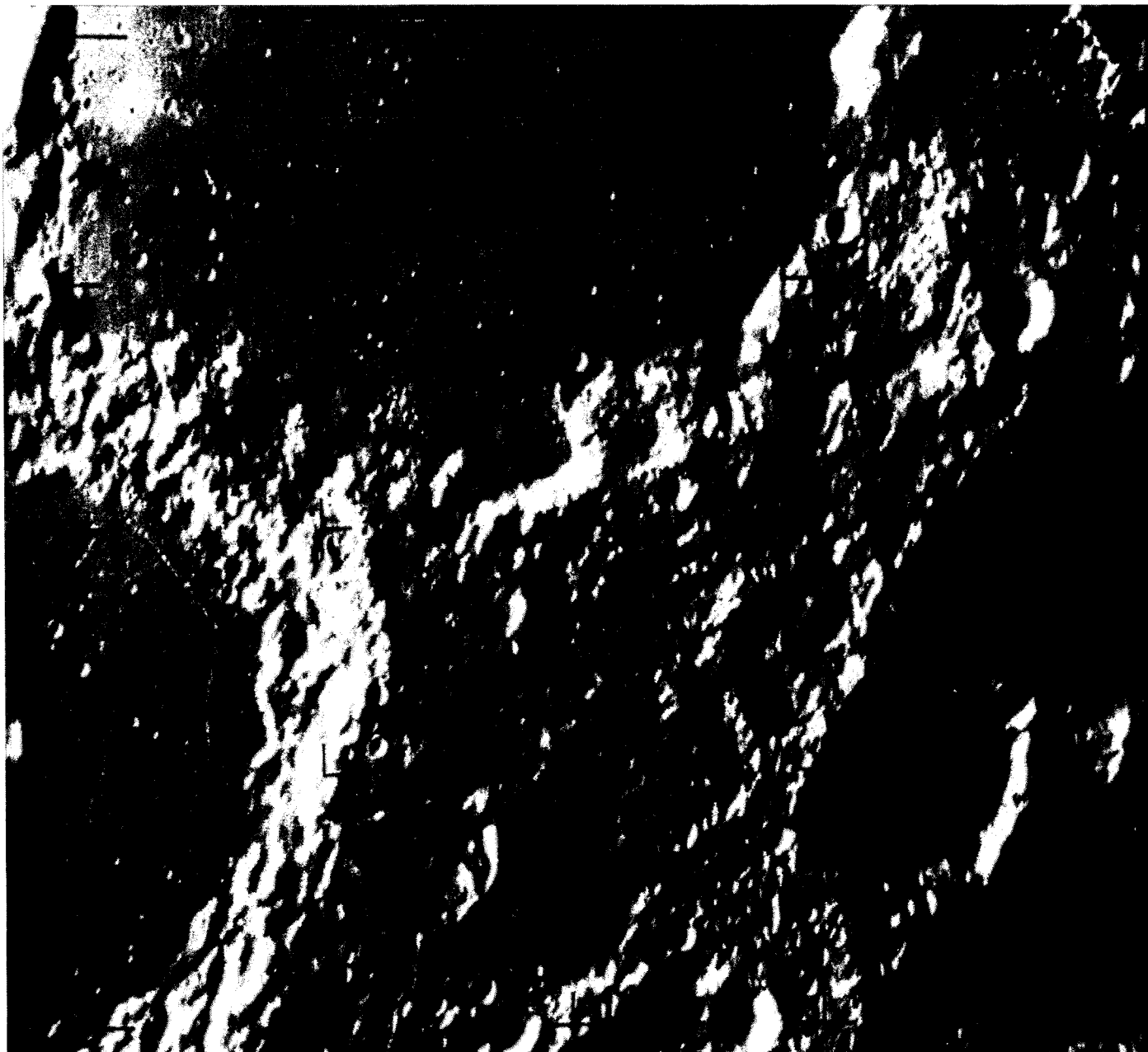
Fig. 20. *Ranger IX* B-camera photograph, showing Ptolemaeus (top), Alphonsus (lower left),
Klein and part of Albategnius (lower right). (Note that the older Ptolemaeus
and Alphonsus are more cratered than Albategnius.)
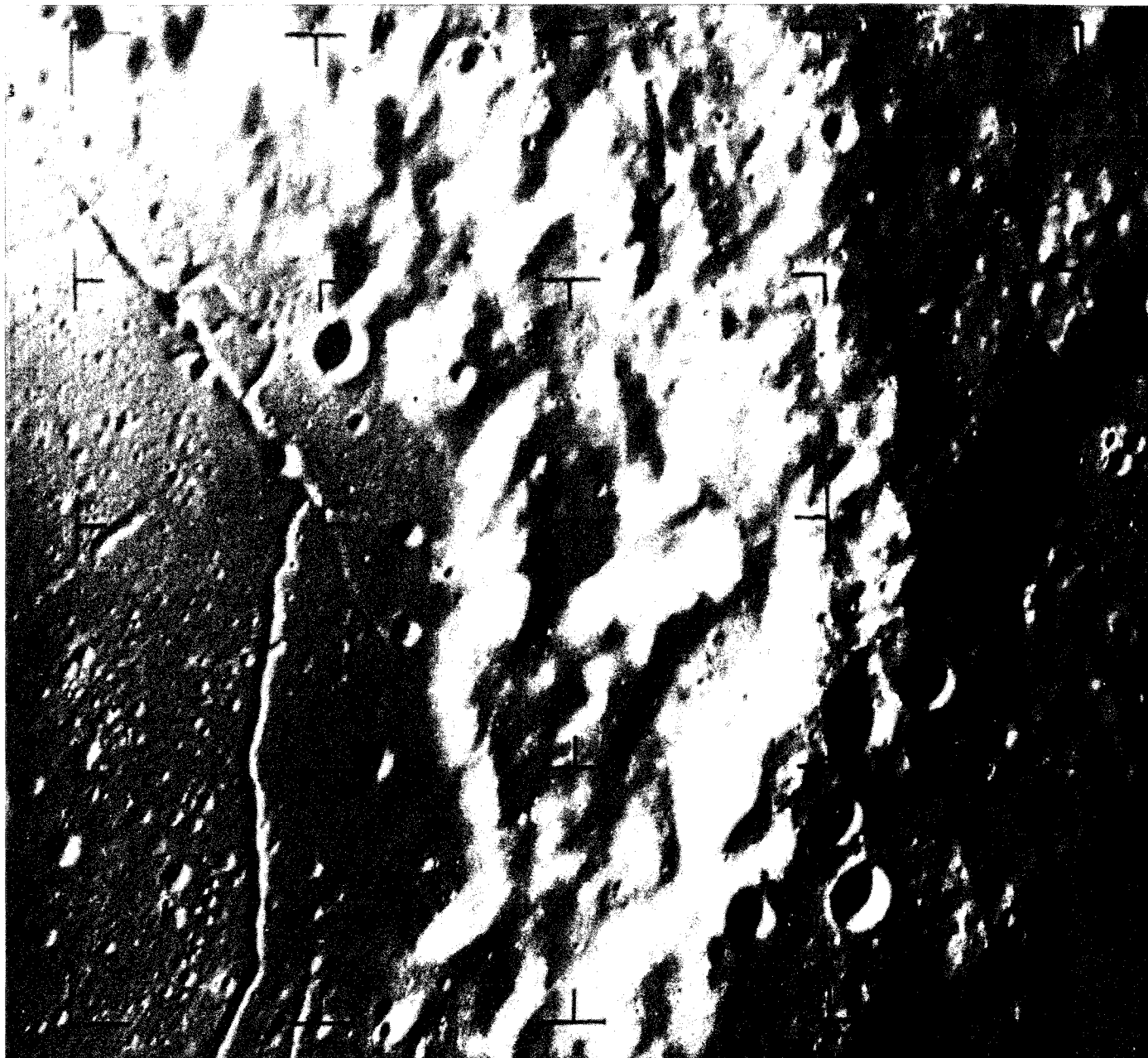
Fig. 21. *Ranger IX* B-camera photograph, showing E rille, dark-halo craters, and relatively smooth highland
crater walls of Alphonsus. (Covers an area approximately 51 km in width; craters as
small as 125 m can be detected. Resolution is about three times
that of best Earth-based photographs.)
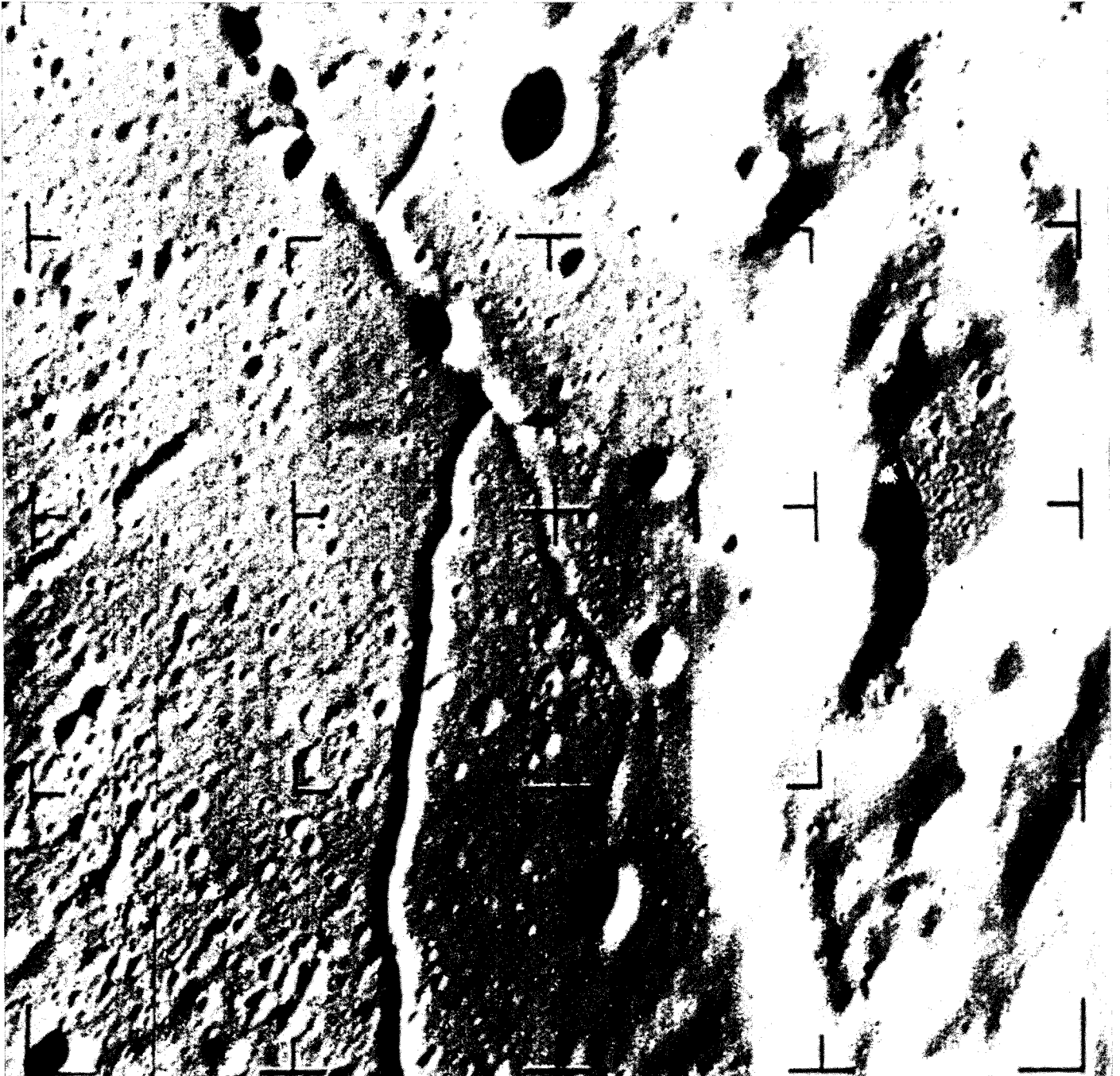
Fig. 22. *Ranger IX* B-camera photograph, showing features of Fig. 21 in greater detail. (Note that cache basin left of center has same cratered appearance as floor of Alphonsus.)
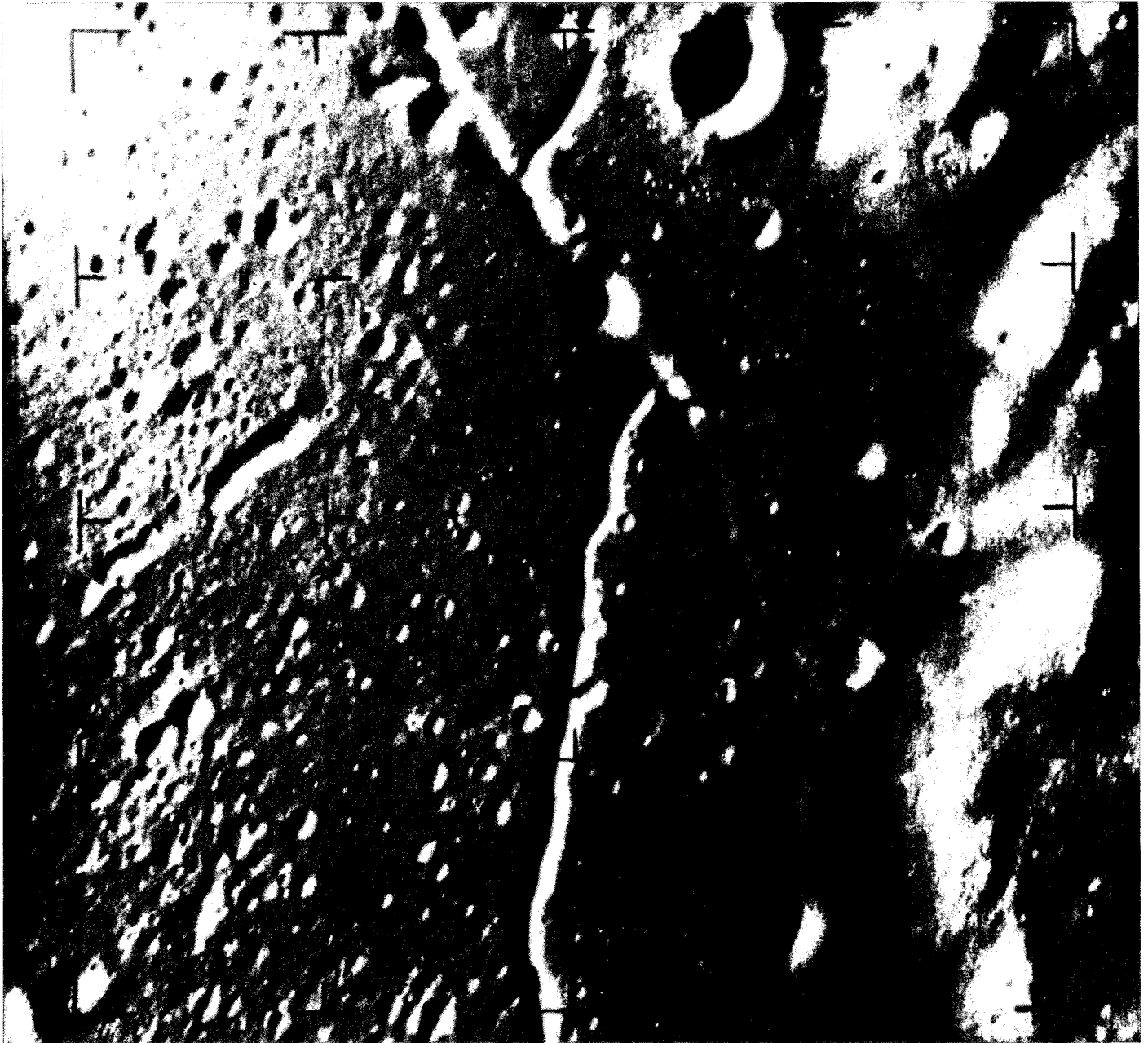
Fig. 23. *Ranger IX* B-camera photograph, showing filled-in rilles in vicinity of dark-halo craters.
(Note relatively small number of craters in dark-halo areas surrounding craters.)
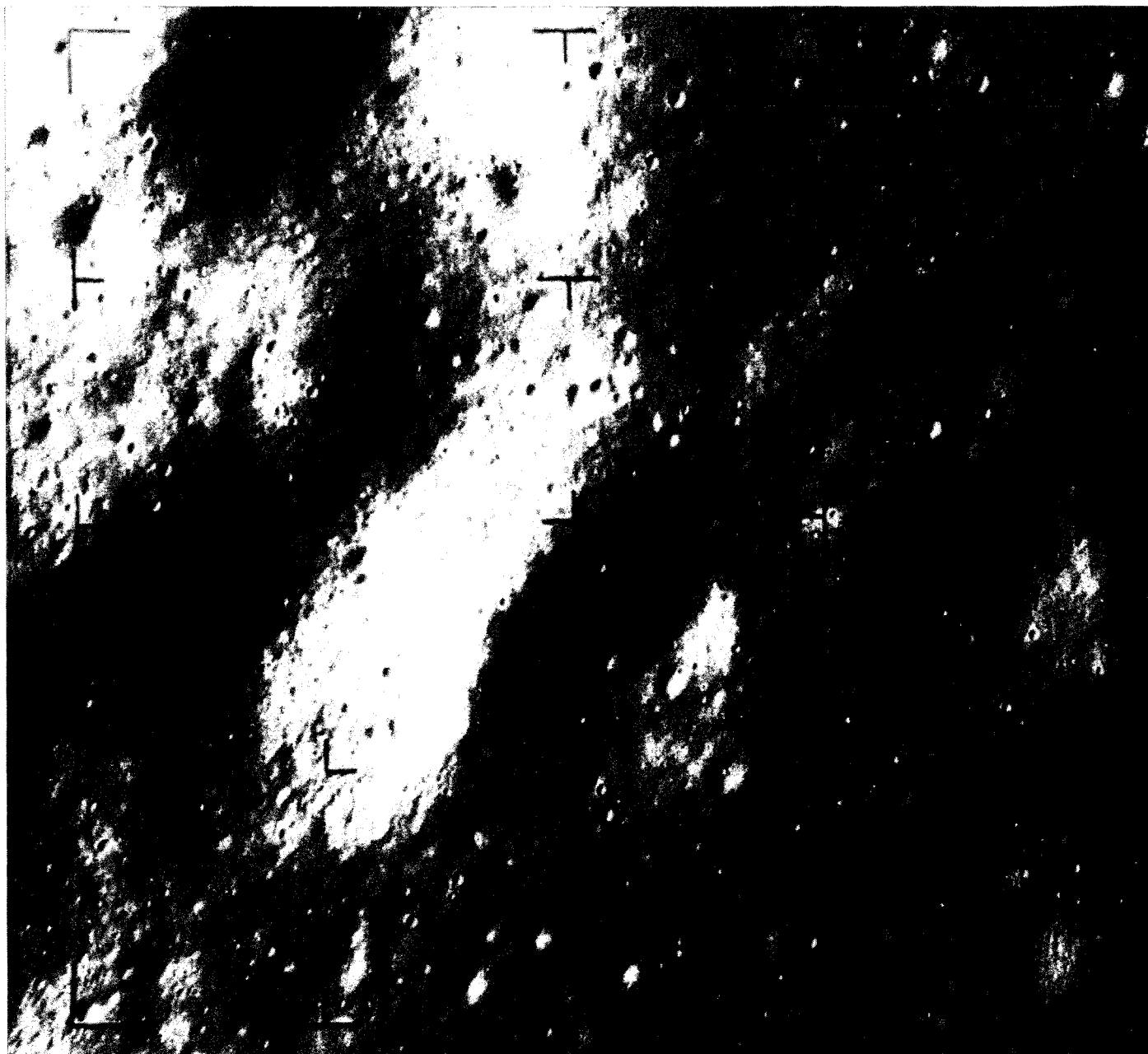
Fig. 24. Last complete *Ranger IX* B-camera photograph. (Covers an area slightly over 2.5 km in width. Note "tree-bark" structure also observed in *Ranger VII* photographs.)

REFERENCES

1. *Ranger VII: Part I, Mission Description and Performance,* Technical Report No. 32-700(I), Jet Propulsion Laboratory, Pasadena, California, December 15, 1964.

2. *Ranger VII: Part II, Experimenters' Analyses and Interpretations,* Technical Report No. 32-700(II), Jet Propulsion Laboratory, Pasadena, California, February 10, 1965.

3. *Ranger VII Photographs of the Moon: Part I, Camera A Series; Part II, Camera B Series; Part III, Camera P Series,* NASA SP-61, August 27, 1964; NASA SP-62, December 15, 1964; and NASA SP-63, February 10, 1965, respectively, Government Printing Office, Washington, D.C.

4. *Ranger VII Lunar Charts RLC 1–5,* United States Air Force, Aeronautical Chart and Information Center, St. Louis, Missouri.

5. Hapke, B., Photometric and Other Laboratory Studies Relating to the Lunar Surface," *The Lunar Surface Layer, Materials and Characteristics,* ed. by J. W. Salisbury and P. E. Glaser, New York: Academic Press (1964), pp. 323–344.

6. Willingham, D., *The Lunar Reflectivity Model for Ranger Block III Analysis,* Technical Report No. 32-664, Jet Propulsion Laboratory, Pasadena, California, November 2, 1964.

7. Shorthill, R. W., and Saari, J. M., "Thermal Anomalies on the Totally Eclipsed Moon of December 19, 1964," *Nature,* Vol. 205, March 6, 1965, pp. 964–965.

8. Salisbury, J. W., and Smalley, V. G., "The Lunar Surface Layer," *The Lunar Surface Layer, Materials and Characteristics,* ed. by J. W. Salisbury and P. E. Glaser, New York: Academic Press (1964), pp. 411–444.

9. Gault, D. E., Quaide, W. E., and Oberbeck, V. R., *Interpreting Ranger Photographs from Impact Cratering Studies,* presented at Conference on the Nature of the Lunar Surface, sponsored by the IAU Commission 17 (The Moon) and NASA Goddard Space Flight Center, Greenbelt, Maryland, April 15–16, 1965.

10. Rindfleisch, T., *A Photometric Method for Deriving Lunar Topographic Information,* Technical Report No. 32-786, Jet Propulsion Laboratory, Pasadena, California, September 15, 1965.

III. INTERPRETATION OF THE RANGER RECORDS*

Gerard P. Kuiper, Robert G. Strom, and Rudolf S. Le Poole**

Lunar and Planetary Laboratory
University of Arizona
Tucson, Arizona

A. Ranger VIII and IX Coverage

The *Ranger VIII* and *IX* missions have enriched science with two massive files of pictorial documents of remarkable quality and immense value. Their influence will be felt for many years as supporting investigations progress. In this Report, a full assessment of the scientific implications cannot yet be given.

Ranger VIII impacted in Mare Tranquillitatis on February 20, 1965, 01:58 GMT, at 24.8°E longitude and 2.6°N latitude, after having transmitted back to Earth over 7000 pictures. The paths swept by the A and B cameras are indicated in Fig. 1. The high-resolution coverage occurs in typical mare terrain, crossed by a complex system of ridges already well recorded by Earth-based photography (Ref. 1, Figs. 6 and 7). This part of Mare

Tranquillitatis is on the blue end of the scale of mare colors (Ref. 1, Figs. 13 and 14), in contrast to Mare Cognitum, which is on the yellow end. The color differences between and within the maria are not large; but they are distinct and important, associated as they are with the process of mare deposition (Ref. 1, p. 32). The *Ranger VIII* records thus cover one extreme of the mare color scale, those of *Ranger VII* the other. The similarities between these maria (as noted below) are therefore likely to extend to all lunar maria.

The vertical path of *Ranger VIII* over the lunar surface is illustrated in Fig. 2, with the directions of the A- and B-camera axes indicated. It is seen that the same terrain features are viewed with the B camera at two to three times the distance of the A camera; but since the focal length of the B camera is three times that of the A camera, the scales of corresponding photographs are similar, making possible stereoscopic viewing right up to impact. This expected application was a factor in the decision not to change the orientation of the spacecraft
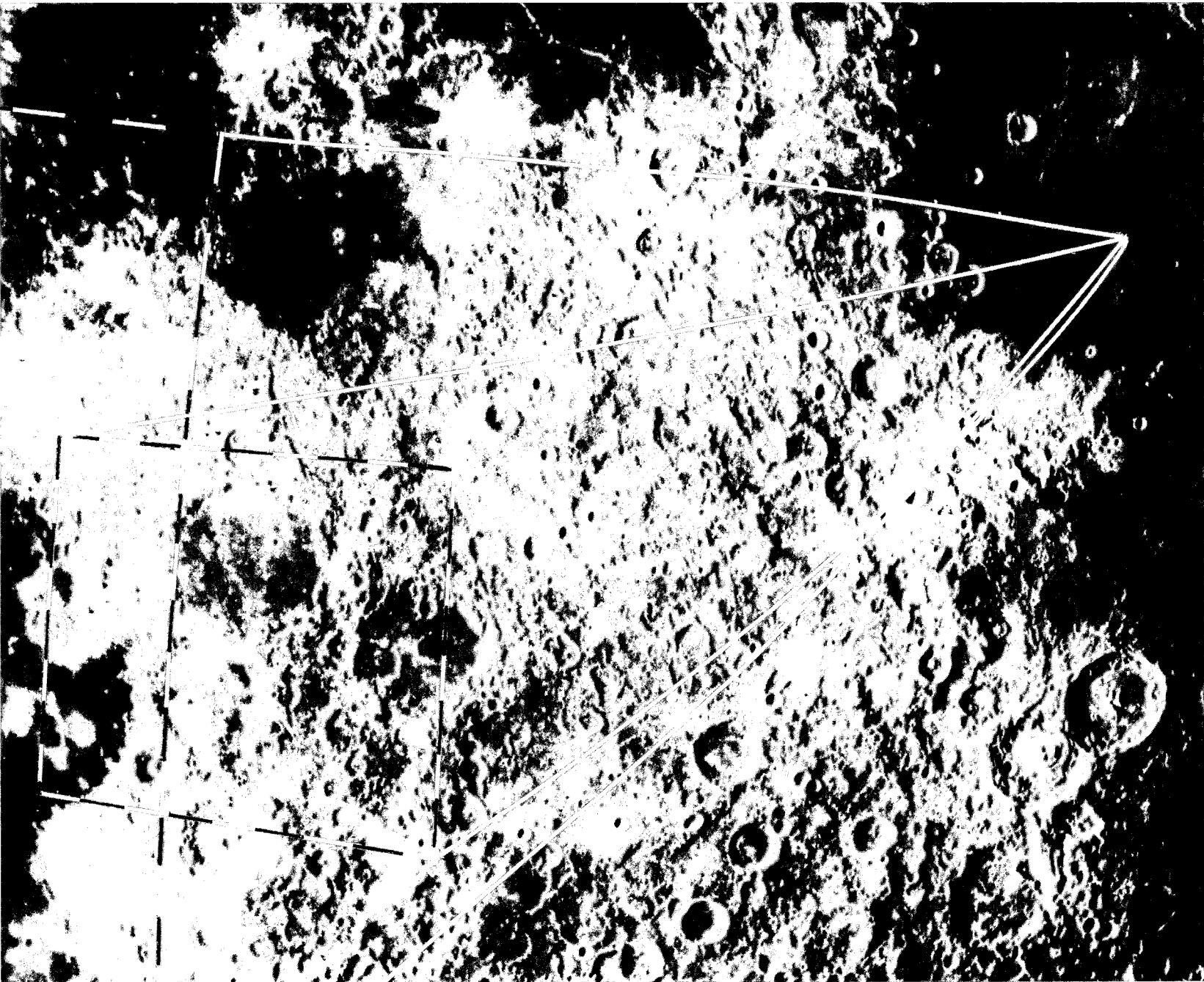
Fig. 1. Coverage by *Ranger VIII* A and B cameras. (Dashed squares outline first A [large] and B [small] fields; solid lines are overall boundaries of later frames.)
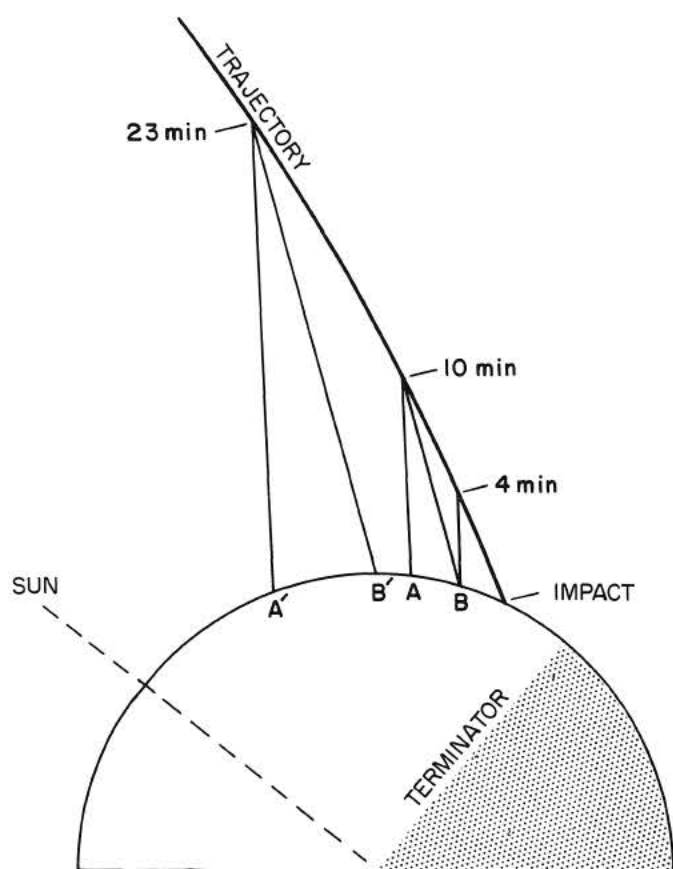
Fig. 2. Vertical section through trajectory of *Ranger VIII*, showing coverage by A and B cameras. (May be combined stereoscopically.)

before impact by performing a terminal maneuver. *Ranger VIII* covered both upland and mare terrain, doing double duty in that sense, and its records have provided a very rich source of information.

Rangers VII and *VIII* having covered the range of mare colors, it appeared opportune to direct *Ranger IX* to one of the several large lunar craters. Among the obvious candidates was Alphonsus, whose central peak had been suspected of emitting gases, and which had eight prominent dark-halo craters on its floor (e.g., Ref. 2, Figs. 1 and 9), all but one associated with peripheral rilles on the crater floor. The impact (March 24, 1965, 06:08 GMT) was planned for an area between the central peak and a group of prominent dark-halo craters (Fig. 3), at 2.4°W longitude, 12.9°S latitude, with the A camera sweeping in from the side of Mare Nubium and the B camera from the opposite direction (Fig. 4). This configuration was achieved by commanding the spacecraft to execute its "nominal" terminal maneuver, which at the

same time assured a minimum of image trailing close to the lunar surface. Thus, while in the case of *Ranger VIII*, the highest resolution in one coordinate was traded for increased overall coverage, the geometry of the *Ranger IX* approach favored the camera orientations provided by the nominal terminal maneuver and also yielded maximum attainable camera resolution.

The floor of Alphonsus was found to resemble mare-type terrain in almost every respect. All three *Ranger* missions, including *Ranger IX*, achieved maximum resolution for maria; in addition, good records of intermediate resolution were obtained for uplands and crater rims.

The emphasis in the *Ranger* program on mare-type terrain reflects the conviction that the maria are more likely to be comparatively "simple" and interpretable, since they are less precipitous than the uplands and have a shorter and less complex history. Because of the absence of large mountain systems, and a dense, overlapping distribution of craters, the maria also seemed to be the logical initial choice for unmanned and manned landings. In retrospect, these estimates appear to have been valid, although there are some reservations concerning the "simplicity" of the mare surface, owing to the discovery of the prevalence of collapse depressions, first detected by *Ranger VII* and later confirmed by the *Ranger VIII* and *IX* records.

B. Reconnaissance of Mare Surface

During the past decade, the nature of the lunar surface has been intensely debated. To the traditional hypotheses considering either *volcanism* or *meteoritic impact* as the controlling factor were added views of the lowlands of the Moon having been covered with thick layers of *dust*, or, alternatively, of *debris;* and conflicting theories about the Moon's *origin* (fission from the Earth and capture by the Earth during geologic time, in addition to the concept of a double planet). Increasingly powerful techniques of observing the lunar millimeter, centimeter, and meter emissions led at first to assumptions that the Moon was covered with a nearly uniform, low-density layer, several meters thick, believed to have originated by erosion. As the angular resolving power of these new methods increased, however, the striking *heterogeneity* of the lunar crust that had long been apparent from telescopic optical observations was confirmed; and the gap between interpretations made from optical and long-wave data, which had been widening for several years, now appears to be closing rapidly.

The *Ranger* records are destined to play a most important role in this development. By extending the optical range of lunar-surface studies by fully three orders of magnitude, they have closed the worst information gap, i.e., that concerning surface structures with scales from 0.5 km to 0.5 m. At still smaller dimensions, the thermal, radar, and radio emission data, and observations on differential denudation, supplemented by laboratory experiments (polarization, discoloration, solar-wind effects), define the lunar conditions reasonably well.

The method of presenting data and hypotheses is the one customarily used in the physical sciences: from among the apparent alternatives, that hypothesis is selected and tested which, on the basis of all available information, appears the most plausible. The alternative, of

Fig. 3. Impact area of *Ranger IX* (frame A37).

Fig. 4. Coverage by *Ranger IX* A and B cameras. (Corners of fields fall on solid lines meeting at impact point.)

presenting an analysis of multiple hypotheses, was not normally carried into print.

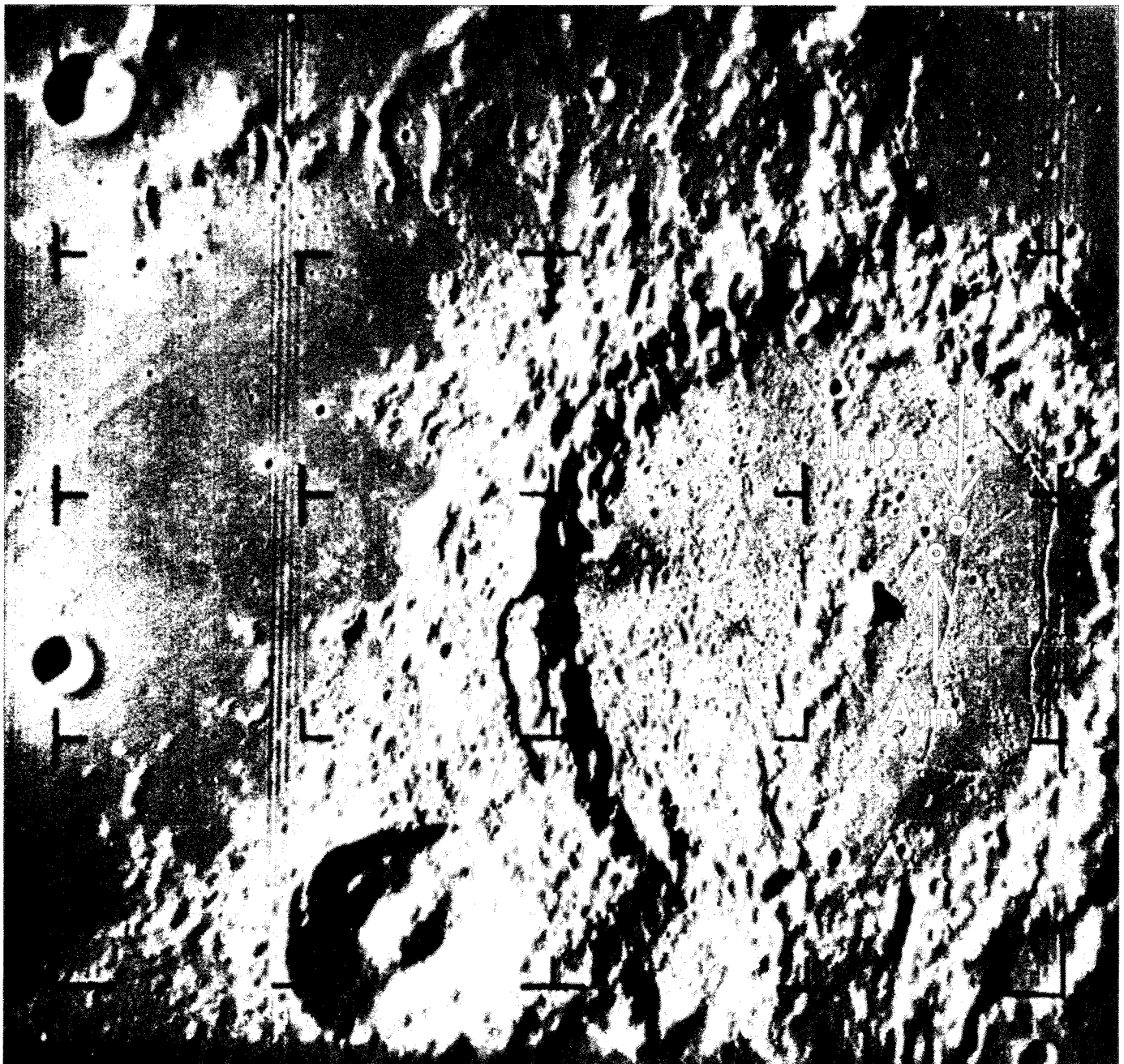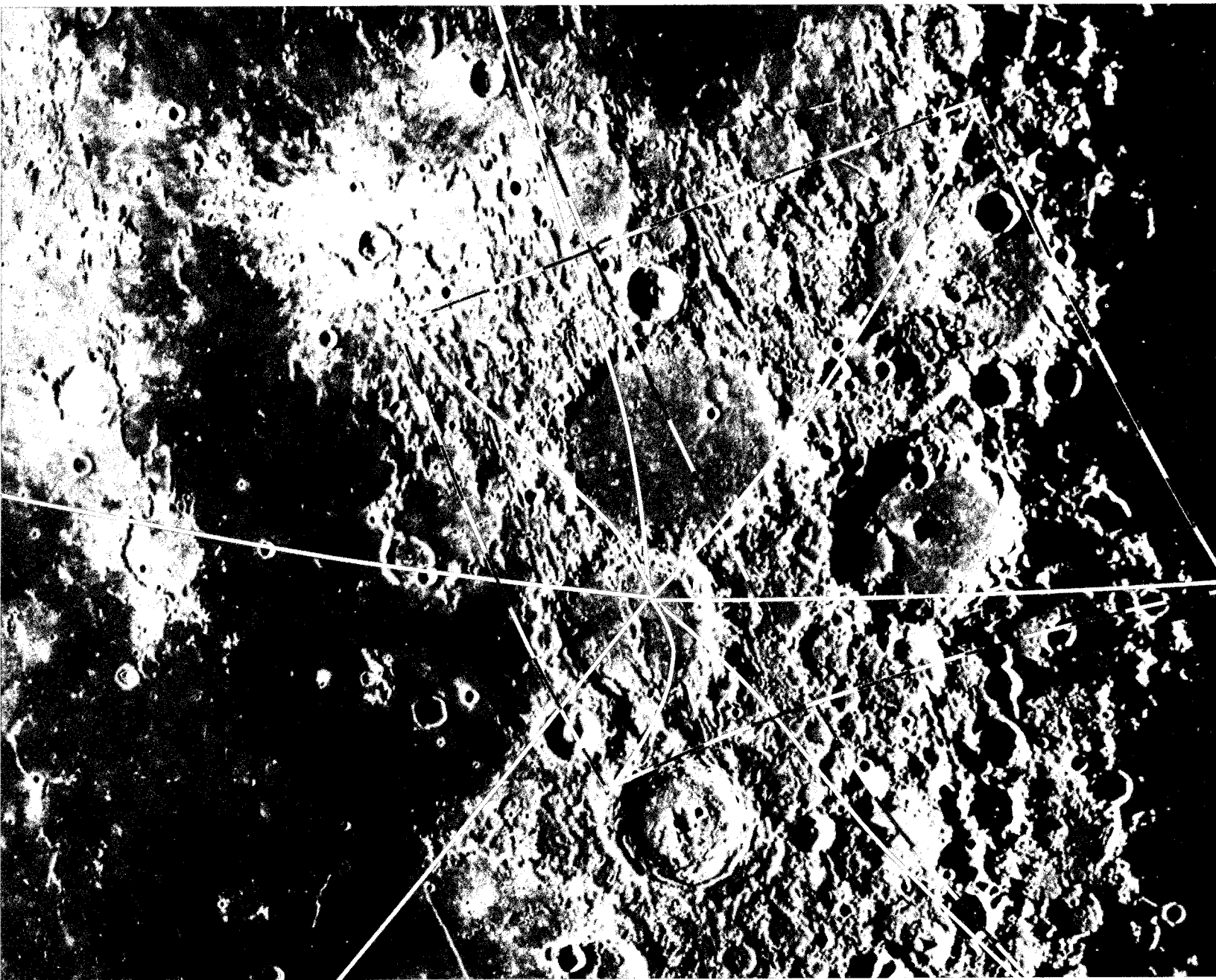Earth-based observations of the Moon indicate (see Ref. 1) that (1) the lunar maria are *lava fields,* in several areas built up of visible flows having distinct flow fronts and sharply bounded characteristic colors; and (2) these lavas were not produced by the impacts that caused the near-circular mare basins, but instead came to the surface from *available magmas,* often after a considerable lapse of time since the epoch of basin formation. By analogy with the processes inferred from meteorites, the principal heat source producing the lunar magmas appears to have been the Moon's own radioactivity; the meteorites were mostly, if not entirely, derived from asteroids, bodies much smaller than the Moon and therefore correspondingly more subject to heat losses. *Since the asteroids melted in their interiors, the interior of the Moon must also have melted.*

It was further shown (Ref. 1), on the basis of vacuum experiments with molten rock, that the lunar maria must initially have been covered with a layer of *rock froth,* possibly some 5–10 m thick. The low lunar surface gravity will enhance the frothing process. This frothy layer, partly destroyed and compacted near the surface by numerous small impacts, and ablated and recemented at the surface by the solar wind, is probably responsible for the *porous surface layer,* several meters thick, required by the radar reflection data and, for the uppermost layers, by the millimeter and centimeter emission curves. For the terrae, the porous layer required by the radar-reflection data presumably dates back to the period of accretion, although it, too, must have been modified by after-effects.

The texture of the lunar surface as inferred from the *Ranger VII* records, the smallest lineaments found, and the crater counts, all indicate that, between craters of 1-m diameter and larger and outside the belts surrounding large impact craters, the thickness of the fragmented layer of the mare surface is at most 1–2 m. This was found compatible with the present impact rate of cosmic particles, known to be roughly 1 g/cm^2/4.10^9 years.

An unexpected discovery was the *collapse depressions,* frequently from 100–300 m in diameter but present in both smaller and larger sizes as well. Although much larger depressions (1–10 km in diameter) had been known to exist in a few large "flooded" craters—particularly Ptolemaeus and Albategnius—the profusion of these smaller depressions, covering one-fourth to one-half of the mare

floor, came as a surprise. Figure 5 shows part of the last *Ranger VIII* A frame, which may be compared with *Ranger VII* frame A199 (Ref. 1, Fig. 31); both the shallow circular depressions with nearly level floors and circular dimple craters occur in similar dimensions and numbers. Their visibility in Fig. 5 is somewhat enhanced by the lower Sun angle (15 deg, vs. 23 deg for *Ranger VII*).

The *Ranger IX* photographs again show a similar pattern (Fig. 6), if allowance is made for the still lower Sun angle of 10 deg. They further provide the opportunity to compare the occurrence of depressions on the Alphonsus floor and on the mountains forming the crater wall (Fig. 7). This is important because the wall must be at least as old as the floor and, if the depressions were eroded craters, the wall should show at least as many depressions per unit area as the floor. Quite the opposite is found. Figure 8 shows part of the same region depicted in Fig. 7 at increased resolution. The opposite wall is shown in Fig. 9, which also includes part of Mare Nubium. This mare must again be of about the same age as the crater floor and wall (in Sections E and I, a small age difference is found between wall and floor, the wall being pre-Imbrium and the floor early post-Imbrium). An amazing difference exists in the crater density between Mare Nubium or the Alphonsus wall on the one hand, and the Alphonsus floor on the other. The comparison of wall vs. floor may be made at greater resolution in Fig. 10. In all four comparisons (Figs. 7–10), the sharp impact craters are similar in frequency, but the shallow, round depressions are practically absent from the crater walls and the strip of Mare Nubium shown. This cannot be a result of post-mare slumping because the wall slopes are gentle (~5–20 deg) and many nearly level areas are present. Mare Nubium is almost entirely level. The *Ranger IX* data thus confirm that *the depressions are internal in origin, with their distribution depending on local structural properties.* The collapse hypothesis is strengthened by the occurrence of several linear rille-like groupings of depressions. (This question will be discussed further in connection with Fig. 75.)

When the *Ranger VII* Experimenters' Report (Ref. 1) was written, I was unaware of the existence of terrestrial circular collapse depressions other than those found in limestone country. The geometry and appearance of these depressions are remarkably similar to those of lunar depressions (Ref. 1, pp. 50–52), although the cavitation process was obviously different. We have since observed that circular depressions are very common in large, nearly level terrestrial pahoehoe flows (Ref. 3), a fact not mentioned in standard geological texts. This close terrestrial
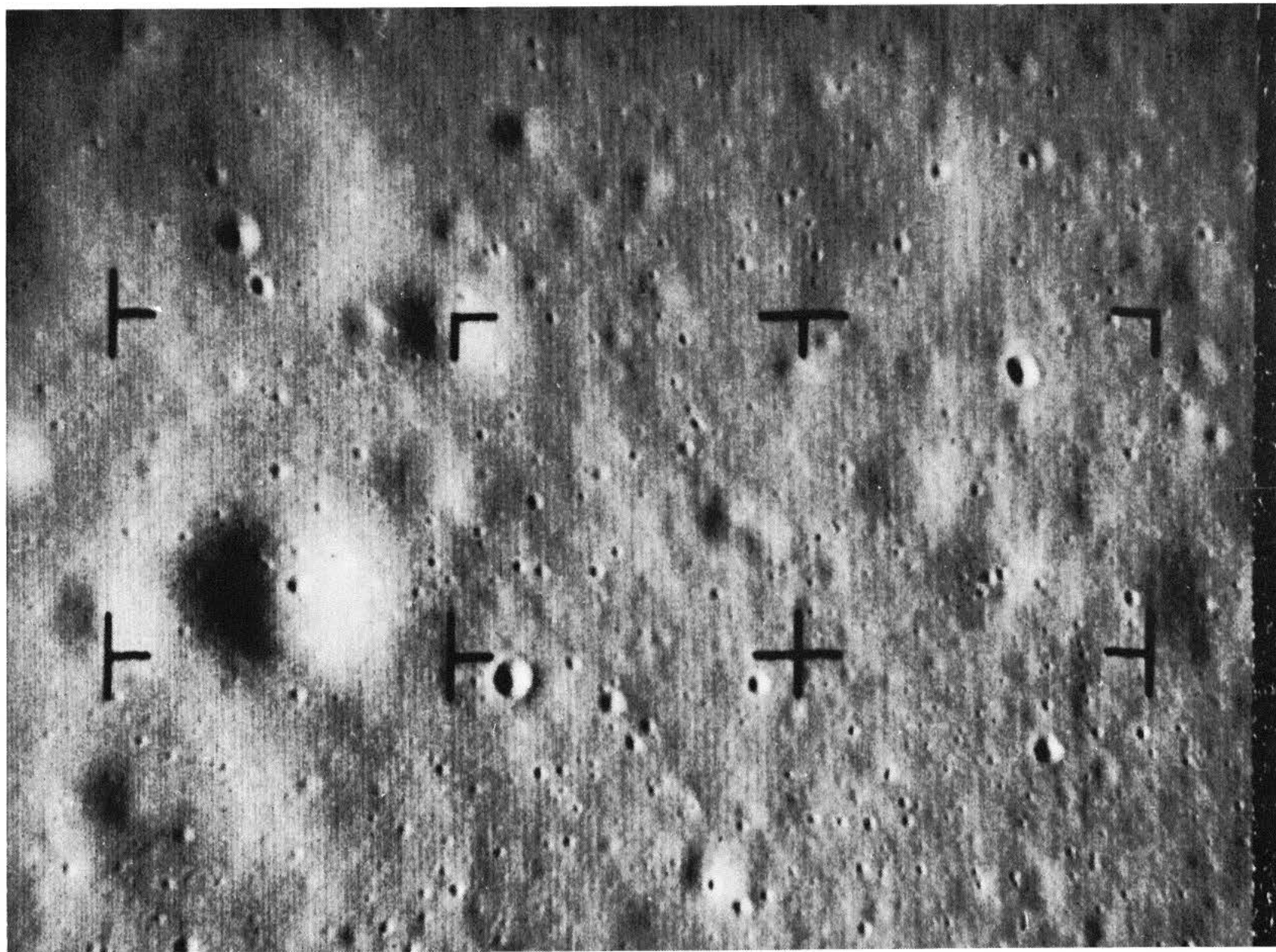
Fig. 5. Last *Ranger VIII* A frame, cut off at impact. (Dimension 1.71 km [N–S].)
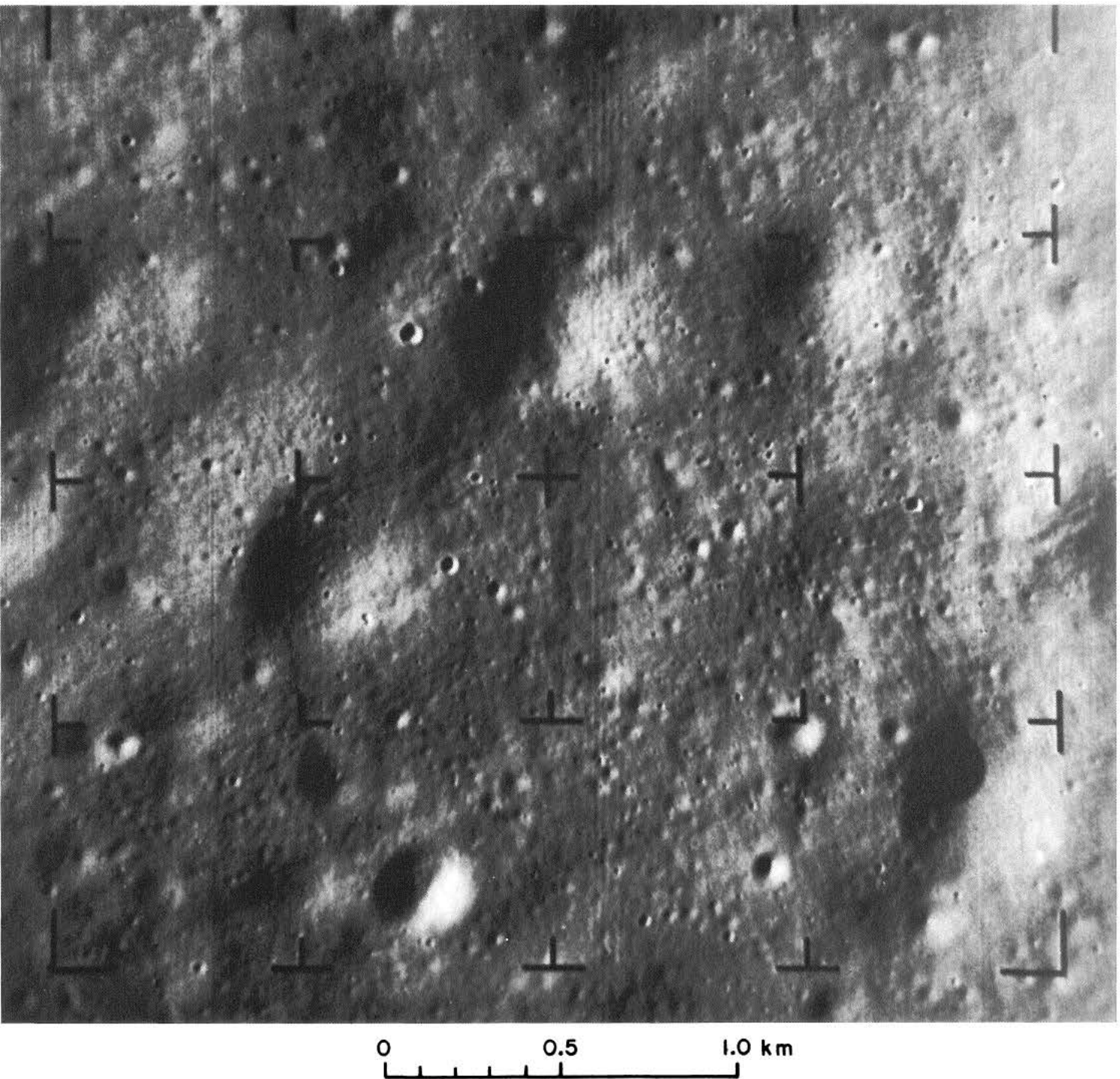
0   0.5   1.0 km

Fig. 6. Last *Ranger IX* A frame (A70). (Note "tree-bark" pattern and large fractional coverage of collapse depressions. Dimensions 3.07 [N–S] × 3.26 km [E–W].)
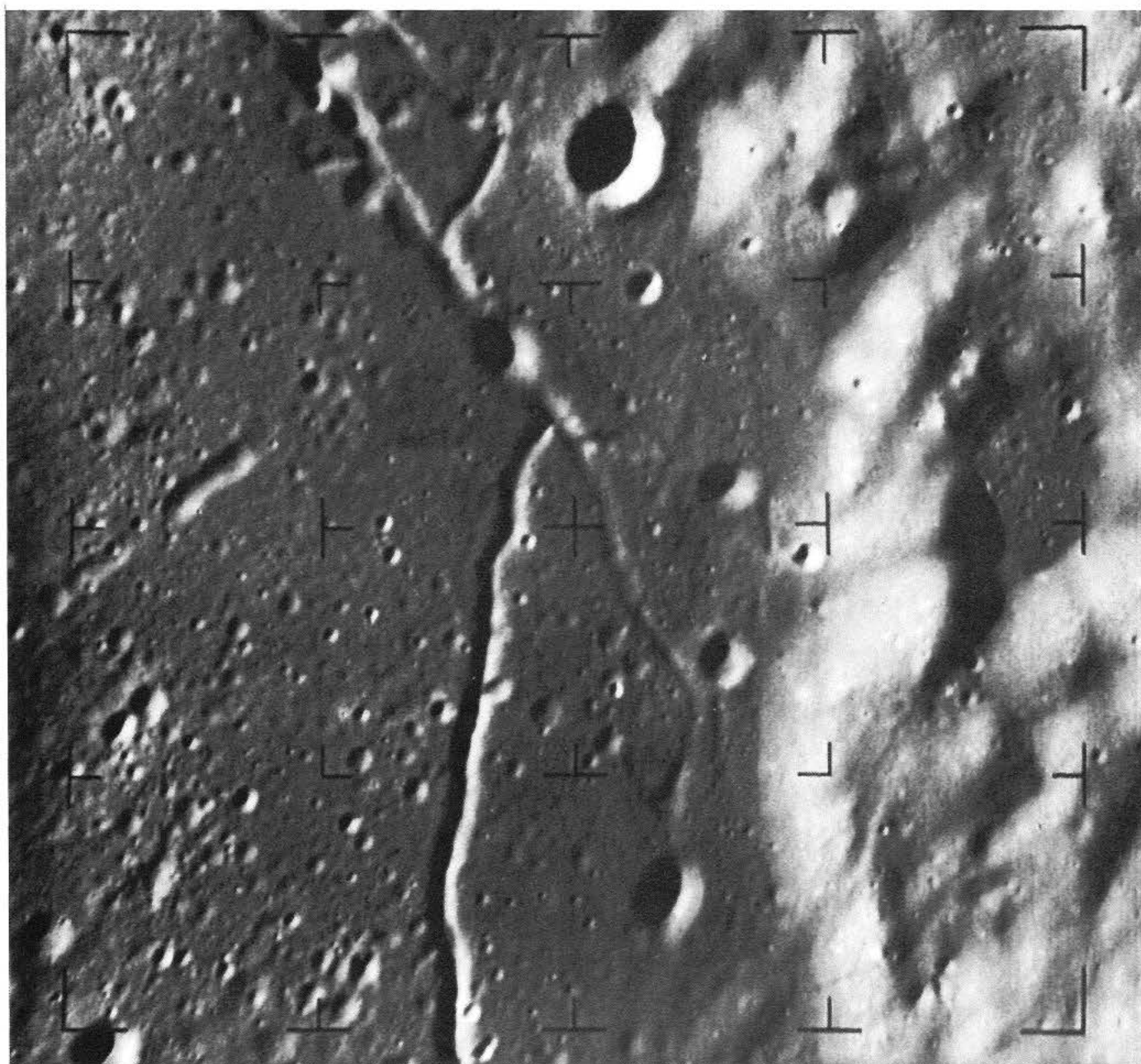
0   5   10 km

Fig. 7. *Ranger IX* frame B75, showing NE corner of floor of Alphonsus with peripheral rille system, three dark-halo craters and ejecta, and part of surrounding walls. (Floor contains numerous depressions, as does "lava lake" surrounded by soft hills forming crater walls. Dimensions 26.6 [N–S] × 31.0 km [E–W].)
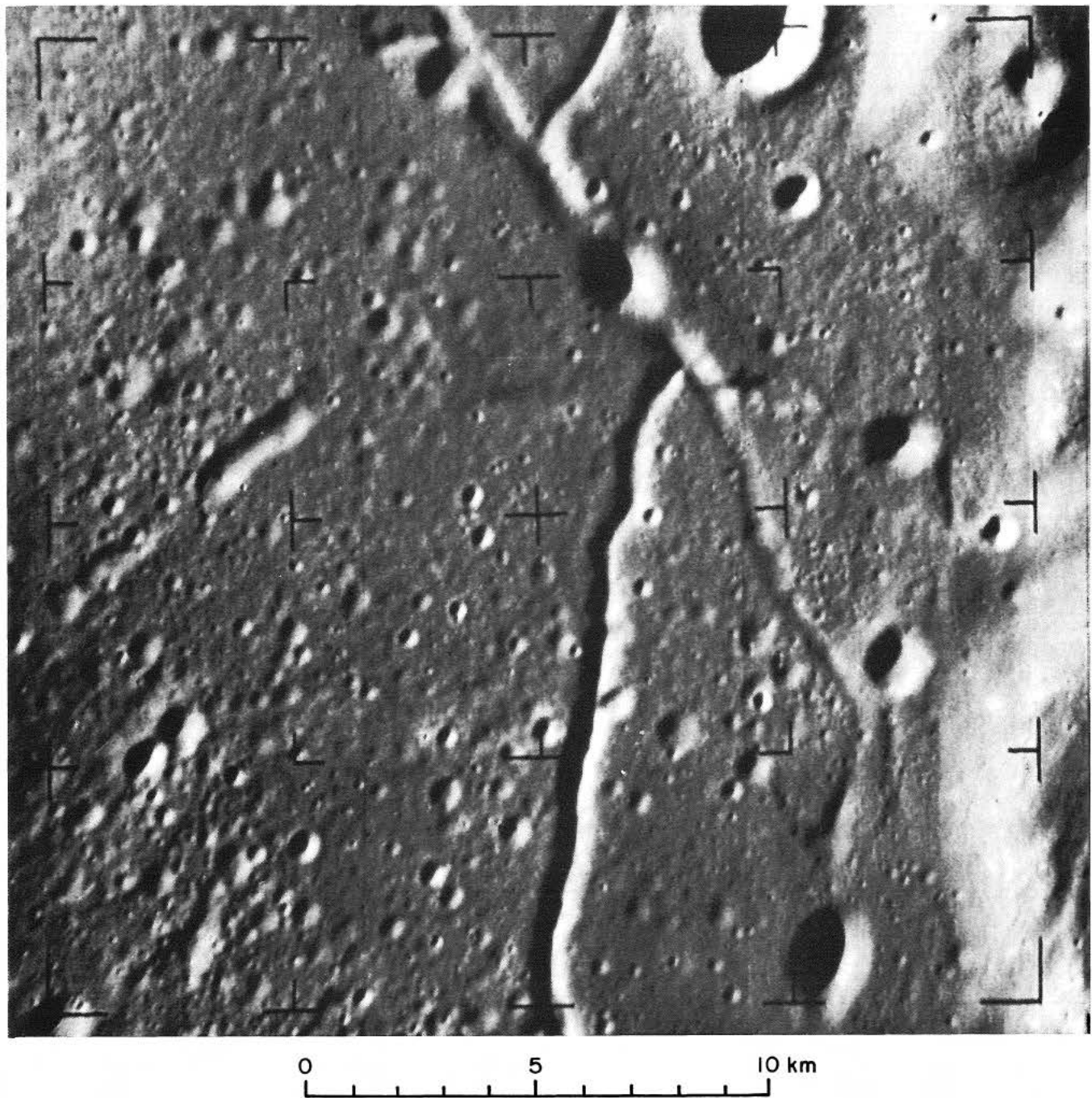
Fig. 8. Frame B78, showing same area as Fig. 7, but closer in to Moon, with additional resolution. (Dimensions 20.5 [N–S] × 23.9 km [E–W]. Dome 1 in. from left edge shown in Fig. 119.)
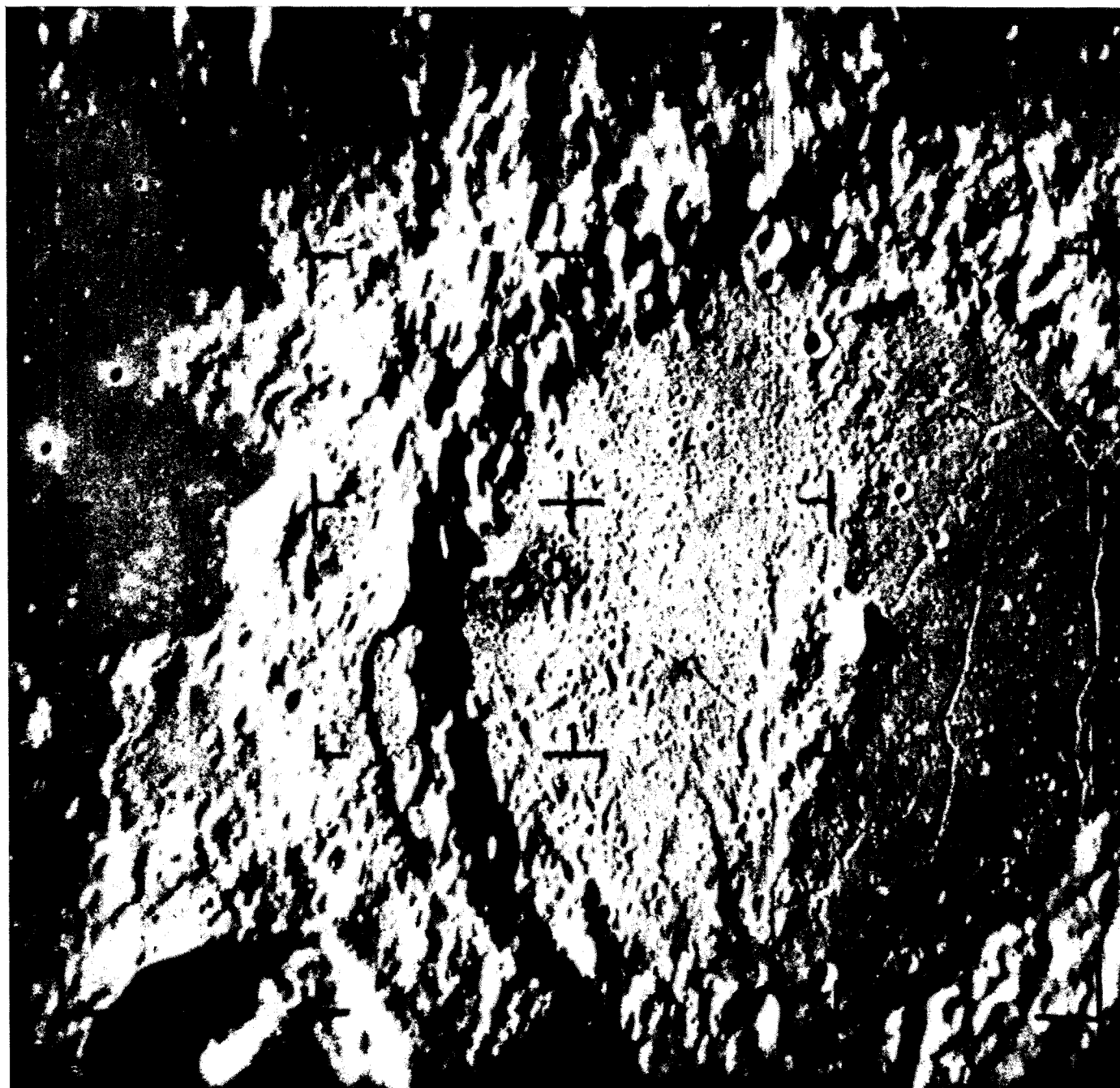
Fig. 9. *Ranger IX* A-camera coverage (A45) of Alphonsus, most of surrounding crater wall, and adjacent part of Mare Nubium. (Note contrast between numerous depressions on crater floor and their absence on Mare Nubium.)
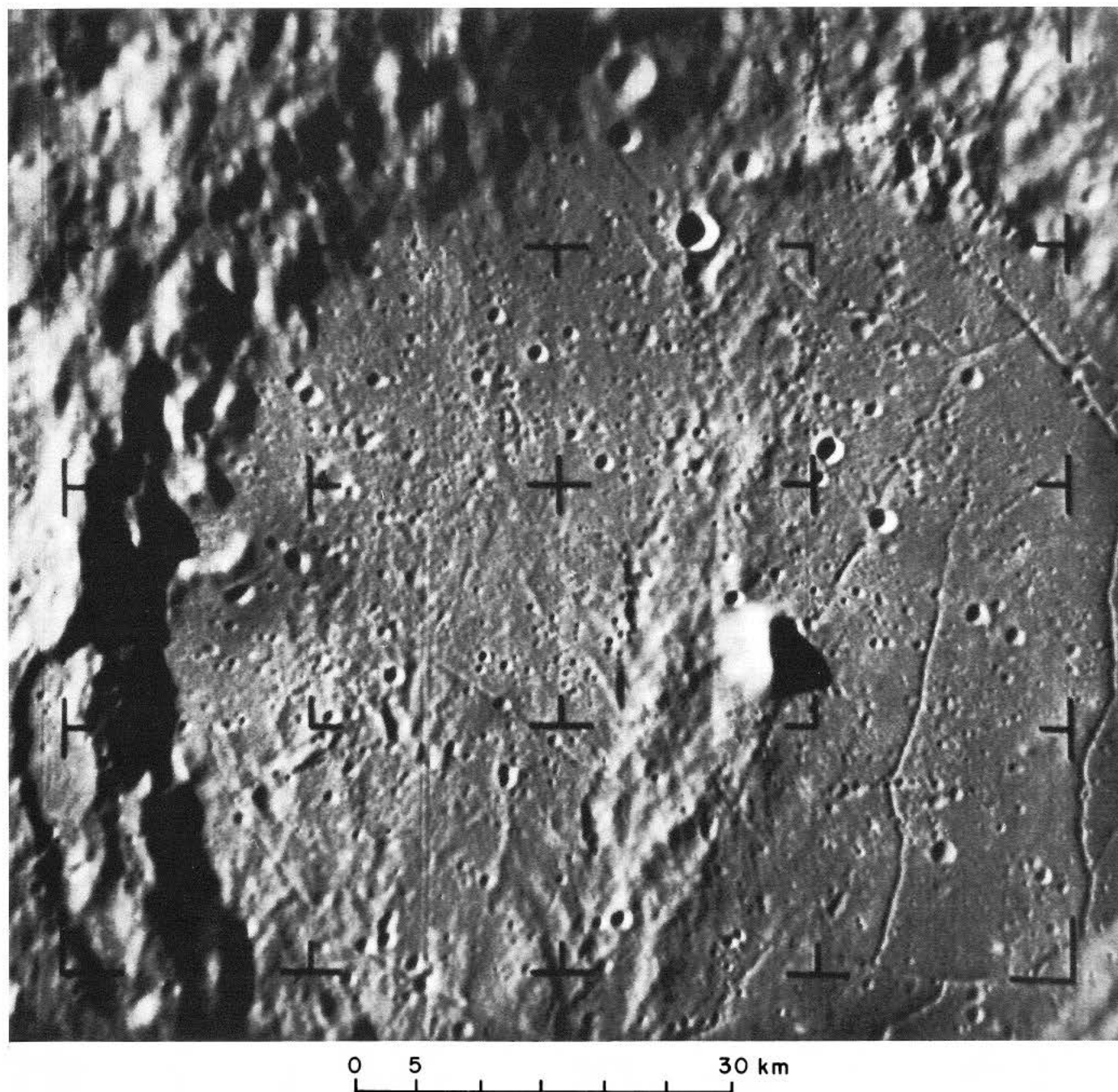
Fig. 10. *Ranger IX* A-camera coverage (A54) of floor of Alphonsus; same area as in Fig. 9, but closer in. (Note comparative paucity of collapse depressions on peak, central spine of crater, and crater walls. Dimensions 86.3 [N–S] × 91.1 km [E–W]. Three domes are seen left of center-right reticle, NE of Alphonsus peak, shown in detail in frames B84–86. Other dome is near mark just below.)

analog gave indications of possessing some aspects of mare deposition that would warrant detailed comparisons. It was found that while nearly level pahoehoe flows without exception exhibit collapse depressions, pure aa flows never do. Composite flows of aa overlying pahoehoe show collapse depressions that match the lunar dimple craters almost perfectly. This confirms the *Ranger VII* conclusion that the mare surface has a *two-layered structure*. (The subject is developed further in Sections C–E.)

Important data which assisted in the interpretation of the *Ranger* records were obtained by Saari and Shorthill (Ref. 4) on the thermal distribution over the eclipsed Moon. With the permission of these authors, one of their several remarkable heat scans, obtained with the 74-in. reflector of the Helwan Observatory, Egypt, on December 19, 1964, is reproduced in Fig. 11. It has 200-line scans and a resolution of about 10 arc sec; the effective wavelength of the record is 11 μ. Figure 12, obtained just before the eclipse on the full Moon, is added for comparison. The Saari and Shorthill scanning system records the 11-μ radiation and visible light simultaneously on separate channels. Since the librations in Figs. 11 and 12 are practically the same, distances on the disk may be transferred from one record to the other.

The whitish spots in Fig. 11 are areas whose temperatures exceed those of their surroundings. Pending a full evaluation of the records by the authors, I make the following comments based on a cursory inspection. Most "hot spots" are identifiable craters, with Tycho, Copernicus, and Langrenus being among the largest in area. Certain small craters, however, have a higher thermal response. The east–west gradient across the picture is probably due both to the more advanced cooling toward the west limb caused by the motion of the Earth's shadow across the lunar disk and to the fact that the west limb is on the sunrise side. Maria Humorum, Nubium, Serenitatis, and Tranquillitatis are somewhat warmer than the neighboring uplands. This can be explained only partially by their visual absorptions (lower albedos) of solar radiation; however, the fact that the contrast is no greater indicates that a rather uniform layer (at least a few millimeters thick) of very low conductivity covers the entire Moon. Where the layer is destroyed, consolidated rock is exposed in the craters and their walls. The frequency of the hot spots is greater on the maria by a factor of 3 to 5, which appears to indicate that (1) they have been produced primarily by post-mare craters and (2) the top of the consolidated rock layer is deeper in the terrae than in the maria. The fact that more than half of the post-mare craters show as hot spots indicates that, at least

during the past 10^9 years, the accumulation rate of dust has been exceedingly low (on the order of 1 mm). This means that, at present, *the sputtering rate* (Ref. 1, p. 61) *may be comparable to, or in excess of, the dust production rate,* which would be consistent with the sharp color boundaries found on the Moon (Ref. 1, pp. 26–39). The hot spots are discussed further in Section F.

The Saari–Shorthill results owe their power to the great increase in angular resolution over that achieved in earlier thermal mapping. Since a 100-in. telescope has a theoretical resolving power at 11 μ of 1 arc sec, further resolution gains in the thermal region are possible. Also, as Dr. Frank Low's work has shown, successful high-resolution measurements can be made at 20 μ from a high-altitude observatory, making possible thermal mapping of the Moon during the dark phase, when the mean temperature over the disk descends to about 90°K—too low for 11-μ measurements (energy maximum $\sim$30 μ). Low has discovered areas both much colder ($<$ 70°K) and much hotter than the 90°K average (Ref. 4). The potentials of high-resolution thermal studies of the Moon are very great, as, of course, are those of studies at 1 mm and beyond. At 1.2 mm, the 200-in. telescope has a theoretical resolving power of 60 arc sec, a value actually attained by Low. This development is important because of the unexpectedly thin, dusty cover on most of the post-mare craters, first discovered for a few objects by Shorthill *et al.* (Ref. 5) and confirmed by Sinton (Ref. 6).

Several other recent results are relevant to the subject of this Part. B. Hapke and co-workers (Ref. 7) have clarified the photometric and polarimetric properties of the lunar surface and examined the effects of darkening and discoloration by (solar) proton bombardment (Ref. 8). The sputtering effects of the solar wind have been examined by several authors (e.g., Ref. 9). Laboratory studies and a monograph on lunar-surface conditions have been published by J. W. Salisbury and P. E. Glaser (Ref. 10), and important conclusions on the upper few meters of the Moon have been derived from radar and radiofrequency intensity measurements (Ref. 11). Monographs and compendia on the Moon have been published at the rate of about one per year (see Supplementary References).

The *Ranger* records permit visual examination of surface structure in the range of 1–1000 m, which was practically inaccessible to previous optical, thermal, or radio and radar techniques. In this range, there occur numerous craters—both primary and secondary, collapse depressions, rilles and crater chains, and the ridges and the elements
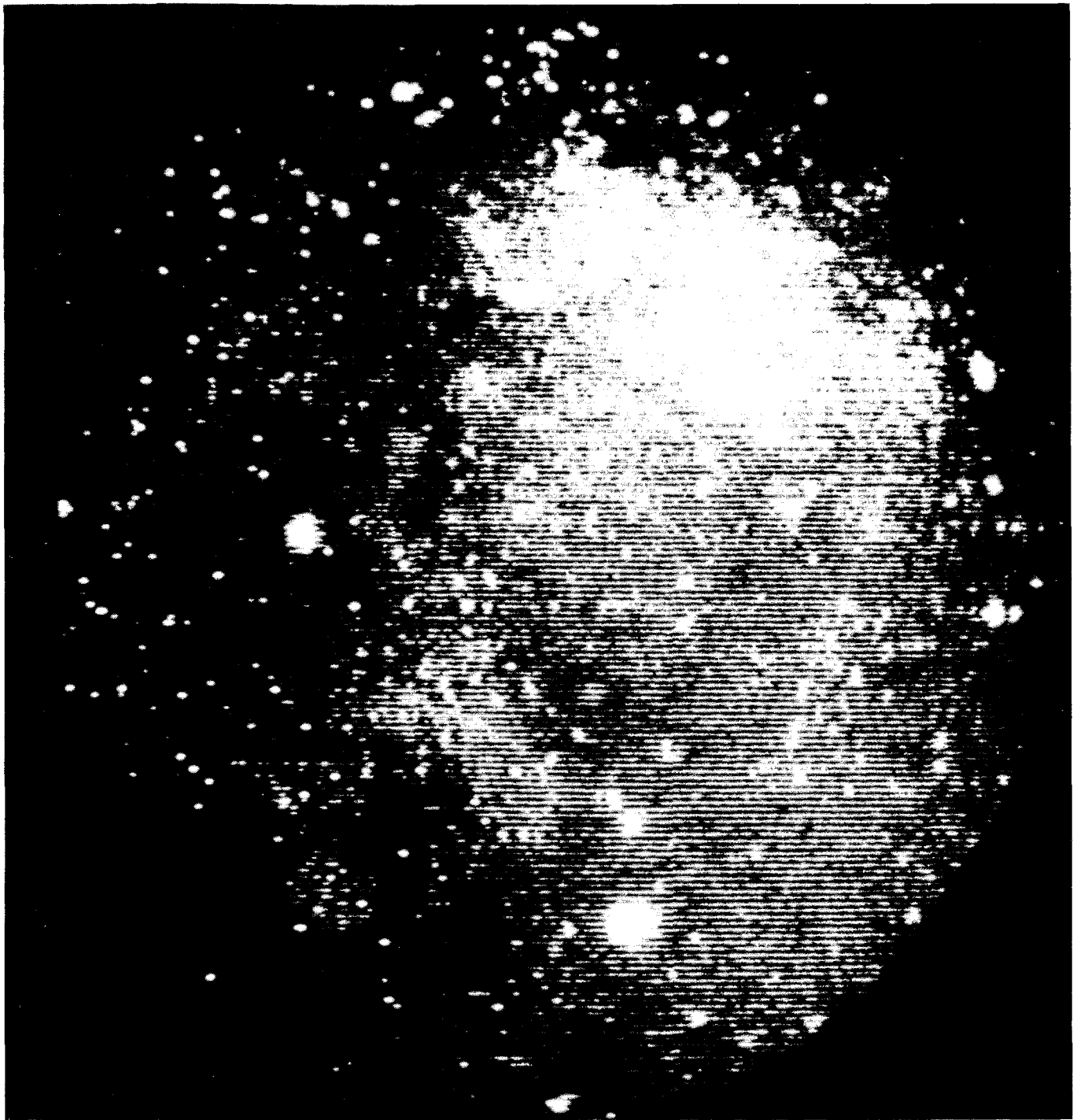
Fig. 11. Heat scan of lunar surface at 11 μ, obtained during total eclipse, December 11, 1964, with 74-in. telescope, Helwan, Egypt, by Drs. J. M. Saari and R. W. Shorthill of Boeing Company, Seattle, Washington. (Courtesy J. M. Saari and R. W. Shorthill.)

Fig. 12. Scan of full Moon, shortly before eclipse of December 11, 1964, obtained by Saari and Shorthill with 74-in. telescope, Helwan, Egypt, made in visual light, for comparison with Fig. 11. (Courtesy J. M. Saari and R. W. Shorthill.)

making up major crater rays. The discussion of the crater frequency in the *Ranger VII* Experimenters' Report (Ref. 1) was brief, because a clear separation between primary, secondary, and collapse craters had not been made. With the added information provided by *Rangers VIII* and *IX* and the improved interpretation of the collapse craters, a tentative separation now appears possible, and it leads to important results. *The shape of the frequency curve of primary craters can be interpreted on the basis of the known frequency distribution of impacting meteorites, small asteroids, and comets*; a proportionality or *rate factor* for the entire curve remains somewhat uncertain but seems to be in accordance with the estimated increase in the rate of collisions in the asteroid ring since its formation; *secondary craters in the three* Ranger *impact areas are comparatively rare; and the collapse depressions predominate by a factor of up to nearly 100 over impact craters in the diameter range of 30 m to 1 km.* The counts and the discussion of the primary craters are presented in Section F. The separation required in Section F of the "sharp" (primary) craters from the "soft" ones, which are generally collapse depressions, is preceded by the review, in Sections C–E, of the several types of negative structures.

One more introductory remark should be made concerning the general appearance of the mare floor. From the *Ranger VII* records it was found that, between craters, the floor is remarkably smooth. The records obtained by *Rangers VIII* and *IX* led to the same conclusion and, because of the lower Sun angles (15 and 10 deg, respectively, vs. 23 deg for *Ranger VII*), provided more precise information. The smoothness of the mare floor between craters is consistent with the conclusions derived from radar reflections. In the optical range $\lambda \simeq 0.5 \ \mu$, on the other hand, the Moon is extremely rough; the full Moon shows no limb darkening.

The smoothness at $\lambda > 10$ cm and the extreme roughness at $\lambda < 3–10$ cm may, on the maria, have been produced by the following agents: (1) The initial lava deposit, covered with a thick layer of *rock froth* whose cavities are statistically of diameters below 1–3 cm. (2) The effect of *meteoritic bombardment* that for craters with $D > 1$ m will have covered the intervening space with a thin layer of debris (probably less than 10 cm thick on the average). To the extent that this debris derived from the rock froth of the upper 5–10 m, the particle dimensions will reflect its cavitation ($D < 1–3$ cm). The debris would have fallen mostly in small open crevices and holes, thereby further reducing the roughness at $\lambda > 10$ cm. (3) *Sputtering*, which has been estimated by Wehner (Ref. 9) to have removed some 17 cm from the lunar

surface, if the present rate were assumed throughout lunar history, and if the surface density were that of silicate rock. A rock-froth cover would have lost much more. Furthermore, sputtering would have worked preferentially at protuberances and be ineffective in crevices, thus causing a doubly effective leveling effect. *The transition from roughness to comparative smoothness at 3–10 cm may then be due to the cavitation size of the rock froth that is continually abraded and scattered.* Sputtering constantly regenerates the roughness at the 1-μ scale, however, as was found both experimentally and theoretically by Wehner (Ref. 9) and others.

In addition to erosion by sputtering, erosion by "sandblasting" occurs (Ref. 1, p. 61). In the *Ranger* pictures, its effects may not be distinguishable from those of sputtering.

Because the sputtering rate on the Moon is significant in comparison with competing processes, its somewhat unfamiliar properties are recounted here from Ref. 9 (p. 313 ff):

"Sputtering is mainly due to low energy ions. High energy particles penetrate deeply into the lattice and expend their energy in processes other than sputtering . . .

"From an evaluation of published astrophysical observations and measurements by Explorer X, Lunik II, and Mariner II, one arrives at a flux of 2×10^8 protons/cm^2 sec with 600 km/sec average velocity at one astronomic unit from the sun. For solar storm conditions, we assume that the flux increases by one order of magnitude and that the particle velocity goes up to 1000 km/sec. We assume, furthermore, that 15% α-particles accompany the protons with the same velocity. The effects of heavier ions can be neglected in view of their much smaller flux densities . . .

"Sputtering tends to level surfaces because atoms sputtered from the sides of protrusions tend to be ejected in a direction toward the surface and attach themselves in crevices, holes, deep areas, etc. A polished surface, on the other hand, develops a higher degree of microscopic roughness under sputtering because differently oriented crystallites have different sputtering yields. From yield studies on rough surfaces, such as threaded targets, we estimate that the sputtering rate on porous, slag-like surfaces may be decreased by a factor of two or more because many of the sputtered atoms cannot clear the surface.

"Some information on the influence of the angle of incidence on sputtering yields was obtained by bombarding thin target wires with hydrogen-ion beams. In section, the wire becomes wedge shaped, indicating that the sputtering rate is considerably higher where the beam strikes obliquely. We estimate that the partially oblique incidence at the moon increases the sputtering rate by a factor of two . . .

"In agreement with Reiffel (4), the results show that the He component in the solar wind is more important to sputtering than the proton component. The combined sputtering rate for Cu is 1.1 Å/year and for Fe or stones is on the order of 0.4 Å/year. Thus, if it is assumed that the solar wind has remained the same over the period of the moon's existence (4.5×10^9 years), the moon would have lost a layer roughly 17 cm thick . . .

"One can safely conclude that most of the sputtered atoms have ejection velocities higher than the escape velocity of the moon . . .

"The target surfaces show many modifications after prolonged bombardment. One observes, for instance, the formation of a brittle crust with particles or spheres cemented together by atoms which are sputtered back and forth in the spaces between grains or spheres. Sputtering of oxide powders shows that the bombarded surface becomes enriched with metal. For instance Fe_2O_3 powder is reduced to Fe_3O_4 or to FeO, and finally to Fe. In fact, after long bombardment, iron or copper oxide powders become covered with closely spaced needles and spires with a metallic appearance when viewed at oblique angles. In the process of sputtering and of breaking up of molecules, oxygen atoms are more likely to escape (or to be incorporated in volatile hydrogen compounds) than metal atoms. The surface of such a sputtered powder target acquires a fibrous structure with an opaque appearance with photometric properties which seem to match closely those of the lunar surface . . .

"Heavy metal atoms are probably favored for being retained, while light atoms have a higher probability for escaping. We predict, therefore, a lunar surface somewhat enriched in heavy metals."

C. Terrestrial and Lunar Collapse Depressions

Reference is made to the *Ranger VII* Experimenters' Report (Ref. 1) for a description of the main character-

istics of the lunar collapse depressions. This description and the suggested interpretation appear to apply without change to the *Ranger VIII* and *IX* records, as typified by Figs. 5 and 6. What was missing in the *Ranger VII* Report was a close terrestrial analog of the lunar circular depressions. Such an analog has now been found.

A number of flights were made over a dozen comparatively uneroded basaltic flows in New Mexico, Arizona, and California, and aerial photographs were obtained under various illuminations. Sample photographs are included here, pending fuller publication in the *Communications of the Lunar and Planetary Laboratory*. Important assistance was given us by U. S. Government agencies, which provided original records of their photogrammetric coverage and new coverage at low Sun angles of areas of special interest. Ground studies were also made, and information was collected from persons who have made the study of the flows their avocation.

Figures 13–23 are aerial photographs of flow units and individual "craters" of the 30-mile-long McCartys Basalt Flow south and east of Grants, New Mexico. The northern tip of this flow, along U. S. Highway 66, has been described by Nichols (Ref. 12); however, we have found the thicker, less accessible southern portions to be more instructive. On the basis of archaeological finds in and just outside of the flow, the age of the flow is estimated by Dr. A. E. Dittert of the New Mexico Museum of Anthropology to be 1500–1800 years. Erosion has not yet destroyed its main characteristics. Figures 13 and 14 give two views of one of the areas examined. The 15-mm-long white line near the lower right corner is a distance marker (135 ft = 41 m) placed there by a ground party. The elevated area resembling a large, flat, inflated cushion is the major portion of one flow unit and is 25–30 m high. The terminal walls of the cushion are severely fractured, and secondary flows have emerged from some of the fractures, both in the foreground (left) and in the right margin. Many near-circular depressions are seen, such as **A**, the triple group **C**, and several around **E** (better shown in Figs. 15 and 16). Composite depressions are also evident: **B**, **D**, and others are double; **S** is sextuple. Each component of the composite depressions tends to have its own circular symmetry, as may be seen by comparing Figs. 13, 14, 15, and 16. Figures 17 and 18 are near-vertical views of the area with a Sun angle of about 25 deg; Figs. 19–22 show nearby areas with the same illumination.

Both the single and composite depressions show *fracture systems* roughly paralleling the contours (Figs. 13–22,

Fig. 13. Aerial view of southern portion of McCartys Basalt Flow, New Mexico, with 135-ft (41-m) distance marker
in right foreground and several collapse depressions designated by letters for further reference. (Secondary-flow
units resulting from breaks in flow front are noted in left foreground and in right margin. N is up. E–W
dimension of frame measured through crater A is 500 m, Sun angle approximately 15 deg. LPL photograph.)

Fig. 14. Same general area as in Fig. 13. (NE is up. LPL photograph.)
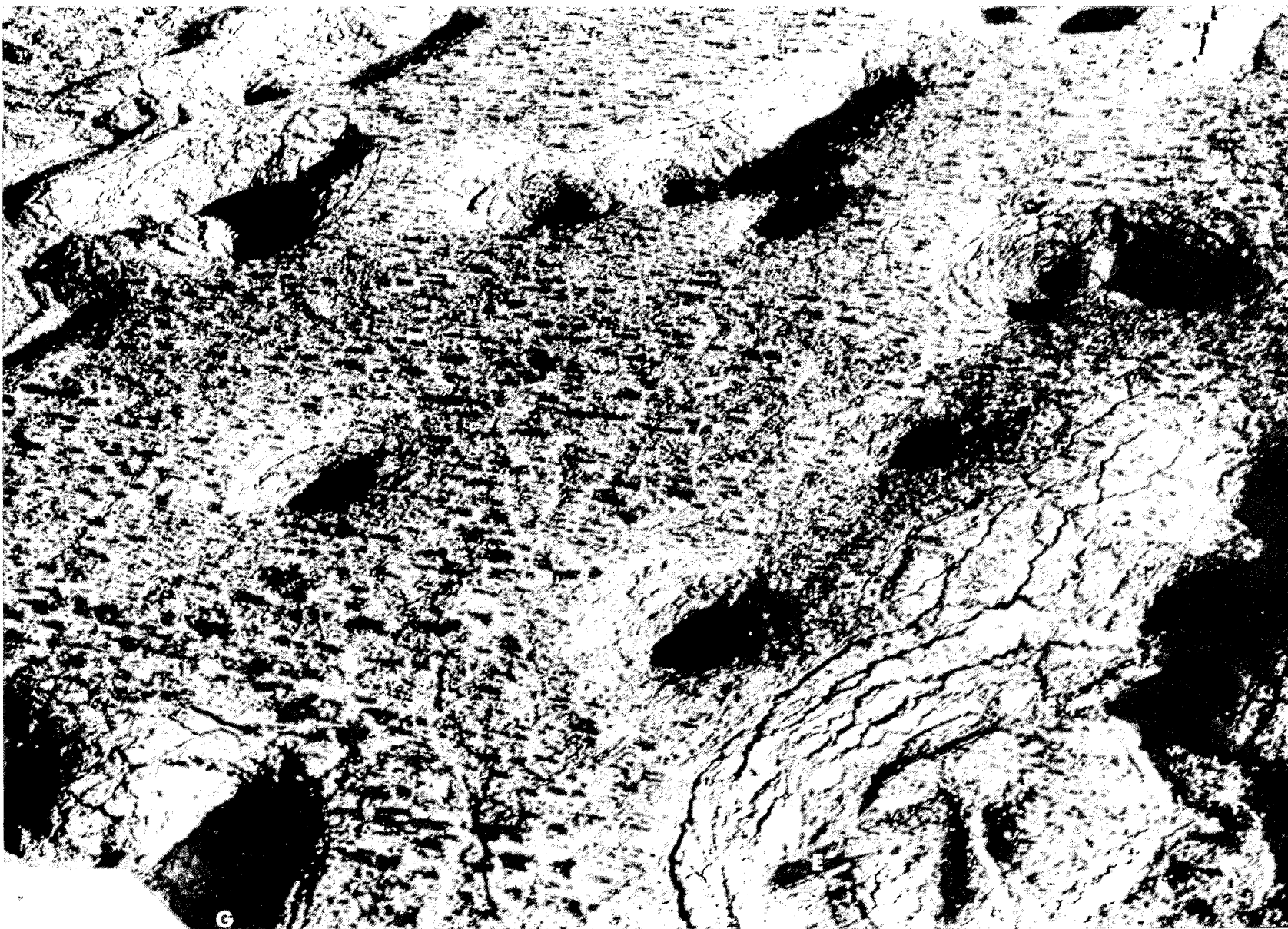
Fig. 15. Closer view of several collapse depressions shown in Fig. 13. (Note peripheral
fracture systems around depressions. LPL photograph.)
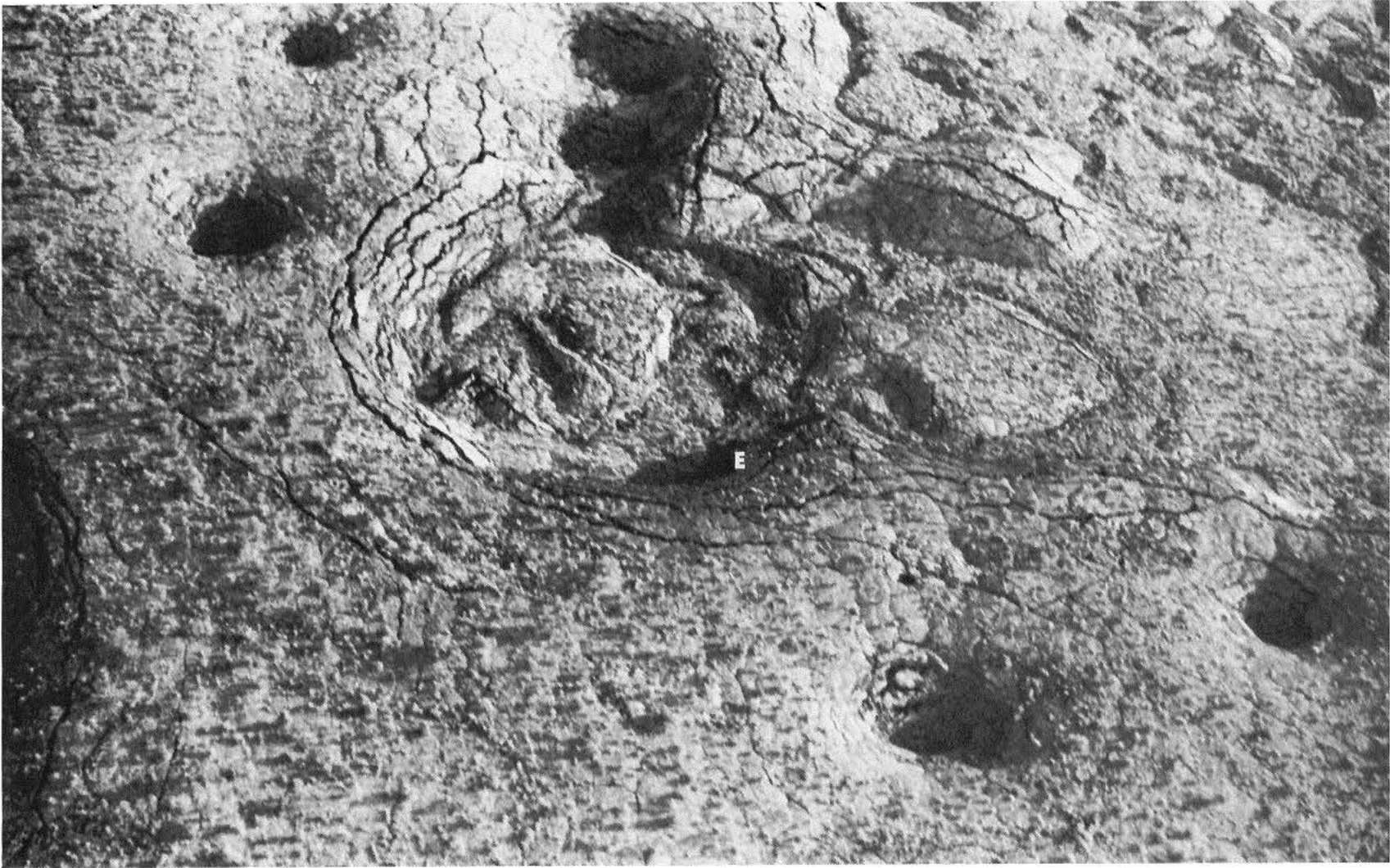
Fig. 16. Aerial view of other collapse depressions shown in Fig. 13. (Note fracture systems and sporadic small breaks, or holes, in crust. LPL photograph.)
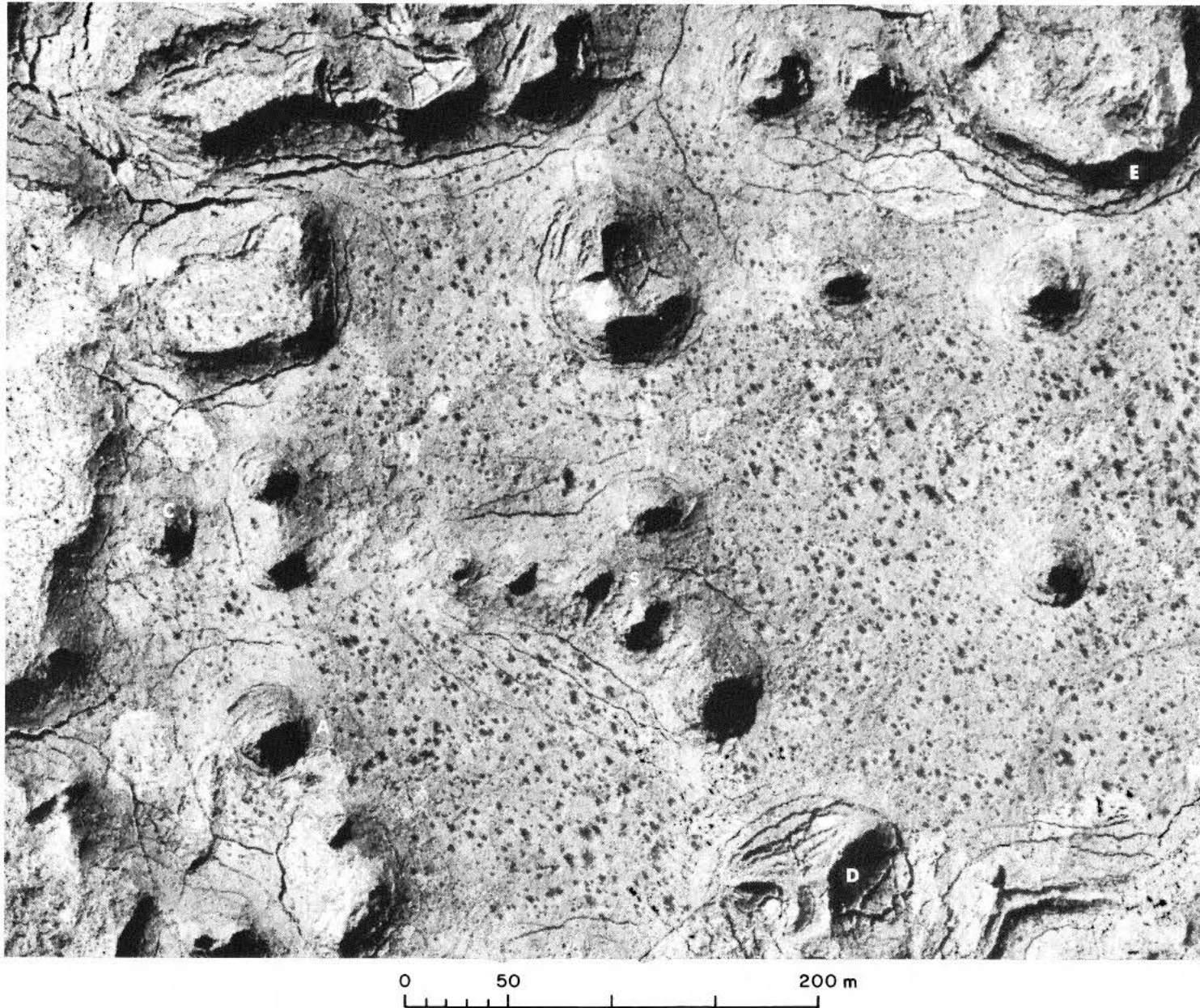
Fig. 17. Near-vertical aerial view of portion of McCartys Flow and its collapse depressions — circular, multiple, and nearly square — and peripheral fracture systems. (For key to letters, see Fig. 13. NW is up. Dimensions 470 × 590 m. Sun angle approximately 25 deg. U. S. Government photograph.)
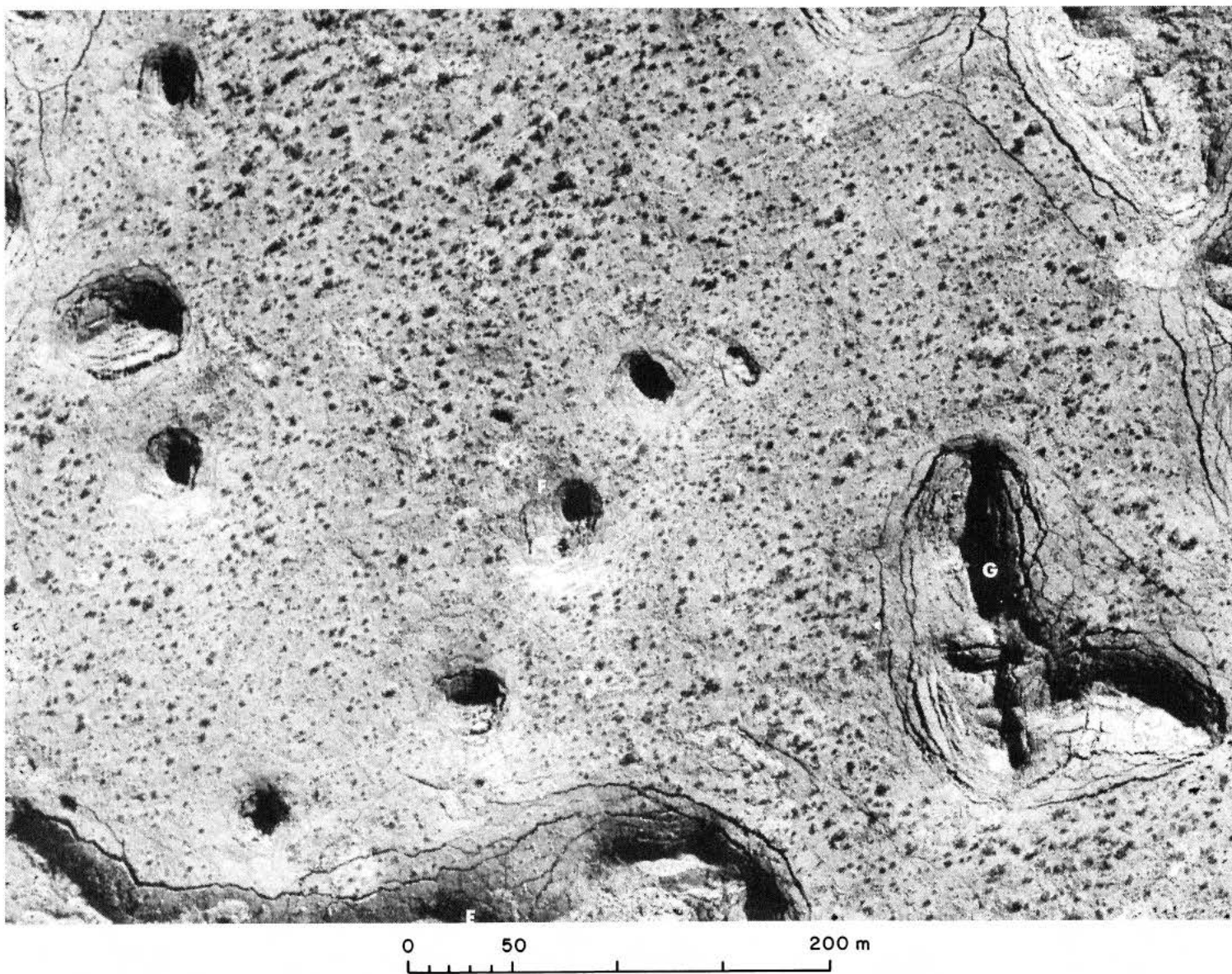
Fig. 18. Same view as in Fig. 17, but adjacent region. (See Fig. 13 for identification. Same scale as in Fig. 17. NE is up. Dimensions 470 × 590 m. U. S. Government photograph.)
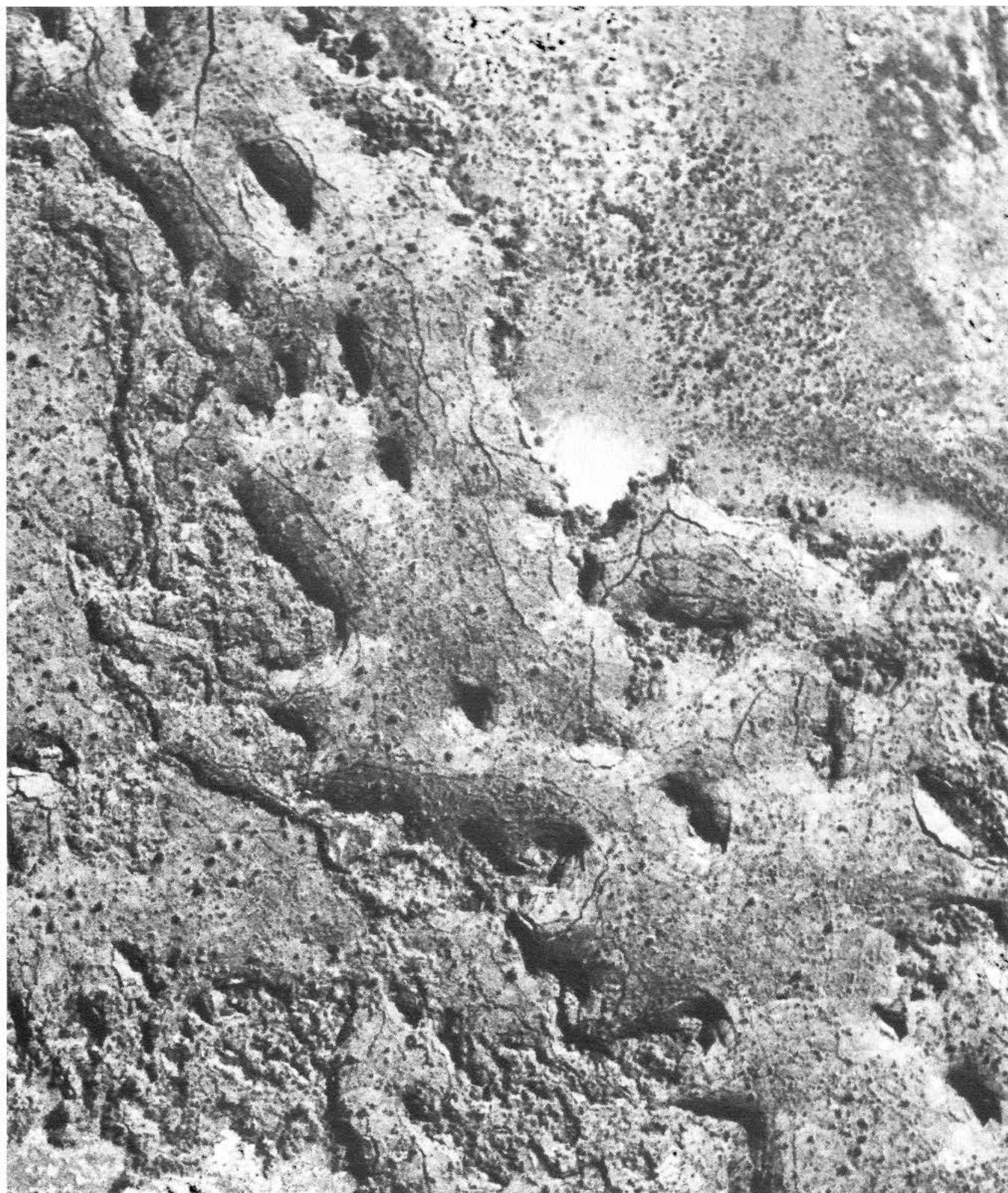
0   50   200 m

Fig. 19. Near-vertical view of flow unit in S tip of
McCartys Flow, showing several major collapse
craters and two secondary-flow units
containing smaller craters. (Sun
angle approximately 25 deg.
NE is up. U. S. Government
photograph.)

←⎯⎯

Fig. 20. Near-vertical view of flow unit in S portion
of McCartys Flow, showing single and double
collapse craters. (Insert in lower left corner
is enlargement of nearly square fracture
system at center of upper margin. NE
is up. Sun angle approximately
25 deg. U. S. Government
photograph.)

⎯⎯→

0 50 200 m
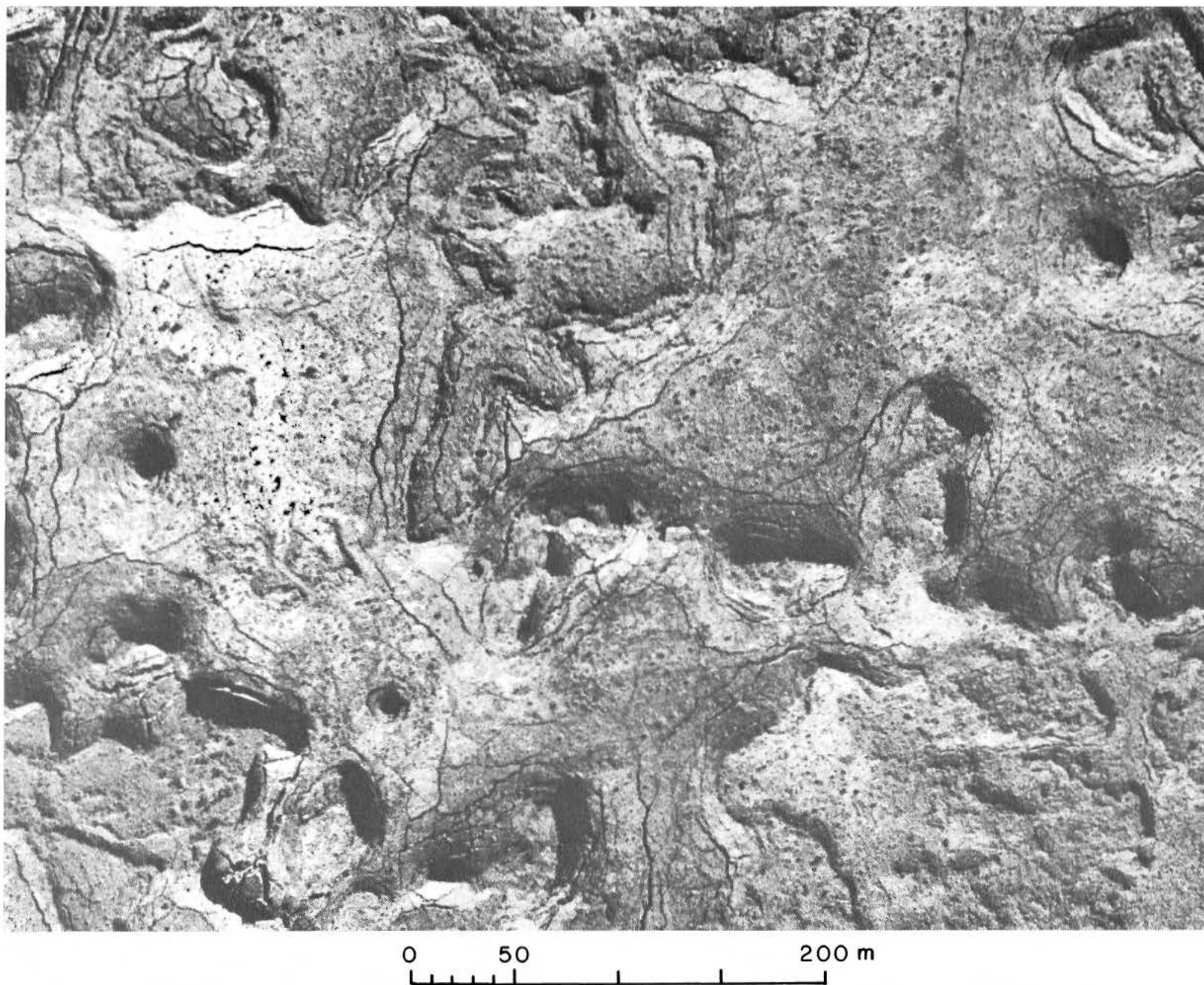
Fig. 21. Area in S portion of McCartys Flow, showing primary-flow unit with occasional circular sinks and associated secondary-flow units with small sinks. (Sun angle approximately 25 deg. NE is up. U. S. Government photograph.)

Fig. 22. Three adjacent flow units in S portion of
McCartys Flow, two having clusters of sinks
and normal circular depressions. (NE is
up. U. S. Government photograph.)
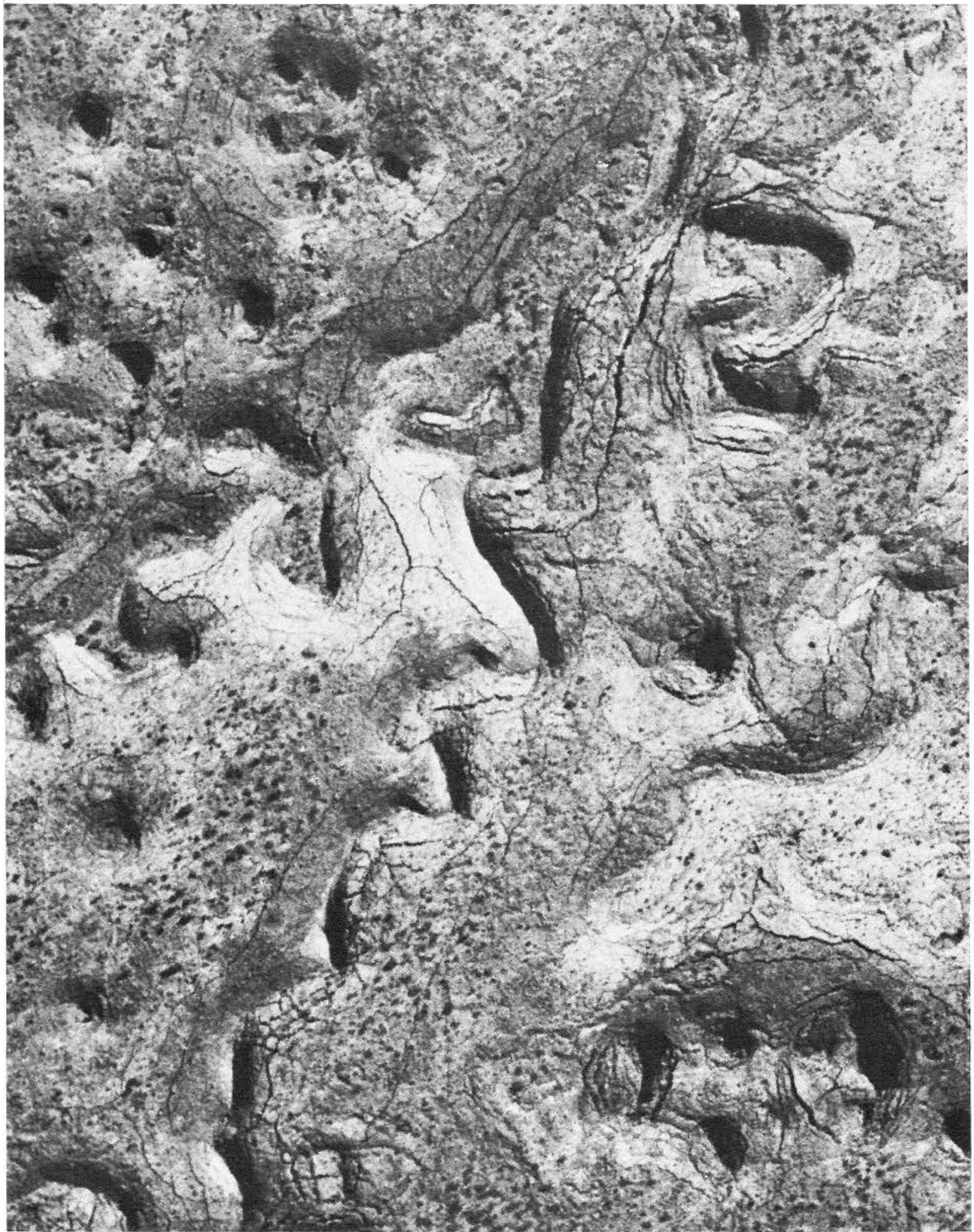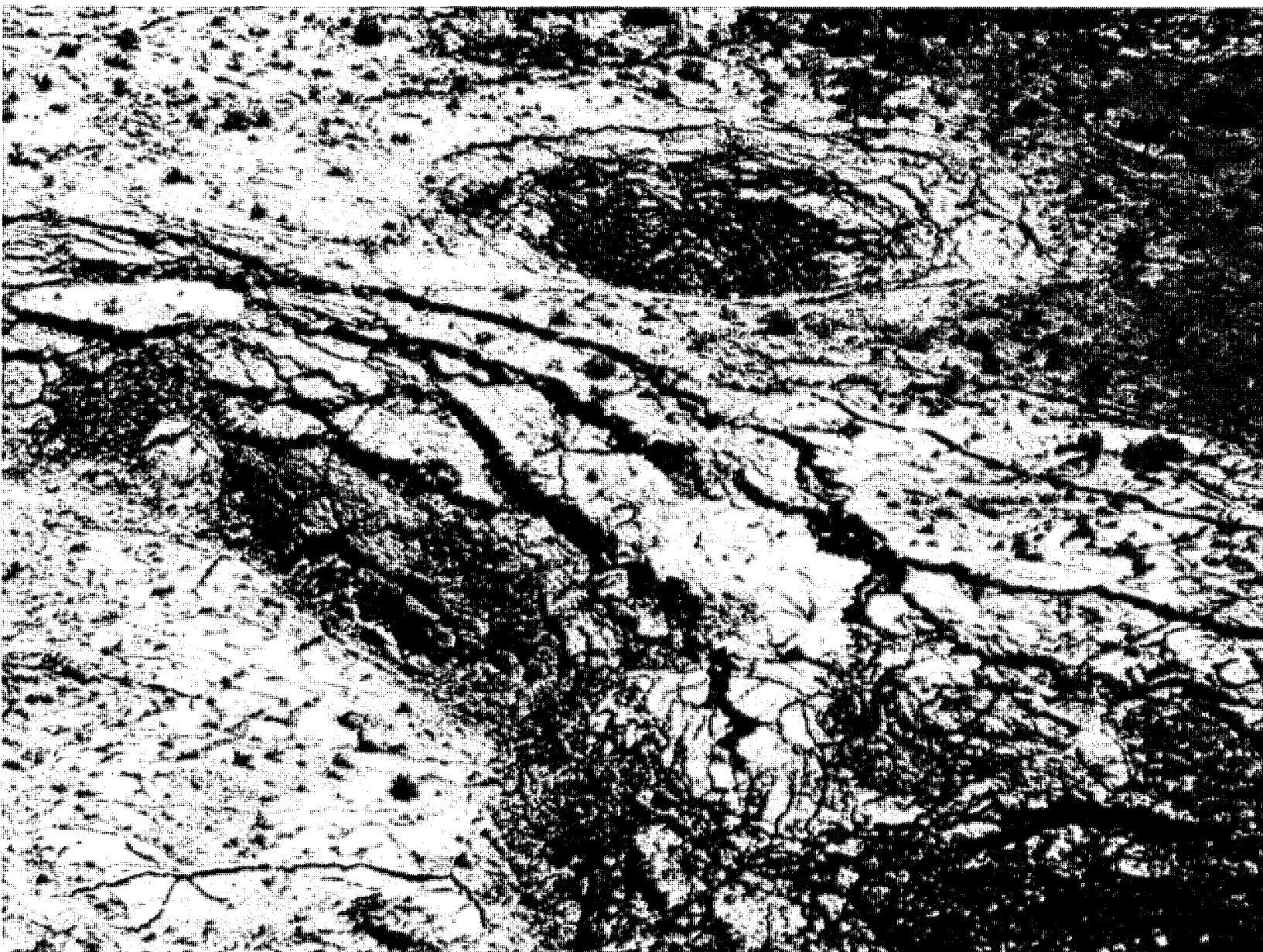
Fig. 23. Low-altitude aerial view of two collapse depressions in S portion of McCartys Flow. (Diffuse light. LPL photograph.)

and especially Fig. 23). The depressions have no rims, dip inward at first very gently, and fracture completely only near the center. This is also seen from the ground, as in Fig. 24, which shows the western half of **A**, and Fig. 25, a small collapse depression observed from the edge. The diameter of **A** is about 100 m, measured at the first peripheral fracture; the steeper part of the pit is about 45 m in diameter (see Fig. 17). The depth of **A** is roughly 25 m—close to the thickness of the flow. There is a considerable range in the diameters of the depressions, but their depths are not very different, often approaching the depth of the flow unit itself. The terrestrial depressions tend to be somewhat smaller but steeper than the lunar depressions.

The sometimes gigantic dimensions of the collapse depressions must be experienced from the ground to be appreciated. The broken masses expose the underlying structure of the flow, which implies that *the lunar mare floor, too, can be explored through the depressions.* Figures 26–31 illustrate this point. Figure 26 shows a fractured slab of ropy pahoehoe, measuring some 16 m at the top, which occurs just below the letter **S** in Fig. 17. The view from this point toward **D** is shown in Fig. 27, and the view toward **C** in Fig. 28. The southern slope (outlined by four roughly parallel fractures in Fig. 17) and the entire trough are seen from the western end in Fig. 29. The offset crater above **S** in Fig. 17 ends in a cave like most craters, as shown in Fig. 30. Figure 31 presents the interior of a typical small cave.

Both aerial and ground inspection have shown that *the depressions are due to the collapse of lava chambers that drained.* The drainage was apparently caused by the rupture of the confining flow fronts before the inner chambers had completely solidified (Figs. 13, 19–22). Inspection has shown the existence of numerous subterranean passages. Mr. Fred Wagoner of Albuquerque, New Mexico, who has studied the McCartys Flow for many years and has examined and partially mapped 900 caves in the flow, reported to the writer that the deepest cave examined was over 100 m deep; that three systems of lava tunnels exist, radiating from three sources of lava; that he has found one tunnel 11 km (7 miles) long and many tunnels well over 1 km; that one tunnel with a diameter of 100 ft (30 m) has a near-horizontal ice layer 40 ft (12 km) thick at the level of the center, with air both above and below the ice; and that below the −50-ft (−15-m) level, the year-round temperature in all parts of the caves is a constant 31°F.

The implications for future lunar research are many. Among those being investigated is one of the more remarkable properties of the flow—a strong magnetic anomaly near its southern tip.

That the McCartys Flow is in no way exceptional may be seen by reference to other flows. Figure 32 shows part of a somewhat older flow 40 miles south of Socorro, New Mexico, just east of the Rio Grande. The depressions, remarkable for their symmetry, have been partly filled with sand blown in from the surrounding desert. Forty miles northwest of El Paso, Texas, and 18 miles west of La Mesa, New Mexico, is another flow, part of which is shown with high Sun in Fig. 33. In addition to the five circular sinks near the center and toward the upper left, there is a row of four plus two in a common trough— much like the sextuplet **S** on the McCartys Flow—and several are visible in the lower right. Most of these sinks exhibit surprisingly circular symmetry.

A very remarkable flow, of similar dimension (about 42 miles or 68 km long) and age as the McCartys Flow, occurs west of Carrizozo, New Mexico, and north of White Sands. Two sample areas are shown in Figs. 34 (oblique) and 35 (vertical), both taken with high Sun. The floors of the near-conical sinks in Fig. 35 are distinguished by their light color (possibly due to wind-blown dust). Many thousand such sinks are observed in the Carrizozo Flow. Their average dimensions are about the same as those of the pits on the McCartys Flow.

The *following generalizations* apply to these and numerous other flows that have been examined: (1) nearly level, fairly thick pahoehoe flows exhibit near-circular collapse features—the thicker the flow, the deeper and larger the depressions; (2) the pure aa flows examined (the Bonito Lava Flow and that of the SP Crater, both north of Flagstaff, Arizona, and several between Grants and Zuni, New Mexico) do *not* have collapse features; and (3) aa flow units superposed on larger pahoehoe flow units *do* have collapse features, apparently because the collapse occurs in the underlying pahoehoe.

The depressions of category (3) resemble certain classes of lunar depressions very closely, as illustrated by the two sample areas of the Carrizozo Flow shown in Figs. 36–43. In the two regions seen in Figs. 36 and 37, a major lava tube in the pahoehoe flow has ruptured on top and extruded a dark layer of aa. Both Figures show the underlying pahoehoe partly exposed, with scattered, near-circular collapse depressions. There are several sinks in

Fig. 24. Panoramic view of collapse depression A identified in Fig. 13. (LPL photograph.)

Fig. 25. Small collapse depression in McCartys Flow, showing slope, fractures, and central pit. (LPL photograph.)
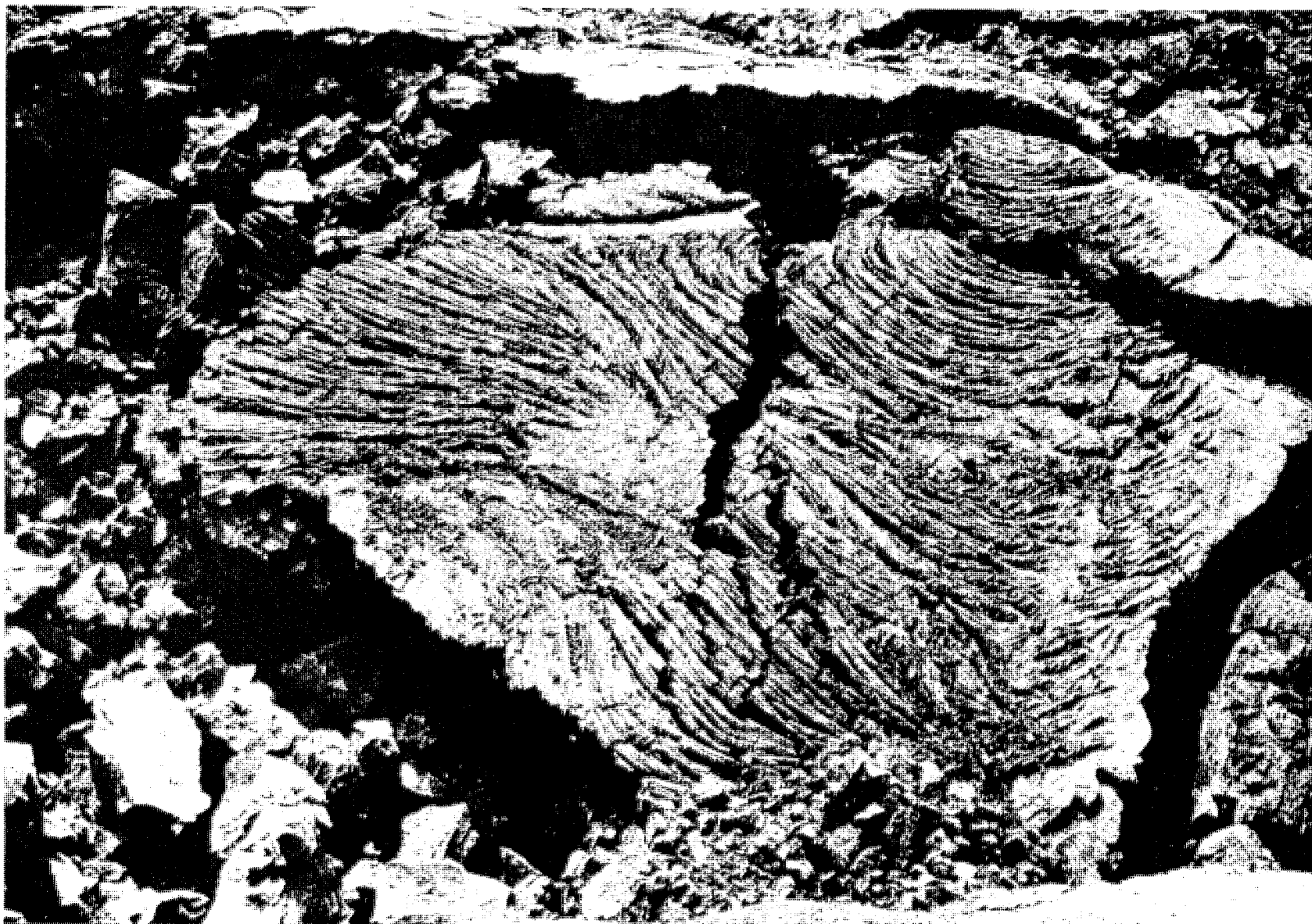
Fig. 26. Fractured block of pahoehoe on saddle in multiple depression S seen in aerial photograph,
Fig. 17, 5 mm below letter S; about 16 m wide at top. (LPL photograph.)

Fig. 27. Longitudinal view of multiple depression S from vantage point of Fig. 26,
looking toward crater D in Fig. 17. (LPL photograph.)

Fig. 28. Longitudinal view of multiple collapse depression S from vantage point of Fig. 26, looking toward crater C in Fig. 17. (LPL photograph.)
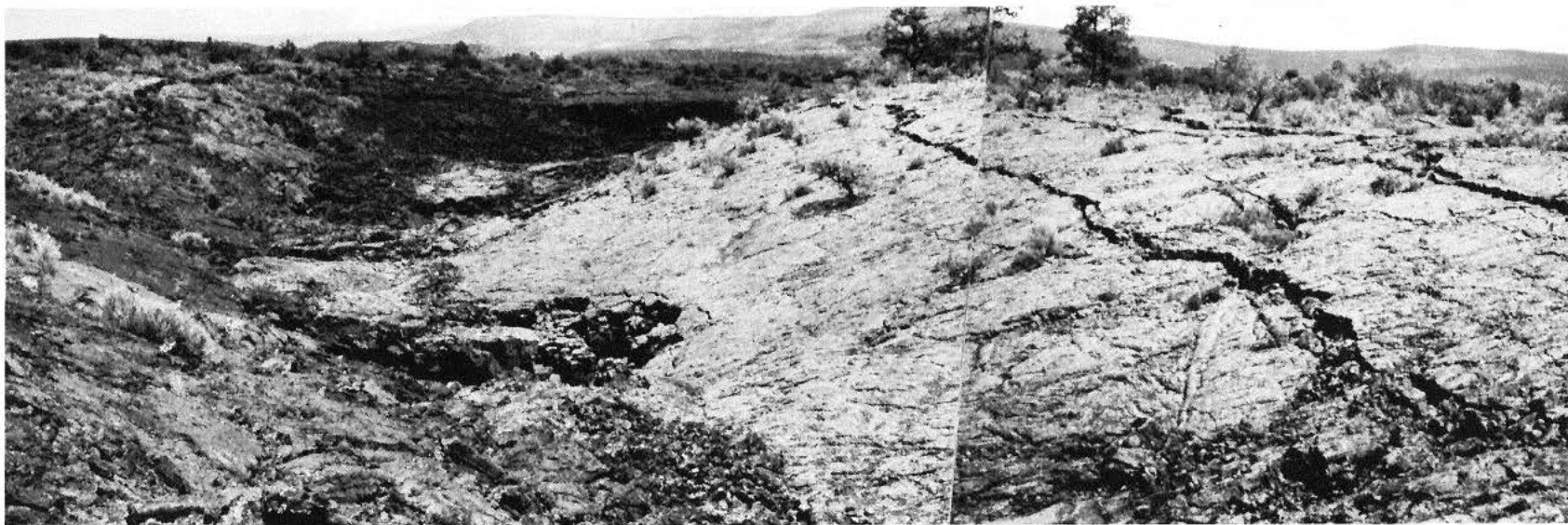
Fig. 29. Composite longitudinal view of multiple collapse depression S, looking from its extremity toward crater C in Fig. 17. (Note nature of fractures on slope and appearance of individual pits in floor. LPL photograph.)

Fig. 30. Appearance, from rim, of offset sixth member
of multiple depression S in Fig. 17. (Note cave at
bottom, common in these structures.)

Fig. 31. Typical view of cave, showing solid but
irregular sculptured basalt ceiling. (Total
depth of cave approximately 15 m.
LPL photograph.)

Fig. 32. Aerial view of part of basalt flow 40 mi S of Socorro, New Mexico, showing
collapse depressions partially filled with desert sand. (LPL photograph.)
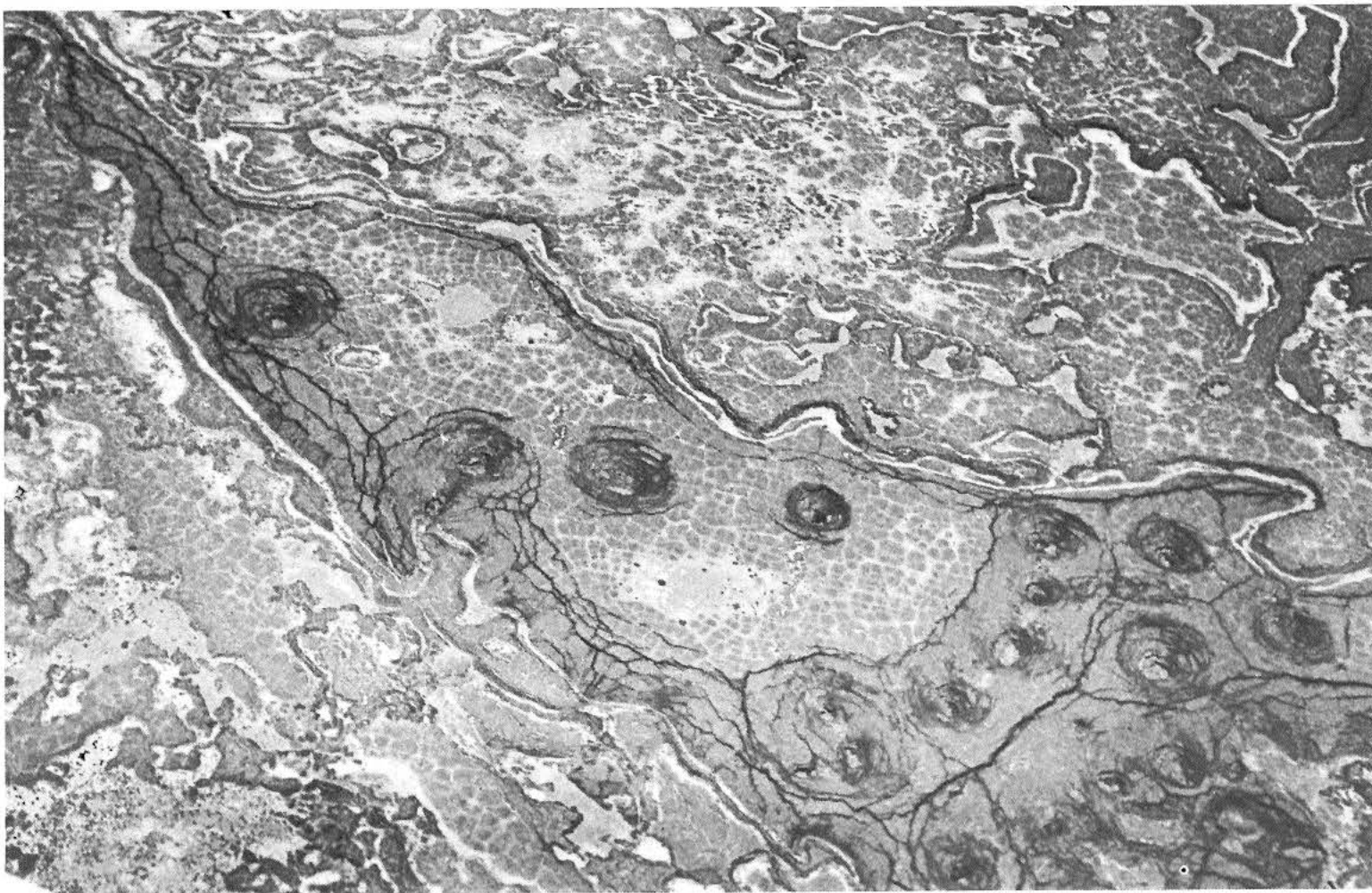
Fig. 33. Aerial view of part of basalt flow 18 mi W of La Mesa, New Mexico, taken in diffuse light, showing numerous conical collapse depressions, six of which are in a common trough. (Note surrounding fracture systems and delicate orthogonal fracture pattern in lavas between the sinks. LPL photograph.)
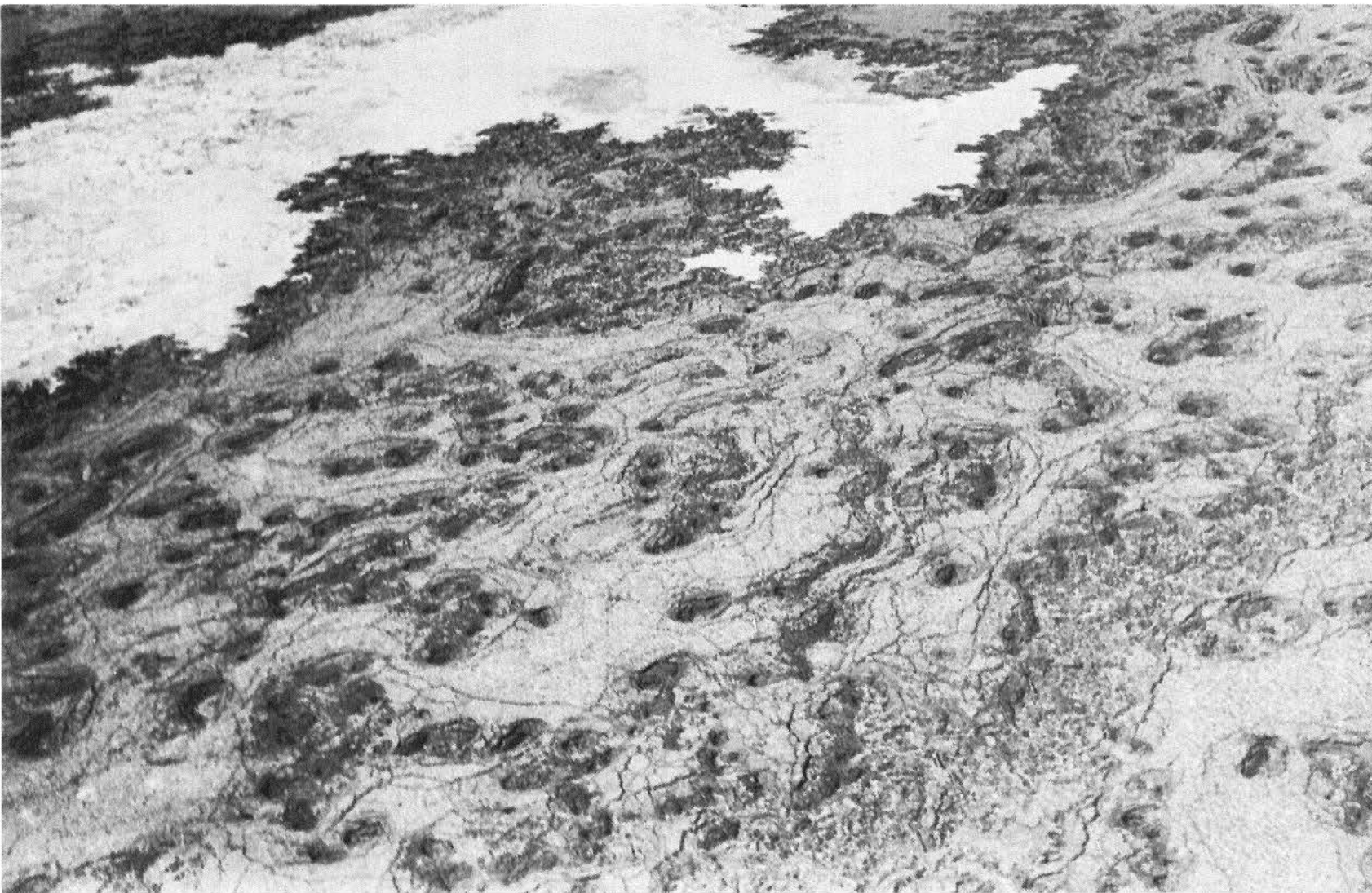
Fig. 34. Aerial view of part of Carrizozo Basalt Flow, New Mexico, with conical sinks and
fracture systems similar to those in McCartys Flow. (LPL photograph.)

0   50   300 m
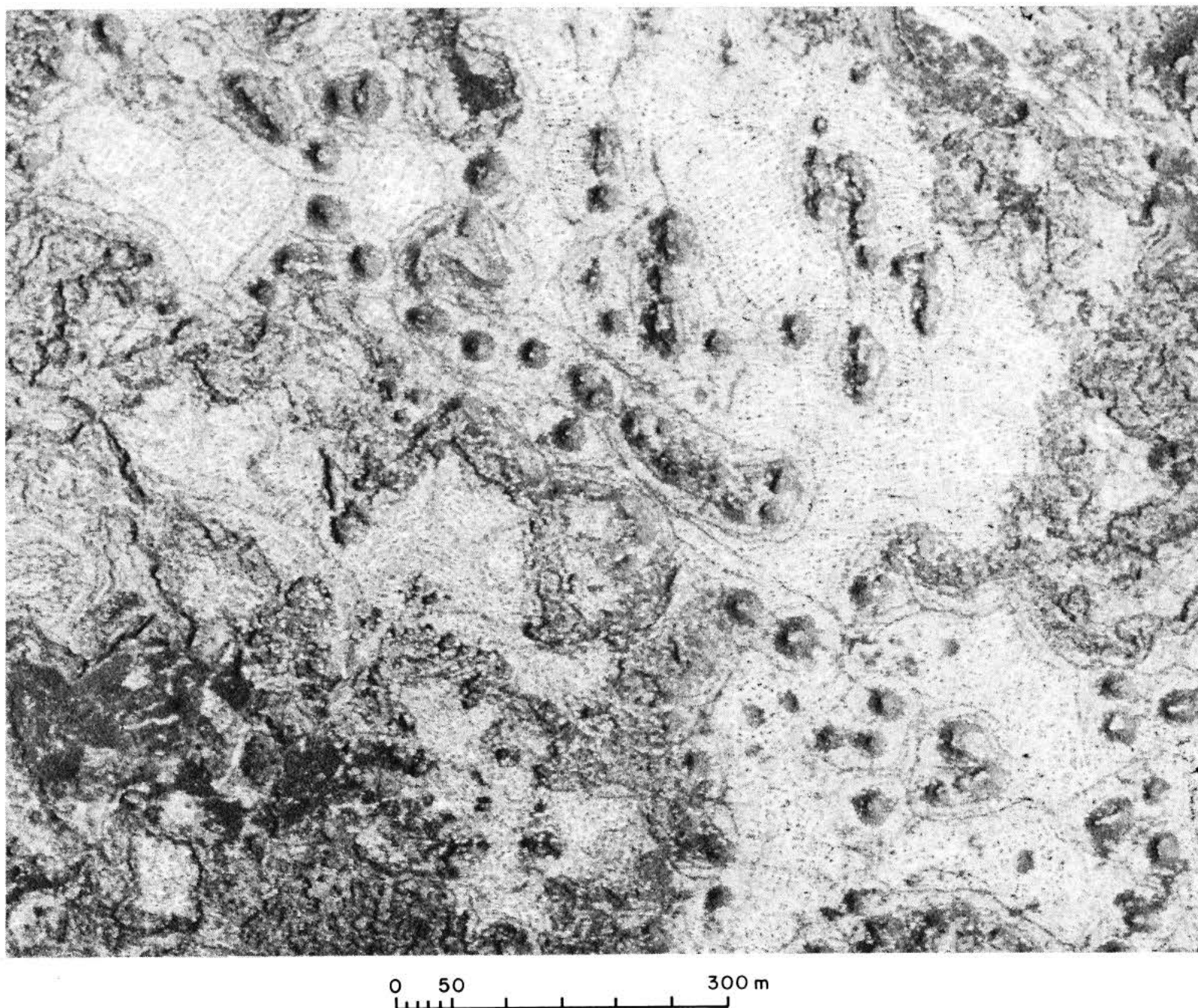
Fig. 35. Vertical view of part of Carrizozo Flow, showing single and multiple conical sinks, orthogonal fracture pattern in undisturbed portions of basalt, and some small parts (dark) covered by aa. (U. S. Government photograph.)
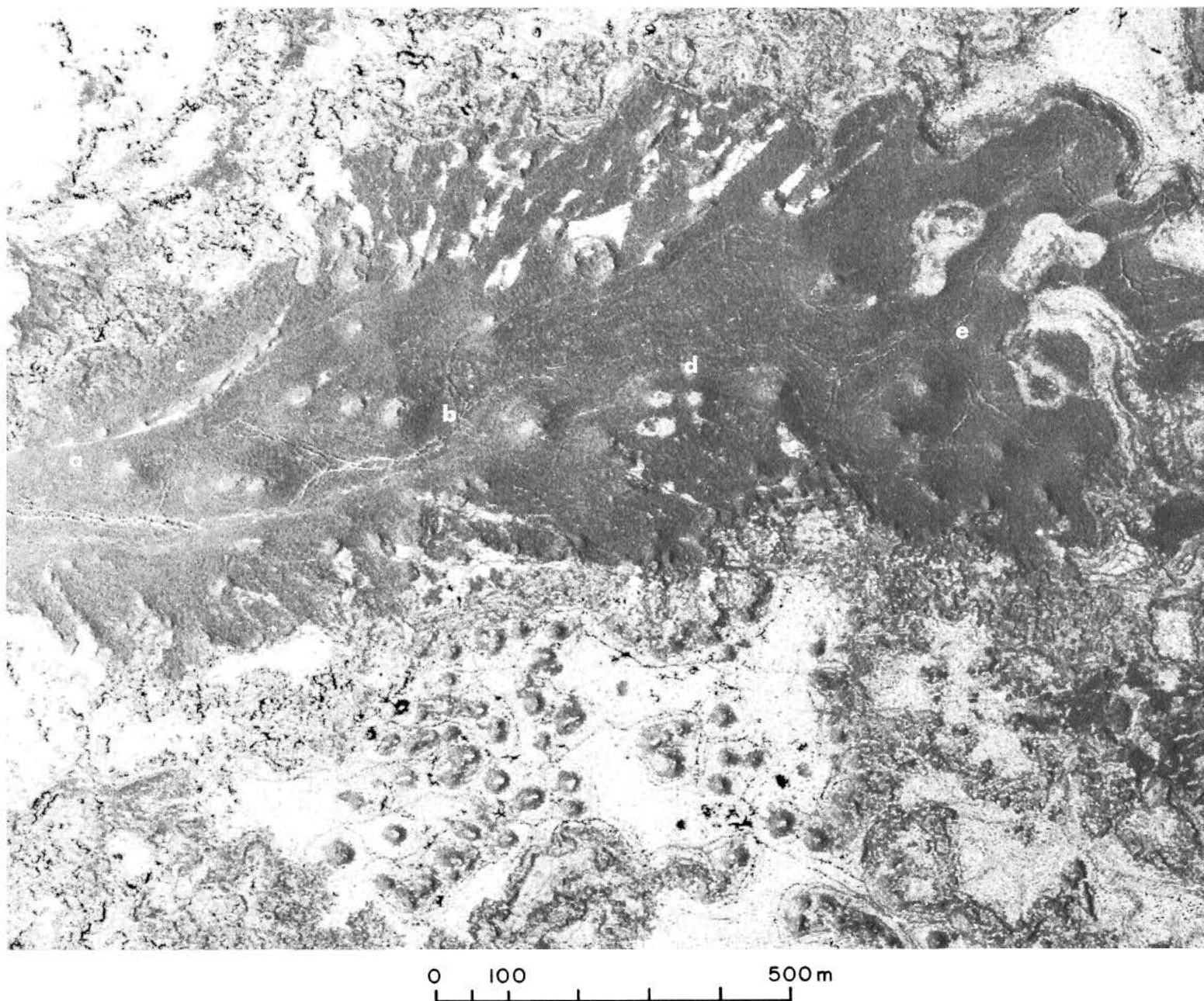
Fig. 36. Near-vertical view of part of Carrizozo Flow; lower portion is typical pahoehoe, showing conical
sinks and orthogonal fracture pattern in lighter areas; dark portion is pahoehoe covered by aa and
shows sinks closely resembling lunar dimple craters in profile. (U. S. Government photograph.)

0   50   300 m
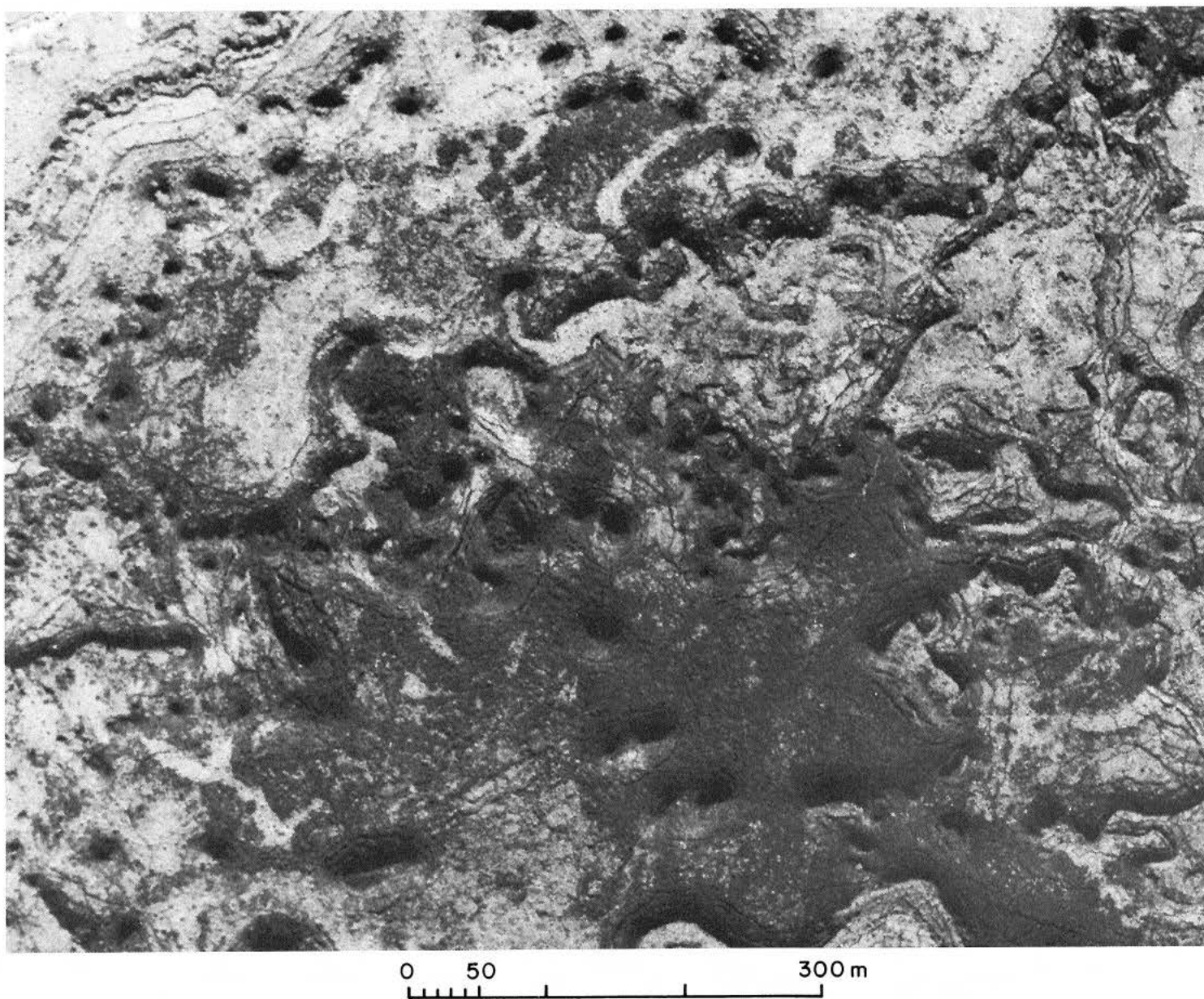
Fig. 37. Region of Carrizozo Flow adjacent to that of Fig. 36, also showing portions covered by
aa and having dimple-crater-type depressions. (U. S. Government photograph.)

the aa, but they are wider, shallower, and more Moon-like in profile than those found in pure pahoehoe. Close-up photographs taken from a small plane are reproduced in Figs. 38–43. The flow unit in Fig. 38 has blunted depressions, while the one in Figs. 39–43 has pointed or grooved depressions that are quite like the dimple craters on the Moon. (Most of the small white patches are lichens; the large whitish areas are pahoehoe. There is no normal vegetation on the flow.) *The striking resemblance to lunar dimple craters* may be seen by comparing Figs. 42 and 43 with Fig. 44 (lower half). Even *the linear break at the center* is of similar proportion and dimension. Another similarity exists in the "tree-bark" pattern first noted in the *Ranger VII* photographs (Ref. 1, pp. 55–60, 153–154). Mr. Whitaker was the first to remark that the depressions observed in these photographs appeared to be enveloped, roughly along the contours, by a delicate system of fractures or furrows. The half-tone reproductions (Ref. 1, pp. 56, 57, 59, 154) lost much of this somewhat marginal information; but the photograph of the model (Ref. 1, p. 60) retains the general impression conveyed by all of the records. In Fig. 45, Mr. Whitaker has outlined his interpretation of *the pattern around the depressions* based on the available *Ranger VII* P frames and A199. This swirling pattern may be compared with that appearing in Figs. 39–43. Apart from the granularity of the aa cover, the correspondence is remarkable.

A physical and dynamic interpretation of the collapse depressions in terrestrial lava fields must await fuller exploration, including three-dimensional mapping. However, studies of the related problem of surface collapse over coal and ore mines are described in standard engineering texts on mining. These studies appear to account, at least in part, for two statistical properties of the depressions in lava flows: their tendency toward circularity, and the near-vertical orientation of the fracture planes,

with a slight inward leaning at the surface level (see Figs. 25 and 23). Both properties are a consequence of the tendency of the rock to fracture along almost cylindrical surfaces placed upon the cavity (with the cylinder more nearly circular than the cavity itself), provided that the rock medium is reasonably isotropic and not fractured or stratified along strongly inclined planes. On the Moon, these conditions are presumably fulfilled. (Conversely, departures from symmetry would signify anisotropic subsurface conditions on the Moon.) At the surface, the area of fracture and depression above mines usually extends somewhat beyond the outline of the subsurface cavity itself, apparently due to the fact that outside the main cylindrical fracture, additional roughly concentric fractures develop, with associated small inward displacements of the surface layer. Such displacements have been established for the main depression of the San Manuel, Arizona, mine, for example (see Fig. 143 in Section K).

In addition to the purely dynamic causes of collapse, exemplified by the collapse depressions over mines and by the milder forms of karst topography in limestone country discussed before (Ref. 1, Fig. 32), a physical cause for circular symmetry has been noted. Inspection of some of the drained lava chambers in the McCartys Flow near Grants (Figs. 13–31) has shown that the thickness of the ceiling varies tremendously (from much less than 1 to over 10 m). Clearly, at the time of drainage, considerable temperature and/or composition differences must have existed, with much of the flow already solidified and fluid columns and connecting channels remaining. The ceilings are thinnest above the fluid columns that drained—a correlation obviously having a single thermal cause. The thin spots above the axes of the fluid columns will have become centers of weakness in the crust, and centers of collapse upon drainage of the columns.

Fig. 38. Aerial view of aa flow unit overlying pahoehoe in part of Carrizozo Flow. (Note near-circular collapse depressions and surrounding fracture patterns resembling those on Moon. Bright patches are lichens; no other vegetation on flow. LPL photograph.)

Fig. 39. Aerial view of aa flow unit in Carrizozo Flow, shown vertically in Fig. 36. (Depressions resemble lunar dimple craters and small crater chains. Small, bright patches are lichens. For scale, see Fig. 36, regions a, b, and c. LPL photograph.)
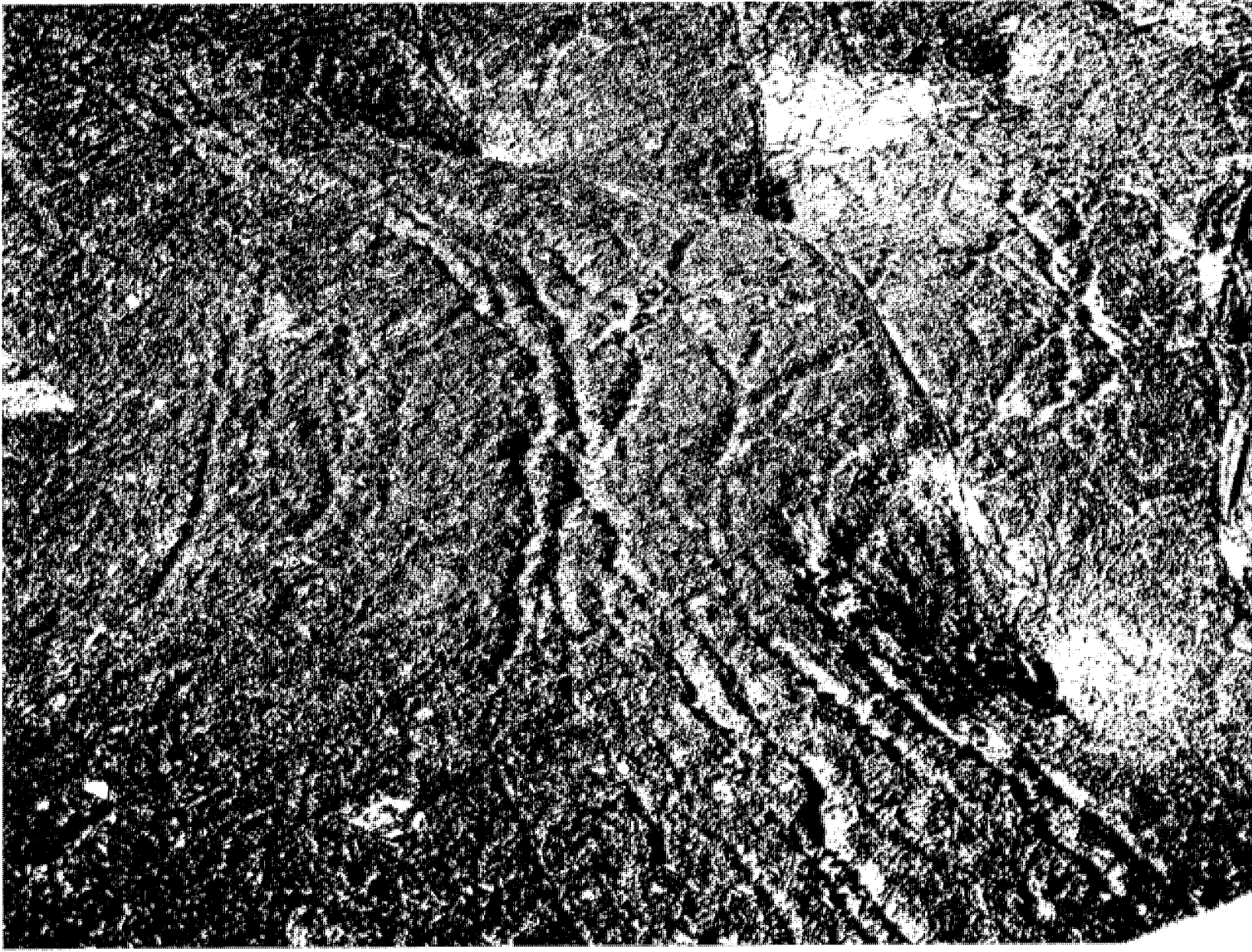
Fig. 40. Close-up of aa flow unit shown in Figs. 36 and 39. (For scale, see Fig. 36, regions d [bottom] to e [upper left]. LPL photograph.)
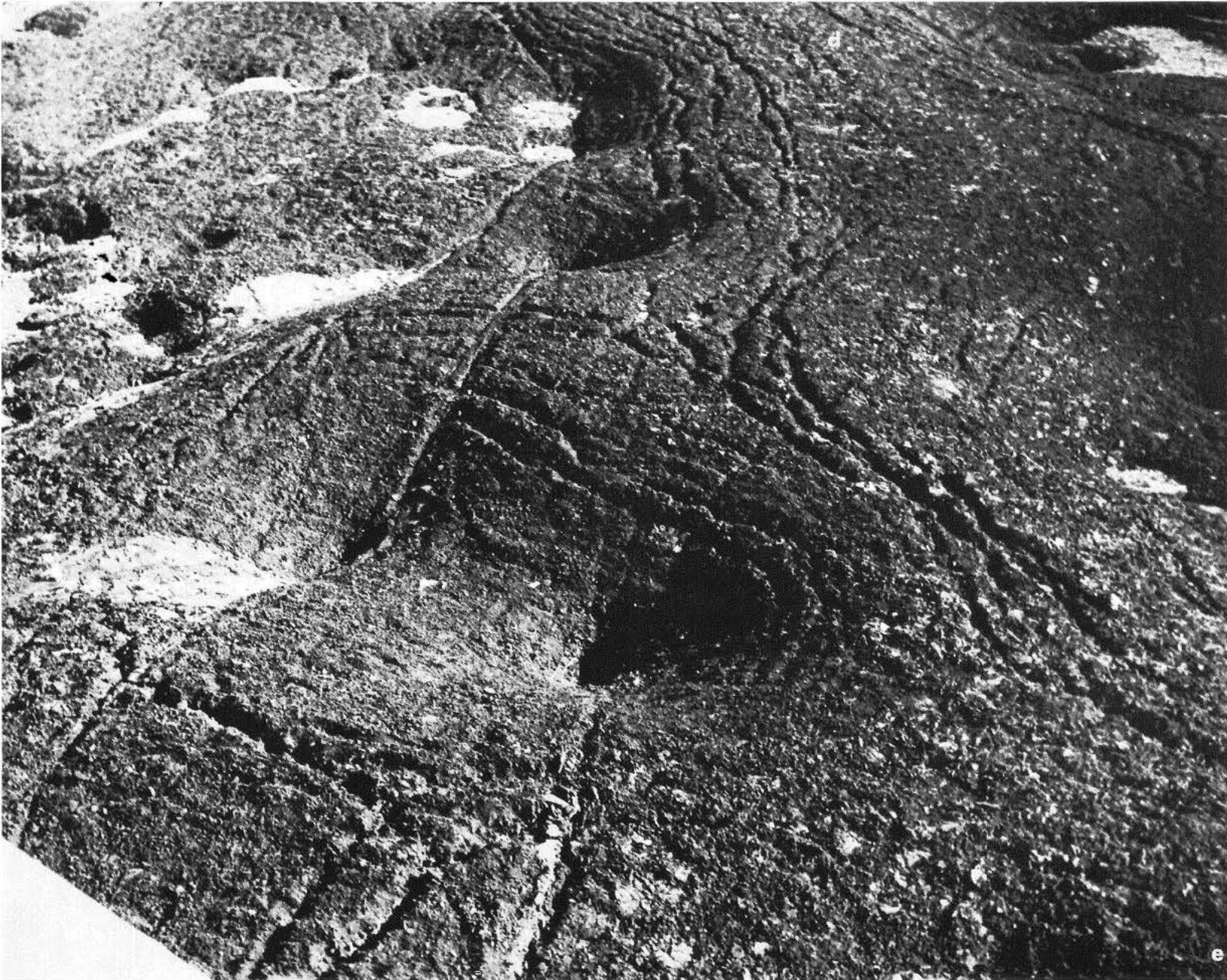
Fig. 41. Aerial photograph of detail in aa flow unit in Carrizozo Flow, shown in Fig. 36. (Note resemblance to lunar
dimple craters and tree-bark pattern. For scale, see Fig. 36, regions d [top] to e [lower right]. LPL photograph.)
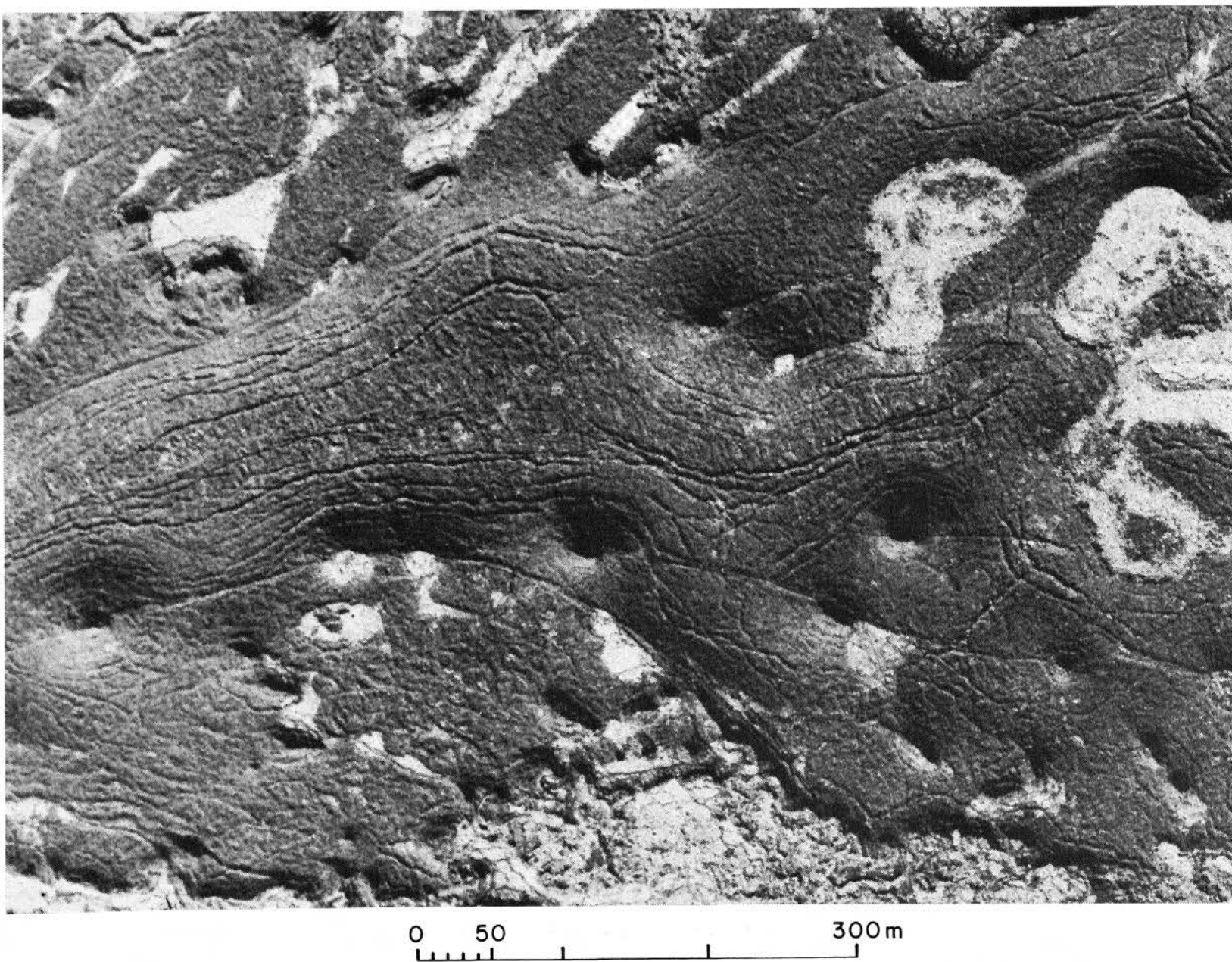
Fig. 42. Close-up of aa deposit on pahoehoe shown in right half of Fig. 36. (U. S. Government photograph.)
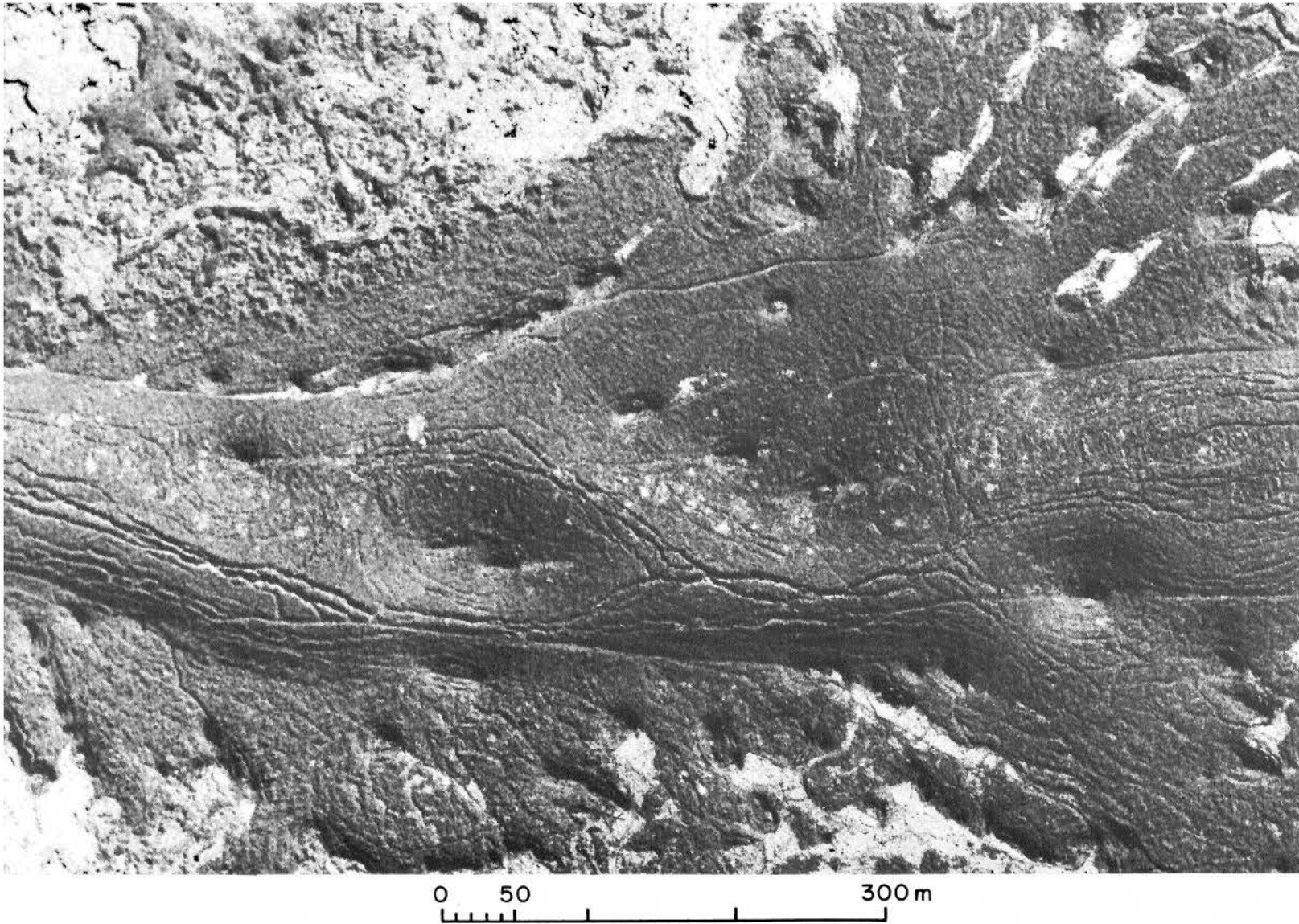
Fig. 43. Close-up view of left half of Fig. 36, adjacent to area shown in Fig. 42. (U. S. Government photograph.)

Fig. 44. Selection of dimple craters from *Ranger VIII* records, each reproduced more than once to optimize visibility of central break, or cave. (Numbered 1–13, counted in horizontal rows, starting top left: 1–2, P17; 3–6, same feature in P18; 7–9, B90; 10, P10; 11–13, same feature in P11; horizontal lines are 50 m long.)

$\longrightarrow$
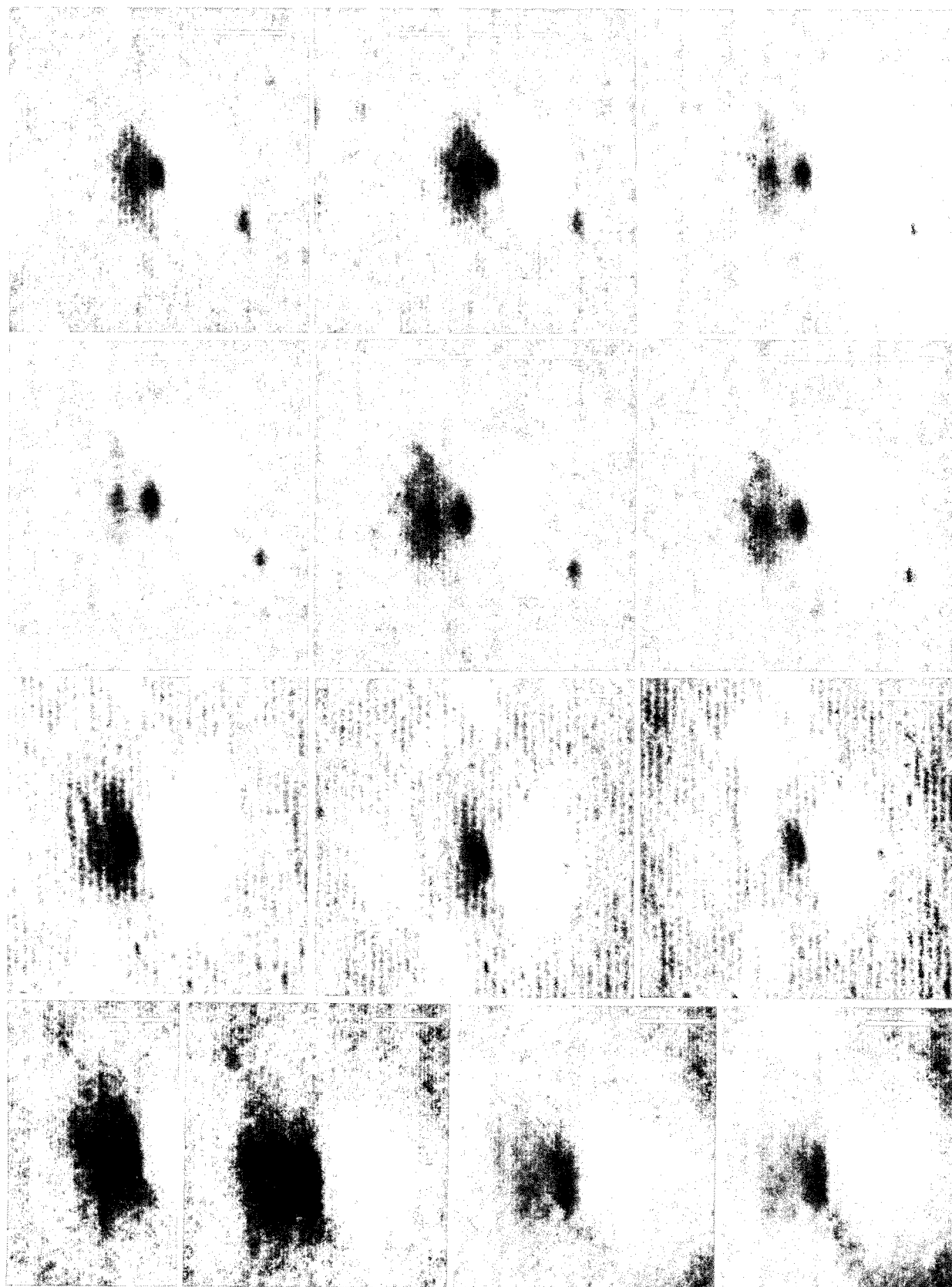
LENGTH OF LINE = 50 m

Fig. 45. Part of *Ranger VII* frame A199, with structural lines (fractures) observed in A and P frames by E. A. Whitaker. (For identification, the same letters are used as in Ref. 1, Fig. 31, p. 51. Compare also with Figs. 14–16, 19, 34, and 39–43 in this Part.)

$\longrightarrow$
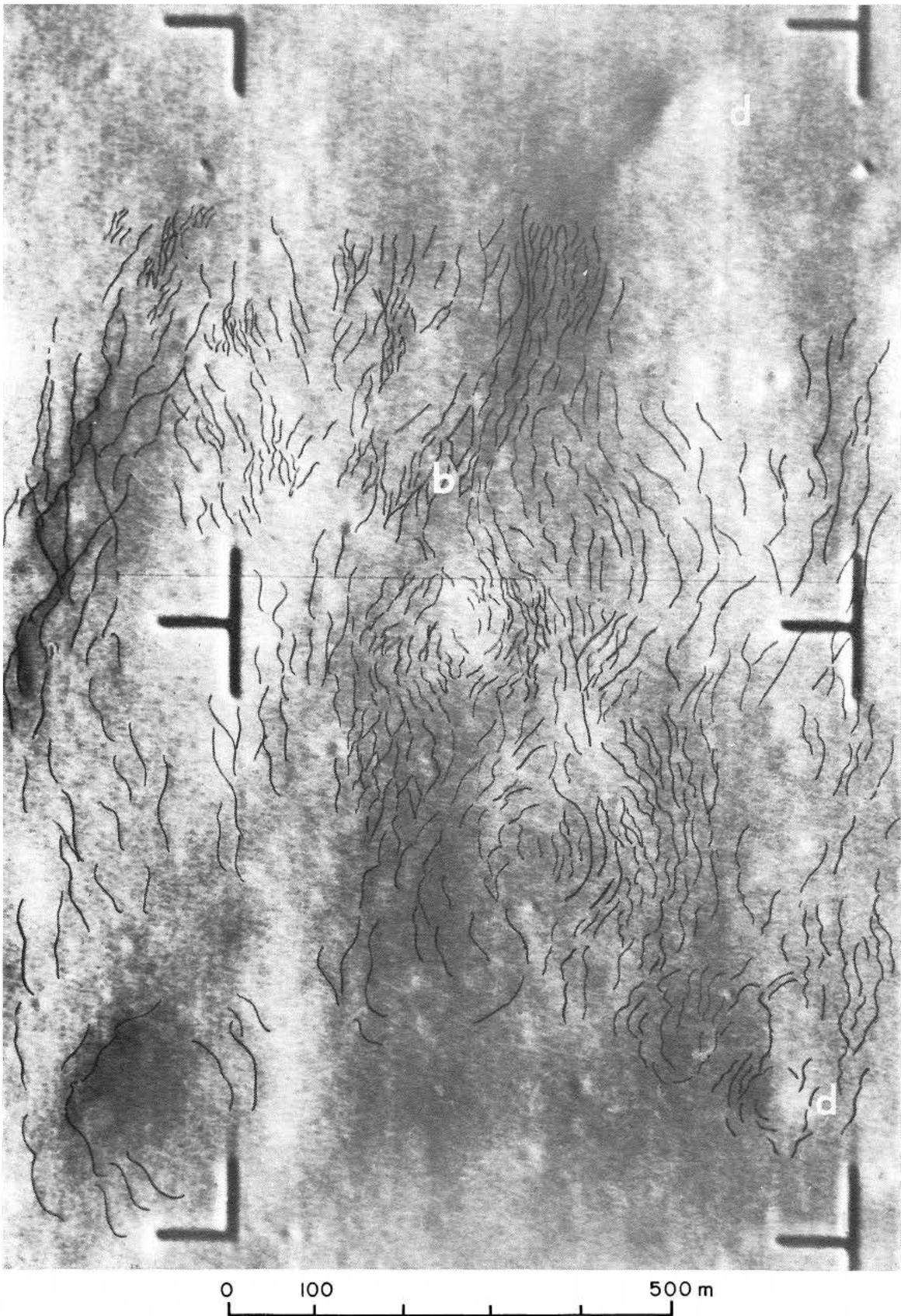
D. Ranger VIII: *The Structure of Mare Tranquillitatis*

Ranger VII supplied a mass of new information pertaining to the mare floor, and covered several classes of lesser features. In order of prominence, these are: (1) primary- and secondary-impact craters and circular collapse depressions; (2) square, linear-beaded, and irregular collapse depressions; (3) mare ridges; (4) lineaments of various types, including parts of (2) and (3); and (5) fine structure (tree-bark pattern or otherwise) between craters. The lineaments are discussed in Section G; comments on the other classes are made in this Section on the basis of Figs. 46–59 and other material.

Figure 46 reproduces part of the last *Ranger VIII* B frame. In this Figure, as in most of the other *Ranger* frames reproduced, the fiducial marks have been removed by hand retouching* in order to avoid distraction from the subject matter. Also, wherever desirable, a metric scale has been added. The reproductions of the *Ranger* frames have not been rectified (except for Figs. 135 and 136 in Section K), so that the scales are not quite the same in the two coordinates.

The pan-shaped depression in Fig. 46 is about 1 km in diameter at the rim and has on its floor a somewhat irregular rhombic pattern that extends outward to the north. The two directions, seen especially outside the crater, are close to the *diagonal grid directions* (Section G). A prominent furrow occurs along the western edge of the floor, the straight portion of which is parallel to one of the grid directions. (The continuation of this furrow is seen near the right edge of Fig. 49.) On the northwest wall of the crater are some twenty *rocks*, 3–10 m in diameter and about one-third or one-fourth as high; a similar number of rocks are less clearly shown on the east–northeast wall. Only one or two rocks appear on the crater floor itself, and none is discernible outside the upper rim. The rocks are not accompanied by impact craters (Ref. 1, p. 54). Since the floor shows the same general grid pattern found outside the rim, it is assumed that the depression was formed by collapse and is not of explosive maar origin. Maar-type explosive craters are found on the Moon (see below) but differ greatly from the crater in Fig. 46. The rocks are probably the result of irregular fracturing of the walls during the collapse. Reference is made to Figs. 16, 23, 25, 26, 28, 38, 40, and 43, and particularly to Fig. 143 in Section K, for terrestrial analogs of this phenomenon. No precise match is

*Performed by T. E. Weller of the Lunar and Planetary Laboratory.

expected because of the absence of a terrestrial rock-froth layer. Also, many areas on the Moon have been subjected to very severe *shocks* that could have caused projecting rocks to break off and roll down. The slope of the pan-shaped depression is about 150 m wide and the tilt about 12 deg, so that the depth is about 30 m. This is not very different from terrestrial depressions such as those shown in Figs. 28 and 29, or in the foreground of Fig. 23. The depth of the large dimple crater in Fig. 46 is 12–15 m.

Part of the last *Ranger VIII* B frame may be combined stereoscopically with part of the last A frame. The two records are shown together in Fig. 47. One roundish depression, clearly visible stereoscopically, has a fault in the wall that casts a shadow. The fault is sharp within the resolution of the frames (1.5 m), indicating very limited erosion since its formation.

Figures 48 and 49 reproduce, respectively, part of the last *Ranger VIII* A frame (see Fig. 5) and part of the next-to-last B frame, on which are plotted the centers of the last 12 frames taken by the best of the P cameras (P_1). The records produced by this camera, which has a 3-in. focus, are nearly free from electronic interference.

Some of the last 12 P frames themselves are reproduced in Fig. 50. Figures 50(e) and (f) show prominent depressions, both having intricate floor patterns. The crater in Fig. 50(e) has eight or ten *rocks* on its floor and slope, and rocks are suspected in two other cases, both on the slopes of depressions. One of these can be seen in the lower right margin of Fig. 50(d); the other is in area **h** (not reproduced separately here) of Fig. 49. The very shallow depressions, such as those visible in Fig. 49 near **g**, **h**, and **i**, are hardly distinguishable from the general mare terrain at the higher resolution of Fig. 50.

On the basis of the above data, and of Fig. 55, we may generalize as follows: Whenever the resolution is adequate, the walls and floors of *the deeper collapse depressions show fine structure* in the form of sweeping *furrow* patterns and individual *rocks*, 2–10 m in diameter. No rocks are visible outside the depressions. These observations set the depressions apart from impact craters and strengthen the hypothesis that they are of collapse rather than impact origin.

The crater density increases somewhat toward the smaller scales, indicating that the increase in a log $N/$

log D plot occurs with a slope steeper than -2 (see Section F). In the frames taken closest to the lunar surface, the very small craters drop out and the larger craters appear eroded, but the erosion appears to affect only the uppermost layer of 1 m or so. Areas **l** and **m** (not reproduced here) contain a prominent dimple crater, shown in Fig. 44, which appears to have a break (a cave) at the bottom.

The last frames taken by the two 1-in.-focus P cameras (P_3 and P_4) are of particular interest. Three of these show the two adjacent depressions seen in Fig. 48 between areas **b** and **c**. They are reproduced with increasing resolution in Figs. 51–53. Figures 51 and 52 also show a remarkable dimple crater about 60 m in diameter having a central hole or cave, some 5×12 m in size, which is clearly distinguishable from the slopes themselves. *This hole is one of the best documented caves on the Moon.*

The deeper of the two large depressions shown in Fig. 53 has a rock-like mass on its southern slope. This rock is seen much better in Fig. 54, which reproduces the third-to-last P_2 frame. Figure 54(a) presents the frame as recorded, 54(b) the mask used to reduce the interference pattern (the mask having been derived, after some local retouching, from the *last* P_2 frame, which shows little lunar detail), and 55 the composite print. Several rocks, 2–3 m in diameter, are now visible on the inner slope and the floor of the pan-shaped depression, which is not unlike the crater reproduced in Fig. 46, but is smaller (about 200 m in diameter at the outer rim instead of 1000 m). Prominent tree-bark patterns are seen on the floors of both depressions. The explanation of the crater and the rocks is probably the same in both instances.

We note several additional points of interest in Figs. 46–53. (1) Between the craters of $D \ll 10$ m, the mare floor has a monotone, though streaky, windswept appearance, very different from that resulting from the well known "saturation-bombing" pattern observed in some highland areas near Tycho.* It is true that the scale of

---

*Examples are at 0° longitude, 40°S and at 8°E, 44°S.

the Tycho fields is different, but the logarithmic frequency law of diameters is nearly linear up to the sudden turnover point near 1 m (see Section F), so that the comparison is relevant. *An explanation other than erosion by repeated impacts* ("gardening") is therefore needed. (2) Numerous small, very shallow, yet nearly circular depressions occur down to diameters of 10 m and less. Whether these minor depressions are also due to collapse and have perhaps been somewhat eroded by sputtering, or whether they are due to puffs of fine debris from primary impacts all through lunar history cannot be determined by inspection; however, on other grounds, the second alternative is improbable. (3) Occasional fairly sharp craters exhibit well displayed central rock masses [Figs. 46, 48, 49, 50(b), and 50(e)]; these could be secondary-impact craters. (4) Many of the 2- to 10-m craters have slopes in excess of 15 deg, while the slopes of some are less steep. (5) Some collapse craters have fine structure on their inner walls, suggesting that only minor erosion has occurred since their formation [Figs. 46, 50(e), 50(f), and 54].

The last *Ranger VIII* P picture occupies 13% of the width of a full frame and was taken only 0.08 sec before impact, with a slant range of 190 m. It covers a field of about 23 m. The smear during the exposure is about 1.1 m. One crater, some 75 cm wide, appears at the bottom of the strip. Some streaks are only 15 cm wide on the Moon. Unfortunately, the smear is 30 deg from east to west, so that the light and shadows of craters mostly overlap.

The existence of small dimple craters with central caves indicates that the low-density rock-froth surface layer on the mare is of limited thickness because, by analogy with terrestrial dimple craters (Figs. 42 and 43), the cavitation is likely to occur in the denser layer below. The example of Figs. 51 and 52, with $R \cong 25$ m, slope $\simeq 12$ deg, and depth to cave $\simeq 5$ m, would lead to a value of not over 2 m. A dimple crater in Figs. 49 (**I**) and 44, with $R \simeq 75$ m, slope $\simeq 12$ deg, and depth $= 15$ m, suggests a cover thickness of < 8 m.

Fig. 46. Section of last *Ranger VIII* B frame (B90), showing pan-shaped depression with rocks on inner slope and prominent dimple crater. Scan lines removed by double copying. (See also Fig. 41, right margin. Dimensions 1200 $\times$ 1200 m.)

Fig. 47. Views of two roundish depressions in *Ranger VIII* frames B90 and A60, respectively.
(May be combined stereoscopically. Dimensions 490 × 490 m.)
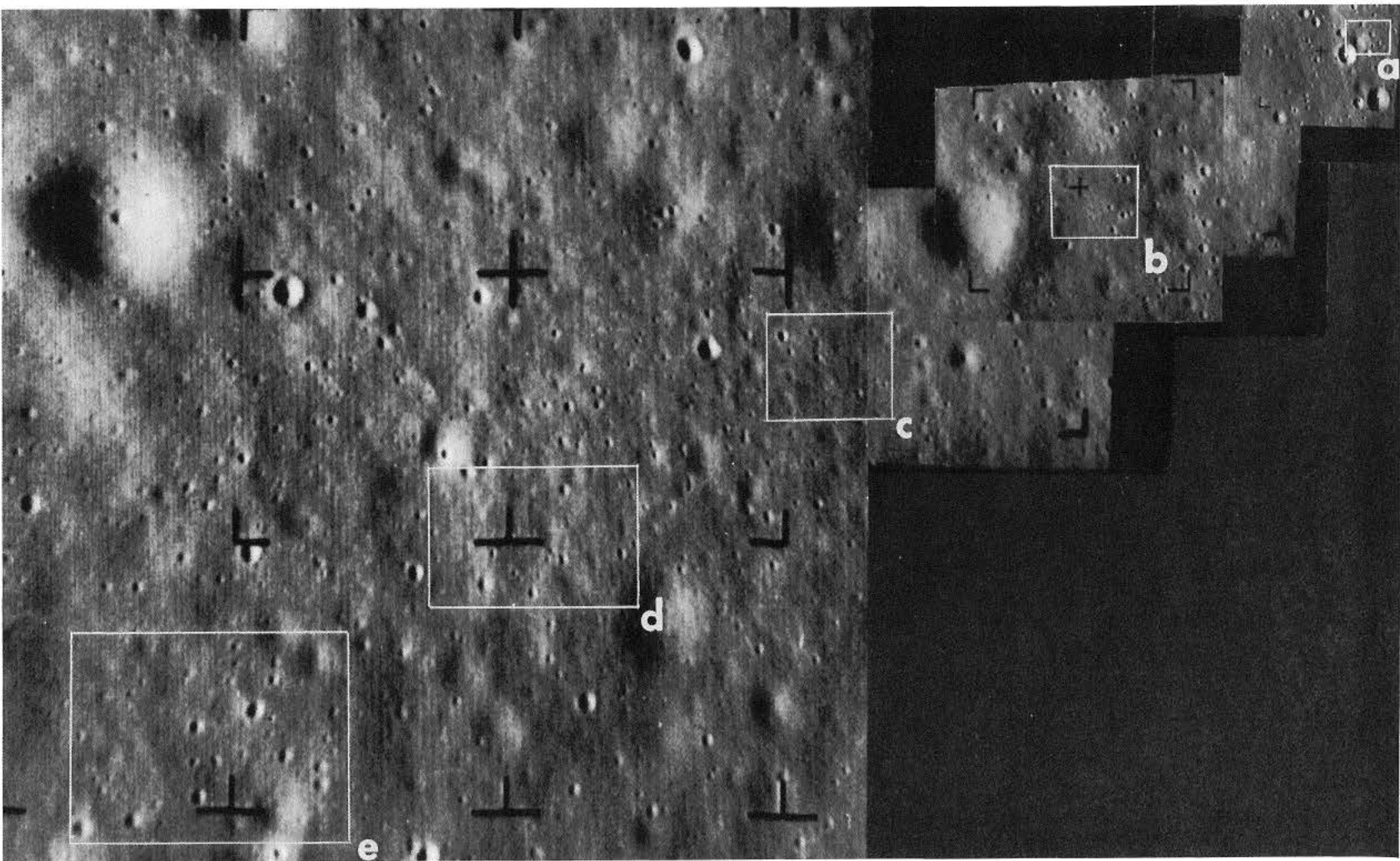
Fig. 48. Part of last *Ranger VIII* A frame (A60), with P-frame mosaic showing coverage of last five
P₁ frames. (Four are reproduced in Fig. 50. Dimensions 2200 × 1300 m.)
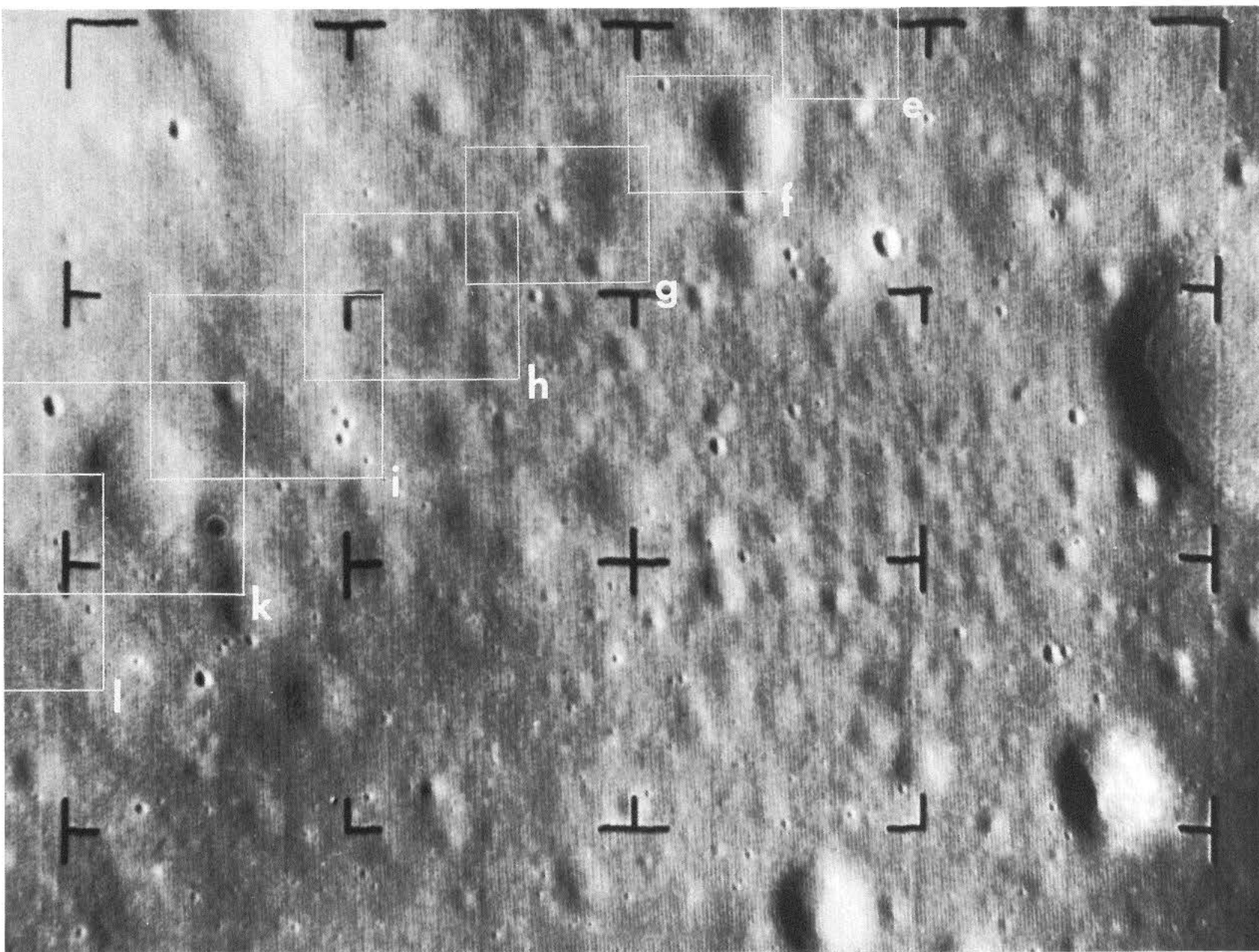
Fig. 49. Part of next-to-last *Ranger VIII* B frame (B89), showing pan-shaped depression of Fig. 46 (right) and coverage of seven P_1 frames marked e to l (left). (Some of the latter are separately reproduced in Fig. 50. Dimensions 4400 × 2700 m.)
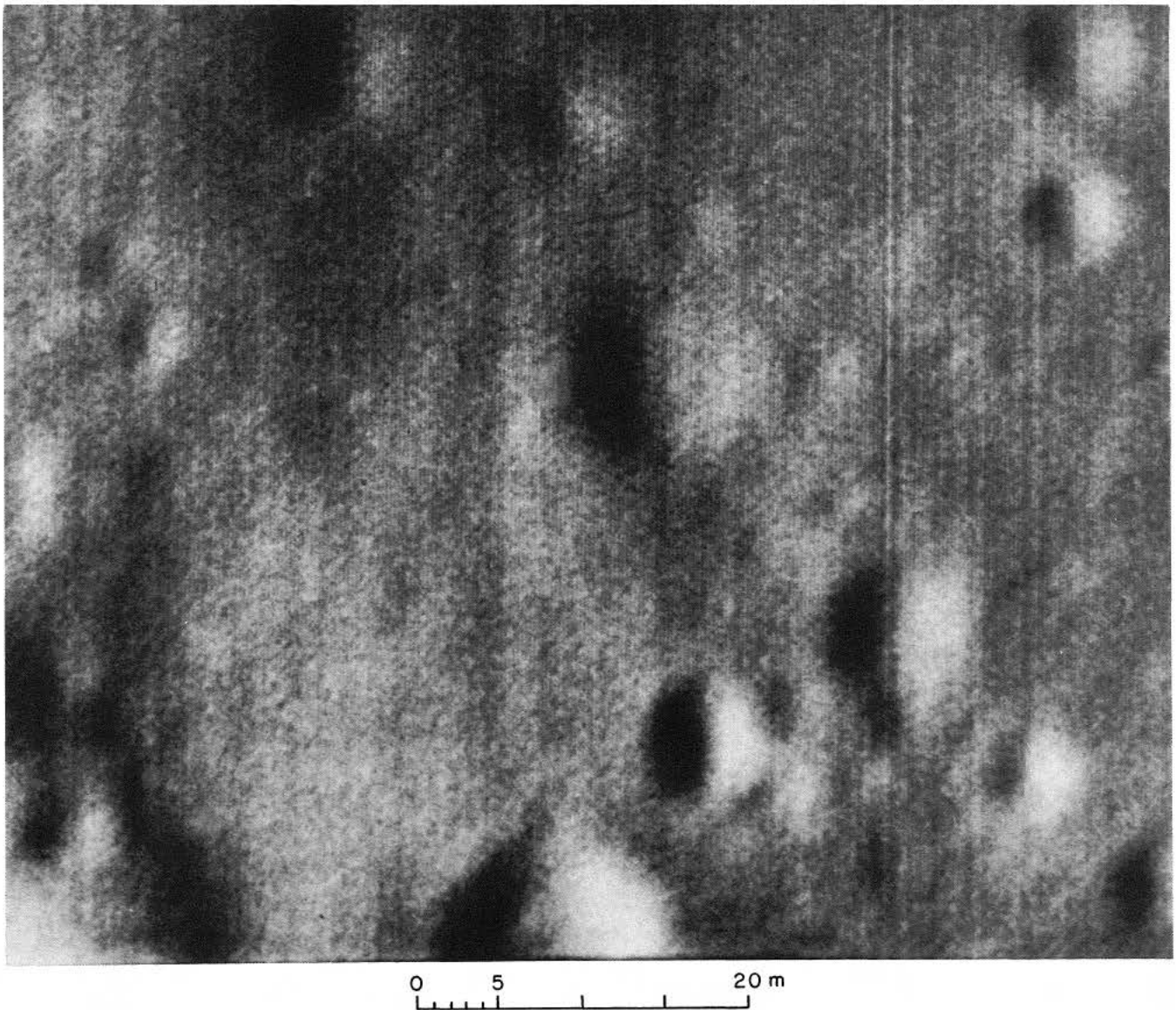
Fig. 50(a). Last *Ranger VIII* P₁ frame (P20), at location a in Fig. 48. (Note washed-out appearance of craters and diagonal trend of shallow grooves. Dimensions 73 × 46 m. Average smear due to motion 1.1 m, indicated in amount and direction in upper right corner.)

0   10   50 m
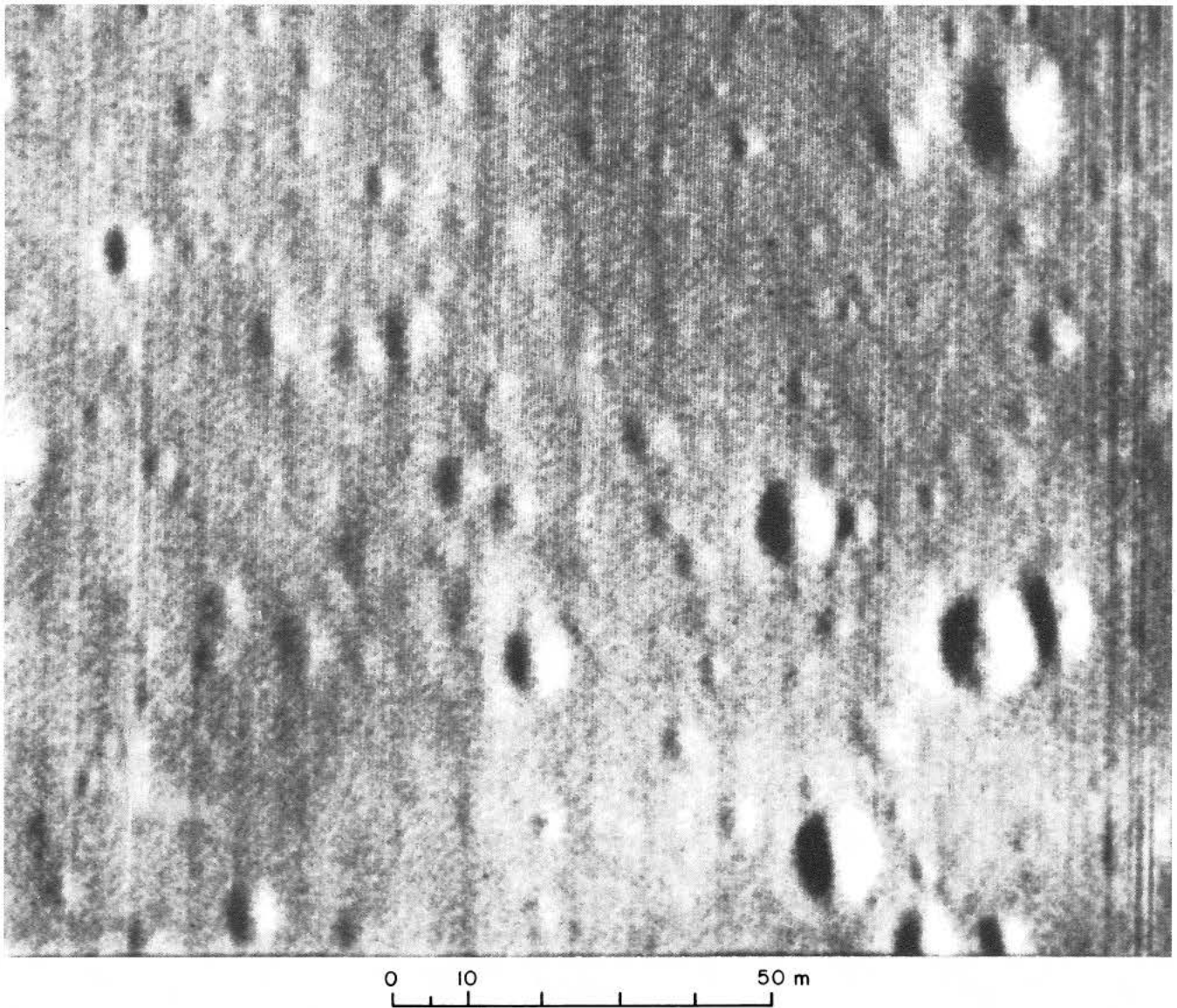
Fig. 50(b). Next-to-last *Ranger VIII* P₁ frame (P19), at location b in Fig. 48. [Washed-out appearance of small craters noted in Fig. 50(a) still evident. Dimensions 160 × 100 m.]
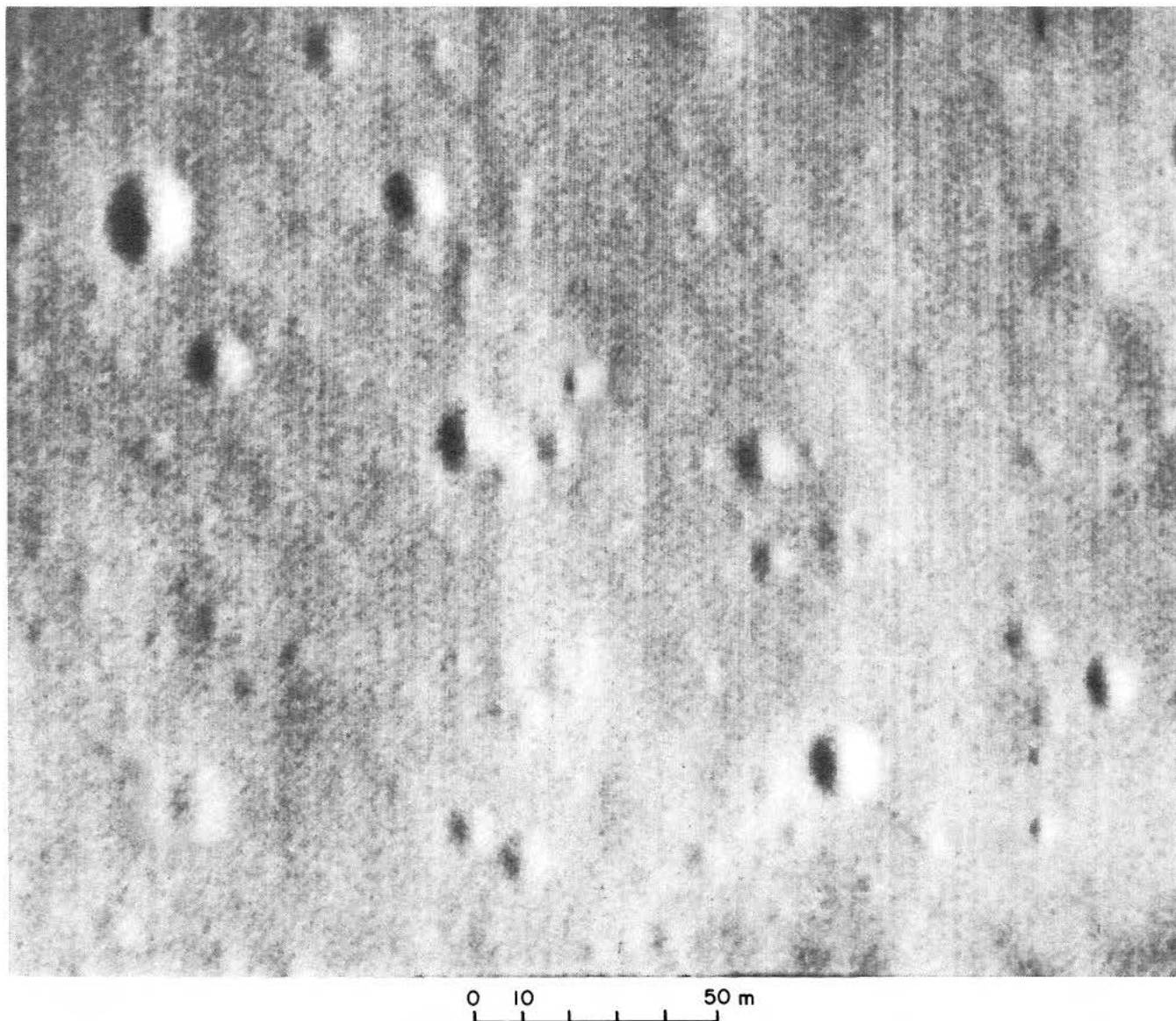
Fig. 50(c). Third-to-last *Ranger VIII* P$_1$ frame (P18), at location c in Fig. 48. (Dimensions 250 × 160 m.)
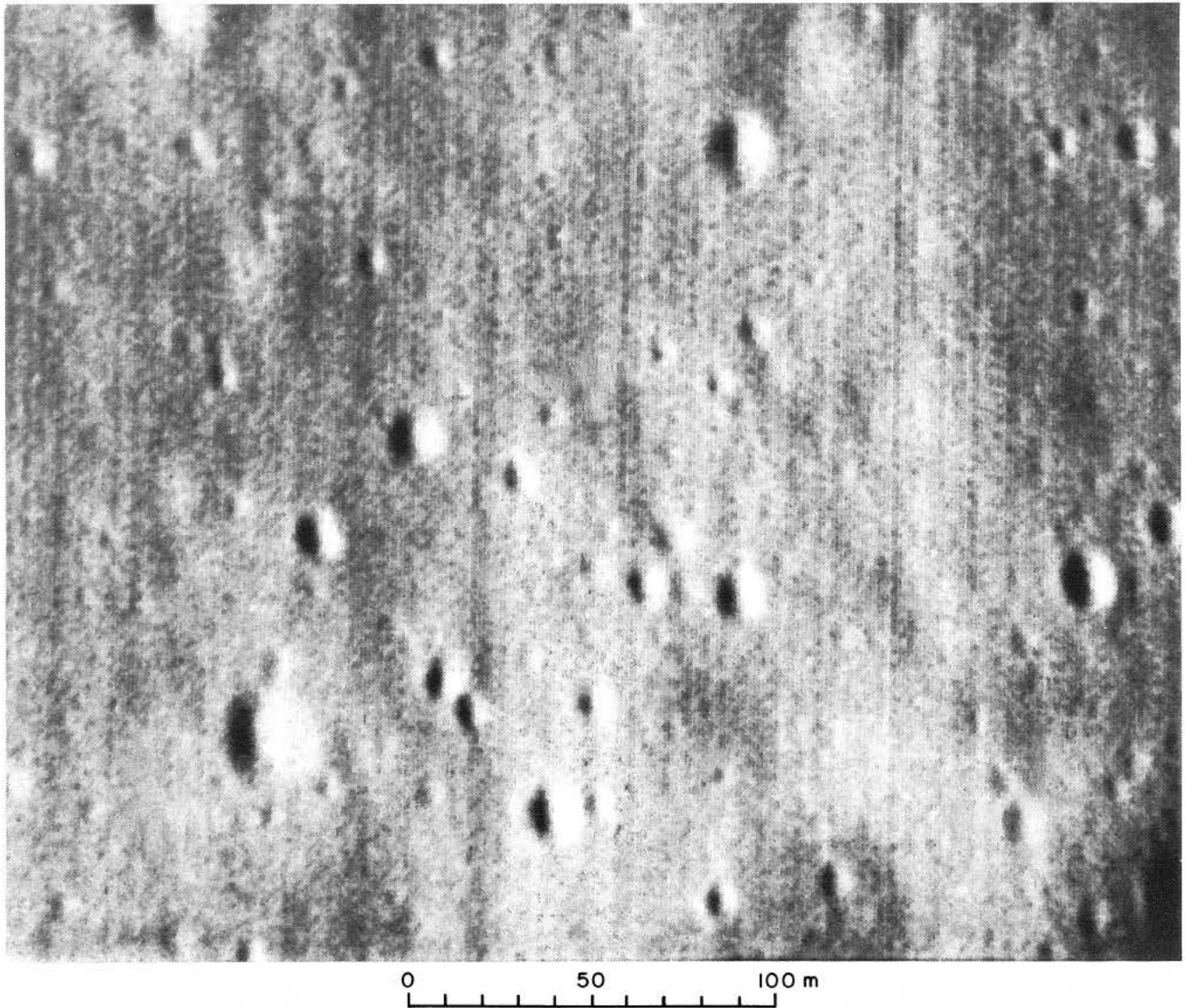
Fig. 50(d). Fourth-to-last *Ranger VIII* P₁ frame (P17), at location d in Fig. 48. (Dimensions 340 × 220 m.)
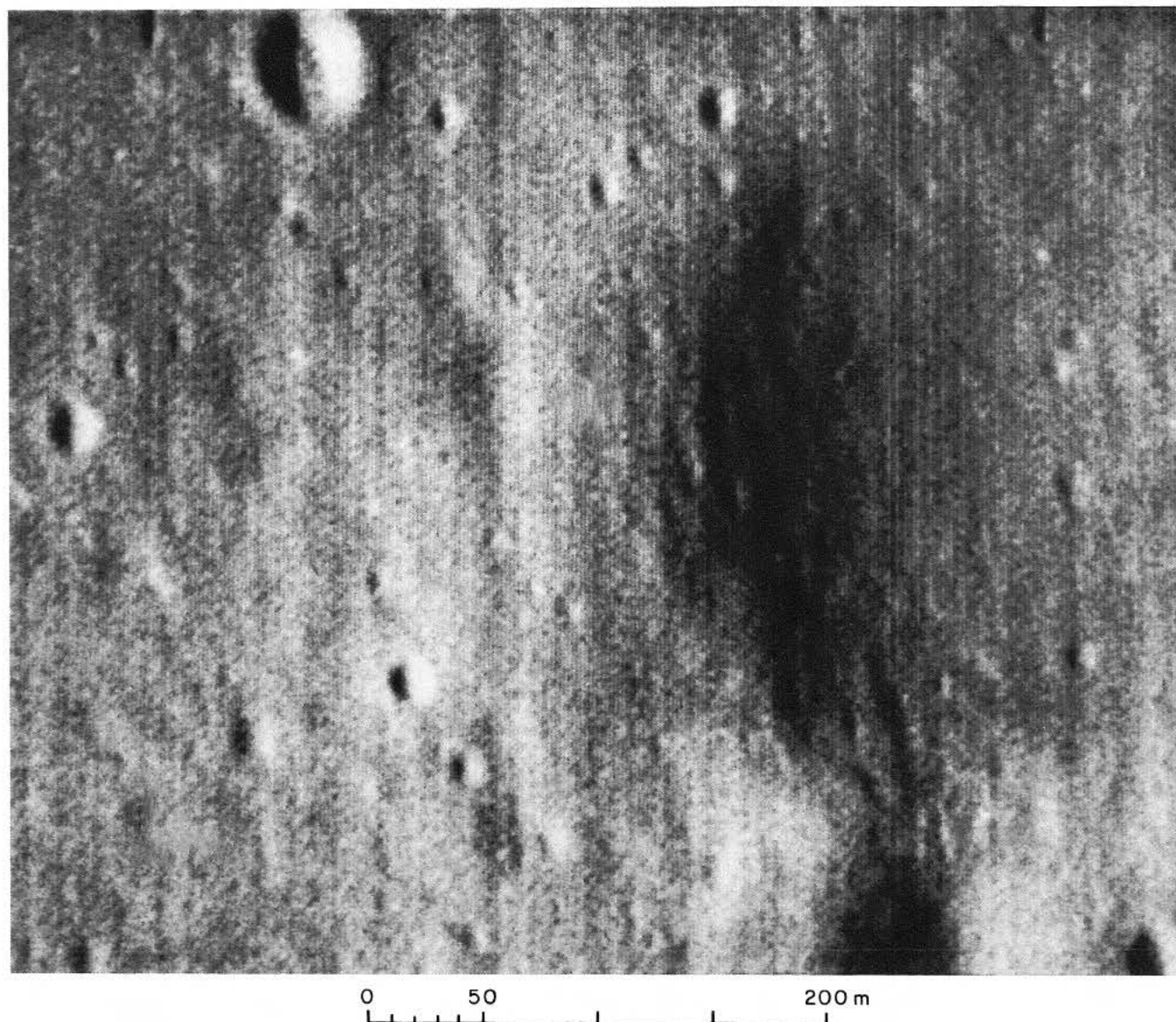
Fig. 50(e). *Ranger VIII* P$_1$ frame (P15), at location f in Fig. 49. (Dimensions 520 × 340 m.)
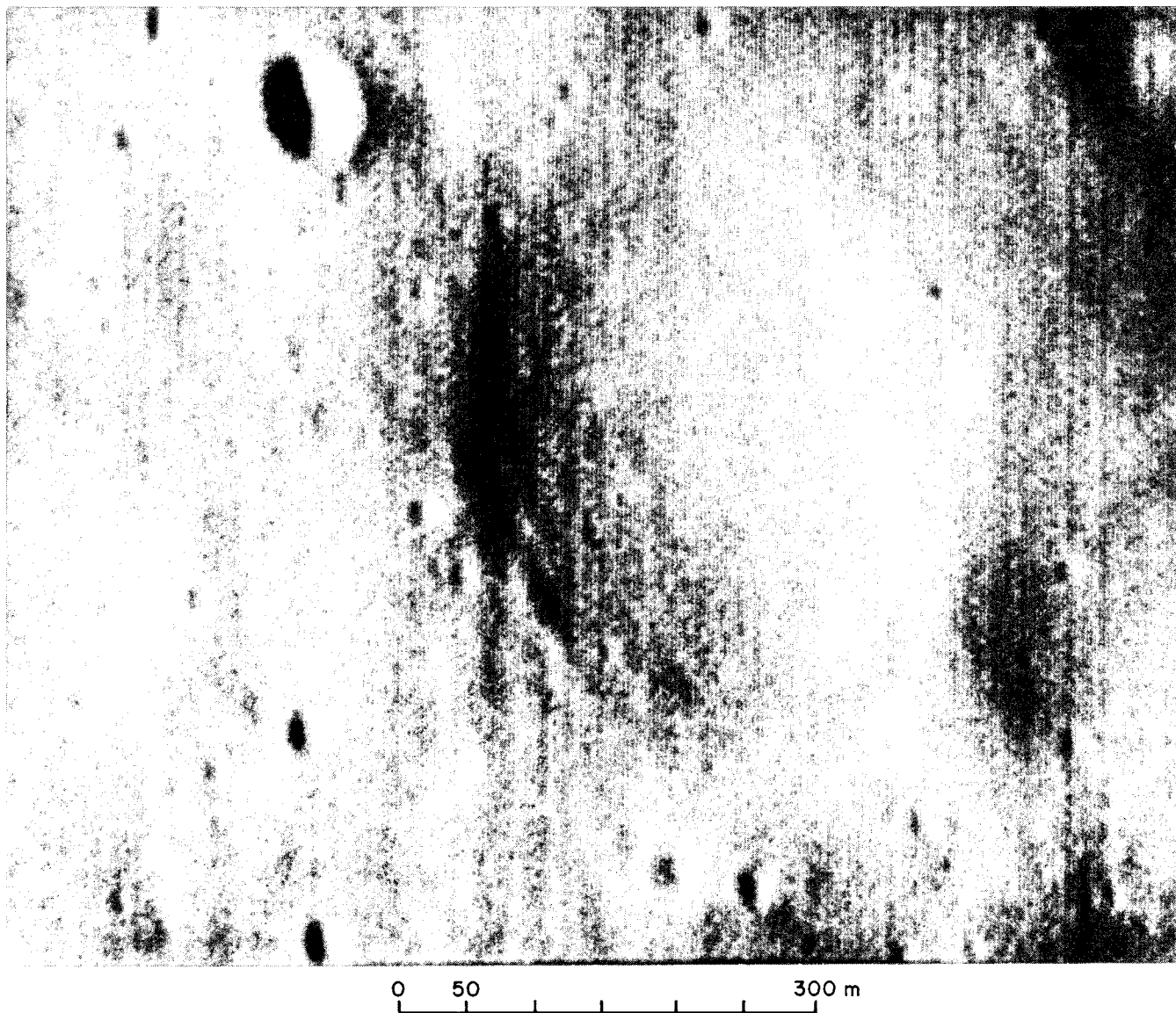
Fig. 50(f). *Ranger VIII* P$_1$ frame (P12), at location k in Fig. 49. (Dimensions 870 $\times$ 570 m.)
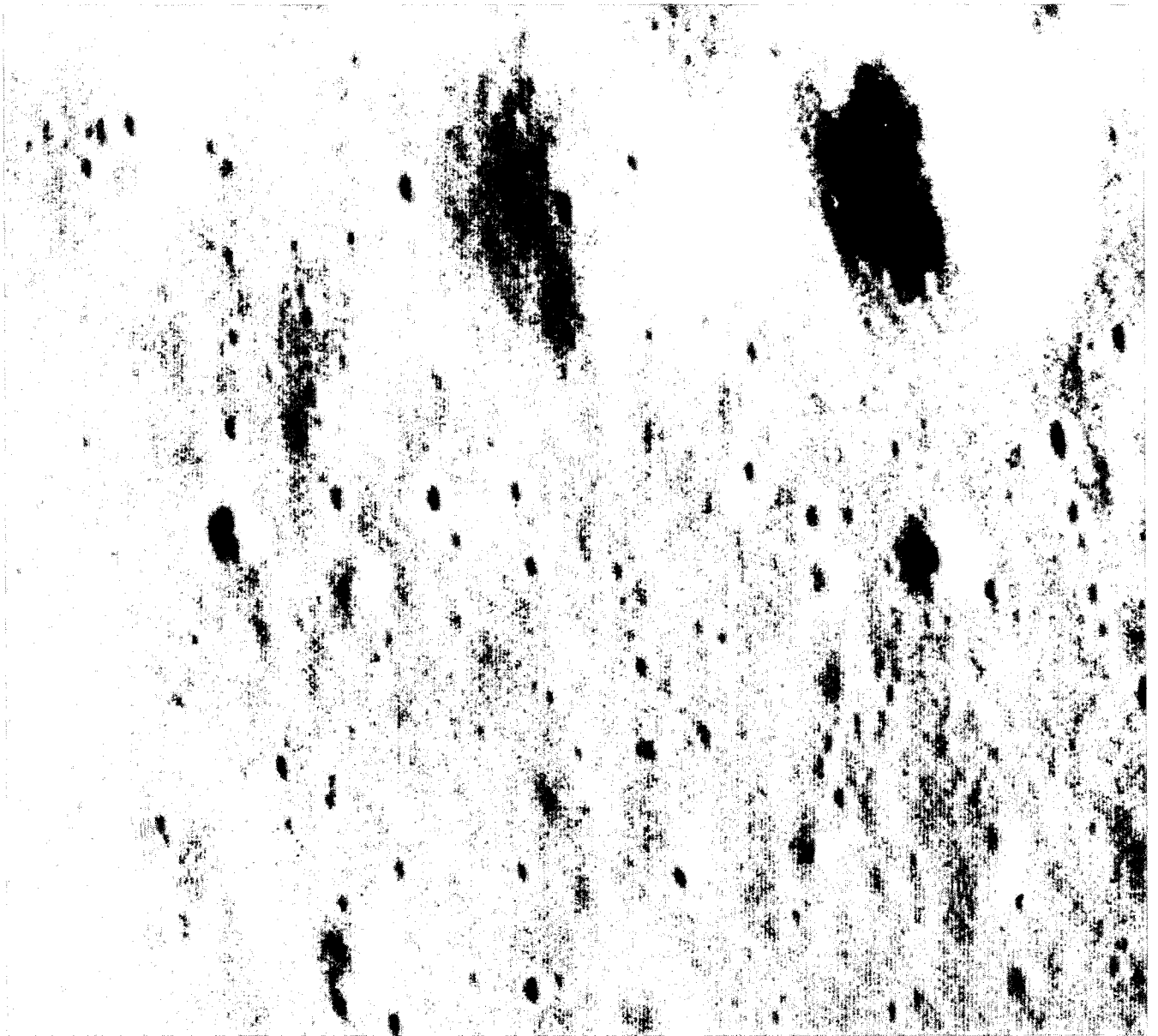
Fig. 51. *Ranger VIII* P_4 frame (P17), showing area between b and c in Fig. 48.
(Dimensions 830 × 590 m.)

0   50   200m
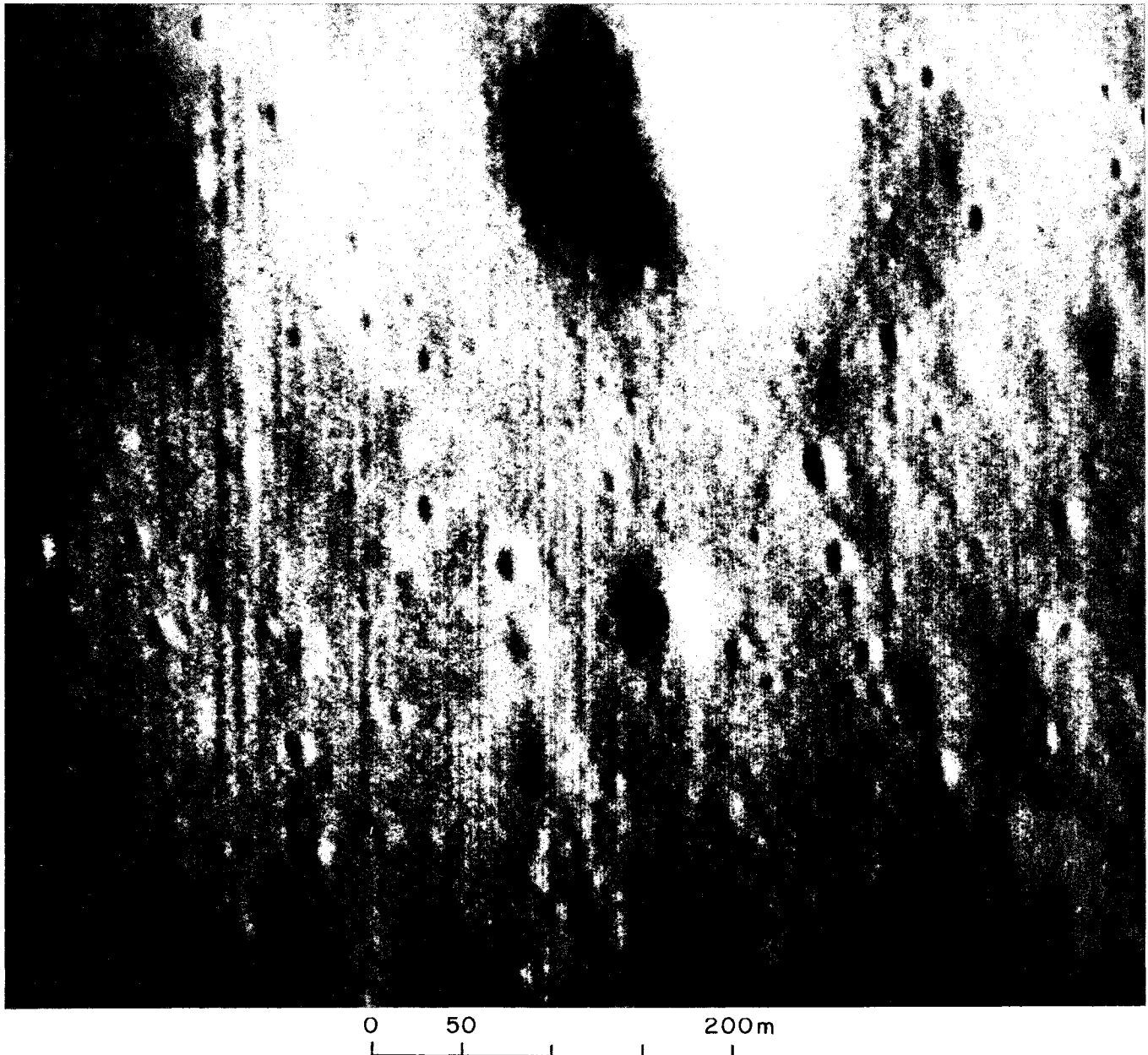
Fig. 52. *Ranger VIII* P$_3$ frame (P18), covering part of Fig. 51 with somewhat increased resolution. (Note dimple
crater showing central dark hole, or cave, also seen in Figs. 51 and 44. Dimensions 640 × 460 m.)

0   50   200 m
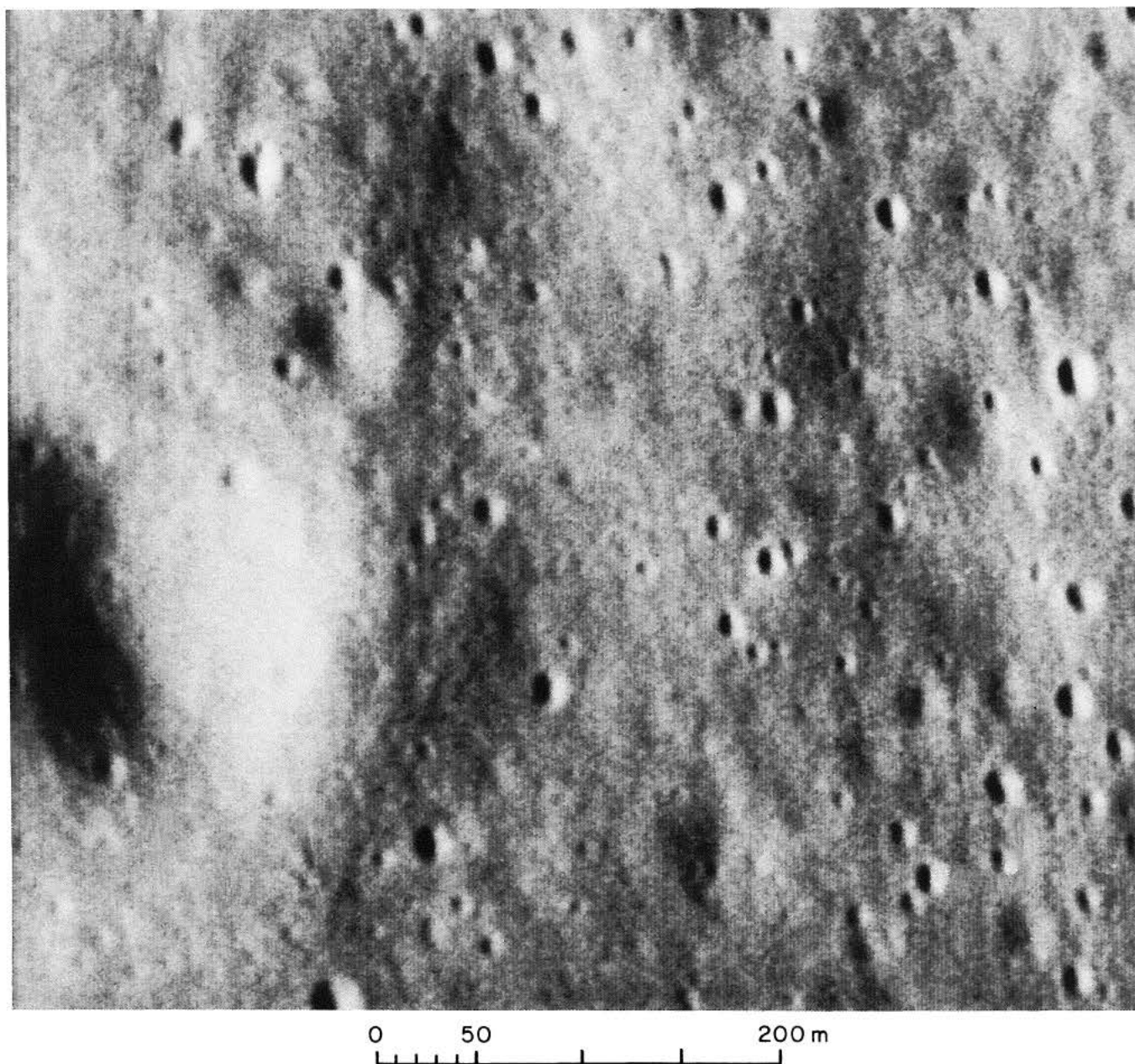
Fig. 53. *Ranger VIII* P$_3$ frame (P18), showing area overlapping Fig. 52, with increased resolution. (Dimensions 560 × 400 m.)
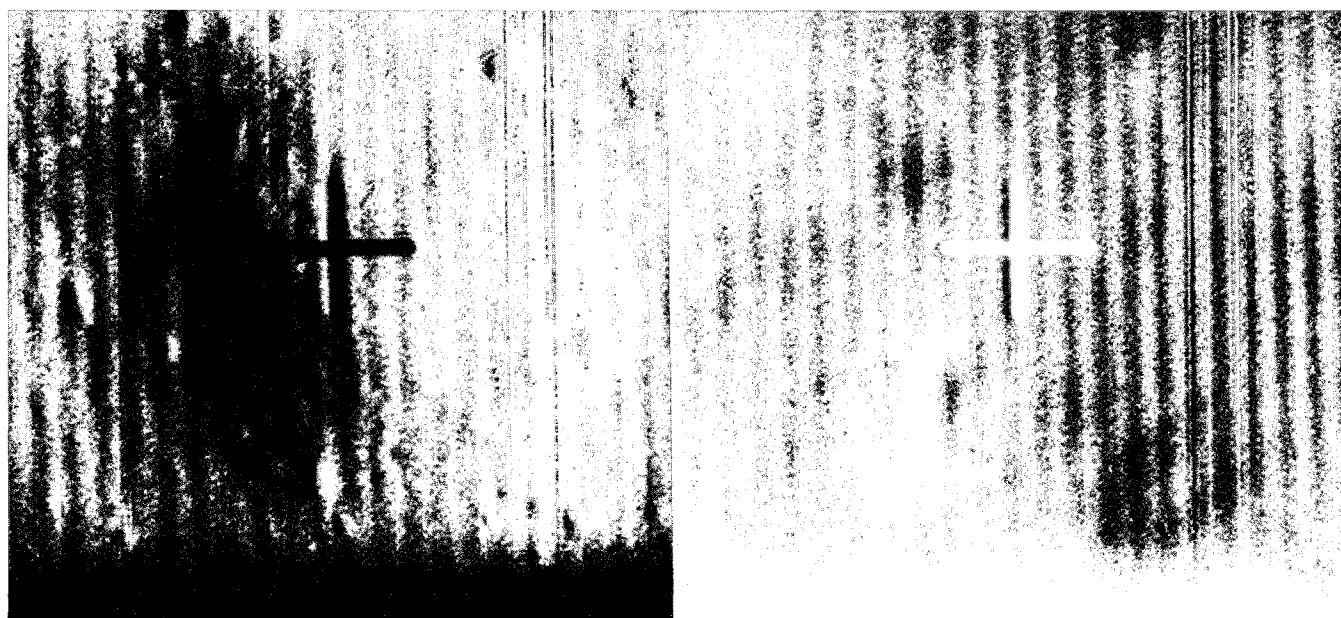
Fig. 54(a). Third-to-last *Ranger VIII* P_2 frame (P18). (Reproduced as recorded, with electronic interference shown.)
(b). Negative of last *Ranger VIII* P_2 frame (P20). [Smeared lunar detail due to spacecraft
motion and comparatively long focus of camera, used as mask
to cut interference in Fig. 54(a).]
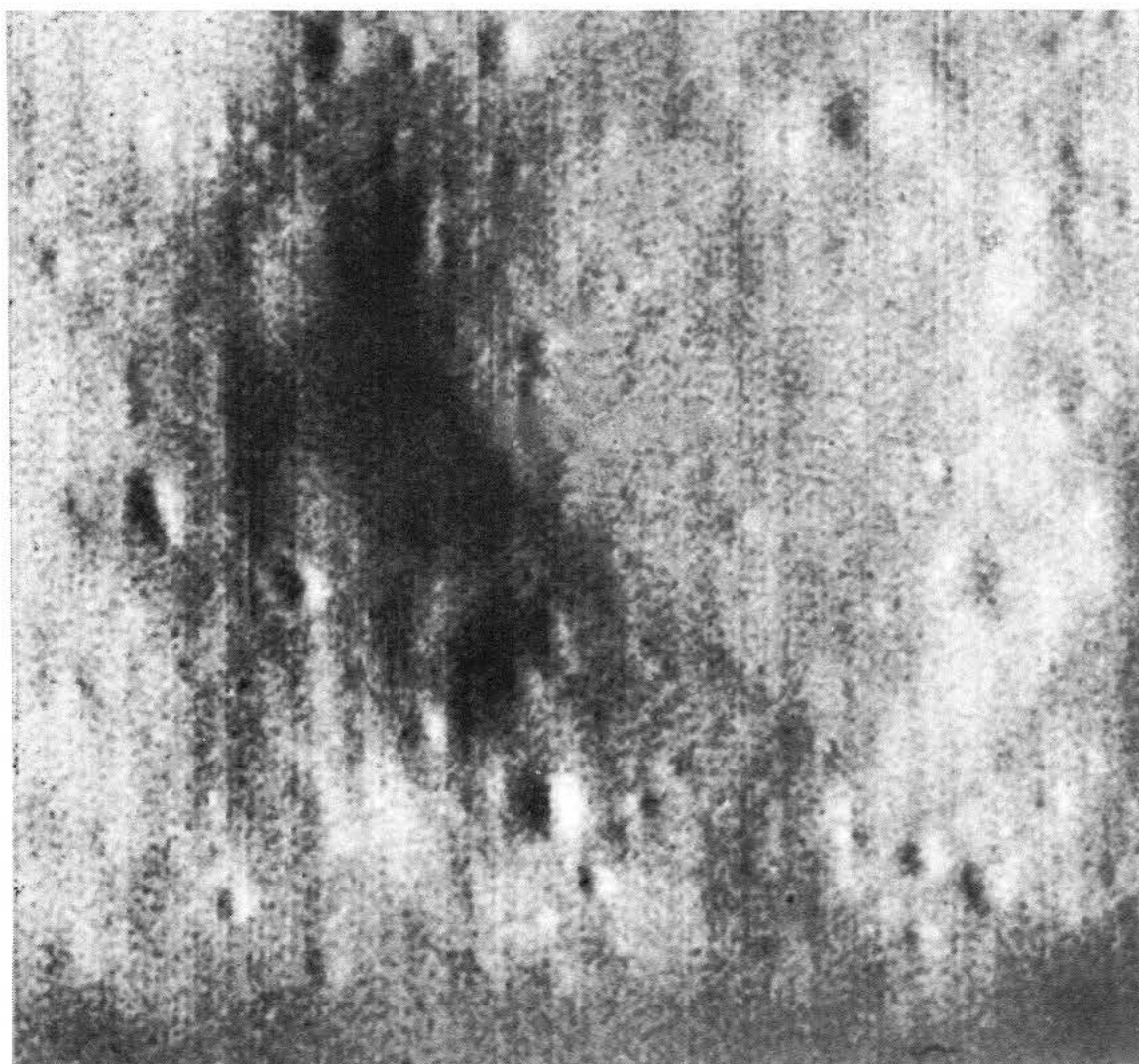
Fig. 55. Same frame as in Fig. 54(a), but printed together with positive mask of 54(b), and after minor retouching of central reticle. (Note pan-shaped depression with rocks on slopes and floor. See Fig. 46 for similar, larger depression. Dimensions 205 × 175 m.)

Fig. 56. Part of second-to-last *Ranger VIII* A frame (A59), showing typical mare floor covered with collapse depressions of varying sizes and depths. (Two coalescing domes, each about 100 m in diameter, occur in lower right-hand corner and several lesser domes on rims of collapse depressions [see Fig. 119]. Dimensions 5.1 [E-W] × 5.4 km [N-S].)
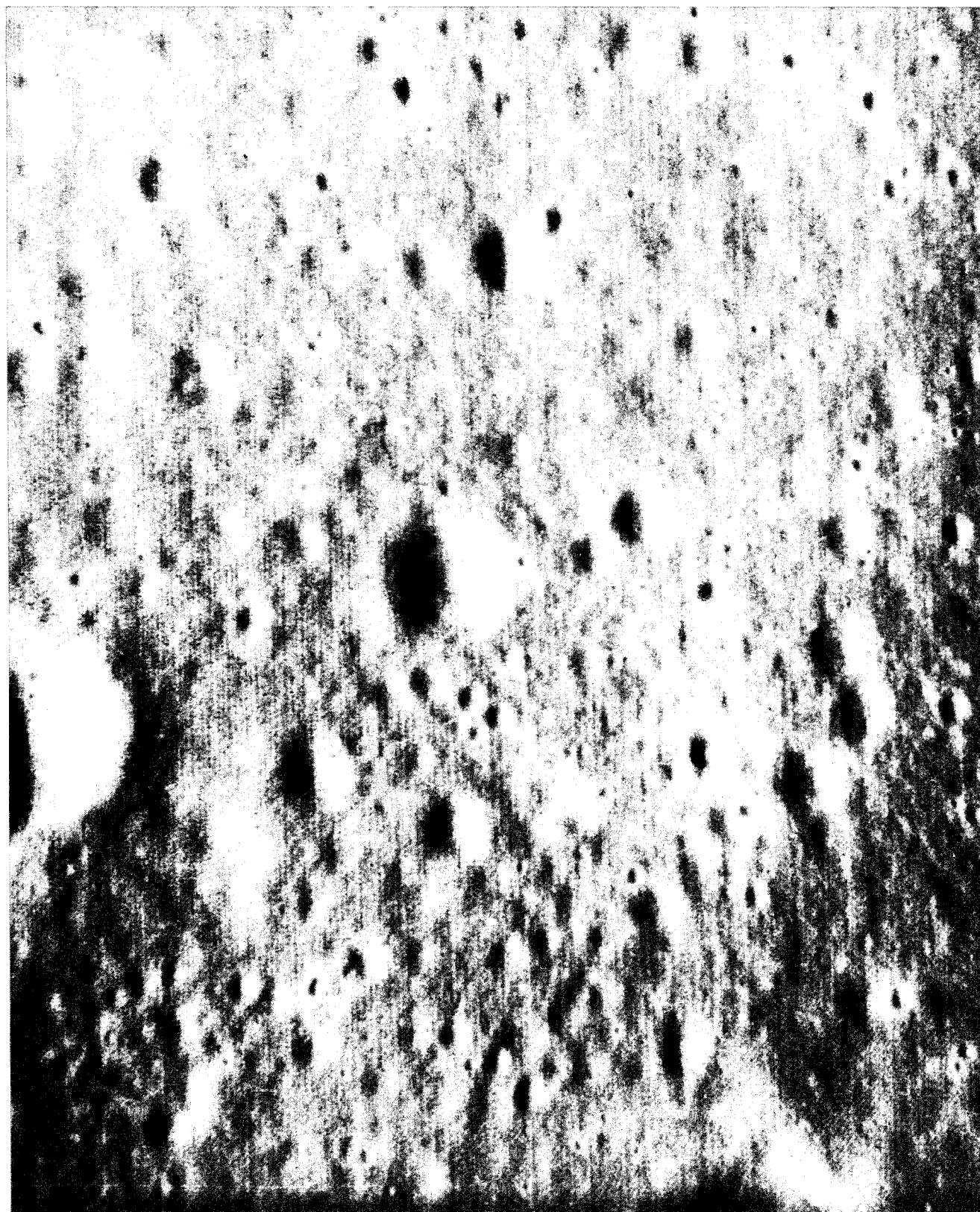
0   0.5   1.0   2.0 km

Fig. 57. Part of third-to-last *Ranger VIII* B frame (B88), showing square depression, shallow linear-beaded depression aligned with grid system, primary-impact crater, and various shallow depressions. (Several low domes are noted, one on floor of square depression, and a double coalescing dome just N, roughly 100 m in diameter. Dimensions 5.0 × 3.0 km.)
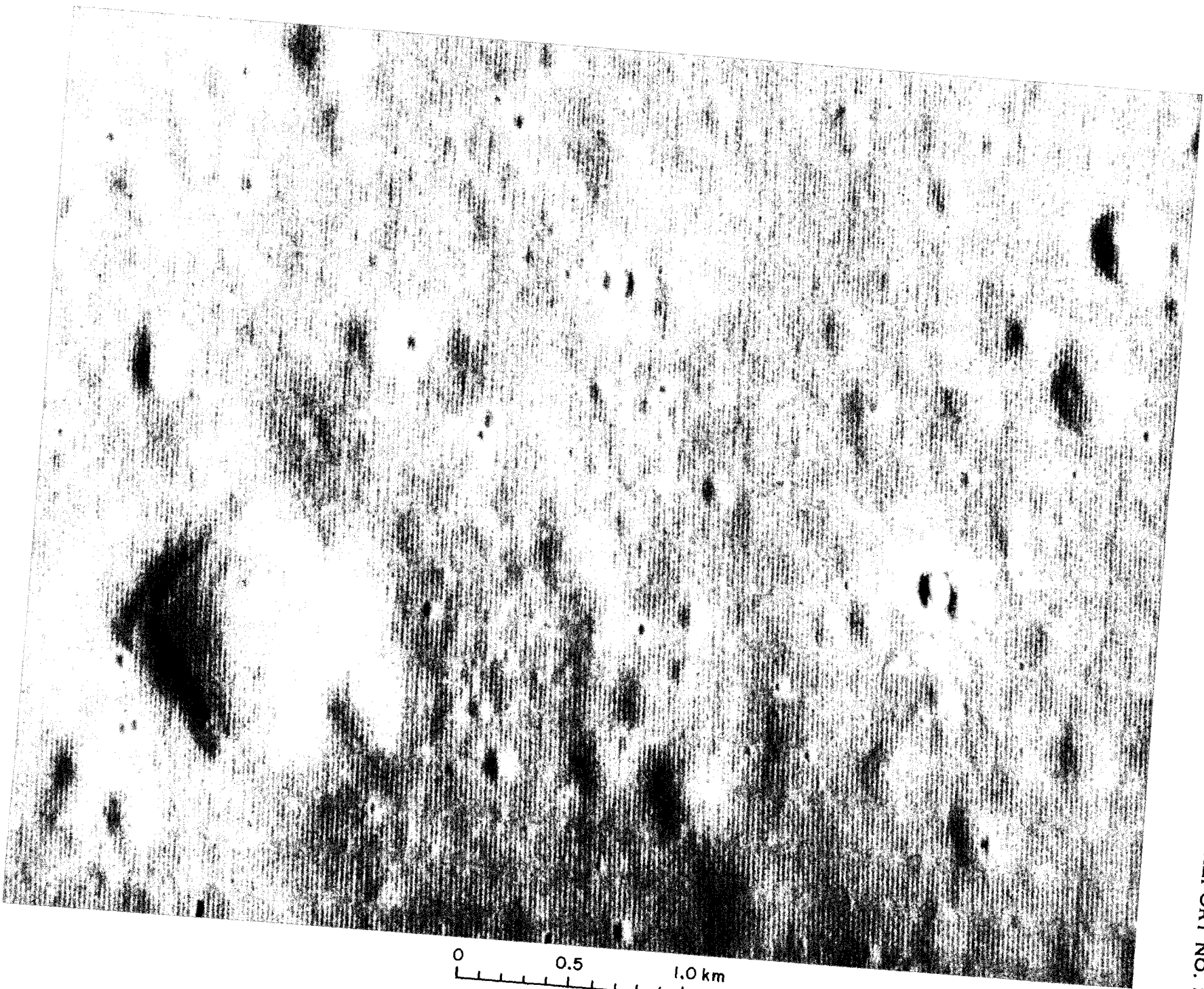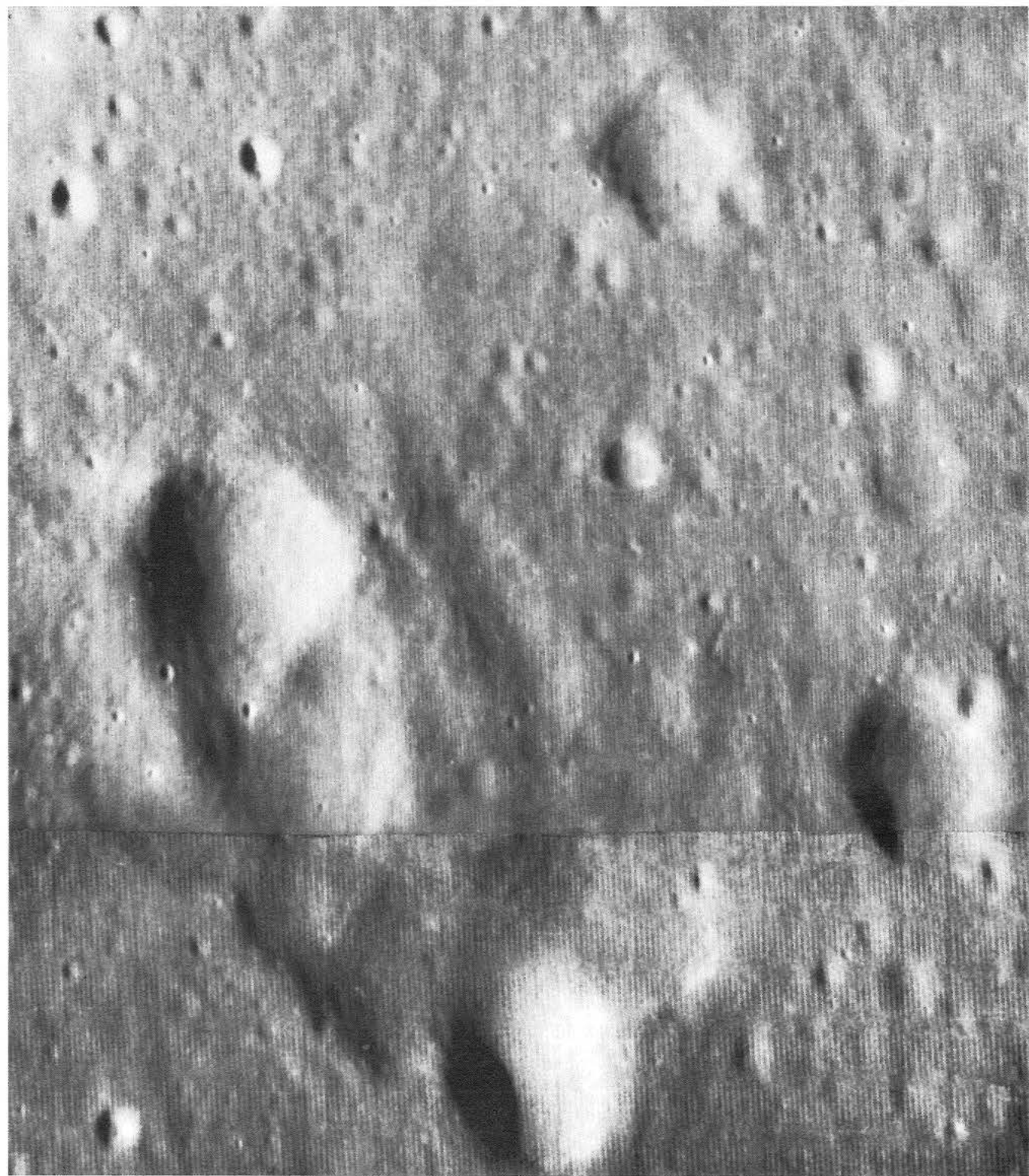
Fig. 58. Mosaic of *Ranger VIII* frames B86 and 87,
showing large irregular depression, two nearly
square depressions (partly shown in Fig. 57),
and smaller detail.

←——

Fig. 59. Full-Moon photograph of part of Mare Tranquil-
litatis, with *Ranger VIII* coverage indicated. (Photograph
shows ray system of Theophilus, which is located
below lower edge of frame. I is impact point.
Four craters are identified: A, Arago;
M, Moltke; S, Sabine; and Ma,
Mädler. U.S. Navy–ACIC
photograph.)

——→
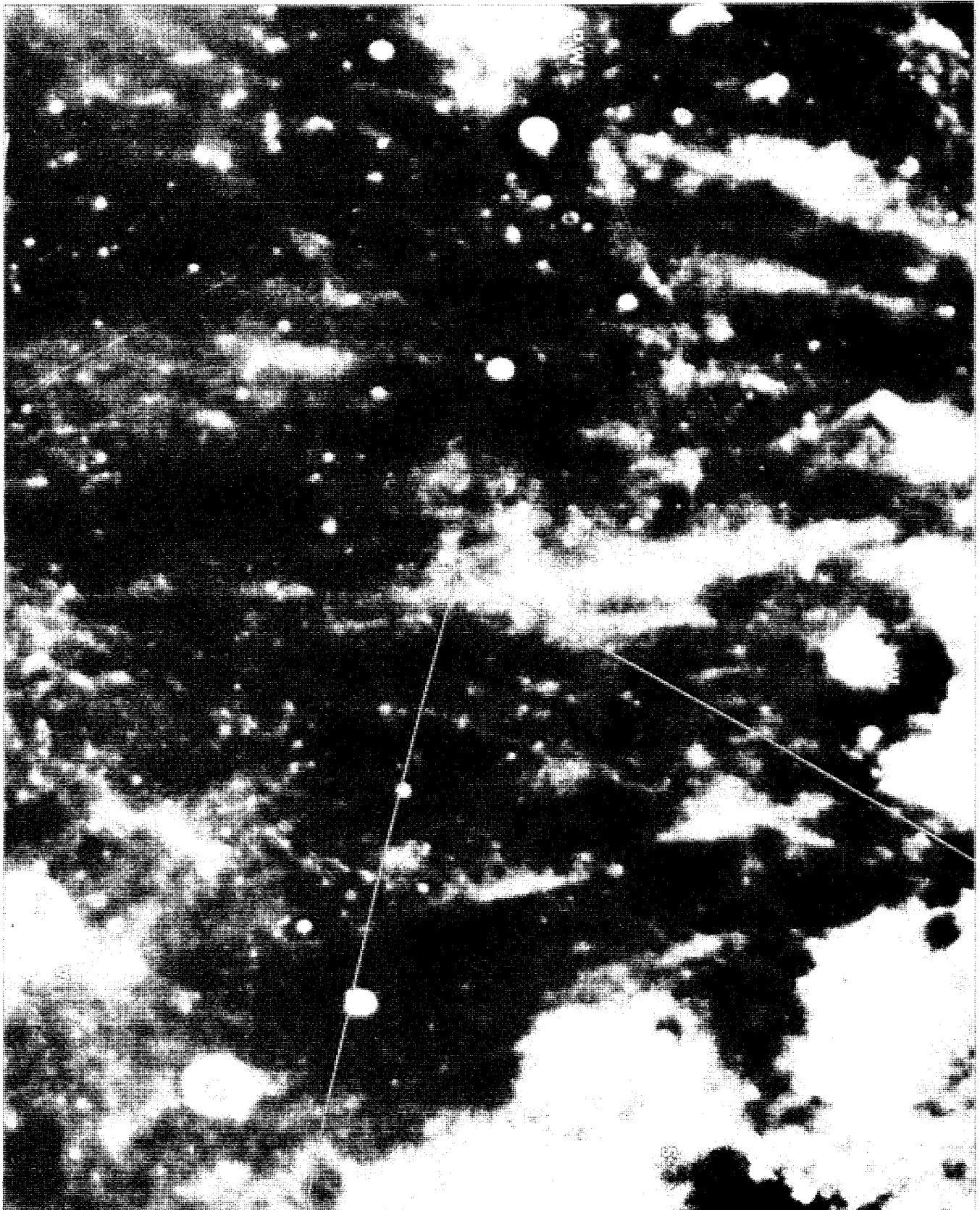
The dimensions of the smallest observable white-halo craters also indicate a small thickness of the low-density layer in Mare Tranquillitatis. Figure 5 shows three such small craters, and a very small fourth one is discernible in Fig. 46, just north of the dimple crater near the northern rim of the large, pan-shaped depression, and confirmed in another frame. The first three craters are about 10, 10, and 8 m in diameter, and the small one is 2–3 m. If the presence of a white halo is attributed to solid rock having been struck, rather than rock froth, then the low-density layer must have been less than 1 m thick near the small crater and less than 2 m near the other three craters.

A thin froth cover on Mare Tranquillitatis may account for the fact, noted above, that several of its collapse depressions have *rocks* on the inner walls and floor, a phenomenon not observed in the other two *Ranger* impact areas.

There is another observation which suggests that *Mare Tranquillitatis has an exceptionally thin insulating cover.* The Saari–Shorthill records show more hot spots there than anywhere else on the Moon. This indicates that larger areas around each crater were laid bare or covered with solid rock fragments by the crater-forming process in Tranquillitatis than in other maria.

Circular depressions on Mare Tranquillitatis are frequent in the diameter range of 100–300 m, but occasional objects have diameters as large as 1 km. Figure 5 shows a typical field, as does Fig. 56, in which one-fourth to one-half of the area is covered with such depressions. Only a few dimple craters occur in Fig. 56, and impact craters are also comparatively infrequent.

In addition to circular depressions, *nearly square, roughly linear,* and *irregular* depressions are found on the mare floor; examples are reproduced in Figs. 57 and 58. The square depressions, like the large circular one in Figs. 46 and 49 (all nearly 1 km across at the outer rim), have peripheral furrows on their floors. Such peripheral furrows also occur in Mare Cognitum (see Ref. 1, p. 51, and *Ranger VII* atlas frame A199). The furrows tend to be linear and parallel to the grid system. These various depressions are probably all due to collapse, but it is not immediately clear whether any outside agent (e.g., debris from, or fractures due to, Theophilus) has contributed to their formation. This question is examined in Section G for four sample areas, with the result that no appreciable number of lineaments, other than those due to the three global grid systems, is found to be

present. However, elsewhere a few linear depressions are roughly oriented toward Theophilus (as discussed below).

Since Theophilus has a weak but rather extended *ray system,* covering essentially all of Mare Tranquillitatis (see Supplement No. 2 to USAF *Rectified Lunar Atlas,* sheets 19C and 13C), the effects of this system on the structure of the mare floor need to be examined. Figure 59 reproduces a full-Moon photograph of the part of Mare Tranquillitatis covered by *Ranger VIII.* The impact (**I**) narrowly missed one of the more prominent Theophilus rays. Two areas shown in Fig. 59 call for special study—the X-shaped feature between Sabine (**S**) and Moltke (**M**), and the ray near the impact point. The former are seen clearly in B54 and adjacent frames, and partly in A43 and adjacent frames. If these two frames, which have nearly the same scale, are viewed stereoscopically, it is found that the ray, apart from brightening the surface slightly, has left no visible marks. *The density and orientation of the collapse depressions do not vary perceptibly across the ray.*

The other area, seen in Figs. 57 and 58, shows no evidence of the effects of the ray. It appears that the Theophilus rays are quite different in structure from those of Copernicus and Tycho described in Ref. 1 (Section III-D). The latter consisted of ray elements that issued from single, or small clusters of, white craters. *No trace of such craters has been found in the case of Theophilus. It is concluded that Theophilus was not formed by a comet but by an asteroidal body.* The distinction between these two classes of impact craters made in Ref. 1 is thus confirmed.

There remains the question of whether any of the large rectangular and grossly linear collapse depressions like those in Figs. 57 and 58 might have been induced by Theophilus. If so, one would expect their directions to conform to the ray system of Fig. 59.

The direction of the ray narrowly missing **I** in Fig. 59 is N 10°W. Region R8-3 lies squarely on this ray, but it has no peak in that direction; the nearest prominent lineament peak is at N 45°W, one of the three global grid directions. The other ray points N 18°W and passes through a corner of test region R8-1, on the side of region R8-2. The former has its main peak at N 40°W, the latter at N 43°W. However, small secondary peaks in the approximate direction of the ray do occur (representing only one and two lineaments, respectively).

A few additional linear-beaded depressions are found, by inspection of the ACIC photomosaics RLC-6 (scale 1:1,000,000), RLC-7 (scale 1:250,000), and RLC-8 (scale 1:100,000),* to be aligned with Theophilus. Among them are three between 20 and 22.5°E longitude and near 0° latitude (seen in Fig. 103 of Section H); however, they align with the diagonal grid pattern as well. Therefore, if Theophilus has contributed to their origin, it is likely to be of the type found in other lunar lineaments: where two lineament systems run parallel, as happens between maria, they reinforce each other, and the lineaments are enhanced. This explanation seems plausible for two further reasons: (1) the depressions occur in a zone of weakness (the Hypatia graben) and (2) they are surprisingly similar in width and appearance to some of the shorter rille-like structures on the floor of the crater Alphonsus (Section E), which are regarded as being due to collapse along fissures. Linear-beaded depressions (crater chains) in a single trough occur also in terrestrial lava fields. Examples are found in Figs. 13, 15 (two cases), 17, 19, 28, 29, 33, 35, 39, and 43. We return to this subject in Section K, in connection with the discussion of Figs. 137–139.

It may be surprising at first that *two types of collapse features* are coexistent on the lunar maria, i.e., the pan- or bowl-shaped depressions with fairly flat, roundish bottoms and the dimple craters. On the other hand, the same is true on the Earth (Figs. 15, 16, 23, and 42). Much of the difference between the two types may be attributed to the difference in their diameters. Both types

---

*Made available to the writer prior to their publication.

appear to be due to drainage of a subsurface lava chamber, with the flat-bottomed depressions caused by the chamber ceiling holding together and the dimple craters by a ceiling so thin that it shattered or folded into a sharp crease (Fig. 44). The assumed origin of the two types is illustrated in Fig. 60.

The *timing* of the Theophilus impact and its ability to effect collapse in Mare Tranquillitatis requires further study. The implication appears to be that the crater formed before the mare interior had solidified fully, and questions are raised concerning the relative date of formation of the Hypatia graben, which is intersected by three depressions; the date of formation of the unusually large central mountains in Theophilus; and the effective date of formation of the grid system in the mare. Presumably, all are very early post-mare.

Figure 61 contains a stereo set of an elongated collapse depression not unlike some of the elongated lunar depressions observed. A curious feature is the raised upper rim, which serves as a warning that a *raised rim does not necessarily imply impact origin.* Apparently, the lava flow domed up before it partly collapsed.

Discussion of the ridge and rille systems in Mare Tranquillitatis and of the craters in the adjacent highland areas is deferred to a later publication. For coordinates, dimensions, and the study of lineaments, reference is made to the excellent AF-ACIC photomosaics RLC-6 to RLC-11, with scales of 1:1,000,000, 1:250,000, 1:100,000, 1:50,000, 1:15,000, 1:5,000, and 1:2000, respectively.

Fig. 60. Vertical sections of lava field before collapse (above) and after (below). (c, collapse depression; d, dimple crater [schematic].)
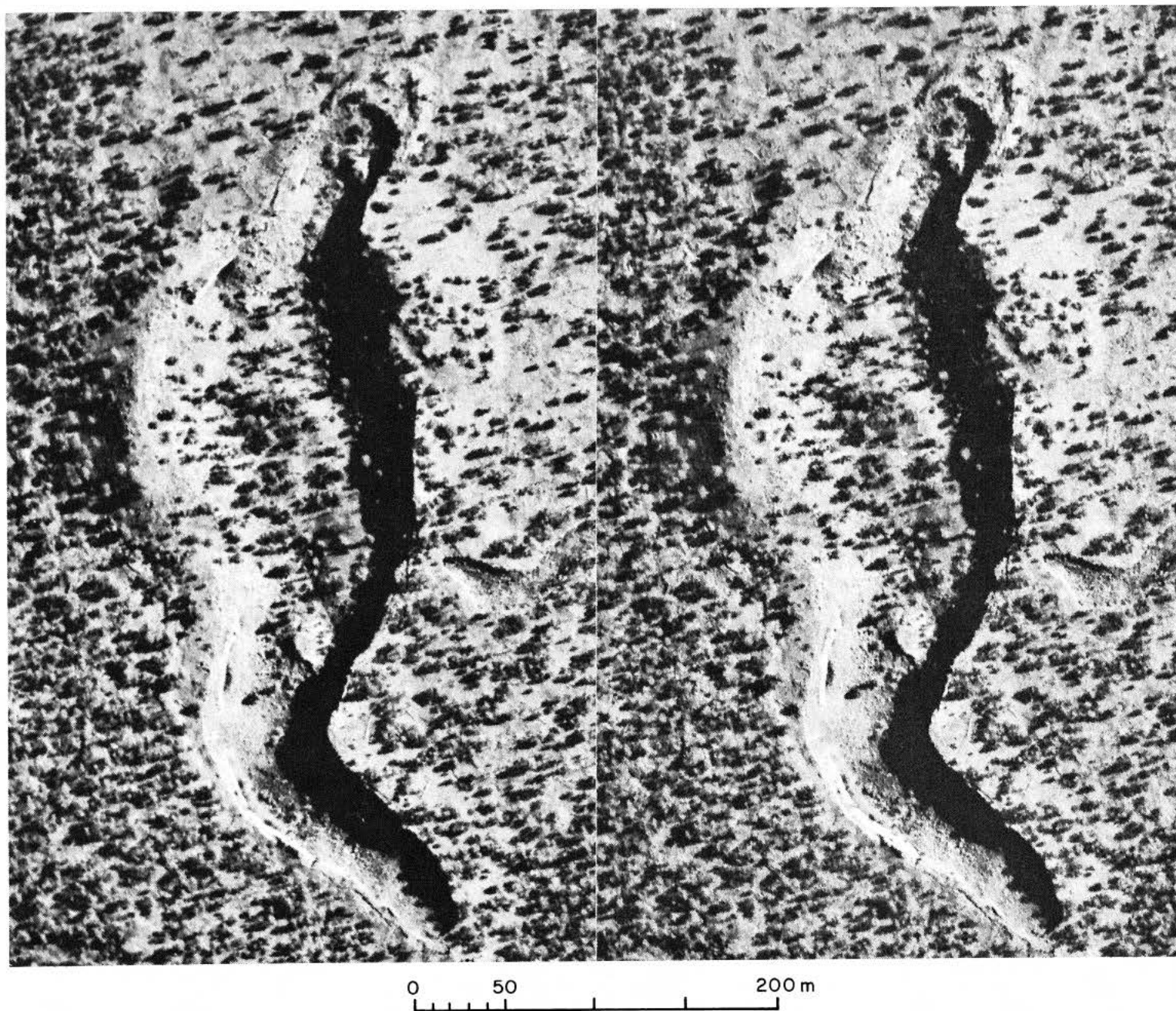
Fig. 61. Stereo pair of terrestrial collapse depression W of Grants, New Mexico. (For stereoscopic viewing, place pair at upper left and lower right. Dimensions 540 × 330 m. U.S. Government photographs.)

E. Ranger IX: *The Structure of the Crater Alphonsus and Surroundings*

The *Ranger IX* records are the most highly perfected of the three sets of *Ranger* photographs, and the photographic atlas summarizing the results is probably the most beautiful astronomical document in existence. The records are nearly free from electronic interference and have the full resolution of the cameras in the focal plane (10–20 μ). The frames have been reproduced with the printing contrast compensating for initial contrast differences, so that remarkable homogeneity has been achieved. The lunar-surface detail shown is infinitely varied and interesting. Because the B-camera fields nearly contained the impact point and the A-camera fields just contained it, the image trailing was negligible for both cameras throughout the mission.

Although some of the records (e.g., Figs. 7 and 8) seem to suggest that the crater walls of Alphonsus are much brighter than the floor, the full-Moon photographs reproduced in Fig. 62 demonstrate that this is not correct and that *the tone differences* in Figs. 7 and 8 *are due to slope differences*. The central peak, however, is indeed much brighter, as are some "perfect" impact craters. The dark-halo craters and Mare Nubium stand out as dark patches. The floor of Ptolemaeus seems slightly darker than its surroundings, but only because of the lesser frequency of small, bright patches. It is curious that, although the floors of the giant craters are structurally mare-like, they have the albedos of highlands (see also Fig. 12).

The area covered by *Ranger IX* contains the large craters Ptolemaeus, Alphonsus, Arzachel, Albategnius and Hipparchus, nearly in the center of the lunar disk. These craters may be examined *stereoscopically* on matching pairs drawn from the *Ranger IX* A- and B-camera series (e.g., A14 + B1, A15 + B2, A16 + B4, A28 + B12, A40 + B20, etc.), from *Rangers VII* and *IX*, from *Ranger VII* and Earth-based photographs, and from *Ranger IX* and Earth-based photographs. It is found that the floor of Ptolemaeus is high above the floor of Alphonsus (and of Mare Nubium), and that of Alphonsus is above Arzachel's. Numerous small lava lakes are observed at various levels between these giant craters, including some in the Alphonsus walls, high above the crater floor. Photogrammetry based on these beautiful new data is still to be performed.

According to their wall structures, the five large craters appear to be late pre-Imbrium, although their floors were affected by flooding that apparently occurred in the post-Imbrium period. For instance, the central spine on the Alphonsus floor was, according to its orientation, structurally determined by the Imbrium impact. Thus, the flooding of the Alphonsus floor was local in nature, with the pre-Imbrium substructure partly remaining. The lineaments on the crater floor, analyzed in Section G, confirm these relative dates.

The *Ranger IX* impact point and camera orientations were selected so as to acquire maximum information on (1) the central peak of Alphonsus, a "white" mountain suspected of having experienced eruptions; (2) the several dark-halo craters and the associated rilles on the floor; (3) the crater walls; (4) interrelations between the five large craters and their surroundings; and (5) the nature of the crater floor.

We shall now summarize tentative conclusions drawn on these topics:

1. *The central peak* is well shown in Fig. 10 and, on a much larger scale, in A61–67 of the *Ranger IX* atlas (for maximum visibility best viewed stereoscopically in consecutive pairs). The coordinates, orientation, and dimensions may be obtained from the ACIC photomosaic, RLC-14 (scale 1:250,000). At the base, the mountain measures about 8.5 km in the northwest–southeast direction; the crestline is some 4 km long; and the height is approximately 1150 m.

   The shape of the mountain is seen well in near-horizontal views of a three-dimensional model made

Fig. 62. Full-Moon photograph of Alphonsus–Ptolemaeus area. (Dark patches on floor of Alphonsus outline deposits by dark-halo craters. Central peak of crater is shown bright, but crater walls have albedo similar to that of crater floor. See Figs. 3 and 9 for identification. U.S. Navy–ACIC photograph.)
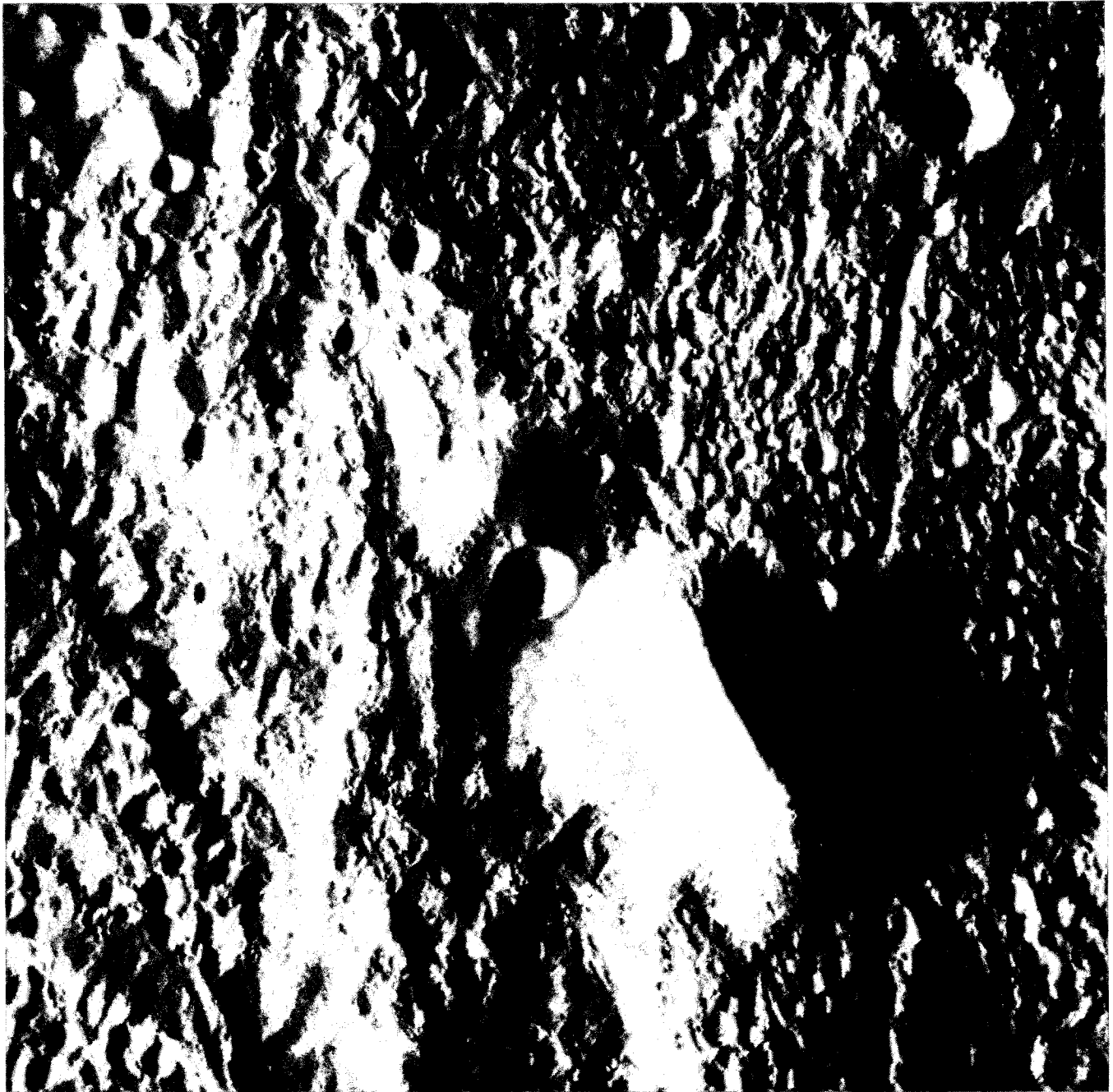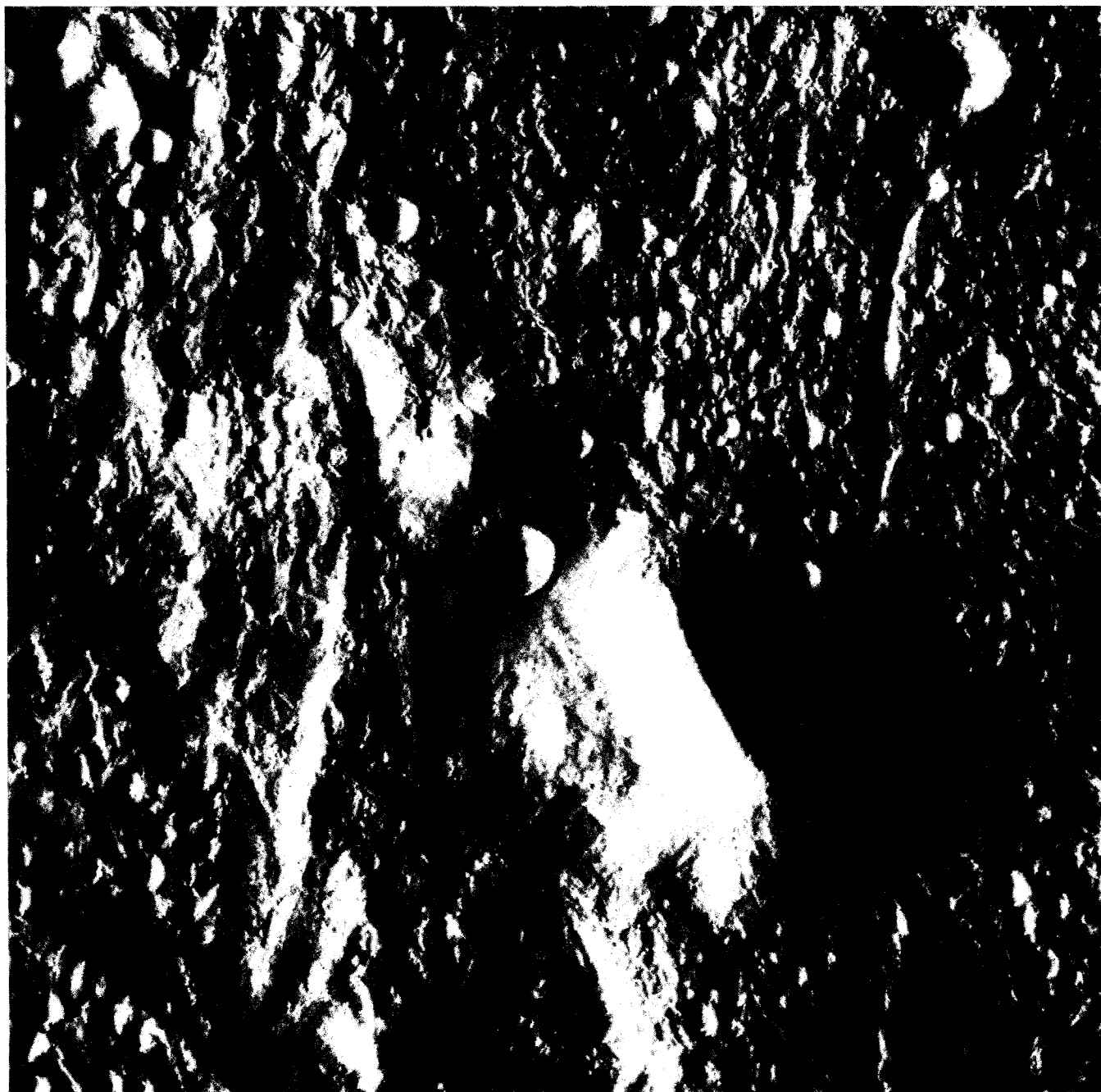
Fig. 63. Stereo pair of scale model of Alphonsus peak area, with evening illumination to match *Ranger IX* aspect. (Model by R. Turner.)

by R. Turner of LPL. This model was based on all available records—*Ranger* and Earth-based—of the area, rectified with the aid of the orthographic grid. The elevations were derived from shadow lengths and the photometric characteristics, which were simulated by using a large laboratory stand with adjustable parallel lights. The model measures 120×120 cm and has a scale of 1:21,000. The vertical views are about 18×18 cm, with a scale of 1:140,000. The model is first shown vertically, as viewed from *Ranger*, but with three different illuminations: in Fig. 63(a) and (b), a stereo pair, it is illuminated as in the *Ranger IX* records; in Fig. 64, from the opposite direction; and in Figs. 65 and 66, from the north and south, respectively. Figure 67 shows two near-horizontal views from the northwest, from somewhat different elevations. Figure 68 is a view from the north, Fig. 69 from the south-southwest, and Fig. 70 from the west, with the light coming from the east.

Several conclusions may be drawn. The visibility of topographic detail depends critically on the height and azimuth of illumination. While Fig. 63 closely matches *Ranger IX* frames A63 and A64, the general illumination of Fig. 64 is required (with Earth-based data used to fill gaps) to show the central peak obliterating the rilles on its east flank. The rilles are all but invisible with the light coming from the north or south (Figs. 65 and 66). This suggests that there is a serious deficiency in our knowledge of east–west rilles and ridges on the Moon.

The views in Fig. 67 are probably those traditionally assumed for the central peak, but one would not readily be prepared for the aspects in Figs. 68, 69, or 70. Figure 68 illustrates the difficulty of grasping, from low-altitude views, the general terrain structure (compare with Fig. 64). Figure 70 shows surprising aspects of the central peak. By comparison with the surrounding terrain, the central mountain is nearly featureless, as if it were covered with snow. (The white appearance is in part due to contrast; the reflectivity is only about 25%, vs. 10% for the surroundings.) The dense cover of collapse depressions seen on the crater floor is absent from the peak down to its base. No major caldera is present; only minor features, less than about 200 m in diameter (one just east of the crestline, well below the summit) are seen in frames A65 and A66. Very small crest craters are not uncommon on the lunar white mountains.

In the *Ranger VII* Experimenters' Report (Ref. 1, p. 71), a brief reference was made to the white mountains and their presumed volcanic origin. A detailed comparison of lunar and terrestrial volcanic white mountains was published later (Ref. 13); Fig. 71, a photograph from this publication, illustrates the remarkable appearance of these mountains before the rains dissolved the sublimate. The lunar vacuum will selectively remove many volcanic sublimates but will probably leave some of them ($PbCl_2$, MgO, CaO, etc.) almost indefinitely. Infrared spectroscopy (a program now underway) may provide a definite answer to this intriguing problem; if so, it will have led to the first lunar chemistry.

2. The entire *Alphonsus rille system* and all *eight prominent dark-halo craters* are seen in Figs. 9 and 10, with parts of them shown on a larger scale in Figs. 7 and 8. For a step-by-step coverage at intermediate scales, reference is made to the *Ranger IX* atlas.

The eight dark-halo craters are placed squarely on the rilles and must therefore be associated with them rather than being due to impact. They have ejected thin blankets of dark material that have partially filled the rilles. The blankets can be studied in detail on the three craters covered by Figs. 7 and 8, and in the mosaics that have been prepared of the most suitable records, reproduced in Figs. 72 and 73.

The dark deposits have no sharp boundaries, although some terracing can be seen, which indicates that the deposits are explosive debris, or ash, rather than lava. This conclusion is confirmed by the occurrence of clusters of small craters and grooves (diameters about 25–30 m), as in Figs. 72 and 73. Their presence indicates that substantial blocks were ejected by the craters along with finer material.

Since the radii of the deposits vary from about 3 to 7 km, the velocities of ejection must have been of the order of 100 m/sec. (This velocity yields $r = 6$ km on a 45-deg ejection trajectory and $r = 3$ km on 15- or 75-deg trajectories; the range r is proportional to V^2.) The craters themselves average 2 km in diameter, and the volumes of the deposits and of the craters appear to be comparable, as is seen in the Addendum to this Section (prepared by R. Le Poole). The two craters shown have no elevated rims and exhibit radial slumping bands on their inner slopes.
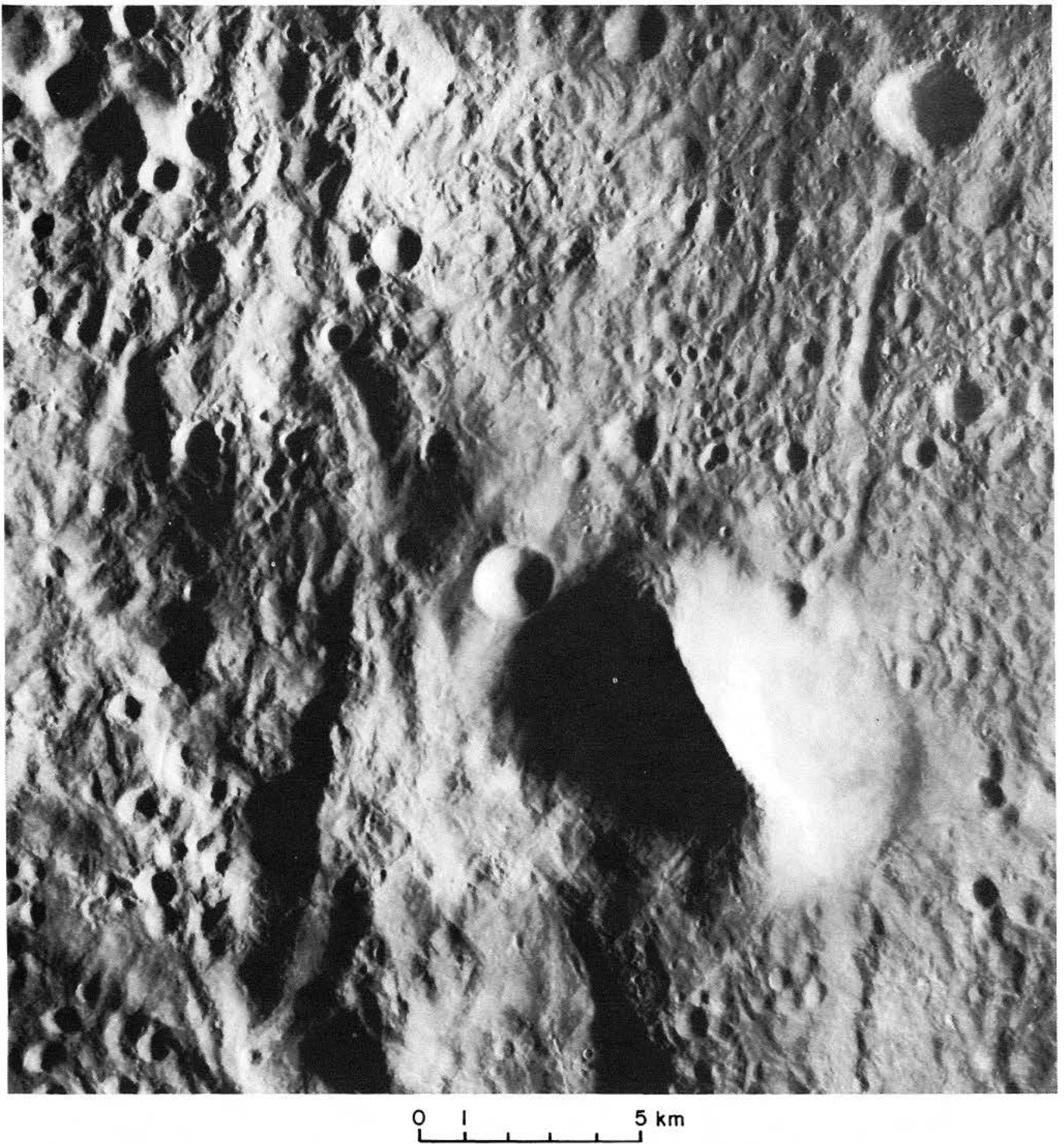
Fig. 64. Same as Fig. 63, but with morning illumination. (Note obliteration of rilles E of peak.)
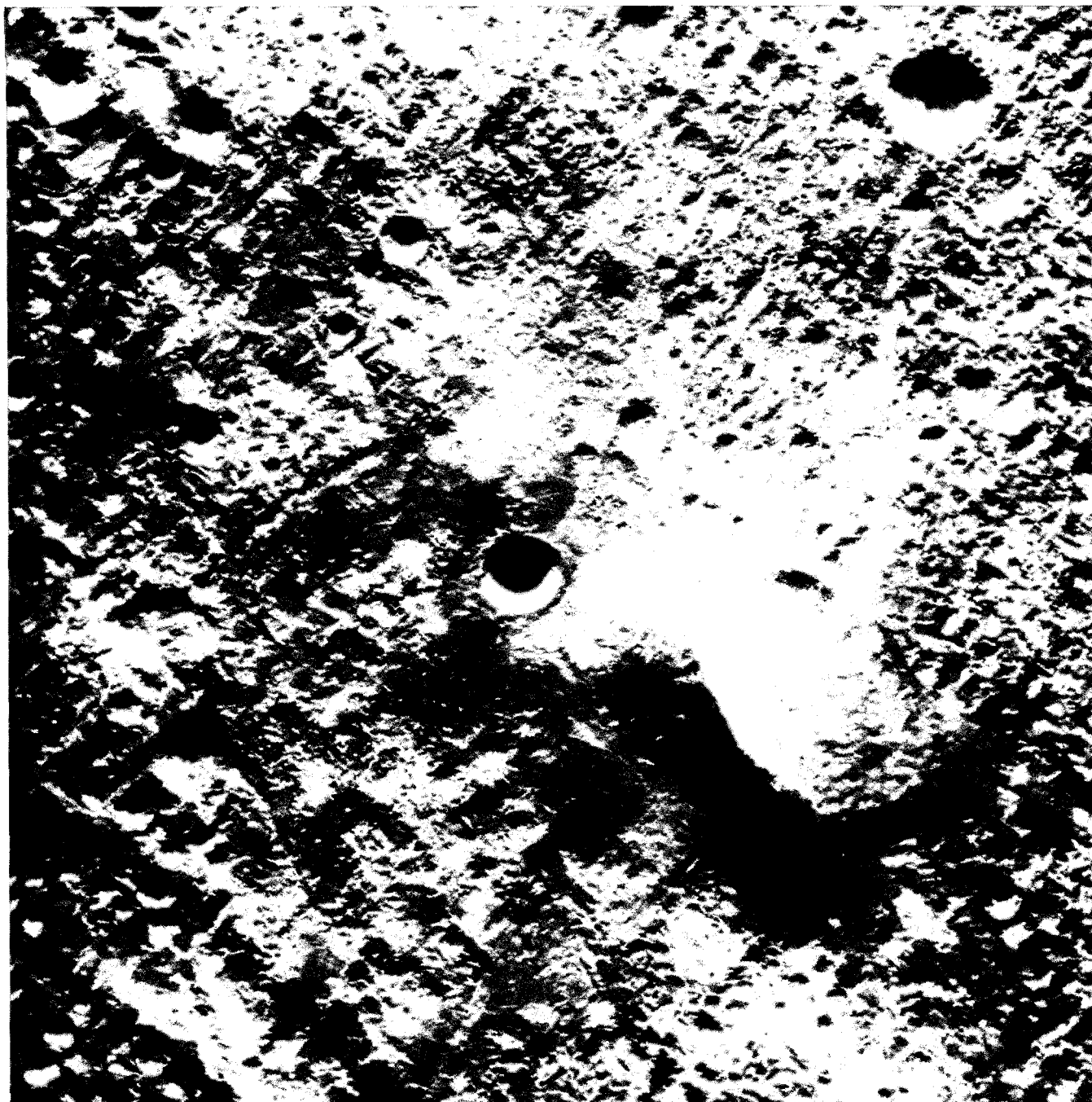
Fig. 65. Same as Fig. 63, but with N illumination (never realized on Moon) to verify directional effects in visibility of rilles and other structural units. (N–S rilles have become nearly invisible.)
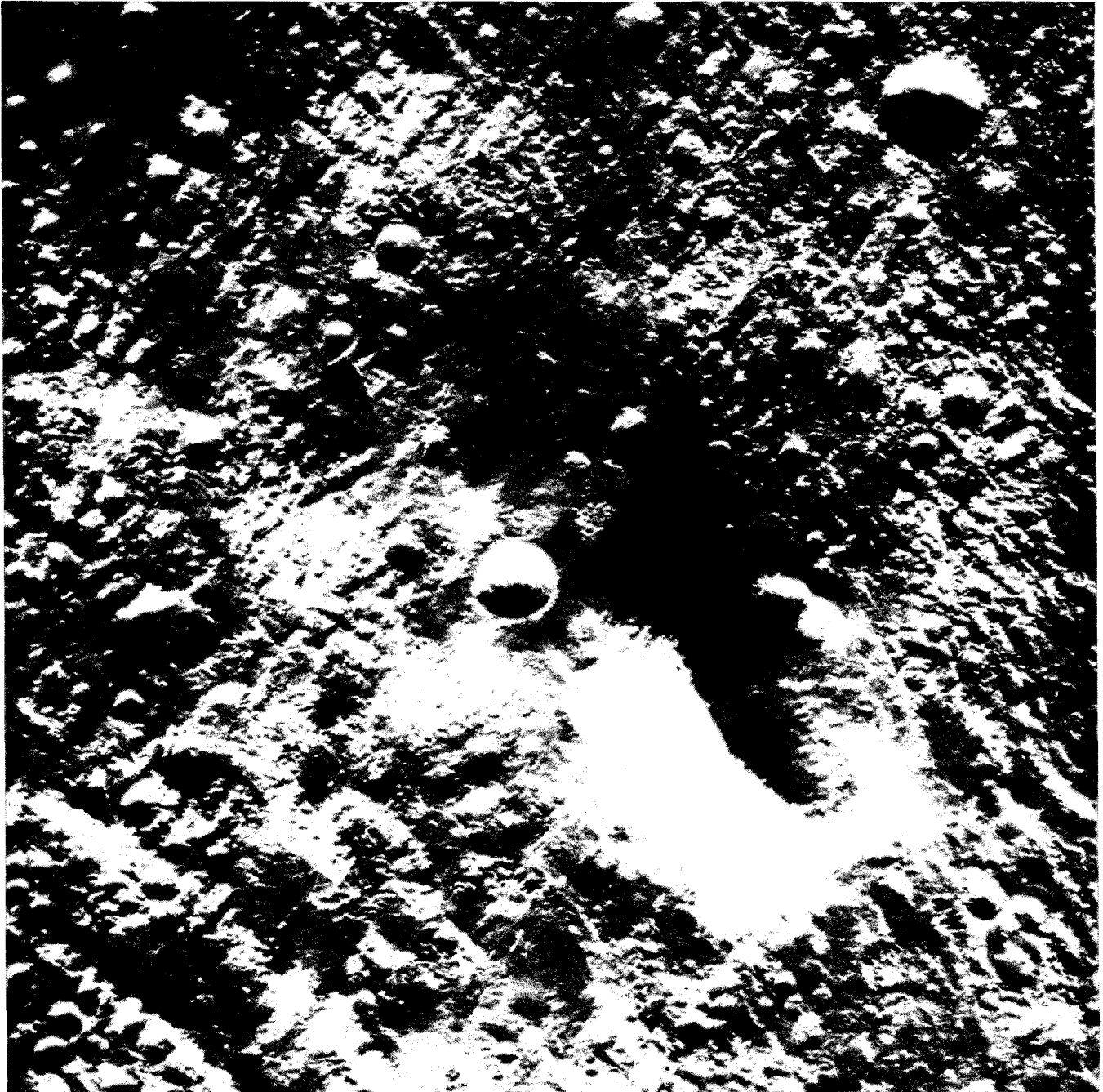
Fig. 66. Same as Fig. 63, but with S illumination.
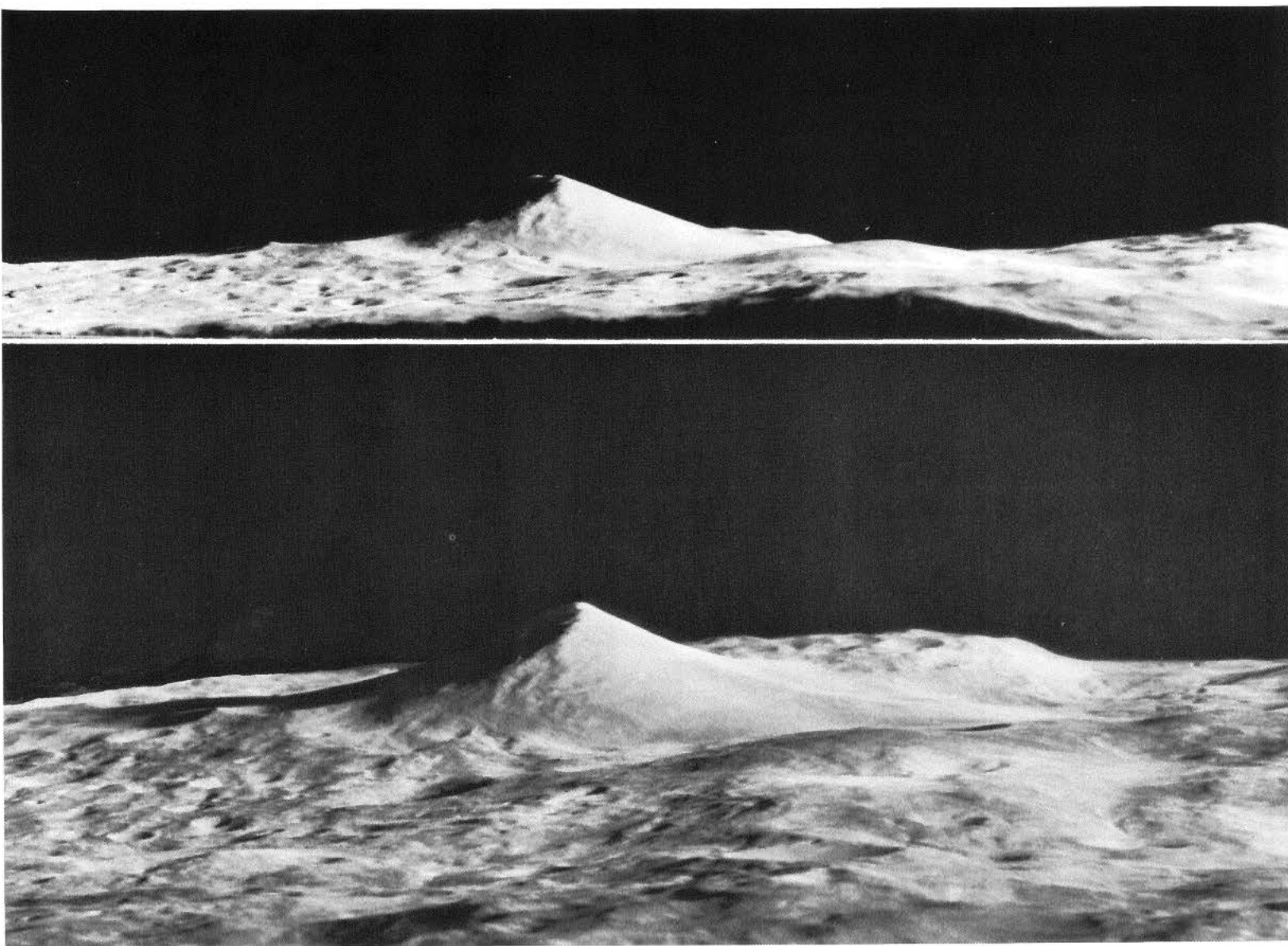
Fig. 67. Two nearly horizontal views of Alphonsus peak, seen from NW, with somewhat different elevations.
(Note invisibility of large crater at right in upper view.)
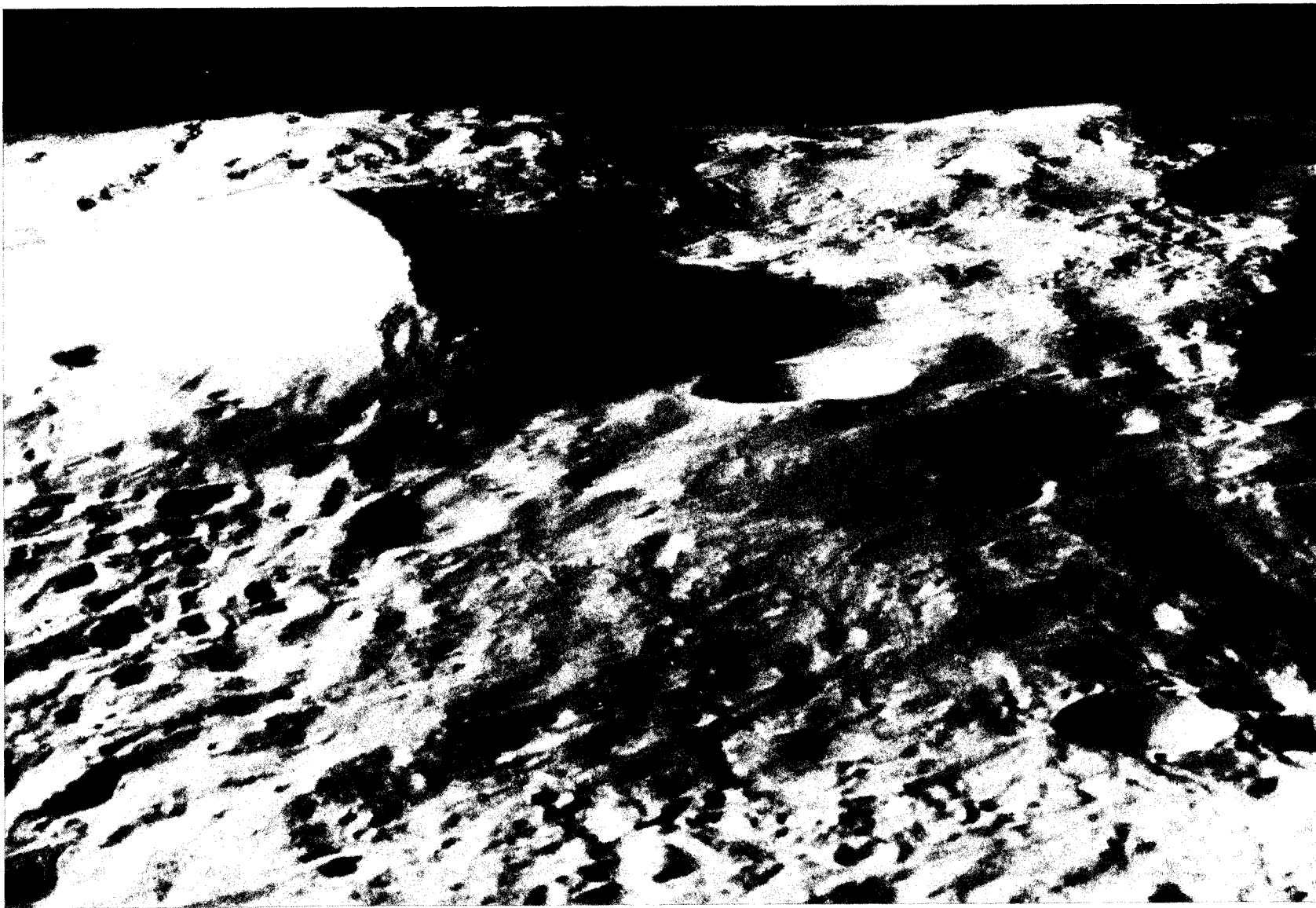
Fig. 68. Alphonsus peak region, seen from N under E illumination. (Valleys with scarps at right are part of central spine of crater.)
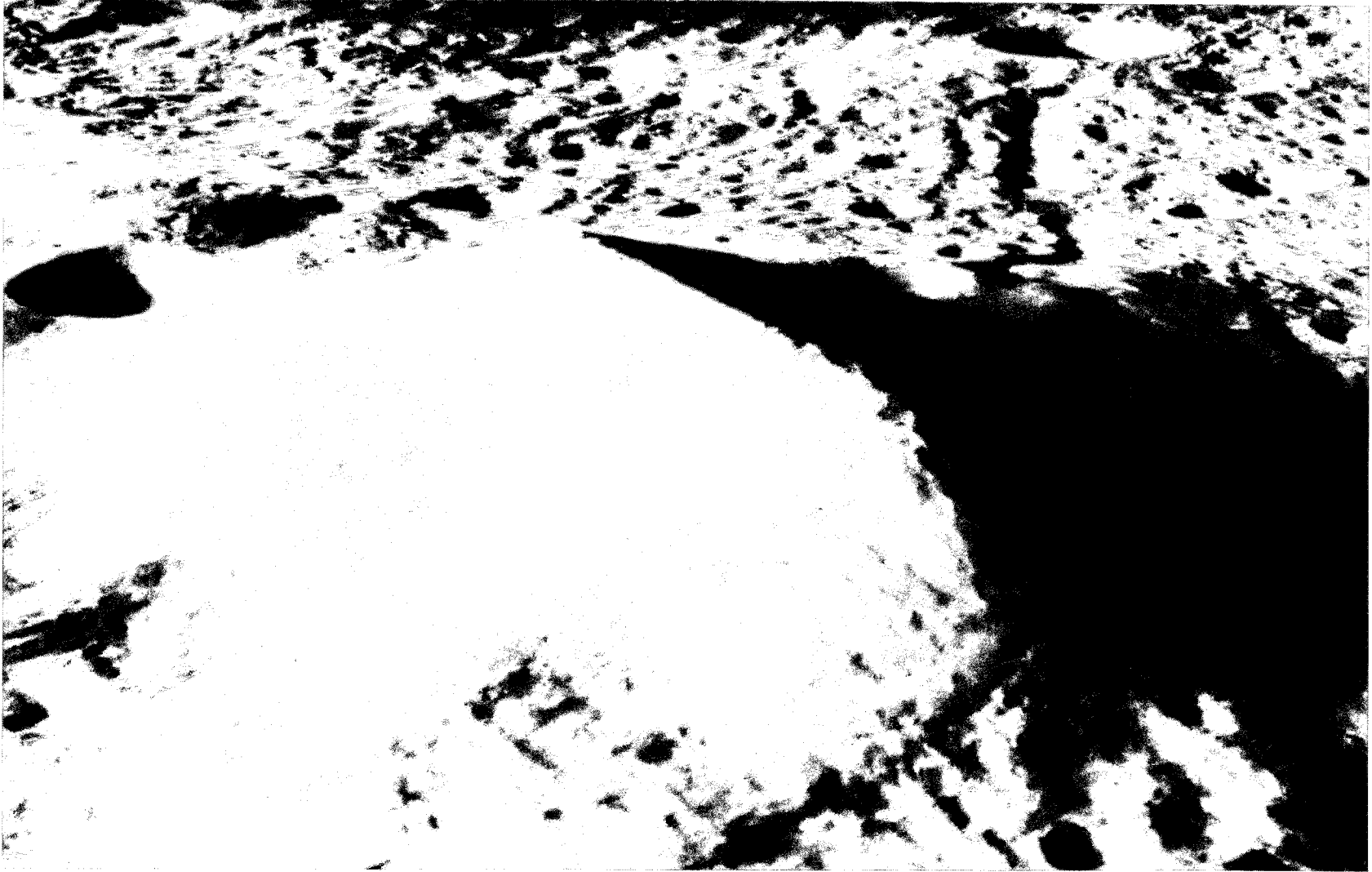
Fig. 69. Alphonsus peak, seen from SSW with W illumination, showing long crest and smooth W slope.

Fig. 70. Alphonsus peak, seen from W with light coming from E.

Fig. 71. White sublimate deposits on Laimana Crater, Hawaii, photographed February 22, 1960, after month-long eruption. (Photograph by H. Pierce, Hilo.)

←——

Fig. 72. Dark-halo crater on E part of Alphonsus floor and its deposit, based on mosaic of *Ranger IX* frames B77, 78, 79, and 80. (Note field of secondaries across rille to W, and light, wrinkled deposit on crater wall. Numerous outcroppings are seen, particularly W of rille, some marked with white dot just below the feature. A lava ridge extends from r upward, crossing wall of collapse crater above.)

——→
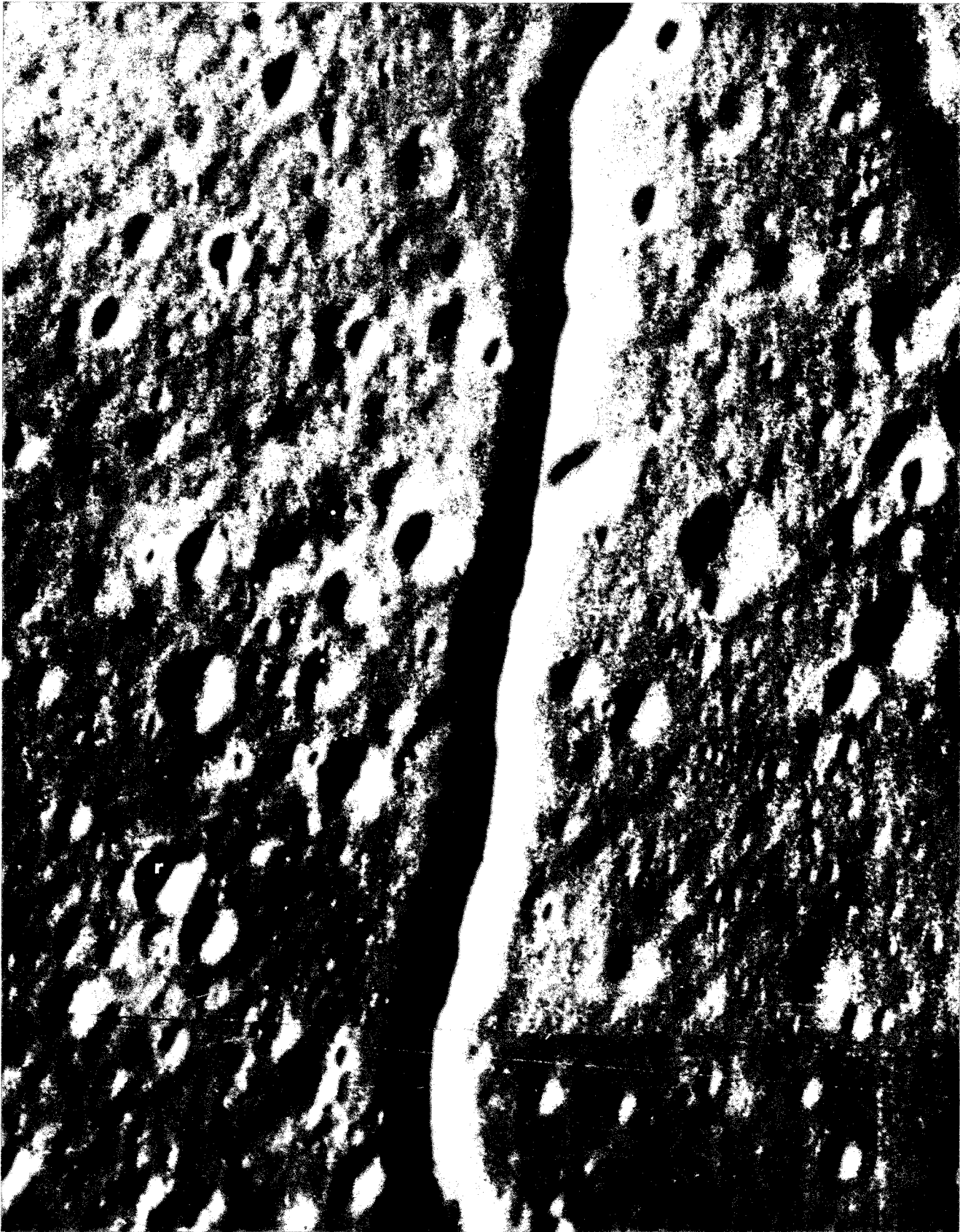
Fig. 72.

Shallow depressions are less numerous in the blankets than on the surrounding crater floor, but conical dimple craters about 100–300 m in diameter appear in similar numbers in both areas, although their walls are darker within the blankets than outside.

The dark blankets around the craters are not sharply bounded. Stereoscopic viewing of enlargements of consecutive frames shows *the blankets to be very rough, with occasional single masses scattered beyond them*. Some isolated dark masses, however, appear to be *outcroppings*; a group of four such masses and a nearby ridge crossing a crater wall are marked in Fig. 72. There are, besides, numerous *low domes* on the floor, some with *well marked summit craters. The Alphonsus floor is very complex and has the unmistakable appearance of volcanic terrain.*

It is concluded that both the dark-halo craters and the Alphonsus central peak are of volcanic origin; yet their appearances are in marked contrast. Apparently, the peak is a large mass added to the landscape by a slow process of cone building, the later stages of ejection having nearly closed the vents. The process was accompanied by the release of vapors that covered the cone with sublimates. The dark-halo craters, on the other hand, correspond to the terrestrial maar formation, as pointed out by R. Strom, in which a single explosion (on the Earth caused by either water or gas, but on the Moon presumably by gas only) scattered the crater volume over the surrounding terrain. No white sublimate deposit would be expected in this case.

The Alphonsus rilles appear to be V- or U-shaped channels, 0.6–1.0 km wide, mostly without raised rims, and with inner slopes of 10–20 deg or sometimes less. Some rilles are quite shallow and tend to break up into a chain of shallow depressions (see Figs. 10, 7, 8, 6, and *Ranger IX* atlas).

Depressions on the adjacent crater floor extend right up to the border of the rilles, as if the rilles did not exist, and sometimes even onto the rille slope. Fine fractures ($D < 25$ m) may run parallel to the rille (frames B81 and 82), and there is evidence that at several points, the rille has developed a local explosion center similar to, but much smaller than, the dark-halo craters.

Three main directions are represented in the Alphonsus rille system: (a) Mare Imbrium (the three principal north-northwest–south-southeast rilles), (b) one diagonal grid system, and (c) one north-south rille passing the central peak (see also Section G). The three rilles aligned with Imbrium may have set off the flooding of the crater floor, with subsequent magma withdrawals leading to the rille's collapse. Alphonsus' central peak appears to be of somewhat later date, since it overlaps two of the rilles. It may have continued to grow for some time after the crater floor had solidified and after the depressions had formed.

About 100 dark-halo craters have been observed on the Moon, most of them in maria or mare-type terrain; in addition, several hundred dark spots appear in the Copernicus region which are probably unresolved dark-halo craters showing only their dark nimbi. We return to these briefly in Section K. Two well known dark-halo craters occur in Mare Nectaris (Ref. 2), and the *Ranger VIII* records show one with increased resolution on the outer slope of Sabine (see Fig. 103 in Section H). This object is not located on a visible rille.

3. The Alphonsus *crater walls* reach a maximum of about 2.0 km above the floor. As Fig. 9 indicates for the north and west sectors, the mountains forming the crater wall are remarkably smooth and rounded, an effect probably attributable to the violent shaking caused by the Imbrium impact. In addition, there is much evidence of subsidence and local melting probably having occurred during the same general period. On a larger scale, this is also true for the northeastern sector in Figs. 7 and 8.

Fig. 73. Dark-halo crater on NE part of Alphonsus floor and its deposit, based on mosaic of *Ranger IX* frames B80, 81, and 82. (Approximate boundary of ejecta blanket outlined by two short, white bars that may be extended to intersect.)

The central part of the eastern sector is reproduced in Fig. 74. In it and in Figs. 7 and 72, a major graben is observed, running from the high-level lava lake to the crater floor, and furrows follow the base of the several mountains facing the floor. Numerous small, white projections, several with calderas on top, are visible in the walls, indicating *volcanism* (fumaroles) of a type presumably similar to that of the central peak but on a smaller scale and dispersed. Frames B77 and B78 give additional coverage. The lava lake shows collapse depressions much like those on the crater floor; but the crater walls have a very different pattern. Large, conical depressions do occur, but the shallow, circular depressions, so abundant on the floor, are absent from the walls. A large dome with a summit crater is seen in Figs. 7 and 74 just north of the lava lake.

The absence of broken and tilted rock slabs in the walls is attributed to the pre-mare origin of Alphonsus. The walls probably consisted originally of unconsolidated accreted material, not crystalline rock. The *absence of numerous fractures* in the rounded mountains, otherwise to be expected from the very violent Imbrium impact, is consistent with this view. Instead, the mountains have an appearance of "toasted marshmallows," to use the apt comparison made by Mr. Whitaker. The shallow furrows observed running roughly along the contours of some of these mountains, and along their inner borders on the crater floor, suggest partial subsidence into a plastic base—not unexpected for the Imbrium period, when lavas surfaced, probably as a result of the Imbrium fractures, in several adjacent areas. The crater walls are likely to be *typical examples of what happened in the lunar terrae* during the period of maximum subsurface melting, when a layer of unconsolidated accreted material

did not fully melt but was subjected to the passage of large quantities of steam and other vapors.

A more detailed study of the crater walls must await a photogrammetric evaluation of the records and the availability of contour maps.

4. We have noted the curious contrast between the appearance at full Moon of the area containing the five large central craters (Figs. 62 and 12) (being continental or terra-type in albedo) and the structure of the Alphonsus floor, with its dense cover of shallow collapse depressions (being mare-type). We must inquire *how general is the spread of these collapse depressions*. The *Ranger IX* data solve the problem; the result of the study based on them is summarized in Fig. 75, where areas containing the depressions are shown with hachures. These areas have one other common property: they are strictly *level* (apart from the sinks), indicating that they were formed from a *molten state*, if not entirely up to the surface, at least very close (within meters) to it. These level areas, covered with shallow, circular collapse depressions, are referred to here as "lava lakes." The compilation presented in Fig. 75 shows that many level lakes but none of the surrounding terrae are covered by depressions, which removes all reasonable doubt that these depressions are *internal in origin*, as concluded in Section A.

The lakes do not have the same elevation throughout, any more than do the five major craters; some are situated high in crater walls. Apparently, the flooding occurred from different magma chambers and at different hydrostatic pressures. This is consistent with what is observed elsewhere on the Moon, e.g., in the crater Wargentin.

Fig. 74. Central part of E wall of Alphonsus (B73). (Note rounded appearance of wall with numerous sunken valleys, among which is a high-level lava basin showing shallow circular collapse depressions; graben connecting "lake" with crater floor; numerous small, white protuberances, some with visible calderas—presumably extinct volcanoes covered with sublimate; and dome with summit crater, just N of lake.)

0   1   5   10 km

The *Ranger IX* records are also the best source for studying the widespread effects of the Imbrium impact on this region. Although this subject merits separate treatment, we can only raise additional questions here concerning (a) the cause of the very large depressions, known from telescopic observations, in Ptolemaeus and Albategnius; (b) the sequence in which the five large craters were formed; and (c) the significance of the observed lineaments. Detailed mapping and photogrammetry of the area will be valuable aids in future studies.

5. The striking property of the Alphonsus floor is the abundance of collapse depressions, which even have some rilles turning into them locally. We shall now consider *the floor structure* on the larger scale (i.e., smaller structural units).

Figures 76–79 reproduce the last (full) *Ranger IX* B frame (B87), probably the most exquisite record in the *Ranger* series, in four sections. Each major depression shows an intricately woven pattern similar to the tree-bark pattern found in the *Ranger VII* records and seen in the model of the impact area (Ref. 1, p. 60). Dimple craters abound, not only outside but also inside the large depressions; the triple set in Figs. 77 and 79 is especially interesting. Since the dimple craters were most likely formed during solidification of the floor (about 4.5×10^9 years ago), their fresh appearance again testifies to the small amount of post-mare erosion (insignificant at scales well above 1 m). No large outcroppings or domes are seen in this area (Fig. 79), and the terrain is relatively smooth.

Whether or not the composite depressions (small ones inside larger ones) signify a two-layered lava bedding in Alphonsus remains to be determined. The large terrestrial flows are usually multilayered, sometimes with known intercommunication of drainage tunnels; but the surface depressions examined were always due to the latest flow.

The area immediately to the west of Figs. 76 and 78 is covered by the last *Ranger IX* A frame (A70), which is reproduced in Figs. 80–83. The scale and

resolution are somewhat reduced, but the records are of great added interest. The diamond-shaped grid pattern is less marked though definitely present, especially in Figs. 81 and 82. In addition to the large, shallow depressions, many dimple craters are visible, as well as a few sharp craters, one of which (upper right of center in Fig. 83) is discussed below in some detail. A dome some 60 m in diameter, with a summit crater about 10 m across, appears in the lower left corner of Fig. 81, and two similar domes are in the extreme upper left corner. Many lower domes are seen elsewhere, and some updoming also occurs on the floor of the large depression in the lower right corner and at various points in the left margin of Fig. 83. Adjacent areas are covered with less resolution by the earlier B and A frames. We note in B84–86 the domes referred to in Fig. 10, and the fact that *the summit craters are not vertical calderas but conical dimple craters*. This subject is treated more fully in Section H.

The last P frames provide information about the Alphonsus floor on the meter scale. The 1-in. P_3- and P_4-camera pictures in frame P8 match the last full B frame (B87) both in scale and quality, while the remaining frames, P9–12, exceed the scale of B87. The photographs produced by the 3-in. cameras (P_1 and P_2) have three times the scale of the 1-in.-camera pictures on each plate.

Atlas picture $P_1 12$ is reproduced in Fig. 84. It is remarkable for its definition, the fine northwest–southeast lineaments shown, and the rocks visible on the surface. Partial frame B88 has even better resolution, as may be seen from the overlapping parts reproduced in Fig. 85. Stereoscopic viewing of the two frames leads to the following conclusions.

Craters occur down to the smallest resolved size—about 0.5 m. (Their frequency is discussed in Section F.) Remarkably narrow lineaments (widths as low as 0.2 m) are also visible both as positive and negative structures; some of them are marked in Fig. 81. Since the lineaments belong to the diagonal grid system and are presumably nearly as old as the crater floor, *a very low erosion rate* is indicated.

Fig. 75. Areas covered by shallow circular collapse depressions within intercrater region, designated by hachure marks.
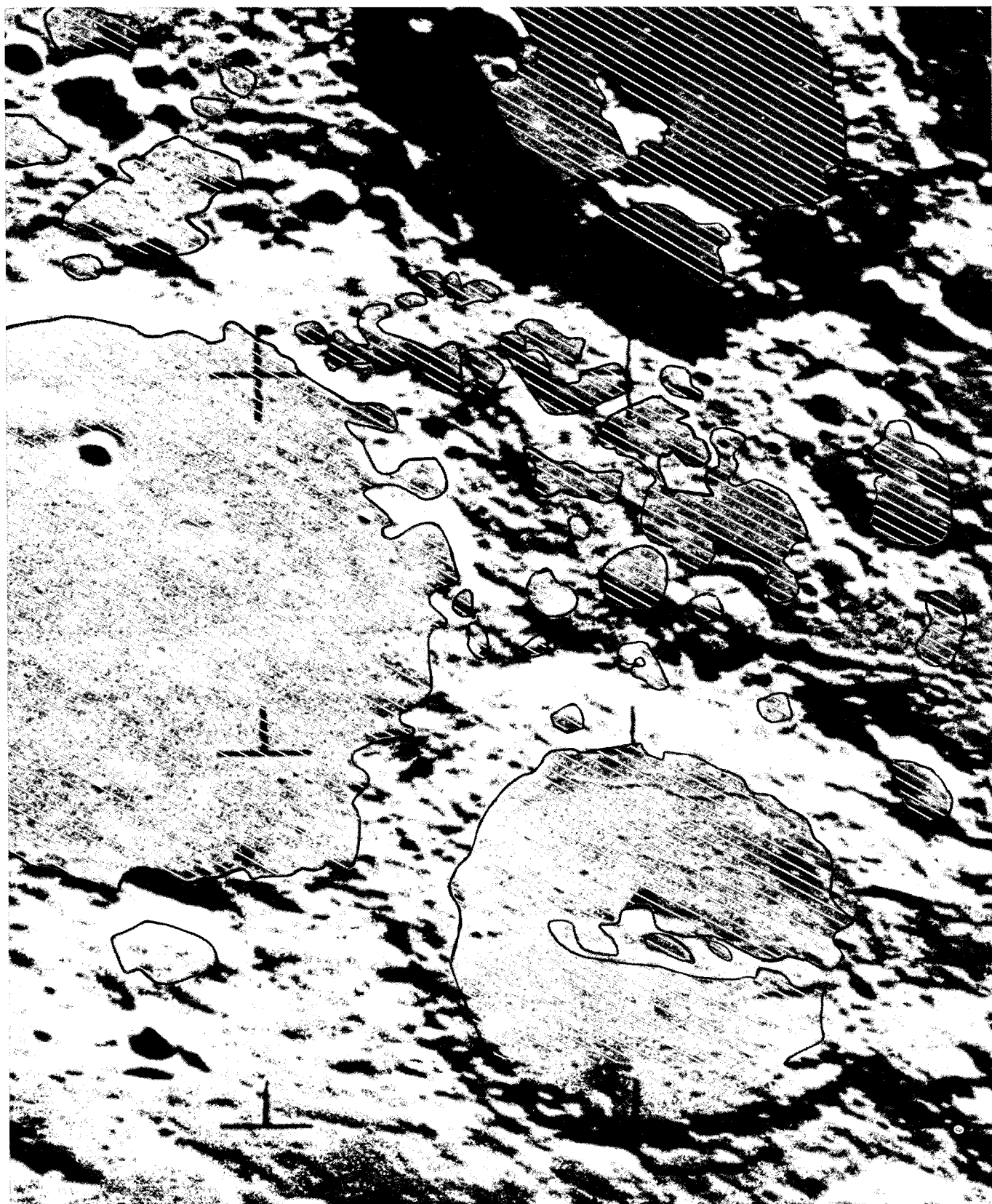
Fig. 76. NW quadrant of last full *Ranger IX* B frame (B87). (Note large depressions, tree-bark structure of floor, dimple craters, shallow depressions, several primary-impact craters, and, in left margin, what may be a secondary crater with central rock mass. Dimensions 1.3 [E–W] × 1.4 km [N–S].)
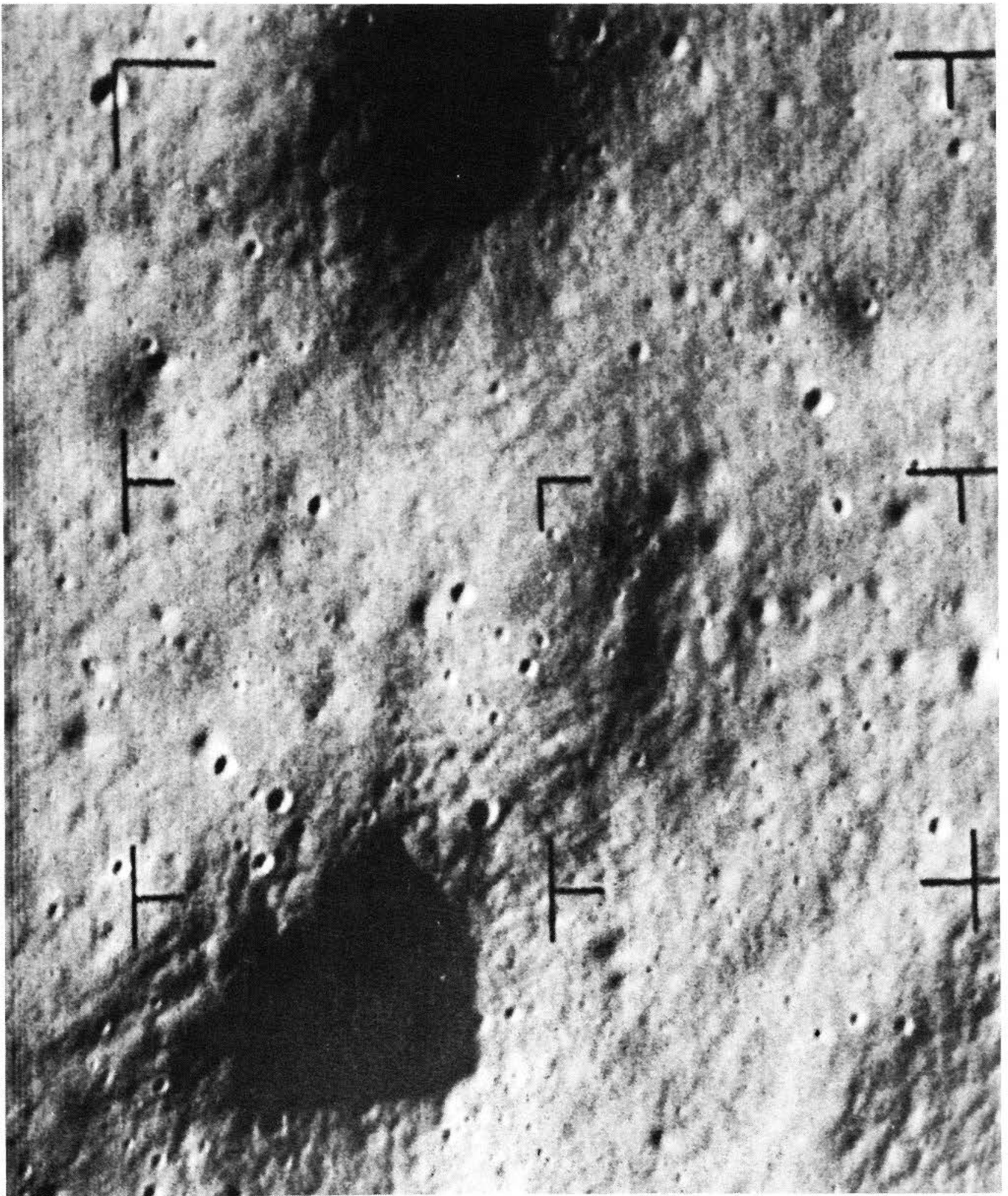
0   100   500m

Fig. 77. NE quadrant of frame B87. (Note updoming in collapse crater in lower right corner, row of three dimple craters, and a few impact craters. Dimensions 1.3 × 1.4 km.)
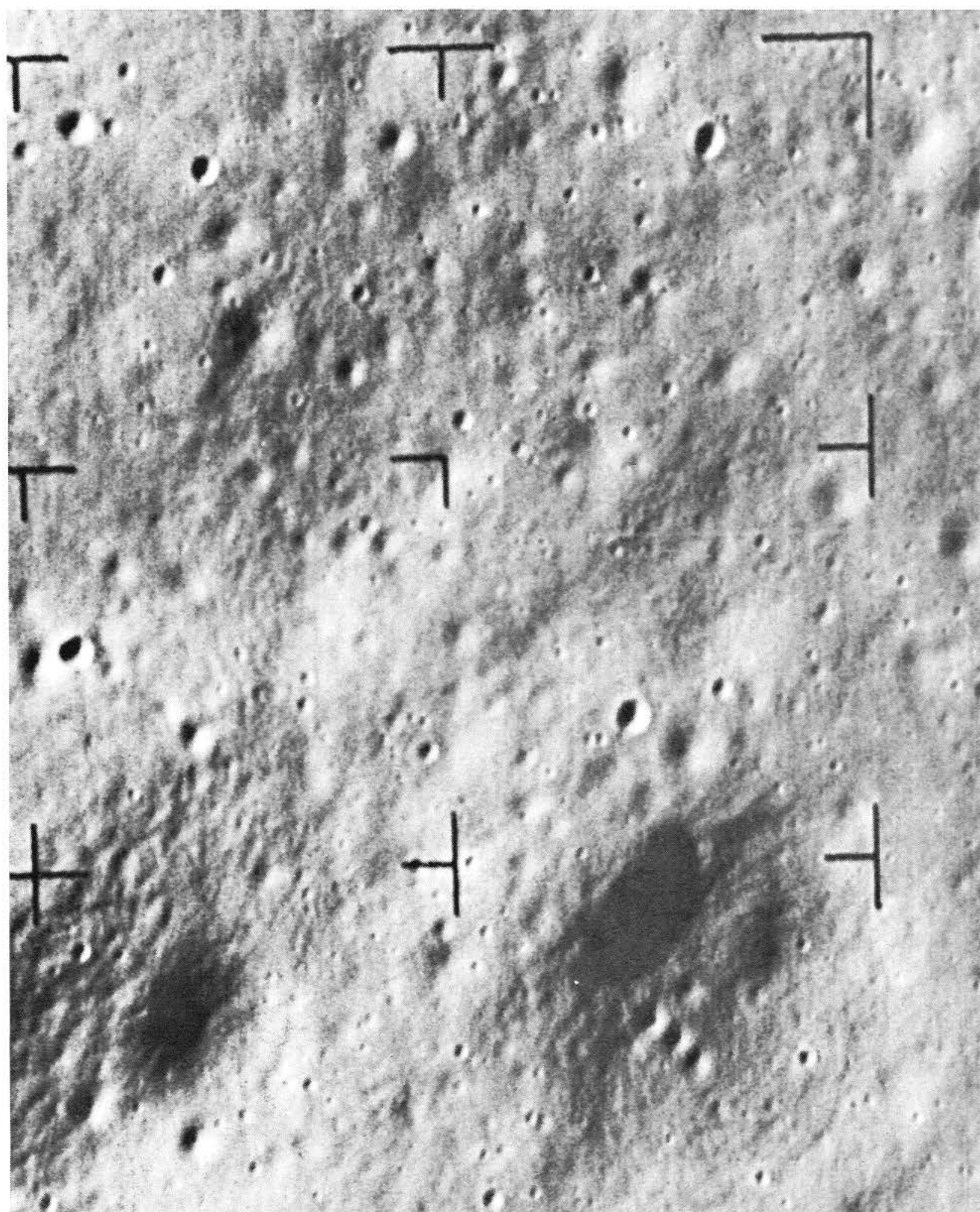
0   100   500 m

Fig. 78. SW quadrant of frame B87. (Note numerous
small protuberances in lower right section.
Dimensions 1.3 × 1.4 km.)
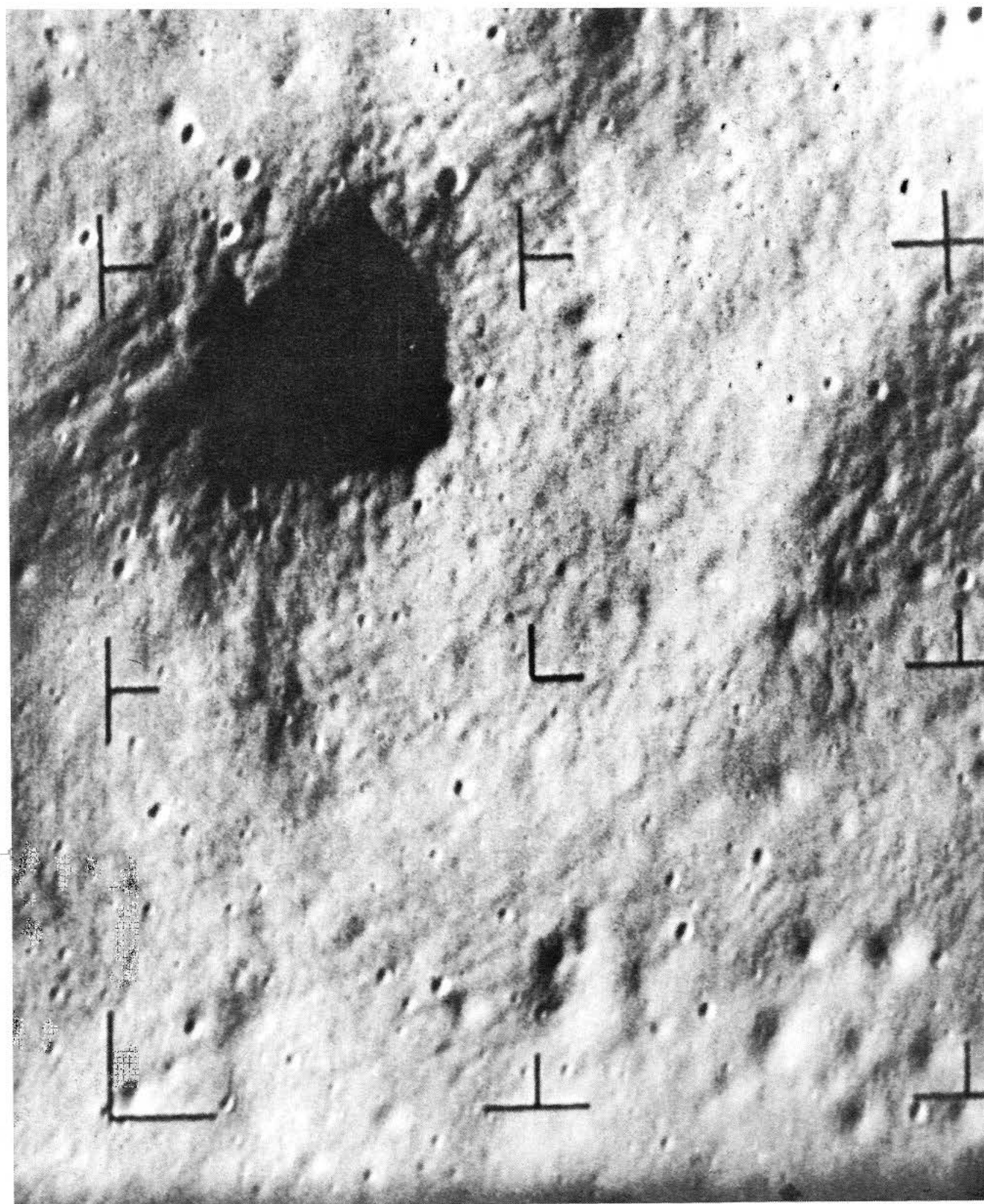
Fig. 79. SE quadrant of frame B87.
(Dimensions 1.3 × 1.4 km.)
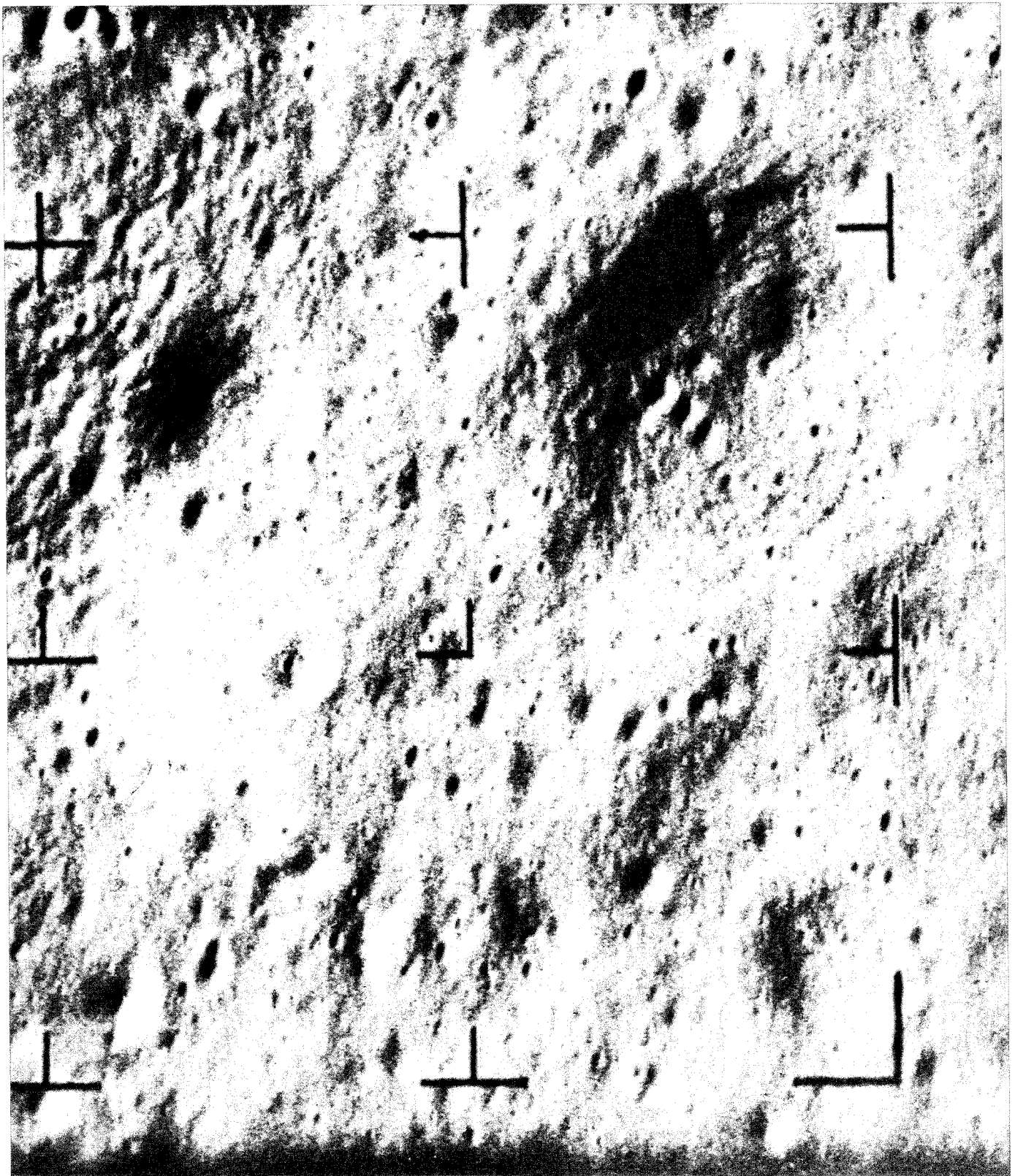
0   100   500 m

Fig. 80. NW quadrant of last *Ranger IX* A frame (A70).
(Dimensions 1.7 [E–W] × 2.1 km [N–S].)
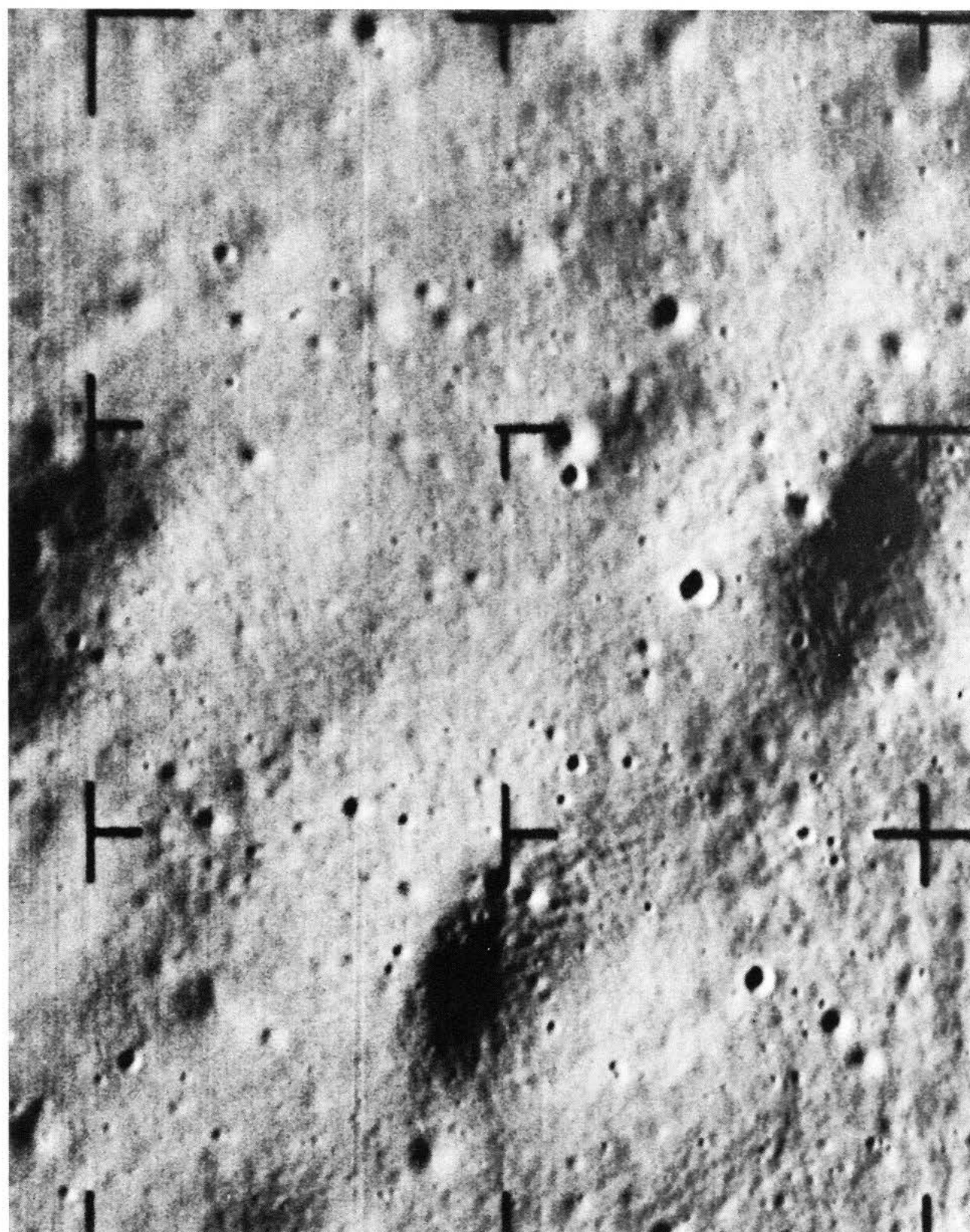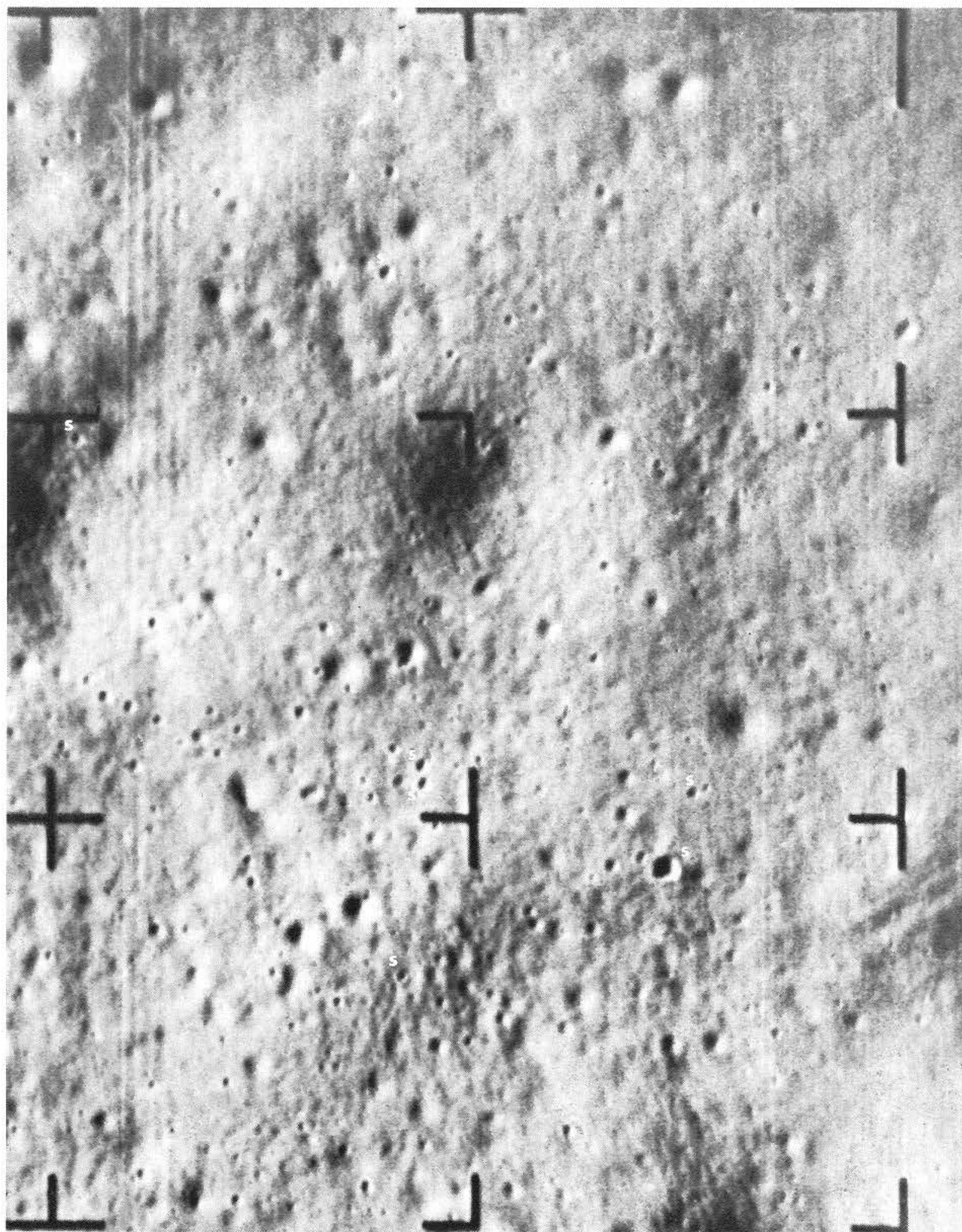
0   100   500 m

Fig. 81. NE quadrant of frame A70 W of region covered
by Fig. 76, with small overlap. (A few "sharp" craters
have been marked S [see Section F].
Dimensions 1.7 × 2.1 km.)

←—

Fig. 82. SW quadrant of frame A70. (Note dome with
caldera in SW corner, and two similar domes in
extreme NW corner; others on floor of dark
central depression. Dimensions
1.7 × 2.1 km.)

—→

0   100   500 m
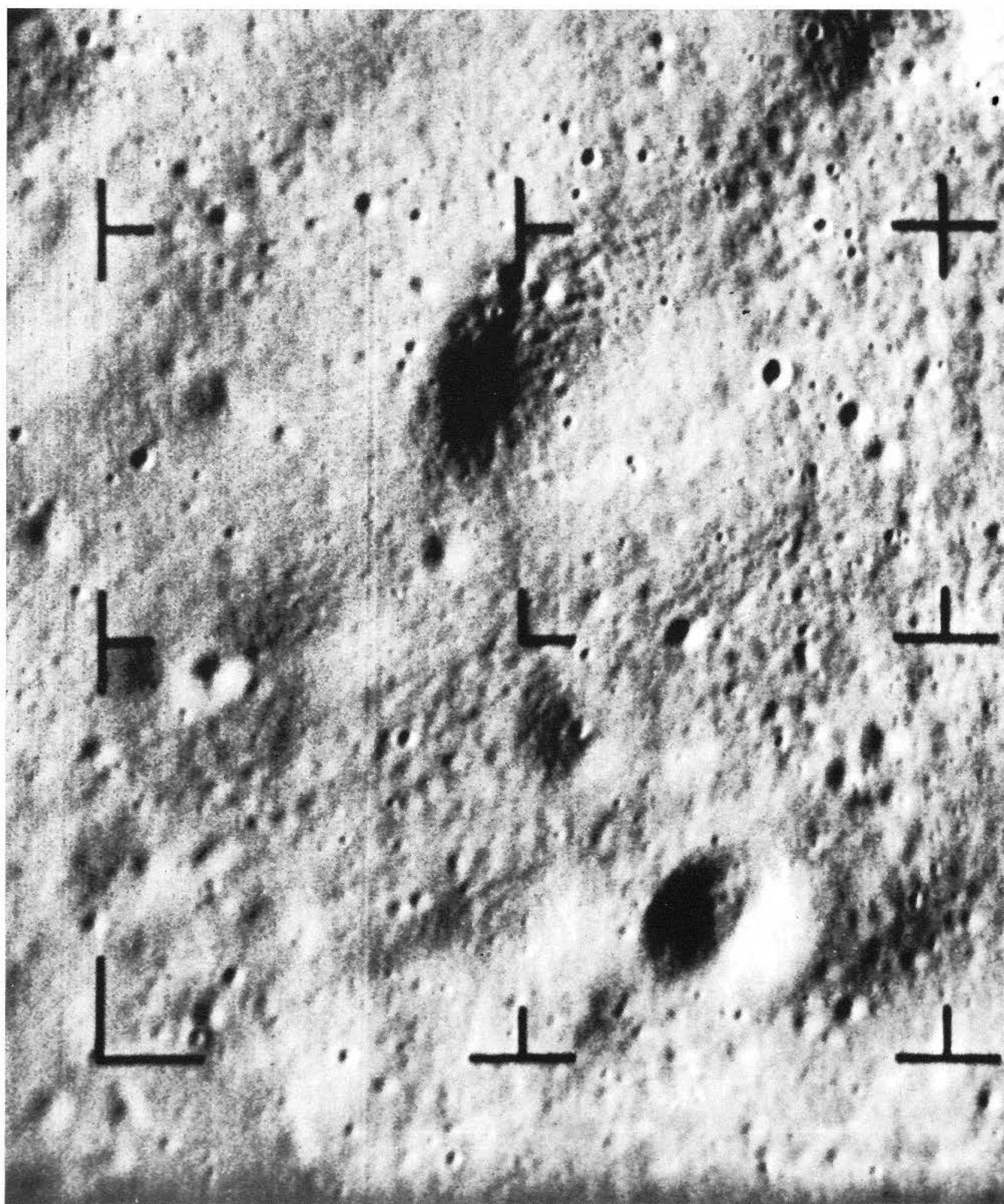
A comparison of Figs. 84 and 85 with Fig. 50(a), showing Mare Tranquillitatis, indicates a large difference in the fine structure of the two regions. This subject is reviewed in Section K, which also includes the *Ranger VII* data.

The rocks noted in Figs. 84 and 85 appear to be due to a nearby primary-impact crater, shown in the mosaic of Fig. 86. This crater is about 50 m in diameter, approximately 100 m from the impact point in *Ranger IX*, and the field of rocks appears to extend—wherever the resolution permits a check —at least 120 m from the crater.

The rocks are marked with arrows in Fig. 86. The actual presence of nearly all of them has been verified stereoscopically in two overlapping frames. Their distribution indicates that they are fragments ejected from the 50-m impact crater, with the largest observed distance from the center of the crater being about 120 m. The prediction of the occurrence of rocks of about 1-m size within 100 or 200 m from their source, made in Ref. 1 (p. 11), has thus been verified empirically. Such confirmation was possible only because *Ranger IX* impacted close to a moderate-size primary crater—a remarkable coincidence, as may be seen by inspection of Figs. 80–83, which show that impact craters of this size are rare. Furthermore, this coincidence has enabled us to determine the bearing strength of the Alphonsus floor (Ref. 13).

Bearing strength is determined as follows: (1) The *distance* of each rock from the center of the crater can be measured; a lower limit to its *velocity of impact* on the Moon is therefore known. (2) The lower limit of the *diameter* of the rock can be measured, as well as its actual *height* above the surrounding surface, the Sun elevation being known (10 deg). (3) It may be assumed that the *bulk density* of the rock is about 2, on the grounds that the material was sufficiently strong and cohesive to survive the explosion that blew the rock out of the crater. (4) The *depth of penetration* into the Moon is somewhat

uncertain. Some vertical compression of the rock will have occurred, so that its present vertical diameter will statistically be somewhat less than its visible horizontal diameter. On the other hand, sputtering may have somewhat changed the height above the surrounding surface. (A protuberance will suffer more mass loss than its level surroundings, but the higher bulk density of the rock will tend to make it more resistant; conceivably, the net height of the rock could even increase with time.) In the computation, we have assumed that half the missing part of the expected original vertical diameter is a fair measure of the depth of original penetration.

The physical nature of the surrounding terrain was briefly reviewed in Section B. From the radar-reflection data, it was inferred that the cavities in the rock froth became dominant at diameters less than about 1 cm. Figure 87 shows two photographs of a typical piece of basaltic rock froth ejected by the Hawaiian crater Laimana (see Fig. 71). This material appears to have been ejected in liquid state and to have solidified in free fall. Its bulk density is about 0.15 and its bearing strength 2 kg/cm^2. The Laimana material may resemble the lunar rock froth; its cavities have dimensions of the right order of magnitude. When fragmented, the material looks like cinder.

The rocks in Figs. 84–86 are typically about 1 m across and extend 15–20 cm above the lunar surface. From two or three well observed examples, *we find the crushing strength of the Alphonsus floor to be 1–2 tons/ft^2, or 1–2 kg/cm^2, averaged for the upper 30–50 cm of the lunar surface.* On the basis of the assumptions made, this will tend to be a lower limit, though the correction is probably less than a factor of 2.

For the cartographic aspects of the *Ranger IX* area, reference is made to the excellent AF-ACIC charts 13–17, with scales of 1:1,000,000, 1:250,000, 1:50,000, 1:10,000, and 1:2000, with a part 1:400.

Fig. 83. SE quadrant of frame A70.
(Dimensions 1.7 X 2.1 km.)
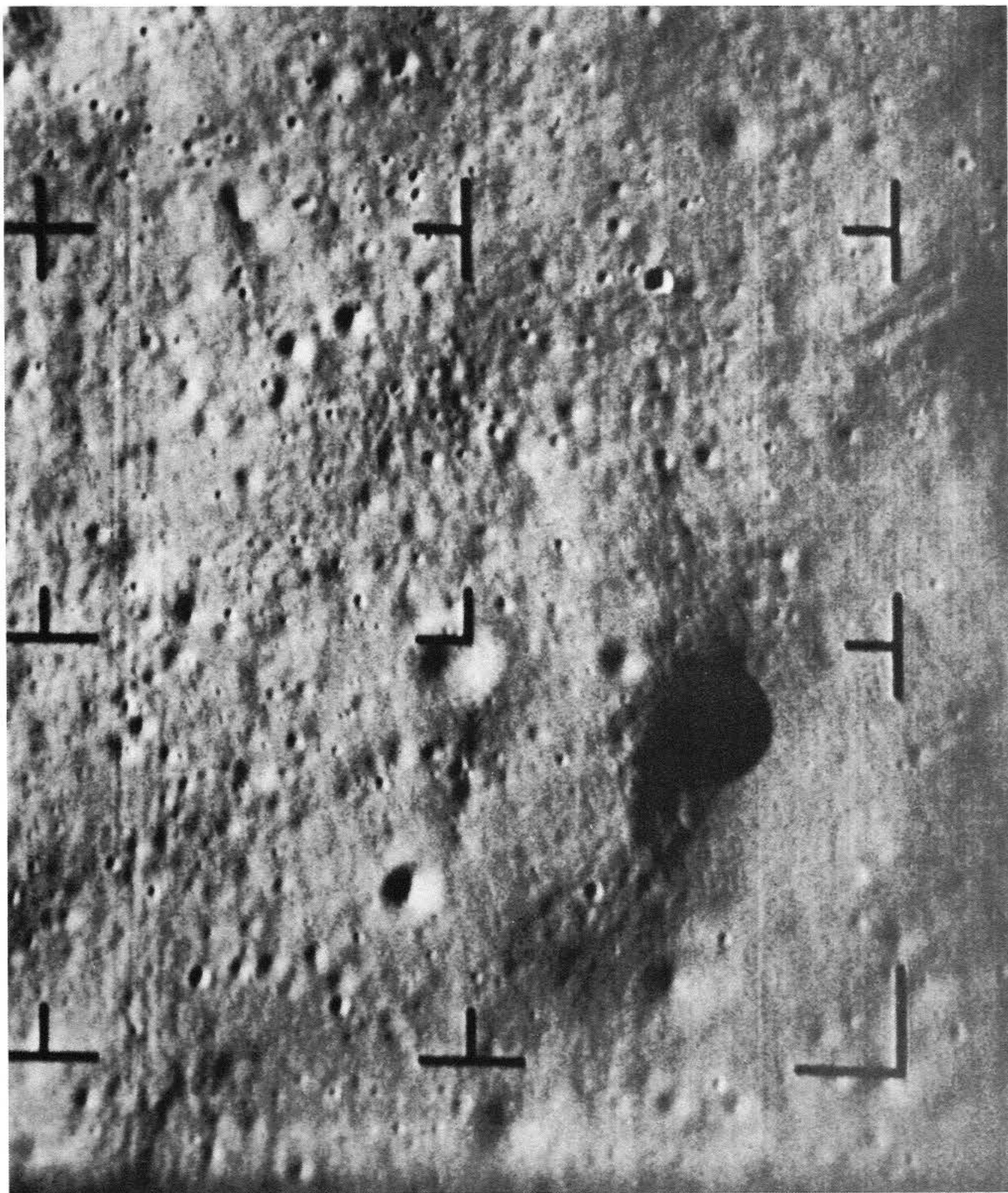
0   100   500 m

Fig. 84. Last *Ranger IX* P₁ frame. (May be compared in overlapping part with Fig. 85.)

←———

Fig. 85. Last (partial) *Ranger IX* B frame (B88). (May be combined stereoscopically with Fig. 84. Highest resolution achieved in *Ranger* series.)
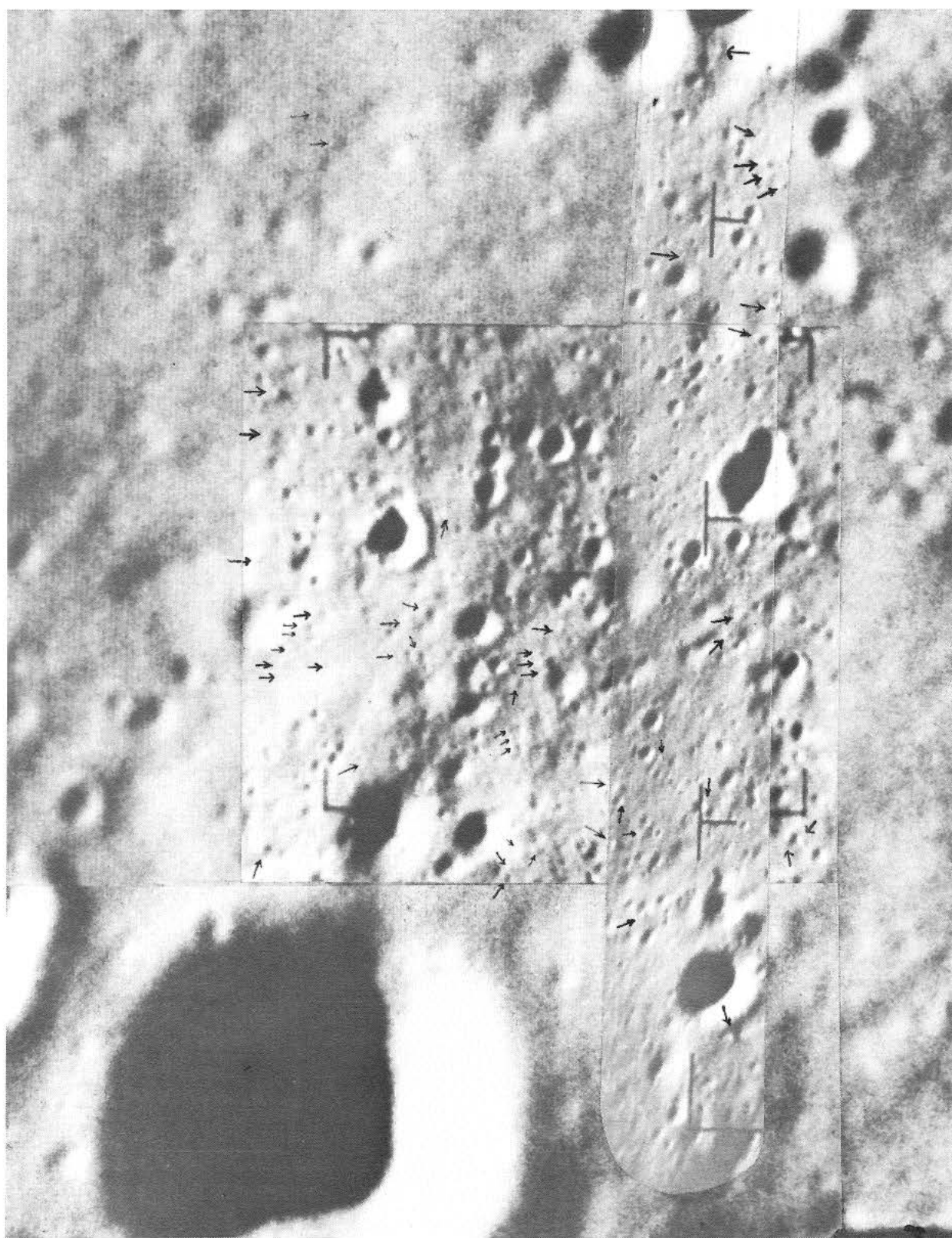
Fig. 86. Photomosaic of *Ranger IX* impact area, showing about 50 rocks (marked by arrows), used in determining bearing strength of floor.

←——

Fig. 87. *Lower view:* basaltic rock of extremely low bulk density (about 0.15), solidified in free fall above Laimana crater, Hawaii, February 1960 (see Ref. 13), together with three typical fragments of similar material. (Largest dimension of rock 9 cm.) *Upper view:* detail of rock, magnified 20 ✕.

——→
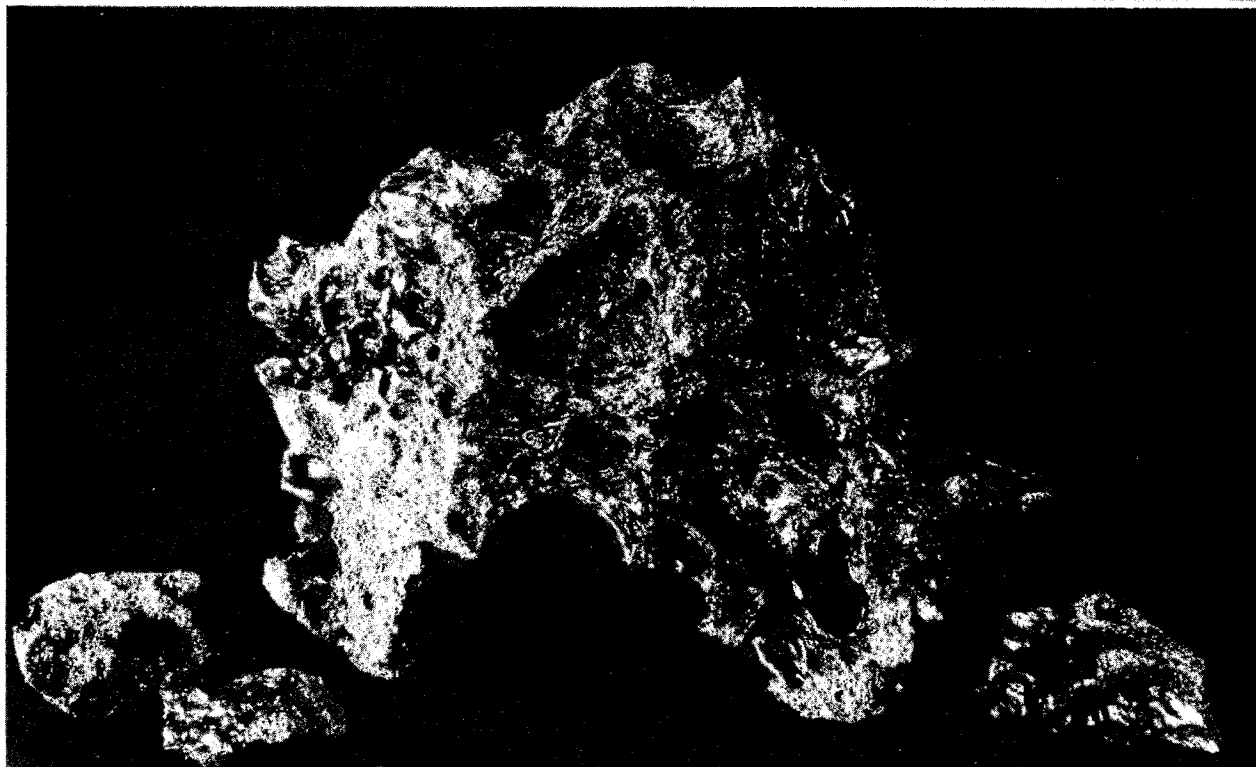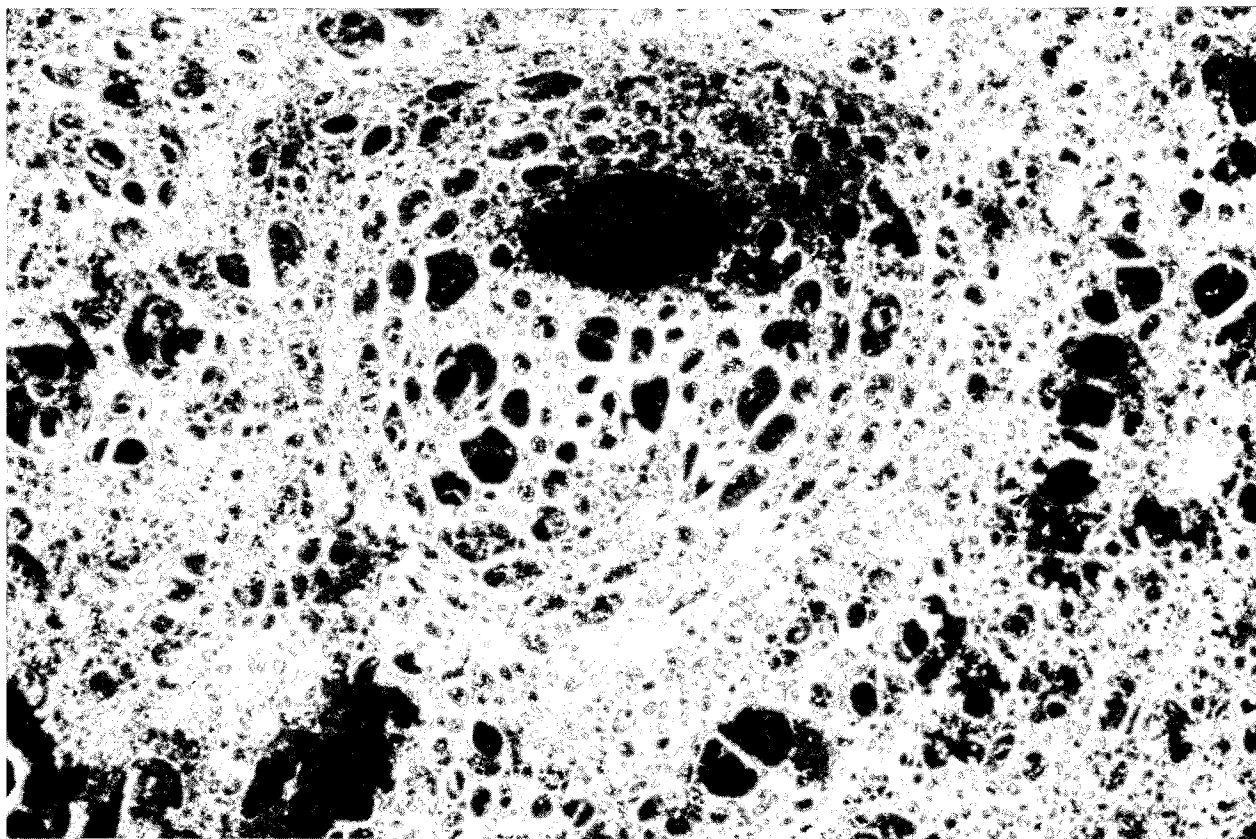
Addendum

A more specific value for the thickness of the ejecta blanket surrounding the dark-halo craters in Fig. 73 can be derived from the results of an experiment performed by Jaffe (Ref. 14). By comparing the appearance of craters showing through the ejecta blanket with laboratory craters covered with a layer of fine sand, the ratio of the thickness of the overlay to the diameter of the crater under consideration is obtained. At a distance of about 6 km from the crater, the thickness of the blanket is found to be of the order of 2–4 m; within a distance of 1 km from the rim, the blanket appears to be 20–40 m thick.

If the dark-halo craters are of explosive origin and the ejecta blankets consist of the crater material, the volumes of crater and blanket must correspond. The craters are about 1.8 km in diameter. If they are near-spherical in shape, with a depth-to-diameter ratio of 1:5, the volume of the crater is about 0.5 km³. The volume of the blanket may be estimated by taking 6.5 m as the average thickness over an area with a radius of 6 km. The blanket volume is then about 0.7 km³. In view of the several uncertainties in this comparison, the agreement found is regarded as confirmation of the hypothesis.

F. Frequency of Post-Mare Craters

The *Ranger* records extend by three orders of magnitude our knowledge of the size–frequency distribution of different classes of lunar craters and their areal densities. They define local differences in these parameters, attributable to such effects as secondaries, internal cratering mechanisms, age differences, and differences in surface properties. Comparisons with present flux rates of interplanetary matter can provide new information on primary-impact cratering and associated phenomena.

1. Collection and Reduction of Data

(a) The *Ranger* records on which craters have been counted and measured were enlarged to a scale of about 2.5 scan lines/mm, making it possible to measure crater diameters to the full accuracy provided by each frame. Because the image quality of the A-camera frame falls off toward the edges, only the central areas were used in order to permit sampling down to the smallest craters visible. The enlarged prints were covered with transpar-

ent drafting plastic, on which the crater outlines were drawn. From the "maps" so produced, the diameters D, were measured and the craters arranged, in increments of equal ΔD, the width of ΔD being about 1 scan line.

(b) The craters were classified into two groups: sharp and soft. A crater was called *sharp* if it had (1) a rim and (2) a rim width-to-diameter ratio of less than 1 to 4. All other craters were called *soft*. This criterion was established on the last A frames and transferred to larger scales through overlapping frames. Examples of sharp craters are indicated in Fig. 81.

(c) The counts thus obtained were first plotted in a linear histogram. A smooth curve was drawn through this plot to represent the most probable distribution, the ordinates giving the number of craters found in the interval ΔD around the abscissa D.

(d) From this graph a new graph was drawn in a log-log plot, giving the numbers per square kilometer, by the transformation $\Delta D_0 = 0.1\ D$. The following procedure was used: the number N at diameter D was read from the smooth curve obtained in (c); N was divided by the area in square kilometers used for the counts to give the number per square kilometer per ΔD; and this number was multiplied by $0.1D/\Delta D$ and plotted on log-log paper.

(e) In the diameter range $D > 3$ km, data were obtained from measurements on Earth-based photographs made by Arthur *et al.* (Refs. 15 and 16). Only the class 1 and 2 post-mare craters were used, since it was found that the criteria for these classes were in good agreement with the author's criteria for sharp craters.

Several difficulties were encountered in collecting and reducing the data. The circumference of a *sharp* crater is easily visible, which makes possible a relatively high accuracy in measurements of D. However, for craters with diameters of less than about 7 scan lines, the decision as to whether the crater is sharp or soft becomes progressively more difficult to make, and there is probably an increasing tendency to include soft craters, which are far more numerous, in the sharp class. In addition, crater incompleteness starts from about the same size down. These two factors leave a rather large uncertainty in N, in spite of the relatively large number of craters. Furthermore, the diameters of these craters are determined with an average accuracy of more than 10–15%, as the resolving power of the photographs is at best about 0.15 D.

The circumference of a *soft* crater may be rather uncertain, and seldom is the crater diameter defined with better than about 10% accuracy. The uncertainty in D being dependent on the shape of the crater (dimple, very gentle slopes, etc.), the actual accuracy in D ranges from 5% to approximately 30%, and averages probably about 12–13%.

Since the illumination angles in the *Ranger VIII* and *Ranger IX* impact areas are only 14 and 10 deg, respectively, shallow depressions having slopes of about 2 deg or even less become visible. The decision as to whether or not these features are craters becomes subjective, unless their size is comparatively large (several tens of scan lines). Since many of the smaller soft craters that are included in the counts are of this kind, the numbers are considered uncertain in spite of efforts to eliminate subjectivity.

Incompleteness for soft craters sets in at about twice the size as for sharp craters.

2. Reliability of the Curves

In order to estimate the "personal equation" involved in the classification and measurement of craters, one of the frames (last *Ranger VIII* A frame) was analyzed independently by R. G. Strom, using the same criteria as the author, with the following results (see Figs. 88 and 89): for sharp craters, agreement within 40% in N or 10% in D, if $D > 10$–11 scan lines; for soft craters, agreement within 40% in N or 15% in D, if $D > 23$ scan lines.

The lack of closer agreement is probably due to small systematic observer differences in D rather than in N. This was found from the "maps" drafted by the observers, and the fact that the cumulative crater numbers of over 10 scan lines for sharp, and over 23 for soft craters, agree more closely—within 12 rather than 40%. Mr. Strom checked several other frames and found a comparable degree of accordance.

In Figs. 90–92, the widths of the bands represent the standard errors in the two coordinates. They are based on the estimated error in D and on the assumption that the standard error in N was determined by the interval $3\Delta D$ at the time the smooth curve was drawn (see 1c).

3. Interpretation

Comparison of the sharp crater curves of the *Ranger VII*, *VIII*, and *IX* impact areas leads to the conclusion

that sharp craters can, on the whole, be identified with primary impact craters for the following reasons: (1) The three distributions are practically the same except for $D < 7$ m (see Fig. 93); the local differences do not exceed the uncertainty limits of each curve. (2) Local cratering mechanisms (e.g., secondary cratering or collapse) are likely to produce appreciable crater-density fluctuations. There is no evidence for the latter; only external origin by primary impacts can readily account for the close similarity of the three size–frequency distributions (provided that the three impact areas are of similar age, which is a reasonable assumption since all three are mare-type).

With the tentative identification of sharp craters as primary-impact craters adopted, the details of the distribution curve may now be considered. Since the three curves agree so well for $D > 7$ m, no separate discussion is needed, and a single distribution curve may be used for the primary-impact craters.

Figure 93 shows that in a log-log plot, the size–frequency distribution of post-mare primary-impact craters consists of three linear parts, with deviations occurring at $D < 7$ m. The linearity implies that the distribution functions are of the form

$$\log N = A + B \log D$$

in which N, as before, represents the number of craters per square kilometer per interval $\Delta D = 0.1\,D$, and D is given in meters.

The three linear parts, repeated in the right-hand curve of Fig. 93, have the following relationships:

(a) 7 m $< D <$ 22 m

$$A = 4.20 \pm 0.15 \qquad B = -2.65 \pm 0.10$$

(b) 22 m $< D <$ 120 m

$$A = 5.65 \pm 0.20 \qquad B = -3.70 \pm 0.20$$

(c) 120 m $< D$

$$A = 1.25 \pm 0.10 \qquad B = -1.68 \pm 0.08 \qquad (1)$$

In order to compare these relationships with available data on meteorite fluxes in the vicinity of the Earth–Moon system, a conversion was made from crater diam-

eters to masses of impacting bodies by means of the equation (Ref. 17)

$$D = 0.00014E^{1/3.4} \qquad (2)$$

where D is expressed in meters and E, the kinetic energy of impact, in ergs. A uniform impact velocity of 14 km/sec is adopted, and it is assumed that there is no need to correct for a correlation between the mass and velocity of the impacting bodies. (Evidence supporting both assumptions has been presented by Whipple and Hughes in Ref. 18.) The conversion (Eq. 2) leads to a mass–frequency distribution of the form

$$\log N = C + K \log m$$

in which N represents the number of bodies per square kilometer per $\Delta m = m/0.38$ that have impacted since the mare formation, and m is given in grams. After conversion, the three parts of the curve become.

(a) $8 \times 10^3 \, g < m < 3 \times 10^5 \, g$

$\quad C = 4.95 \pm 0.15 \qquad K = -0.79 \pm 0.03$

(b) $3 \times 10^5 \, g < m < 2 \times 10^8 \, g$

$\quad C = 6.30 \pm 0.20 \qquad K = -1.06 \pm 0.06$

(c) $2 \times 10^8 \, g < m$

$\quad C = 1.65 \pm 0.10 \qquad K = -0.49 \pm 0.03 \qquad (3)$

4. The Slope Change Between (b) and (c)

Hawkins (Refs. 19, 20, and 21) has shown that there is a significant difference in the mass-frequency distribution of stony and iron meteorites. He finds

$$\log N = -1.1 - \log m \quad \text{for stones}$$

and

$$\log N = -3.8 - 0.7 \log m \quad \text{for irons}$$

where N represents the cumulative number of impacts with mass greater than m on the Moon per square kilometer per year. The two distributions intersect at about $10^9 \, g$, which means that the stones outnumber the irons for masses smaller than $10^9 \, g$, and the reverse is true for masses greater than $10^9 \, g$. Unfortunately, these distribution functions are derived from data that extend upward
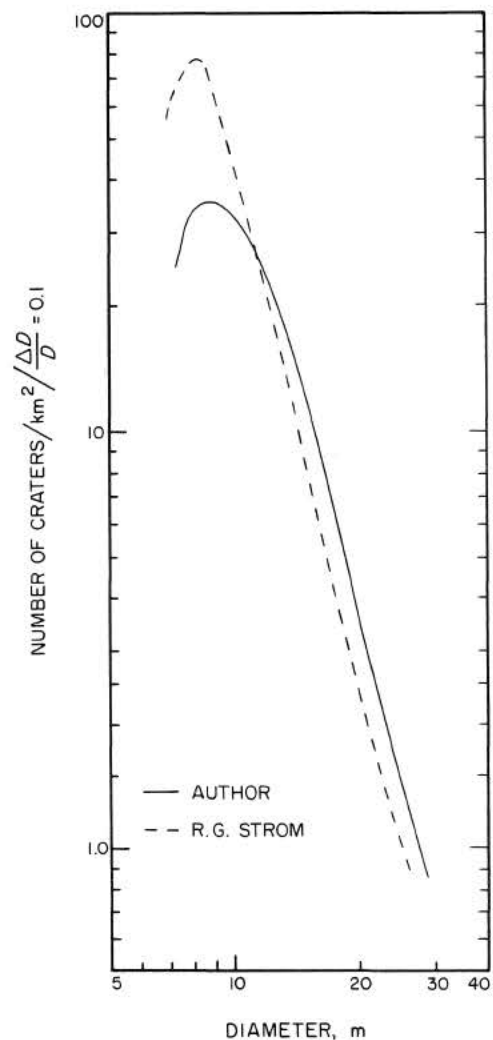
Fig. 88. Size–frequency distribution of "sharp" craters in last *Ranger VIII* A frame, as derived independently by R. G. Strom and the author.

to only $2 \times 10^7 \, g$, so that the extrapolations are considerable. The mass at which the curves intersect is uncertain, probably by an order of magnitude.

The following explanation for this difference in the mass distribution of stones and irons is offered by Hawkins (Refs. 19 and 21). He assumes that both stones and irons are asteroidal fragments produced by collisions in the asteroid belt (see also Ref. 18). These collisions are comparable to a grinding process. Now the slope (K) of the mass–frequency distribution of resulting particles appears to be dependent on the amount of grinding. Prolonged grinding has the effect of steepening the slope (Ref. 22). A moderate degree of crushing yields
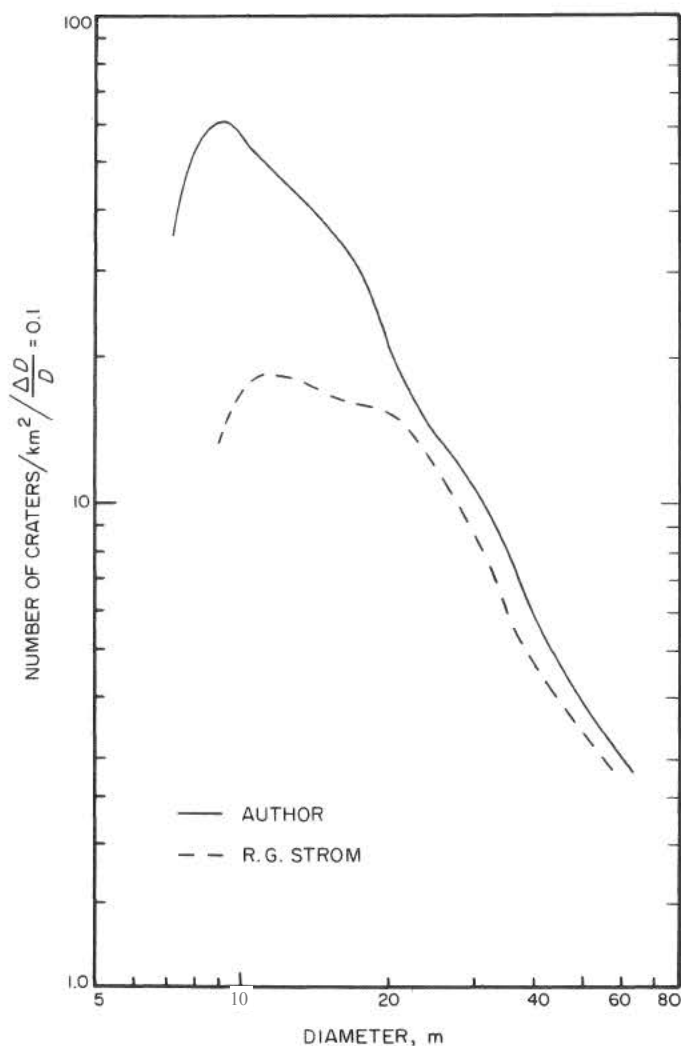
Fig. 89. Size–frequency distribution of "soft" craters in last *Ranger VIII* A frame, as derived independently by R. G. Strom and the author.

a slope of about -0.6, while extensive crushing gives a slope of approximately -1. The fact that stones appear to be "extensively ground" and irons reached only a preliminary state of grinding, is explained by the large difference in crushing strength (Ref. 21).

In order to compare the areal density of sharp craters with the absolute flux of meteorites, the cumulative numbers must be converted into incremental numbers, with increments $\Delta m = 0.38\ m$. After conversion, we find, from the Hawkins data,

$$\log N = -1.5 - \log m \qquad \text{for stones}$$

and

$$\log N = -4.5 - 0.7 \log m \qquad \text{for irons} \qquad (4)$$

in which N = number of impacts per square kilometer per $\Delta m = 0.38\ m$.

Figure 94 shows a comparison of Hawkins' numbers $\times 10^9$ years with the *Ranger* counts, converted to meteorite masses. The relationships are roughly parallel, but there is a displacement that appears beyond the limits of uncertainty of the data. From a comparison of the stone curve of Hawkins with curve (b), the total meteoritic flux for the post-mare period (presumably about 4 billion years) is roughly 50 times smaller than that obtained from a constant flux rate at the present intensity. [Since Hawkins' iron curve was extrapolated over several orders of magnitude, its comparison with (c) has much less weight.]

From the structure and orbital elements of the meteorites, it has been inferred that they originate in the asteroid belt and are produced there by collisions. Anders (Ref. 23) has found from the observed distribution of asteroid diameters and the Hirayama families that the original size–frequency distribution may have been Gaussian, with a maximum at $D \sim 60$ km or $m \sim 10^{20}$ g. If this is correct, the smaller bodies (meteorites) produced would initially be fragments from collisions of the original asteroids, and their numbers would increase proportionally with time. Later, as the total cross section of the small bodies approached or exceeded that of the original asteroids, the production rate of small bodies would have increased with an ever-increasing power of the time.* At present, the meteorite production rate is undoubtedly many times greater than the original rate, as determined from the frequency curve of asteroid cross sections or magnitudes (Ref. 24). How large the factor is cannot be estimated from the asteroids because the statistical data extend only to a magnitude of 16 instead of the magnitude of 35–40 that would be required for coverage of the mass range of interest here. The factor could well be anywhere from 10 to 100.

The empirical ratio of 50, found above, is therefore not unreasonable. It is uncertain for several reasons: (1) the conversion of the *Ranger* crater diameters to masses of the impacting bodies is uncertain, with the relationship depending on the density and other physical properties

---

*I am indebted to Dr. W. K. Hartmann for discussion of this subject, on which he has prepared a manuscript.
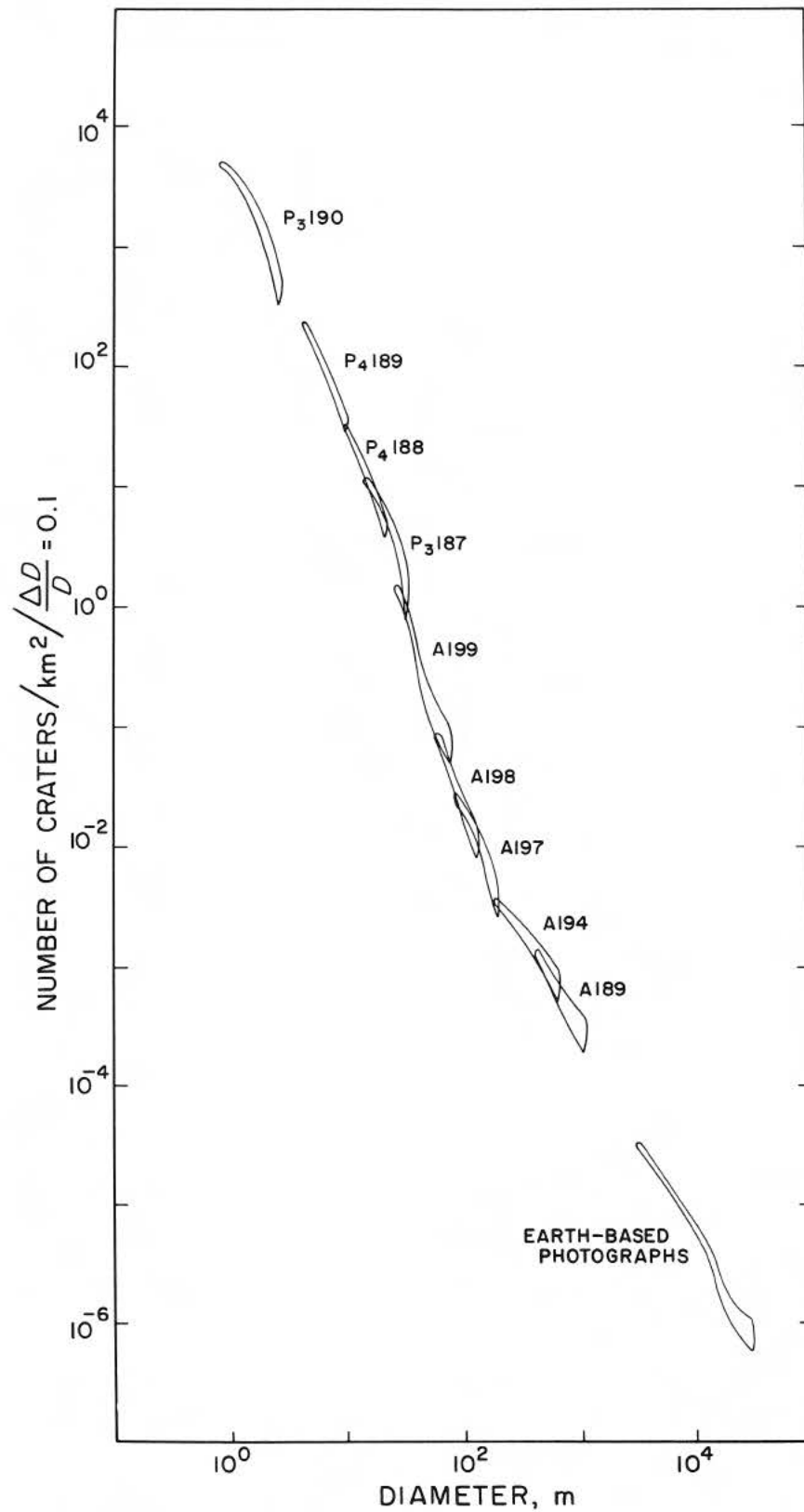
Fig. 90. Size–frequency distribution of sharp craters in *Ranger VII* impact area. (Widths of segments represent the uncertainty in the actual position.)
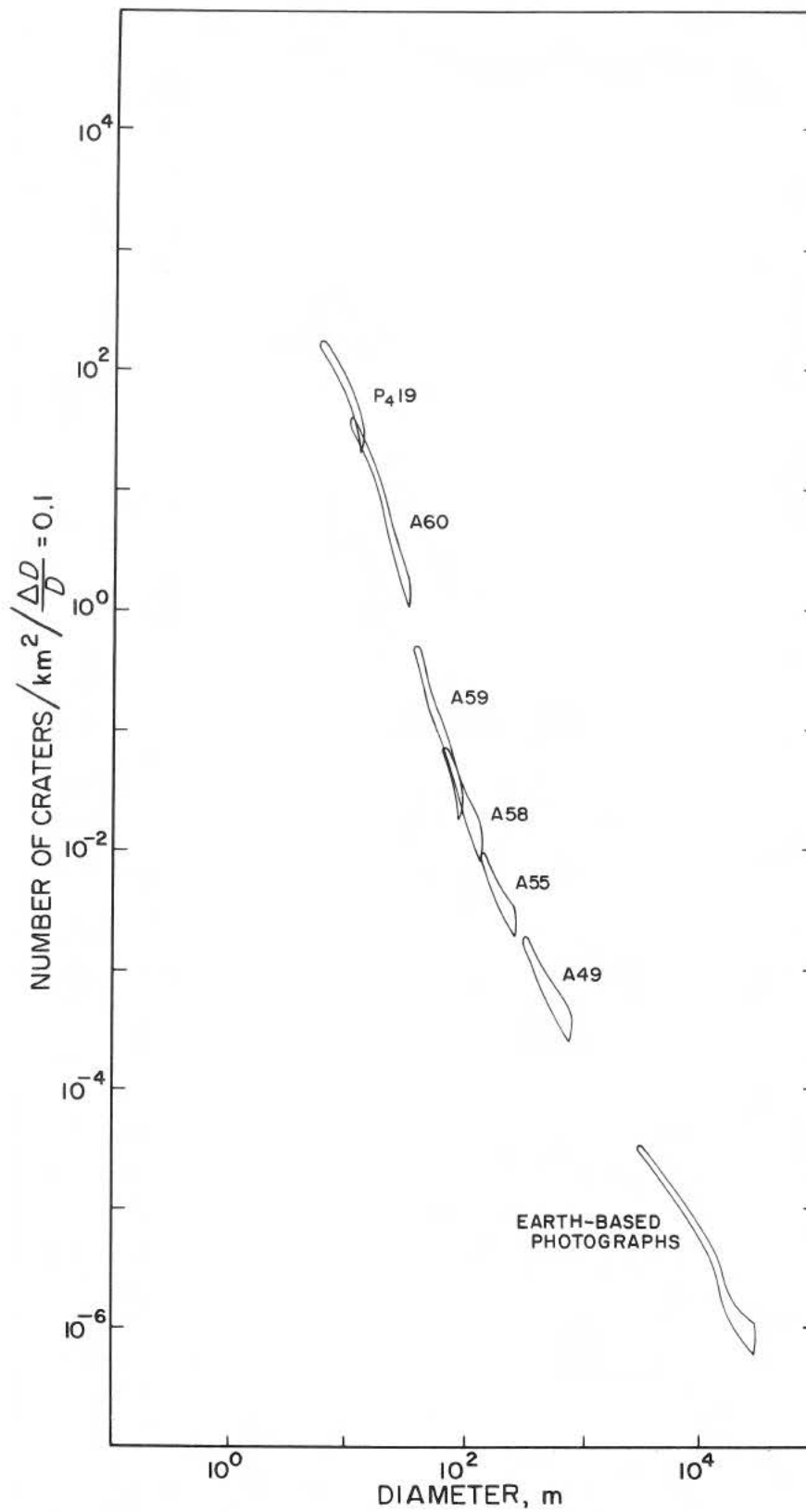
Fig. 91. Size–frequency distribution of sharp craters in *Ranger VIII* impact area. (Widths of segments represent the uncertainty in the actual position.)
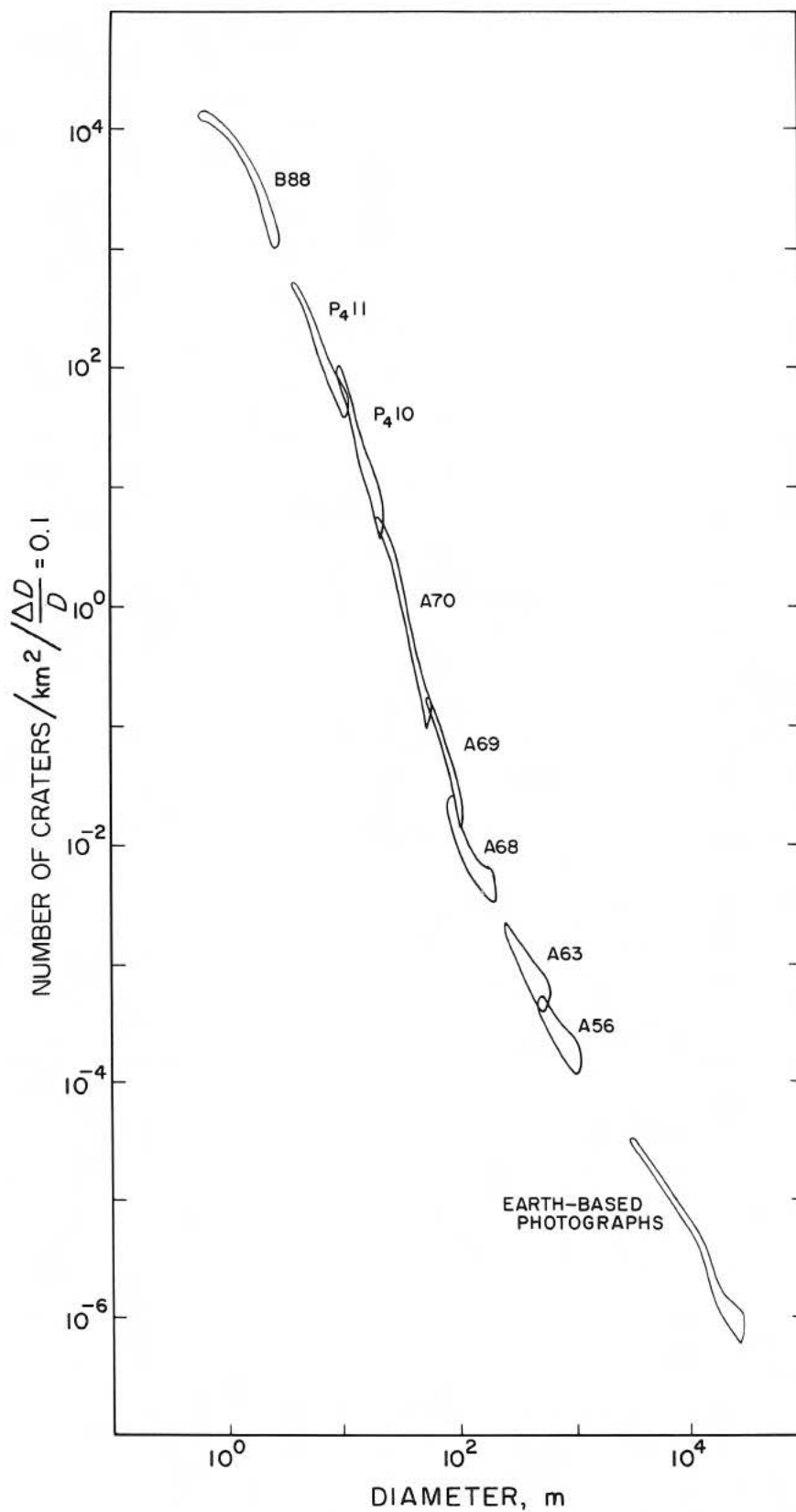
Fig. 92. Size–frequency distribution of sharp craters in *Ranger IX* impact area. (Widths of segments represent the uncertainty in the actual position.)
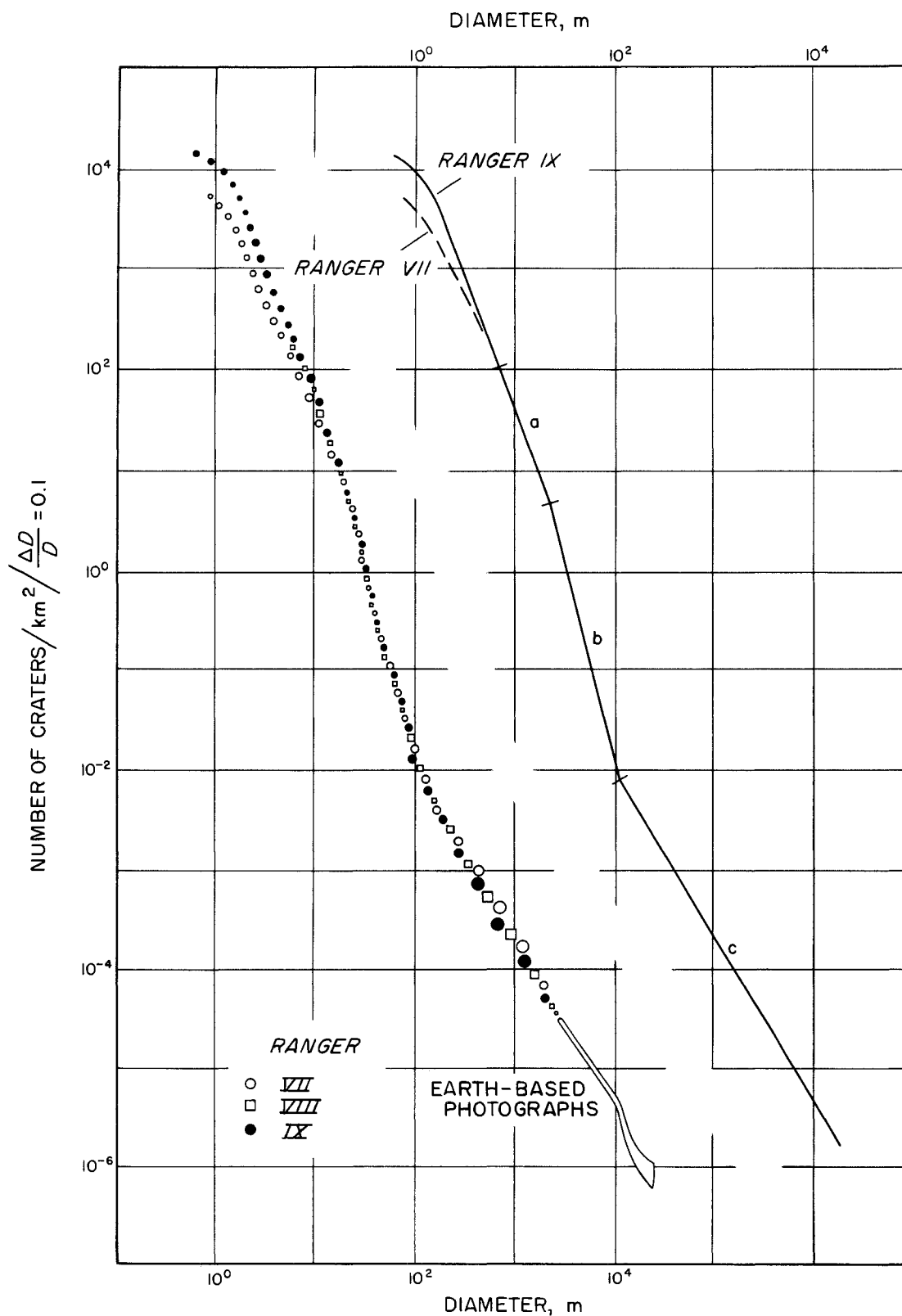
Fig. 93. Comparison of size—frequency distribution of Figs. 90, 91, and 92 (left), and schematic representation of size—frequency distribution of post-mare primary-impact craters (right).
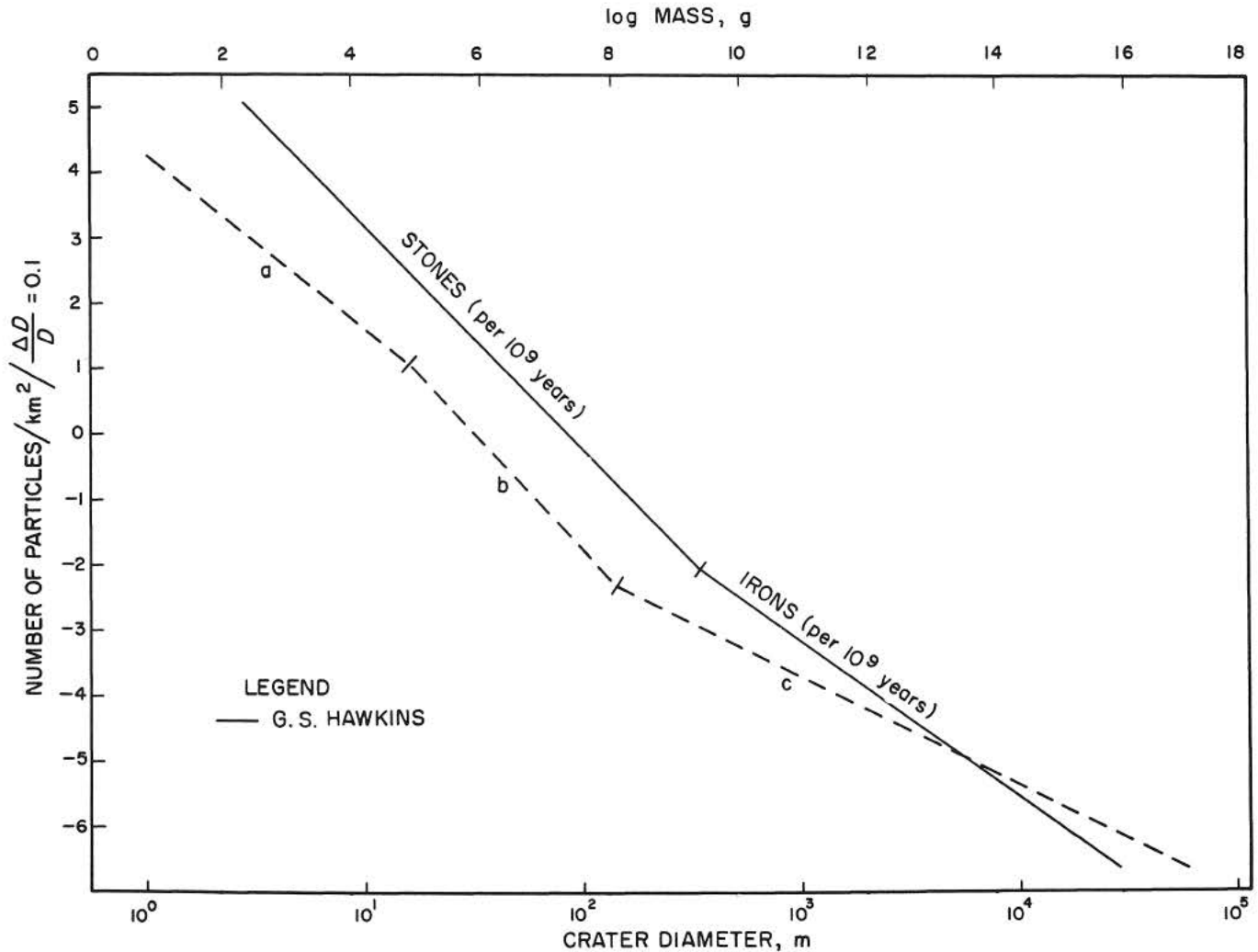
Fig. 94. Comparison of present particle flux with actual distribution on Moon.

of the mare surface layers; (2) the average impact velocity on the Moon is somewhat uncertain; (3) the present meteoritic flux on the Moon is uncertain, both because of errors in the geocentric flux and the scaling factor to be applied to the Moon. The rate factor may therefore be 10–50—a reasonable amount because the collisional meteorite production process presumably started roughly at the time of mare formation.

Thus, parts (b) and (c) of the curve of post-mare sharp craters may tentatively be interpreted as being due to stones and irons, respectively, with the observed flux accounted for as to order of magnitude.

5. The Slope Change Between (a) and (b) of Eq. (3)

We noted before the existence of a linear relationship between $\log m$ and $\log N$ for the impacting bodies respon-

sible for the primary lunar craters, and have commented on the possible interpretation in terms of a grinding process. On this basis, fragments are being produced in the asteroid belt according to the distribution law

$$dN = ar^{-b} \, dr \qquad (5)$$

in which r is the radius of a particle in centimeters. The Poynting–Robertson effect will cause a particle to spiral into the Sun, with its "lifetime" t

$$t = 10^7 r \rho q^2 \qquad (6)$$

where r is the radius of the particle in centimeters, ρ its density, and q its perihelion distance in astronomical units (A.U.). The mean eccentricity e, has been assumed

to be 0.15, and t is expressed in years. With $\rho \simeq 3.5$ (stones, which are the more numerous) and $q \simeq 2$ A.U.,

$$t = 1.40 \times 10^8 r \qquad (6a)$$

If the age of the asteroids T is 4.5×10^9 years (Ref. 24), the present ratio R of the number of particles still orbiting the Sun and the number of particles produced throughout T is

$$R = \frac{t}{T} = \frac{1.40 \times 10^8 \, r}{4.5 \times 10^9} = 0.031 \, r \qquad \text{for } t < T$$

$$R = 1 \qquad \text{for } t > T$$

$$(7)$$

The lifetime t equals the age T of the asteroids for a particle of radius $r_0 = (0.031)^{-1}$ cm $= 32$ cm, which is equivalent to a mass of $(4/3) \, \pi \, (32)^3 \times 3.5$ g $= 4.7 \times 10^5$ g.

Thus, by Eq. (5),

$$dN = Rar^{-b}dr \qquad (8)$$

or, by Eq. (7),

$$dN = a'r^{-(b-1)} \, dr \qquad \text{for } r < 32 \text{ cm}$$

and

$$dN = ar^{-b}dr \qquad \text{for } r > 32 \text{ cm}$$

In the source region of the asteroid ring, the meteorite population will thus be reduced for particles with masses smaller than $\sim 5 \times 10^5$ g by the Poynting–Robertson effect, with the diameter–frequency distribution lowered by 1 and the mass–frequency distribution by $\frac{1}{3}$ in the exponent. The correspondence of such a distribution change with the observed difference between parts (a) and (b) of Eq. (3) suggests a possible interpretation of this difference in terms of the Poynting–Robertson effect. However, for this interpretation to be correct, the probability of collision of particles originating from the asteroid ring with the Earth–Moon system must be nearly mass-independent in the mass range considered here. The fulfillment of this requirement has not yet been established. The probabilities of collision with the terrestrial planets have been discussed by Öpik (Ref. 25).

6. Surface Modification

At diameters smaller than about 7 m, the number of craters decreases, compared to an extrapolation of part (a) of the curve, first in the *Ranger VII* impact area and

down from $D \simeq 2$ m on the Alphonsus floor. These deviations can be interpreted in terms of surface modification. Jaffe (Ref. 14) has performed experiments to show the dependence of the appearance of a crater on the thickness of an overlay of fragmental material. From his investigations, it was estimated that covering a sharp crater with a fragmental layer about $\frac{1}{30}$ D thick is enough to change its appearance to that of a crater which would be classified as soft. Thus, *the thickness of the disturbed layer on the floor of Alphonsus appears to be of the order of 7 cm* ($\frac{1}{30}$ of 2 m), while *in the* Ranger VII *impact area this depth seems to be increased by about a factor of 3*. This increase is attributed to the Tycho and Copernicus rays in the impact area.

Two other independent determinations of the amount of post-mare "erosion" provide about the same results. (1) From the primary-crater distribution, one can obtain a cumulative areal coverage of the maria with craters having diameters $D > D_0$. The size–frequency distributions of parts (a), (b), and (c) can also be written as

$$dN = pD^{-k} \, dD \qquad (9)$$

where D is given in meters, and N per square kilometer. Thus,

(a)	$p = 1.6 \times 10^5$	$k = 3.65$
(b)	$p = 4.5 \times 10^6$	$k = 4.70$
(c)	$p = 1.8 \times 10^2$	$k = 2.68$

(10)

Let

$$\int_{x_1}^{x_2} dA$$

represent the total area (in square meters) of all primary craters per square kilometer, having $x_1 < D < x_2$. Then, by Eq. (5), dA can be written as

$$dA = \pi \left(\frac{D}{2}\right)^2 dN = \frac{\pi}{4} \, pD^{-(k-2)} \, dD \qquad (11)$$

(D in meters).

Assuming the largest post-mare crater to have a diameter of 100 km, one finds from Eqs. (10) and (11) that part (c) contributes

$$\int_{120}^{10^5} 1.4 \times 10^2 \, D^{-0.68} \, dD = 1.6 \times 10^4$$

(D in meters) or a coverage of 1.6%.

In the same way, one finds for (b)

$$\int_{22}^{120} 3.5 \times 10^6 \, D^{-2.70} \, dD = 6 \times 10^3$$

(D in meters) or 0.6%.

Thus, *the post-mare primary-impact craters with* $D > 22$ m *cover 2.2% of the maria.*

Extrapolations of relation (a) to very small crater diameters would fix that value (D_0) at which the entire mare surface would have become covered. One finds

$$\int_{D_0}^{22} 1.2 \times 10^5 \, D^{-1.65} \, dD = [1.9 \times 10^5 \, (D_0)^{-0.65} - 2.7 \times 10^4]$$

(D in meters).

By equating this expression to $10^6 - 2.2 \times 10^4$ (1 km² − area covered by craters with $D > 22$ m), one finds for D_0

$$[1.9 \times 10^5 \, (D_0)^{-0.65} - 2.7 \times 10^4] = 9.78 \times 10^5$$

or

$$D_0 = 0.08 \text{ m}$$

Since small primary craters have a depth-to-diameter ratio of roughly 1 to 4, this indicates that, except near large primary craters, *the mare surface cannot have been fragmented by primary impacts to an average depth of more than a few centimeters.*

(2) Another estimate of the rate of accumulation of fine debris on the mare surface can be made from the thermal data of Saari and Shorthill (Ref. 4), which were obtained during the lunar eclipse of December 19, 1964 (see Section B).

The hot spots in the maria in the northern hemisphere have been identified as completely as possible with the class 1 and 2 post-mare craters of Arthur's catalog (Refs. 15 and 16), the same classes used in the size–frequency distributions of Figs. 90–93. It was thus possible to find the percentages of "hot" craters in terms of all class 1 and 2 craters, depending on the crater diameter (see Fig. 95). The proportion appears to be fairly constant at 75% for diameters larger than 18 km, whereas it drops to zero at about 2 km. Since the scanning beam had a diameter of about 18 km on the lunar surface, the drop in Fig. 95 can be considered as being due to its limited resolution. Therefore, the conclusion that 75% of the post-mare primary-impact craters have not been covered with enough fragmented material to eliminate the thermal anomalies resulting from crater formation appears justified. In fact, 75% represents a lower limit, since any failure to identify a hot spot with a crater and any error in selecting primary-impact craters would decrease this percentage.

From these data, it is obvious that *the accumulation rate of fine debris cannot exceed a few millimeters per* 10^9 *years*, which agrees well with the two other observations described.

Comparison of the production rate of fine debris with the rate of sputtering (about 0.5 Å/year, Ref. 9) shows that sputtering may be more important than fragmentation in modifying the lunar surface on a small scale. This would imply that the thin debris layer is replaced once
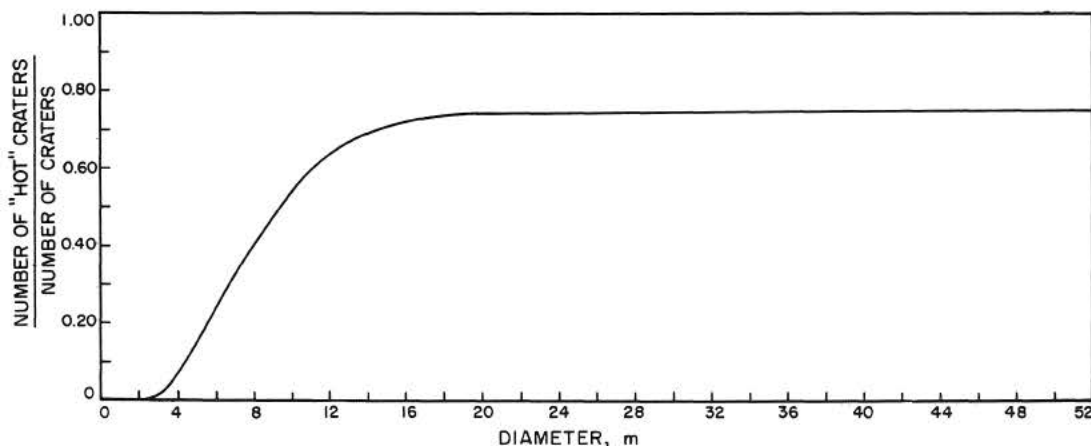
Fig. 95. Ratio of primary craters designated as "hot" to total number of primary craters, as a function of crater diameter.

every 3×10^8 years. Since sputtering is more effective in smoothing the surface, its prevalence over impact erosion would account for the smooth appearance of the mare-type surface in the high-resolution *Ranger* photographs (see also Section B).

7. Soft Craters

Since most of the soft-crater counts remain to be done, only some general remarks are made on their distribution. Figure 96 shows a comparison of the sharp- and soft-crater distribution in the last *Ranger VII, VIII,* and *IX* A frames. It appears that soft craters are the more numerous by factors up to nearly 100 at $D = 100$ m.

One further finds that soft craters *do* show significant local differences, ranging up to a factor of 3, in areal densities. For example, the soft craters in the last *Ranger VII* A frame show an excess in the range of 100–200 m. This excess can be identified with the "loop" of craters which crosses this frame. In the *Ranger VII* and *IX* frames, there is also evidence for a bimodal distribution around preferential diameters of about 20 and 100 m,
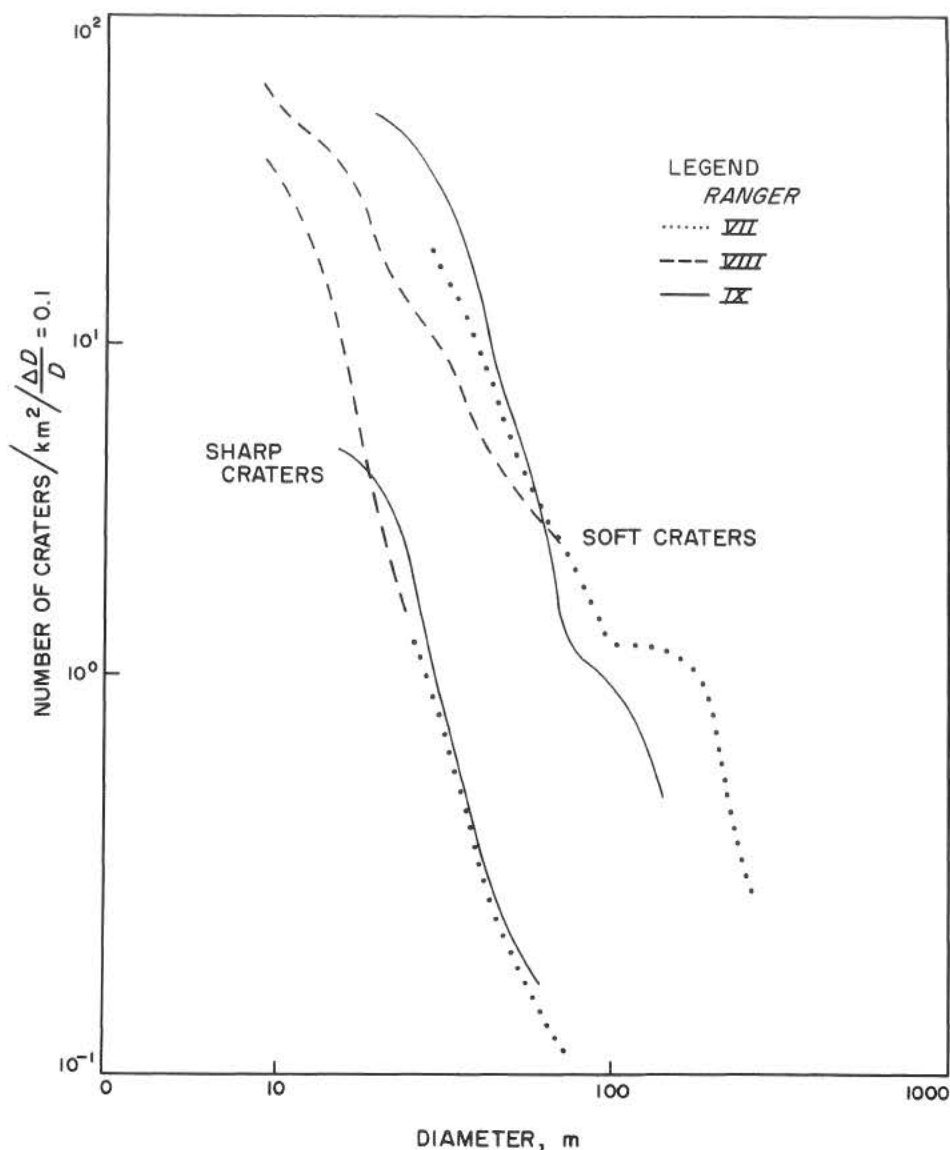
Fig. 96. Size–frequency distributions of sharp and soft craters in last
Ranger VII, VIII, and IX A frames. (Note excess of soft
craters in Ranger VII frame for $100 < D < 200$ m.)
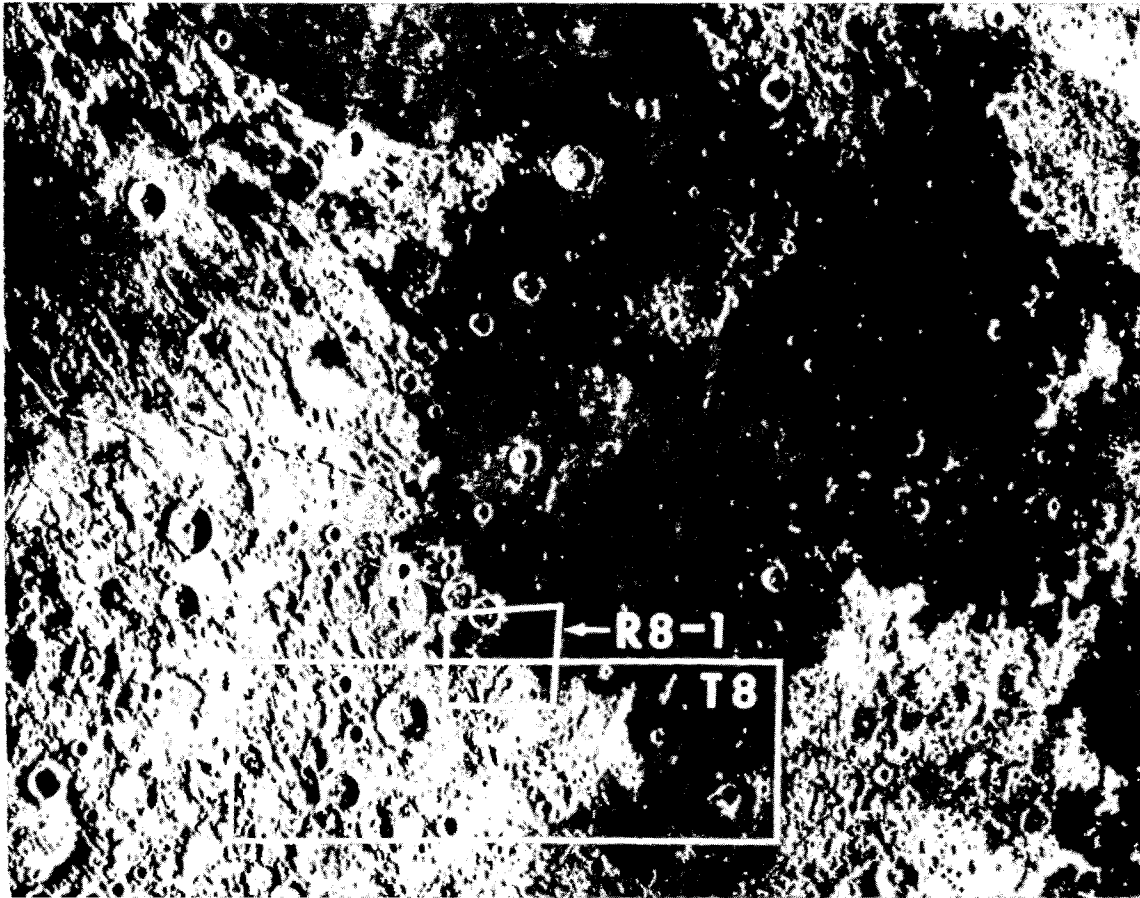
Fig. 97. Location of areas mapped for lineaments from Earth-based (T8)
and *Ranger VIII* (R8-1) photographs.

respectively, each covering a similar fraction of the mare surface.

Data on the size–frequency distributions of terrestrial collapse depressions in lava flows are needed for a better interpretation of the lunar soft-crater distributions.

G. Small-Scale Lineaments in the Ranger VIII and IX Photographs

In a previous study (Ref. 1, Section H) of the *Ranger VII* photographs, it was shown that small-scale lineaments occur in Mare Cognitum, and that their directions correspond to the directions of major lineaments in the terra adjacent to the *Ranger VII* impact site. It was also pointed out that the *Ranger VII* lineaments form parts of global lineament systems which were determined in an earlier study (Ref. 26) using Earth-based photography.

The *Ranger VIII* and *IX* photographs show small-scale lineaments which are similar, but more pronounced because of the lower Sun angle, in Mare Tranquillitatis and on the floor of Alphonsus. The directions of these small-scale lineaments also coincide with the directions of large-scale lineaments in the terra areas adjacent to Mare Tranquillitatis and Alphonsus, and therefore confirm the findings reported in the *Ranger VII* experimenters' analyses (Ref. 1, Section H).

Following the procedure adopted in the *Ranger VII* Report (Ref. 1, Section H), the small-scale lineaments were mapped from selected *Ranger VIII* and *IX* photographs and their directions compared with large-scale lineaments in the terra areas adjacent to the impact sites. The locations of the areas mapped for small-scale lineaments from *Ranger VIII* photographs (R8-1 to 4) and the terra area (T8) mapped for large-scale lineaments adjacent to the *Ranger VIII* impact site are shown in Figs. 97 and 98. The lineaments were mapped on *Ranger*

VIII photographs B90 (the last B frame), B87, B76, and the frame between B39 and B40. Since the *Ranger VIII* B camera was oriented at an angle with respect to the lunar surface which distorted the true directions of the lineaments, it was necessary to rectify the B photographs before mapping the lineaments.

Figures 99 and 100 are representative lineament maps of *Ranger VIII* areas R8-4 and R8-1. As in the *Ranger VII* photographs, the lineaments are represented by small crater chains, elongate craters, and linear depressions and ridges, and are probably manifestations of fractures. It is significant that, although area R8-4 covers only a small

region (3.4 km^2) entirely within Mare Tranquillitatis, the directions of the lineaments in area R8-1, which are primarily in the uplands, correspond closely to those in area R8-4. In Fig. 99, a large collapse depression (diameter 900 m) is shown near the lower right-hand corner of the map. Extending north from this crater is a broad, gentle, plateau-like elevation shaped like a triangle (see Fig. 46, and frame B90). The lineament density is five times greater on the plateau (104 lineaments/km^2) than in the surrounding area (21 lineaments/km^2). The lineament density on the crater floor also appears to be somewhat greater than in the general area outside the crater. These facts suggest that the plateau has been gently
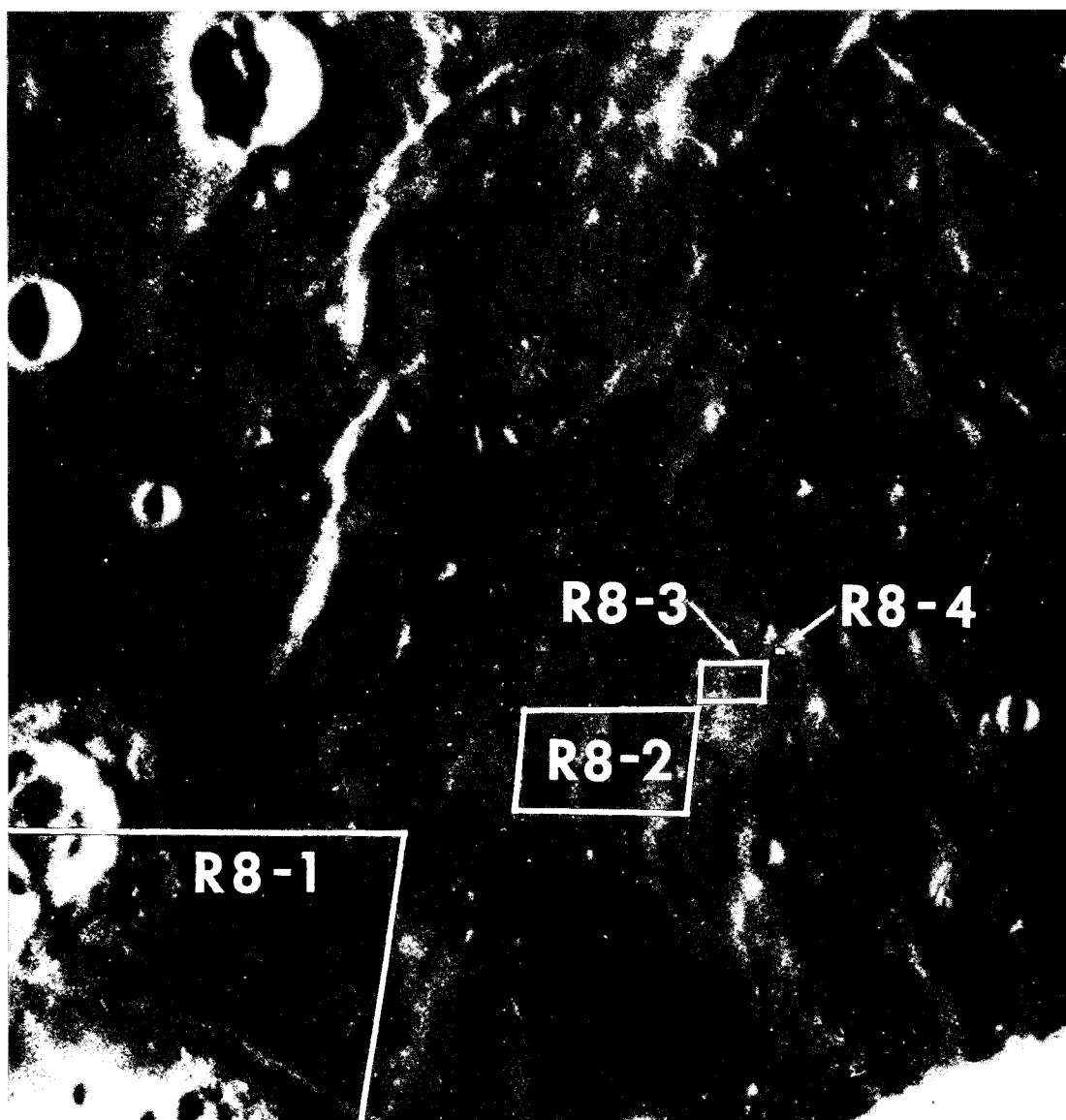
Fig. 98. Location of areas (R8-1 to 4) mapped for lineaments from *Ranger VIII* photographs.
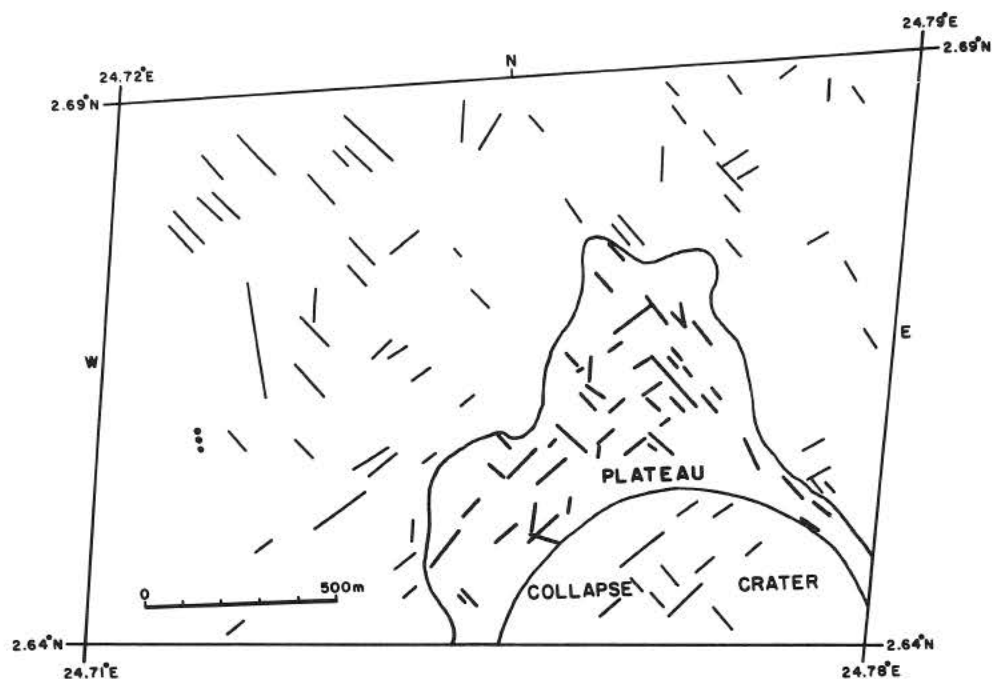
Fig. 99. Lineament map of area R8-4. (Shaded area is broad, gentle, plateau-like elevation. Based on rectified *Ranger VIII* photograph B90. See Fig. 46.)
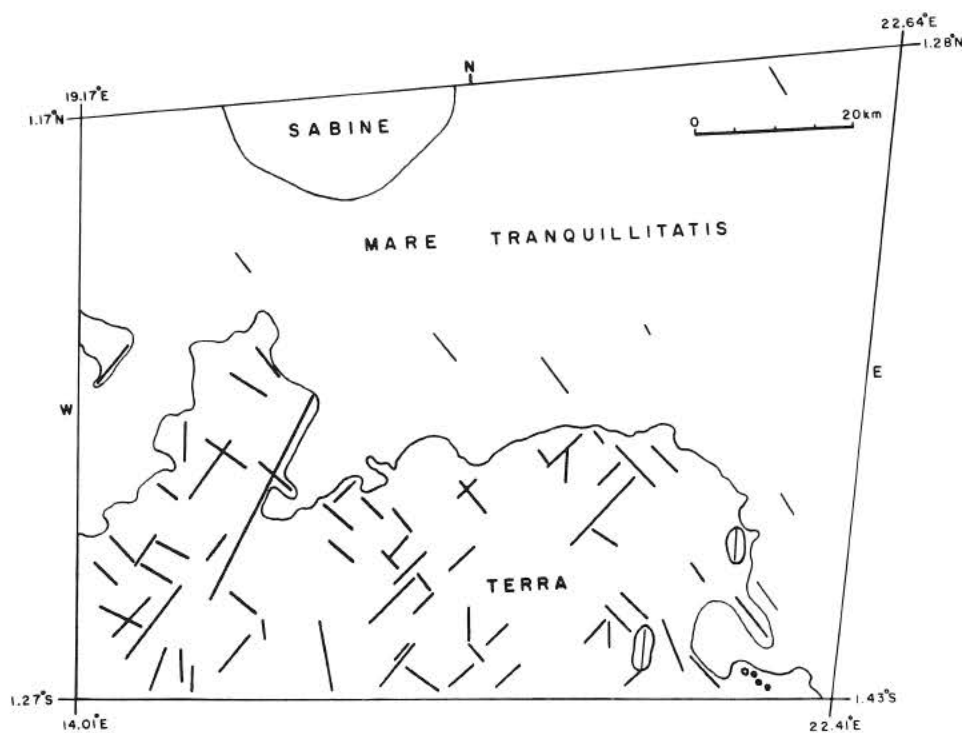
Fig. 100. Lineament map of area R8-1. (Based on rectified *Ranger VIII* photograph between frames B39 and 40. See Fig. 103.)
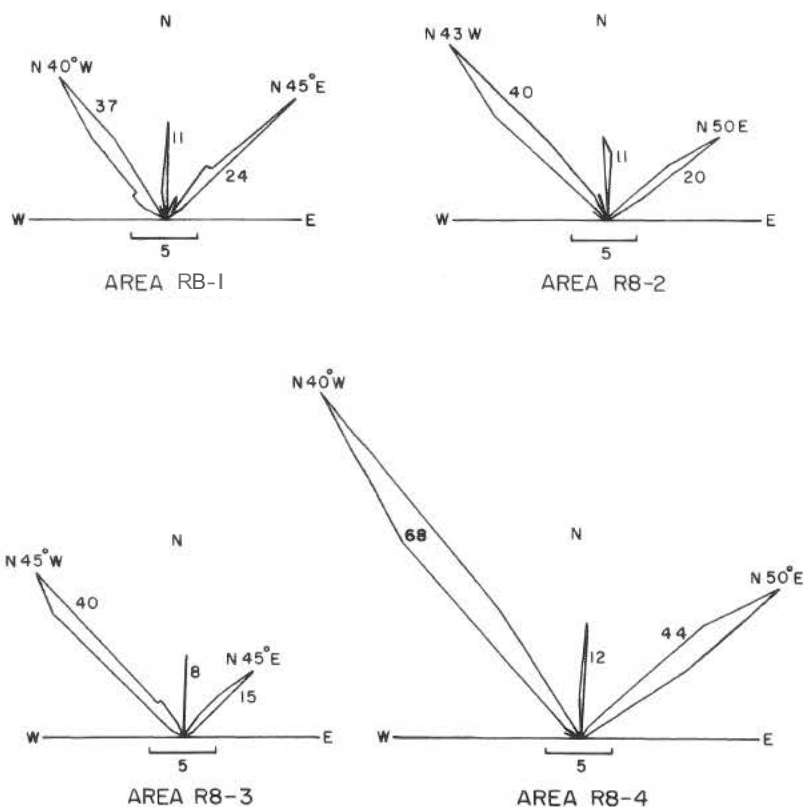
Fig. 101. Azimuth–frequency diagrams of lineaments
in *Ranger VIII* areas R8-1 to 4. (Number near
each peak refers to the number of linea-
ments represented by that peak.)
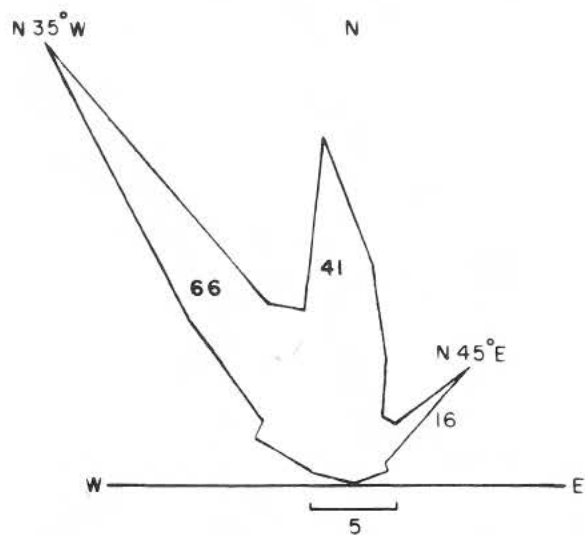
Fig. 102. Azimuth–frequency diagram of lineaments
in terra (T8) adjacent to *Ranger VIII* impact site.
(Number near each peak refers to the number
of lineaments represented by that peak.)

uplifted, thus intensifying the pre-existing fracture pattern. In addition, the collapse of the large crater also appears to have intensified the pre-existing fracture pattern on the crater floor.

Figure 101 presents lineament azimuth–frequency diagrams of *Ranger VIII* areas R8-1 to 4. The diagrams show that the lineaments are oriented in three principal directions (northeast–southwest, northwest–southeast, and north–south), the strongest system being the northwest–southeast one. Figure 102 is a lineament azimuth–frequency diagram of terra area T8, adjacent to the *Ranger VIII* impact site. The lineaments in this area were mapped from Earth-based photographs (Ref. 26), and their true selenographic azimuths were computed on the IBM 7072 computer of the University of Arizona Numerical Analysis Laboratory. The diagram shows that the large-scale lineaments follow three principal directions which are practically identical to the directions of small-scale lineaments in the *Ranger VIII* photographs. The northwest–southeast lineaments form part of the Imbrium radial system and the global northwest–southeast system. Unfortunately, the directions of the Imbrium radial system and the global northwest–southeast system coincide in the *Ranger VIII* impact area. The small-scale *Ranger VIII* lineaments oriented in that direction may therefore belong to either system. However, the flooding of Mare Tranquillitatis occurred after the initial development of the Imbrium radial system, as indicated by the flooded valleys on its western shore, so it is probable that the majority of northwest–southeast-directed lineaments in Mare Tranquillitatis belong to the global system. The other two major directions belong to the global northeast–southwest and north–south lineament systems.

In addition to the fine lineaments, there are several trough-like depressions which consist of craters or have a crateroid appearance. Details of four of these depressions are shown in Fig. 103 along the Hypatia rille, and features of this type occur throughout Mare Tranquillitatis. Figure 104 is an Earth-based photograph of Mare Tranquillitatis on which 36 of these structures are indicated; although some of them are difficult to see in the reproduction, they are quite evident in the original photograph. The trough-like depressions are also well portrayed on ACIC chart LAC 60. The azimuths of the 36 structures shown in Fig. 104 were measured on the ACIC chart and plotted in an azimuth–frequency diagram (Fig. 105). This diagram shows that the majority of the structures are oriented in three principal directions which roughly coincide with the three main directions of lineaments in the adjacent terrae and with the small-scale

lineaments in Mare Tranquillitatis (compare Fig. 105 with Figs. 101 and 102). Furthermore, many of the troughs occur on ridges. All of these facts indicate that the majority of trough-like depressions seen in the *Ranger VIII* and Earth-based photographs of Mare Tranquillitatis are structurally controlled and may be due to collapse and/or maar-type cratering.

Examples of linear volcanic troughs in the Galapagos Islands which are remarkably similar to those in Mare Tranquillitatis are shown in Fig. 106.

The relationships between small-scale lineaments on the floor of Alphonsus and large-scale lineaments in the surrounding terrae are very much like those of similar features in the Mare Tranquillitatis area. Figures 107 and 108 show the areas (R9-1 to 3) mapped for small-scale lineaments from *Ranger IX* photographs (A70, A68, and A56) and the terra area (T9) mapped for large-scale lineaments adjacent to the *Ranger IX* impact site. Figures 109 and 110 are lineament maps of *Ranger IX* photographs A70 and A56.

Figure 111 shows azimuth–frequency diagrams of the small-scale lineaments in areas R9-1 to 3, and Fig. 112 is an azimuth–frequency diagram of large-scale lineaments in the adjacent terra (area T9). An inspection of the diagrams reveals that the small-scale lineament directions on the floor of Alphonsus are very similar to the directions of large-scale lineaments in terra area T9. The peaks at N 45–55°W, N–S, N 12–22°E, and N 40–50°E correspond to the northwest–southeast, north–south, north-northeast–south-southwest, and northeast–southwest global lineament systems, respectively. The north-northeast peak is missing in the diagram representing the last A frame (area R9-3) but appears in the next-largest area (R9-2). Apparently, this system is not represented by very small-scale lineaments on the floor of Alphonsus. However, one of the two major structural trends on the central spine of Alphonsus is in the north-northeast direction.

It should be noted that the relative intensities of the peaks representing the global systems are roughly the same on the floor of Alphonsus and in the adjacent terra. However, the peak at N 14–22°W, whose direction corresponds to the Imbrium radial system in the area, is much weaker on the floor of Alphonsus than in the adjacent terra. This indicates that *the stresses which produced the Imbrium radial system were much more intense in the area surrounding Alphonsus than they were on the crater*

Fig. 103. South-shore area of Mare Tranquillitatis E of
Sabine (margin), showing Hypatia Rilles I and II,
dark-halo crater on outer wall of Sabine,
and four prominent linear-beaded
depressions near rille.
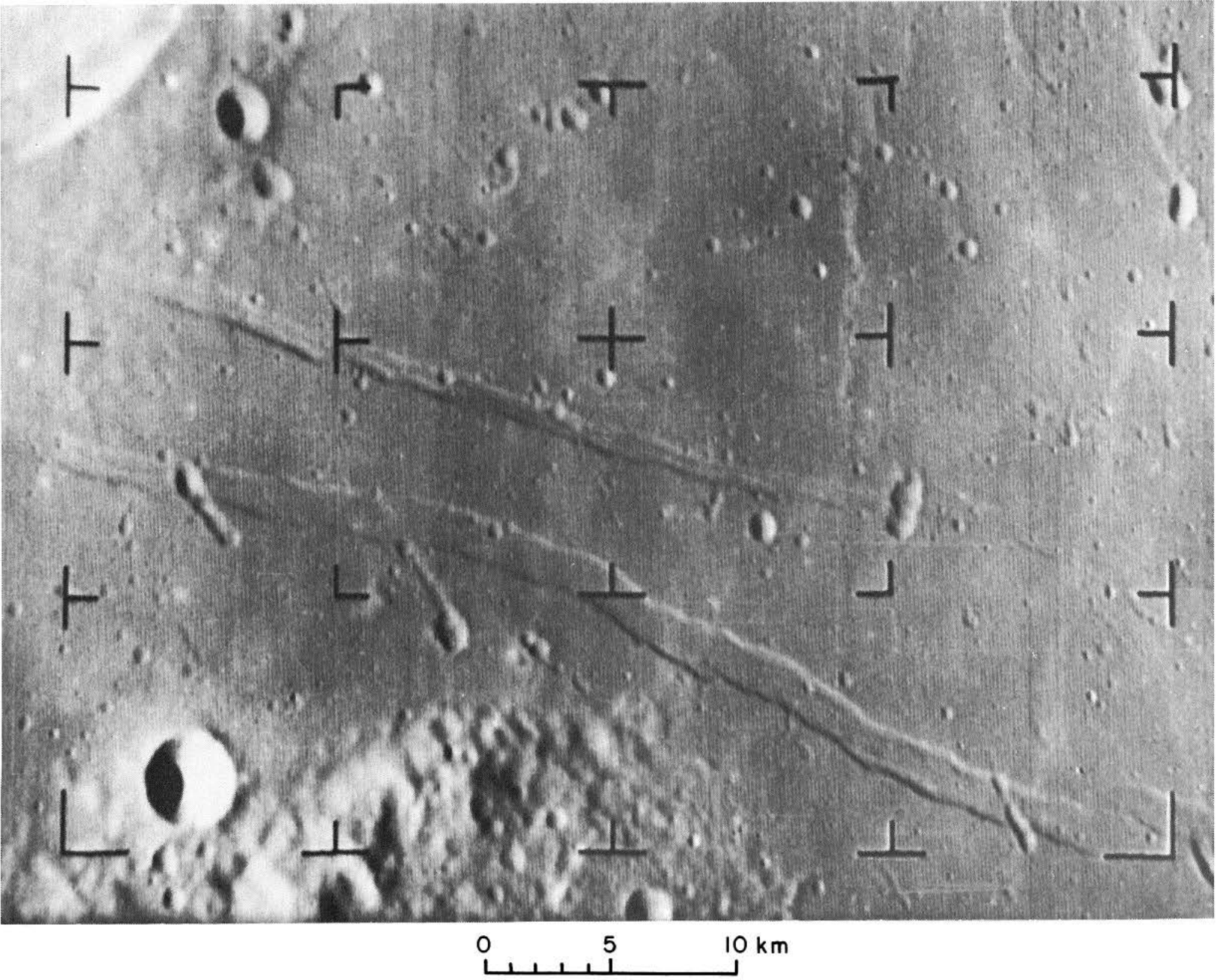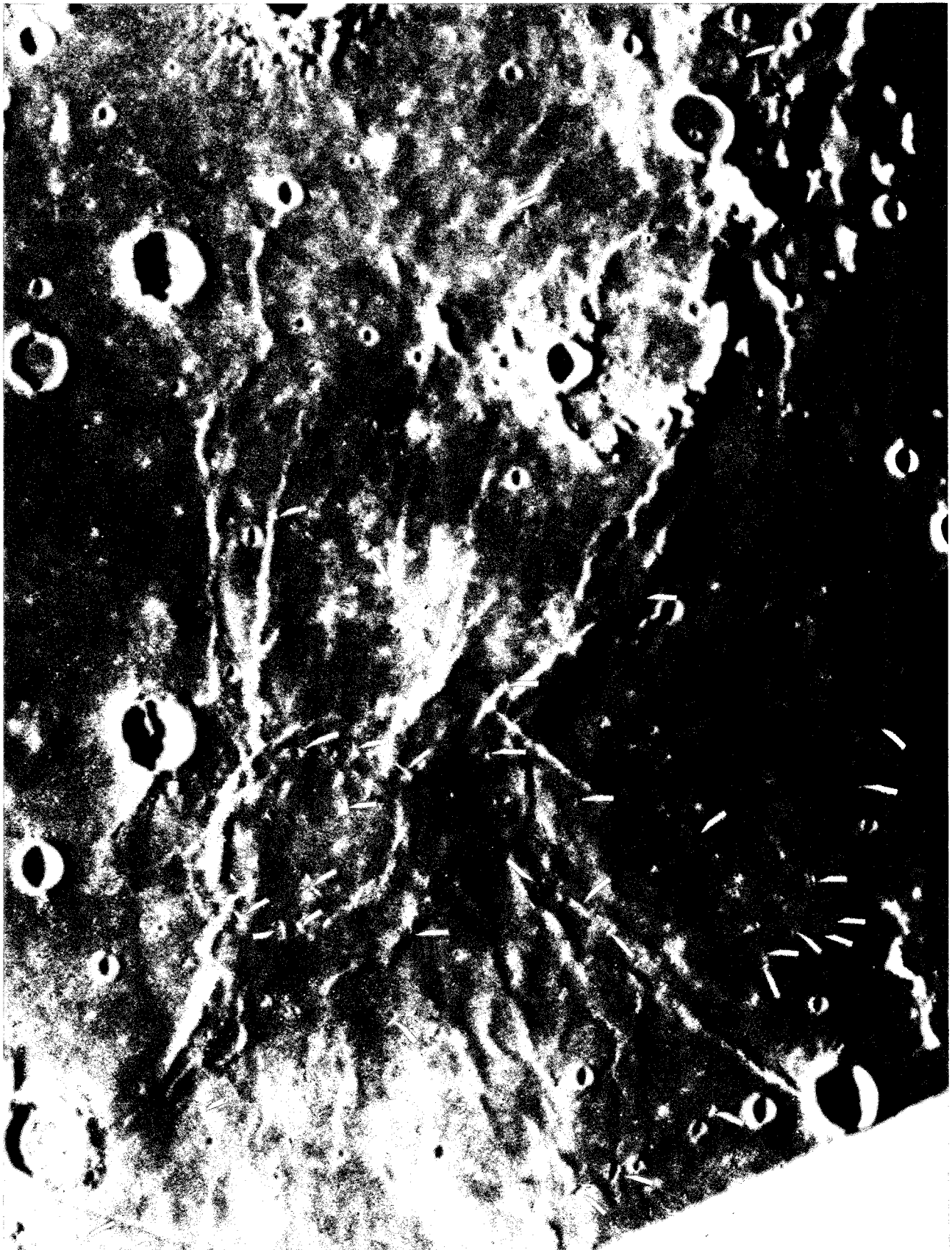
floor. Therefore, the flooding of Alphonsus probably took place *after* the main development of the radial system, but at a time when there were weak residual stresses remaining from the formation of the radial system. Since the walls of Alphonsus are cut by the Imbrium system, they must be older than that system. If the floor of the crater were the same age as the walls, then one would expect a comparable degree of lineation, which is not the case. Furthermore, a large valley belonging to the Imbrium radial system cuts the southern interior wall of Alphonsus and seems to have been flooded by the floor material. These facts indicate that *Alphonsus was formed before the Imbrium event but was flooded subsequent to the formation of Mare Imbrium,* when the stresses which produced the radial system were declining. Thus, the *formation of the Imbrium system extended over a considerable period of time.*

The major axes of the central peak and the central spine, the two most prominent structures on the floor of Alphonsus, coincide with the direction of, and were probably formed along subcrustal fractures associated with, the Imbrium system. It should be noted that although *the axis of the spine coincides with the Imbrium direction, the fine structure on the spine forms part of the global lineament systems.* Since this is also true of the fine structure of mare ridges, which are probably dike-like intrusions (Ref. 1, pp. 60–71), it is probable that *the central spine of Alphonsus is also a dike-like intrusion* along an Imbrium radial fracture, with subsidiary branches following fractures of the global lineament systems.

In summary, the azimuthal distribution of small-scale lineaments in Mare Cognitum, Mare Tranquillitatis, and on the floor of Alphonsus coincides with the distribution of large-scale lineaments in the adjacent terrae. These findings lead to the conclusion that the fracture pattern in the lunar crust is very basic in nature, extending down to scales in the meter range. The small-scale fractures in the mare material indicate that the material is relatively strong and cohesive. This supports the contention that the mare material is primarily lava overlain by only a thin ($\leq$ 1 m) layer of fragmental material.
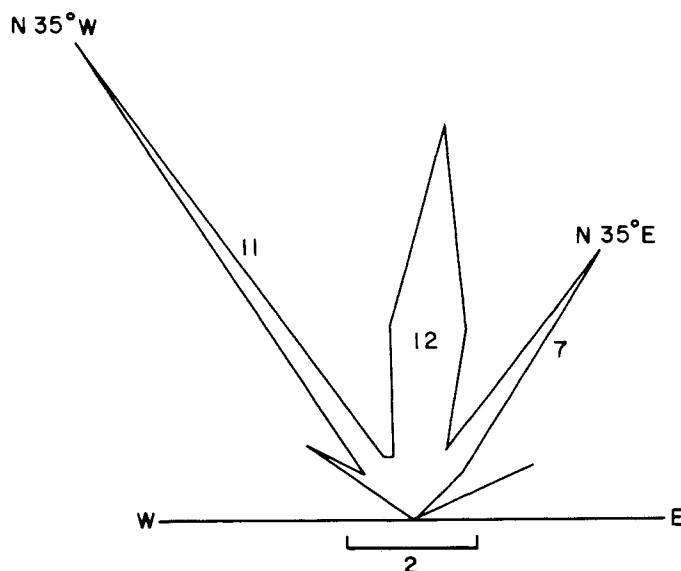
Fig. 105. Azimuth–frequency diagram of trough-like depressions shown in Fig. 104. (Number near each peak refers to the number of depressions represented by that peak.)

Fig. 104. Trough-like depressions in Mare Tranquillitatis (indicated by white lines).

0   500 m
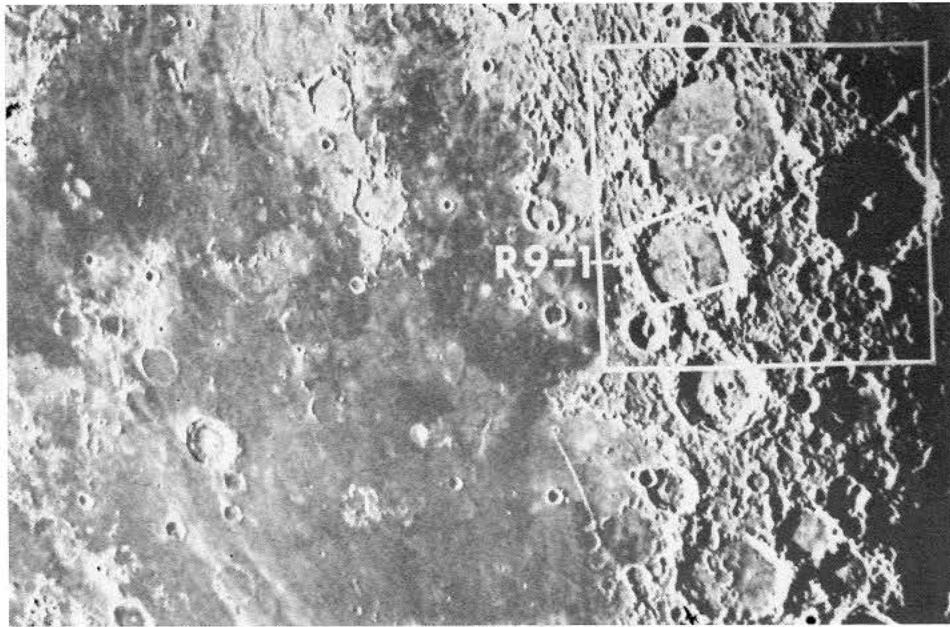
Fig. 107. Location of areas mapped for lineaments from
Earth-based (T9) and *Ranger IX* (R9-1) photographs.

Fig. 106. Oriented, linear volcanic craters located along
fractures that are radial to Volcan Wolf caldera in
Galapagos Islands. (Note remarkable similarity
between these linear structures and the linear
depressions shown in Fig. 103.)

←
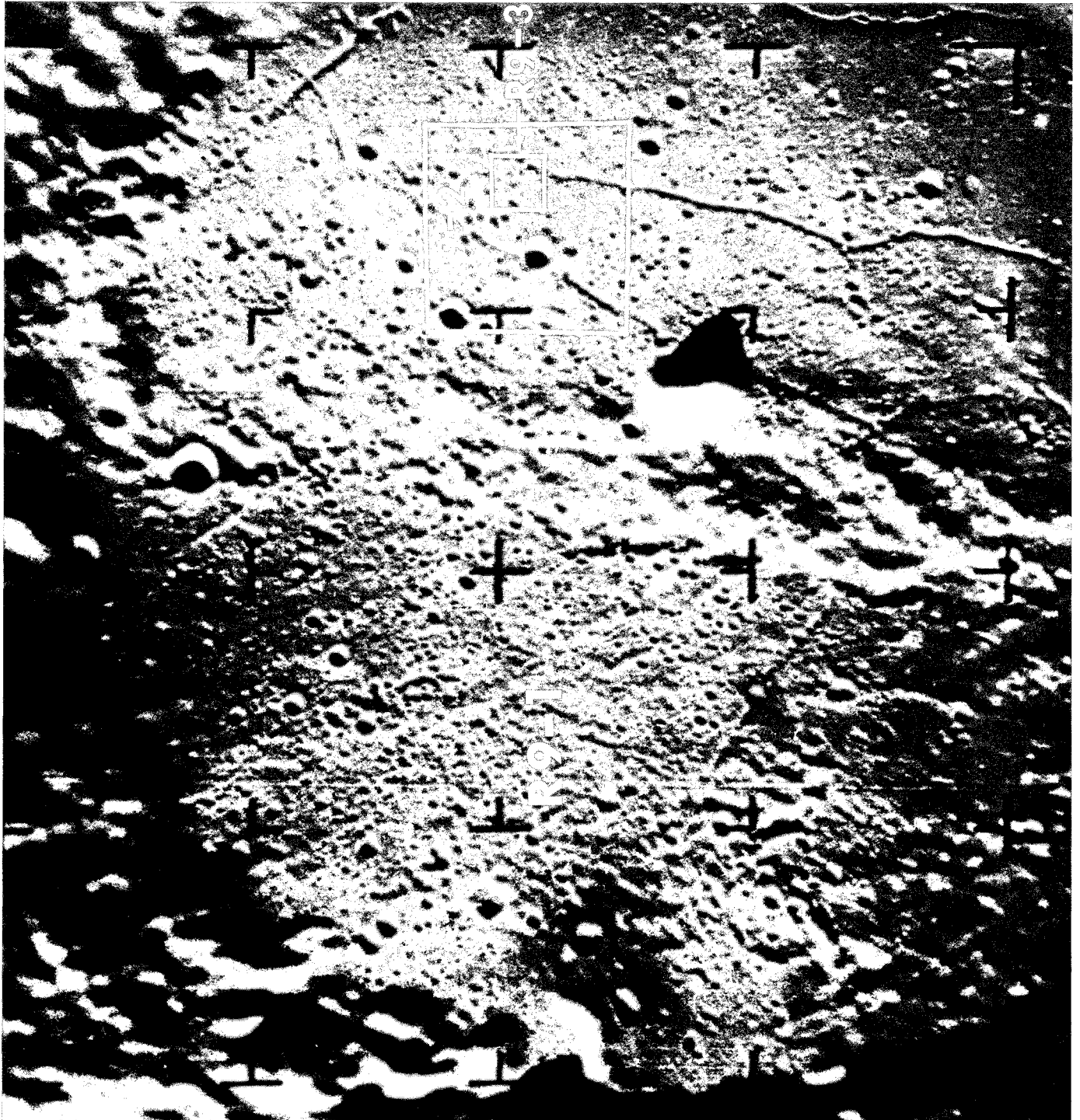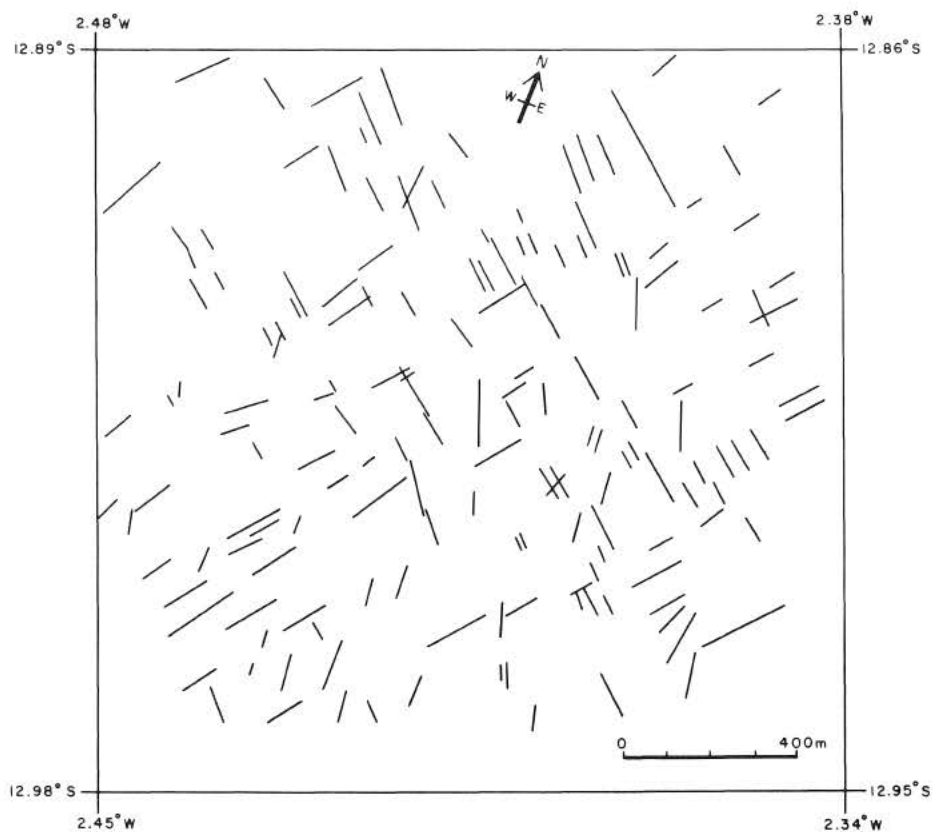
Fig. 109. Lineament map of area R9-3, based on
Ranger IX frame A70. (See Figs. 80–83.)

Fig. 108. Location of areas (R9-1 to 3) mapped for
lineaments from Ranger IX photographs.
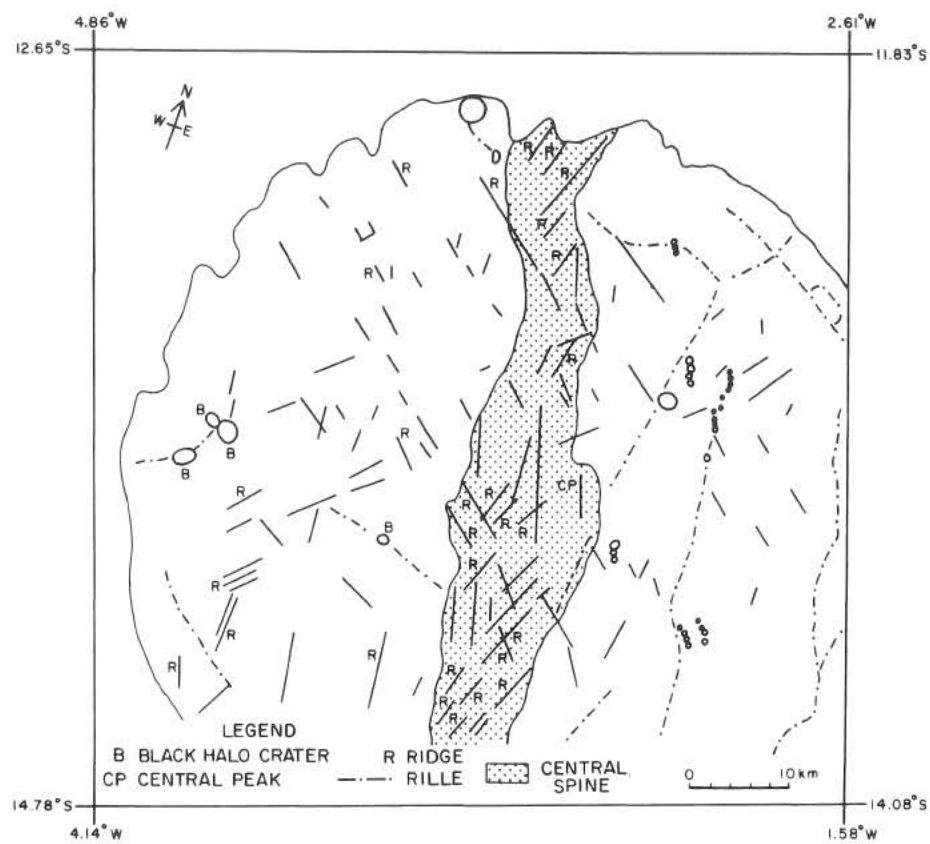
Fig. 110. **Lineament map of area R9-1, based on**
Ranger IX **frame A56. (See Figs. 10 and 108.)**
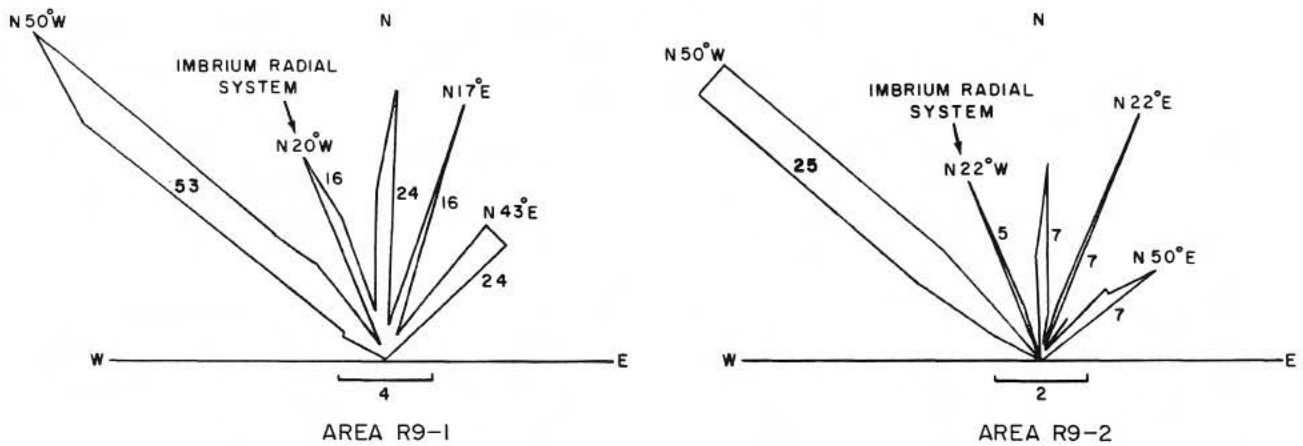
Fig. 111. Azimuth–frequency diagrams of lineaments in *Ranger IX* areas R9-1 to 3. (Number near each peak refers to the number of lineaments represented by that peak.)
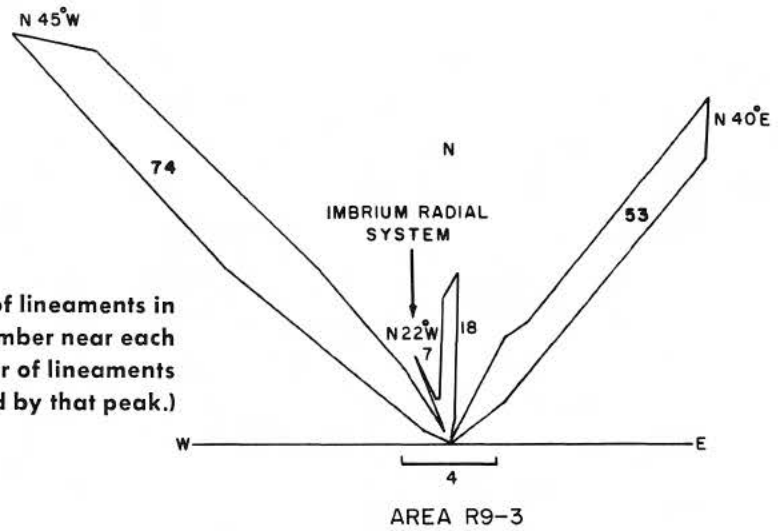
Fig. 112. Azimuth–frequency diagram of lineaments in terra adjacent to *Ranger IX* impact site (T9). (Number near each peak refers to the number of lineaments represented by that peak.)
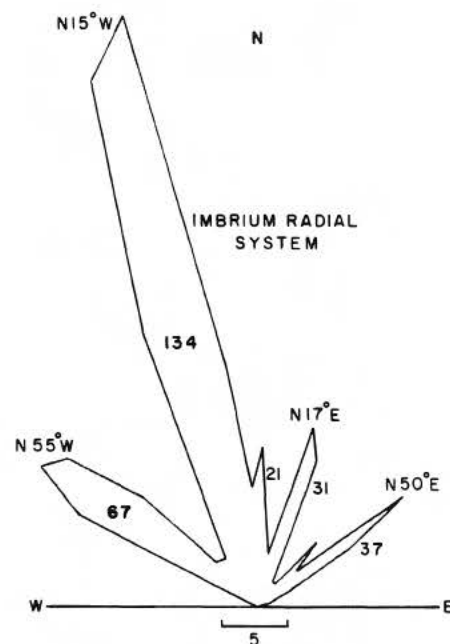
H. Small Domical Structures in the Ranger Photographs

Small domical structures found in the *Ranger VII, VIII*, and *IX* photographs are the only positive topographic relief (except for the ridges) found on mare-type terrain, and they provide some insight into lunar subsurface activity.

Several of the domes occur on crater floors. In Fig. 113, five or six domical structures, ranging from 1.5 to 3.5 km in diameter and up to 300 m high, are seen on the floor of Theon Junior (diameter 18.5 km); the south-ernmost dome may have one or more summit craters. Theon Junior is usually considered a sharp, class 1 impact crater.

Figures 114 and 115 show two domical structures within soft craters in Mare Cognitum; the larger dome (Fig. 114) is 60 m in diameter and the smaller one (Fig. 115) about 25 m. There are protuberances in several other craters in the *Ranger VII* B frames, but they are considerably sharper, and the craters in which they occur are relatively sharp. These protuberances may be secondary ejecta that produced the craters, or they may be the result of slumping of the crater walls.

0   10 km

Fig. 113. *Ranger VIII* **photograph of domes on floor of Theon Junior.**
(Early B frame not represented in atlas.)
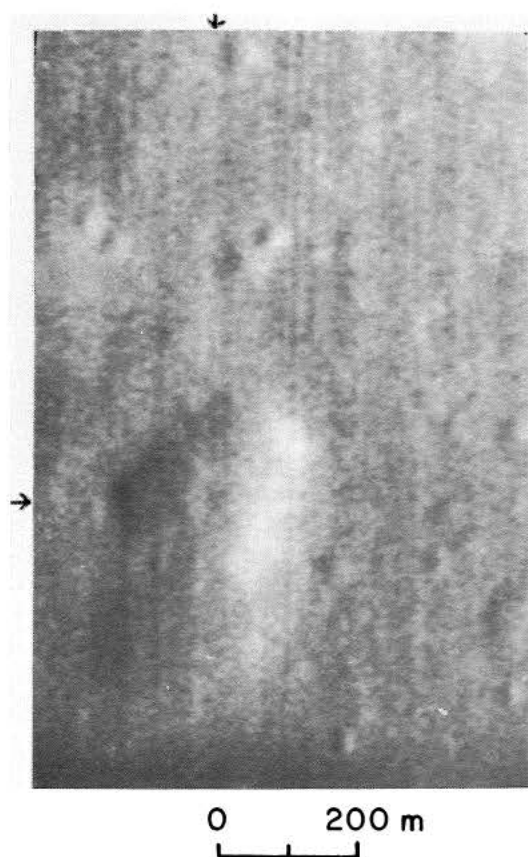
Fig. 114. Section of *Ranger VII* frame P174, showing dome on floor of a collapse structure on Mare Cognitum. (See also frame B199.)

Fig. 115. Section of *Ranger VII* frame B200 in same general area as Fig. 114.

A gentle dome, 95 m in diameter, is seen on the bottom of a 500-m collapse crater in Alphonsus (Fig. 79, upper right corner). This domical structure has a broad, relatively flat top and is about 3.5 m high; the detail on its surface is no different from that of the surrounding area. Another dome, 90 m in diameter, is shown on the floor of a large collapse crater in Fig. 116, and there are several smaller domical structures on its inner slopes. This crater forms one of a chain of four collapse structures.

Domical structures displaying a morphology similar to that of the above-mentioned domes occur in intercrater areas. Two small domes are located about 500 m north of the large, square-shaped collapse structure in Mare Tranquillitatis (Fig. 57). They may be verified in *Ranger VIII* photograph A59 and in several P_3 and P_4 frames which overlap the same area. The domes are very close together and may coalesce slightly. The larger one is 120 m in diameter and the smaller one 85 m; their heights are approximately 5–8 m. At the scale of the records, neither dome shows a summit crater.

In the lower section of Fig. 117 an elongate domical structure is seen, which is 600 m wide, 1.1 km long, and about 26 m high. This dome is just visible near the left edge of Fig. 8, 5 km above the lower corner; near its crest is a row of three rimless craters, 70 m in diameter each. The line of craters is parallel to the long axis of the dome and the trough-like depression visible near the center of the left margin in Fig. 8. The northernmost crater has a narrow, irregular depression leading away from it. The prominent bright crater on the western slope does not appear structurally related to the dome (it may be due to impact). The dome is best seen with the crater covered.

The domes in Figs. 118 and 119 exhibit excellent detail. The low dome in Fig. 118 is 760 m in diameter and 20–30 m high; it may be seen on a smaller scale in *Ranger IX* photographs A65–68. On its eastern half, there is a large teardrop-shaped crater, 190 m in diameter. Peripheral on the floor of the pointed end are dark furrows, about 10 m wide, which may be fractures. There are several fine rilles on the northwestern flank of the dome, three of them (marked **a**, **b**, **c**) only a few meters wide, all ending in sharp, rimless craters. The surface detail of the dome is no different from that of the surrounding area; i.e., no lava or ash deposits are in evidence.

Figure 119 shows a complex domical structure, seen on a smaller scale in Figs. 8 and 10. The main dome has a very shallow depression, about 75 m in diameter, on its summit. The elevated area continues to the northeast, though it breaks up into separate domical components, some of which have summit collapse craters. A prominent component with a summit crater (dimple) occurs just

Fig. 116. *Ranger IX* frame A69, showing string of four collapse craters on Alphonsus floor, crossed by weak diagonal lineament system; floor of third from top has several domes.
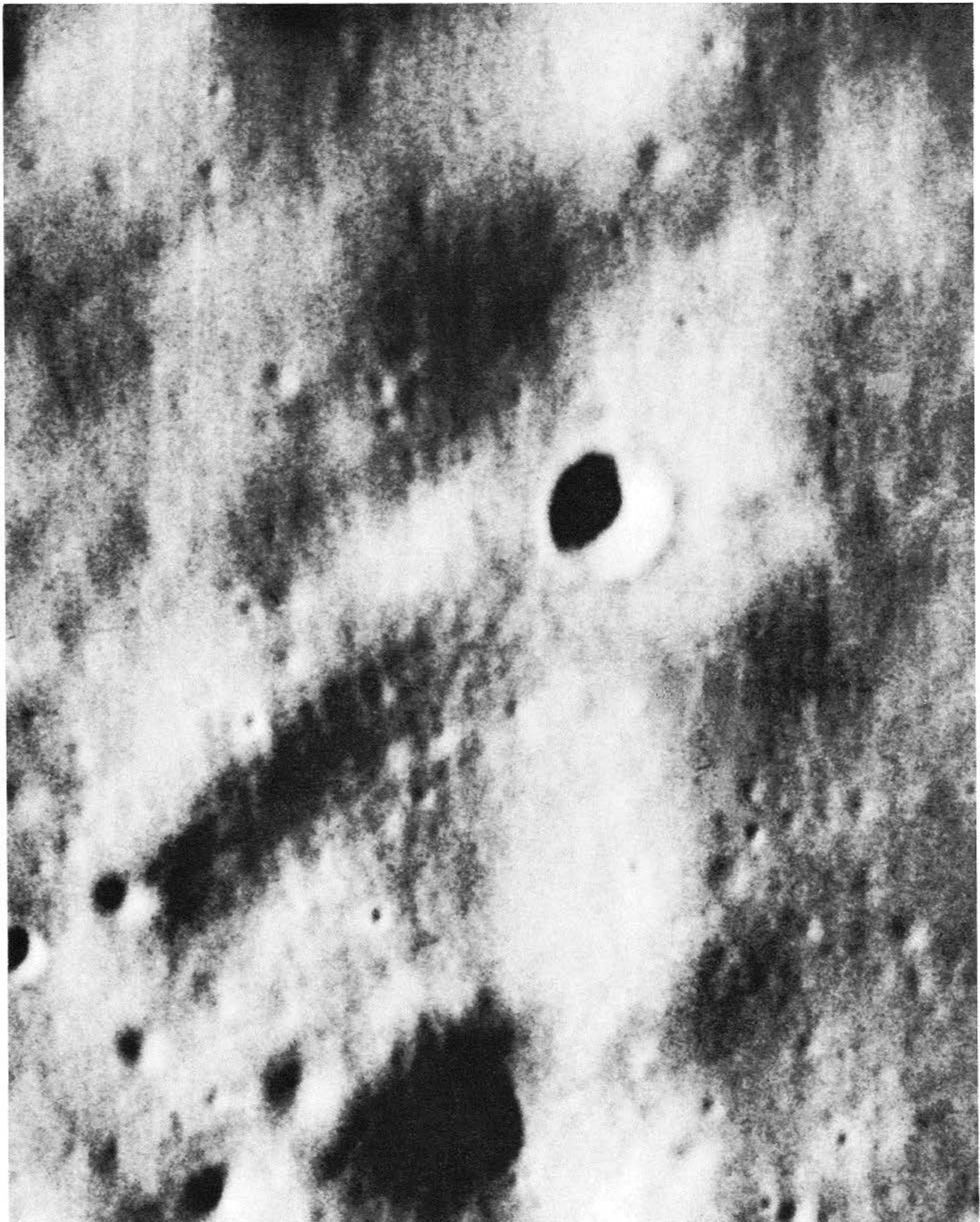
0   100   300 m
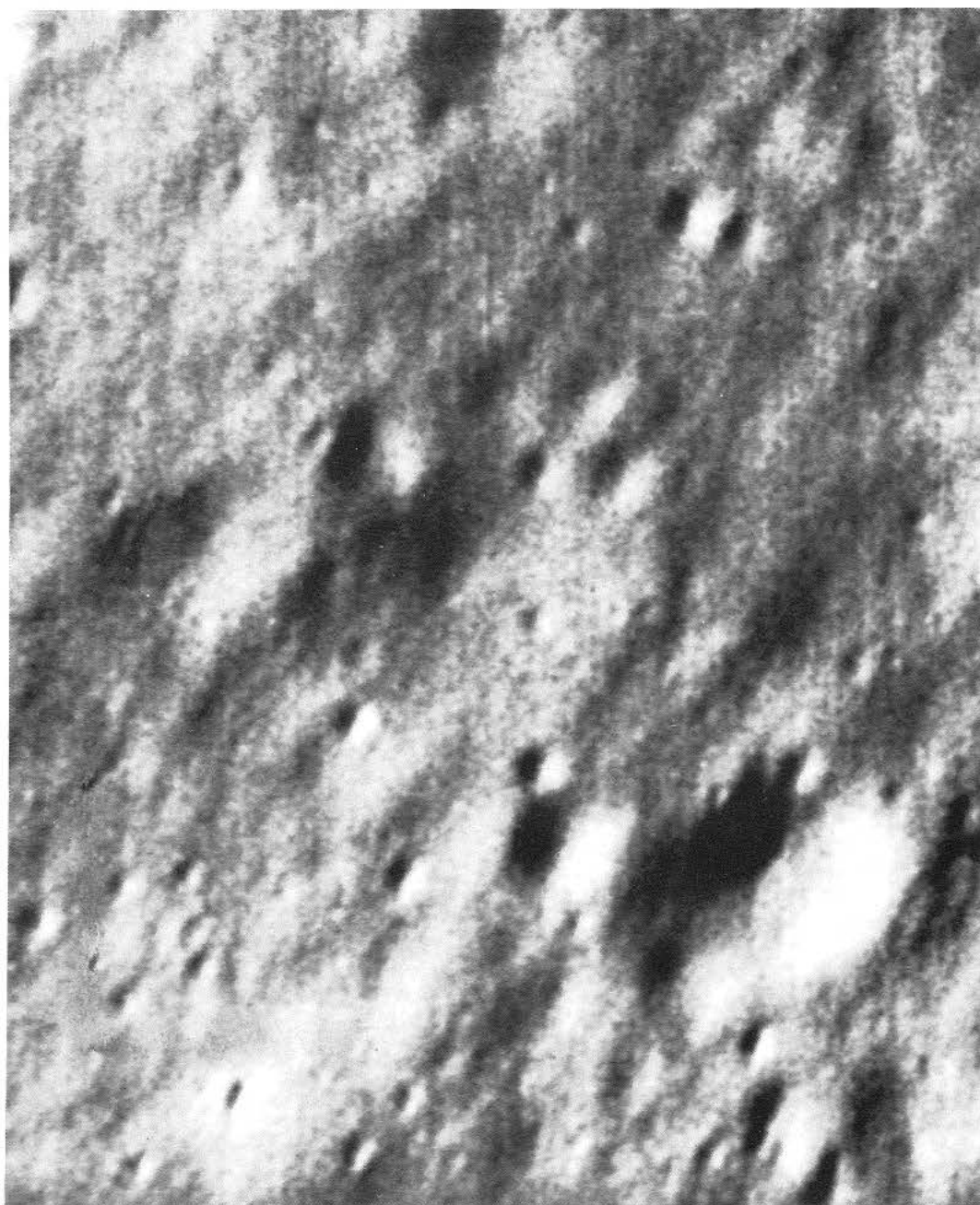
0   500 m

Fig. 117. *Ranger IX* frame B82, showing elongate dome on Alphonsus floor
(above 0 of scale).

Fig. 118. *Ranger IX* frames B85 and 86, showing
dome on Alphonsus floor. (Letters a, b, and c
mark narrow rilles ending in craters.)

⟶

0   100   300 m

Fig. 119. *Ranger IX* frames B84 and 85, showing two
domes on rim of shallow circular collapse depression.
(Summit crater on W dome is clearly a dimple crater.
See Figs. 8 and 10 for general location.)

0   500 m

west of the main dome. Inspection of the *Ranger IX* records shows that complex uplifted areas are common all over the Alphonsus floor. They may also occur in the *Ranger VII* and *VIII* fields, but because of the higher Sun angles, such extremely low structures are difficult to see.

The smallest dome yet found occurs in the last *Ranger IX* P₃ photograph (Fig. 84). This dome is 5 m in diameter, approximately 20–30 cm high, and has a 1-m summit crater.

The domes described above are only the more prominent ones visible in the *Ranger* photographs. There are many other such structures which are less pronounced but definitely domical. These are visible primarily in the *Ranger VIII* and *IX* photographs because of the low Sun angle.

The domical structures that occur on the floors of craters in the *Ranger* photographs have the same appearance as the domes in areas between craters and are probably of a similar origin. With the exception of those in Theon Junior, the domes are situated in soft craters which have been shown to be collapse depressions; therefore, they are of internal origin rather than being fragments that produced the crater.

Domical structures in the *Ranger* photographs have the following characteristics: the surface detail of the domes is no different from that of the surrounding area; there is no evidence of lava effusion or ash ejection from the domes or their summit craters; slopes at the edges of the domes, where they are steepest, average about 5–10 deg; some domes have summit craters, while others do not; and the summit craters are usually rimless.

Generalized cross sections of two large domes (Kies and Milichius) visible in Earth-based photographs, five small domes in the *Ranger* photographs, and a tumulus on the floor of Kilauea caldera, Hawaii, are shown in Figs. 120 and 121. It is apparent that there is little or no difference between the large domes, the small domes, and the terrestrial tumulus, and it is probable that all are of similar origin. The lack of evidence for lava effusion or ash ejection associated with dome formation indicates that they were not constructed by the build-up of successive outflowings of lava such as occur in the formation of terrestrial spatter cones and shield volcanoes, nor by the build-up of ash deposits like those found in terrestrial cinder-cone formations. This is also indicated by the extremely gentle slopes of the domes, the fact that many domes do not possess summit craters, and the identical surface details on the domes and in the surrounding areas. Rather, it seems probable that just as

in the formation of terrestrial tumuli, the surface has been uplifted by the hydrostatic pressure of subcrustal lava. The term *tumuli* should be restricted to the smaller domes (≤500 m); the larger ones (≥500 m) are more accurately referred to as *laccoliths*. However, this is an arbitrary classification, because there is a complete range in dome diameters from over 12 km to as little as 5 m. In addition to size, the distinction between laccoliths and tumuli is based on origin: laccoliths resulted from a deep-seated magma source, while tumuli (see Fig. 121) were caused by the hydrostatic pressure of superficial fluid lava beneath the solidified crust of a gently dipping lava flow. The summit craters found on many of the domes are probably due to collapse of the surface which resulted from loss of support following a partial withdrawal of lava or magma. Domes without summit craters may not have experienced a withdrawal of magma.

Domical structures on the floors of collapse craters may also have resulted from the hydrostatic pressure of lava following the collapse. Similar structures occur on the floors of collapse depressions in terrestrial lava flows (see Section C). Figure 16 shows a collapse depression (E) about 100 m in diameter in the McCartys Flow, New Mexico, which has a domical structure on its floor (note similarity of the flat, dark dome on the floor of the large collapse crater in Fig. 77). The domical structures on the floors of terrestrial collapse depressions are comparable to those on the Moon and probably have a similar origin.

Special mention should be made of the domes on the floor of Theon Junior, a sharp, class 1 crater of the type usually thought to be of impact origin. If this is the case, then the impact must have tapped a subsurface magma supply which partially flooded the crater floor and produced the domes.

On the basis of the conclusion that the small-scale lunar domes (≤ 100 m) are similar to *terrestrial tumuli and*, as the evidence indicates, *originated in the same manner*, a further conclusion can be drawn concerning the constitution of mare material. Terrestrial tumuli are found only on lava flows and are usually formed after the surface of the flow has solidified but prior to the solidification of the lava under the crust. This indicates that the *mare material is primarily lava*, as was deduced in the experimenters' analyses of the *Ranger VII* photographs (Ref. 1), and that the *small-scale lunar domes were formed prior to the complete solidification of the lava*. The presence of domes on the floors of lunar collapse depressions further indicates that the *collapse depressions were formed soon after the deposition* of the lava.

(a)
~360 m
12 km
KIES DOME (FROM EARTH–BASED PHOTOGRAPHY)

(b)
~260 m
10 km
MILICHIUS DOME (FROM EARTH–BASED PHOTOGRAPHY)

(c)
~26 m
760 m
DOME IN *RANGER IX* -85

(d)
~26 m
616 m
DOME IN *RANGER IX* -82

(e)
~8 m
120 m
DOME IN *RANGER VIII* -88

(f)
~3.5 m
95 m
DOME ON FLOOR OF COLLAPSE CRATER
RANGER IX -87

(g)
~25 cm
5 m
DOME IN LAST P_3 FRAME (P12) OF *RANGER IX*

(h)
~3 m
30 m
TUMULUS ON FLOOR OF KILAUEA CALDERA, HAWAII
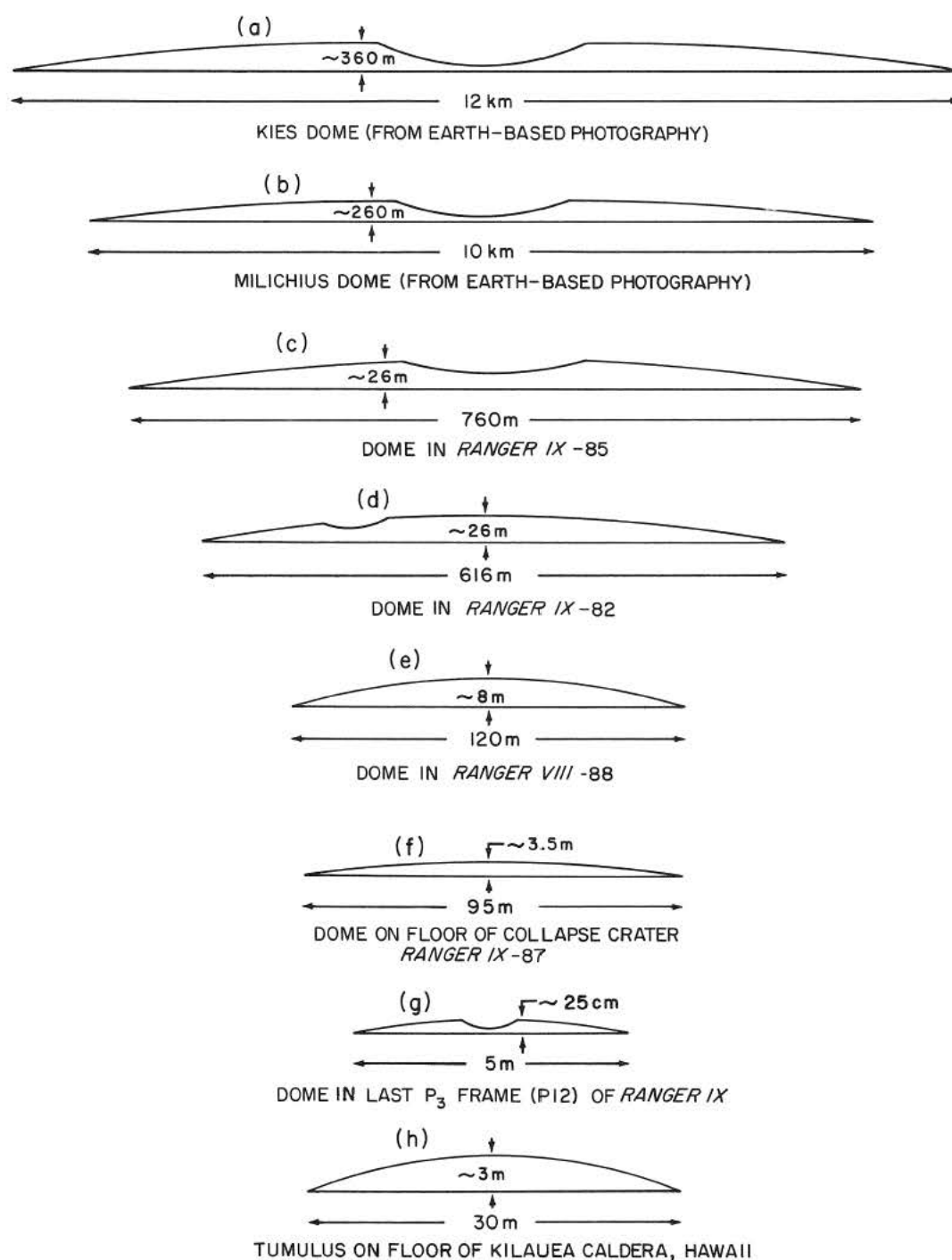
Fig. 120. Generalized cross sections of the Kies and Milichius domes, five small domes in *Ranger* photographs, and a tumulus on floor of Kilauea caldera, Hawaii.

Fig. 121. Tumulus on floor of Kilauea caldera, Hawaii. (LPL photograph.)

I. Sinuous Rilles

Sinuous rilles are among the most peculiar types of features on the lunar surface. Their origin has been a subject of debate for many years, and to date no explanation has been offered which adequately accounts for their unusual morphology. Recently, a class of terrestrial features (lava drainage channels) having very similar morphologies has come to our attention; it is believed that the lunar sinuous rilles originated in a manner similar to these terrestrial analogs.

Lunar sinuous rilles are relatively rare features, only 25–30 having been observed. The best known examples are Schröter's Valley and the Prinz, Marius, and Conon rilles (Figs. 122–126). Sinuous rilles have several distinctive characteristics. They always have a widening or a small crater at one end. The craters at the ends of four of the Prinz rilles (indicated in Fig. 123) are rimless, and at least two rilles—the one immediately adjacent to Prinz (Fig. 123) and the Hadley rille (Fig. 124)—begin at crater chains. Usually, the craters at the ends of sinuous rilles are breached. The courses of the rilles consist of curves with very short radii (5–50 km), giving them the appearance of meandering river beds. In some instances, the rilles form arc segments as great as 180 deg. They sometimes have widenings or crater-like depressions along their courses. The Marius and Hadley rilles show several distinct discontinuities along their courses (illustrated in Figs. 124 and 125) which appear to be bridges or some type of obstructions of the rilles. In most instances, the sinuous rilles are of uniform width along at least 80% of their length, and they are usually rimless. However, the Conon rille has a definite raised rim along most of its length (see Fig. 126), and it is possible that one of the Prinz rilles has a very low rim. All discernible sinuous rilles start in high areas and terminate in low regions. This is particularly apparent in the Prinz region (Fig. 123), where the rilles trend in the same direction.

Explanations of the sinuous rilles have been offered recently by Quaide (Ref. 27) and Cameron (Ref. 28). Quaide considers the rilles to be tension fractures caused by arching of the rigid crust. His primary evidence for this interpretation is the rare presence of craters along the course of several sinuous rilles which he believes to be the result of volcanic activity localized by the fractures. Quaide also cites the rectangular block of mountains known as the Aristarchus uplift, which contains Schröter's Valley, as evidence that Schröter's Valley and other sinuous rilles in the region are due to arching of the lunar crust. However, there is no evidence of arching

associated with other sinuous rilles such as the Marius, Hadley, or Conon rilles, and fracturing is not an adequate explanation of why all sinuous rilles start at a relatively prominent crater which is situated at the higher end of the rille. Also, the discontinuities in the Hadley and Marius rilles are very abrupt; the rilles have the same width at these points as they do elsewhere along their course. If they were fractures, they would be expected to die out gradually as they approached the discontinuity. The geometry of the rilles also militates against the fracture hypothesis. There is no precedent on Earth for sinuous fractures associated with major uplifts having arc segments as great as 180 deg. Furthermore, uplifts produce numerous branching fractures with a more-or-less radial trend rather than just one sinuous fracture. As previously mentioned, the Conon rille has a raised rim along most of its length. Fracturing cannot account for this, since fractures do not have raised rims. Thus, it appears that fracturing cannot adequately explain either the morphology or the geometry of sinuous rilles.

Cameron (Ref. 28) considers the sinuous rilles to be valleys eroded by nuées ardentes (ash flows). However, this hypothesis also meets with serious difficulties. A nuée ardente erosion valley would not have discontinuities along its course, as do the Hadley and Marius rilles. It is also doubtful that an erosion valley would have a raised rim like that of the Conon rille. Cameron shows a map and photograph of a valley eroded by a nuée ardente in Japan (Ref. 28, pp. 2427–2428). The valley, which is about 15 km long and begins at the Asama volcano, does not appear to have the same characteristics as the sinuous rilles. There are no curves with short radii, and the valley widens appreciably at its terminus—from about 1 km near its beginning to more than 4 km near the end of the flow. This is to be expected of a nuée ardente because of its extreme mobility and tendency to spread laterally. Sinuous rilles, on the other hand, usually die out gradually at their termini and are more or less constant in width throughout the remaining portions. A widening at the end opposite the crater from which the rille apparently originates has never been noted in sinuous lunar rilles. All of these observations are contrary to the nuée ardente hypothesis for the origin of sinuous rilles.

There is a class of terrestrial features which exhibit the characteristics of lunar sinuous rilles more closely. These are the *lava drainage channels,* also known as lava gutters, found in numerous lava fields throughout the world. A lava drainage channel is an open channel through

0   50 km

Fig. 122. Schröter's Valley, the largest sinuous rille. (Dimensions: length, 200 km; width, 2–5 km; depth, over 300 m. LPL photograph.)

0   20 km

Fig. 123. Group of sinuous rilles near Prinz and a portion of Schröter's Valley. (White arrows indicate rimless craters at beginning of four such rilles. Note that rilles trend in same direction. Lick Observatory photograph.)

Fig. 124. Hadley Rille at base of Apennine mountains.
(Discontinuities of rilles indicated by white arrows.
Note crater chain at beginning of rille.
Lick Observatory photograph.)
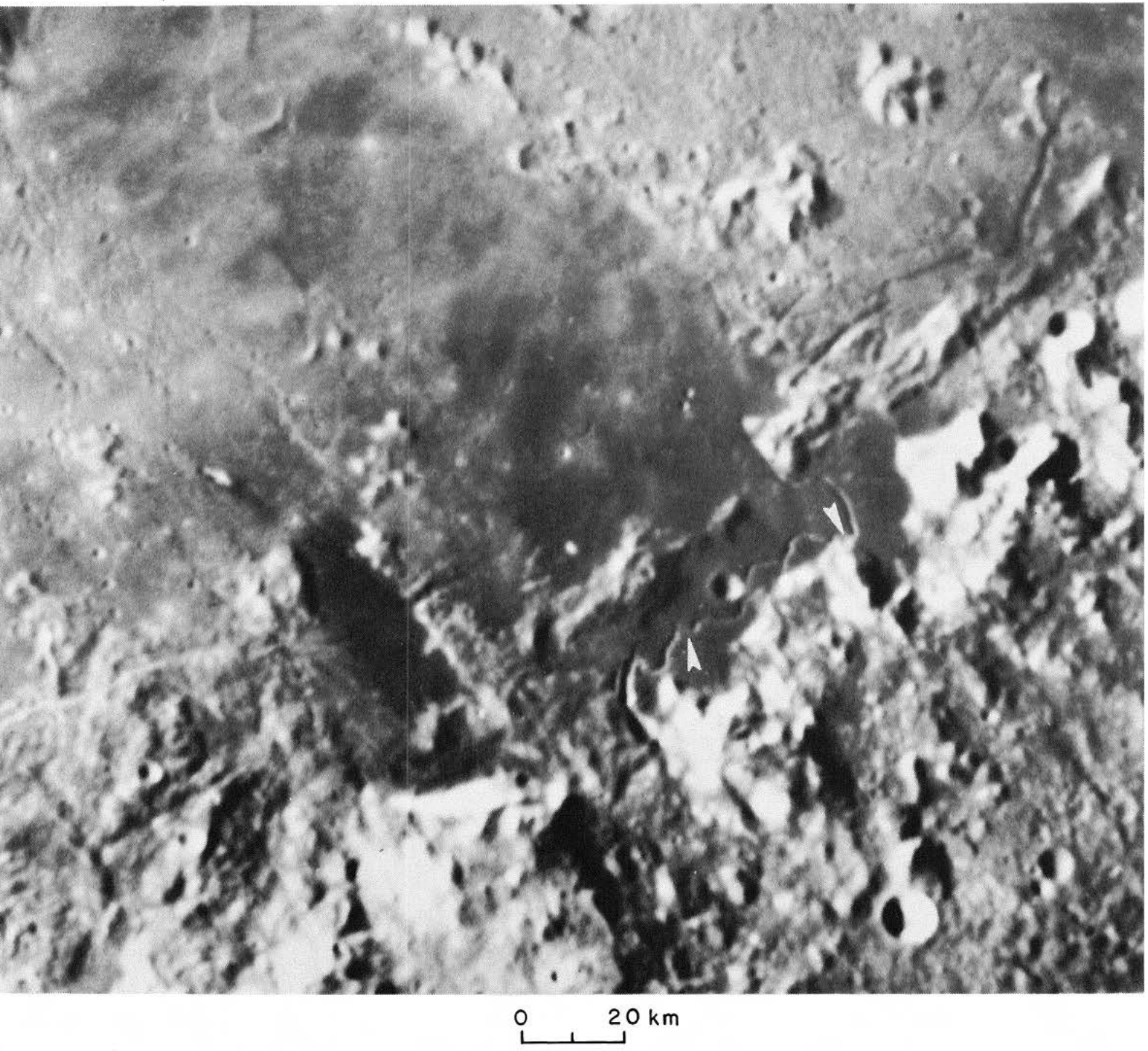
0   20 km

0   20 km

0   20 km

Fig. 126. Conon Rille in Apennine mountains. (Note raised rim along
much of rille's course. Mt. Wilson photograph.)

Fig. 125. Marius Rille in Oceanus Procellarum. (White
arrow indicates discontinuity of rille. Scale refers
to unforeshortened N–S dimension. Lick
Observatory photograph.)

←

which a lava river feeds a flow (see Figs. 127–130). The volume of lava in a channel may fluctuate considerably (Ref. 29); at times, the channel may be full to overflowing, and at other times, the surface of the lava river may be well below the banks of the channel. During times of overflow, solidifying lava along the banks builds up natural levees that may confine the lava river several feet above the level of the surrounding flow. As the activity ceases, the lava river drains away, leaving an open channel.

Lava drainage channels have the following characteristics in common with the sinuous lunar rilles. The courses of the channels usually consist of curves with short radii; in some cases, the channels form arc segments as great as 180 deg (see Fig. 127). The sinuous nature of the channels is due to pre-existing irregularities in the topography and slight changes in the direction of slope. Frequently, there are discontinuities where the lava has risen to the top of the rim and solidified to form a bridge, or to block the channel. Several of these discontinuities are indicated in Figs. 128 and 129. At some localities along the channels, small craters occur (see Figs. 127 and 128), which appear to be collapses over bridged portions of the channels. As is the case with the lunar sinuous rilles, lava drainage channels are of relatively uniform width along 80–90% of their length and gradually die out at the end of their course. Often the channels have raised rims which are natural levees built up by successive overflowings of lava. However, there are channels lacking raised rims, where apparently the lava has never overflowed the banks. Lava drainage channels always begin at a crater or a crater chain, or with a widening of the channel, and in most instances, the originating craters are breached. Also, the originating crater is always at a higher elevation than any other part of the channel.

The greatest dissimilarity between lava drainage channels and lunar sinuous rilles is the difference in size. Schröter's Valley, the largest sinuous rille, is about 200 km long, 5 km wide, and over 300 m deep. The others are of the order of 20–100 km long, 0.5–2 km wide, and a few tens of meters deep. The largest lava drainage channel found to date is only 5.5 km long, 36–90 m wide, and a few meters deep. Therefore, lunar sinuous rilles are about 4–40 times larger than terrestrial lava drainage channels. However, the size of lava drainage channels depends significantly on the volume of lava emitted, although velocity of flow, viscosity, and temperature of the lava

are contributing factors. Obviously, a lava drainage channel the size of Schröter's Valley or the Hadley rille requires a much greater volume of lava than the terrestrial channels shown in Figs. 127–130. Single lava flows observed on the Moon (Ref. 1) are generally of greater dimensions than single terrestrial flows. One of the flows in Mare Imbrium has a minimum length of 150 km, a width of 25–50 km, and a thickness of about 50 m. This flow has covered an area of 5600 km^2 with a volume of 280 km^3. Other flows in the same vicinity have similar dimensions. The largest known single terrestrial flow is a Columbia River plateau basalt flow in Oregon, which has a volume of about 800 km^3 (Ref. 30). A single Icelandic fissure eruption has covered a 100-km^2 area with a lava volume of 5–10 km^3 (Ref. 31). However, single terrestrial flows of such dimensions are exceedingly rare; they are usually 5–10 times smaller. Known lunar flows are, therefore, 10–20 times more extensive than average single terrestrial flows. Hence, one would expect larger lava drainage channels on the Moon than on Earth. Furthermore, the diameters of the craters at the ends of sinuous lunar rilles are 7–40 times greater than the diameters of the largest originating craters of terrestrial lava drainage channels, so it is not surprising that the sinuous rilles are larger than the lava drainage channels.

There is one important dimensional similarity between the lunar and the terrestrial features, i.e., the ratio of the diameter of the originating crater to the width of the rille or channel (D/W). The lunar ratio is 1.3 to 3 (1.9 average), and the ratio for 17 terrestrial channels is 1.5 to 3 (2.2 average). Since there is a definite genetic relationship between lava drainage channels and their originating craters, the similar ratio of lunar sinuous rilles also suggests a genetic relationship.

The evidence presented here (morphology, spatial relationships, and mode of occurrence) strongly suggests that the lunar sinuous rilles are lava drainage channels rather than fractures or nuée ardente erosion valleys. Since terrestrial lava drainage channels are found almost exclusively in basaltic lava flows (because of the low viscosity and consequent high mobility of molten basalt), it is possible that the lunar flows may also be basic in composition. This is consistent with the great areal distribution of individual flows in Mare Imbrium and with the presence of collapse depressions and small-scale domes discussed in Sections C and H. Such features indicate a highly fluid lava, and hence, a lava of basic (e.g., basaltic) composition.
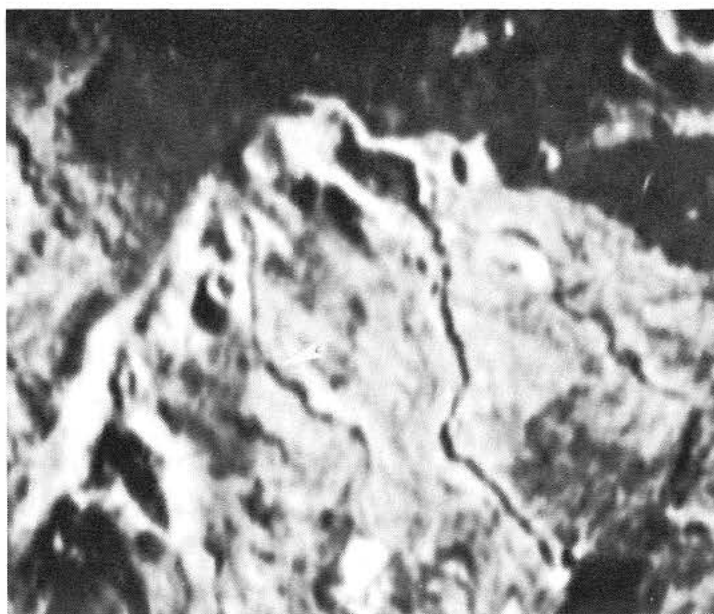
0   500 m

Fig. 127. Lava drainage channels on floor of Sierra Negra caldera in Galapagos Islands. (White arrow indicates a crater-like depression along one of the channels. Note remarkable similarity between these channels and the lunar sinuous rilles.)

Fig. 128. Lava drainage channels in Iceland. (White arrows indicate collapse craters and bridges or obstructions along channels.)

→

0   100 m
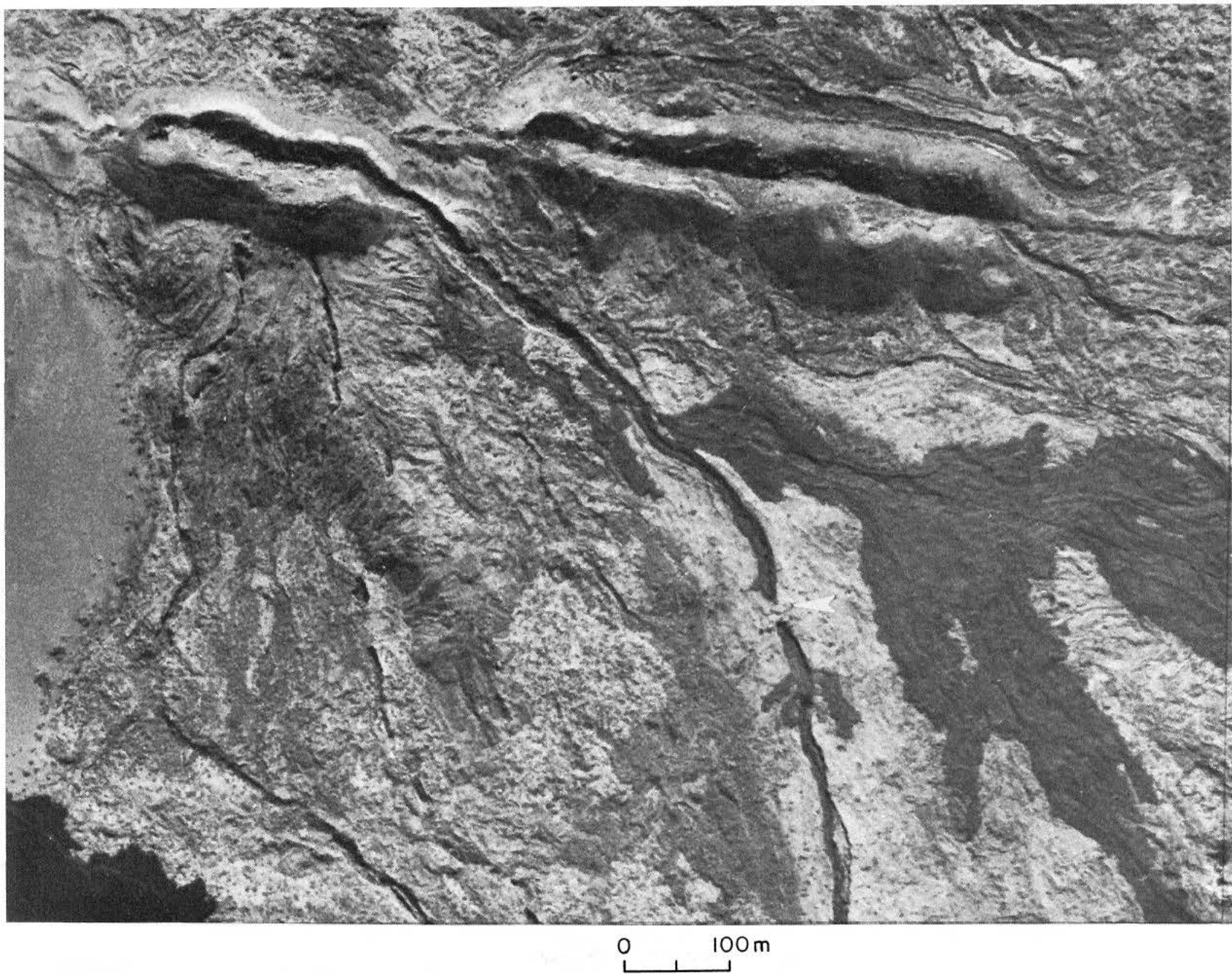
Fig. 129. Lava drainage channels in Hawaii. (Lava bridge along one of the channels indicated by white arrow. U. S. Government photograph.)

0   100 m

J. Properties of Mare Material Inferred From the Presence of Collapse Depressions

The interpretation of soft craters in the *Ranger* photographs as collapse depressions implies certain properties for mare material. Since analogies between terrestrial and lunar collapse depressions appear justified (see Section C), it is very probable that the gross properties of the material in which terrestrial collapse depressions occur are, in general, analogous to those of the lunar mare material.

Terrestrial collapse craters occur on lava flows, and it is inferred that the lunar collapse depressions are also associated with lava. In the *Ranger VII* Report (Ref. 1, pp. 29–33), flow structures in Mare Imbrium were discussed which are remarkably similar to terrestrial lava flows. It was also pointed out that the boundaries of several of the flows correspond exactly to color boundaries in Mare Imbrium. At the recent Oregon Lunar Geological Field Conference (August 1965), photographs of these flow structures were shown to Drs. McBirney, Macdonald, Waters and Williams. These eminent volcanologists agreed that the Imbrium structures are very similar to terrestrial lava flows, and that their gross morphology is more like that of lava than ash flows. On December 3, 1965, U.T., one of the Imbrium flows was visually observed and photographed through the LPL 61-in. telescope at the Catalina Observatory. The photograph is reproduced in Fig. 131(a), and another, taken of the same flow at opposite illumination but with a higher Sun angle, is shown in Fig. 131(b). Figure 131 shows that the flow crosses two very low ridges and stops abruptly at the prominent Imbrium ridge I-1. A very narrow crack lined with smaller craters was observed visually opposite the lava flow at the base of the sharp crest of I-1, and on the flow, a chain of very small craters was noted along the crest of the low ridge marked 2. These visual observations were confirmed by A. Herring and R. Le Poole. It appears highly probable that the flow emanated from either 2 or the more prominent ridge I-1. Since the flow boundaries cross 2 and end abruptly at I-1, it is more likely that the flow originated from the latter and that the crack lined with small craters is its point of origin. This view strongly supports the interpretation first put forth in the *Ranger VII* Report (Ref. 1) that the *mare ridges are dike- or sill-like structures*. In the present case, *the*

dike has apparently broken through the surface to form the lava flow. The flows observed in Mare Imbrium apparently represent the last phase of filling the basin.

O'Keefe and Cameron (Ref. 32) have suggested that the maria consist of ash rather than lava flows. However, there is no evidence that collapse craters occur on such flows, and it seems unlikely that they would form there. Collapse craters on lava flows are due to loss of support resulting from the drainage of lava beneath the solidified crust of the flow. This drainage takes place through complex systems of tubes or lava tunnels of varying diameters. Collapse takes place where the roof of the tube is too thin to support its own weight. Since the thickness of the roof varies from place to place, the collapses occur in a more or less random fashion, as described in Section C. The carrier mechanism of an ash flow is gas, and it is unlikely that gas would give rise to the hydrodynamic parameters necessary to produce collapse depressions. Therefore, it is probable that the material filling the maria and the flooded craters is primarily lava, although ash deposits may occur locally.

To date, all investigated lava flows that have collapse depressions consist of basalt. Furthermore, the collapse craters occur only on the pahoehoe-type lava. Aa basalt flows and flows of acidic and intermediate composition (e.g., rhyolite and andesite) are apparently devoid of these structures. The pahoehoe basalt flows which display collapse depressions have the following characteristics: (1) at the time of extrusion, they were of fairly low viscosity; (2) the flows are relatively thick (~ 15 m); (3) the gradient over which the lava flowed is very gentle (≤ 1 deg); and (4) they flowed by the flow-unit mechanism. Under these conditions, the pahoehoe lavas built up relatively thick flows (~ 15 m) with a solidified crust underlain by fluid lava. At different times during the extrusion, the lava ceased to flow, the crust at the terminus of the flow cracked open, and the fluid lava beneath the solidified crust poured out of the cracks to form new flow units and thus produce collapse depressions along thin portions of the drained lava tubes. Pahoehoe lava is extruded at a higher temperature than aa lava but with considerably less gas content. The gas soon escapes, and the flow quickly congeals with a minimum amount of crystallization. Aa lava issues at a lower temperature but

Fig. 130. Lava drainage channels in Hawaii. (U. S. Government photograph.)

←
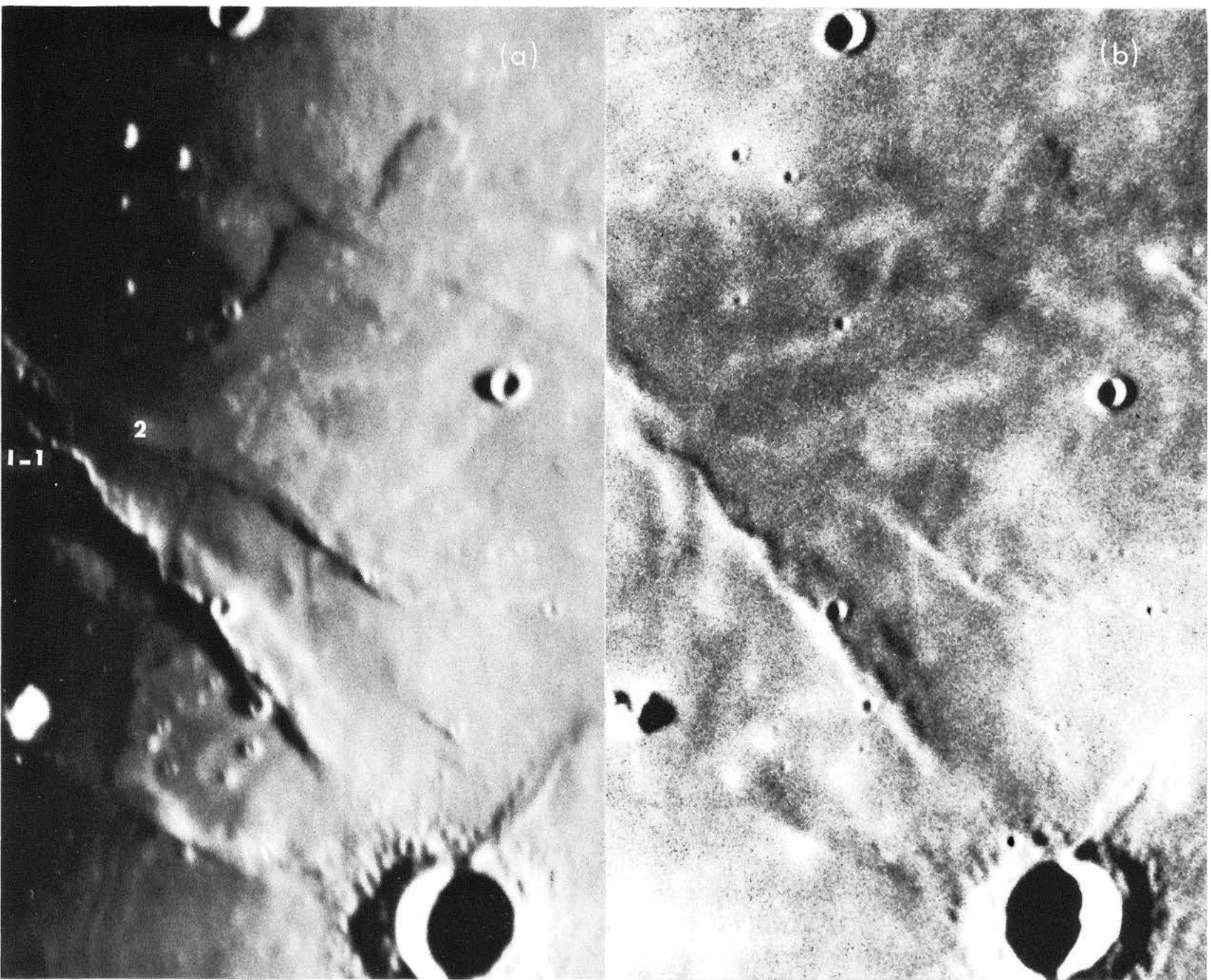
0   50 km

is so highly gas-charged that it is initially even more fluid than pahoehoe (Ref. 33). Therefore, aa lava moves rapidly, forms thin flows, and usually advances by the single-unit flow mechanism. These factors are unfavorable for the production of collapse depressions and are the principal reasons why aa lava flows lack such structures. Several collapse depressions occur in aa flows on the McCartys and Carrizozo lava fields, but they are due to the collapse in the pahoehoe lava underlying the very thin aa flows. In some cases, the thin aa lava has flowed into the depressions, while in others, the collapses have occurred in the pahoehoe after the deposition of the aa. Apparently, the added weight of the aa lava was enough to collapse portions of tubes in the pahoehoe which were initially stable.

Acidic and intermediate lavas behave quite differently from basic lavas. Basic lavas melt at rather low temperatures because of the low silica and high lime and magnesia contents, and the low viscosity and high gas content lead to rapid boiling. Acidic and intermediate lavas are considerably more viscous. Primarily because of their high silica content, they melt at relatively high temperatures and solidify at temperatures at which basic lavas remain fluid. Therefore, lavas of acidic and intermediate composition flow only for short distances, usually consist of a single flow unit, and build thick, compact flows devoid of lava tubes. These factors are unfavorable for the formation of collapse depressions and explain why lavas with such compositions lack this type of structure.

In addition to collapse depressions, there are other lunar structures which testify to the volcanic nature of the maria, including lava drainage channels (the sinuous rilles discussed in Section I), tumuli (Section H), flow fronts and mare ridges (this Section), large domical structures (probably laccoliths), maar craters, and volcanic mountains. An extensive dome field with associated sinuous rilles and ridges is shown in Figs. 132 and 133, and the dark-halo craters shown in Figs. 72, 73, and 103 are examples of maar craters. It is also possible that many of the elongate beaded depressions with raised rims are maar-type craters located along fractures (see Figs. 103, 104, and 106). On Earth, maar craters are commonly associated with terrestrial lava fields (e.g., in Oregon and Mexico). Numerous isolated mountains that occur in the lunar maria probably have a volcanic origin. The "white" mountain in Mare Cognitum photographed by *Ranger VII* has a summit crater, as do many other peaks in the maria. This fact, together with the high albedo of such peaks, implies volcanic activity and associated sublimate deposition.

The above considerations strongly suggest that the lunar mare-type terrain consists of lava having properties similar to those of terrestrial pahoehoe. However, the lunar lava probably has a relatively thick froth layer overlying more compact rock. Furthermore, the lunar lava is assumed to be rather basic in composition, that is, low in silica content and rich in lime, magnesia, and iron. These inferences are supported by the presence in the *Ranger* photographs (see Section H) of small-scale domes which have been interpreted as tumuli. This type of structure is prevalent on terrestrial pahoehoe basaltic lava flows but is rare on, or absent from, aa basalt flows, acidic and intermediate flows, and ash flows.

Fig. 131(a). Sunrise illumination of Lambert region of Mare Imbrium, showing flows on mare surface and dike-like ridge. (LPL photograph.)
(b). Same area as in Fig. 131(a), but opposite illumination. (Mt. Wilson Observatory photograph.)

←

Fig. 132. N part of Marius volcanic field, showing numerous domes and mesas, many with split top; dark lava deposit extending nearly to upper margin, seen with better illumination in Fig. 125; dike-like N–S ridges passing through center; and sinuous rille on W side, not photographed before. (LPL photograph.)

⟶
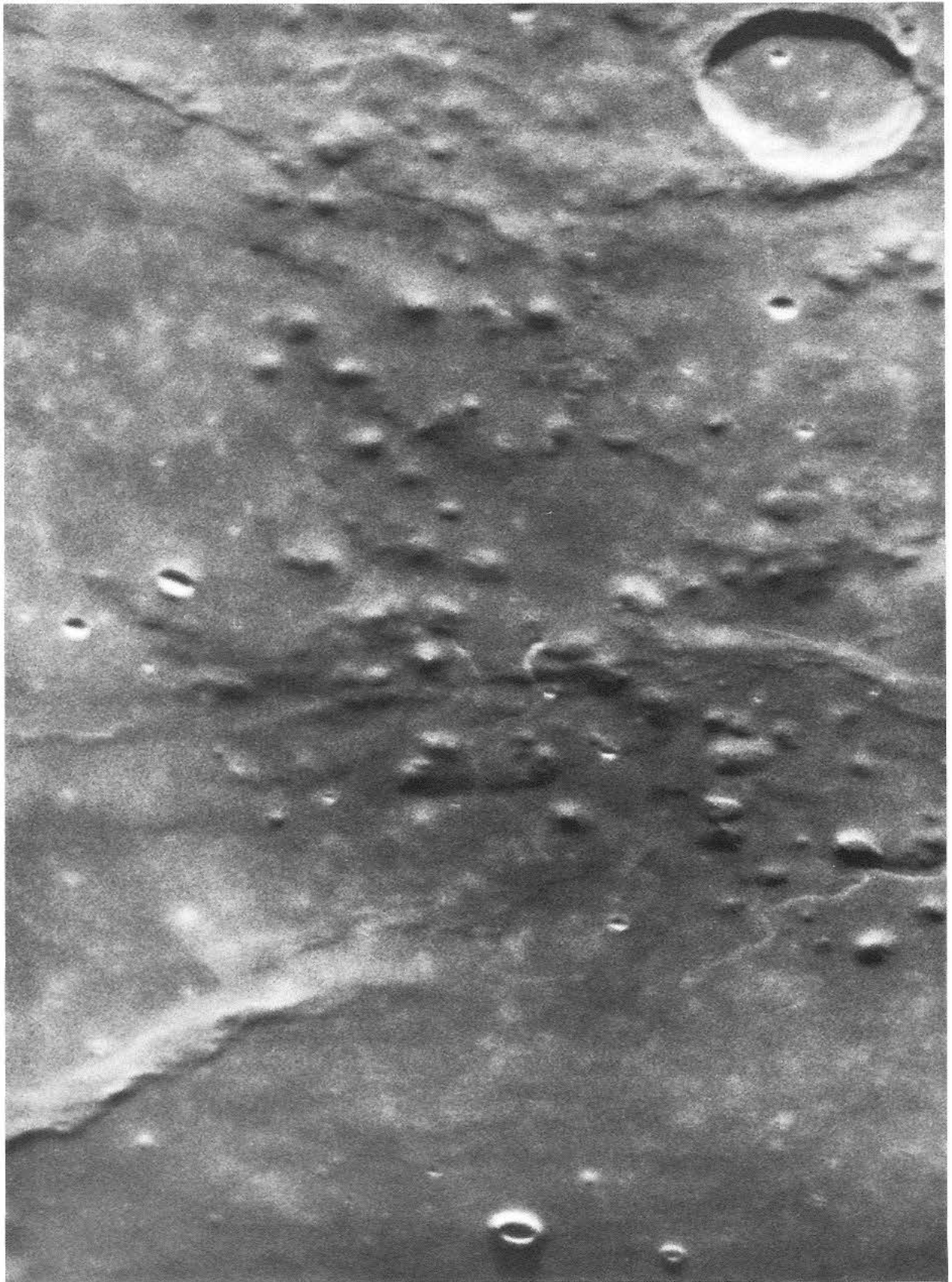
Fig. 133. S part of Marius volcanic field, showing scar-like depressions at left and corona-like feature at lower left, accompanied by several small, whitish craters. (LPL photograph.)

K. Concluding Remarks

The *Ranger* missions are among the Nation's most brilliant scientific achievements. Each of the last three flights carried out flawlessly its over 100 commands, and each returned a vast collection of photographic records of incomparable resolution and quality. These records have *closed the worst information gap* extant concerning the Moon, covering dimensions from about ½ m to ½ km in the widely separated areas of Mare Cognitum, Mare Tranquillitatis, and the Alphonsus floor.

The *Ranger* records supply data that help answer some basic questions about the nature of the *mare surface*. It is inferred from them that the maria are lava deposits overlain with a layer of low-density rock froth a few meters thick, the uppermost part of which has been eroded by micrometeorite impacts and sputtering. From the radar-reflection data, it is inferred that the mare surface becomes very rough at 1 cm. This critical dimension is assumed to be due to the "bubble" size of the rock froth, effective not only in the original deposit, but in its eroded form due to sputtering and its fragmented form due to impacts. The dust layer on this rough material is well below 1 cm. Beneath the visible cover of rock froth, an intricate system of tunnels developed in the lava deposits through drainage and relocation, which caused the surfaces of the maria and the mare-type terrain to exhibit near-circular collapse depressions. A number of identifiable caves have been found among these depressions. The close parallels noted between the lunar collapse features and those observed in terrestrial lava flows have opened up a wide field for further investigation and have suggested the development of field methods for *lunar-surface exploration*.

The sources and modes of deposition of the mare lavas have long been uncertain, but some answers to these questions have now emerged. Telescopic observation of Mare Imbrium provided the first good information not only on the existence of a succession of major lava flows on the maria (Ref. 1) but also on a likely source of the lavas [Section J and Fig. 131(a)]. Apparently, *the sources of the last phases of the mare flooding were associated with the ridges.*

The Marius field of lava domes (Ref. 2, p. 300) appears to have been a very active volcanic field. Part of it is seen in Fig. 125, together with a system of major flows some 70 km wide whose front faces north. The field, as photographed with the NASA 61-in. telescope, is reproduced in Figs. 132 and 133. It illustrates (1) many typical volcanic vents and associated lava channels, bearing witness to the extraordinary local volcanic activity, and (2) the tremendous gains in resolution that must still be made before one can hope to understand the Moon adequately.

The deposition of the lavas and their solidification and cooling were accompanied by several groups of phenomena that have left observable marks on the surface: the *sinuous rilles* (Section I), the *domes* (Section H), the *lineaments* (Section G), the *tree-bark structure* on all three maria, and the many *outcroppings*, such as those on the Alphonsus floor (Section E). These phenomena, together with the *collapse depressions* (Section C, D, and E), the *ridges* discussed in the *Ranger VII* Report (Ref. 1), and the observed *lava flows* and their probable *sources* on Imbrium (referred to above), round out the interpretation of *the maria as lava deposits*.

With this explanation now well established, further research can be directed toward the determination of the individual *sources* for each of the maria and the details of the flooding process. Inspection of Figs. 125, 132, and 133 suggests that part of this investigation can be accomplished from the Earth, provided an intensive effort is made at the best astronomical sites available.

After the deposition of the mare floors and the formation of the many associated features (drainage tunnels, collapse structures, domes, faults, ridges, dark-halo craters, rilles, and other lineaments), meteoritic impacts added *primary-impact craters*. Their frequencies are derived and tentatively interpreted in Section F, and their numbers are found to be *consistent with the meteorite counts*. Down to diameters of 22 m, these craters cover about 2.2% of the mare surface and down to 1-m diameters about 18%. However, among the post-mare craters, some very large objects occur, such as Archimedes and Plato, with flooded floors, clearly formed immediately post-mare. In addition, there are several moderate-size craters whose central mountains indicate that the subsurface layers of the mare were still hot when they were formed. The latter group is characterized by having central *vents* instead of central peaks: Timocharis, Lambert, Euler, and Pytheas in Mare Imbrium, and Plinius and Maskelyne in Mare Tranquillitatis. The unusual frequency of these two classes of large and very large post-mare craters formed within a comparatively short interval implies that they were the concluding phase of the initial intense (mostly pre-mare) bombardment of the Moon (attributed to impacts by *circumterrestrial* rather than asteroidal bodies; Ref. 34), which included the phase of mare formation itself. Figure 134 shows schematically
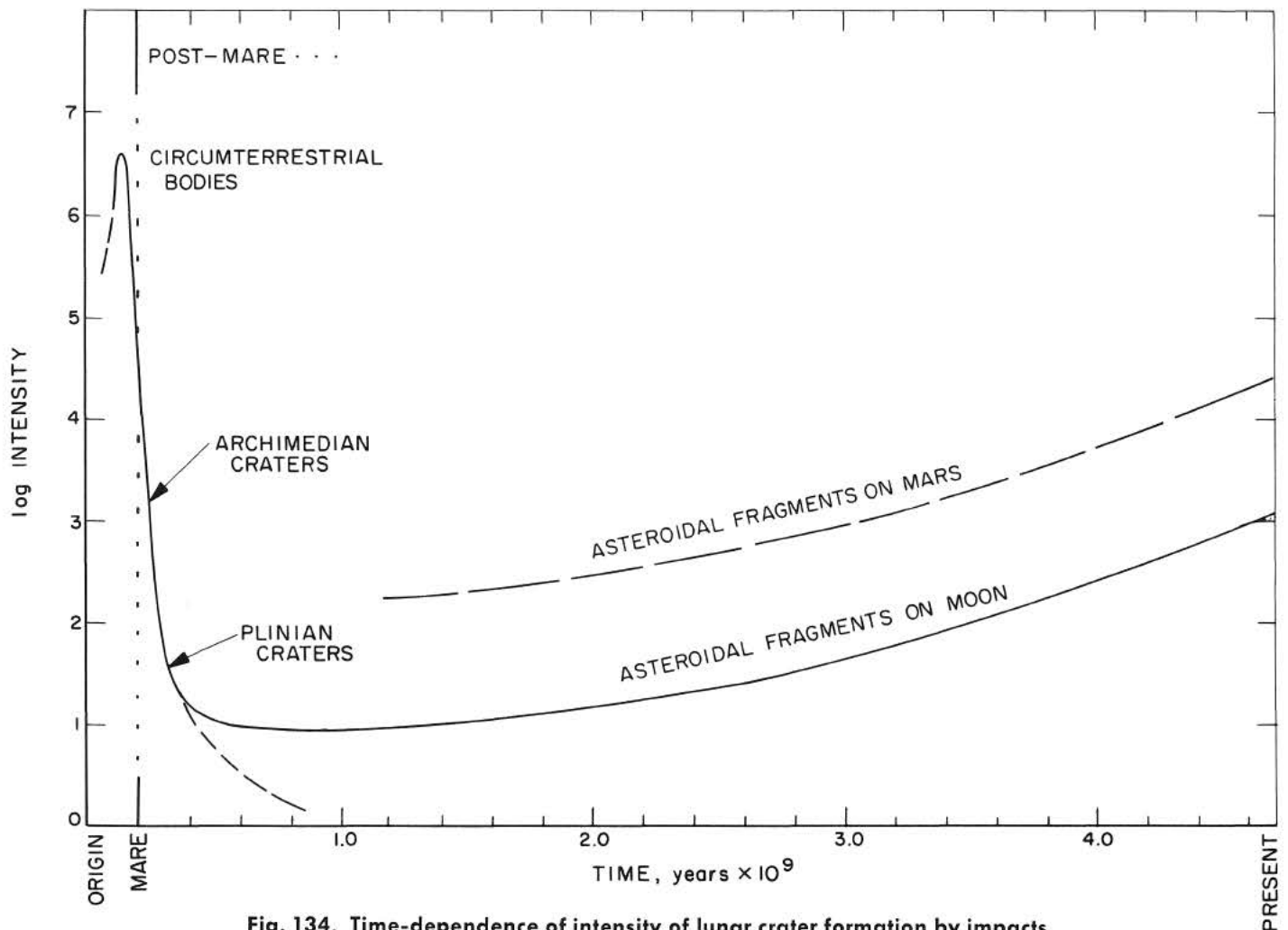
Fig. 134. Time-dependence of intensity of lunar crater formation by impacts.

the time-dependence of the intensity of lunar bombardment and primary-crater formation according to this concept. The asteroidal impact rate increases with time because each collision in the asteroid ring increases the total exposed cross section of the asteroids (Refs. 35 and 23, and Section F-4).

The above interpretation has recently received support from two sources: (1) the primary crater counts and their explanation by Le Poole (Section F) confirm the increase in asteroid-type impacts during geologic time by at least one order of magnitude, and (2) the *Mariner IV* data indicate that the crater-forming rate on Mars has been about 15 times that on the lunar maria, which is consistent with the greater impact rate expected on Mars because of its greater proximity to the asteroid ring (see also Ref. 23). On the other hand, the lunar pre-mare crater density appreciably exceeds that on Mars and

clearly has a cause (impacts by circumterrestrial bodies) not operative on that planet.

Although the interpretation of the larger telescopically observed craters being due to primary impacts is widely accepted, efforts to discover alternative explanations for some of the large craters may prove fruitful. There are a number of puzzling cases among the large craters that appear to involve additional mechanisms. The *Ranger* data are a vast source of information also for the investigation of large craters. Time has not permitted the inclusion of such studies in this Report; in fact, except for a few experimental runs (Ref. 36), the basic photogrammetric evaluations have not yet been made. The ACIC mapping program referred to earlier, coupled with photogrammetry, will in time supply a foundation for quantitative studies of the three *Ranger* impact areas.

The analysis of the ridges on Mare Tranquillitatis, which were well covered by *Ranger VIII*, is another important unfinished item in the *Ranger* evaluation program. A third is the discussion of the results of the picture analysis and clean-up performed by JPL, a process which has led to improved representation of the pictures themselves and has made possible the preparation of photometrically calibrated contour maps. Figures 135 and 136 show two rectified, electronically cleaned pictures of the last *Ranger VII* P$_3$ frame, the former without alteration of the originally recorded instrumental resolution and the latter with correction for image blur (camera blur, electron-beam blur, and finite bandwidth combined). These Figures, together with Fig. 50(a) (*Ranger VIII*) and Figs. 84 and 85 (*Ranger IX*), provide the best available comparisons between the impact areas.

If allowance is made for the different Sun angles, it is seen that the *Ranger VII* and *IX* impact areas do not vary appreciably in their populations of small craters, but that the *Ranger VIII* impact area deviates. There are two known causes for this deviation: image motion during exposure (1.1 m), and differences in aspect and illumination. The second effect causes all craters to appear shallower in the *Ranger VIII* pictures than in the *Ranger VII* and *IX* records. Le Poole estimates that, for this reason, a crater with a true depth-to-diameter ratio of 1:5 appears as 1:8 in the *Ranger VIII* frames. Also, the image motion will transfer an increasing fractions of craters with $D = 8$ m and less into the "soft" class. There seems to be a third effect, however, which causes Fig. 50(a) to appear different from 50(b)–(d), and is therefore probably *local* in nature. This difference may be the result of a small local "deposition" effect (of recent date, to explain the absence of sharp craters); a layer 0.3–0.5 m deep would account for the appearance of Fig. 50(a).

The linear pattern, evident particularly in Fig. 136, was recognized in Strom's earlier discussion (Ref. 1, p. 68, Fig. 48), although the prints used by him showed the system less clearly and included only a few lineaments. The directions noted in Fig. 136 are the same, however, as those found in earlier pictures; i.e., *they belong to the global lunar grid pattern*. This is very remarkable in view

of the smallness of the features observed here, and implies considerable cohesiveness of the lunar crust even in the upper meter or so.

Another problem briefly considered in the *Ranger VII* Report (Ref. 1, p. 44) is the nature of the long, narrow valleys ("grooves" or "scars") in Mare Cognitum, which are approximately oriented toward Bullialdus. With the additional evidence now available, the interpretation of these valleys may be improved. Figures 137 and 138 compare the Bullialdus features and others like them with the *Ranger VIII* and *IX* linear depressions discussed before, of which samples are shown in Fig. 139. It is concluded that they all have basically the same kind of structure, namely, that they consist of aligned groups of from three to six adjacent or merging round collapse depressions, often around 0.6 km in width and 3 km long but sometimes having only half or a third these dimensions. The high-resolution pictures in Fig. 139(b) and (c) show sharp folds and furrows on the floors and walls of the depressions, quite like those found in the larger isolated collapse depressions; most of them belong to the lunar grid system. The trough in Fig. 139(c) is accompanied by numerous depressions of the dimple-crater type. A remarkably similar set of terrestrial collapse depressions, clearly associated with two major near-vertical fissures, is shown in Fig. 140.

The linearity of the beaded troughs observed on the Moon as well as their directions and their distinguishable fine structure all indicate that the collapses took place along dynamically determined structural lines or planes (not lava tunnels). There remains the question of whether the collapses resulted from the withdrawal of magma in these planes or occurred much later in the solid state. The presence of domes in some of these depressions favors the former explanation; also, the soft outlines of the troughs suggest that the collapse took place when the top layers were still in a *plastic state* and draped themselves over the cavities.

Rille-like depressions and beaded troughs occur also as part of the radial systems surrounding Langrenus, Aristoteles, Aristillus, and other craters. Examples are

Fig. 135. Last *Ranger VII* P$_3$ frame, rectified and filtered to remove spacecraft-induced noise, and corrected for vidicon shading. (JPL photograph.)
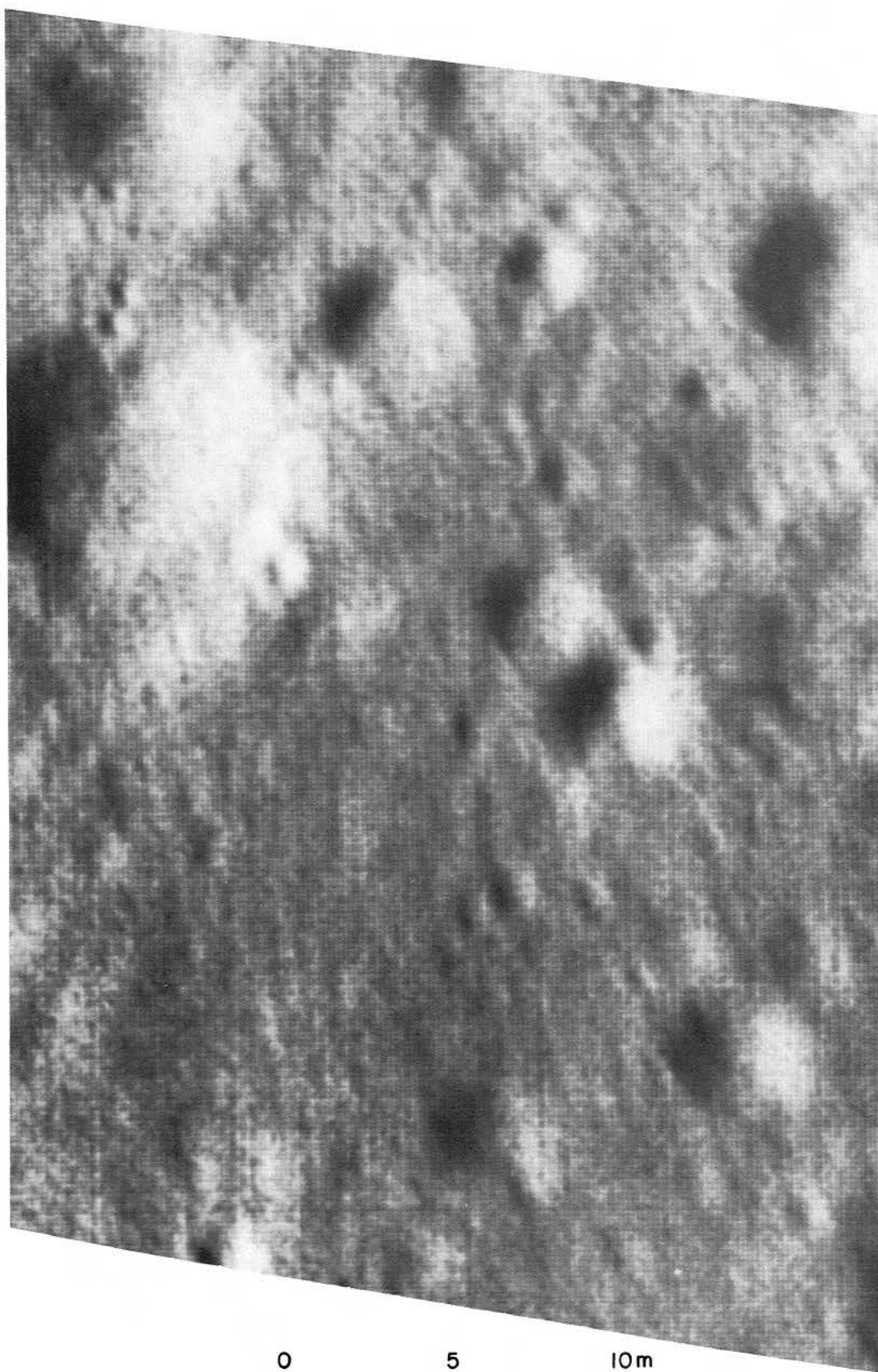
Fig. 136. Last *Ranger VII* P$_3$ frame, corrected in the same way as Fig. 135, but with additional correction for finite blur by camera, electron beam, and finite bandwidth. (JPL photograph.)
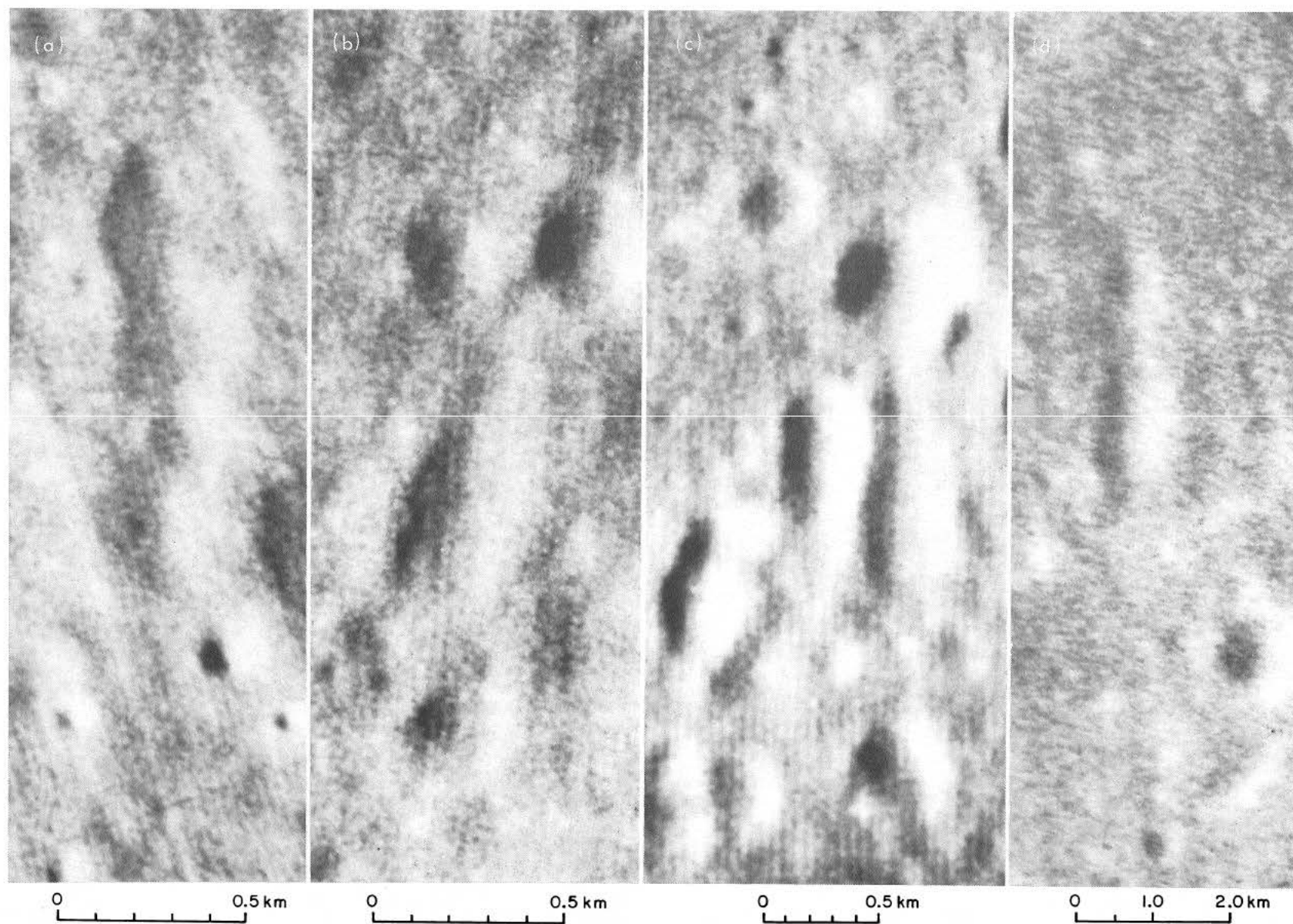
Fig. 137. Linear-beaded collapse depressions observed in *Ranger VII* records: (a) A198, (b) A198, (c) A197, (d) A192.
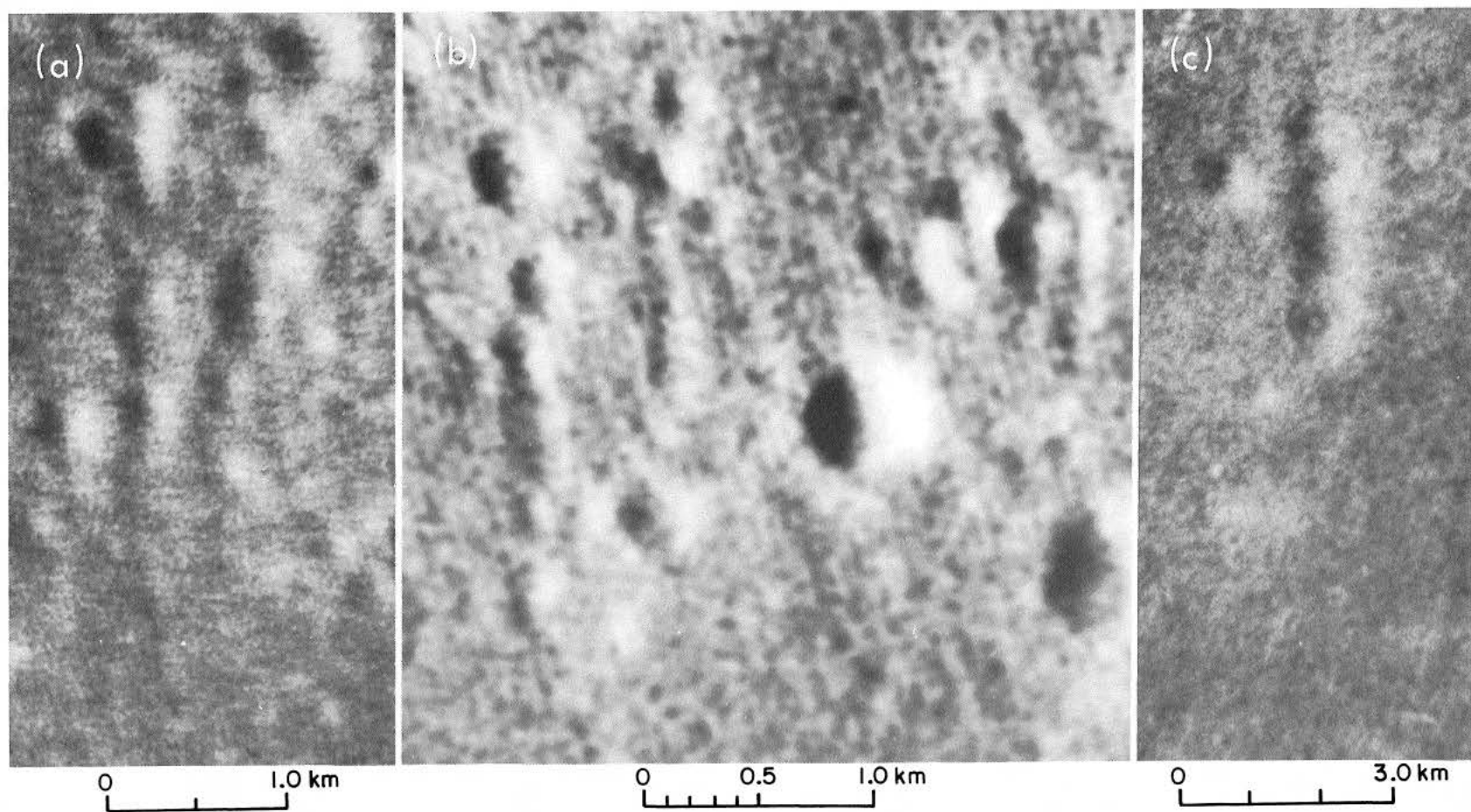
Fig. 138. Linear-beaded collapse depressions observed in *Ranger VII* records: (a) A195, (b) A196, (c) A187.

Fig. 139. Linear-beaded collapse depressions:
(a) *Ranger VIII* frame B82, (b) *Ranger IX*
frame A67, (c) *Ranger IX* frame B84.
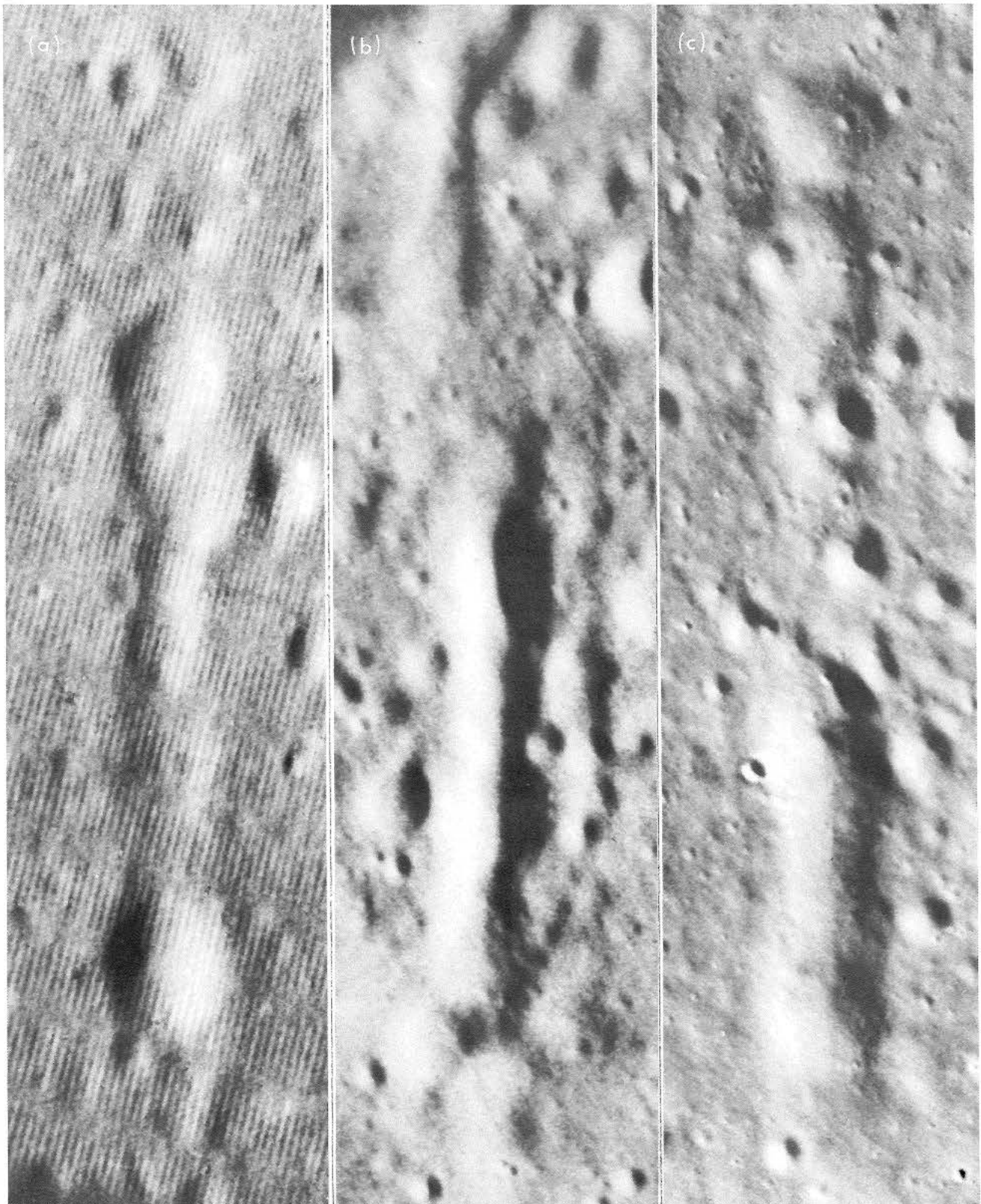
Fig. 140. Linear-beaded collapse depressions over
two parallel fissures, Hawaiian Islands.
(U. S. Government photograph.)

reproduced in Figs. 141 and 142. These radial systems have often been regarded as "scars" or "gouges," but their interpretation as collapse troughs over fissures appears more plausible. One argument is that the radial troughs are by far the strongest where their direction coincides with other known grid directions (as noted in the legends), a property mentioned in Section D with reference to Theophilus. To what extent the weaker and shorter troughs are due to collapse only, collapse stimulated by impact, or pure impact, cannot readily be ascertained from the present data.

In this connection, the Copernicus system of beaded valleys (Ref. 1, Section III-H) presents some special aspects. The apparent increased frequency of the valleys within the large rays crossing Mare Imbrium and the roughness of the rays seen on the terminator would suggest the cause to be impact, unless the excess is due to photometric causes only (Ref. 1, p. 58). Stimulated collapses propagating along pre-existing structural lines of weakness are known to occur over subsurface mines; since they occur in cold and brittle rock, they lead to rougher interior contours. Information on the structural and engineering properties of the mare crust can probably be derived with the aid of existing studies of mine stopes and the causes of surface subsidence over mines (Ref. 37). Examples of large subsidence areas over mines and their associated fracture systems and surface motions are shown in Figs. 143–146.

The fracture systems seen in Figs. 143 and 145 are similar to those of the depressions in lava fields (Fig. 23 ff), except that the latter appear less brittle and blocky. As has been stated, this is presumably due to the somewhat plastic nature of the crust that still prevailed at the time the collapses in the lava fields occurred. Radially oriented collapse depressions on the slope of a volcano are shown in Fig. 147.

Yet another approach to the investigation of the nature of the mare surface is to study the effects of surface texture on crater ray deposits. Recently, considerable progress has been made in recording these deposits through the program of full-Moon photography with the 61-in.

telescope at the U. S. Naval Observatory near Flagstaff, Arizona, using long exposures (30–60 sec) on exceedingly fine-grain plates of high contrast. Examples are reproduced in Figs. 59 and 62, and some crater-ray deposits are shown in Figs. 148–151.

The Copernicus field, part of which is shown in Fig. 148, is especially instructive. It contains hundreds of what appear to be dark-halo craters, most of which are so small that only their dark, fuzzy nimbi are visible. Well over 100 of these spots are shown in Fig. 148. Their location with respect to the exceptionally dark volcanic fields bordering Sinus Aestuum is interesting. They do not coincide with the summits of the dark domes and mounds (seen clearly in Photographic Lunar Atlas, Sheets D4a, b, and e) but seem to be randomly distributed on their lower slopes and in the valleys. There is some evidence of the steeper mounds having a deposit of ray material from Copernicus on the exposed side. This, together with the varying degrees of contrast shown by the dark spots and the strong rays partly covering some halos, indicates that the dark-halo craters as a class are older than the Copernicus rays. Their present visibility is attributed to the roughness of the ejecta of the dark-halo craters (noted in the discussion of Figs. 72 and 73). Differential sputtering will, then, after some time, expose the nimbi.

The same differential effect is operative on ordinary impact craters such as Eratosthenes C, D, and E (all about 3.5 km in diameter) and Draper C ($D = 7$ km) in Mare Imbrium, as well as Eratosthenes itself (see Fig. 149). In each case, the ejecta blanket has a fairly sharp outer boundary, which is about 1 crater diameter away from the crater rim for the four smaller craters. The ejecta belts are markedly darker than the surroundings wherever the ray deposit is moderate or light; however, heavy ray deposits are not visibly reduced by the ejecta belts (see Fig. 149). The dark belts are quite pronounced for Eratosthenes A and B ($D \simeq 6$ km each) where the Copernicus ray deposit is thin (Rectified Lunar Atlas, Sheets 12c and d). Inspection of the Saari-Shorthill heat map (Fig. 11) indicates that Eratosthenes A + B and D + E are "hot spots"; i.e., they have better than average

Fig. 141. Radial linear collapse structures SW of Langrenus. (Direction coincides with diagonal grid system, causing enhancement. Longest valleys are 80–100 km long. LPL photograph.)
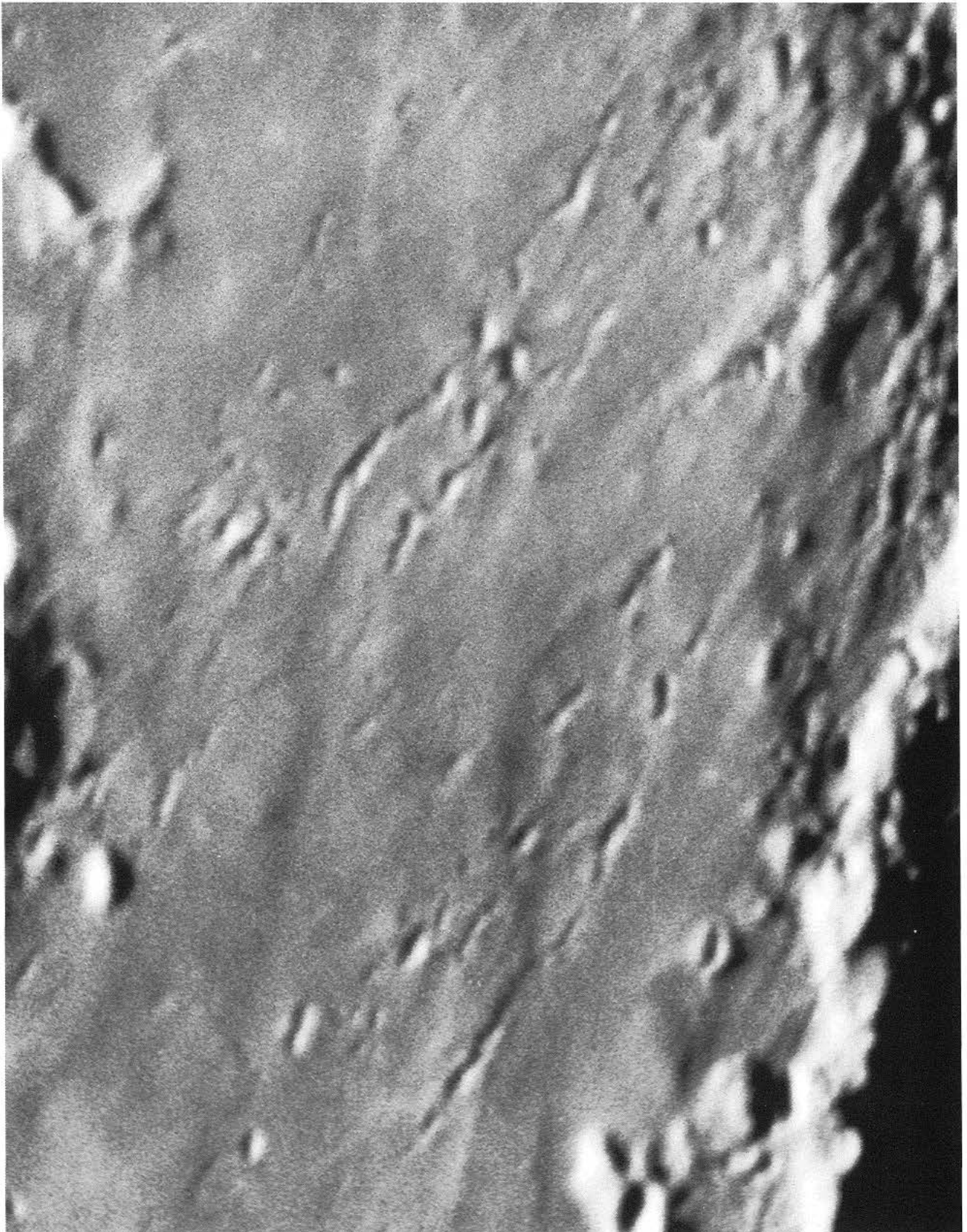
Fig. 142. Radial linear collapse structures NW of
Aristoteles. (Direction coincides with peripheral
Imbrium system. Longest valley is 80 km
long. Lick Observatory photograph.)
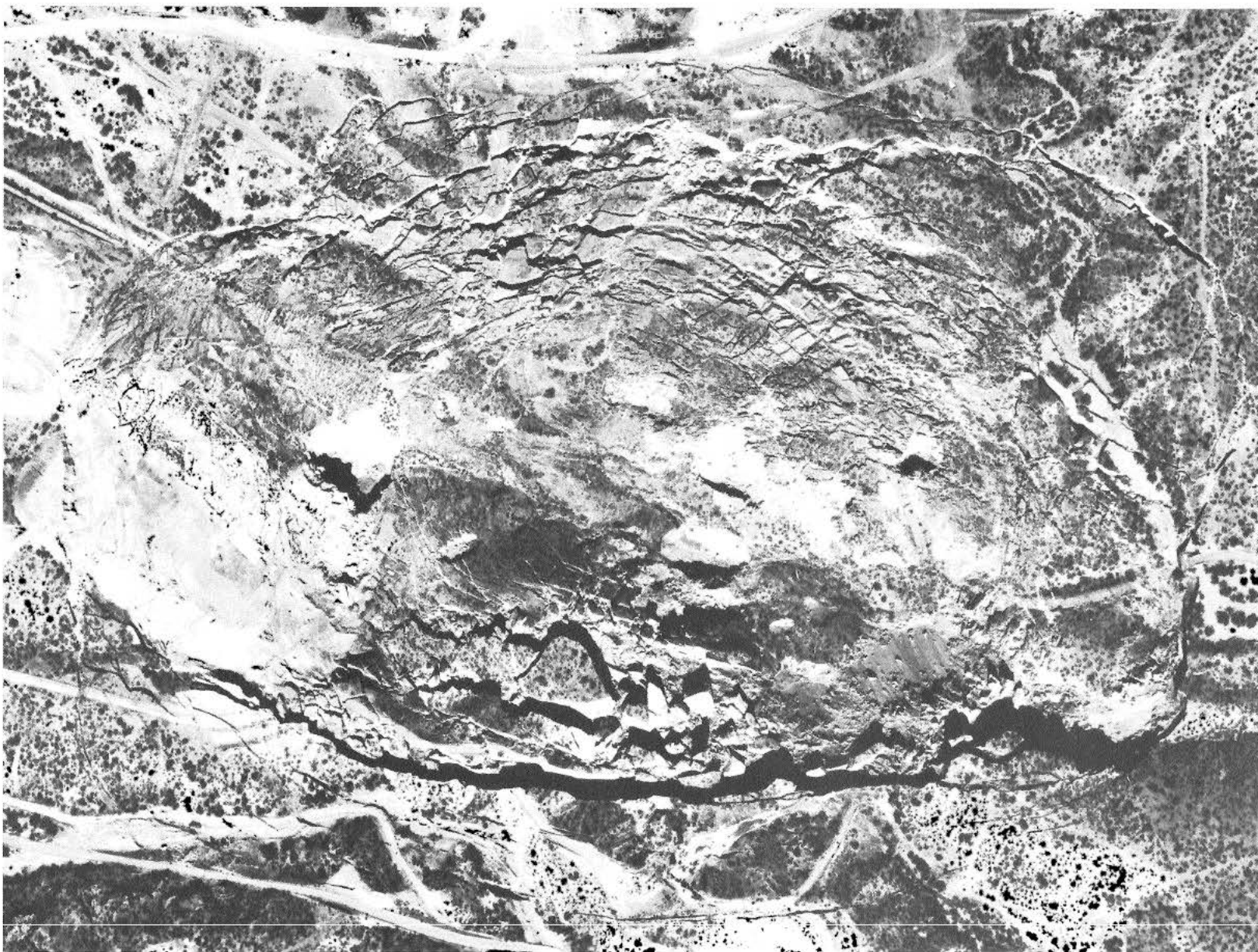
Fig. 143. One of three recent collapse depressions and surrounding fracture systems above underground copper mines in San Manuel, Arizona (see Fig. 144), photographed September 1, 1960. (U. S. Government photograph.)
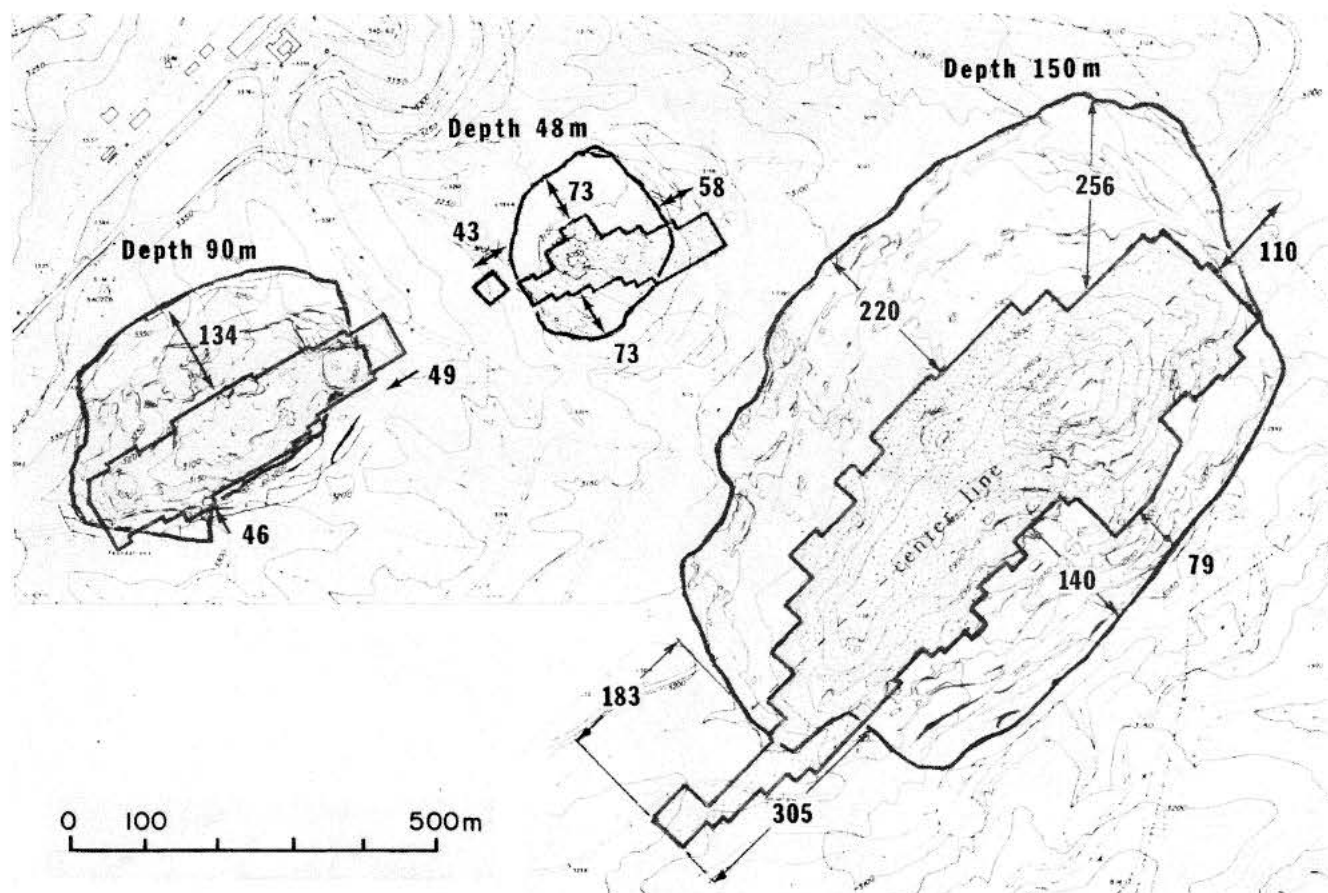
Fig. 144. Outline of three collapse depressions, the largest of which is shown in Fig. 143, compared with subsurface cavities having depth of approximately 1200 ft. (Courtesy A. W. Hatheway.)

Fig. 145. Aerial photographs of collapse depression shown in Fig. 143, taken January 13, 1966. (LPL photographs.)

→
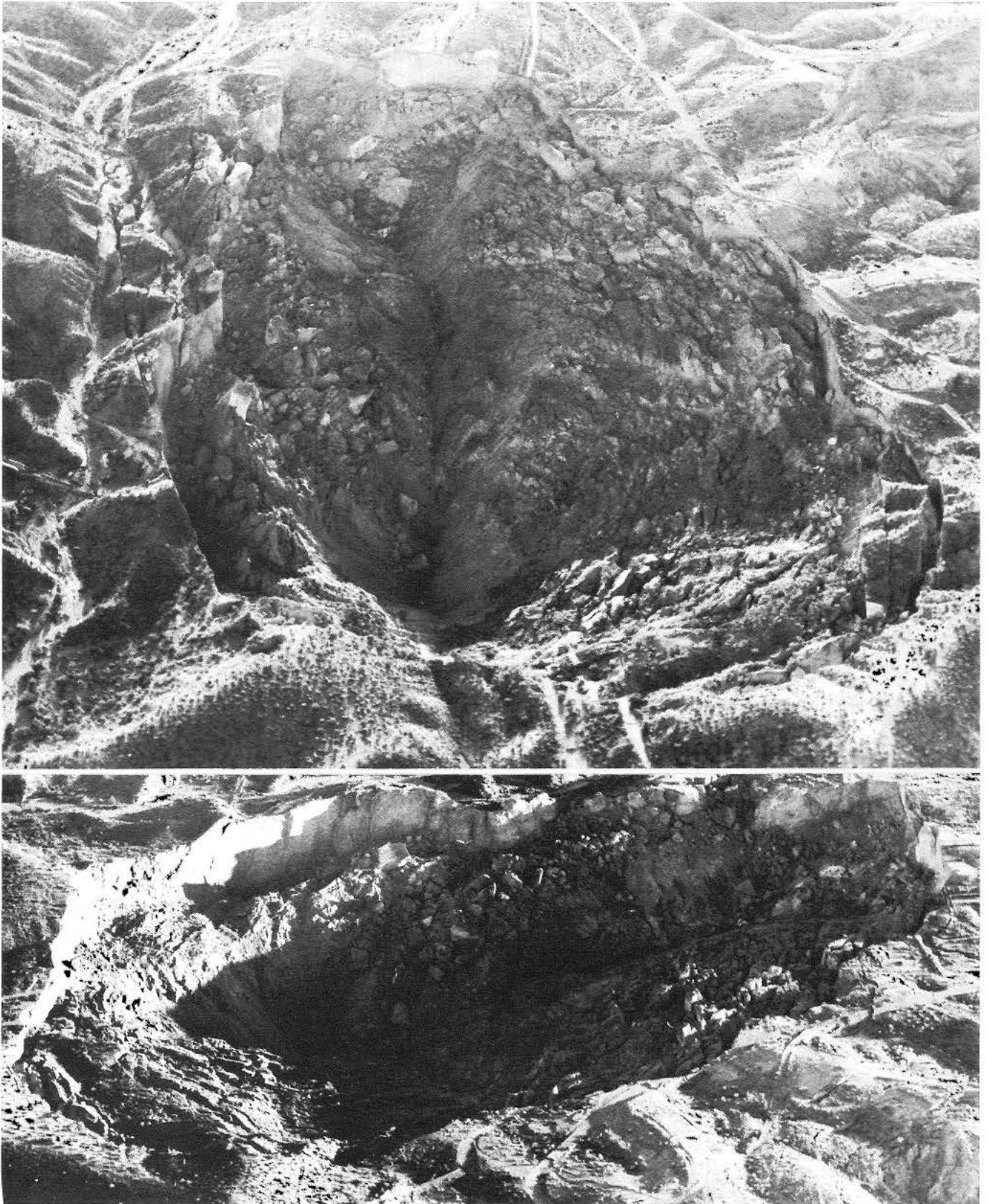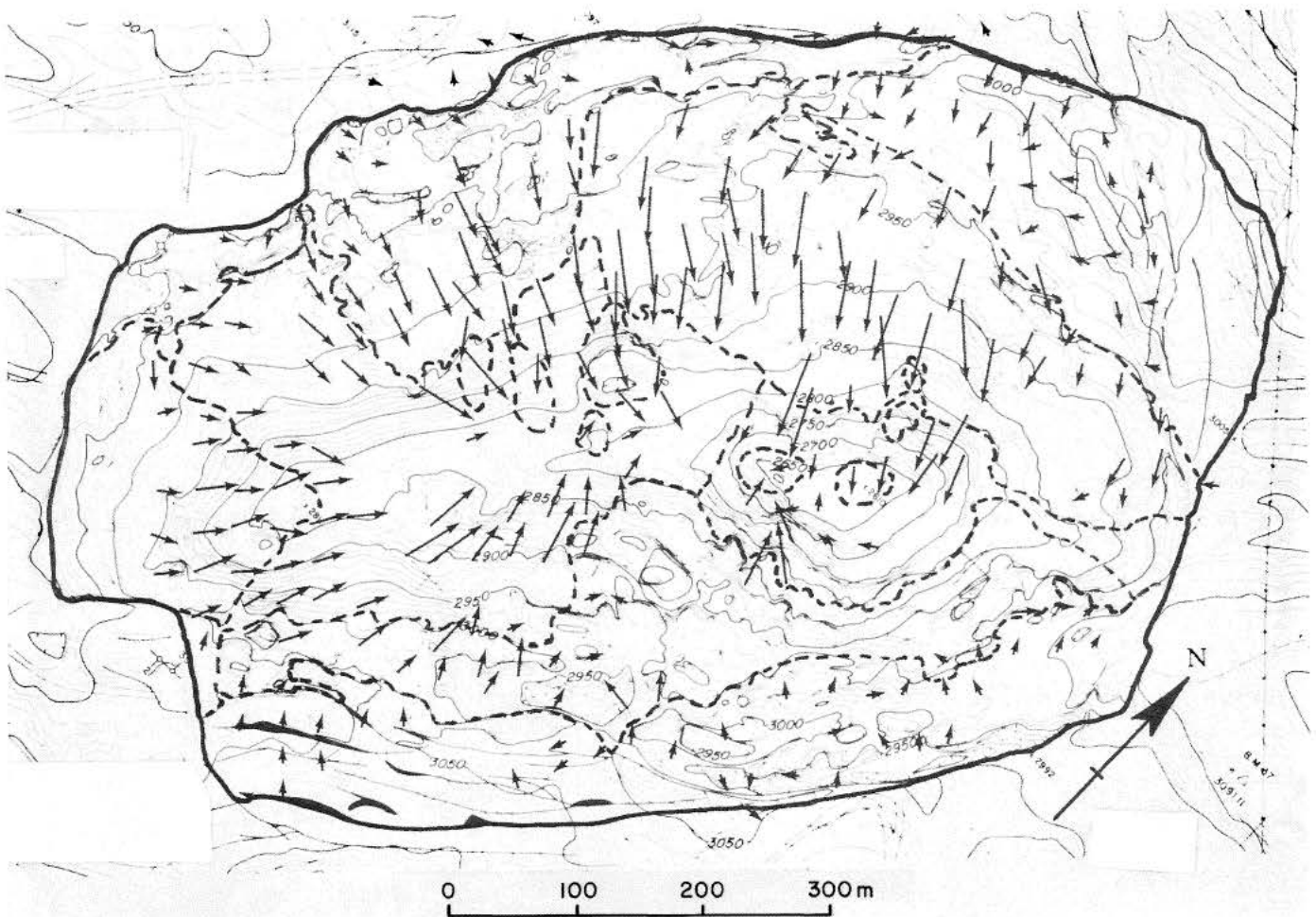
Fig. 146. Surface movement within collapse depression shown in Figs. 143 and 145 during 1957–1961, based on geodetic measurements of markers cemented into surface rock. (Courtesy A. W. Hatheway.)
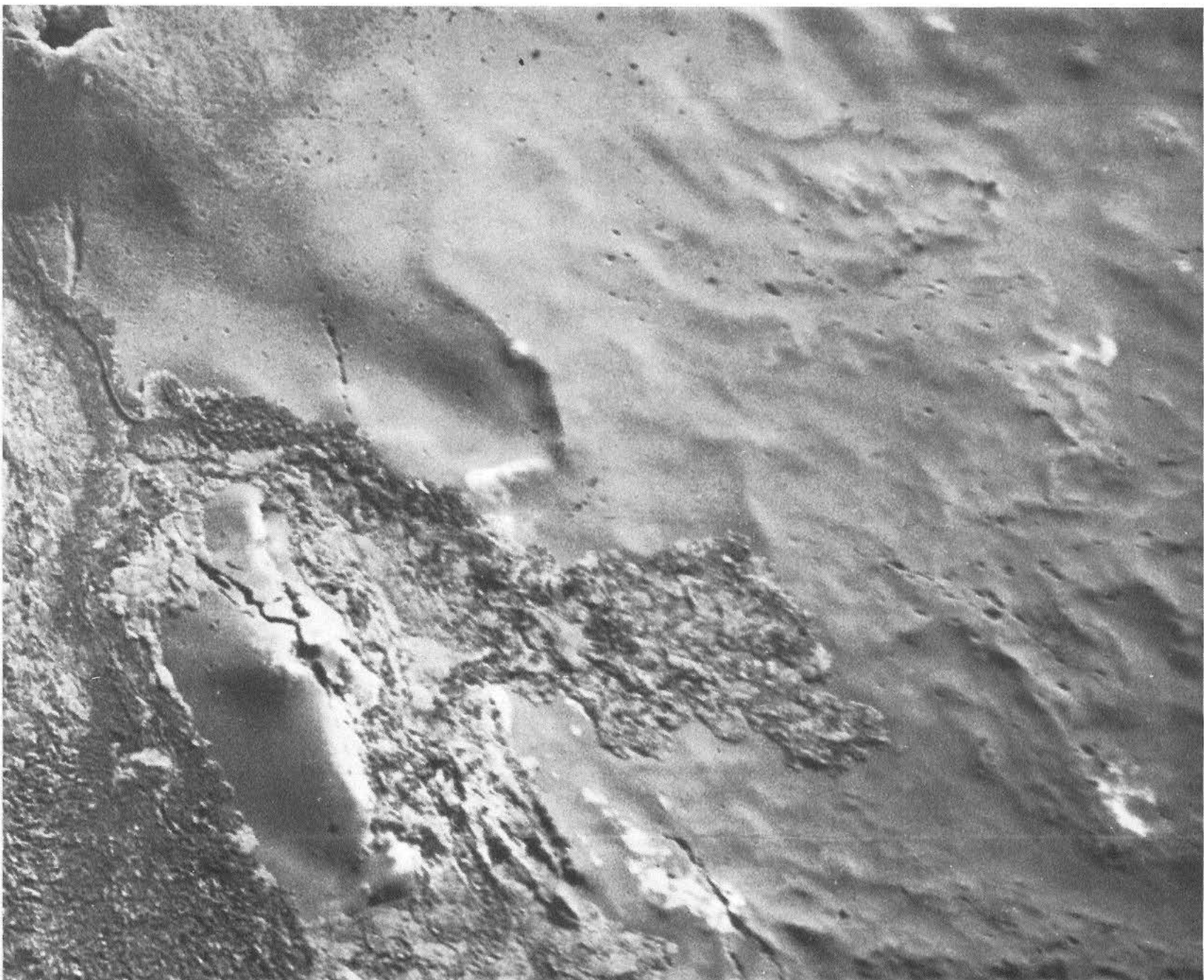
Fig. 147. Radial linear collapse structures on Laimana Crater, Hawaii. (LPL photograph.)
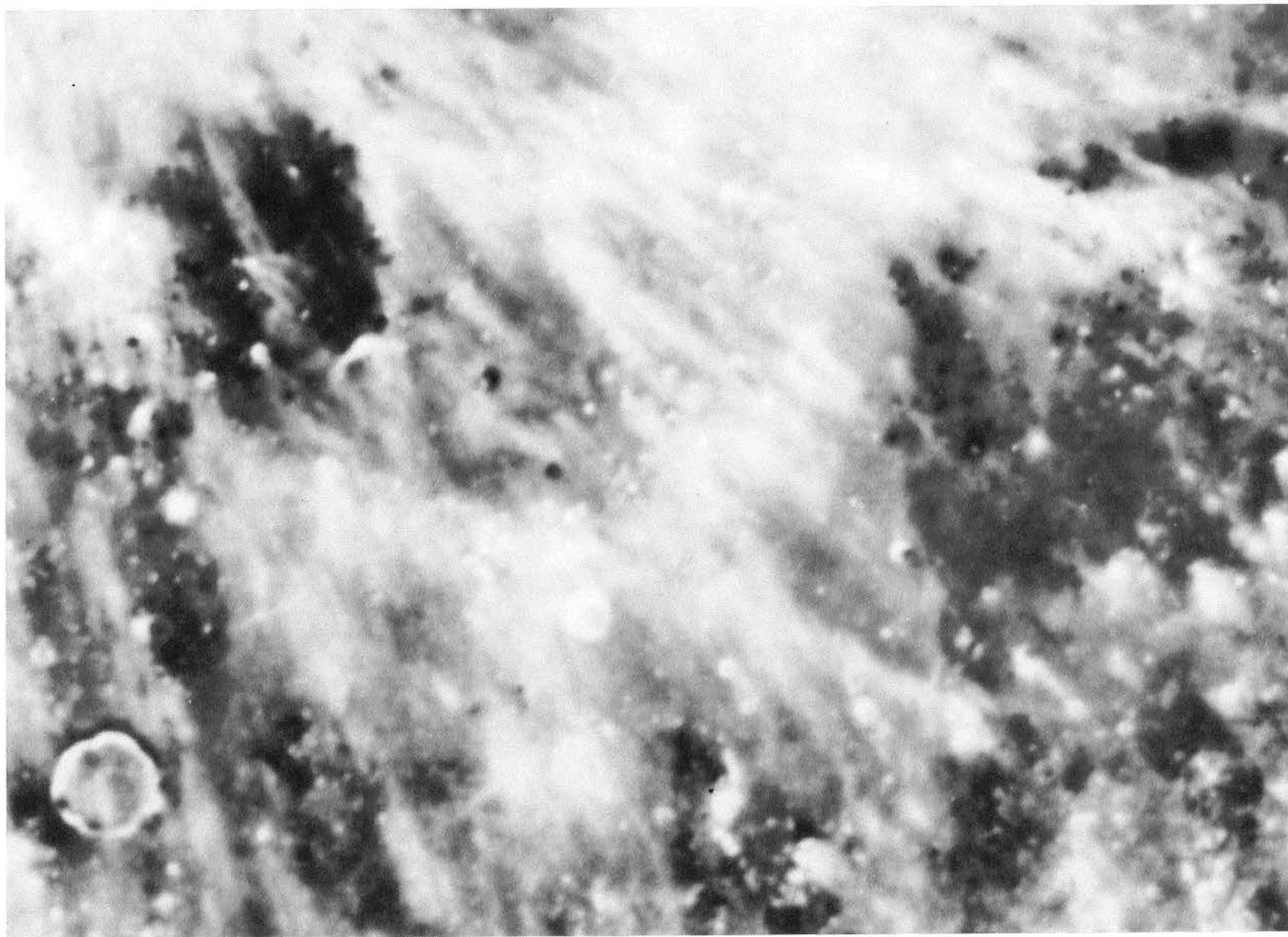
Fig. 148. Section of Copernicus ray system, from about 7–16° W and 0–8° N. (Prominent crater in lower left corner is Gambart. Numerous dark-halo craters show through ray deposit. U. S. Navy–ACIC photograph.)

Fig. 149. Full-Moon photograph of Eratosthenes region,
showing differential denudation of ejecta blankets
around primary-impact craters. (U. S. Navy–
ACIC photograph.)

Fig. 150. Full-Moon photograph of region around Birt,
showing N–S rille ending in darkened, presumably
blocky, region containing mound. (U. S. Navy–
ACIC photograph.)
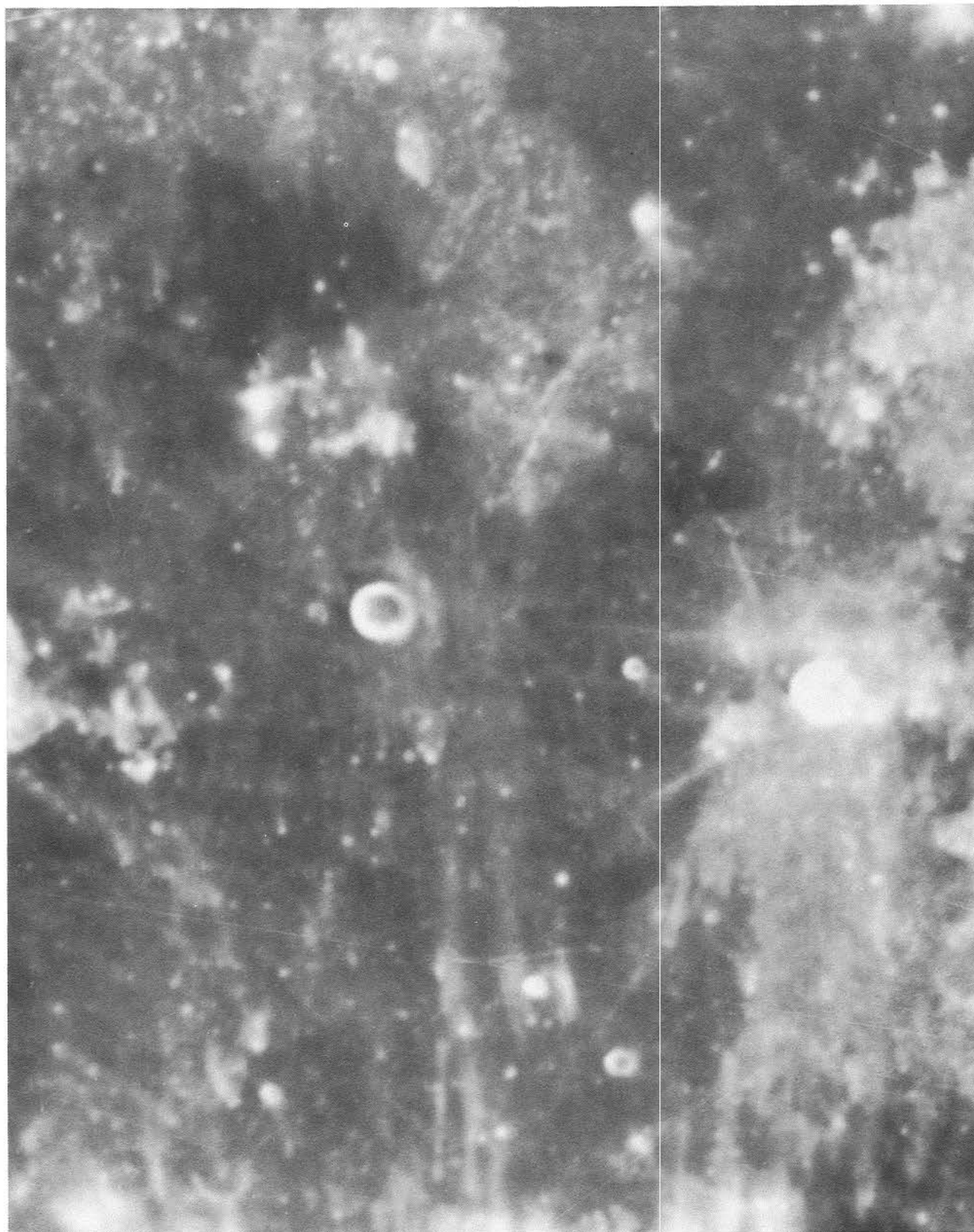
Fig. 151. Full-Moon photograph of E part of Mare Cognitum, showing differential denudation around
dark mountain ridge, also observed in *Ranger VII* photographs. (U. S. Navy–ACIC photograph.)

conduction to the deeper layers of the mare. This is consistent with the concept of a broken, rocky surface deposit.

The concept that *differential denudation of ray deposits yields a measure of the roughness of the lunar surface in the decimeter range* has application also to Mare Nubium and Mare Cognitum. In the *Ranger VII* pictures, a dark mountain range attracted attention (Ref. 1, Fig. 28 and p. 72) which had been suspected to be of recent origin. This conclusion now appears unwarranted. The evidence indicates that the range is pre-Tycho, just like the dark portions of the crater floor of Pitatus, the dark, split dome on the rille west of Birt (Fig. 150), and several other features whose age is almost certainly essentially that of Mare Nubium itself. The outlines of the dark patch in Mare Cognitum on a full-Moon photograph are soft like a crater halo (Fig. 151), and unlike the sharp outlines of the mountain range inside it, as observed by *Ranger VII*.

The *bearing strength of the typical mare surface* is of concern for both instrumented and manned soft-landing operations. Two aspects of this problem have become apparent during the *Ranger* photographic reduction program. First, the widespread occurrence of collapse depressions and the caves observed in some of them are indications of the fragile and unstable nature of much of the mare surface and, therefore, of the obvious risks to landing operations. Because of similar difficulties, it is operational practice not to retrieve rocket payloads that accidentally drop into the Carrizozo Lava Flow discussed in Section C. There are, however, identifiable areas on the maria that appear to be free from the collapse depressions—i.e., *the ridges* and at least *some portions of Mare Nubium*. The surface distribution of such regions ought to be more fully explored before landings are attempted.

The second aspect of the soft-landing problem is the bearing strength on the "micro" scale, which involves not the easily identified terrain features but the nearly level terrain between obstacles. In the *Ranger VII* Report, an estimate was given on the basis of a probable identification of the uppermost mare surface with rock froth, somewhat compacted by particle impact (Ref. 1, pp. 11 and 39). The *Ranger IX* impact area afforded the opportunity to determine the limiting bearing strength directly (Section E), and an order-of-magnitude value (1 kg/cm² or 1 ton/ft²) consistent with the *Ranger VII* discussions was obtained.

After detailed lunar studies have clarified the post-mare developments, the *pre-mare* period will come into better focus, and the great problems of the origins of the Moon and the Earth will become more tractable. One aspect of these problems is the early thermal history of the Moon and, in particular, any observable effects that might still remain of a high solar-luminosity phase assumed to have followed immediately the period of pre-solar contraction. A direct tie-in of the solar and lunar time scales would be of vast scientific importance. It may be possible also to arrive at some prediction of the water content of the uppermost layers of the terrae; they may be very dry because of the hot vacuum treatment. In this connection, efforts must be made to analyze spectroscopically the reddish glow of the gases that are expelled from the lunar crust from time to time (Ref. 38).

The terrae and maria are sometimes thought to parallel the continents and ocean basins of the Earth, but this analogy is almost certainly in error. The terrestrial continents appear to be blocks 35–40 km thick, floating plastically in the mantle from which they were apparently differentiated during geologic time. The 5- to 6-km-thick basaltic ocean floors likewise originated during geologic time as a result of repeated volcanism (Ref. 39). The lunar terrae, on the other hand, are not differentiation products but appear to be surface residues of the accreted material that initially formed the entire Moon. (The closest views of this type of material are found in the *Ranger IX* coverage of the Alphonsus wall [see Fig. 74] and the *Ranger VIII* coverage of the Delambre region.) This pre-mare material appears to have been very severely shaken by gigantic impacts such as those that caused Mare Imbrium (reducing all original steep slopes) and metamorphosed by hydrothermal action during the period of maximum subsurface melting. It is therefore not surprising that no visible fissures exist that are definitely pre-mare, although the presence of a pre-mare lineament system is indicated by the numerous polygonal pre-mare craters and ridges in the terrae. As Strom has pointed out, the fact that at least the Nectaris and Imbrium lineament systems cut the global system (shown by ridges) indicates that the latter must be older. The maria themselves were caused by the flooding of pre-existing basins (the most prominent of which were due to impacts of circumterrestrial bodies).

Unlike the deposition of basalt on the floors of the terrestrial oceans, the lava deposition in the maria did not occur sporadically all through geologic time but appears to have taken place during a limited interval some

4.5×10^9 years ago. Conclusions that have occasionally been drawn about the maria being much younger (a few times 10^8 years) are based on the facile assumption that the age of a lunar province is proportional to its crater density. This assumption ignores such evidence as that which has led to the concepts represented in Fig. 134.

Lineaments disclose roots leading to the deeper crustal layers and are thus potentially important sources of information. The fact that the global grid system of the Moon can be traced to the submeter crustal properties is very remarkable. On the Earth, very prominent lineaments have been discovered not only on the continents but also, e.g., on the Pacific floor (Ref. 39). Some of these are over 4000 km in length, and together they represent, at least in the eastern Pacific, a roughly zonal system. Parallel to these lineaments, large displacements of the crust (wrench faults) have been found, which have alternately been interpreted as being due to (1) polar displacements within the body of the Earth, causing sheer forces through zonal changes in the linear velocity of rotation which act on a crust supported by a plastic base, and (2) convection currents in the Earth's mantle, with drag forces exerted on the overlying crust. The equivalent of either of these processes is likely to be nonexistent on the Moon: (1) the inertial ellipsoid of the Moon's body has a forced rotation in the tidal field of the Earth, whereas the position of the axis of rotation within the body of the Earth is in indifferent equilibrium; (2) because the Moon is much less massive than the Earth, its internal temperature will be less and its body more rigid, as is in fact demonstrated by the considerable deviation of the Moon from hydrostatic equilibrium. Consistent with, and thus confirming, the above conclusions, one finds no substantial displacements along any of the lunar lineaments. Furthermore, unlike the Pacific floor lineaments, which appear to be of comparatively recent geologic age ($\leq 10^8$ years), the lunar grid system probably dates from the pre-mare to the early post-mare period, and must be related to the thermal and tidal properties

pertaining at that time. Yet another difference between the Moon and the Pacific floor system is that the grid lines on the Moon are not normally divisions between different physiographic provinces. On the Pacific floor, the opposite is frequently the case (Ref. 39). A preliminary study made by Strom of the Martian grid system observed in the *Mariner IV* records indicates that the Mars system somewhat resembles that of the Moon.

The terrestrial continents have lineament systems that are more similar to those found on the Moon and on Mars. Reference is made to a study of the Australian lineaments (Ref. 40), which are much older than the very prominent system in the northeastern Pacific (Ref. 39), and along which no displacements have been noted. Similar results have been derived for the Canadian Shield, among others.

A practical as well as a scientific objective must finally be to determine more precisely the nature of the upper 1 cm–1 m of the lunar maria. The radar and optical evidence indicate strongly that outside craters larger than 1 m and outside the ejecta belts immediately surrounding large impact craters, the surface is comparatively smooth down to dimensions of 1–3 cm, where the surface becomes extremely rough and vesicular. It appears further that the importance of ejecta from primary craters has been overrated and that, in particular, many long valleys attributed to ejecta (scars) are in reality depressions along fractures.

The dynamics and engineering aspects of the lunar collapse depressions occurring in the honeycombed and vesicular mare deposits are likely to develop into a major subject of scientific interest as well. The problem of finding shelter will be paramount after landing operations. The *Ranger* records have shown that the lunar maria are honeycombed with accessible cavities that might serve this purpose.

REFERENCES

1. Kuiper, G. P., "Interpretation of Ranger VII Records," *Ranger VII, Experimenters' Analyses and Interpretations,* Technical Report No. 32-700, Pt. II, Jet Propulsion Laboratory, Pasadena, California, February 10, 1965, pp. 9–73.

2. Kuiper, G. P., "The Exploration of the Moon," *Vistas in Astronautics,* Vol. II, New York: Pergamon Press, Inc. (1959).

3. Kuiper, G. P., "Circular and Composite Collapse Depressions on Earth and Moon, I," *Communications of the Lunar and Planetary Laboratory,* University of Arizona (In press); also, "The Moon and the Planet Mars," *Advances in Earth Science* (Contributions to the Conference on the Earth Sciences, M. I. T., Sept. 1964), Chapter 2, ed. by P. M. Hurley, Cambridge: The M. I. T. Press (1966), pp. 21–70.

4. Saari, J. M., and Shorthill, R. W., "Nonuniform Cooling of the Eclipsed Moon: A Listing of Thirty Prominent Anomalies," *Science,* Vol. 150 (1965), pp. 210–212; Low, F. J., "Planetary Radiation at Infrared and Millimeter Wavelengths," *Lowell Observatory Bulletin,* No. 128, Vol. 6, No. 9 (1965), pp. 184–187.

5. Shorthill, R. W., Borough, H. C., and Conley, J. M., "Enhanced Lunar Thermal Radiation During a Lunar Eclipse," *Publications of the Astronomical Society of the Pacific,* Vol. 72 (1960), pp. 481–485; Shorthill, R. W., and Saari, J. M., "Cooling Curves for Some Rayed Craters During a Lunar Eclipse," *op. cit.,* Vol. 73 (1961), pp. 335–336.

6. Sinton, W. M., "Eclipse Temperatures of the Lunar Crater Tycho," *Lowell Observatory Bulletin,* Vol. 5, No. 3 (1960), pp. 25–27; Sinton, W. M., "Temperatures on the Lunar Surface," *Physics and Astronomy of the Moon,* Chapter 11, ed. by Z. Kopal, New York: Academic Press, Inc. (1962), pp. 407–428.

7. Hapke, B., "Photometric and Other Laboratory Studies Relating to the Lunar Surface," *The Lunar Surface Layer, Materials and Characteristics,* ed. by J. W. Salisbury and P. E. Glaser, New York: Academic Press, Inc. (1964), pp. 323–344; Hapke, B., and Van Horn, H., "Photometric Studies of Complex Surfaces, with Applications to the Moon," *Journal of Geophysical Research,* Vol. 68, No. 15 (1963), pp. 4545–4570; Hapke, B., "A Theoretical Photometric Function for the Lunar Surface," *ibid.,* pp. 4571–4586.

8. Hapke, B., *Optical Properties of the Moon's Surface* (Paper presented at Conference on the Nature of the Surface of the Moon, Goddard Space Flight Center, Greenbelt, Maryland, April 1965), CRSR 198, Center for Radiophysics and Space Research, Cornell University, Ithaca, New York, June 1965; Chow, H. Y. C., *Effects of Several Parameters on the Optical Properties of Some Rock Powders, with Applications to the Moon,* CRSR 200, Center for Radiophysics and Space Research, Cornell University, Ithaca, New York, June 1965.

9. Wehner, G. K., "Sputtering Effects on the Lunar Surface," *The Lunar Surface Layer,* ed. by J. W. Salisbury and P. E. Glaser, New York: Academic Press, Inc. (1964), pp. 313–322.

10. *The Lunar Surface Layer,* ed. by J. W. Salisbury and P. E. Glaser, New York: Academic Press, Inc. (1964); *Studies of the Characteristics of Probable Lunar Surface Materials,* ed. by J. W. Salisbury and P. E. Glaser, AFCRL-64-970, Special Report No. 20, Office of Aerospace Research, U. S. Air Force Cambridge Research Laboratories, Bedford, Massachusetts, January 1964.

REFERENCES (Cont'd)

11. Evans, J. V., and Pettengill, G. H., "The Radar Cross Section of the Moon," *Journal of Geophysical Research,* Vol. 68 (1963), p. 5098; Pettengill, G. H., and Shapiro, I. I., "Radar Astronomy," *Annual Review of Astronomy and Astrophysics,* Vol. 3, ed. by L. Goldberg, Palo Alto: Annual Reviews, Inc. (1965), p. 377; Thompson, T. W., *A Study of Radar-Scattering Behavior of Lunar Craters at 70 cm,* Report RS64, Center for Radiophysics and Space Research, Cornell University, Ithaca, New York, November 1965.

12. Nichols, R. L., "McCartys Basalt Flow in New Mexico," *Bulletin of the Geological Society of America,* Vol. 57 (1946), pp. 1049–1086.

13. Kuiper, G. P., "Lunar Results from Rangers 7 to 9," *Sky and Telescope,* Special Supplement, Vol. 25, No. 5 (May 1965), pp. 293–308, and *Communications of the Lunar and Planetary Laboratory,* University of Arizona, Vol. 3, No. 49 (1965), pp. 33–60.

14. Jaffe, L. D., "Depth and Strength of the Lunar Dust," Personal communication, 1964, and *Journal of Geophysical Research,* Vol. 70 (1965), pp. 6129–6138.

15. Arthur, D. W. G., Agnieray, A. P., Horvath, R. A., Wood, C. A., and Chapman, C. R., "The System of Lunar Craters, Quadrant I," *Communications of the Lunar and Planetary Laboratory,* University of Arizona, Vol. 2, No. 30 (1963), p. 71.

16. Arthur, D. W. G., Agnieray, A. P., Horvath, R. A., Wood, C. A., and Chapman, C. R., "The System of Lunar Craters, Quadrant II," *Communications of the Lunar and Planetary Laboratory,* University of Arizona, Vol. 3, No. 40 (1964), p. 1.

17. Shoemaker, E. M., Hackman, R. J., and Eggleton, R. E., "Interplanetary Correlation of Geologic Time," *Advances in the Astronautical Sciences,* Vol. 8, New York: Plenum Press (1963), pp. 70–89.

18. Whipple, F. L., and Hughes, R. F., "On the Velocities and Orbits of Meteors, Fireballs, and Meteorites," *Journal of Atmospheric and Terrestrial Physics,* Special Supplement, Vol. 2 (1955), pp. 149–156.

19. Hawkins, G. S., "Asteroidal Fragments," *Proceedings of Lunar and Planetary Exploration Colloquium* (May 23–24, 1961), Vol. 2, No. 4, North American Aviation, Inc., Downey, California (1961), pp. 5–10.

20. Hawkins, G. S., "Impacts on the Earth and Moon," *Nature,* Vol. 197 (1963), p. 781.

21. Hawkins, G. S., "Interplanetary Debris Near the Earth," *Annual Review of Astronomy and Astrophysics,* Vol. 2, ed. by L. Goldberg, Palo Alto: Annual Reviews, Inc. (1964), pp. 149–164.

22. Gaudin, A., *Principles of Mineral Dressing,* New York: McGraw-Hill Book Co., Inc. (1944).

23. Anders, E., "Fragmentation History of Asteroids," *Icarus,* Vol. 4, No. 4 (1965), p. 339.

24. Anders, E., "Meteoritic Ages," *The Solar System, Vol. IV—The Moon, Meteorites, and Comets,* Chapter 13, ed. by B. M. Middlehurst and G. P. Kuiper, Chicago: University of Chicago Press (1963), pp. 402–495.

REFERENCES (Cont'd)

25. Öpik, E. J., "Collision Probabilities With the Planets and the Distribution of Interplanetary Matter," *Proceedings of the Irish Academy,* Vol. 54, Section A, No. 12 (1951).

26. Strom, R. G., "Analysis of Lunar Lineaments I: Tectonic Maps of the Moon," *Communications of the Lunar and Planetary Laboratory,* University of Arizona, Vol. 2, No. 39 (1964), pp. 205–216.

27. Quaide, W., "Rilles, Ridges, and Domes—Clues to Maria History," *Icarus,* Vol. 4, No. 4 (1965), pp. 374–389.

28. Cameron, W. S., "An Interpretation of Schröter's Valley and Other Lunar Sinuous Rilles," *Journal of Geophysical Research,* Vol. 69 (1964), pp. 2423–2430.

29. Wentworth, C. K., and Macdonald, G. A., "Structures and Forms of Basaltic Rocks in Hawaii," *Bulletin of the United States Geological Survey,* No. 994 (1953), p. 98.

30. Williams, H., Personal communication, August 1965.

31. Billings, M. P., *Structural Geology,* New York: Prentice-Hall, Inc. (1954), p. 514.

32. O'Keefe, J. A., and Cameron, W. S., "Evidence from the Moon's Surface Features for the Production of Lunar Granites," *Icarus,* Vol. 1, No. 3 (1962), p. 271.

33. Washington, H. S., "The Formation of Aa and Pahoehoe," *American Journal of Science,* Vol. 6 (1923), pp. 409–423.

34. Kuiper, G. P., "On the Origin of the Lunar Surface Features," *Proceedings of the National Academy of Sciences,* Vol. 40, Section 8 (1954), pp. 1108–1111.

35. Kuiper, G. P., "On the Origin of Asteroids," *Astronomical Journal,* Vol. 55, No. 1186 (1950), p. 164; Kuiper, G. P., *et al.,* "Survey of Asteroids," *Astrophysical Journal Supplement Series,* Vol. III, No. 32 (1958), pp. 289 and 330 ff.

36. Hedden, R. T., *Lunar Charting Experiments Utilizing Ranger VIII Materials in the AS-11A Analytical Plotter,* ACIC Technical Paper TP-20, September 1965.

37. Lewis, R. S., and Clark, G. B., "Rock Mechanics," *Elements of Mining,* 3rd Edition, Chapter 17, New York: John Wiley and Sons, Inc. (1964), p. 621; Briggs, H., *Mining Subsidence,* London: Edward Arnold and Co. (1929); Hatheway, A. W., *Engineering Geology of Subsidence at San Manuel Mine, Pinal County, Arizona,* Master's thesis, Department of Geology, University of Arizona (1966).

38. Lunar and Planetary Branch Cartography Division, ACIC, *Lunar Color Phenomena,* ACIC Technical Paper No. 12, 1964; Middlehurst, B. M., "A Lunar Eruption in 1783?" *Sky and Telescope,* Vol. 28, No. 2 (1964), pp. 83–88; Green, J., "Tidal and Gravity Effects Intensifying Lunar Defluidization and Volcanism," *Annals of the New York Academy of Sciences,* Vol. 23 (1965), pp. 403–469; Middlehurst, B. M., and Burley, J. B., *Transient Lunar Events: Possible Causes,* Paper Presented at Conference on Extra-Terrestrial Resources, Colorado Springs, Colorado, November 1965 (In press); Middlehurst, B. M., "Lunar Events: Possible Causes," *Nature* (In press); Middlehurst, B. M., and Burley, J. B., "Lunar Events: A Historical Review," *Proceedings of the National Academy of Sciences* (In press).

REFERENCES (Cont'd)

39. Menard, H. W., *Marine Geology of the Pacific*, New York: McGraw-Hill Book Co., Inc. (1964).

40. Hills, E. S., "A Contribution to the Morphotectonics of Australia," *Journal of the Geological Society of Australia*, Vol. 3 (1955), pp. 1–15.

Supplementary References

1. "Geological Problems in Lunar Research," *Annals of the New York Academy of Sciences*, ed. by H. E. Whipple, Vol. 123, Art. 2 (1965).

2. Baldwin, R. B., *The Measure of the Moon*, Chicago: University of Chicago Press (1963).

3. *Physics and Astronomy of the Moon*, ed. by Z. Kopal, London: Academic Press, Inc. Ltd. (1962).

4. *The Moon—Symposium No. 14 of the International Astronomical Union*, ed. by Z. Kopal and Z. K. Mikhailov, New York: Academic Press, Inc. (1962).

5. Fielder, G., *Lunar Geology*, London: Lutterworth Press (1965); Fielder, G., *Structure of the Moon's Surface*, London: Pergamon Press, Ltd. (1961).

ACKNOWLEDGMENTS

IV. PROGRESS IN THE ANALYSIS OF THE FINE STRUCTURE AND GEOLOGY OF THE LUNAR SURFACE FROM THE RANGER VIII AND IX PHOTOGRAPHS*

Eugene M. Shoemaker**

with contributions by
James D. Alderman
Warren T. Borgeson
Michael H. Carr
Richard V. Lugn
John F. McCauley
Daniel J. Milton
Henry J. Moore
Harrison H. Schmitt
Newell J. Trask
Don E. Wilhelms
Sherman S. C. Wu

United States Geological Survey
Flagstaff, Arizona

A. Introduction

The pictures acquired from the *Ranger VIII* and *IX* missions contain a wealth of new data about the lunar surface and supplement our knowledge of the Moon in several ways.

First, the *Ranger VIII* and *IX* pictures greatly augment the information about the fine structure of the lunar

---

*Final manuscript received February 10, 1966.

**All Sections not identified by author were written by Mr. Shoemaker.

surface obtained from the *Ranger VII* mission. Other parts of the Moon were shown to be similar to the part first photographed with high resolution by *Ranger VII* in Mare Cognitum, and, in a general way, predictions based on the data obtained in this mission were confirmed. In addition, certain features, such as the small lineaments, that were only faintly discernible in the *Ranger VII* pictures, were found to be more prominent and much more widespread than had been anticipated. The improved portrayal of small features of low relief is due mainly to the fact that the *Ranger VIII* and *IX* target areas were closer to the terminator at the time of impact than was the target area of *Ranger VII*.

Both the *Ranger VIII* and *IX* pictures contain much new information as to the detailed topography of the lunar plains. In the *Ranger VIII* mission, the decision was made to maintain the cruise-mode orientation of the spacecraft during the final approach to the Moon's surface, specifically for the purpose of obtaining good stereoscopic coverage along the surface trace of the trajectory. The pictures thus acquired provide the best material for photogrammetric measurement of the shape of small features on the Moon among all of the photographs obtained from the entire *Ranger* series.

Inasmuch as the *Ranger VIII* and *IX* pictures cover major samples of the lunar highland areas as well as of the plains, they contain a great deal of new information on areas of complex geology. It is possible to map the geology of selected areas from these photographs at many different scales, ranging from 1:1,000,000 (the scale employed in the Earth-based telescopic mapping program) up to approximately 1:10,000 (a scale typically employed for highly detailed geologic mapping on Earth).

Finally, the *Ranger VIII* and *IX* data, combined with those from *Ranger VII*, provide the basis for preliminary planning and evaluation of the scientific tasks that may be successfully executed by astronauts in the early landings on the Moon of Project *Apollo*. On the basis of the high-resolution *Ranger* pictures, it is now possible to identify many of the types of geologic features that will be of specific interest and to estimate the time and evaluate the activities that will be required for the astronauts to conduct meaningful investigations.

The reduction and synthesis of the data obtained from the *Ranger VIII* and *IX* missions is still in a preliminary stage. This report presents an analysis of the data, as it bears upon the above categories, based largely upon qualitative considerations. The quantitative analysis, for the most part, must await completion of the detailed photometric and photogrammetric reduction of the pictures that has just begun. However, many general conclusions can be drawn at this time which are expected to be modified or refined only slightly by the final program of analysis.

B. New Data on the Fine Structure of the Lunar Surface

The most significant new information about the fine structure of the lunar surface obtained from the *Ranger VIII* and *IX* missions includes: (1) the frequency distribution and morphology of small craters on several different classes of lunar terrain; (2) the morphologic details of very small craters that are related to the mechanical properties of the lunar-surface material; (3) the distribution and orientation of small lineaments and their spatial relation to certain types of craters, especially on the floor of Alphonsus; and (4) the small topographic details of broad, sloping surfaces, such as the walls of Alphonsus.

On the basis of the size distribution and the shapes of craters observed in the high-resolution *Ranger VII* pictures of Mare Cognitum, a model of ballistic erosion and deposition on the mare surface was formulated (Ref. 1, pp. 130–132), leading to several explicit predictions about the surface features to be seen in the target areas of *Rangers VIII* and *IX*. Most craters observed in Mare Cognitum were interpreted in this model to be of impact origin, and the population of small craters was considered to be in a steady state. The possible presence of other types of craters was recognized, but, in my opinion, no conclusive evidence for their presence could be found in the *Ranger VII* pictures.

In the model developed from the *Ranger VII* data, the ratio of craters of secondary-impact origin expected to have been formed on Mare Cognitum to craters of primary-impact origin is about 50:1 for craters of 1-m diameter. The predicted cumulative distribution functions of primary- and of secondary-impact craters converge at a crater diameter between 2 and 3 km. About 500 times as many craters greater than 1 m in diameter were predicted as were actually seen. This predicted number of craters is far too large to be observed because their cumulative area exceeds the area of the mare surface by more than an order of magnitude. Thus there should have been frequent superposition of craters and destruction of old craters by newer ones during the long history of the mare surface.

The predicted cumulative distribution function of primary-impact craters and the observed distribution function of eumorphic* craters shown in the *Ranger VII*

---

*In the *Ranger VII* experimenters' report (Technical Report No. 32-700, Part II, Jet Propulsion Laboratory, December 15, 1964), the term *primary crater* was used to describe a class of craters with a certain well defined shape (Ref. 1, p. 76). Inasmuch as this class of craters was interpreted to be of primary-impact origin later in the Report, the designation *primary crater* has acquired strong genetic implications for others with whom I have discussed the *Ranger* data. To avoid confusion, the term *eumorphic crater* will be used here as a descriptive name for a sharp-rimmed, steep-walled crater and is synonymous with *primary crater* as defined and illustrated by Shoemaker (Ref. 1, pp. 76–85).

pictures of the mare surface converge at a crater diameter of about 400 m; the predicted and the observed cumulative distribution functions of all craters converge at about 300-m crater diameter. The crater size at the points of convergence was interpreted as the upper limit of the steady part of the observed distribution functions. In other words, the size–frequency distribution of craters in the size range of 1 to 300 m was considered to be in a steady condition. If the flux of primary and secondary objects is of constant size distribution, the size distribution of impact craters 1 to 300 m in diameter does not change with time. Old craters of any given size smaller than 300 m are destroyed as rapidly as new craters of that size are formed.

When applied to other lunar plains, the model derived from the *Ranger VII* data requires that similar parts of the crater size-distribution functions be in a steady condition. The upper limiting crater size of the steady part of the distribution on any one plain would depend on the age of the plain, which is reflected by the number of large craters it contains. The steady parts of the distribution functions should be nearly identical for all plains. Thus it was expected that the distribution of small craters in Mare Tranquillitatis, which has approximately twice as many large craters as Mare Cognitum, would be nearly the same as that in Mare Cognitum. Similarly, the floor of Alphonsus, which has about 10 times as many craters larger than 1 km in diameter as Mare Cognitum, would also have nearly the same distribution of small craters as Mare Cognitum. When account has been taken of the photometric effects on recognition of shallow craters, for pictures taken at different distances from the terminator, these predictions have been borne out, as shown by N. J. Trask in Section 1 below.

I believe that the model developed from the *Ranger VII* data, which led to the identification of steady-state populations of small craters on the lunar plains, has been essentially confirmed by the *Ranger VIII* and *IX* data. The final test of the model must await the detailed photometric reduction of the *Ranger* pictures. Crater populations can then be compared by shape, and account taken of the varying recognizability of extremely shallow craters at different angles of solar illumination.

Several types of craters of other than impact origin are believed to be identifiable in the *Ranger VIII* and *IX* pictures, and, in fact, half or more of the craters observed on the floor of Alphonsus may prove to be of these other types. The presence of other crater types in no way invalidates the model of ballistic erosion and deposition. It simply means that a complete theory of the lunar surface must take into account all of the operating processes and recognize that many processes besides impact have contributed to the topography and to the fine structure of the surface.

One of the most important new conclusions to be drawn from the *Ranger VIII* and *IX* data has to do with the mechanical properties of the material at or near the lunar surface. Several of the *Ranger VIII* and *IX* pictures reveal the very small surface details of craters comparable in size to terrestrial craters produced experimentally by impact and by explosion. By comparing small lunar craters with experimental craters, H. Moore shows, in Section B2, that a few of the small lunar craters revealed in greatest detail occur in material of low cohesion. Such material probably extends locally at least to a depth of 1 to 2 m in the areas photographed with high resolution near the impact points of *Rangers VIII* and *IX*. This means that the Moon's surface at these places is underlain by fragmental material with a grain size less than the line-pair separation resolution of the *Ranger* photographs. A fragmental layer of this kind is precisely what is predicted by the ballistic model of erosion and deposition developed from the *Ranger VII* crater shape and size–frequency distribution data and is essentially confirmed by the *Ranger VIII* and *IX* data; I believe that this fragmental layer is indeed observed. The ballistically generated fragmental layer may overlie either solid rock or fragmental deposits of volcanic or other origin.

On the basis of the ballistic model, it is expected that most of the surface layer of fragmental debris is very fine-grained, at least close to the surface. Because the layer has low cohesion, the porosity is probably not abnormally high at depths exceeding a few tens of centimeters. Only highly cohesive material will sustain, under pressure, an abnormal amount of void space between the grains. Material beneath the ballistically generated fragmental layer could have abnormally high porosity, however, if it is cohesive and highly vesicular.

The bearing strength of the surface must still be considered indeterminate, but the chances are good that it is moderate to fairly high. On the basis of Moore's results for the cohesion of material near the surface, I believe there is reason for optimism about the problem of the foot pads of the *Apollo* spacecraft sinking after touchdown on the lunar surface.

Among the most striking features observed in the *Ranger VIII* and *IX* pictures are the systems of small lineaments and the parallel alignment, with the lineaments, of many small elongate craters and chains of small craters. These features are especially prominent on the floor of Alphonsus, as shown by M. H. Carr in Section B3, but are also observed on the maria.

The small lineaments, elongate craters, and crater chains are also aligned with major, telescopically resolvable lineaments that have a well defined orientation and regional pattern on the Moon. This parallelism indicates that the small lineaments and aligned craters are secondary, or younger, structures that are superimposed on the terrain on which they occur, rather than primary structures, such as flow ridges or collapsed lava tubes of typical basaltic lava flows. The small lineaments are probably formed over joints and fissures, as suggested in Section B4. Many of the very small, aligned craters probably have been formed by local drainage of the weakly cohesive or cohesionless ballistically generated fragmental layers into underlying fissures.

Finally, the density of craters on broad, sloping surfaces observed in the *Ranger IX* photographs, particularly on the walls of Alphonsus, provides important clues about the fine structure of the lunar surface and the processes by which it is formed. Care must be taken in evaluating the difference in appearance between these sloping surfaces and the relatively level areas, such as the floor of Alphonsus, because part of this difference is due solely to photometric effects arising from variations of the component of slope in the phase plane. Surfaces sloping toward the Sun are brighter, and shallow craters are more difficult to detect on them than on level surfaces of the same albedo. After allowance has been made for the photometric effects, however, there is clearly a deficiency of small craters on the walls of Alphonsus as compared with the floor.

I believe that the small crater population is in a steady state on the walls, just as on the floor of Alphonsus, but that the rate of destruction of small craters on the walls is greater than on the floor. The increased rate of crater destruction may be due primarily to downslope mass movement of material with low cohesion. There is no need to postulate that the walls are younger than the floor or that they are covered with some unusual deposit of material.

1. Size and Spatial Distribution of Craters Estimated From the *Ranger* Photographs, Newell J. Trask

The *Ranger VIII* and *IX* photographs, together with the earlier *Ranger VII* photographs, have made possible the measurement of size and spatial distribution of small craters on the Moon in three contrasting terrains: (1) ray areas on the maria, (2) ray-free parts of the maria, and (3) relatively flat highland-basin terrain exemplified by the floor of Alphonsus. Size–frequency distributions of craters in the two widely separated mare areas photographed, one in Mare Cognitum and the other in Mare Tranquillitatis, are closely similar. Crater densities on the floor of Alphonsus are higher than on the maria for craters of large diameters but, significantly, are very close to the densities on the maria for craters of small diameters. In addition, data from *Ranger IX* point to important differences in crater densities in different parts of the lunar terrae.

Detailed comparison of the maria with the floor of Alphonsus is difficult because of the probability that several types of craters are present, possibly in different proportions, in each area. In this Section, the main emphasis is placed on the size–frequency distributions of total craters regardless of form or origin. Recently acquired high-resolution telescopic photographs are used here to make comparisons of areas studied in the *Ranger* photographs with other similar areas for the range of crater sizes resolvable at the telescope.

a. Distribution of Craters in the Maria

Data on the size–frequency distribution of craters in Mare Tranquillitatis were compiled from the *Ranger VIII* A- and P-camera photographs for diameters less than 3 km and from Lick Observatory plate L-24 for the larger craters. The cumulative crater size–frequency distribution obtained for Mare Tranquillitatis is compared with the crater distribution in Mare Cognitum, based on the *Ranger VII* photographs, in Fig. 1. The data for Mare Cognitum are typical of areas between the rays down to diameters of 10 m and of the ray areas for smaller diameters (Ref. 1, p. 110). The crater size–frequency distributions in both maria show an abrupt change of slope (on the log-log graph) in the vicinity of 3-km crater diameters; the steepest slopes are observed in the 0.5- to 3-km size range. Below 0.5 km, the average slope in both maria is slightly greater than -2, down to the smallest craters measurable. The measured spatial densities are slightly greater in Mare Tranquillitatis than in Mare Cognitum in each size class. This difference is
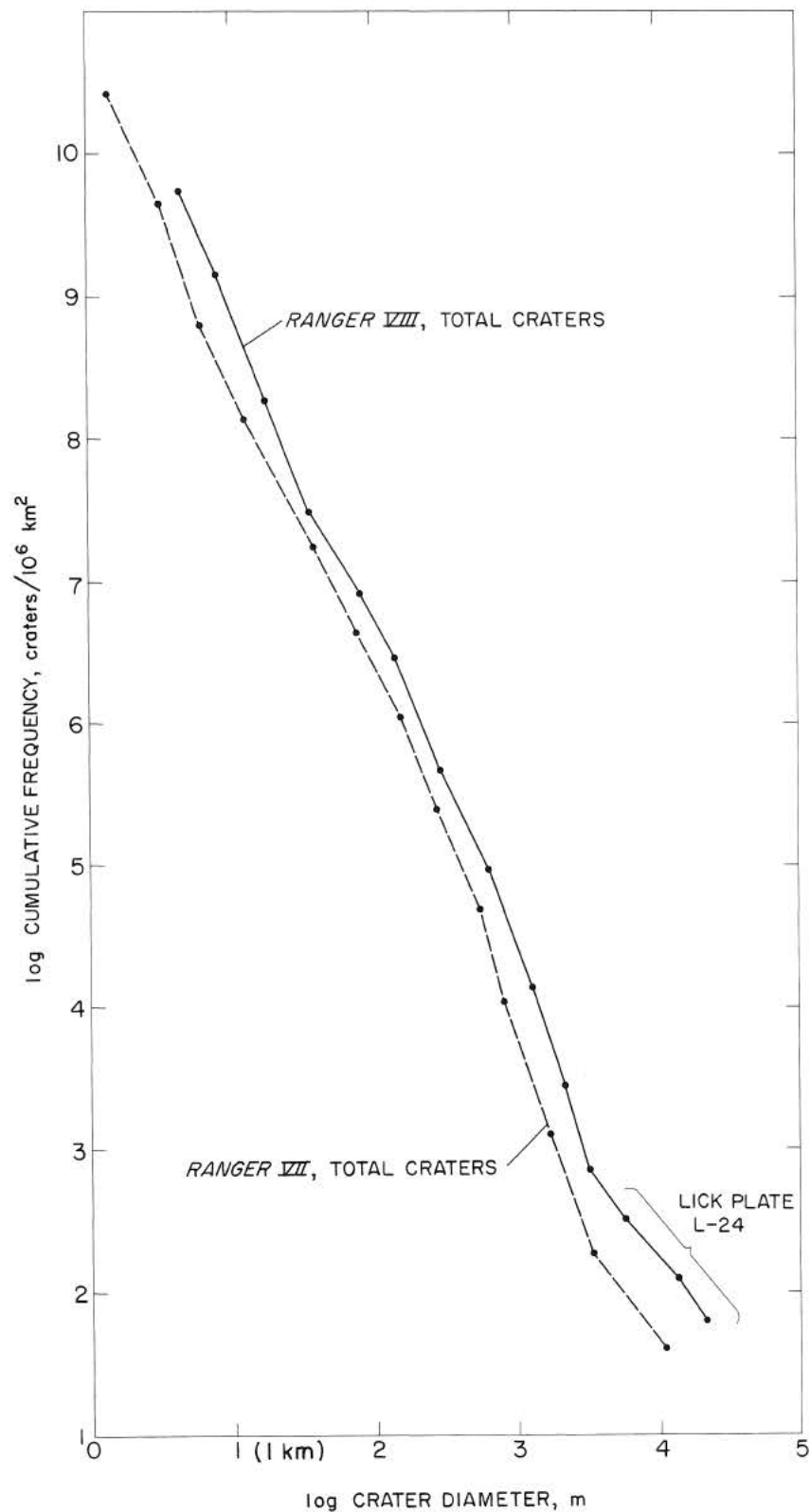
Fig. 1. Cumulative size—frequency distribution of all craters in Mare Cognitum (*Ranger VII*, B and P cameras) and Mare Tranquillitatis (*Ranger VIII*, A and P cameras, and Lick plate L-24).

real for crater diameters over 1 km and has been documented by earlier studies (Ref. 2). In the smaller size classes, the differences could be entirely apparent because the lower Sun angle in the *Ranger VIII* photographs of Mare Tranquillitatis permits discrimination of more very shallow craters than in the *Ranger VII* photographs of Mare Cognitum. The differences in the size classes greater than 1 km may not be statistically significant because of the low total number of craters in these classes.

The crater size–frequency distributions for Mare Tranquillitatis and Mare Cognitum can be compared with distributions for other mare surfaces by using photographs taken recently by G. Herbig with the 120-in. reflecting telescope at Lick Observatory. These photographs permit study of the distribution of craters down to diameters of 1.5–2 km. Three additional mare areas were studied for comparison with the areas covered by *Rangers VII* and *VIII*: Mare Serenitatis, part of Mare Imbrium, and part of Oceanus Procellarum (Fig. 2). In all of these mare areas, there is an abrupt change of slope of the crater size–frequency distribution between crater diameters of 2 and 6 km (Fig. 3). The larger numbers of craters in the smaller size classes, giving rise to slopes of the size-distribution curve between

-3 and -4, could not be measured on earlier Earth-based photographs (Refs. 2, 3, and 4). When allowance is made for the fact that the numbers of the smallest craters observable on the three Lick plates are slightly low (because of loss of contrast as the resolution limits of the plates are approached), it is clear that the crater size distributions obtained from telescopic photographs in other mare areas correspond closely to the distribution in Mare Cognitum. Mare Tranquillitatis has a distinctly higher crater density than the other maria studied.

Of the many craters portrayed in the *Ranger* photographs, the class of circular craters with sharp raised rims (here referred to as eumorphic craters) can be most easily discriminated from the rest. My counts of craters in this class for *Ranger VII* (Fig. 4) agree closely with Shoemaker's (Ref. 1, p. 118). The size–frequency distribution of craters in this class for Mare Tranquillitatis is identical with that for Mare Cognitum, within the limits of probable random variation of the counts for the small numbers of craters actually observable on the photographs (Fig. 4).

The eumorphic craters were interpreted by Shoemaker (Ref. 1) as being of primary-impact origin. Some of the
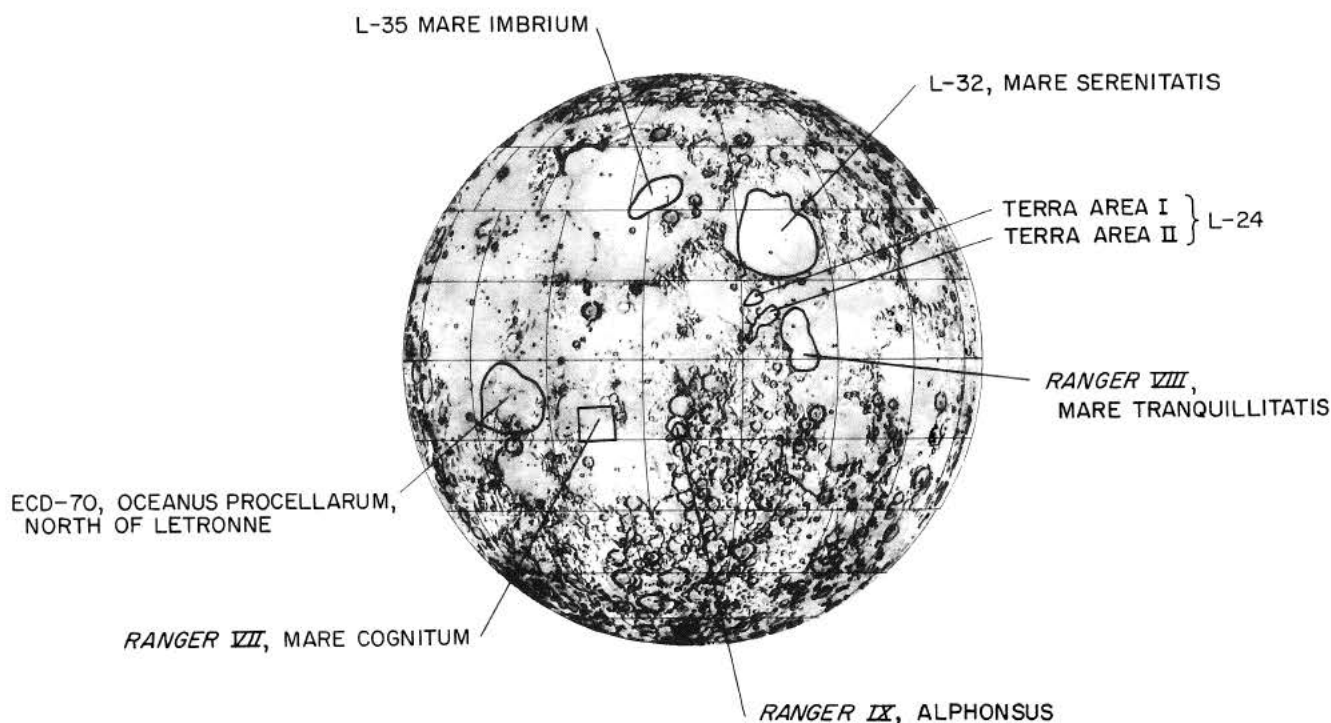
Fig. 2. Index map of the Moon, showing locations of areas studied for size–frequency distribution of craters.

Fig. 3. Size—frequency distribution of craters in mare areas, based on *Ranger* photographs and on Lick Observatory telescopic photographs. (Locations of areas are shown in Fig. 2. A—eastern Mare Serenitatis, light central portion, Lick plate L-32; B—Mare Imbrium, N and W of Archimedes, Lick plate L-35; C— Mare Cognitum, *Ranger VII* A- camera frames 155 and 179; D—Oceanus Procellarum, N of Letronne, Lick plate ECD- 70; E—western Mare Tran- quillitatis, Lick plate L-24 and *Ranger VIII* A- camera frame 43.)

$\longrightarrow$

log CUMULATIVE FREQUENCY, craters/10⁶ km²

log CRATER DIAMETER, m
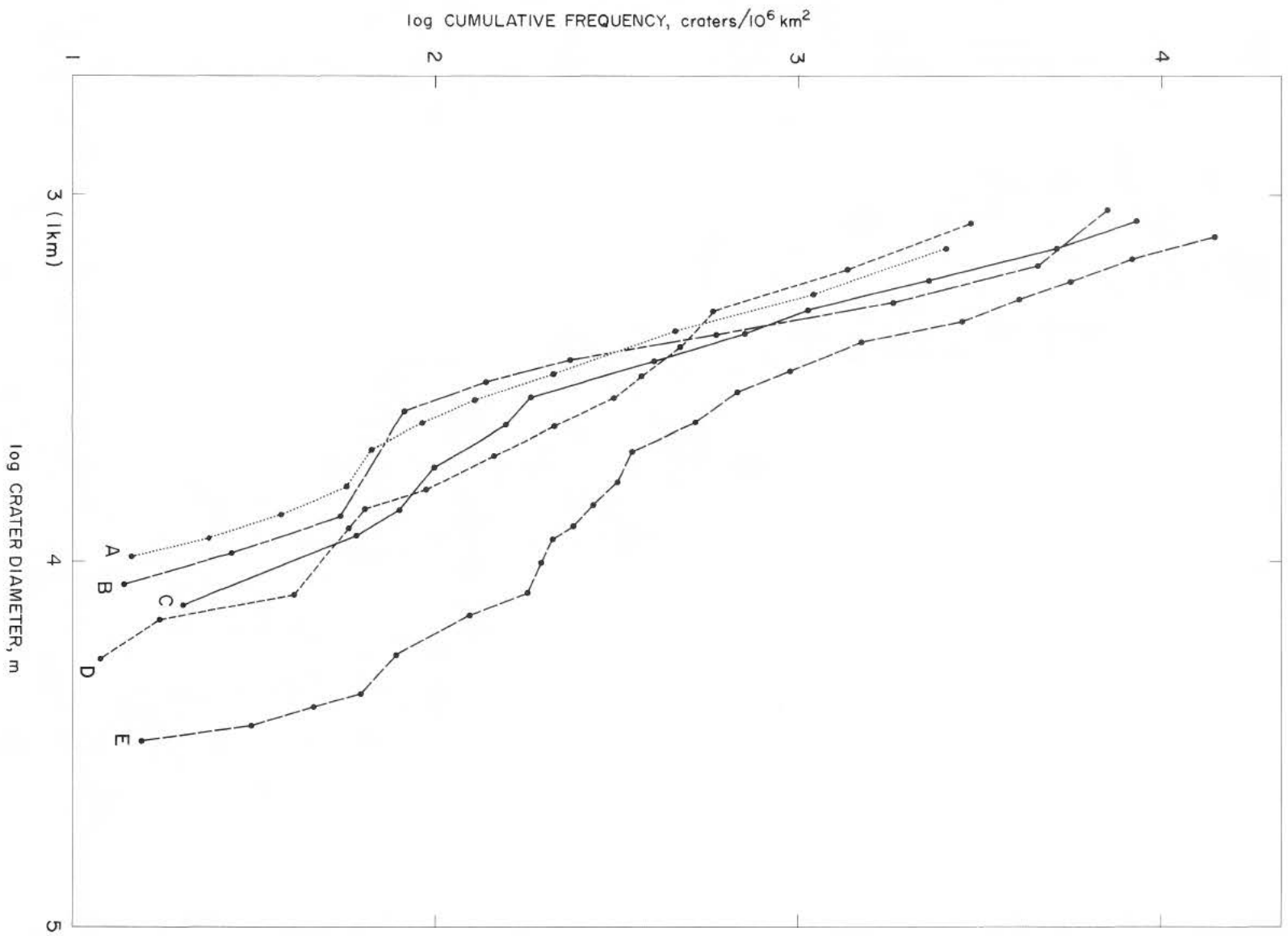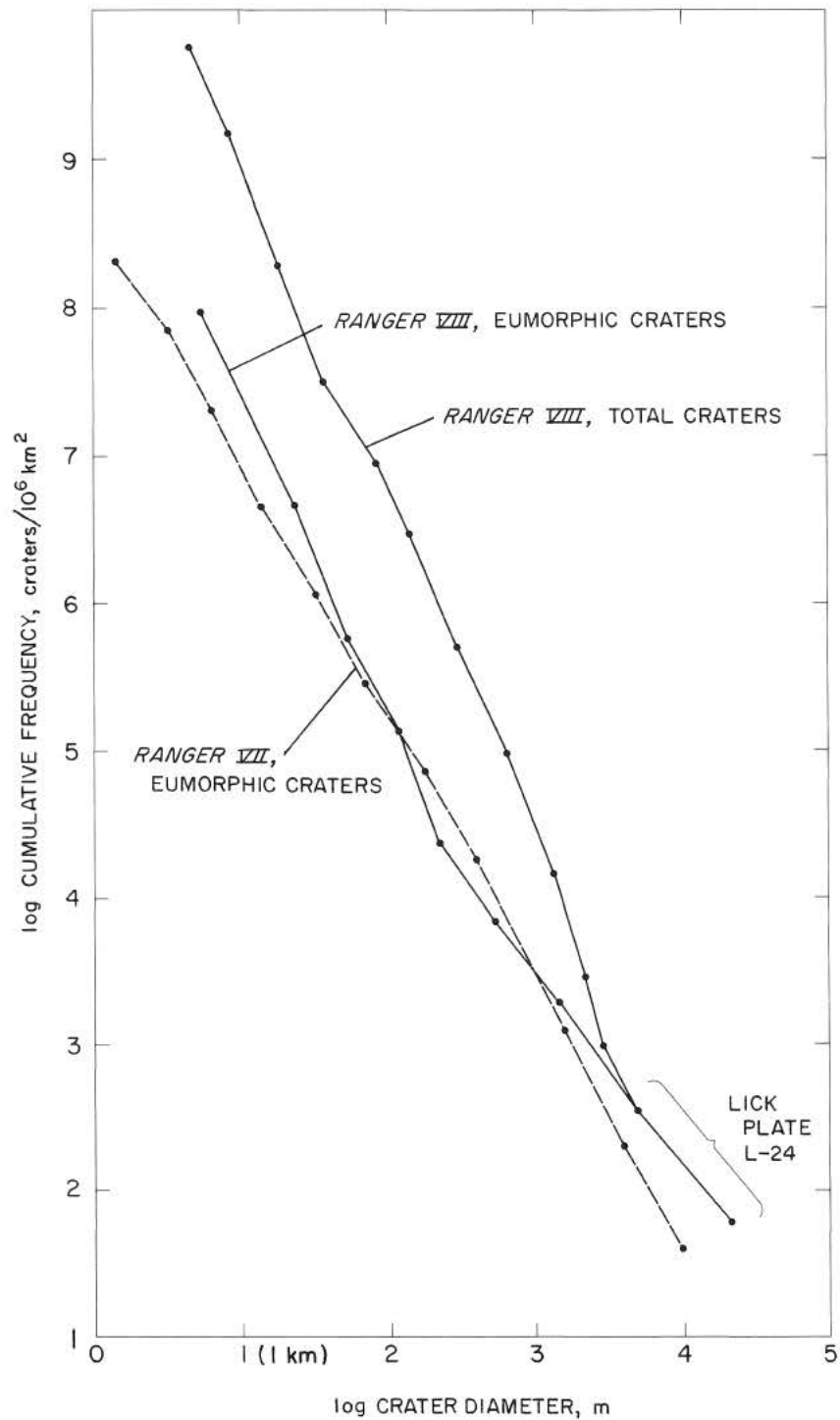
Fig. 4. Cumulative size–frequency distribution of eumorphic craters on Mare Cognitum (*Ranger VII*) and Mare Tranquillitatis (*Ranger VIII*). (Distribution of total craters from Lick plate L-24 and *Ranger VIII* shown for comparison.)

fresh circular craters on Mare Tranquillitatis may be isolated secondary-impact craters associated with the large crater Theophilus, and similar to the circular secondary craters of Tycho shown in the *Ranger VII* A-camera series. Classification according to form of the remaining craters shown in the *Ranger* photographs is still in a preliminary stage.

b. Distribution of Craters in the Terrae

The *Ranger IX* mission provided very high-resolution photographs over parts of the flat floor and east rim of the crater Alphonsus. Geologic mapping in the equatorial region of the Moon by the U. S. Geological Survey indicates that material similar to that on the floor of Alphonsus is widespread in other parts of the terrae. These relatively smooth, flat areas within and between the walls of large craters in the terrae superficially resemble the maria but have a higher albedo and a higher density of telescopically resolvable craters (Refs. 5 and 6).

The size–frequency distribution of craters on the flat part of the floor of Alphonsus is illustrated in Fig. 5. For crater diameters above 1 km, the count applies to the entire floor, exclusive of the central peak and elongate central ridge; for small crater diameters, it applies only to the crater floor east of the central ridge. Because of the relatively small area of the floor of Alphonsus, no meaningful statistics can be obtained for craters with diameters greater than 5 km. The size-distribution curve maintains a slope of -2 from about 1-m crater diameter, the smallest observed, to about 500-m diameter. For diameters above 500 m, the curve has an average slope of -2.7.

The size distribution of craters on the floor of Alphonsus can be compared with the distributions in similar flat areas in the terrae, for which good Lick Observatory plates are available. Crater distributions for two areas near Mare Tranquillitatis (Fig. 2) were obtained from Lick plate L-24 (Fig. 6). Again, meaningful statistics for craters with diameters greater than 5 km cannot be obtained because of the small areas involved. The distributions agree closely for crater diameters near the limit of resolution of the Lick plate, and the distribution of small craters on other flat areas of the lunar terrae is probably similar to that on the floor of Alphonsus.

A significant observation made in the *Ranger IX* photographs is the apparent low density of craters on the exterior rim of Alphonsus, as compared to the

density of craters on the floor. Photographs of the rim show craters down to 250-m diameter. At this diameter, the density of recognizable craters is approximately 2½ times less than on the floor (Fig. 7). The crater density on the highlands east of Alphonsus varies from place to place. Some low, flat areas in this upland region (Fig. 8) are similar to the floor of Alphonsus and have similar crater density. Other parts of the highlands are gently rolling to rugged; some are covered with craters, whereas others appear to be only sparsely cratered. Since no single crater distribution can adequately describe such an area, a separate distribution has been obtained from each of three selected B-camera photographs (Fig. 7). The areas studied are outlined in Fig. 8. Low, flat areas similar to the floor of Alphonsus, areas in shadow, and areas inclined toward the Sun so that they appear bright and featureless (such as the west-facing east wall of Alphonsus) have been omitted from the crater counts. A restricted highland area with a relatively high average slope has a low density of craters smaller than 2 km in diameter compared with the floor of Alphonsus, but the density of craters larger than 2 km in a broader highland area matches the density on the floor of Alphonsus.

c. Interpretation

A striking aspect of the crater distributions noted in photographs from all three *Ranger* missions is the tendency for the total crater densities to converge at small crater diameters, despite differences in the densities of large craters. This observation is consistent with the models of the cratering process on the maria proposed by Moore (Ref. 7) and Shoemaker (Ref. 1), in which the size–frequency distribution of small craters is in a steady state. In these models, craters with diameters below a certain limiting size are destroyed as rapidly as they are formed, with the destruction proceeding not only by the superposition of larger crater on smaller but also by the erosion of rims and the infilling of crater floors by the impact of small fragments and the deposition of ejecta from such impacts. The steady-state crater density is the limiting high density toward which any part of the lunar surface evolves with time; below a certain limiting size, small crater densities tend to be the same on all parts of the Moon's surface that have reached the steady-state density. For a surface of a given age, the limiting crater diameter for the steady-state size–frequency distribution of craters slowly increases with time.

A possible steady-state size–frequency distribution function for craters of all sizes on the level parts of the Moon may be estimated by combining the distributions of small craters observed in the *Ranger* photographs
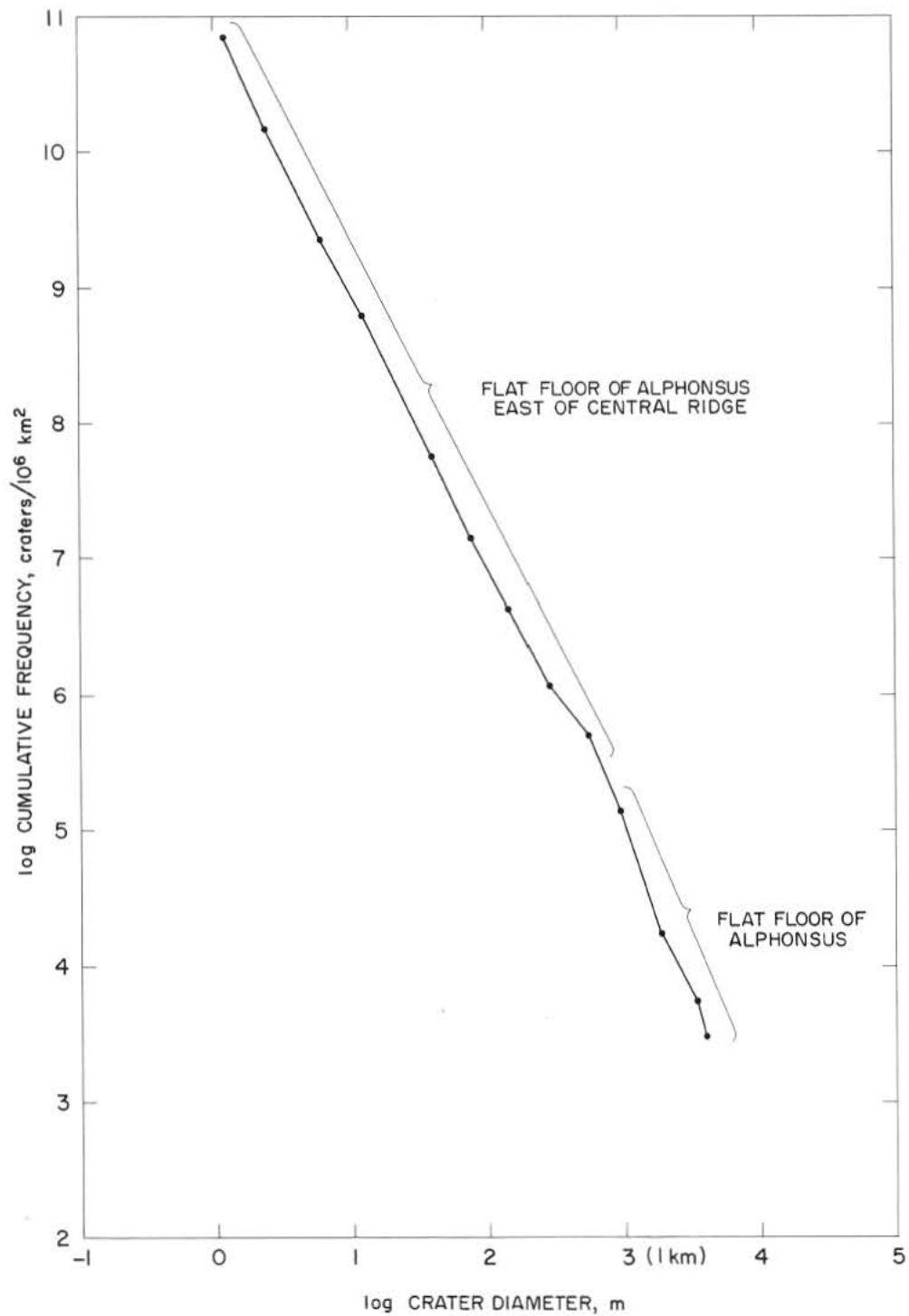
Fig. 5. Cumulative size–frequency distribution of craters
on floor of Alphonsus.
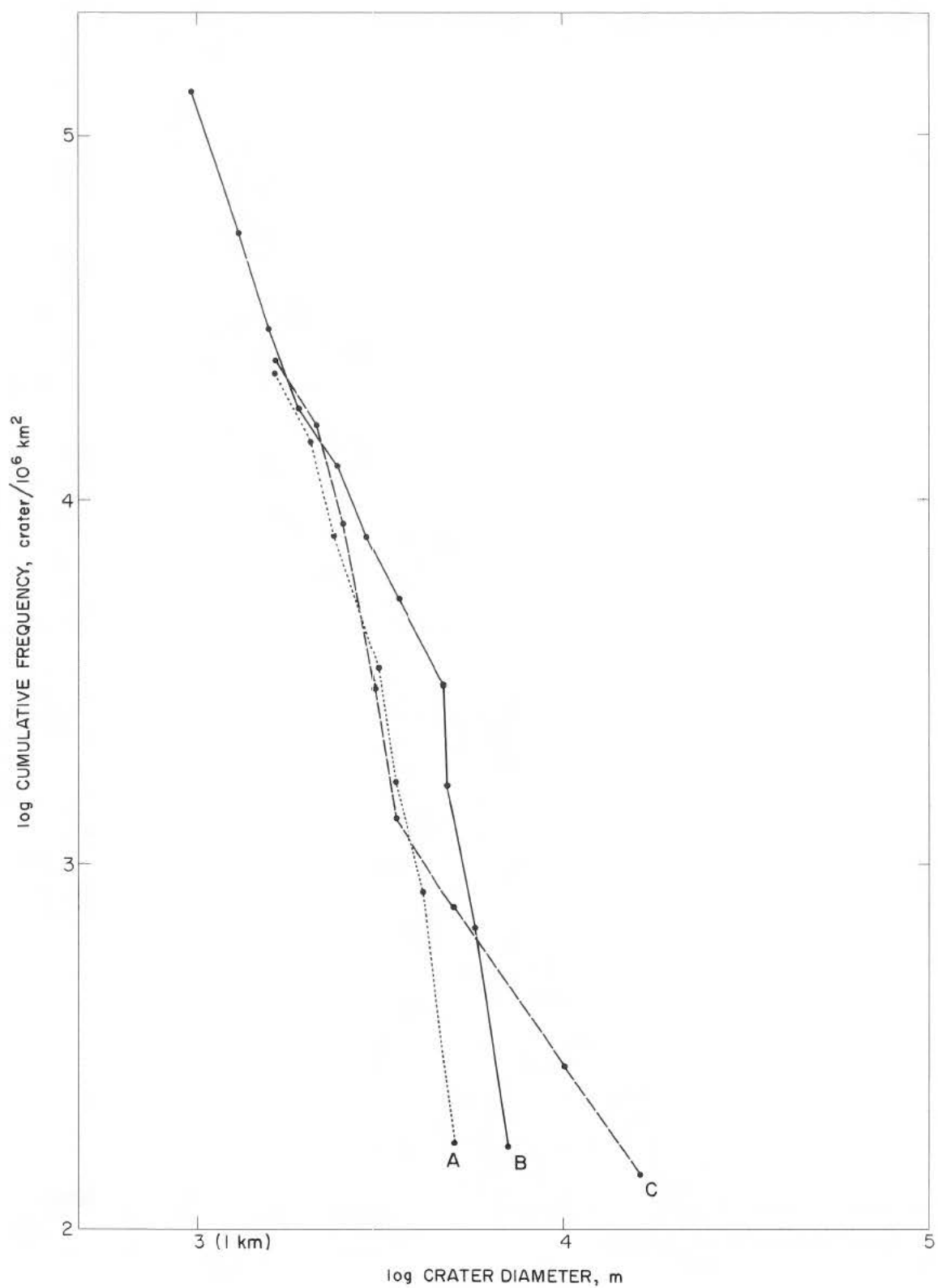
Fig. 6. Cumulative size—frequency distributions of craters
in lunar terrae. (Locations of areas are shown in Fig. 2.
A—terra area I, Lick plate L-24; B—floor of
Alphonsus, exclusive of central peak and
ridge (*Ranger IX*); C—terra area II,
Lick plate L-24.)

←
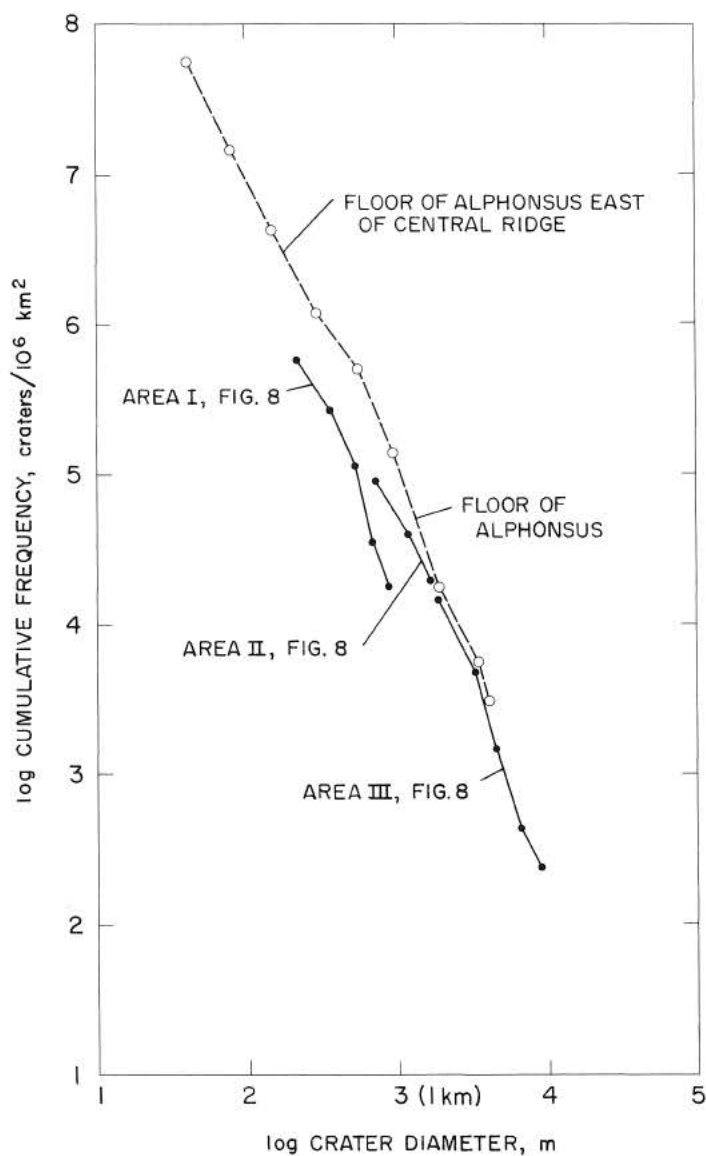
Fig. 7. Cumulative size—frequency distribution of craters
on rim of Alphonsus and adjacent highlands compared
with size—frequency distribution of craters on floor
of Alphonsus. (Locations of areas are shown
in Fig. 8.)

0   100 km   ············· AREA I
|_____| — — — — AREA II
          APPROXIMATE SCALE EAST-WEST   ——————— AREA III
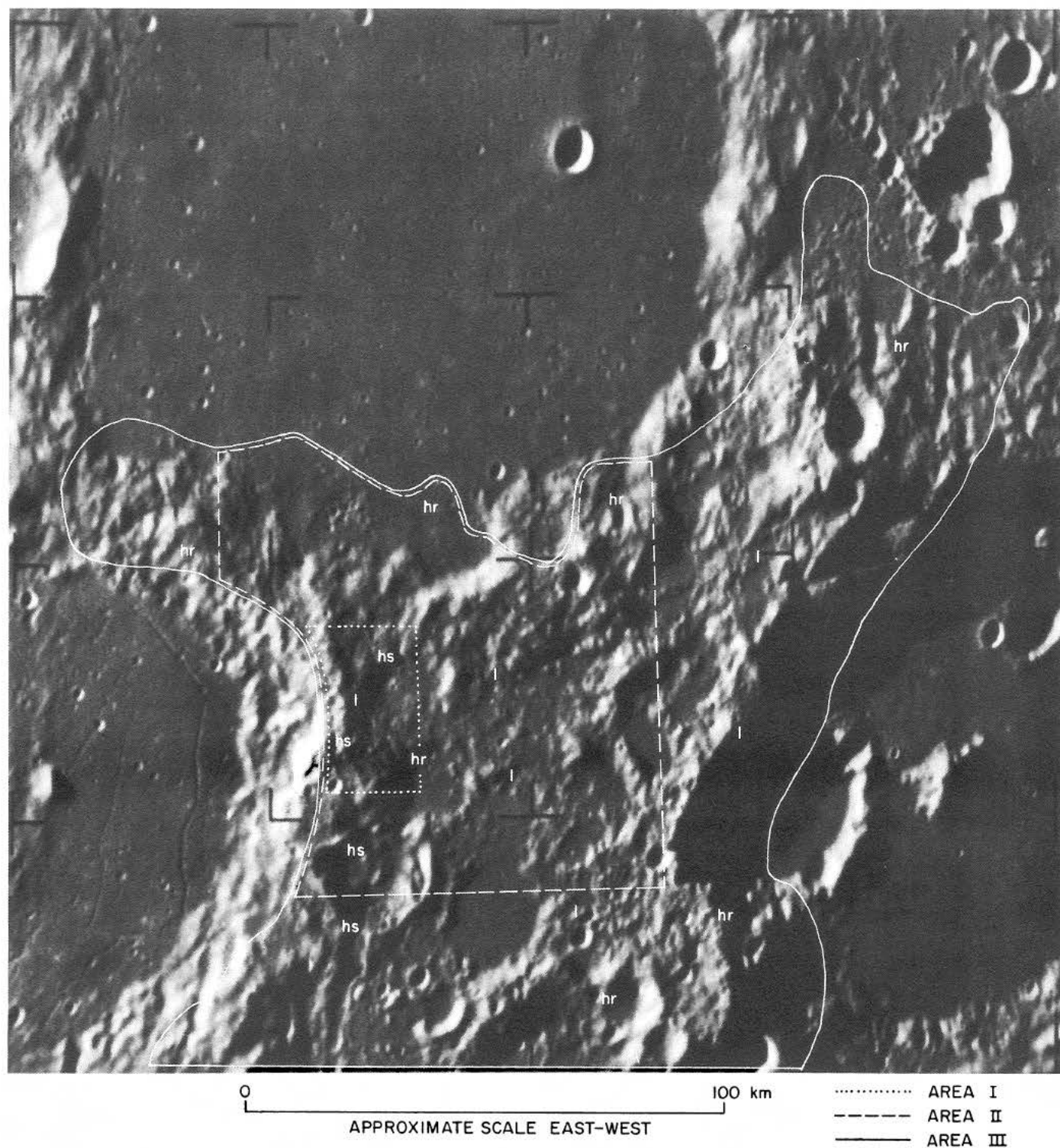
Fig. 8. *Ranger IX* B-camera frame 15, showing areas studied for crater size–frequency distribution given
in Fig. 7. (Different types of terrain in lunar highlands indicated by symbols: l—low, flat areas
with crater densities the same as on floor of Alphonsus; hs—high, smooth areas with
few craters; hr—high, rough areas with many craters.)

with the distribution of large craters observed in certain ancient parts of the terrae. In some parts of the terrae, craters 10 km in diameter and larger overlap one another and are packed together so closely that the superposition of another crater of the same size would result in complete or partial destruction of one or more of the pre-existing craters (Refs. 8 and 3). This may represent a condition of steady-state crater density for large craters. A crater size–frequency distribution fitted to the data of Young (Ref. 9) and those of Palm and Strom (discussed by Baldwin in Ref. 10) for ancient craters in the terrae, and to the data for the smallest craters observed in the *Ranger* photographs (Fig. 9), is represented by the power function:

$$N = 10^{10.9}d^{-2} \qquad (1)$$

where N is the cumulative number of craters per 10^6 km^2 with diameters greater than d (in meters). For a simple power distribution function with an exponent of -2, the area occupied by craters in each decade of diameters is constant.

If the power function given by Eq. (1) is taken as representative of the steady-state crater distribution for the level parts of the Moon, it may be used to determine what part of an observed distribution in level terrain may be in a steady state. The rates of crater formation and destruction on a surface having such a distribution would balance each other so that there is no net change in distribution with time, but these rates are not known. Moore (Ref. 7) suggested two possible rates and combined them in a way to give a power function representing a steady-state distribution very close to that given by Eq. (1) and illustrated in Fig. 9. If more shallow craters are present on Mare Cognitum than can be counted under the conditions of illumination encountered by *Ranger VII*, the distribution there may be in a steady state at diameters below a few hundred meters, in agreement with the interpretation of Shoemaker (Ref. 1), while the distribution on the floor of Alphonsus may be in a steady state at all diameters below about 1 km.

The occurrence of secondary-impact craters in significant numbers is interpreted here as the principal cause for the rapid increase in the density of craters with diameters between 2 and 6 km on the maria. The high-resolution Lick Observatory photographs show that many of the craters in this size range occur in clusters at the ends of diffuse ray elements. It is also the size range in which craters that are clearly secondary to such large primary craters as Copernicus, Langrenus, Aristoteles, and Theophilus become abundant. Craters of other origins probably also contribute to the rapid increase in crater density at these diameters. A few irregularly shaped craters with diameters of about 1 km discernible on the *Ranger VIII* photographs, appear to be localized along mare ridges and may have been formed by internal processes of the Moon.

At least two interpretations seem possible for the local differences in crater density in the highlands east of Alphonsus. Low densities may occur where there has been relatively recent mantling of older craters by volcanic materials, possibly related to suspected volcanism within Alphonsus itself. A second suggestion is that small craters are obliterated by various surface processes more rapidly in the highlands than on the relatively smooth, flat floor of Alphonsus. The density of craters 3 km in diameter and larger is essentially the same in the two areas. Small craters may be destroyed more rapidly in the highlands because of slumping or mass movement of weakly consolidated materials on the slopes of the rolling highland terrain.

2. Cohesion of Material on the Lunar Surface
Henry J. Moore

The highest-resolution *Ranger* photographs show craters within the size range of experimental craters produced by chemical and nuclear explosives and missile impacts in natural materials. Craters and other features down to 25 cm across may be seen in the last partial B frame and the last P frames of the *Ranger IX* photographs. The smallest craters observed are comparable in size to those produced experimentally by impact and to similar craters produced by shallow, subsurface bursts of explosives. Some inferences about the lunar-surface materials can be made on the basis of data from these experiments if one assumes that the craters examined resulted from projectile impacts. These inferences suggest that a layer of fragmental material that is probably weakly cohesive to noncohesive underlies the lunar surface.

Calculations on the distribution of craters produced by the influx of meteoroids and of other solid objects from space that may be expected on the Moon show that the lunar surface should be completely covered with impact craters of various sizes. Moore's calculations (Ref. 7) suggest that on a billion-year-old lunar surface, 10% of the area should be covered by recognizable craters with diameters between 0.1 and 1.0 m, 10% by craters, 1.0–10 m across, and possibly 10% by craters 10–100 m across. In each of these size intervals,
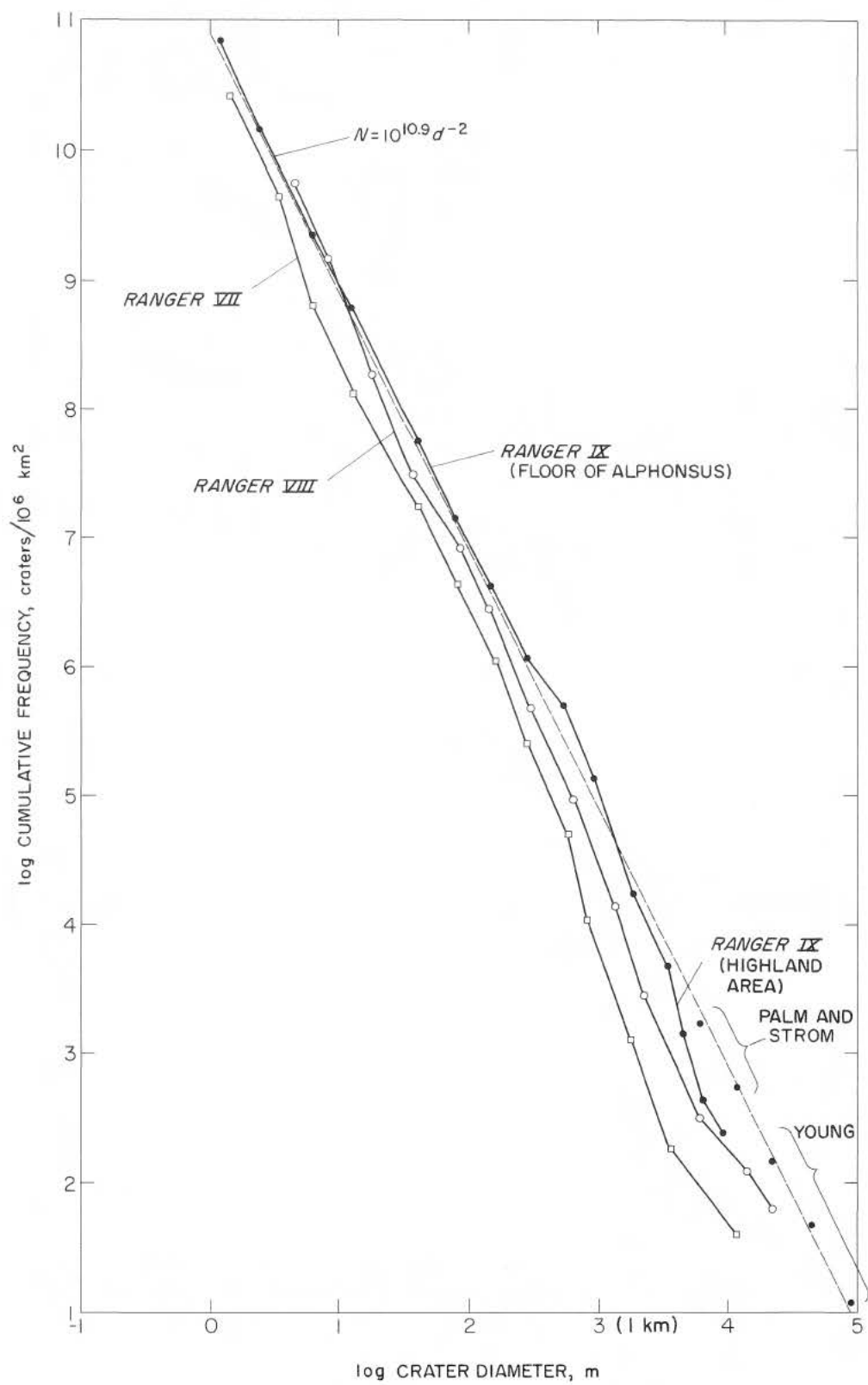
the shape of the craters would range from fresh, un-modified forms to forms produced by erosion and in-filling. The erosion is caused by the ejection of debris during crater formation by impact; the infilling results from the deposition of the debris, which preferentially collects in depressions because of gravitational forces. The form and size–frequency distribution of craters seen in the *Ranger* photographs closely resemble those predicted for impact craters. Similar results might also be produced by the impact of fragments ejected from very large craters along rays (Ref. 1, pp. 75–134, and Ref. 7). It is not to be construed that all the craters seen on the *Ranger* photographs have resulted from impact, for clearly they have not. Only those which have sharply defined raised rims and which appear to be the least modified will be compared with experimental craters.

a. Comparison of Crater Morphologies

The two lunar craters considered here appear on the last partial B-camera and the last two P-camera photo-graphs of *Ranger IX* (Figs. 10 and 11). These craters were selected because their sizes are consistent with the sizes of experimental craters produced by explosives and missile impacts and because they appear to be relatively unmodified in form. In addition, they have asymmetrical rims (higher on one side than the other) and are morpho-logically similar to craters of nearly the same size which were produced by inert missiles with oblique trajectories at White Sands Missile Range, New Mexico (Ref. 11). Although the craters photographed by *Ranger IX* are used as examples, the following reasoning is applicable to other craters observed in the highest-resolution *Ranger VII* and *VIII* photographs.

The important features associated with the two craters under consideration are: (1) little evidence of blocks on the rims and around the craters; (2) low, lumpy struc-tures on the walls, the rims, and around the craters; (3) asymmetrical rims which are higher and wider on one side than the other; (4) slopes that are less than 45

deg and probably near 35 deg or less; and (5) a scalloped rim on one crater.

A conspicuous absence of large, sharply defined blocks around these craters implies the existence of one of the following situations: (1) large blocks were not ejected from the craters because the surface materials were com-posed of fragments or rock units with linear dimensions too small to be resolved in the photographs ($\approx$25 cm); (2) large blocks were ejected and subsequently reduced to finer material; or (3) the entire surface was covered by some material after the craters were formed which obscures the blocks. The conclusion to be drawn in either of the first two cases is that the surface around the craters is underlain by fragments generally below the resolution of the photographs.

In order to illustrate the paucity of blocks in the *Ranger* photographs, two craters formed by chemical explosives in basalt are shown in Fig. 12. The craters were produced by 40,000 and 1000 lb of TNT detonated about 7.9 and 3 m, respectively, below the surface (Ref. 12). The basalt in which the craters were formed has densities between 2.2–2.75 g/cm^3 and an unconfined shear strength near 10^8–10^9 dynes/cm^2.

Blocks in and around these two explosive craters are conspicuous, whereas no such blocks are apparent in the *Ranger* photographs. Blocks up to 2.4 m in length are found in and around the large crater and up to 1.5 m in and around the small one. Many of the blocks around the craters exceed 25 cm. Some blocks are found beyond one crater diameter from the rims, although they are concentrated near the rims. If the illumination condi-tions were the same as those under which the *Ranger* photographs were taken, the blocks around the craters in basalt would produce shadows about 5 times the length of the blocks.

The *Ranger* photographs show a few low mounds, some on crater rims, walls, and flanks, and others pecu-liarly isolated in relatively uncratered areas. These mounds

Fig. 9. Comparison of cumulative size–frequency distri-butions of craters photographed by *Rangers VII*, *VIII*, and *IX*. (Equation of curve for steady-state crater size–frequency distribution determined by combining data of Young, and Palm and Strom with data for small craters observed in the *Ranger* photographs.)
←

are rare and cast weak, short shadows. The author has observed craters produced by explosives and by missile impacts (Ref. 11), with similar associated low mounds. These mounds are composed of lumps of fragmental debris ejected from the craters rather than discrete blocks. The lumps are found on the crater rims and flanks, and also, isolated, at considerable distance from the crater. For missile-impact craters up to 5.5 m across,
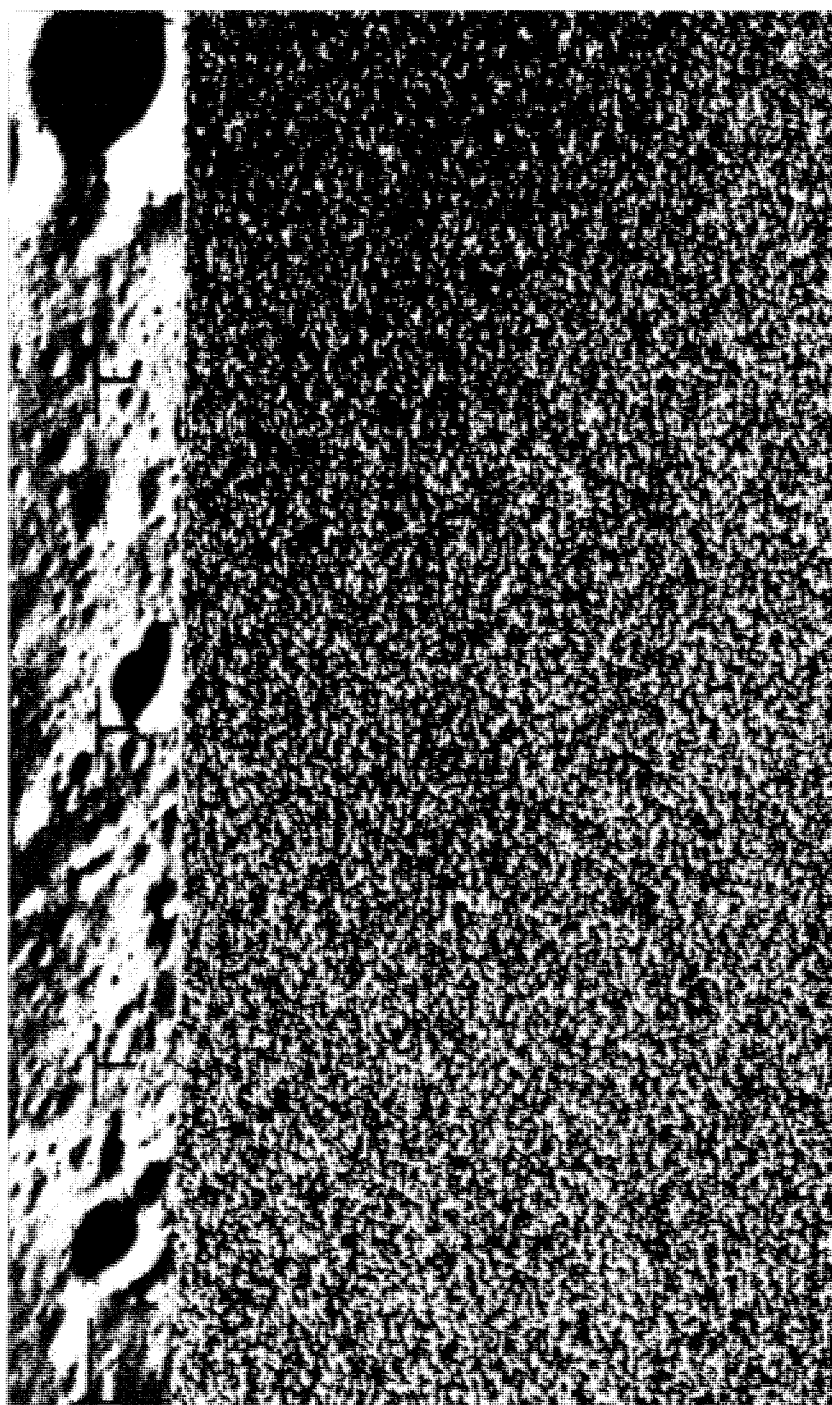
Fig. 10. Last partial *Ranger IX* B-camera photograph. (Largest crater is about 25 m across; next-largest three are about 10 m across.)
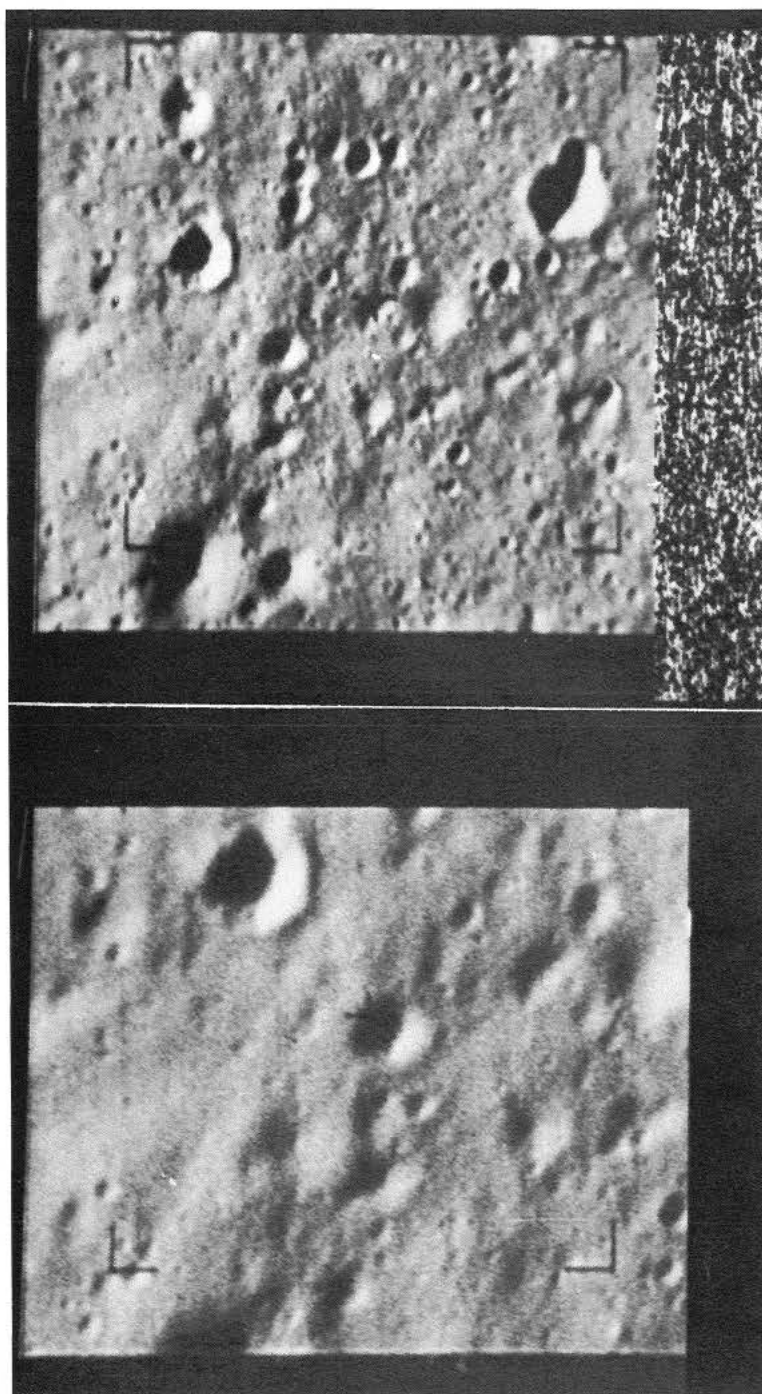
Fig. 11. Last *Ranger IX* P-camera photographs. (Largest crater in upper frame is about 25 m across.)

Fig. 12. Two craters produced by chemical explosives in basalt. (Large crater is 29 m across, small crater about 10 m across. Blocks up to 2.4 m in length occur in and around large crater, and up to 1.5 m in and around small crater. Craters produced by 40,000 and 1000 lb of TNT, respectively, by Sandia Corporation.)

isolated lumps up to several feet in length and 15–30 cm high have been observed. Similar lumps around craters produced by chemical explosives are well illustrated in Ref. 13.

A crater produced by 40,000 pounds of TNT detonated at 13 m (Ref. 12), partly in basaltic cinders and partly in basalt flow rocks (Fig. 13), has greater similarity to the lunar craters. The crater is about 41 m across and 13 m deep. Ejecta are predominantly blocks of flow basalt on the left flank and noncohesive basaltic cinders and clinkers on the right flank. Low ridges and small rocks may be seen on the right flank, but large blocks are rare. The upper right section of the crater is scalloped (partly as a result of slumping and sliding of noncohesive cinders) much like part of the rim of the large crater shown in both frames of Fig. 11.

Craters produced by missile impacts at White Sands Missile Range (Figs. 14 and 15) are similar to many craters of comparable dimensions shown in the *Ranger*

photographs. In both cases, raised rims completely surround the craters, but the rims are higher and wider on one side than on the other. The impact crater shown in Fig. 14 is 9 m across and 2.7 m deep. The target was weakly cohesive gypsum (cohesion $\approx 6 \times 10^6$ dynes/cm^2) saturated with water. The inclined projectile trajectory resulted in a thicker and wider deposit of ejecta on one side of the crater than on the other. After the initial formation of the crater, slumping of the walls produced the lumps on the floor. Hummocks of debris, along with small blocks, occur around the crater, and a few blocks up to 30 cm across are found in and around the crater. Another crater (about 3.2 m across) with an asymmetric rim (Fig. 15), was produced by oblique projectile impact into moist gypsum (cohesion $\approx 6 \times 10^6$ dynes/cm^2); it is similar in form to a number of small lunar craters shown in Figs. 10 and 11.

In craters produced by missile impact in weakly cohesive alluvium (cohesion $\approx 1 \times 10^6$ dynes/cm^2), local slopes of crater walls exceed 60 deg in places, and in

Fig. 13. Crater formed partly in basalt and partly in basaltic cinders. (Crater is about 41 m across. Left side is in basalt, right side in basaltic cinders. Cinder block on upper left rim is 5.8 m long. Crater produced by 40,000 lb of TNT at 13 m by Sandia Corporation. Note difference in form and texture between right and left sides of crater.)
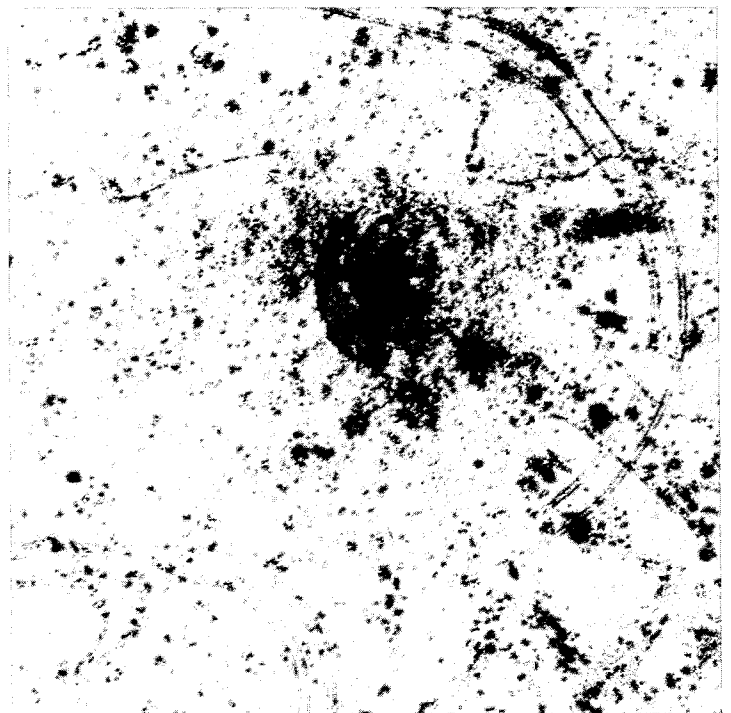
Fig. 14. Crater produced by missile impact in water-saturated gypsum. (Crater is about 9 m across. Projectile kinetic energy was 1.6×10^{15} erg and angle of impact near 45 deg. Note asymmetry of ejecta blanket. U.S. Army photograph.)
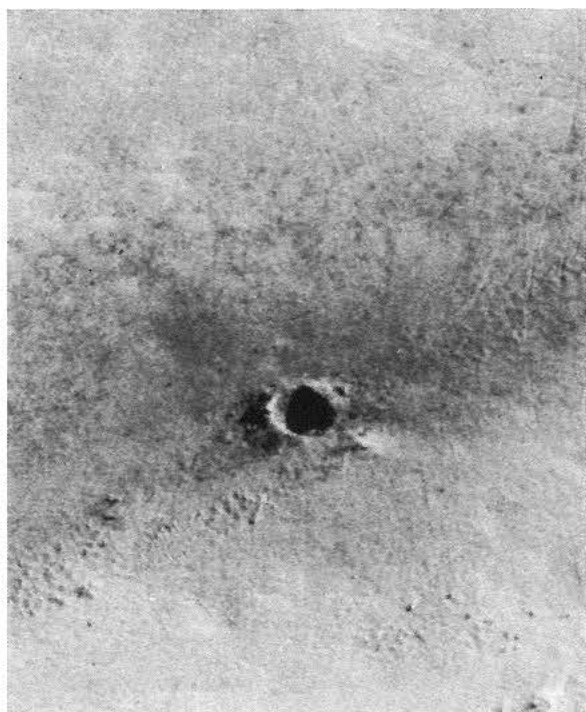
Fig. 15. Crater produced by missile impact in moist gypsum. (Crater is 3 × 3.6 m across. Kinetic energy of missile at impact was 5.9 × 10¹⁴ erg. Note asymmetry of ejecta and paucity of blocks. U.S. Army photograph.)

some cases are vertical. For craters 5.5 m across in alluvium with a cohesion near 5×10^5 dynes/cm², the slopes are composed predominantly of fragmental debris at the angle of repose, namely, 25–38 deg. No evidence has been found for slopes as high as 60 deg in the walls of small lunar craters, and very few appear to exceed about 38 deg. The steepest walls of the small lunar craters are probably underlain by fragmental material at the angle of repose; this angle should be essentially the same for lunar as for terrestrial noncohesive fragmental material (Ref. 14).

b. Interpretation

The combined evidence resulting from comparison of the morphology of lunar and experimental craters suggests that the lunar surface materials are weakly cohesive to noncohesive. The paucity of blocks indicates that the near-surface materials do not have high cohesive like flow basalts and rocks of comparable strength. The low mounds shown in the *Ranger* photographs may be piles of fragmental material ejected from craters, similar to the mounds observed around missile-impact craters.

The fragmental material piled around the terrestrial craters has a grain size generally less than 25 cm. The moderate slopes of the walls of the small, sharp-rimmed lunar craters also suggest that the lunar materials are noncohesive and fragmental.

In the comparison of the small lunar craters with the experimental craters, it should be kept in mind that stresses in the materials due to relief are one-sixth those that would be developed at the surface of the Earth. For example, materials on the Moon with a cohesion of 1 bar will behave somewhat like materials with a cohesion of 6 bars on the Earth (Ref. 14).

It is also important to note that cohesion and bearing strength are not synonymous. Flow basalts and granite have both high cohesion and bearing strength, whereas the sand in a sand pile has no cohesion but high bearing strength. In addition, low-density and noncohesive fragmental layers may have high bearing strength, as is the case at Mono Craters, California, where some surfaces which are underlain by pumice fragments (estimated density ≈ 0.4 g/cm³) will permit the passage of jeeps and pedestrians.

3. The Structure and Texture of the Floor of Alphonsus
Michael H. Carr

The principal characteristics that distinguish the floor of Alphonsus from other areas photographed with high resolution in the *Ranger* missions are the extent to which the floor is cratered and the large number of observable linear features. Although craters are the most obvious topographic features, many linear structures are also present, such as ridges, depressions, and breaks in slope. Many craters are aligned along, and evidently related to, the linear structures. The size–frequency distribution of craters on the floor of Alphonsus varies from place to place. Areas with significantly different crater distributions and densities can be distinguished, so that the floor can be divided into several geologic units, each of which is characterized by a different size–frequency distribution of craters.

a. Textural Units

The relatively flat part of the floor of Alphonsus has been divided into six units on the basis of albedo, relief, structural patterns, and distribution of small craters (Fig. 16). The size–frequency distributions of craters on four of the floor units are shown in Fig. 17. All observable depressions were classed as craters in determining the size–frequency distributions. Most of the units differ

significantly in the distribution of craters larger than 0.3 km, but the density of craters less than 0.3 km in diameter is essentially the same. Some differences are also observable, however, among the smaller craters. The paucity of large craters in unit 2, for example, allows small, very indistinct craters to be distinguished, bringing the total crater count up to that of unit 3, for which many of the very small craters counted had sharp outlines. Although there are no significant differences in their crater counts, units 3 and 4 have a different appearance because many of the craters larger than 0.5 km in diameter in unit 4 have more subdued outlines than craters of equivalent sizes in unit 3. A unit labeled **dh** on the map is distinguished from the others by its low albedo; units 2 and 5 are distinguished mainly on the basis of linear texture and relief, rather than crater size–frequency distribution. A more detailed description of some of these textural units as geologic units is given by McCauley in Section D2.

b. Lineaments and Structurally Controlled Craters

Lineaments observed in the *Ranger* photographs of Alphonsus are plotted in Figs. 18, 19, and 20 at the approximate scales of 1:400,000, 1:77,000, and 1:13,000, respectively. The linear features are ridges and linear depressions, breaks in slope, and straight crater walls. At the smallest scale, 1:400,000, four distinct sets of lineaments can be distinguished on the basis of azimuthal frequency (Fig. 21). Three of these, the northwest–southeast, the northeast–southwest, and the north-northeast–south-southwest sets, belong to the lunar grid system of lineaments (Ref. 15); the fourth is radial to the center of Mare Imbrium. On the rim and central ridge of Alphonsus, the north-northeast–south-southwest set and the Imbrium radials are more prevalent than on the floor, but at the map scale of 1:400,000, all four sets are distinguishable on the floor. In contrast, at the larger scales, which reveal the finer details of the floor of Alphonsus, the northwest–southeast and northeast–southwest sets dominate the structural pattern, and the Imbrium radials and the north-northeast–south-southwest set are almost entirely absent.

In nearly all cases, the observable lineaments are undeflected as they cross topographic features, except at the largest scales of observation. If the lineaments are caused by planar structures intersecting the surface, then the dips of these structures are close to vertical. In a few cases, the directions of dip have been determined from the deflections of surface trends of the lineaments across topographic relief; in the observed cases,

structures controlling the northwest–southeast set dip steeply to the southwest, and structures controlling the northeast–southwest set dip steeply to the northwest. The lack of observable shallow dips does not mean that there are none present, as shallow dipping structures are very difficult to discern on aerial photographs. The only recognized exceptions to the generally steep dips are seen in the last complete B photograph (Fig. 20), where many of the lineaments are deflected as they cross shallow craters. The apparent shallow dips observed here may reflect true dips of the underlying structures, or the deflections of the lineaments may result from downslope creep in the top few meters of the lunar surface.

Lineaments control the location and shape of many craters on the floor of Alphonsus in all of the textural units, and on the central ridge and rim. Craters that are unambiguously controlled by the lineaments are plotted in Fig. 18. To avoid including possible lines of secondary craters that might be unrelated to local structure, a conservative approach was used in identifying the structurally controlled craters. Only groups of craters aligned along depressions, ridges, or breaks in slope were plotted; other lines of craters are not considered to be controlled by the lineaments. Many of the craters along a lineament are elongate in a direction parallel to the lineament; some of these have straight walls, whereas others are circular in outline except for a linear depression breaching one side of the crater. Most, but not all of the structurally controlled craters are rimless. None of the circular craters with sharp, raised rims and outer flanks that are concave upward (eumorphic craters) appear to be structurally controlled, but every other morphological type of crater is observed among the structurally controlled group of craters. Comparison of the craters having demonstrable structural control with the rest of the craters on the floor of Alphonsus suggests that a majority of such craters may be structurally controlled.

c. Interpretation

The alignment of craters along lineaments that are part of a Moon-wide structural system is very strong evidence that many craters on the floor of Alphonsus were formed by mechanisms originating within the Moon. These craters may have been formed in a variety of ways, among which subsidence may have predominated. Although the majority of the aligned craters have no observable rims, many do, a fact which indicates that subsidence alone cannot explain all of the aligned craters.
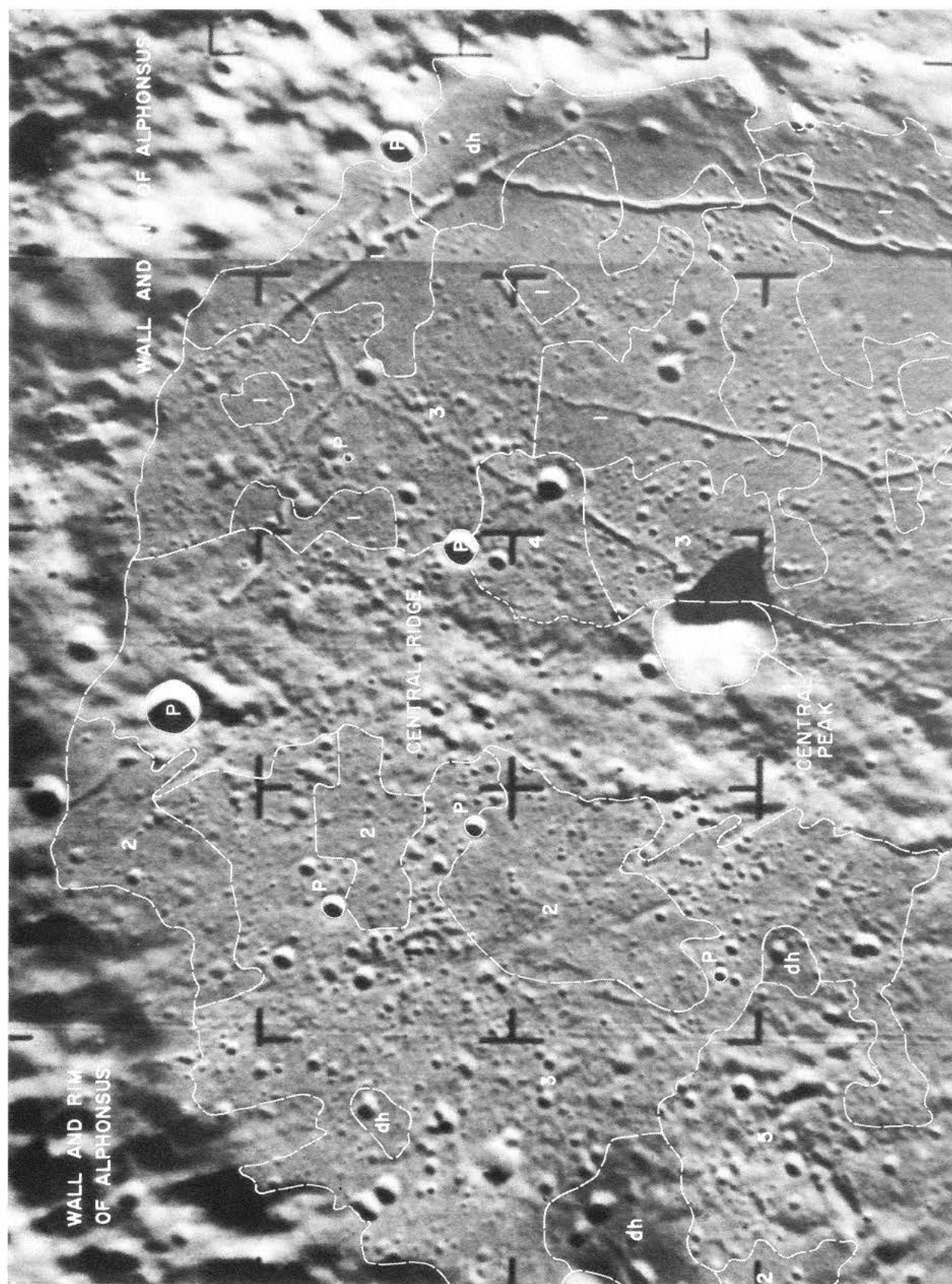
EXPLANATION

dh Material surrounding dark-halo craters; exhibits low albedo and relatively few craters. Craters especially low in frequency in the size range 0.1 to 0.5 km in diameter. Associated with rilles and elliptical craters 0.8 to 3 km in diameter which have broad, low rims that are convex upward.

UNIT 1 Resembles dh but has a larger number of craters and a higher albedo. Has relatively few craters in the size range 0.3 to 1.0 km, and craters less than 0.3 km in diameter commonly have a more subdued form than in units 2, 3, and 4.

UNIT 2 Material with intermediate albedo and marked linear texture. Crater density intermediate between units 1 and 3 for craters larger than 0.5 km in diameter. Size–frequency distribution resembles that of unit 3 for craters with diameters less than 0.5 km.

UNIT 3 Material with intermediate albedo and relatively high density of craters.

UNIT 4 Resembles unit 2 but lacks its marked linear texture. Appears to overlie subdued older features and fills part of a rille.

UNIT 5 Material with prominent ridges and depressions approximately 1 km apart. Crater density probably same as for unit 3 but cannot be determined because of the rough terrain.

P Circular craters with sharp raised rims having outer flanks that are concave upward (eumorphic craters) .

Fig. 16. Distribution of textural units in northern part of Alphonsus floor. (Base mosaic prepared from *Ranger IX* A-camera photograph 57 and B-camera photograph 87.)
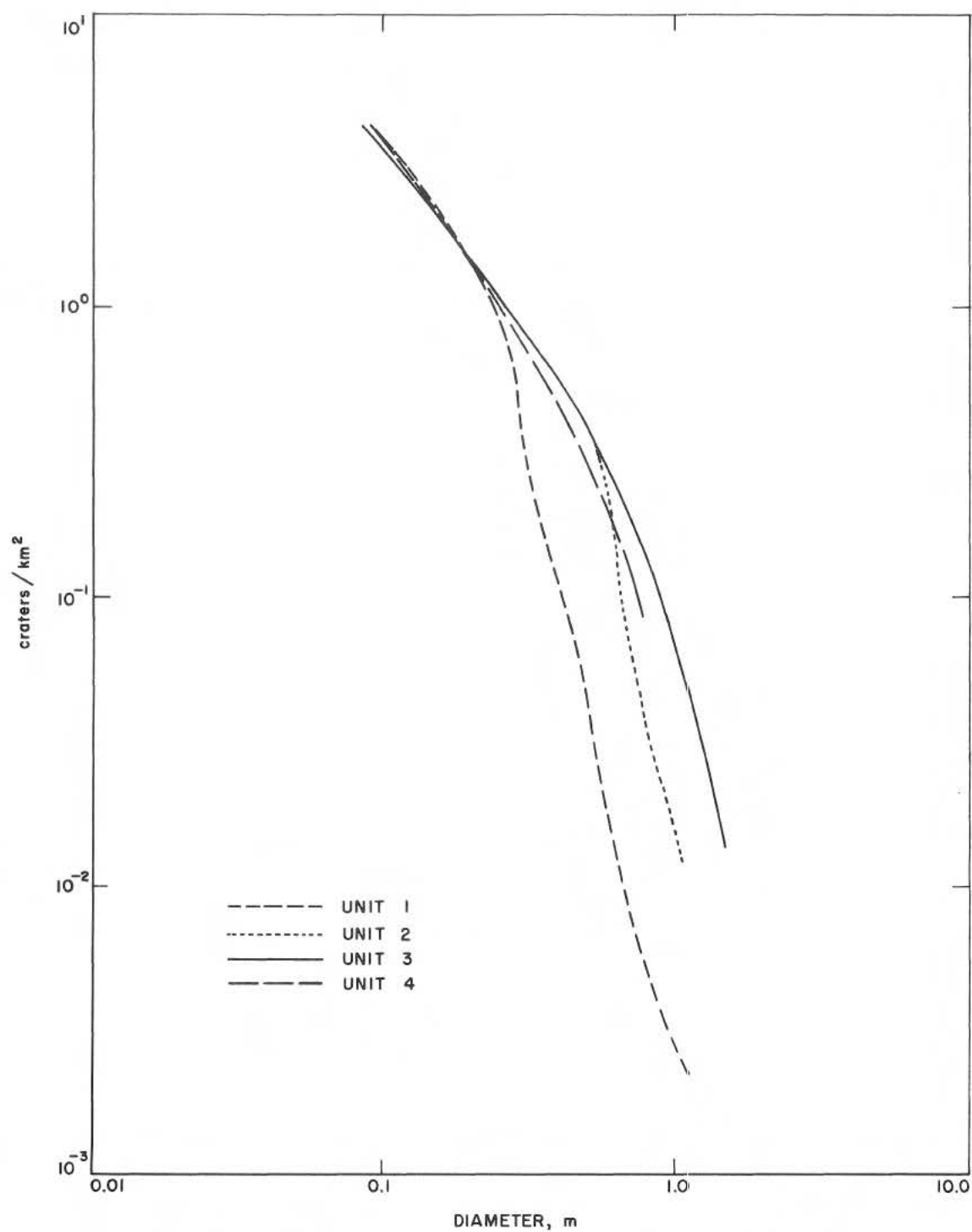
Fig. 17. Size–frequency distribution of craters in different textural units
on floor of Alphonsus.

The raised rims of dark-halo craters appear to be the best examples of constructional features around structurally controlled craters. The dark rims, pitted with many small craters up to 50 m across, are broad and gently sloping, and partly cover or fill adjacent rilles and craters. The dark material extends up to 4 km from the central crater. No linear features, lobate structures, or scarps resembling flow fronts have been observed on the dark rims, which resemble, in form, a broad deposit of pyroclastic material with little or no associated lava extrusions. Craters with such pyroclastic rims are common on Earth, particularly where the eruptions are andesitic or basaltic.

Minakami (Ref. 16) measured the ejection angles and velocities of material thrown out of the andesitic volcano Asama. The measured velocities ranged from 176 to 183 m/sec, with ejection angles of 37–43 deg. On the Moon, similar ejection velocities and angles would throw material on ballistic trajectories as far as 17 km. Volcanic eruptive activity could therefore account for dark halos extending 4 km from the main crater, if the ejection velocities of fragments were comparable to those on Earth.

Textural units 1, 2, and 3 are here interpreted as being similar in origin to, but older than, the dark-halo material, with unit 1 the youngest and unit 3 the oldest on the basis of crater density. Unit 4 surrounds a large crater on a rille. Although the rim material of the crater is not dark, the unit appears to blanket the surrounding terrain and is therefore interpreted as ejecta from the crater. In form, the crater resembles the dark-halo craters and is assumed to have a volcanic origin. Unit 5 appears to be an area where the presumed volcanic material filling the floor of Alphonsus (represented by units 1–4) is thin or absent and underlying, older materials of the floor are exposed.

The lineaments observed in Alphonsus are believed to reflect underlying fractures and faults. Strom (Ref. 15) has suggested several mechanisms for the origin of the lineaments on the Moon. The relationship between the lineaments on the floor of Alphonsus and the lunar grid system suggests that the process of formation of small, close-spaced fractures on the lunar surface is related to the processes that cause the major structures on the Moon. Separate deformational processes could be invoked to explain the minor fractures by assuming that their orientation is controlled by the orientation of the major fractures. This hypothesis, however, does not explain the absence of the Imbrian and the north-northeast–

south-southwest sets at large scales. If it were entirely true, the two sets of lineaments should be absent at all scales. A more likely explanation is that northeast–southwest and northwest–southeast fractures are still being formed and that the same processes causing the broad features, kilometers across, also cause fractures that are spaced centimeters apart. According to this hypothesis, small, close-spaced Imbrian and north-northeast–south-southwest fractures are absent because the processes that formed these lineaments are no longer operative, although movement may have occurred along them since their main period of formation.

4. Lunar Patterned Ground

In the last A-camera and the last few P-camera frames from *Ranger VII*, a distinctive pattern of gentle ridges or mounds and intervening troughs was discovered whose appearance was likened to the bark of the Ponderosa pine. The high-resolution pictures acquired from *Rangers VIII* and *IX* have shown that this pattern of small ridges and troughs is very widespread on the Moon. As it was seen in the highest-resolution frames of all the *Ranger* target areas, there is reason to suspect that it may occur over most of the lunar surface.

A general descriptive term is needed for this pattern of low ridges and troughs, and I will here refer to it as *lunar patterned ground*. It has some resemblance to certain types of patterned ground formed in the permafrost areas of the arctic and subarctic regions on Earth, but no implication that *lunar patterned ground* is necessarily related to permafrost is intended.

Good examples of lunar patterned ground are shown in the last *Ranger VII* P_1-camera photograph (Ref. 1, p. 112), the last *Ranger VIII* B-camera photograph (Fig. 36 in Section E), and the next-to-last *Ranger IX* B-camera photograph (Fig. 20). In these examples, the lunar patterned ground occurs on different types of geologic terrain but is similar in all of the areas. Individual ridges or mounds range from 5 to about 30 m in width and from 15 to about 200 m in length. Relief on the mounds, normal to the general slope of the lunar surface, has not yet been accurately measured but is estimated at from 10 to a few tens of centimeters. The slopes on the sides of the mounds are extremely low, and the patterned ground is, therefore, difficult to detect, except under conditions of low-angle illumination. For this reason, in the pictures from all three *Ranger* missions, it is most easily seen on low scarps and crater walls that are inclined almost parallel with, or at very small angles to, the Sun's rays; the patterned ground is generally
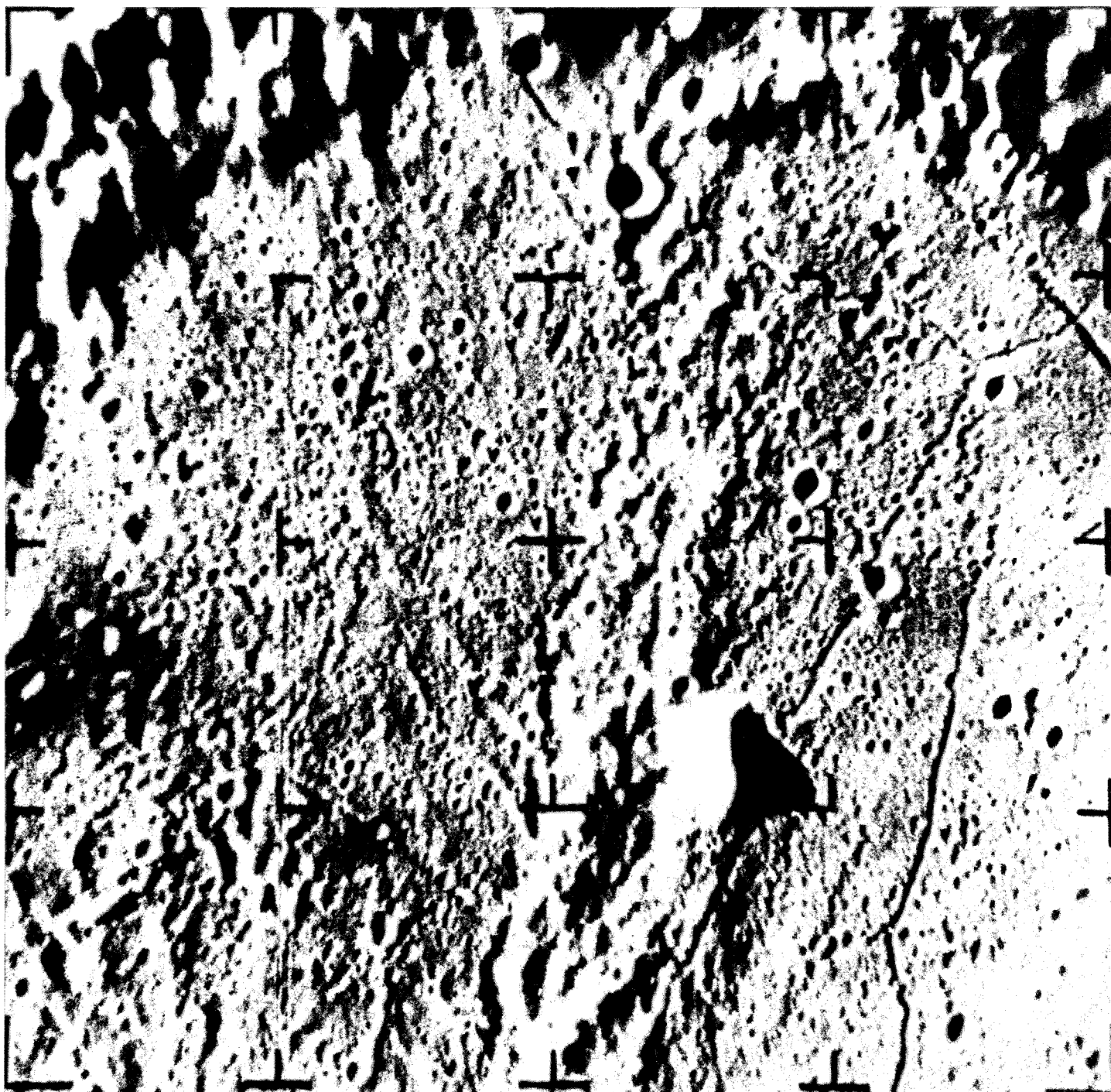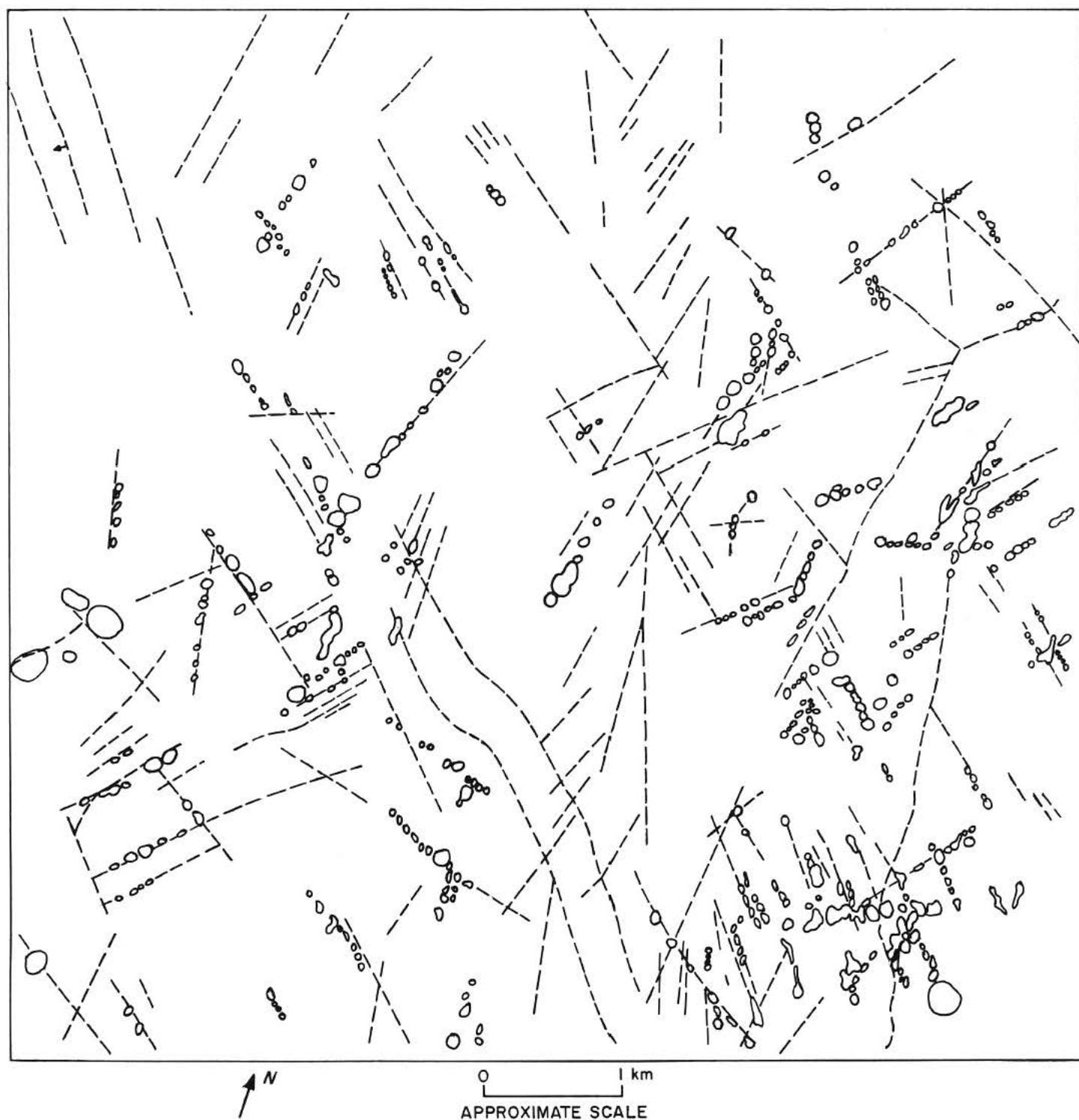
Fig. 18. *Ranger IX A-camera photograph 57, showing lineaments and structurally controlled craters in Alphonsus.*
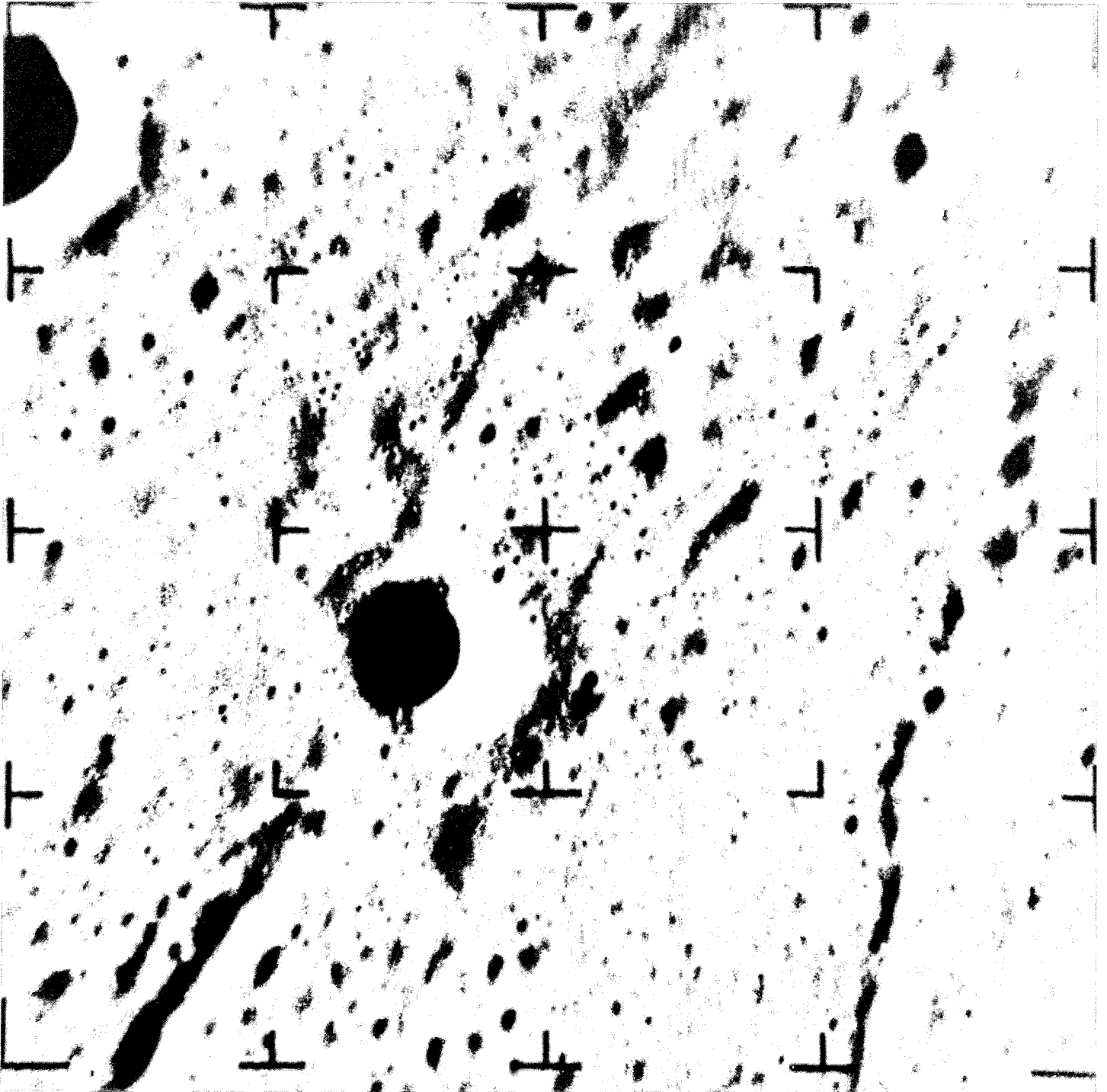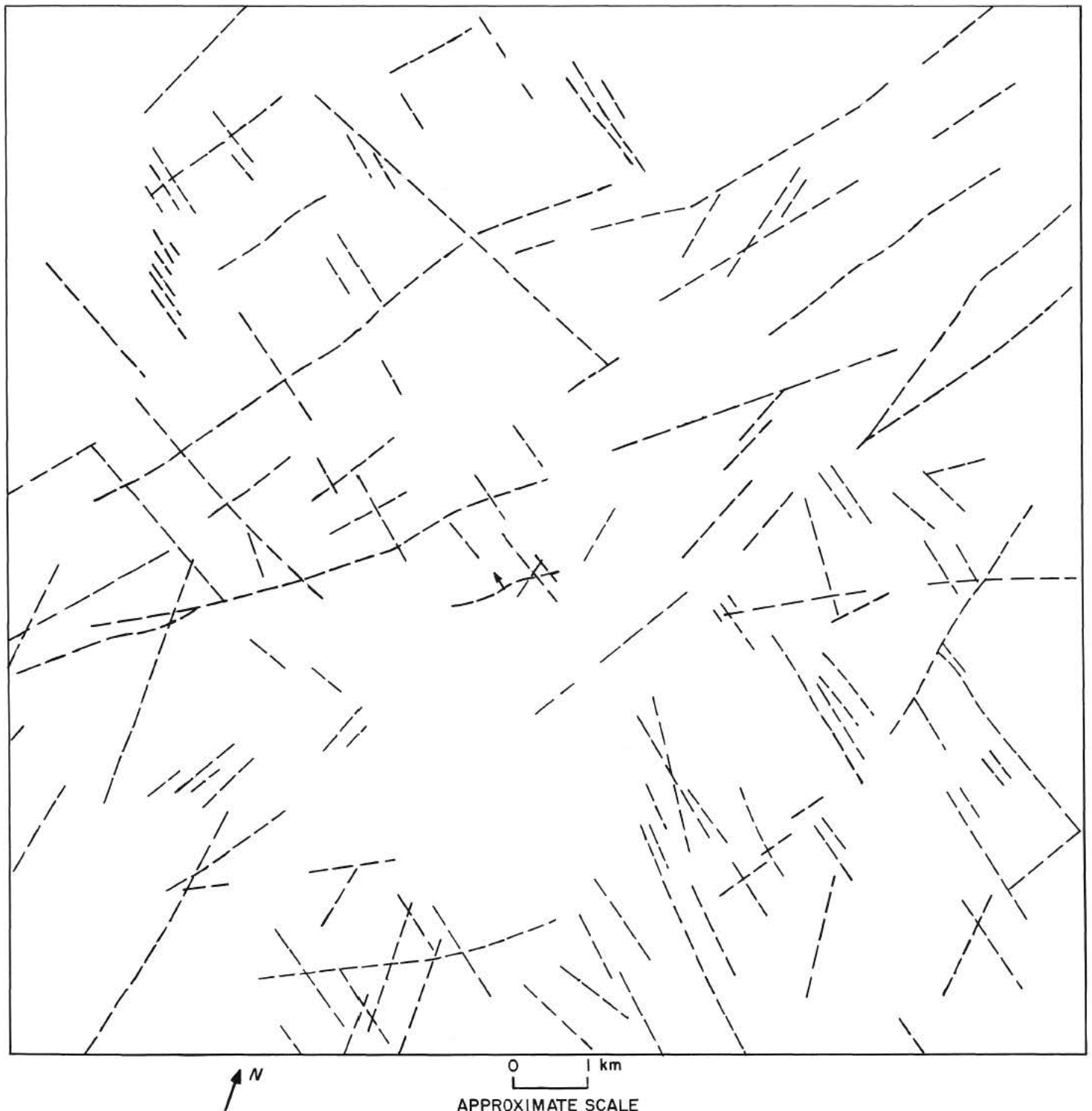
Fig. 19. *Ranger IX* A-camera photograph 68, showing lineaments on floor of Alphonsus.

N

0   1 km

APPROXIMATE SCALE
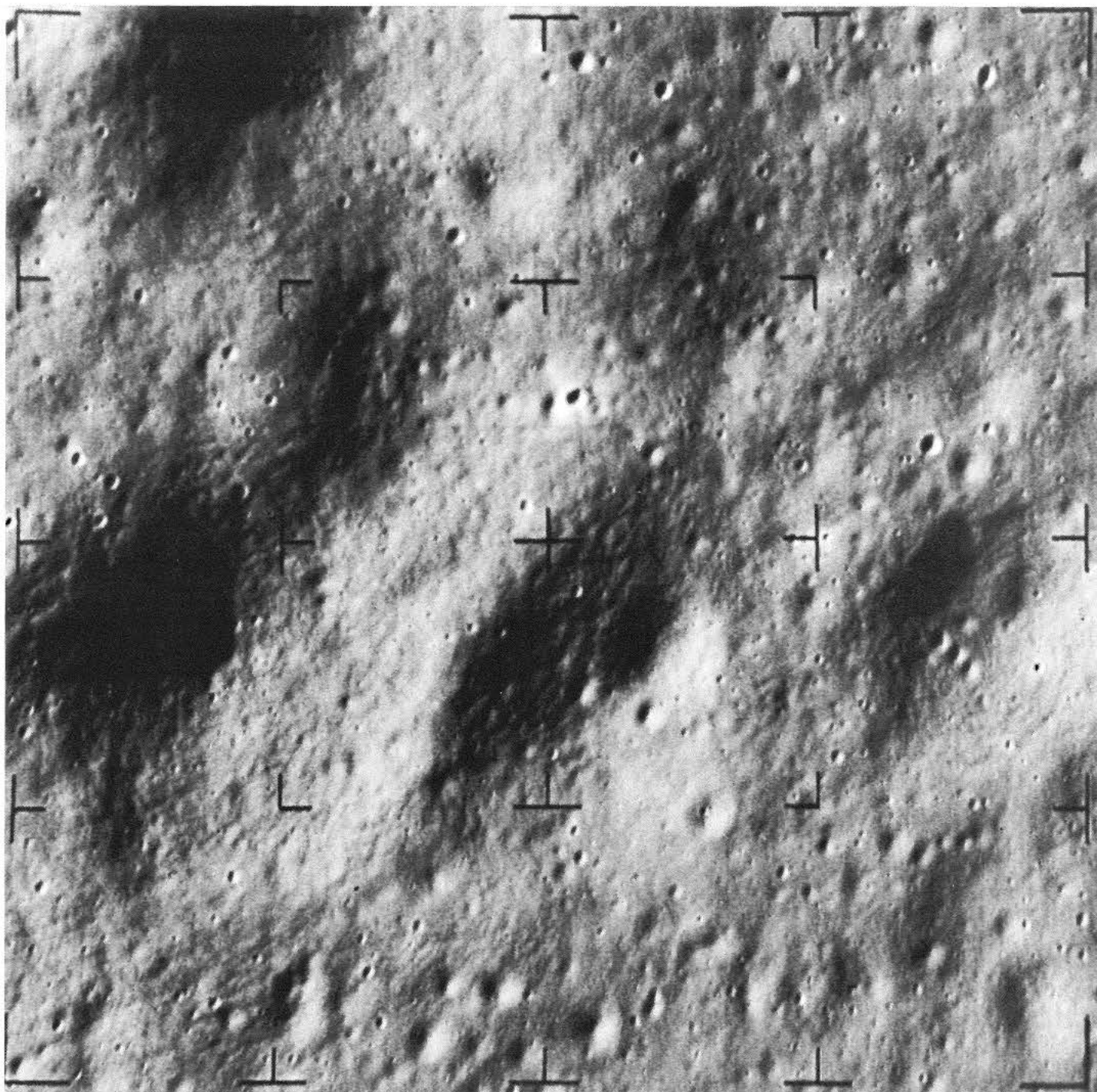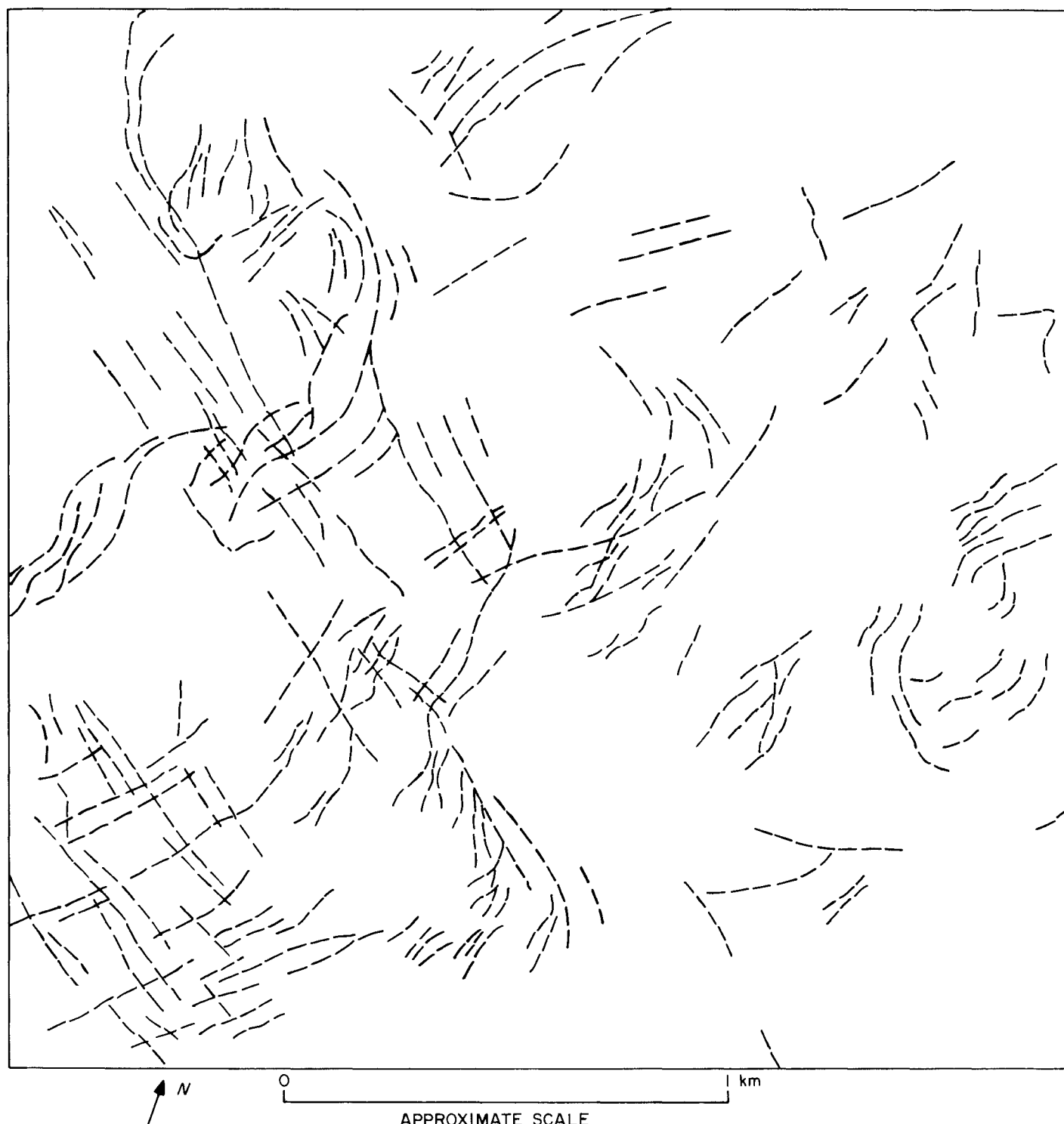
Fig. 20. *Ranger IX* B-camera photograph 87, showing lineaments on floor of Alphonsus.
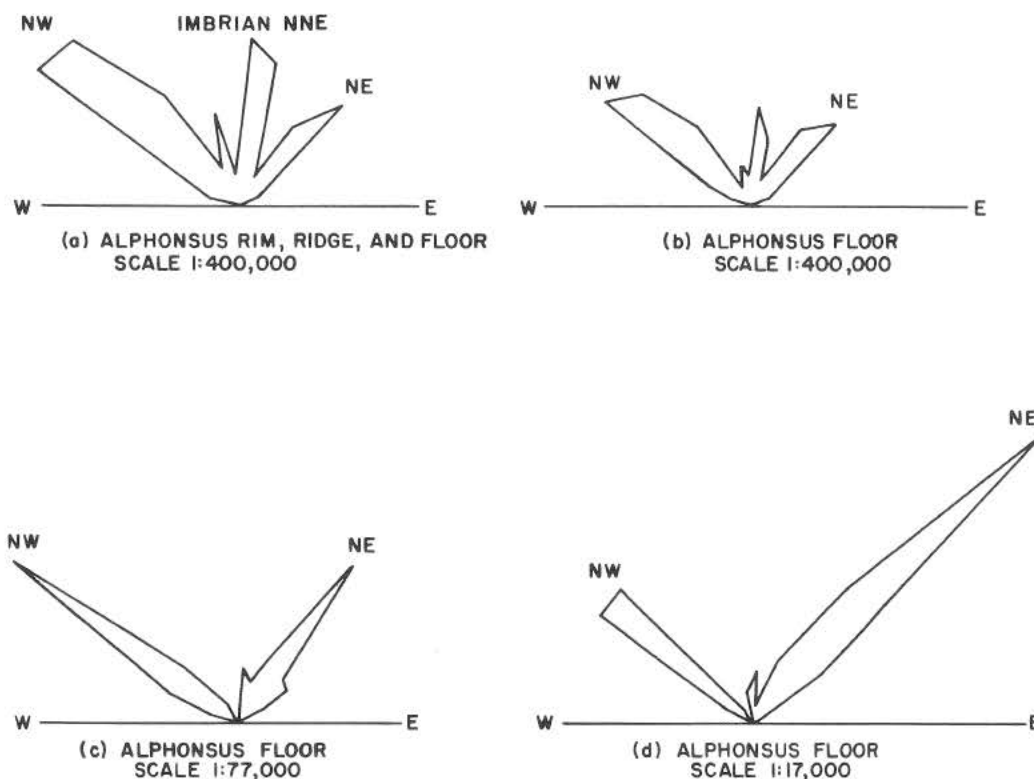
Fig. 21. Azimuth–frequency diagrams for lineaments in Alphonsus.

shown best in the *Ranger IX* pictures, which were taken with the lowest angle of solar illumination.

The troughs between the mounds have been mapped as small lineaments by Carr (Fig. 20) and by Schmitt (Fig. 37 in Section E). In each of the areas in which it has been observed, the predominant orientations of the linear elements of the lunar patterned ground tend to be parallel with the larger lineaments seen in the *Ranger* pictures and with dominant regional lineaments observed with the telescope. This parallelism suggests that the patterned ground is controlled by underlying structures, which, in turn, are controlled by the regional structural pattern. Two dominant orientations are generally found in the patterned ground at each locality, typically separated in azimuth by 60 to 90 deg. Thus, viewed over a broad area, the lunar patterned ground exhibits a grid pattern. Local departures from the principal grid orientation are common, however. The grid is most easily seen in pictures in which the coherent noise and video scan lines have been suppressed or removed.

The *Ranger VII* pictures that show the patterned ground are all high-resolution photographs of part of a ray

of Tycho on Mare Cognitum. The observed patterned ground occurs on the floor, walls, and rim of two secondary craters of Tycho and also on nearly level parts of the ray that are relatively free of resolved craters. Elements of the grid are oriented northwest and north-northeast, intersecting at an angle of about 70 deg. A series of *en echelon* scarps on the wall at one secondary crater and a sinuous set of subdued scarps cutting across the floor of the other are parallel or subparallel with the dominant north-northeast element of the grid. These scarps were interpreted by Shoemaker (Ref. 1) as having been formed by slumping within the craters. Both elements of the grid are approximately parallel with major lineament systems in the Mare Cognitum region plotted by Strom (Ref. 1).

The most prominent lunar patterned ground seen in the *Ranger VIII* pictures of Mare Tranquillitatis occurs on the rim and floor of the large crater shown in the southeast corner of the last B-camera photograph. Orientation of the troughs (Fig. 38 in Section E) is not as uniform at this locality as in other examples of lunar patterned ground, but the most prevalent orientations are again northwest and north-northeast. Systematic minor differences in orientation of the grid elements from

one part of the crater rim to another suggest that the patterned ground is controlled at least in part by the local structure of the rim. The north-northeast element of the grid is roughly parallel with a long, shallow linear depression that transects the wall of the crater, whereas the northwest element is approximately parallel with the long axes of numerous very shallow, elongate, oriented craters that occur in nearby parts of the mare.

Lunar patterned ground occurs over most parts of the floor of Alphonsus shown in the highest-resolution *Ranger IX* photographs. The elements of the grid intersect nearly at right angles here and are oriented northwest and northeast. As Carr has shown, these elements are approximately parallel to much larger linear features in the floor of Alphonsus and to major lineaments in this region of the Moon. Deviations from the prevailing grid orientation generally occur where the patterned ground crosses crater walls. These deviations or deflections are of the type that would be expected for the surface trace of a plane, in some cases dipping away from the center of the crater and in others toward it. Where the grid is deflected toward the center of the crater, it is also possible that the deflection is due to downslope creep. In Fig. 20, a row of dimple craters, each about 40 m in diameter, is oriented subparallel with the northwest grid element.

It seems highly probable that the lunar patterned ground is related to joints (fractures) and fissures in material that underlies the lunar surface at shallow depths. Each trough in the patterned ground may be localized over an individual joint or fissure. The depth to the jointed material probably does not much exceed a few meters where patterned ground is observed; if the depth were much greater, it would be difficult to account for spacing of the troughs as close as 5 to 10 m. In most places, the jointed material probably directly underlies the ballistically generated fragmental surface layer.

The jointed material almost certainly differs in origin, and probably in physical characteristics, from place to place. Where the patterned ground was observed in Mare Cognitum and Mare Tranquillitatis, the jointed material probably consists of thrown-out blocks of rock, which form a layer of rocky debris on the crater rims and breccia under the crater floors. On the floor of Alphonsus, the jointed material may be consolidated volcanic ash. The strength of the jointed material need not be very great, as only weakly consolidated sediments are known to be capable of sustaining joints on Earth.

It is, perhaps, significant that the most prominent patterned ground seen in the *Ranger VIII* pictures of Mare Tranquillitatis occurs on the rim and floor units of a relatively large crater. These are the places where material derived from depths on the order of tens of meters below the original mare surface should lie close to the present surface, and, hence, where rocky material is most likely to occur at shallow depth, whereas relatively cohesive volcanic material might underlie the ballistically generated surface layer in adjacent parts of the mare. In addition, the ballistically generated surface layer itself should be thinner on the rim and floor of the crater than on the adjacent older parts of the mare.

The troughs and ridges of the patterned ground may have been formed by jostling of the underlying joint blocks. In the jostling process envisioned, the relatively cohesionless fragmental surface layer tends to be heaped up slightly toward the centers of the joint blocks and thrown away from the edges of the blocks. Troughs would thus be formed over the joints. Some loss of fine-grained surface material probably also takes place by drainage down open joints or fissures between the blocks, thereby deepening the troughs.

A very crude analog of the lunar patterned ground may be represented by a pattern of fissures developed along the Atacama fault zone in northern Chile (Fig. 22), which was brought to my attention by G. E. Ericksen of the Geological Survey. Here, a grid of fissures has developed as a result of horizontal strain adjacent to a recent trace of displacement in the fault zone. Open fractures or fissures occur in Jurassic volcanic rocks that are covered with about 1 m of colluvium. The surface pattern is formed by drainage of the colluvium into the fissures. In this case, the pattern of linear depressions has developed as a result of simple distension of the surface rather than by jostling of the joint blocks, as postulated for lunar patterned ground.

Jostling of joint blocks on the Moon may take place primarily as a consequence of the passage of seismic surface waves propagated from relatively high-energy impacts. It is also possible that surface waves of significant amplitude are generated by seismic events originating in the lunar interior. The jostling must occur with sufficient frequency to maintain the lunar patterned ground against ballistic erosion and deposition, which tends to erase or destroy it. Intermittent jostling is probably an active process at the present time. In addition, there may be active tectonic processes leading to
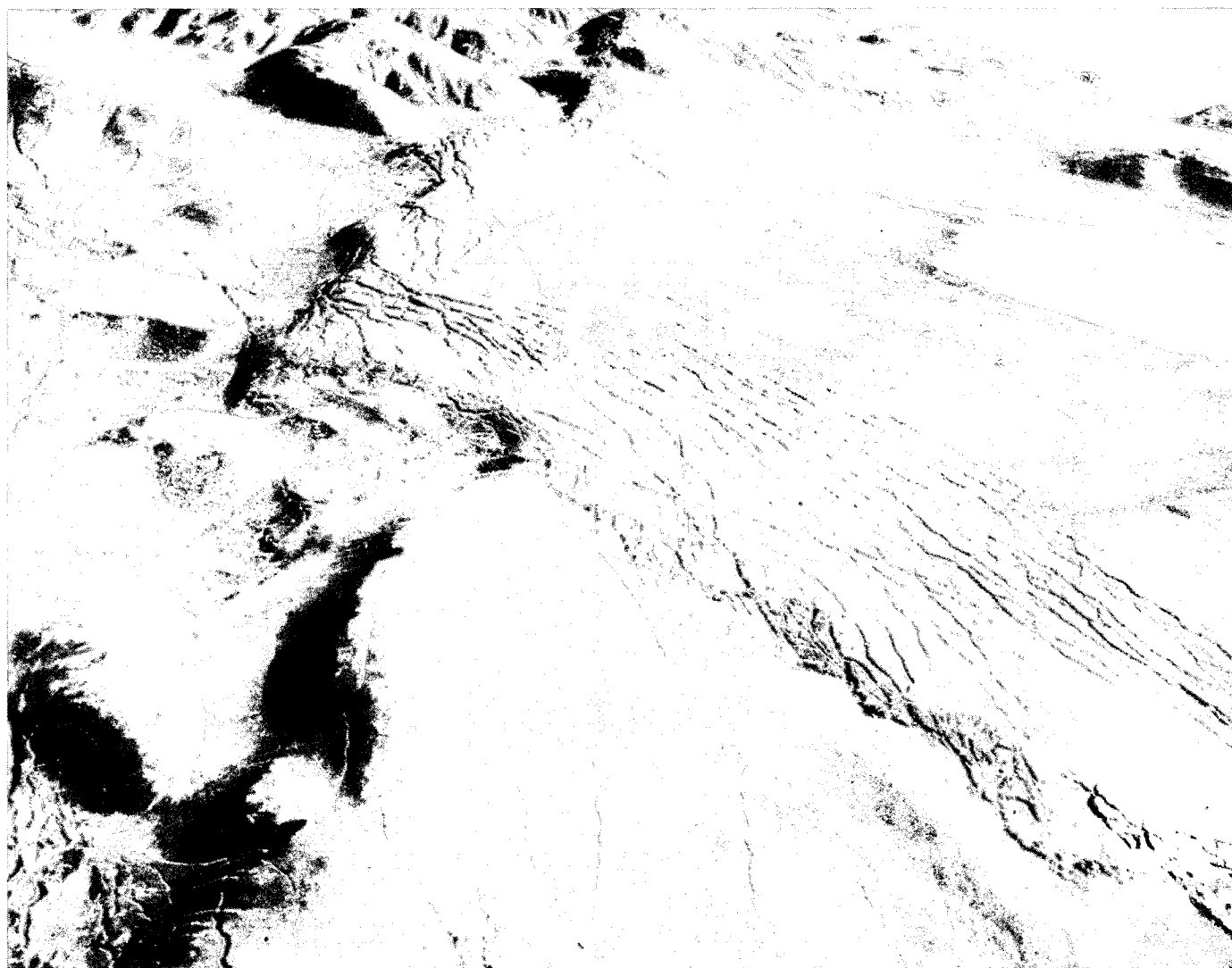
Fig. 22. Oblique aerial photograph of part of the Atacama Desert, Chile, showing a pattern of linear depressions developed over fissures in the Atacama fault zone.

further development of joints or opening of pre-existing joints in preferred directions, as Carr has suggested for the floor of Alphonsus in Section 3.

C. Preliminary Photogrammetric Analysis of the Topography of Small Areas on the Moon

The Geological Survey is investigating the photogrammetric reduction of selected stereoscopic pairs of *Ranger* photographs for the purpose of obtaining control for the compilation of detailed topographic maps by photometric methods. This control is required in order to determine the local photometric function of small areas on the lunar surface and to connect photometrically derived profiles in the direction normal to the phase-

angle plane (Ref. 1, pp. 129–130). A general study of the photogrammetric reduction of *Ranger* pictures has been carried out by J. D. Alderman, W. T. Borgeson, and S. S. C. Wu.

As a part of the photogrammetric investigations, H. J. Moore and R. V. Lugn set up an experimental stereo model with an ER-55 plotter and, using two A-camera photographs from the *Ranger VIII* mission, studied the problems of design and use of an anaglyphic projection instrument suitable for analysis of *Ranger* photographs. Such stereo models aid greatly in the analysis and plotting of the geology and in the general stereoscopic study of the lunar surface. A topographic map compiled from their model is presented in this Section in order to illustrate

the type of result that may be obtained by anaglyphic projection techniques and to provide a preliminary base map for the geological analysis by N. J. Trask of the area represented by the model (described in Section D3). The preliminary photogrammetric results reported here are entirely experimental in nature but represent an approximate solution of the topography of the area studied.

1. Investigation of the Photogrammetric Reduction of the *Ranger* Images, James D. Alderman, Warren T. Borgeson, and Sherman S. C. Wu

In addition to high-resolution monoscopic pictures of the lunar surface, *Ranger* flights have provided a limited amount of usable stereoscopic coverage. This coverage will permit more detailed and accurate measurement of local slopes than can be accomplished with Earth-based methods, yielding information of importance to basic geological and engineering investigations.

Recovery of slope data from *Ranger* images involves a number of factors that are alien to conventional photogrammetry. The major problems are: (1) the narrow-angle lens systems of the *Ranger* cameras, (2) camera tilt, (3) camera calibration, (4) small base-to-height ratios, (5) image motion and image blur, and (6) video scan lines, image size, scale differences, low Sun angle, and lunar photometric effects. Initial studies have been concerned with the feasibility of systematic data reduction, rather than with actual attempts to produce quantitative base materials. The latter objective will be accomplished during a subsequent data-reduction program.

a. System Limitations

Narrow-angle lens systems. All *Ranger* cameras were narrow-angle lens systems, five of the six cameras on each spacecraft having extremely narrow-angle lenses. The use of such systems was required for compatibility with a 1-in. vidicon. The most severe limitation imposed, however, was the small format size selected for the P cameras because of the need for very rapid scanning and readout between frames. The terminal velocity of the *Ranger* spacecraft (8600 ft/sec) made rapid scanning necessary, particularly for the recovery and transmission of the last high-resolution frames. For that reason, an 0.11-in.-square format size that could be exposed, scanned, and transmitted in 0.21 sec was chosen for all the P cameras.

Good narrow-angle lens systems, like the central part of a wide-angle lens, have high resolution but are inherently ill-suited for stereoscopy, particularly if the optic axes of individual frames are parallel or divergent. In such systems, the space rays from corresponding photographic points intersect at angles so acute that the vertical (z) determination is highly imprecise. The situation can be compared to a surveying problem, in which a base line 200 ft long is used to determine the distance to a point 5 miles away; an error of 1 sec of arc leads to an error of 17 ft in the computed distance.

Available photogrammetric plotters (with the exception of the AP/2 and some first-order plotters) are designed for wide-angle camera systems with 70- to 120-deg fields of view. Other characteristics of first-order plotters limit their use in the recovery of the geometry of the *Ranger* pictures. When set in stereo plotters, the *Ranger* images occupy only the part of the angular field equal to that of the taking camera. The six components of orientation for each frame are difficult to control under these conditions, and only a precise presetting of the components will permit recovery of the geometry. Conventionally, the components are determined by ground control. A universal photogrammetric instrument such as the AP/2 plotter, designed to accommodate pictures taken with a narrow-angle system, should permit more precise geometric reconstitution because the x- and y-tilts can be more closely controlled on this plotter than on any other.

The P_1 and P_2 cameras have an angular field of view of 2.1 deg and a focal length of 3 in.; they are virtually useless for photogrammetric purposes, although, in theory, these cameras provide the maximum possible ground resolution. The P_3 and P_4 cameras have an angular field of view of 6.3 deg, a focal length of 1 in., and an 0.11 × 0.11-in. format. The angular fields of the P_3 and P_4 cameras are larger than those of the P_1 and P_2, but provide images of smaller scale. Although still weak, these increased angular fields present greater photogrammetric potential. The B camera, with an angular field of 9.3 deg, a focal length of 3 in., and a format of 0.44 × 0.44 in., offers only slightly more in terms of reconstituting the geometry than the P_3 and P_4 cameras. The A cameras have an angular field of 25 deg, a focal length of 1 in., and a format of 0.44 × 0.44 in.; the pictures taken with these cameras provide the strongest possible stereo models available in the *Ranger* series.

Unfortunately, only a few high-resolution A-picture combinations are available for stereo models (see Table 1).

Camera tilt. Camera tilt is objectionable even under optimum photogrammetric conditions where the z (alti-

Table 1. Stereoscopic pairs of *Ranger* photographs from which useful photogrammetric measurements can be made

Model No.	Camera and photo No.	Original scale[a] (on vidicon)	Range, km	Altitude, km	Tilt		Base/height ratio
					deg	min	
1	A57	1/342,000	35.009	30.859	28	11	1/5
	B83	1/1,104,000	82.594	62.737	41	12	
2	A54	1/2,123,000	55.395	49.053	27	41	1/8
	B81	1/1,418,000	106.068	81.103	40	08	
3	A58	1/949,000	24.772	21.785	28	26	1/3
	A59	1/556,000	14.506	12.726	28	41	
4	A58	1/949,000	24.772	21.785	28	26	1/8
	B87	1/629,000	47.021	35.402	41	09	
5	A69[b]	1,807,000	21.057	19.571	21	39	1/4
	A70[b]	1,297,000	7.746	7.194	21	46	
6	A52	1/3,287,000	85.767	76.452	26	57	1/2.5
	A56	1/1,733,000	45.216	39.949	27	51	
7	A51	1/3,673,000	95.838	85.612	26	43	1/3
	A54	1/2,123,000	55.395	49.053	27	41	
8	A57	1/1,342,000	35.009	30.859	28	11	1/6
	A58	1/949,000	24.772	21.785	28	26	
9	A56	1/1,733,000	45.216	39.949	27	56	1/9
	A57	1/1,342,000	35.009	30.859	28	11	
10	A54	1/2,123,000	55.395	49.053	27	41	1/10
	A56	1/1,733,000	45.216	39.949	27	51	

[a]Principal distance A camera = 26.09 mm, B camera = 74.8 mm.
[b]*Ranger IX* photographs; all others are *Ranger VIII* frames.

tude) difference of image points is to be determined either analytically or with stereoscopic plotting instruments. If both tilt and relief of unknown magnitudes are present, the direction of image-point displacements is indeterminate. Relief displacement is radial from the nadir point and is a function of the first power of the radial distance from the nadir point to the image point, and of the height of the object. Tilt displacement is radial from the isocenter and varies both with the square of the radial distance and with the cosine of the angle that a line through the image point and isocenter makes with the direction of tilt.

The absolute components of tilt cannot be calculated without ground control. An analytical solution is dependent upon the validity of the tracking and spacecraft-orientation data, and upon the ability of an operator to reference discrete image points in each photo of a stereo pair. Unfortunately, very few well defined common image points exist in the high-resolution *Ranger* stereo pairs. This virtually eliminates the use of a comparator

in analytical profile determination. Hence, a stereo model recovery is superior to any other mode of photogrammetry for these pictures.

The advantages of using a stereoscopic plotting instrument rather than analytic methods are:

1. Datum orientation is more reliable.

2. Slope components can be determined in any direction.

3. Detailed profiles can be compiled across ill-defined areas in the images.

4. Small formats are more easily handled.

5. Photomechanical processing of the pictures is less detrimental.

6. The measurements do not require complete acceptance of trajectory and spacecraft orientation data.

7. The stereo model can be used to aid geological investigations.

The main disadvantages are:

1. The number of usable stereo models is strictly limited.

2. Nearly all available plotters are limited in their ability to accommodate tilt.

3. Most plotters cannot accommodate large z-differences.

4. The range of focal length that most plotters can accommodate is restricted (normally 3½–8½ in.).

Camera calibrations. At the time of exposure of a picture, the rays from the various object points have a unique angular relationship with one another and with the camera axis. The purpose of all camera calibrations and plotter compensations is to allow these relationships to be regenerated with accuracy. Recovery of the image geometry at the instant of exposure requires knowledge of three essential elements: (1) location of the principal point, (2) camera-lens focal length, and (3) distortion of the total system, including distortion introduced by the electronic parts of the camera and the picture reconstruction system.

Location of the principal point. The principal point is defined as the intersection with the image plane of the line perpendicular to the image plane passing through the camera-lens nodal points. When the image plane is perpendicular to the lens axis, the principal point is coincident with the intersection of the optic axis and the image plane. As the principal point is not marked in the images, some kind of fiducial system must be used to define it. It is also necessary that the lens be so aligned that the fiducial system actually defines the principal point, or, at least, a point whose distance and direction from the true principal point are fixed and known. Wide-angle (90-deg) cartographic cameras are required to have a fiducial system that defines the true principal point within 15 μ. In narrow-angle systems, principal-point location is not so critical, and a positional uncertainty of about 75 μ can be tolerated without detriment. Interior orientation of a stereo model is dependent upon reproduction in the plotter of the image plane and the optic-axis relationship of the taking camera. Mislocation of the principal point or points will distort the model in different ways, depending upon the direction of shift. In the case of the *Ranger* pictures, only principal-point displacements in opposite x-directions contribute to significant vertical scale errors.

The principal point is represented by the central reticle of the *Ranger* cameras, normally within ±1 min

of arc, and is not a source of error. It is difficult to align the small cross of the central reticle with the principal point of a projector, however, and a small interior orientation error is introduced when optic centering is performed.

Camera-lens focal length. The second item of interest to the photogrammetrist is the principal distance of the negative. In the original image, the principal distance is the distance from the image plane to the interior nodal point. When the lens is focused for infinity, this distance is equal to the lens focal length, sometimes called the effective focal length. The effective focal length is gaged to give the best average focus over the entire image plane, and is not necessarily the same as the focal length determined on-axis.

In vidicon systems, the focal plane is shifted away from the lens by the interposition of the glass faceplate into the optical path. This introduces a curvature of field, convex toward the lens, which results in negative distortion. The shift in the focal plane can be allowed for, but the curvature of field changes the effective focal length (Ref. 17). For narrow-angle (10-deg) systems, these faceplate effects—especially field curvature—are small.

Radial distortion of the total system. The methods and instruments of photogrammetry treat a picture as a central point perspective of the object imaged. Most of the geometric imperfections of optical systems are displacements directed either radially away from (+) or toward (−) the principal point, and have a magnitude that is a function only of the radial distance from the principal point. When the camera axes of a stereo pair of photographs are parallel and vertical, the chief effects of radial distortion are errors in z. As the angle of convergence increases, radial distortion begins to affect the accuracy of x and y (planimetry).

A rough estimate of maximum distortion allowed for in so-called "distortion-free" images can be derived from experience with cartographic photogrammetry. In pictures considered distortion-free, the distortion is equal to or less than one-fifth the line-pair resolution. Larger distortions can be dealt with by corrector plates in a printer or cams in plotters, or by analytic treatment, provided the distortion has previously been measured. It is necessary to know the distortion of the camera system as a whole, and not just that of the lens.

The vidicon faceplate used in the *Ranger* has an effect on distortion, even when it is optically flat. In essence, it

is part of the lens system. The glass plate lying between the lens and the focal plane displaces the focal plane away from the lens; the displacement along the optic axis is about one-third the glass thickness. This distortion can be removed by insertion of an equivalent glass plate in a ratio printer when diapositives are made.

The electronic link between the vidicon faceplate and the reconstituted picture with which the photogrammetrist works generates distortions of both systematic and random character.

Base-to-height ratio. The base-to-height ratio for the Ranger stereo images is defined as the ratio of the perpendicular distance from the center of the camera at the lower altitude to the optic-axis extension of the second, higher camera, divided by the range (optic center to lunar surface along the optic axis) of the lower camera. This definition is similar to that used in terrestrial stereometric photography, where one of the two cameras is not normal to the base line.

The high-angle trajectory of the *Ranger* spacecraft resulted in stereo images with extremely small base-to-height ratios. The ratio of the base separation of two frames to the range to a common image point is approximately the sine of the angle of convergence. The three-dimensional geometry of the system is strongest when the angle of convergence is 90 deg. A measure of reliability of z-measurements (normalized for $d = 90$ deg) may be expressed as

$$\text{weight factor} = 2 \sin^2 \frac{d}{2}$$

where d is the angle of convergence. It is evident that as d approaches zero, the reliability of determining z on a stereo plotter is drastically reduced. Normally, 12 deg is considered the limiting angle of convergence from which reliable z-measurements may be made in an anaglyphic plotting system; the limiting angle is approximately 8–9 deg in a first-order instrument. A convergence angle as small as 1 deg 55 min can be accommodated on a C-8, with a repeatability of z reading within 0.1 mm (Ref. 18). X parallax measurements with an AP/2 plotter are reputed to be reliable (90% confidence), with a base-to-height ratio of 0.025 (1 deg 25 min convergence). These accuracies can be obtained only with good images; decrease in the quality of the images will increase the limiting angle of convergence required for reliable measurements.

The base-to-height ratios of Ranger images may be derived from coordinates in the following manner:

1. Higher position of spacecraft

   $R_1 = R + H_1$, where R = lunar radius and H = vertical distance of spacecraft to lunar surface

   λ_1 = colatitude of spacecraft

   β_1 = longitude of spacecraft

   The coordinates are

   $x_1 = R_1 \sin \lambda_1 \cos \beta_1$

   $y_1 = R_1 \sin \lambda_1 \sin \beta_1$

   $z_1 = R_1 \cos \lambda_1$

2. Lower position of spacecraft

   $R_2 = R + H_2$

   λ_3 = colatitude

   β_3 = longitude

   The coordinates are

   $x_3 = R_2 \sin \lambda_3 \cos \beta_3$

   $y_3 = R_2 \sin \lambda_3 \sin \beta_3$

   $z_3 = R_2 \cos \lambda_3$

3. Optical-axis intersection on lunar surface of higher spacecraft

   λ_2 = colatitude

   β_2 = longitude

   R = lunar radius

   The coordinates are

   $x_2 = R \sin \lambda_2 \cos \beta_2$

   $y_2 = R \sin \lambda_2 \sin \beta_2$

   $z_2 = R \cos \lambda_2$

Equation for vector from (3) to (1):

$(x_1 - x_2)\mathbf{i} + (y_1 - y_2)\mathbf{j} + (z_1 - z_2)\mathbf{k}$

Unit vector $\mathbf{e}$:

$$\mathbf{e} = \frac{(x_1 - x_2)\mathbf{i} + (y_1 - y_2)\mathbf{j} + (z_1 - z_2)\mathbf{k}}{\sqrt{(x_1 - x_2)^2 + (y_1 - y_2)^2 + (z_1 - z_2)^2}}$$

Equation for vector from (2) to (3):

$$\mathbf{v} = (x_2 - x_3)\mathbf{i} + (y_2 - y_3)\mathbf{j} + (z_2 - z_3)\mathbf{k}$$

Perpendicular distance from (2) to vector (1) to (3):

$$\text{Distance} = |\mathbf{v} \cdot \mathbf{e}| = \mathbf{v} \cdot \mathbf{e} = \frac{1}{\sqrt{(x_1 - x_2)^2 + (y_1 - y_2)^2 + (z_1 - z_2)^2}} \cdot \begin{vmatrix} \mathbf{i} & \mathbf{j} & \mathbf{k} \\ (x_1 - x_2) & (y_1 - y_2) & (z_1 - z_2) \\ (x_2 - x_3) & (y_2 - y_3) & (z_2 - z_3) \end{vmatrix}$$

$$= \frac{\big[(y_1 - y_2)(z_2 - z_3) - (z_1 - z_2)(y_2 - y_3)\big]\mathbf{i} + \big[(z_1 - z_2)(x_2 - x_3) - (x_1 - x_2)(z_2 - z_3)\big]\mathbf{j} + \big[(x_1 - x_2)(y_2 - y_3) - (y_1 - y_2)(x_2 - x_3)\big]\mathbf{k}}{\sqrt{(x_1 - x_2)^2 + (y_2 - y_3)^2 + (z_1 - z_2)^2}}$$

or

$$|\mathbf{v} \cdot \mathbf{e}| = \sqrt{\frac{(y_1 - y_2)(z_2 - z_3) - (z_1 - z_2)(y_2 - y_3)^2 + (z_1 - z_2)(x_2 - x_3) - (x_1 - x_2)(z_2 - z_3)^2 + (x_1 - x_2)(y_2 - y_3) - (y_1 - y_2)(x_2 - x_3)^2}{(x_1 - x_2)^2 + (y_1 - y_2)^2 + (z_1 - z_2)^2}}$$

The base-to-height ratio = distance/range of lower position.   (See Table 1 for numerical base-to-height ratio.)

Image motion and image blur. During the finite time that the shutter is open, any movement of the camera results in a blurring and distortion of the images. The magnitude and direction of image blur and distortion depend on the magnitude and direction of the camera velocity vector relative to the object being imaged, the camera orientation, and the relief of the area being imaged.

When a "between-the-lens" shutter is used, all parts of the picture are exposed simultaneously, and the centers of blurred image points are not displaced from the relative positions they would have had if the camera had been stationary; thus, there is no image distortion, and the picture may be treated as a central point perspective. Image blurring in this case only degrades resolution, as image points are elongated in a direction and by an amount determined by relative camera velocity and camera orientation.

When a focal-plane shutter is used, different parts of the picture are exposed at different times while the camera is at different points in space. In the resulting picture, the image points are displaced from the relative positions they would have had if all parts of the picture had been exposed simultaneously. The resulting displacements may be considered as distortions from a true-perspective center picture, or the picture may be considered as having been produced by a camera in which the perspective center has been replaced by a perspective line. The magnitude and direction of the distortion depend upon the direction and speed of the shutter motion, the direction and magnitude of the camera velocity relative to the object that was imaged, and the camera orientation. Image blurring occurs as an additional effect. Except for the AP/2, existing plotters are not designed to cope with the effect of a focal-plane shutter.

The resolution of the *Ranger* images that are suited for photogrammetry is such that image motion and blur have little effect upon photogrammetric reduction. (For an analysis of image motion and blur see the Appendix to this Section.)

Video scanning, image size, scale differences, low Sun angle

Video scanning. The television scanning systems used in *Ranger* limited the resolution of the cameras. Whereas the lenses had a resolution of 50 line pairs/mm, resolution of the camera systems was approximately 36 line

pairs/mm. Linearity is probably the limiting factor in resolution, and nonlinearity of the scanning is a major contributor to the unknown stereo model distortions. Video "jitter" (random electron beam displacements) tends to produce a model much softer than normal photographs. The full effects of nonlinearity of scanning and jitter are, at present, unknown.

One unavoidable aspect of television pictures that is detrimental to photogrammetry is the scan line. At latent image size, the effect is not particularly harmful, but when the images are enlarged, the blanking spaces become very noticeable. The effect is similar to looking at an object through a one-directional, thick wire screen. When the latent image is enlarged six times and set up in a first-order plotter, this effect creates a pseudo-datum that the operator must penetrate in order to place the floating mark upon the surface. Under these conditions contouring is accomplished with more confidence than is the reading of elevations—a reversal of the normal photogrammetric condition.

Image size. One aspect of image format that has created operator difficulties is the very small size of the images. It is difficult for a photogrammetrist to adjust his long-developed techniques in dealing with formats of 7 × 7 in. or 9 × 9 in. to formats occupying an area of 0.7 × 0.7 in. Interior orientation by alignment of reticles defining center lines of the format is restricted by reticle width (0.005–0.002 in.) and linear separation (0.5 in.)

Image scale differences. Camera stations along the *Ranger* spacecraft trajectory are at greatly different altitudes, and the pictures from cameras of equal focal length are, therefore, at greatly different scales.

When there is a large difference in scale between two photographs of a stereo pair, a plotter operator will not be able to achieve image fusion if he is employing an orthographic viewing system. Scale difference in first-order plotters would be acceptable if zoom oculars were available, but only the AP series of first-order plotters can accommodate a scale discrepancy without a major redesign of the optical system. It may be noted that the photogrammetric system that most closely meets the demand of equal image scale by recovery of all spatial relationships is the double-projection system first designed by Zeiss in 1928.

One problem created by disparate image scale concerns the operator link in the stereo plotter system. It

is separate from, but related to, the problem of accommodating disparate camera altitudes within the mechanical and optical limitations of the plotter. Although the human eye and brain can accommodate some image-scale disparity and still achieve stereo fusion, scale differences exceeding 4–5% will cause eyestrain when long viewing times are involved.

The most harmful effect of altitude difference is the resulting ground-resolution change for each photograph. When small relief features are subdued or eliminated from one photo, the ability to form a stereo model is curtailed.

Low Sun angle. The minimum solar altitude normally used for terrestrial photography is 30 deg. Below this angle, shadows cast by features with slopes greater than 30 deg obscure parts of the detail. In addition, the brightness of a horizontal surface decreases rapidly (approximately 1%/deg) when the Sun angle is below 60 deg. On the other hand, when small features are involved and albedo differences are also small, small shadows enhance detail and generally improve the quality of the image. Thus, a low Sun angle, resulting in small shadows, would have some photogrammetric value in areas of minor relief.

A crude attempt was made to evaluate lighting effects on a model of varying relief and with no albedo differences. The setup consisted of two multiplex projectors tilted 28 deg, separated along the z-axis by about 100 mm. Exposures were made on glass plates in the projectors for convenience in resetting. A spotlight was used as an illuminating source and set at 60 and at approximately 20 deg. Each model was then reset and a comparison made; the model obtained from the images that were illuminated at 20 deg was the poorest.

The low Sun angle, in combination with narrow-angle lens systems, is felt to be the factor that prohibits the reversing of stereo effects. No matter how the high-resolution *Ranger* photographs are oriented, pseudo-stereo (reversal of relief) cannot be achieved. This fact has prompted statements to the effect that true stereo does not exist in the *Ranger* images. It can be demonstrated that equivalent central parts of vertical terrestrial photographs of monotone areas (sand, snow, grain fields) at Sun altitudes of 45 deg tend to produce the same effect.

b. First-Order Plotters

The inherent qualities of first-order plotters, some of which have already been described, led to their selection for use in our first attempts to reconstitute the *Ranger* images.

Four additional factors prompted the choice of these instruments: (1) their heighting accuracy (root-mean-square error of spot elevations) is at least three times better than that of a second-order instrument such as a multiplex; (2) the images are separated by a viewing system for each eye, and there is no ghost picture caused by incomplete image extinction by color or Polaroid filters; (3) data pertaining to relative and absolute orientation can be set in and read out; and (4) theoretically, the base-to-height ratio can be set almost to zero.

The instrument that appeared most suitable for recapturing the unorthodox geometry of the *Ranger* imaging system was the AP/2. Numerous contacts were made with the agencies having a plotter of this type in an attempt to arrange a cooperative research effort. The Geodesy, Intelligence and Mapping Research and Development Agency of the U.S. Army Corps of Engineers agreed to incorporate two *Ranger VIII* models ($P_3 18$–$P_4 17$ and A58–A59) into their AP/2 evaluation program. The Geological Survey furnished trajectory data and copy negatives, and a cursory examination of the *Ranger* pictures was made. The major factor preventing a more complete evaluation was the fact that the lowest viewing magnification (approximately 39 times) severely degraded image quality. (This situation could not be corrected without modification of the AP/2, which was committed to many other programs requiring the existing optical system.) Large magnification in any optical viewing system tends to degrade the images to a point where stereo perception becomes difficult, and—to compound the problem—video scan lines, upon magnification, form a strong pseudo-datum that is almost impenetrable. An attempt to alleviate the scan-line interference by optical-diffraction methods and by photomechanical subduing resulted in image degradation of such a magnitude that stereo viewing was not significantly improved.

Removal of the coherent noise by optical-diffraction methods theoretically offers the ideal way to improve the photogrammetric quality of spacecraft television images, but the presently developed instruments have serious deficiencies which prevent their routine use. A development program to correct the shortcomings of optical diffraction is underway and should be completed in about one year. Its results will be applicable not only to video

systems, but also to others, such as electromechanical scanning systems, for removal of coherent noise. In addition, techniques of image enhancement by selective filtering will improve detection of lineation patterns that are useful for geologic interpretation.

A total of five attempts were made to use other first-order plotters for the reduction of *Ranger* pictures, but their limitations did not allow the exact reconstruction of the original orientation. The instruments used were the Wild A-5, AP/C, and Zeiss C-8. One form line map was compiled in the Wild A-5, using rectified prints of *Ranger VIII* A frames 58 and 59.

Time and cost limitations prohibit the modification of first-order plotters for *Ranger* data reduction by the Geological Survey. The most practical alternative was to modify anaglyphic plotters used in base map construction and stereo photogeological interpretation. Use will be made of first-order plotting systems for specific measurement of crater depth-to-diameter ratios from stereo pairs of extreme base-to-height ratios where vertical and horizontal scale differences can be evaluated.

c. Anaglyphic Plotters

A review of the *Ranger* data indicated that the available anaglyphic-type projectors would not accommodate the *Ranger* stereo image combinations without modification of one or more projector components. With the full realization of the effects of not adhering to a general recovery of the geometric taking conditions, two selected *Ranger VII* stereo pairs, P_4186–P_3187 and A198–A199, were set up in BL 30-mm multiplex projectors for stereoscopic evaluation. The following were the major limiting factors in this effort: (1) projector heights above datum were greatly different, (2) base-to-height ratios were very small, and (3) the condensing-lens housings tended to fall off when the projectors were tilted.

Of the two stereo pairs studied, only the base-to-height ratio of the P-frame pair could be met without considerable modification of the projectors. Despite the fact that the proper conditions for an oriented stereo model could not be fulfilled, the models were cleared of parallax in an approximate orientation to determine whether any stereo potential was available. It was found that the floating dot could be fused repeatedly at the same apparent surface. The stereoscopic viewing of the unoriented models was sufficiently encouraging to suggest that the *Ranger* geometry could be recovered with some degree of reliability through further refinements and by the use of other types of plotters. To initiate additional

investigation of multiplex compatability, several BL 30-mm projectors, four Zeiss 46-mm projectors, and approximately half a dozen lens assemblies were procured from the Topographic Division of the Geological Survey.

The major problems in the application of double-projection plotters to photogrammetric reduction images are:

1. Projector supporting frames allow for only a small Z-separation. In this case, Z is defined as the distance along the optic axis from the perspective center of one camera to a point formed by the intersection of a line perpendicular to this optic axis from the perspective center of the other camera. The perpendicular line is the base line. Compatible stereo frames from the *Ranger* series of pictures exceed the Z-limitations of available projectors and require a supporting-frame modification. The complexities arising from a large Z-difference prohibited the redesign of present supporting frames to accommodate the *Ranger* stereo models (designated in Table 1), except for the A58–A59 combination. The detrimental effects are: magnification of the low-resolution pictures, projector instability; extreme depth of focus requiring very small apertures; insufficient model illumination; and lower projector interference with image projection from the upper projector. Projector modifications are planned which take these effects into consideration.

2. The light source is one of the most critical factors in the recovery of stereo models by double projection. The entire field should be illuminated at nearly equal intensity, as errors introduced by varying light intensity and low light level may be large when picture resolution is low. It has been demonstrated that where light intensity varies, warping of the model, similar to the effects of tilting one projector about the y-axis, may occur over different parts of the model. A large Z-separation of the projectors makes it difficult to obtain sufficient and balanced illumination with the systems available at the present. The redesigned projectors will probably incorporate a light source similar to the spotlight type employed on the Kelsh projectors; as the angular field will not exceed 25 deg, full field illumination can be obtained.

3. The depth of focus of any projection system depends upon the lens aperture and focal length. Depth of focus may be defined as the range of image distance, with a fixed object distance within which image points have a circle of confusion smaller than a given

limit. For good viewing, the diameter of the circle of confusion should normally not exceed 0.2 mm.

Because of the large range difference in the usable *Ranger* stereo pairs, the image from only one projector would be well defined if the principal distance and aperture of the two projectors were kept equal. Reduction of the aperture size of the higher projector would increase the depth of focus, but, unfortunately, would also reduce the amount of illumination if present lighting systems were used.

4. The physical size of the projectors is the limiting factor in recovery of the base-to-height ratio. The maximum settings are one to three for the Balplex, one to four for the BL 30-mm, and one to five for the Zeiss 46-mm projectors. If smaller ratios are obtained for any particular projector pair, either part of the field will be blocked out or the projectors will be brought into physical contact before the desired base-to-height ratio has been established.

Miniaturization of the projectors will not prevent interference of light rays by the lower projector in the models listed in Table 1. It will be necessary to shift the geometry from the projector by use of a parallelogram mirror system or a beam splitter.

To test the validity of using an anaglyphic projection system further, a series of rough models were set up using *Ranger VIII* A-, P_3-, and P_4-camera images. The following conclusions were reached:

1. The conditions are environmentally extrinsic to a photogrammetrist. It will require a training period of nominal duration to allow even the superior operator to adjust to the adverse circumstances of the unusual and very weak geometry.

2. The quality of the *Ranger* images permits considerably more latitude in the model setup than is possible with conventional photographs.

The introduction of principal-point error by deliberate displacement of one *Ranger VIII* P_3 frame (the central reticle was not used as the principal point) showed that no visible effects on parallax, scale, or datum occurred until the displacement was approximately 0.5 mm. However, when the displacement was 0.5 mm in the y-direction, the parallax could not be completely cleared from the model, and in the x-direction, appreciable tilting of the datum was noted. The expected effect was a change in vertical scale. When projectors are constructed

to accommodate the camera taking conditions, this experiment will be repeated.

The principal distance in one projector was varied by placing shims under the diapositive. The datum did not tilt visually until the principal distance had been increased by some 7.0 mm, at which point the image from one projector was almost lost.

A double-projection system is desirable for geologic analysis and mapping, base-map compilation, and the establishment of photometric control. Such a system will be constructed to accommodate the unusual geometry of the *Ranger* images and will be used extensively in subsequent investigations.

Appendix
Image-Blur Analysis

It is easier to visualize the blurring process if, instead of considering a camera with a vector velocity V and a fixed lunar surface, the conditions are reversed and a fixed camera and a lunar surface with a vector velocity $-V$ are used.

For convenience, the ground point is represented by X, Y, Z coordinates in a right-hand orthogonal system whose origin is at the ground position of the projected central reticle (principal point), with $+X$ toward the ground nadir and $+Z$ vertically upward. The corresponding picture coordinates are x and y; $+x$ is measured from the principal point along the principal line toward the nadir, and y is perpendicular to x and parallel to Y. With this set of coordinates, the camera tilt t is contained in the XZ-plane, and its value is determined by the following formula:

$$\cos t = \frac{\text{camera altitude}}{\text{slant range}} = \frac{H}{S}$$

f = lens focal length

S = slant range to ground position of central reticle

$$x = \frac{f(X \cos t + Z \sin t)}{S - (X \sin t + Z \cos t)}$$

$$y = \frac{fy}{S - (-X \sin t + Z \cos t)}$$

Differentiation of these expressions with respect to the time would give velocity components, but the results would be unnecessarily complicated. To avoid this, a datum plane perpendicular to the camera axis and passing through the ground principal point is used instead of the Moon's surface. This new plane intersects the lunar surface along the Y-axis, and the dihedral angle between the plane and the lunar surface is the tilt angle t.

The coordinates of a ground point in the new system are given by the equations

$$X' = X \cos t + Z \sin t$$

$$Y' = Y$$

$$Z' = -X \sin t + Z \cos t$$

Picture coordinates in the new system are given by the following equations. These equations are identical to those used for terrestrial vertical photography when S represents the flight height.

$$x = \frac{fX'}{S - Z'}$$

$$y = \frac{fY'}{S - Z'}$$

$$\frac{dx}{dt} = v_r = \frac{f}{S - Z'}\left(\frac{dX'}{dt} + \frac{fX'}{(S - Z')^2}\right)$$

$$\frac{dZ'}{dt} = \frac{f}{S - Z'}V_{x'} + \frac{X'}{S - Z'}V_{z'}$$

$$\frac{dy}{dt} = v_y = \frac{f}{S - Z'}V'_{y'} + \frac{Y}{S - Z'}V_{z'}$$

where $V_{x'}$ and $V_{y'}$ are components of motion perpendicular to the optical axis. If $V_{z'}$ were zero and Z' fixed, then the above equations would describe the usual terrestrial case of vertical photographs and level flight, with ground points imaged as lines. The length of every line smear would be the same, and each would be parallel to the flight path. Variations in Z', small compared to S, will produce only second-order effects in the length of smear lines. In the case of the *Ranger* P images, although Z' will vary with ground X, the narrow taking

angle ensures that X, and therefore Z', will always be small compared to S. Hence, the above argument for the terrestrial case holds also for the *Ranger* photographs.

The effect of $V_{z'}$, which is parallel to the camera axis, is to displace all image points radially from the principal point by an amount proportional to the radial distance; i.e., the image scale is changed. The scale change during the exposure is that due to the change in the slant range during the time the shutter is open.

For example, substituting JPL data for two late frames of the *Ranger VII* P_4 camera,

$t = 32.1$ deg from vertical

$V = 2.62$ km/sec, 25.8 deg from vertical (In this case, V was within 1 deg or so of being within the vertical plane containing the nadir.)

$V_{x'} = 2.62 \sin (32.1 - 25.8 \text{ deg}) = 2.62 \sin 6.3$ deg m/msec $= 0.287$ m/msec

$V_{y'} = 0$ (not quite true, but close enough for blur analysis)

$V_{z'} = 2.62 \cos 6.3$ deg $= 2.60$ m/msec

Exposure time $= 2$ msec

Blur due to $V_{x'} = 2 \times 0.287 = 0.574$ m

Blur due to $V_{z'}$ is due to change in S of 5.2 m

From JPL data,

$S = 20.35$ km for P_4 frame 181

$S = 1.74$ km for P_4 frame 189

$S = 0.519$ km for P_3 frame 190

(A change of S of 5 m will have a negligible effect on image quality, although there is a small amount of radial distortion.)

Lunar curvature is not considered a factor in the last *Ranger* frames. Relief is a contributing element but has relatively minor significance.

2. Experimental Topographic Map of a Small Area of the Lunar Surface From the *Ranger VIII* Photographs

Henry J. Moore and Richard V. Lugn

During the *Ranger VIII* mission, the decision was made to maintain the cruise-mode orientation of the spacecraft rather than to perform a terminal maneuver, in order to obtain extensive stereoscopic coverage of the lunar surface along the flight path. The trajectory and orientation of the spacecraft were such that some of the stereo photographic coverage obtained had a base-to-height ratio that could be accommodated by modification of an available anaglyphic-projection stereo plotter. This Section presents the preliminary topographic results obtained from experiments undertaken to study the problems of design of an appropriate anaglyphic projection instrument. An ER-55 plotter was used.

a. Procedure

Two consecutive A-camera photographs, 58 and 59, were selected for the preliminary experiment (Figs. 23 and 24), mainly because they have a base-to-height ratio that could be used in the ER-55 projector system. They are the second and third photographs from the end of the A-camera series and show details not seen before in this area of the Moon. The photographs include a relatively large crater, and it was thought that the orientation of the shadow within the crater could be used to provide control which would supplement the information provided by the spacecraft telemetry and tracking. As there is considerable vertical separation in camera stations, it was necessary to adapt the supporting bar of the ER-55 so that this separation could be reconstructed to give the proper relative orientation of the projectors (Fig. 25).

No ground control is available on the Moon for mapping at the scale of the high-resolution *Ranger* photographs; it is therefore necessary to depend for control on the position and orientation of the cameras as obtained from spacecraft tracking and from the spacecraft orientation-system telemetry. To solve this problem using an anaglyphic projection system, the geometry of the flight camera positions and the camera orientation are reconstructed with the stereo-plotting instrument. In order to maintain the correct geometry, the ratio of the scale of the diapositives used in the projectors to the scale of the latent image on the vidicon target of the television camera must be the same as the ratio of the projector principal distance to the camera principal distance. As the principal distance of the projector is 55 mm (Ref. 19) and that of the camera is nominally 26.06 mm, this ratio is 2.11. The Omega D-2 Enlarger was used to make the

diapositive plates. Although the use of this enlarger leads to unknown errors, it was considered suitable for a preliminary study. The lack of precise calibration of the camera principal distance, and the alignment and position of the vidicon are additional sources of error in the present photogrammetric use of the *Ranger* photographs. Among other effects, this error leads to a small unknown vertical distortion and tilting of the stereo model. Other sources of error, such as electronic distortions of the image and image blur, were ignored for this experimental study.

To achieve orientation of the projectors, the images were projected onto a level surface separately, and the ratios of the image format boundaries for each frame were set equal to the ratios obtained from the camera-orientation data provided by the Jet Propulsion Laboratory.* As a check on the projector orientations, measurements were then made of the emission angles at the format extremes and at the central reticles. The two planes defined by the optic axes and verticals from the projectors were parallel, and it was established that the optic axes were essentially parallel. The projectors were adjusted until the base-to-height ratio was the same as the computed base-to-height ratio of the two exposure stations. Finally, the ratios of the optic-axis ranges of the two *Ranger* exposure stations were compared with the ratios of the optic-axis ranges of the projectors and found to be in good agreement. The appropriate data are listed in Table 2.

When the projectors were properly oriented, the stereo model appeared clear of y-parallax, and no further adjustments of the projector motions were attempted. It was then assumed that the stereo model represented a model of the actual lunar surface and that it was correctly oriented.

The projector representing the upper exposure station projected the image 87.8 cm, which is well beyond the optimum projection distance of 52.5 cm. Although such a great projection distance results in a poorly defined image, no effort was made to correct this by lowering the projectors because the appropriate corrections would have resulted in interference from the lower projector. No attempt was made to change the position or orientation of the projectors in order to provide a convenient scale for compilation.

The scale of 1:27,400 was determined by comparing the dimensions in the stereo model that could be equated

_____

*Data tabulation for *Ranger VIII* camera A, as amended (1965).
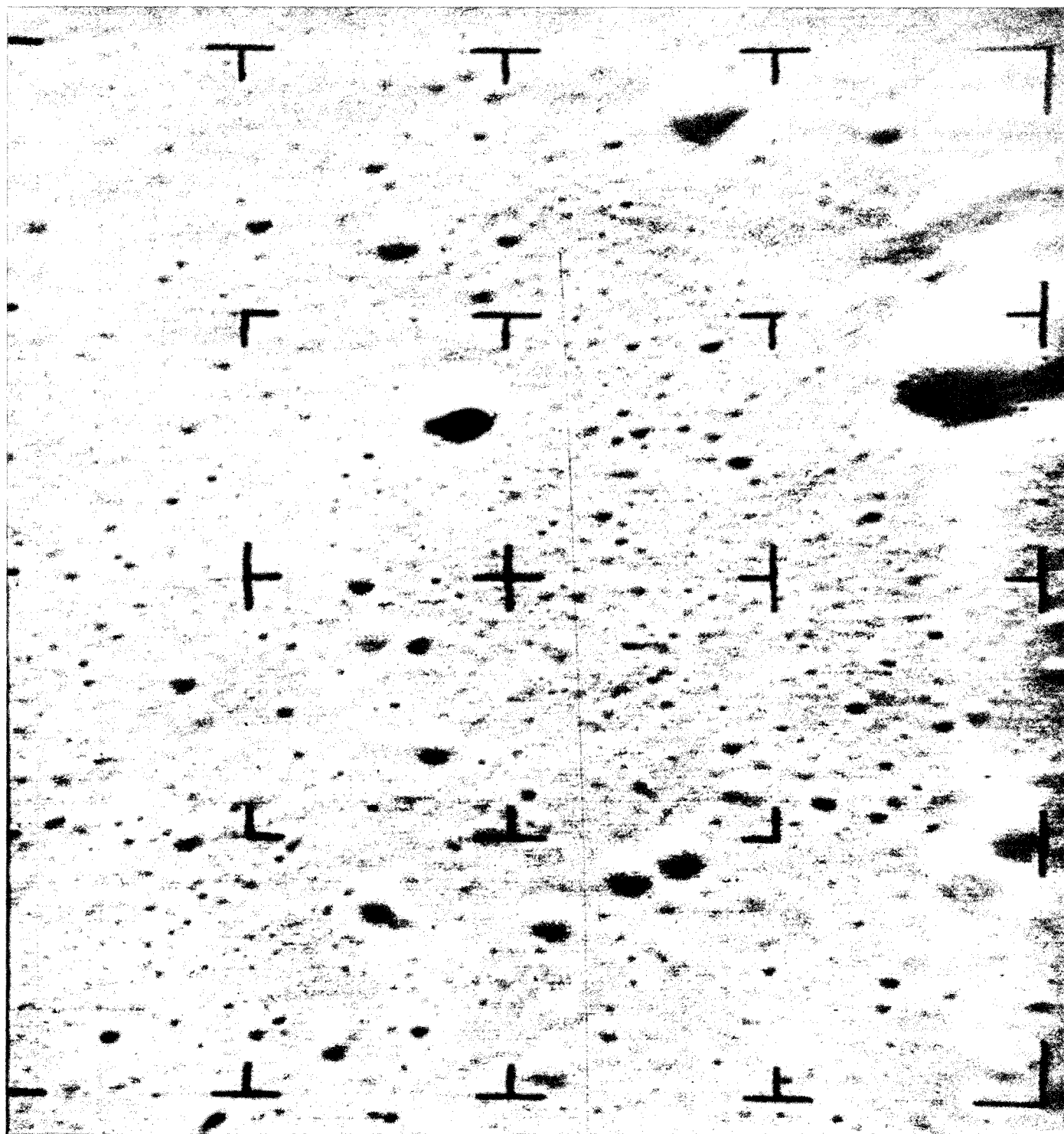
Fig. 23. *Ranger VIII* A-camera photograph 58.
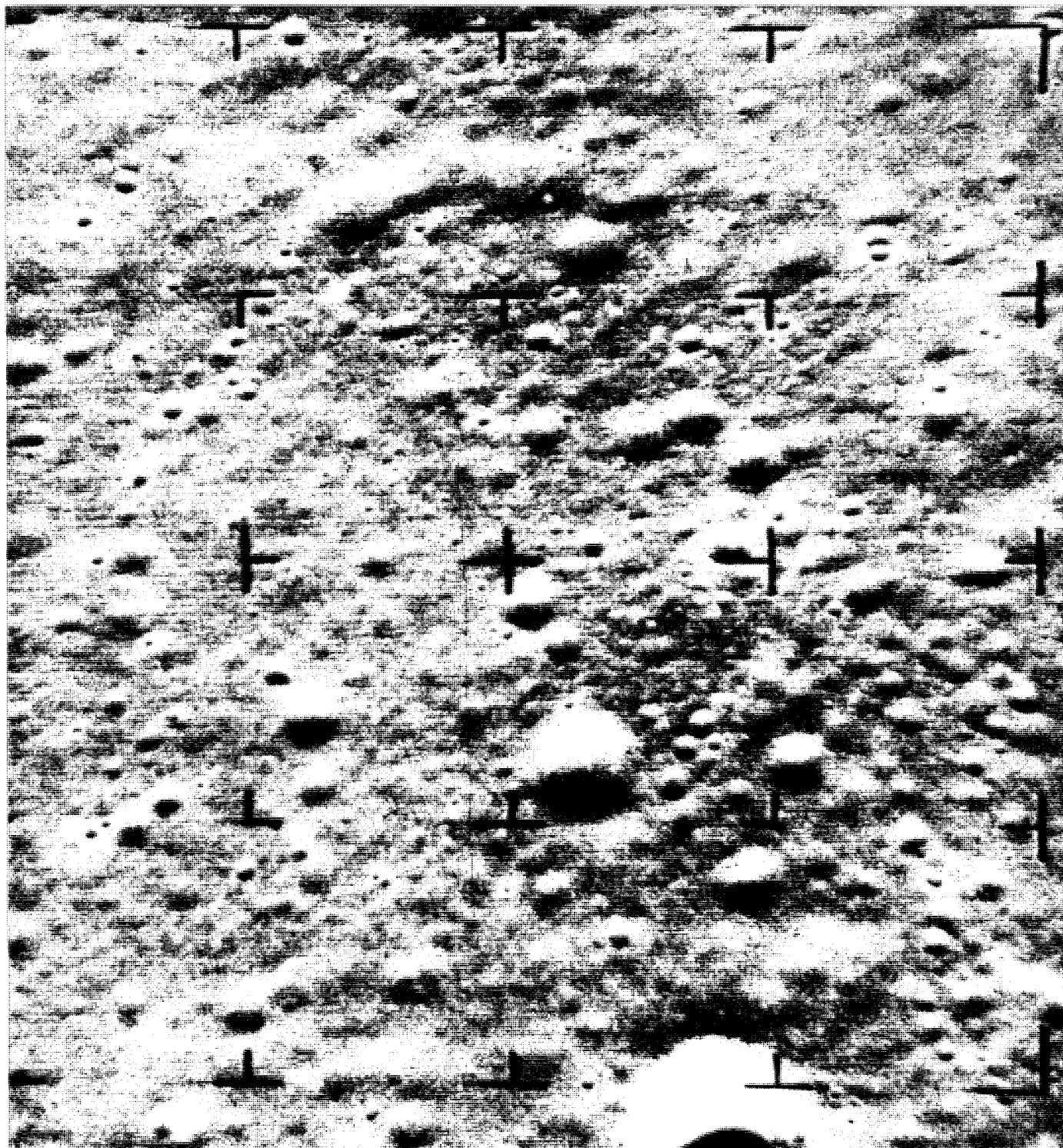
Fig. 24. *Ranger VIII* A-camera photograph 59.
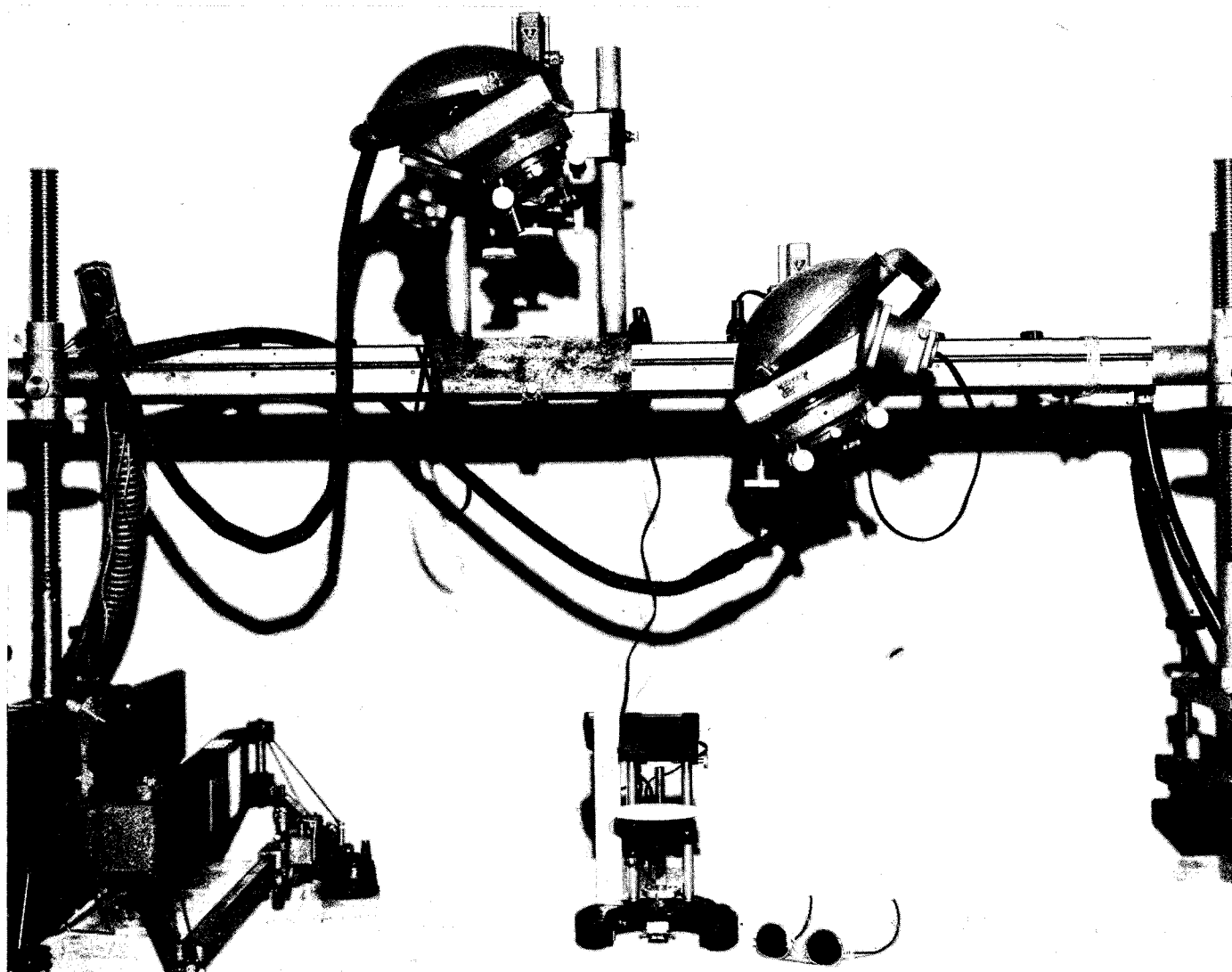
Fig. 25. Photograph of ER-55 plotter, showing setup used for experimental compilation
of topographic map from *Ranger* photographs.

Table 2. Comparison between *Ranger VIII* camera orientations and ER-55 projector orientations

Item No.	Item	JPL data	Model
1	Field of view	25 deg[a]	24.63 and 24.77 deg
2	Optic-axis range (assumed principal point) (A58)	24.77 km	87.8 cm
3	Optic-axis range (A59)	14.51 km	52.7 cm
4	Horizontal distance between principal points on surface	5.16 km	18.6 cm
5	Separation of optic axes	4.53 km	16.3 cm
6	Ratio of items 4 and 3	1/2.82	1/2.83
7	Ratio of items 5 and 3	1/3.20	1/3.23
8	Ratio of items 2 and 3	1.70	1.66
9	Emission angles (A58)		
	NW corner	23.49 deg	22.9 deg
	NE corner	43.86 deg	43.2 deg
	SE corner	39.67 deg	39.8 deg
	SW corner	15.52 deg	15.7 deg
	Center	28.62 deg	28.3 deg
10	Emission angles (A59)		
	NW corner	23.64 deg	23.0 deg
	NE corner	43.91 deg	43.6 deg
	SE corner	39.72 deg	40.2 deg
	SW corner	15.72 deg	16.0 deg
	Center	28.79 deg	28.5 deg
11	Theoretical scales		$1/2.76 \times 10^4$ and $1/2.81 \times 10^4$
12	Measured scale	$1/2.74 \times 10^4$[b]	

[a]Because of a mask on the vidicon faceplate, this angle may be near 24.3 deg.
[b]Obtained using length of north edge of model and corresponding JPL data.

with data received from JPL; ranges and projection distances used in the computation of the scale are listed in Table 2. The altitude of the spacecraft was 21,800 m for the higher camera position. It was arbitrarily decided to compile with a contour interval of 55 m, which represents 2 mm at the map scale.

b. Results

Stereo models obtained from *Ranger* photographs are appreciably degraded compared to models obtained from conventional aerial photographs taken for photogrammetric mapping. Stereoscopic interpretations by two operators were found to be generally the same, although they differed significantly in topographic detail; for example, both operators found that the mare surface was nearly level on the average, although local gentle slopes near 7 deg were present. For the east–west slope of the wall of the largest crater, one operator obtained 31 deg and the other, 26 deg. This result is consistent with

measurements of slopes of craters of slightly larger sizes using shadow techniques (Ref. 20).

The inclination (or slope) of the shadow in the large crater was measured as 14 ±2.0 deg, a result consistent with the local elevation of the Sun at the time of *Ranger VIII* impact. This indicates that the stereo model may have been approximately level, with a possible maximum tilt of 2 deg in the east–west direction.

In detail, the two operators differed significantly. The error of reading the position at a point on the model was found to be about equal to the contour interval used (55 m). Because of the low photogrammetric quality of the photographs, the lack of photogrammetric calibration of the *Ranger* camera, and the errors introduced by the procedures used for this experimental study, the results must be viewed cautiously. One of the experimental maps is shown in Fig. 26, however, to illustrate the product of this technique.

N

0 |——————————| km

EXPLANATION

CONTOUR, APPROXIMATELY LOCATED

SUPPLEMENTARY CONTOUR

DEPRESSION CONTOUR

CRATER RIM

SHADOW OUTLINE

CONTOUR INTERVAL 55 m
ARBITRARY DATUM
SCALE 1:27,500
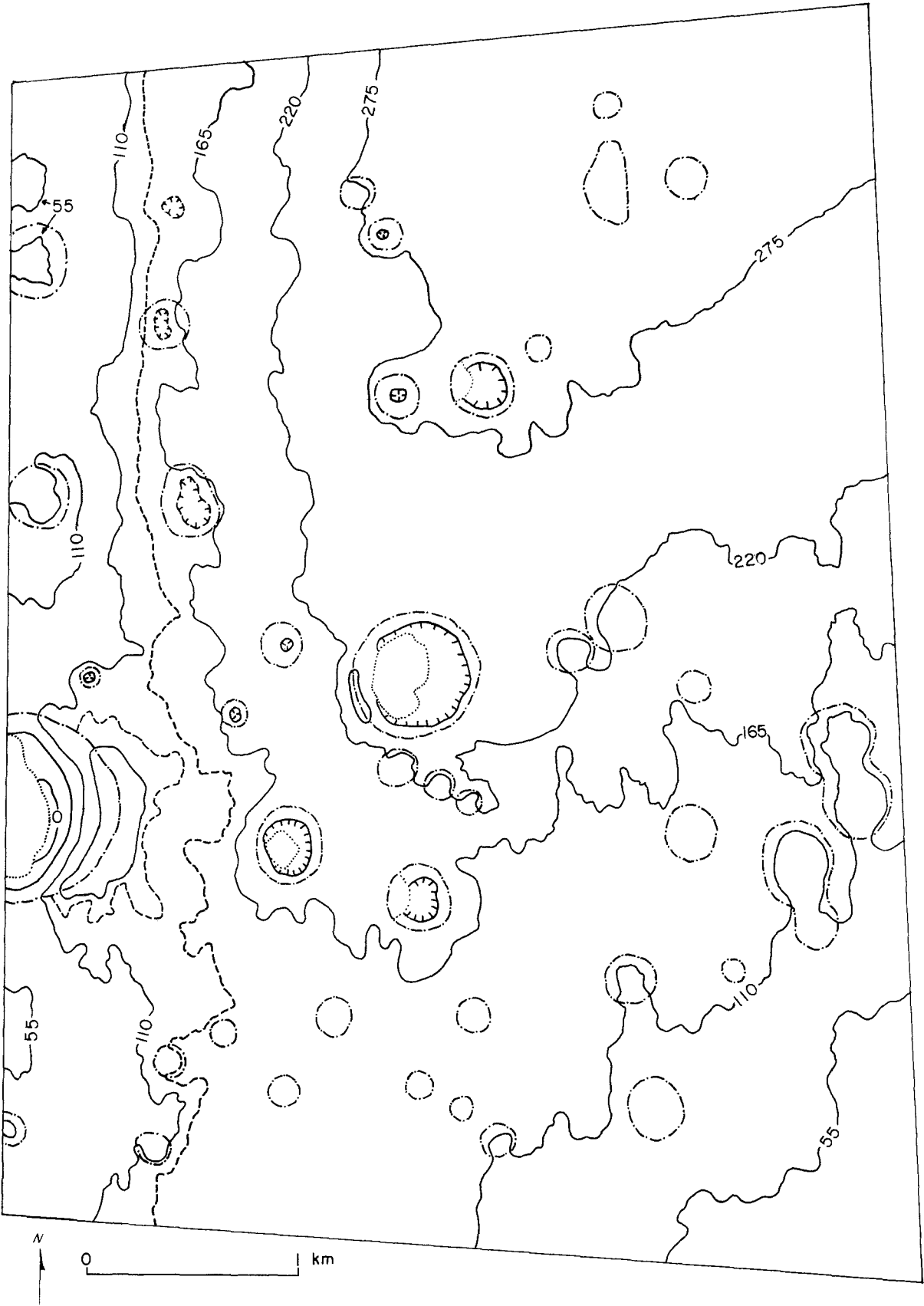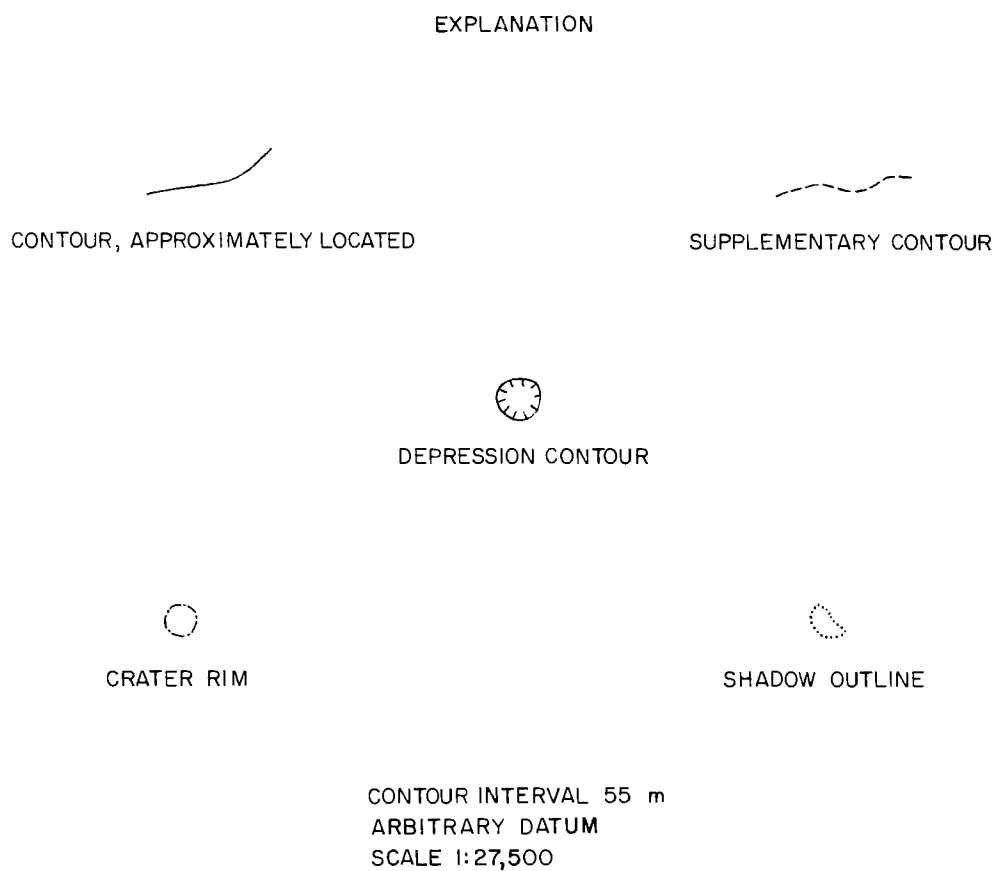
Fig. 26. Topographic map of small area of lunar surface.

c. Conclusions

Although the *Ranger VIII* photographs and the experimental topographic maps do not conform to terrestrial mapping standards, important topographic data are obtainable from selected *Ranger* photographs with the use of applicable photogrammetric techniques. Such data, when combined with photometric measurements from the photographs, can be used to derive the local photometric functions and to provide control over large distances for the preparation of more detailed topographic maps by photometric methods (Ref. 1, pp. 129–130). This investigation is in a preliminary stage, and the techniques used may be significantly improved upon by means of better diapositive printing procedures, corrections for electronic distortions and noises, and modifications of the projectors for accommodation of differences in camera heights, base-to-height ratio, depth of field, and illumination.

D. Use of the Ranger Photographs in Geologic Mapping of the Moon

Two major objectives of lunar exploration are to determine the present structure of the Moon and to interpret its history. The geologist attempts to achieve these objectives by the method of geologic mapping, in which the structures exposed at the surface and the distribution of recognizable stratigraphic units are plotted on suitable topographic or planimetric map bases. The decipherable history of the Moon is recorded in its structure and stratigraphy.

Both the structural and stratigraphic features of a given part of a solid planetary surface are recognized or discriminated primarily by their elements of topographic form and by their array or pattern of physical characteristics, such as albedo, color, and surface texture. Much of these data ordinarily employed in geologic mapping can be recorded in photographs, and, where well exposed, the structure and stratigraphy of a given area can be worked out largely from the data contained in appropriate photographs. Such is the case for the Moon, where the broad features of the geology are being mapped at a scale of 1:1,000,000, chiefly by means of data obtained from telescopic photographs and from direct visual telescopic examination of the lunar surface.

The photographs obtained in the *Ranger* missions provide an opportunity to examine the geology of the Moon locally at much larger scales than has been possible heretofore. The following Sections describe the prelim-

inary results of geologic mapping, at successively larger scales, of selected parts of the Moon on the basis of the data contained in some of the *Ranger VIII* and *IX* photographs. The most detailed study, made by N. J. Trask, has been carried out at a scale comparable to that employed in detailed geologic mapping on the Earth. Many new problems have been encountered in the large-scale mapping; however, it has been shown that the general geologic techniques developed in the earlier telescopic mapping are applicable to the geologic analysis and reduction of high-resolution photographs acquired from spacecraft and that the stratigraphic units thus recognized can be placed within the gross stratigraphic classifications worked out at the telescope.

1. Geology From a Relatively Distant *Ranger VIII* Photograph, Daniel J. Milton and Don E. Wilhelms

The most striking achievement of the *Ranger* missions was the acquisition—in the last seconds before impact—of photographs revealing fine features of the lunar surface whose nature could previously only be inferred by indirect means. The more distant photographs in the sequence from each mission may be less spectacular, but they also contain much new information of interest. They are similar to photographs obtained by Earth-based telescopes but have better resolution (except for the earliest in the sequence). Thus they can be used directly in the small-scale geologic mapping of the Moon carried out by the U. S. Geological Survey.

B-camera photograph 34 of the *Ranger VIII* series (Fig. 27) serves as a good illustration of the methods, product, and, particularly, the problems of lunar geologic mapping. The area shown, which is approximately 100 km on a side, had been covered by preliminary geological maps previously prepared by E. C. Morris and the writers at a scale of 1:1,000,000, or approximately one-third the scale of the photograph. These maps are now being revised, mostly on the basis of the *Ranger* photographs. As yet only qualitative methods have been used, but eventually the descriptions of such features as hummocky terrain and highly cratered surfaces should and will be supplemented by quantitative methods of slope and crater-distribution analysis. Although for this study as much of the mapping as possible was done from B-camera photograph 34, Earth-based photography was used to examine the area at different Sun angles, particularly to determine albedo at full Moon, and other photographs in the *Ranger VIII* series were used to clarify details.
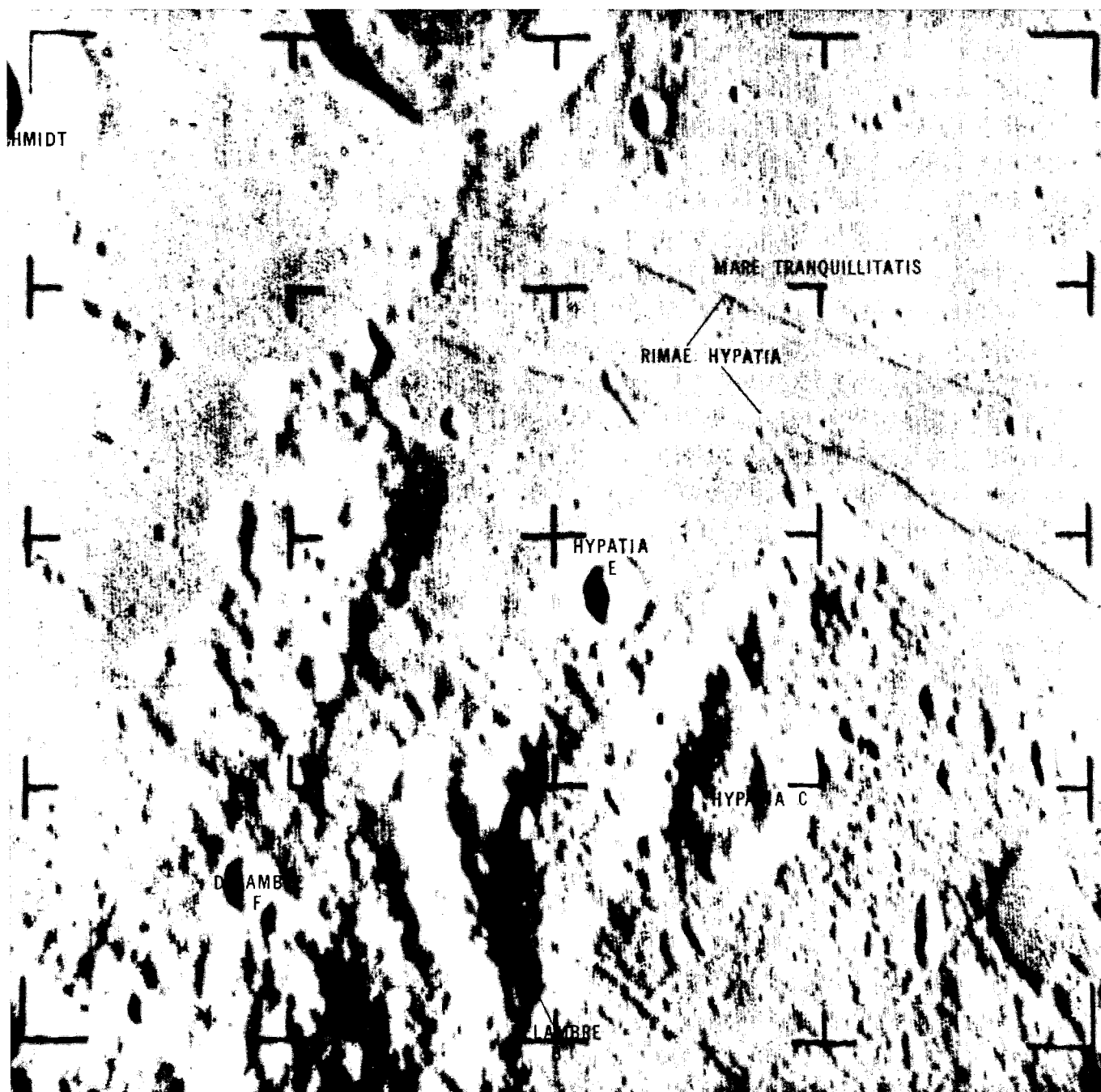
Fig. 27. *Ranger VIII* B-camera photograph 34. (Reticle marks are about 20–25 km apart.)

a. Objectives and Method of Geologic Mapping

Every geologic process produces deposits or structures that partially or completely erase or conceal the evidence of earlier processes. The task of the geologist is to isolate the layers of the palimpsest by the relations of superposition and intersection of the features. From these relations, the chronologic sequence of the events recorded in the layers and structures is deciphered.

In Figs. 28 and 29, some of the salient features shown on B-camera photograph 34 are indicated. The compilation is not complete but serves as a guide to be supplemented by further inspection of the photograph. Figure 28 shows linear features (lineaments); those along which there is a displacement or offset of the surface (faults) are denoted by a solid line with a bar on the down-dropped side, Scarps bounding ridges on the mare surface are marked by a special symbol, and other lineaments are shown by dashed lines. In Fig. 29, more or less round depressions (craters) are outlined. There is a continuous gradation from craters that are sharply defined to ones so subdued as to be near the limit of detection. Those with raised rims, which are generally deeper and have sharp, even crests, are drawn in solid lines; more subdued craters, which are generally shallower, are outlined by dashed lines. A hachured symbol is used to denote the edges of irregular depressions that appear to be transitional between round craters and the depressed areas between parallel lineaments.

Figure 30 is based upon a slightly more interpretive analysis of the photographic data. The lines delineate areas which appear to have different surface texture and albedo. Areas enclosed within a given boundary exhibit similar texture and albedo, suggesting a common origin. A still more interpretive step—to which most of this Section is devoted—is the analysis of these areas as geologic units, which implies a genetic variety and specific age for each. The product of this analysis is the geologic map (Fig. 31).

Classification of mappable geologic units according to relative age is one of the chief goals of geologic mapping. Relative age is determined from the stratigraphic relationship of superposition of the geologic units. On the Moon, the superposition, or overlap, of one unit upon another is in general determined from the areal pattern of the units; the rim material and rays of a ray crater, for example, are recognized as superposed on older geologic units where the rays extend across the older units. In many cases, the stratigraphic relationship of two geologic units cannot be determined solely from their local pat-

terns, and in order to determine relative age, it is necessary to correlate the local units with other geologic units in regions where the stratigraphic relations can be solved.

A basic stratigraphic classification scheme, modeled after the scheme used internationally for geologic mapping on Earth (Ref. 21), has been adopted for the lunar geologic maps prepared by the U. S. Geological Survey. The lunar scheme consists of three parts: (1) a classification of surface materials into formations and groups on the basis of physiographic and optical characteristics, (2) a classification of these units according to stratigraphic sequence, and (3) a corresponding classification or subdivision of lunar geologic time (Ref. 22). The recognized sequence of overlapping geologic units is subdivided into major groups called systems; in ascending stratigraphic order there are the Imbrian, Eratosthenian, and Copernican Systems. Geologic units in the Copernican System overlie the ones in the Eratosthenian and Imbrian Systems, and units in the Eratosthenian System overlie those in the Imbrian System. Geologic units in the Imbrian System overlie still lower, mappable units which have not yet been formally divided into systems but are collectively referred to as pre-Imbrian units. The Imbrian System is further subdivided into two series, the Apenninian (at the base) and the Archimedian (at the top).

The geologic time scale adopted for the Moon comprises (from the beginning of lunar history to the present) pre-Imbrian time and the Imbrian, Eratosthenian, and Copernican Periods, representing the intervals of time during which the materials of the corresponding systems were deposited or formed. The Imbrian Period is divided into the earlier Apenninian Epoch and the later Archimedian Epoch. A task for future lunar exploration will be the determination of approximate dates, in terms of years, for the boundaries of the periods and epochs by isotopic analysis of appropriate samples recovered from the recognized geologic units.

b. Age and Origin of Structures and Geologic Units

Pre-Imbrian structural features. The earliest events recorded in the structure and distribution of geologic units in the area studied are recognizable to a large extent only from structures that have influenced the deposition of later materials. The most prominent of these structures is the arcuate series of broad high ridges, the middle one of which extends from Hypatia E to Delambre B. These ridges constitute the western part of a multiwalled circular feature at least 150 km in diameter. It is apparently a smaller member of a group of very large circular

Fig. 28. Lineaments shown in *Ranger VIII* B-camera photograph 34. (Faults are shown by solid line with bar and ball on downdropped side, mare scarps by solid line with barb pointing downhill, other lineaments by dashed lines. NW–SE trending lineaments on terra belong to the Imbrian sculpture system.)
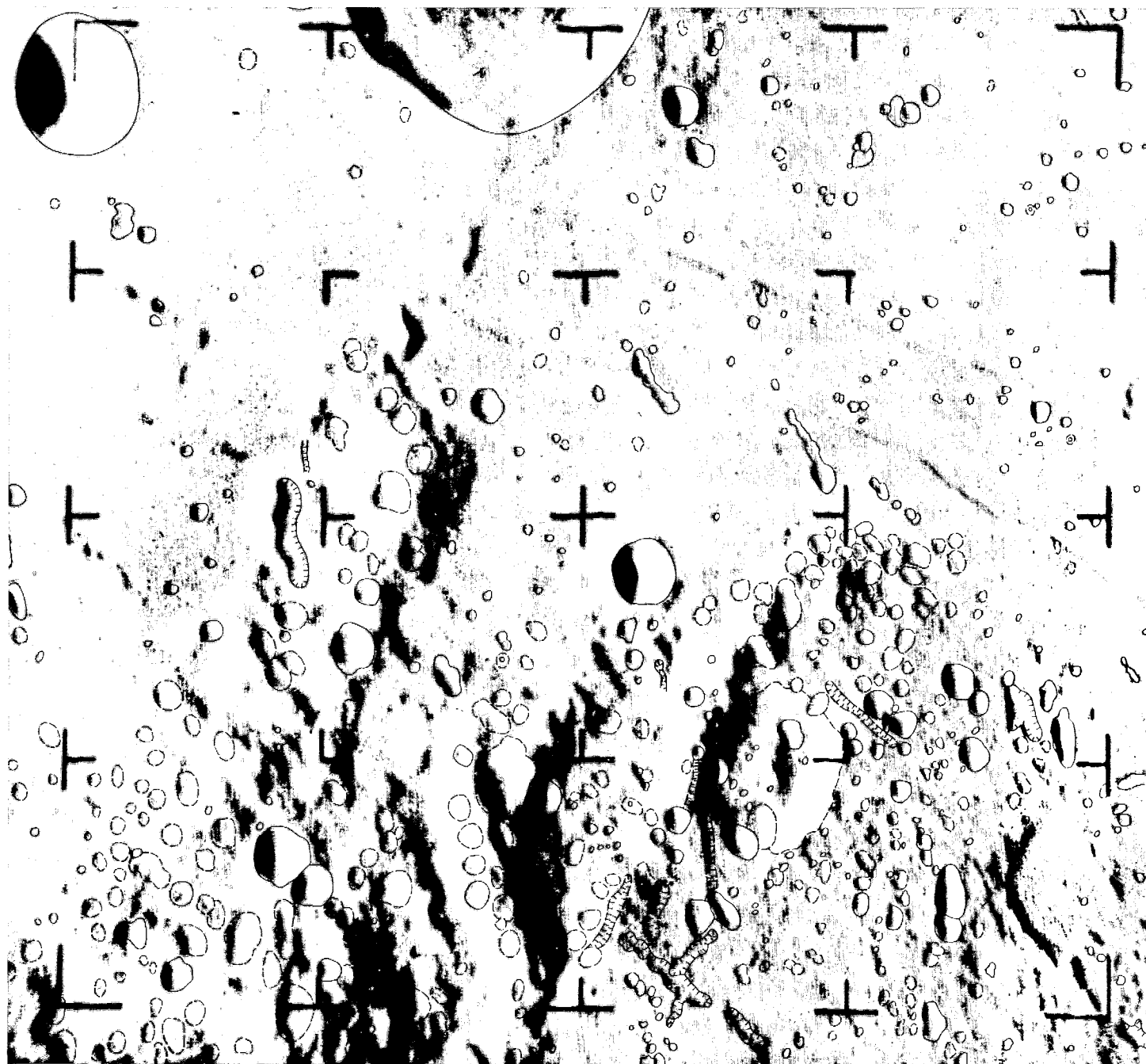
Fig. 29. Craters and other depressions shown in *Ranger VIII* B-camera photograph 34. (Craters with sharp rim crests and raised rims are marked by solid lines, subdued craters by dashed lines.)
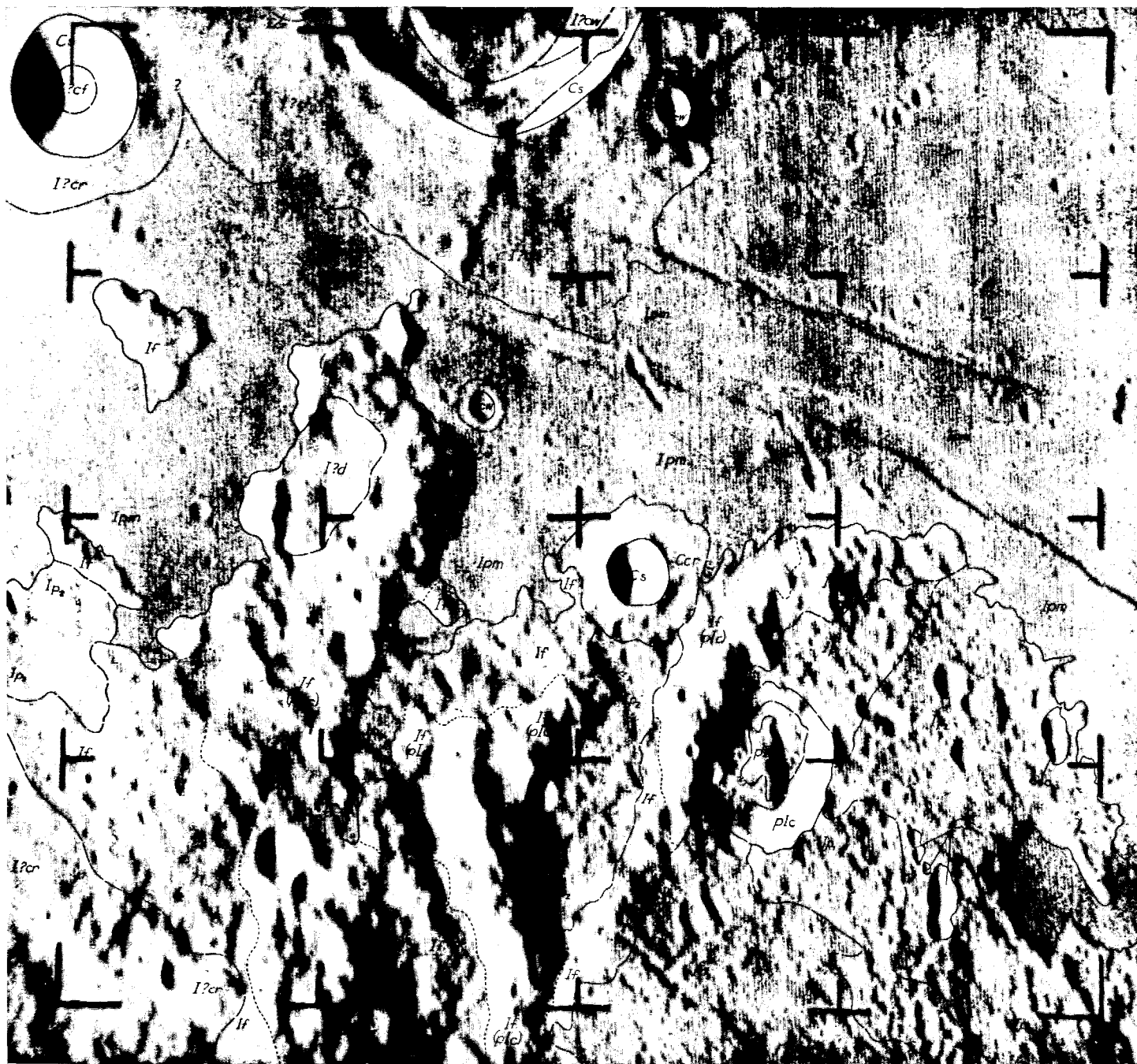
Fig. 30. Geologic units exposed in the area of *Ranger VIII* B-camera photograph 34.
(Explanation of symbols is given in Fig. 32.)

structures represented by the circular mare basins (Ref. 23). As much as this ancient circular feature has been altered by subsequent deformation, its arcuate walls still control the greatest relief in the area. Other large, for the most part ill-defined, structures of similar great age are present, although some are superimposed on and younger than the multiwalled feature. Among these are the crater Hypatia C, an incomplete crater wall curving south from Sabine, and the edge of the Mare Tranquillitatis basin.

Structures and deposits of Imbrian age

Imbrian sculpture and the Apenninian Series. A second major lineament system on the terra, less prominent but more widespread than the ancient arcuate structures, trends northwest–southeast (Fig. 28). In the western part of the map area, this lineament system is represented by close-set ridges and valleys which are superposed on the older, broad arcuate ridges. These are a part of an extensive system of similar ridges and valleys, called Imbrian sculpture by Gilbert (Ref. 24), trending radially away from the Mare Imbrium basin. They are interpreted here as a series of tilted fault blocks. Their pattern is compatible with the hypothesis that the Mare Imbrium basin was formed by impact, which generated a radial fault pattern.

Surrounding the Mare Imbrium basin is a regional geologic unit characterized by a distinctive hummocky topography in which the local relief generally decreases radially away from the basin. This unit is known as the Fra Mauro Formation, after a type locality in the western part of the Moon (Ref. 25), and is interpreted as being a deposit of ejecta from the Mare Imbrium basin. Much of the material around any large impact crater has been ejected with low velocity, forming a rim deposit thinning outward. Fewer but more energetic fragments follow longer trajectories and fall with greater kinetic energy, so that, instead of a continuous deposit of ejecta, they form discrete secondary-impact craters surrounded by local ejecta deposits. The area covered by the *Ranger VIII* photographs lies at a distance from the Mare Imbrium basin at which the continuous deposit of the Fra Mauro Formation is transitional outward into a thin discontinuous deposit, where poorly developed Imbrian secondary craters are more prominent topographically than the ejecta hummocks. This transition zone, mapped as the pitted facies of the Fra Mauro Formation, covers most of the terra west of the central ridge of the map area and appears north of Hypatia C. The Fra Mauro Formation is probably also present on the steeper ridges, but recognition of it is difficult there because the dominant relief is controlled by pre-Imbrian structure. Areas

in which the Fra Mauro Formation is probably very thin and pre-Imbrian rock is near the surface or locally exposed are indicated by dotted boundaries. The depositional hummocks and the secondary-impact craters have a crude orientation radial to Mare Imbrium. It is, therefore, difficult to make a clear distinction between the Imbrian sculpture, produced by faulting, and the Fra Mauro surface texture, produced by deposition and secondary cratering.

The Fra Mauro Formation is the oldest well established and widespread geologic unit in the lunar stratigraphic column; for this reason, it is taken as the basal unit of the Imbrian System, which is the earliest formally defined lunar system, and of the Apenninian Series. In this map area, only the Fra Mauro Formation can be unequivocally assigned to the Apenninian Series.

Archimedian Series. Geologic units assigned to the Archimedian Series in the area studied include three plains-forming units and dome materials on the terra, materials of the craters Sabine and Delambre, and mare material.

Most of the eastern part of the terra in the map area has an appearance fundamentally different from that of the Fra Mauro Formation. Here the terra is characterized by relatively level plains with subordinate craters and irregular elongate depressions. Three plains-forming geologic units have been mapped on the basis of the number and size of craters present.

Where the plains-forming materials are thin, they subdue but do not completely conceal the topographic features of the underlying geologic unit. Thus, the contact of the plains-forming units with the Fra Mauro Formation, which they overlap, is in many places indistinct. A few characteristic hummocks and craters of the latter can be distinguished within the areas mapped as the plains-forming unit. Where the plains-forming materials are thicker, the surface is a level plain with craters and irregular depressions but no intrinsic positive-relief features. The occurrence and thickness of the plains-forming units is apparently controlled by pre-existing structure. The contacts of the units tend to parallel the directions of Imbrian sculpture, perhaps following faults bounding the deeper basins in which the units were deposited.

The distinction between the three plains-forming units is primarily one of crater density, the unit Ip_1 being the most densely cratered and Ip_3 the least (Fig. 28). In

N

0   10   20   30 km
APPROXIMATE SCALE EAST-WEST

GEOLOGY BY DANIEL J. MILTON
AND DON E. WILHELMS

EXPLANATION

COPERNICAN SYSTEM

Csc — Satellitic craters

Characteristics

Shallow craters with low rims. Outlines irregular or composites of two or more merging round craters. Long axis oriented toward Theophilus.

Interpretation

Secondary craters excavated by ejecta from Theophilus.

Ccr — Crater rim material

Characteristics

High albedo. Topography consists of irregular hummocks near rim crest diminishing in size away from the crater. Around smaller craters appears smooth. Grades outward to ray material.

Interpretation

Impact ejecta around crater.

Cs — Slope material

Characteristics

Highest albedo of any lunar materials. Occurs on steep slopes such as crater walls.

Interpretation

Freshly exposed rock, probably both talus and bedrock uncovered during talus formation.

ERATOSTHENIAN SYSTEM

Ecr — Crater rim material

Characteristics

Low albedo, not surrounded by rays. Topography appears smooth or slightly hummocky.

Interpretation

Ejecta from impact craters.

Ecw — Crater wall material

Characteristics

Low albedo. Material on steep to moderate slopes inside craters.

Interpretation

Primarily slump material which has been stable long enough to darken. May include exposed shock breccia and deformed bedrock.

IMBRIAN SYSTEM — ARCHIMEDIAN SERIES

Icr — Crater rim material

Characteristics

Low albedo. Topography around large craters consists of irregular hummocks.

Interpretation

Ejecta from impact craters.

Icf — Crater floor material

Characteristics

Low albedo. Fairly smooth.

Interpretation

Slump and fallback, and possibly later volcanic flows.

Icw — Crater wall material

Characteristics

Medium albedo. Steep to moderate slopes inside craters.

Interpretation

Primarily slump material which has been stable long enough to darken. May include exposed breccia and deformed bedrock.

Ipm — Mare material

Characteristics

Low to moderately low albedo except where covered by ray material. Flat and smooth except for ridges and scarps with very low slopes.

Interpretation

Volcanic flows, may be ash-flow tuff. Possibly covered with ash-fall tuff.

Ipd — Terra dome material

Characteristics

Moderately low albedo. Topography consists of low hill with a single crater on summit, flanks and surrounding area are smooth.

Interpretation

Volcano and volcanic deposits.

Ipl Ip2 Ip3 — Plains forming units

Characteristics

Medium albedo. Form level plains in which craters and irregular depressions are the dominant feature. Ipl is most cratered. Ip3 least cratered.

Interpretation

Volcanic flows, may be ash-flow or ash-fall tuff.

IMBRIAN SYSTEM — APENNINIAN SERIES

If — Fra Mauro formation

Characteristics

Medium albedo. Undulating topography with sublinear, low, convex ridges or low subequidimensional hummocks 1 to 3 km across with rounded crests and irregular slightly elongate to groove-like pits.

Interpretation

Ejecta from Mare Imbrium basin. Both positive features (piles of debris and perhaps single large blocks) and negative features (secondary impact craters) contribute to the relief.

PRE-IMBRIAN

If (plc) — Fra Mauro Formation overlying pre-Imbrian crater material

Characteristics

Albedo same as that of the Fra Mauro Formation. Large elements of the topography controlled by pre-Imbrian crater forms; fine elements controlled by the Fra Mauro Formation.

Interpretation

Areas in which the ruggedness of the pre-Imbrian relief and the thickness of the Fra Mauro are such that both contribute to the total relief. Transitional to areas mapped as If and plc.

plc — Crater materials, undifferentiated

Characteristics

Moderately high albedo. Material in roughly circular areas with moderately rugged relief.

Interpretation

Rim, wall and central peak materials of old degraded craters.

—————— (plc)
Contact

Long-dashed where approximately located or gradational. Dotted where concealed with symbol for buried unit in parenthesis.

Rim of small crater

Craters are of unspecified age and origin. Rim crest sharp and generally raised. May be surrounded by bright halo.

Rim of small subdued crater

Craters are of unspecified age and origin. Rim crest rounded; no raised rim or bright halo visible. Most are probably older, degraded craters.

Mare scarp

Barb points downslope. Gentle slope; may be fault, flow-front, or mantled scarp.

Irregular depression

May be collapse feature or secondary impact crater.

Fault

Linear offset of the surface. Bar-and-ball on apparent downthrown side.

Lineament

Trough or scarp of unknown nature. (May be single fault, graben, buried graben, or depositional feature.)

Fig. 31. Geologic map based on *Ranger VIII* B-camera photograph 34.

general, Ip$_1$ is the thinnest unit, and Ip$_3$ appears to be the thickest, with Ip$_2$ intermediate between them in crater density and apparent thickness. The shapes of the crater-form depressions superposed on the plains units are diverse. Many of the depressions on unit Ip$_3$ are elongate and rimless and may be volcanic collapse features aligned along deep-seated structures.

The plains-forming materials are believed to be volcanic, probably composed of ash from eruptive centers that cannot definitely be identified. The units may have been deposited slowly over a long period of time. All the resolvable craters formed during or since the start of deposition (as well as some older craters) are probably visible at the surface of unit Ip$_1$, whereas most of the craters formed in areas of unit Ip$_3$ during the deposition period may be buried by the youngest volcanic strata.

The precise age assignment of the plains-forming units within the Imbrian Period is uncertain. The Archimedian Epoch of the Imbrian Period includes a series of events that follow a break in the depositional history after the Apenninian Epoch. Near Mare Imbrium, this break is easily recognized, but at the distance from the mare of the area mapped, a distinct break in the depositional sequence is difficult to recognize. The variation in crater density on the plains-forming units suggests that the units have been deposited over a long period of time and that at least the younger ones are Archimedian in age. The latter may, in fact, be contemporaneous with the Procellarum Group, whose material composes most of the maria.

A dome with a single crater on the summit occurs on the peninsula of terra south of the crater Sabine (in the area mapped as unit Id). A narrow depression north of the summit pit is aligned with the pit and may continue onto the dome; however, the moire pattern of the photograph produced by electronic noise makes it difficult to trace the depression with certainty. Taken together, these features resemble a volcano with a summit crater localized on a small rift. The area around the dome is the smoothest part of the terra in the area studied, indicating that a blanket of volcanic material may be spread over about 100 km^2 of the surrounding rolling terrain. Both the photograph used for the base of the map and other *Ranger VIII* photographs that show the dome lack sufficient resolution to permit determination of the stratigraphic relation of the dome material to the adjacent mare material. The lack of superimposed craters suggests that the dome is young, but the area is too small for a valid crater count. Another possible volcanic fea-

ture in the map area is the crater on the west rim crest of Hypatia C, which seems to have a broader raised rim than most other craters, and in which is incised a narrow depression.

The deposits associated with several major craters in or close to the area—particularly Delambre, whose rim material lies in the southwestern corner of the photograph, and Sabine on the north edge—are tentatively assigned to the Archimedian Series. These craters have sharp rim crests, and the rim deposits have relatively few superposed small craters. However, the secondary craters, which normally accompany young craters the size of Sabine, appear to be absent. This suggests that the outermost rim deposits of Sabine may be buried by the upper layers of Procellarum Group mare material. Delambre presents a similar problem. The lack of surrounding secondary craters, which should be abundantly represented on the older terra surface, suggests that the secondaries may have been so modified as to be unrecognizable. It is possible, on the other hand, that craters such as Sabine and Delambre are basically different from large ray craters such as Theophilus and never had associated secondary craters large enough to be resolved in the *Ranger* photographs. If so, the normal criteria for recognizing the superposition of crater-rim deposits are not applicable.

The material at the surface of the maria is younger than any present in the widespread units of the terrae, with the possible exception of unit Ip$_3$, as indicated by crater density and overlap relations at the margins of Mare Tranquillitatis. Correlation, on the basis of crater density, of the mare material in Mare Tranquillitatis with that of Oceanus Procellarum has led to the assignment of the mare material to the Procellarum Group. The Imbrian Period is defined as ending with the completion of deposition of the Procellarum Group.

Structures and deposits of Eratosthenian age. The most prominent structures superimposed on the mare material are the two Hypatia rilles, which appear to be complex graben. An instructive comparison may be made between these rilles and a graben east of Searles Lake, California (Fig. 32), which shows a similar, slightly *en echelon* pattern. According to G. I. Smith of the U. S. Geological Survey, who furnished the photograph, a fault crops out near the contact of the bedrock of the mountain front with the alluvium of the valley, and dips westward into the basement rocks beneath the alluvial valley fill. In the most recent movement on this fault, the upper plate
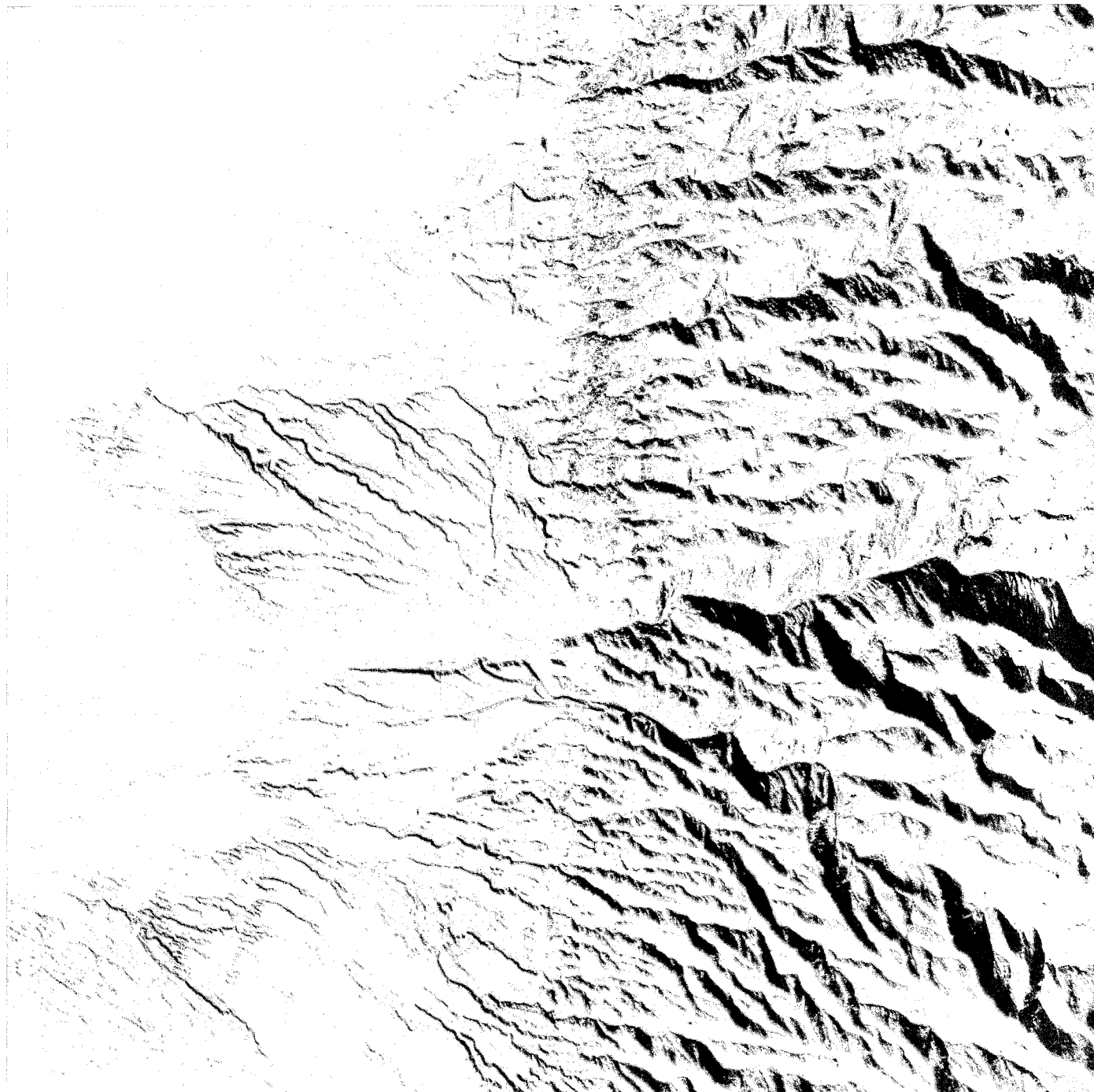
Fig. 32. Vertical aerial photograph of graben on E side of Searles Lake, San Bernardino County, California.
(Small buildings near white dump W of graben give scale.)

slipped toward the valley, carrying the overlying alluvium with it. This resulted in tensional stresses in the thin wedge of the alluvial deposits, which, in turn, led to the collapse of the graben. In the case of the Hypatia rilles, tensional stresses may have been caused by compaction of the mare material itself, rather than by tectonic forces in the underlying material. Secondary craters of Theophilus, a large crater of early Copernican age, appear to be superimposed on the rilles. The rilles are therefore probably of Eratosthenian age.

In addition to the rilles, a number of small craters with relatively dark rim deposits are scattered over the surface of Mare Tranquillitatis. These deposits are assigned to the Eratosthenian System.

Craters and deposits of Copernican age. Several small and large craters of Copernican age lie in or near the map area, as well as some of the rays and secondaries of the crater Theophilus, which is located over 300 km to the southeast. Many of the smaller craters, with elliptical outlines and sharp lips—particularly those in the eastern part of the area—are probably Theophilus secondaries. The lighter areas just visible on the mare in the eastern part of the photograph are rays of Theophilus.

Erosion and mass wasting affect all exposed surfaces on the Moon. The process primarily responsible for these effects is probably micrometeorite bombardment, which continually redistributes near-surface material. On steeper slopes, gravity will cause a net downhill migration of the bombarded material, which is augmented by occasional landslides or rock falls on over-steepened slopes. The high albedo of many steep slopes suggests that fresh material has been exposed recently or is continually being exposed. Such areas are mapped as Copernican slope material. Older or gentler slopes are darker, indicating that the material at the surface is sufficiently stable to permit darkening, presumably by solar irradiation.

c. Summary of Geologic History

The inferred geologic history may be summarized in tabular form:

Pre-Imbrian time	Formation of a multiwalled ring structure, Hypatia C and smaller craters.

Imbrian Period

Apenninian Epoch	Deposition of the Fra Mauro Formation and secondary-impact cratering of old surface by material ejected from the Mare Imbrium basin. Faulting of the Imbrian sculpture system.
Archimedian Epoch	Intermittent volcanism on terra, forming plains and dome units. Faulting and local subsidence, largely along rejuvenated older faults. Delambre, Sabine, Schmidt, and smaller craters formed. Filling of Tranquillitatis basin by Procellarum Group mare material (probably volcanic).
Eratosthenian Period	Small craters formed. Deformation of the mare material by faulting to form the Hypatia rilles and, probably by faulting or folding, to form the mare ridges.
Copernican Period	Hypatia E and smaller craters formed. Rays and secondary-impact craters formed by material ejected from crater Theophilus. Sliding on steep slopes, exposing fresh talus or slope material.

2. Intermediate-Scale Geologic Map of a Part of the Floor of Alphonsus, John F. McCauley

With the success of the *Ranger VII, VIII,* and *IX* missions, it has become possible to carry out regional geologic mapping at scales much larger than those used in previous telescopic studies. By delineating the local stratigraphic units revealed in the high-resolution *Ranger* photographs, the new mapping can portray the detailed physical history of the lunar surface more effectively. The results of a preliminary study of the problems of geologic mapping at the larger scales are presented in this Section.

Inspection of the *Ranger IX* photographic sequence revealed that A-camera photograph 66 and B-camera photograph 74 provided contiguous coverage of approximately 640 km² of the northeastern part of Alphonsus at nearly the same scale (Fig. 33). The area is
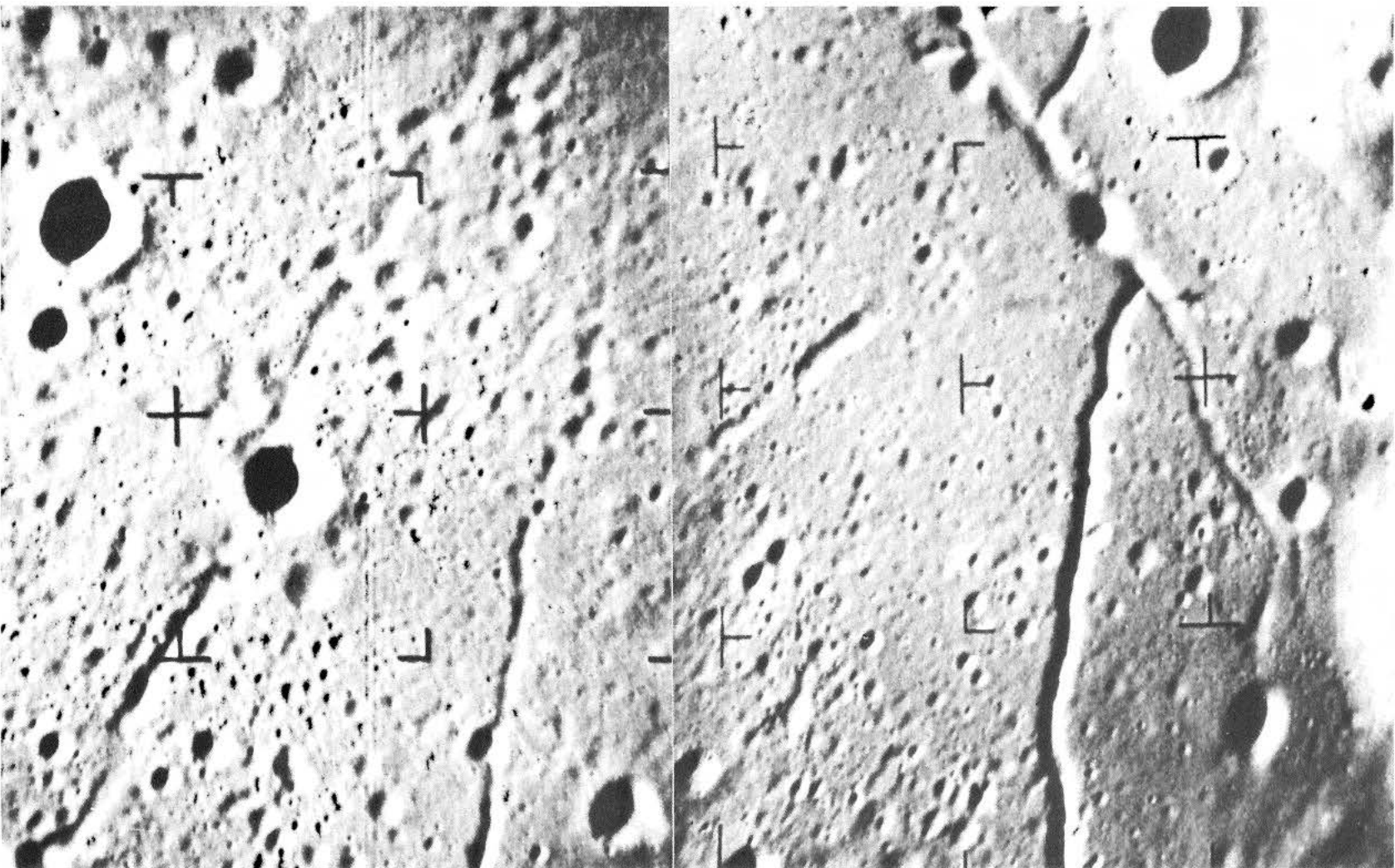
Fig. 33. Mosaic of *Ranger IX* A-camera photograph 66 and B-camera photograph 74, used as base for geologic map of Fig. 34.

geologically complex and of a size appropriate for regional geologic mapping at a scale of approximately 1:100,000. As this scale is an order of magnitude larger than that used for telescopic geologic mapping, the increase in visible detail requires the definition of a variety of new stratigraphic and structural units.

The map prepared for this study shows the distribution of a complex stratigraphic sequence of crater materials and smoother basin-floor materials, all of which have contributed to the filling of the floor of Alphonsus. Nine geologic units, many of which are new subdivisions of units previously recognized in 1:1,000,000 mapping (Ref. 26), are described and classified according to relative age. The work is preliminary, however, and subject to considerable refinement, and the map is intended primarily to demonstrate the technique of geologic mapping at an intermediate scale. When quantitative topographic data have been derived by photogrammetric and photometric techniques, the geologic mapping can be carried out more rigorously. This type of geologic investigation will be applicable not only to other *Ranger* photographs but also to those acquired by unmanned and manned lunar orbiting spacecraft.

a. Stratigraphy of the Floor of Alphonsus

The part of the crater Alphonsus shown on the map exhibits a variety of crater materials, and relatively smooth and more widespread geologic units. Distinctions between the individual geologic units are made on the basis of morphology, slope angles as determined by shadows, surface texture, crater density, and relative albedo. The age relations between the units are established by observed stratigraphic superposition, intersection of structures, and regional correlation. The total crater density on the floor of Alphonsus is higher than on the maria, and a greater variety of crater types can be recognized. A more complex geologic history can, therefore, be deciphered in Alphonsus than on the maria.

Imbrian (?) System. Crater-wall material along the walls of Alphonsus (I?cw) is the oldest geologic unit in the map area (Fig. 34). This wall unit, which appears only along the extreme eastern edge of the map, has not been studied as closely as the floor units of Alphonsus, which are the major subject of this Section. The Alphonsus wall material is characterized principally by moderate local relief and an albedo slightly higher than that of the brightest floor unit. It occurs on closely spaced large hills and terraces which form the walls of the main crater. Typical slopes of the hillsides range from about 5 to

more than 10 deg. Numerous small craters appear on the crests of individual hills, but fewer are recognizable on the flanks. The variety of crater types and the overall crater density on the Alphonsus wall material are less here than on the oldest of the floor units (Icfm in Fig. 34). The contact with the adjacent floor units is well defined locally by subtle linear depressions, which are too indistinct for accurate mapping at this scale. In other places, the contact is indefinite or gradational, suggesting that particulate wall materials have moved downslope and buried the original contact between units. Instability of materials on the hillsides may account, in great part, for the lower observed crater density.

The Alphonsus wall material is considered the oldest geologic unit in the area because of its position in the crater wall and because it is overlapped at the edge of the crater floor by a series of smoother floor units which partially fill the original crater. The exposed wall material may consist either of a regional deposit derived from Mare Imbrium or of deformed and altered material derived entirely from the pre-Imbrian crater Alphonsus. It is tentatively assigned an Imbrian age, pending further detailed regional studies.

Imbrian System. Cratered floor material (Icfm) occurs along the western edge and in the east central part of the map area. It is a regional unit which occurs widely over the floor of Alphonsus and is typified by a crater density significantly greater than that of the average mare (see Sections B1 and B3). A wide variety of types of small craters is present, the most common of which have subdued rims. Irregularly shaped depressions and circular indistinct craters abound. Because of its high crater density, this geologic unit has a rougher surface texture than the other floor units. It has an intermediate albedo which is approximately the same as that of the younger, superposed, smooth floor materials.

Within the map area, the cratered floor material is the oldest floor unit; it is overlapped by several other floor-filling units, and its surface is characterized by more numerous craters. A long history of bombardment by interplanetary and secondary objects is inferred from the numerous partially destroyed or subdued and indistinct craters present on its surface. The unit represents a blanket of material masking the original relief on the floor of Alphonsus. It may consist of regional material derived from Mare Imbrium, intercalated with ejecta from local impact events and with volcanic material that may have partially filled Alphonsus early in its history. The detailed lithology of this unit is likely to be variable

GEOLOGY BY JOHN F. MC CAULEY
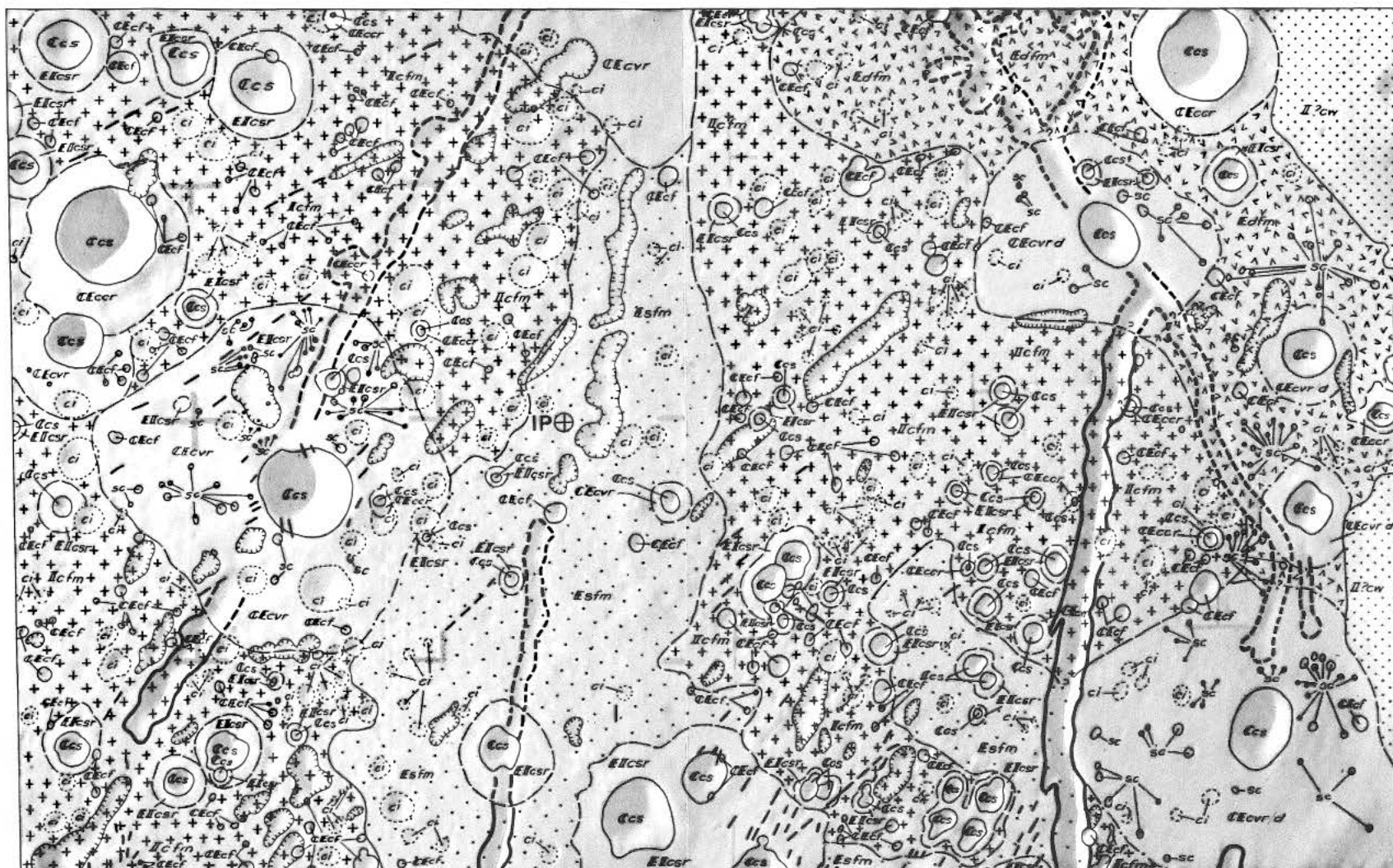
PHOTOGRAPHIC BASE FROM
FA 601, FB 582; R IX

N

IP ⊕ IMPACT POINT
LAT 12.9°S, LONG 2.4°W

0   5   10 Km
Scale
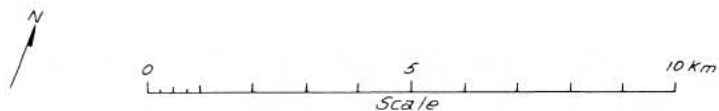
EXPLANATION
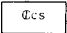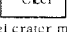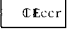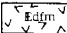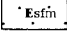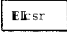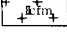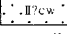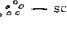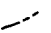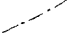
AGE	SYMBOL	DESCRIPTION	INTERPRETATION

Stratigraphic Units

COPERNICAN

Ccs — Crater slope material

Slope materials on the inner walls of craters. Slopes generally exceed 10° and are either in shadow or lack detail because of overexposure on the lighted side.

Granular material which has moved downslope under the action of gravity after the formation of the crater.

CEcf — Funnel crater material

Crater materials inside small craters with no recognizable rim deposits, the internal shape of these is similar to a funnel. In some cases the interior walls appear to be convex upward (dimple craters). The interior slopes generally exceed 10°.

Craters that may result from collapse or subsidence of materials into subjacent cavities. They frequently are aligned along major structural trends and occur on all the floor units. They may exhibit a considerable age range.

CEccr — Concave rim material

Crater rim materials that are concave upward in profile from the edge of the rim deposit to the sharply upturned crater lip. Albedo ranges from medium to high (bright halo craters).

Young craters, probably of impact origin. The rim units consist of finely crushed, shocked materials derived from the older floor materials. The lack of blocks and satellitic craters suggests that the rim materials are of relatively fine grain size.

CEcvr/d — Convex rim material

Crater rim materials that are gently convex upward; cvr d represents dark rim material. Numerous small craters occur on the rim deposits.

Young craters related to structural depressions; probably of volcanic origin. The rim units consist mostly of ash sized fragments. The presence of numerous small craters on the surface of the rim deposit suggests that large coherent blocks may have been ejected from the central vent.

ERASTOSTHENIAN

Edfm — Dark floor material

Relatively smooth material of dark albedo covering part of the floor of the crater on its eastern side. This material is associated with structural troughs and dark halo craters.

Volcanic ash covering the older floor units. Derived from both circular and linear vents aligned with structural depressions.

Esfm — Smooth floor material
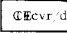
Relatively smooth material of intermediate albedo covering the floor to the northeast of the central peak. This material is also associated with structural troughs and vents.

Volcanic ash covering the older floor units. Derived from both circular and linear vents aligned with structural depressions. The lighter albedo suggests a difference in composition from the darker floor material (Edfm) present elsewhere.

Ecsr — Degraded rim materials

Degraded crater rim materials; subdued in form and appear to be mantled by a thin blanket of surficial material not shown on the map.

Degraded craters thinly mantled by reworked floor material or by volcanic ash. May originally be either of external or internal origin.

IMBRIAN

Ecfm — Cratered floor material

Relatively rough material of intermediate albedo present in irregular patches over the entire crater floor. It exhibits a higher crater density and diversity of crater types than the other floor units.

Oldest basin filling unit. May consist of volcanic materials intercalated with debris from meteorite impact.

IPcw — Alphonsus wall material

Topographically higher, hilly unit of intermediate albedo along the eastern side of the crater. May contain a number of distinct lithologic units which are not here distinguished. It is older than the above floor units.

May consist principally of debris derived from Mare Imbrium but materials of local derivation are also probably present.

Structural Symbols

(ci) — Indistinct craters

Craters that are shallow in relation to their diameter; roughly circular in form, with no recognizable rim deposits. The interior slopes are less than 10°; appear to be thickly mantled older craters.

Old craters of either internal or external origin heavily mantled by younger floor materials. In some cases these circular depressions may be the result of gentle subsidence or differential compaction.

Irregular depressions

Irregularly shaped to elongate or linear depressions, generally shallow and with interior slopes less than 10°. Some are associated with chains of indistinct or funnel shaped rimless craters.

Collapse or subsidence structures generally mantled by younger materials.

— sc

Satellitic craters, small rimless craters that occur abundantly on the rim deposits of the convex rimmed craters.

In general form these craters are similar to funnel craters (CEcf) but their concentration in rim units (CEcvr d) suggests that they may have formed by impact of coherent blocks expelled from a central vent.

Edge of rille. Solid line indicates a sharply defined edge; short dashes indicate a poorly defined edge in some places buried by younger material.

Represents the topographic edge of a structural trough formed by normal faulting.

Lineament or indistinct linear element, may be subtle ridge, depression or unresolved chain of craters.

Contact, dashed where approximately located or where contacts are subdued and inferred to be mantled by surficial material.

Contact between different facies of the same rock unit. Used to differentiate rim and floor units of same texture and albedo.

Fig. 34. Preliminary geologic map of part of Alphonsus.

and its history complex. It is assigned an Imbrian age because of its basal position in relation to the other floor units and its high crater density, which is characteristic of Imbrian units.

Materials of Imbrian or Eratosthenian age. Crater-rim material of subdued form (EIcsr) occurs next in the stratigraphic sequence. The outer boundaries of the rim units are difficult to estimate because of the lack of sharp topographic expression; in addition, the contacts may be obscured by a thin blanket of surficial material that is not shown on the map. The slopes on the inner walls of the craters are generally greater than 10 deg, but their average lower reflectance suggests that they are less steep than the slopes on the walls of younger craters. In some places, the craters in this class are aligned and appear to be structurally controlled (as in the northwest corner of the map area), although the majority seem to be randomly distributed over the cratered floor material (Icfm). The units may include primary- and secondary-impact craters and volcanic vents. The abundance of these craters on the Imbrian (?) cratered floor material and their scarcity on younger units suggest that they are Imbrian or Eratosthenian in age.

Eratosthenian System. Smooth floor material of intermediate albedo (Esfm) occurs in the central part of the map area. It is closely related spatially to a series of linear depressions, which it partially mantles; it is smoother than the cratered floor material and has a lower crater density. The smooth floor material appears to mask a rougher topography of underlying cratered floor material of Imbrian (?) age and is therefore believed to be superimposed on the older floor unit. On the basis of crater density, the smooth floor material is placed in the Eratosthenian System. The unit is inferred to be primarily of volcanic origin on the basis of its areal pattern and apparent relation to possible linear vents.

The eastern part of the map shows a smooth floor unit (Edfm) that is similar in texture to, but darker than, the smooth floor material just described and that is also characterized by a relatively low crater density. This unit overlies the Imbrian (?) cratered floor material but, within the map area, does not lie in contact with the brighter smooth floor material. The similarity in crater density suggests that the two units are of about the same age (Eratosthenian), with the darker material possibly being slightly younger. Because the dark floor unit is also spatially related to linear features, it is believed to be of volcanic origin.

Materials of Eratosthenian or Copernican age. Crater-rim deposits with exterior profiles that are convex upward (CEcvr/d) occur adjacent to or on the Eratosthenian smooth floor materials. Two mappable facies are distinguished on the basis of albedo, one characterized by intermediate and the other by low albedo (the dark halos of craters). No sharp break in slope is present near the lip of the associated craters, and the craters are clearly related to structural depressions that are partially filled by the rim deposits. Both the dark- and intermediate-albedo rim units have numbers of distinct, superimposed, small rimless craters. Although the latter are difficult to distinguish in form from other small craters, they have been classified as "satellitic" craters (sc). They may have been formed by the impact of large blocks of cohesive material ejected from the central vent. Craters having convex rim deposits are interpreted as vents surrounded by blankets of volcanic ash which has been superimposed on older flat-lying blankets composed of the same general volcanic material (Esfm, Edfm). Because they clearly overlap the Eratosthenian smooth floor materials, these units are assigned to the Eratosthenian or Copernican Systems.

Craters with rim deposits that are sharply concave upward near the crater lip (CEccr) appear to be randomly but sparsely distributed over the entire floor of Alphonsus, and are superimposed on all the other units previously described. Some of the smaller craters of this class are surrounded by a bright rim deposit, or halo; other concave crater-rim materials show little or no difference in albedo from the surrounding geologic units. The two largest examples are in the northeastern and northwestern corners of the map area. The rim topography is smooth, and no satellitic or secondary craters have been noted. These craters are interpreted as being of impact origin and, on the basis of morphology, albedo, and stratigraphic position, are assigned an age ranging from Eratosthenian to Copernican. The brightest deposits are believed to be the youngest.

Small, rimless depressions of funnel shape, generally less than 200 m in diameter, are common throughout the map area. The material within these depressions is labeled CEcf on the map (Fig. 34). In some cases, the interior walls of the funnels appear to be slightly convex upward; these are the so-called "dimple craters." They become increasingly more numerous with decreasing size. The structural fabric of the floor of Alphonsus controls their distribution (see Section B3). The funnel craters are present on all the recognizable stratigraphic units and, therefore, are among the youngest features observed

in the area. They may result from the drainage of loosely compacted surficial material into subjacent fissures and cavities. If so, they might be termed "negative vents," in contrast to convex-rimmed craters that are formed by the surface deposition of material ejected from below.

Copernican System. Copernican slope material (Ccs) has been mapped on the inner walls of all those craters having interior slopes that significantly exceed 10 deg, as determined by the presence of sharp umbral shadows within the crater. This unit is generally of high albedo, as determined under full-Moon conditions, and is inferred to consist of fragmental material in an unstable condition that intermittently moves downslope.

b. Structural Features

No detailed analysis of the structural features seen in the area will be presented here, since, in Section B3, Carr gives a structural analysis of the entire floor of Alphonsus at a variety of map scales. Descriptions of the structural features observed are given in the explanation of the map (Fig. 34). Worthy of special note are the indistinct craters, which are shallow, generally circular depressions having no recognizable rim deposits. These craters are particularly common on the cratered floor unit (Icfm); they may be degraded older craters, or they may have been formed as the result of the gentle subsidence of surface materials.

c. Geologic History

From the preliminary geologic map of part of the floor of Alphonsus, it is possible to reconstruct the sequence of events that led to the present configuration of the crater floor. The original crater is pre-Imbrian, and its walls (I?cw) and floor may have been covered with material derived by ejection from the Mare Imbrium region (Fra Mauro Formation). Additional study is required to determine the nature of the wall material more precisely. Subsequently, the crater was partially filled by a sequence of younger deposits (Icfm), which may be in part volcanic in origin and in part derived from local and distant meteorite-impact events. This material was thoroughly cratered during a substantial interval of time after its initial deposition, and faulting and volcanism occurred during and after the early episode of basin filling and cratering. A number of large and small vents formed along major fissures, and a smooth blanket of material (Esfm) was deposited locally on the crater floor. The blanket is thickest near the vents and fissures and thins to a feather edge at the contacts

with the older cratered surface. Another blanket, composed of darker materials (Edfm), formed along the eastern wall of Alphonsus, possibly somewhat later in lunar history. During the entire interval of time from the original blanketing of the crater floor to the time of late volcanic activity along the eastern wall, faulting, subsidence, and drainage of material into subjacent cavities was occurring along with continued cratering by impact.

3. Preliminary Geologic Map of a Small Area in Mare Tranquillitatis, Newell J. Trask

The data received from future unmanned lunar spacecraft, and eventually from manned spacecraft landings, will permit the construction of topographic and geologic maps of the Moon at scales comparable to those used in detailed geologic investigations of the Earth. As a first step in the development of the techniques for large-scale lunar geologic mapping, a preliminary geologic map has been prepared for the small area in Mare Tranquillitatis covered by the overlap of *Ranger VIII* A-camera photographs 58 and 59 (Fig. 35). The map (Fig. 36) was made in conjunction with the topographic map of the same area compiled by Moore and Lugn, described in Section C2.

As the present lunar geologic mapping program of the U. S. Geological Survey is being carried out at a scale of 1:1,000,000, most of the geologic units studied are necessarily of regional extent. The map shown here has a scale approximately 30 times larger and gives a more complete indication of the density of contacts and diversity of materials that will be encountered within small areas on the lunar surface. Lunar terrain of the type covered by the geologic map (a ray-free mare terrain) will probably be encountered in early manned exploration. The scale of approximately 1:27,400 in Fig. 36 is large enough to allow the plotting of geologic contacts and structures that would be encountered in short manned traverses. By comparison, systematic geologic mapping of the United States is currently proceeding at scales of 1:62,500 and 1:24,000. Additional, improved geologic and topographic maps of selected areas on the Moon, at approximately the same scale, will be needed to plan missions for maximum return of significant scientific information.

a. Method of Geologic Mapping

The geology shown in Fig. 36 was worked out by stereoscopic examination of *Ranger VIII* A-camera photo-

Fig. 35. *Ranger VIII* A-camera photograph 59, showing area of geologic map of Fig. 36.

N

0   1 KILOMETER

CONTOUR INTERVAL 55 METERS
ARBITRARY DATUM

GEOLOGY BY NEWELL J. TRASK
BASE MAP BY H.J. MOORE AND R.V. LUGN

EXPLANATION

COPERNICAN SYSTEM

Bright crater material

Bright crater rim material (Cbr) and material on walls of craters with bright rims (Cbw). Craters have sharp rims with outer profiles that are concave upward. Craters probably of impact origin.

Intermediate crater material

Crater rim material of medium albedo (CEmr) and material on walls of craters with rims of medium albedo (CEwr). Crater rims are sharp. Craters are probably of impact origin.

Intermediate crater material, subdued

Material like CEmr and CEmw but crater rim is subdued.

Material of rimless pits

Material in circular depressions with steep walls and a bowl-shaped floor with no raised rim. Pits are probably collapse features.

Cratered cone material

Material on rims (CEcr) and walls (CEcw) of low nearly conical mounds with summit craters. Cratered cones may be small volcanos.

Dark crater material

Crater rim material with low albedo (same albedo as mare material in this area) (Edr) and material on walls of craters with dark rims (Edw). Rim material locally exhibits subdued radial ridges. Craters probably of impact origin.

Dark crater material, subdued

Crater rim material with low albedo, occurring on craters with low, rounded raised rims (Edrs) and material on walls of craters with dark, subdued rims (Edws). Origin of craters uncertain.

Chain crater material

Material of small aligned overlapping craters of similar morphology. Many craters have distinct raised rims; others have very low rims. Probably most chain craters are volcanic; a few may be lines of secondary impact craters.

ERATOSTHENIAN SYSTEM

Material of indistinct craters

Material in shallow depressions with very low rims and gently sloping interior walls. Origin of craters uncertain.

IMBRIAN SYSTEM

Mare surface material

Material that has probably been repeatedly stirred by formation of small unresolved craters. Most of the material is probably fragmental and locally derived from underlying volcanic flows and ash falls.

Contact, dashed where approximately located, dotted where covered.

Mare ridge, arrow shows tapered end.

Rounded mare scarp showing trace of foot of scarp. Barb points downslope.

Irregular depression, may be a collapse feature.

Lineament

Subdued scarp, shallow linear depression or line of very shallow irregular depressions. Probably reflect fractures in lunar subsurface.

Fig. 36. Preliminary geologic map of a small area in Mare Tranquillitatis. (Base map is topographic map prepared by photogrammetric methods from *Ranger VIII* A frames 58 and 59 by Moore and Lugn, Section C2.)

graphs 58 and 59 with a conventional stereoscope and the ER-55 plotter used for the topographic map. Study of the rectified model projected by the plotting device permitted a close-up stereoscopic view of the surface and added important details to the study. The projected model was particularly helpful in the delineation and study of crater rims.

At present, the discrimination of geologic units in the *Ranger* photographs depends on observation of the same physical characteristics used to distinguish map units on the small-scale geologic maps prepared from Earth-based photography and visual telescopic observation (Refs. 27 and 28). Albedo and topographic form are the principal characteristics of the lunar-surface materials on which the discrimination of mappable units is based. In the case of the large-scale *Ranger* photographs, data on normal albedo are lacking at sufficient resolution for mapping. Relative albedo can be estimated from the *Ranger* photographs by using the topographic map of Moore and Lugn to distinguish the differences in brightness that are due solely to differences in slope. Three relative units of albedo—dark, medium, and bright—have been visually estimated for the photographs. A program of quantitative determination of albedo from the *Ranger* photographs is under development by the Geological Survey.
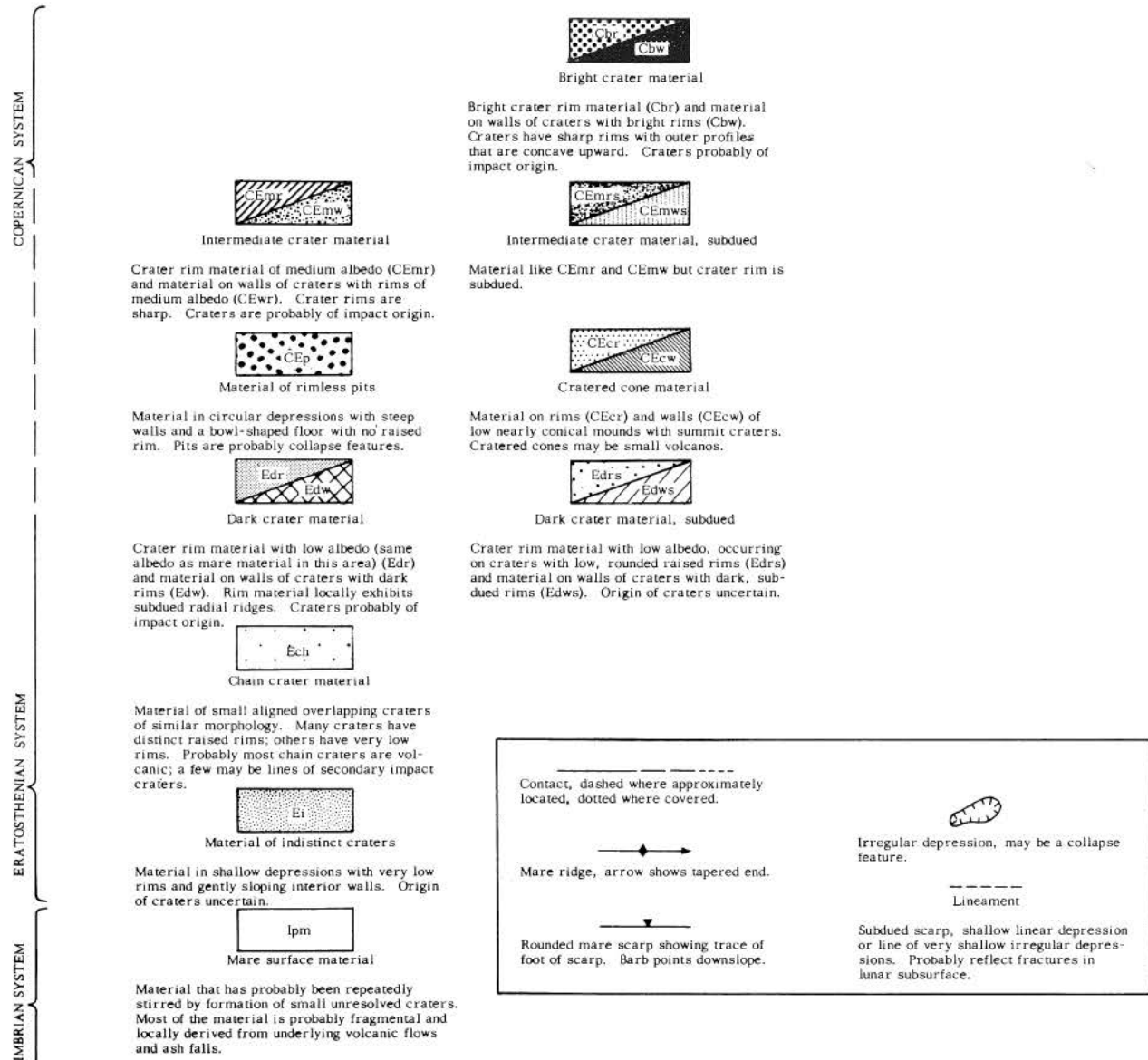
b. Stratigraphy

The geologic units on the mapped part of Mare Tranquillitatis consist of crater materials and the regional materials on which the craters have formed. The crater materials can be classified on the basis of crater morphology and the relative albedos of the crater rims. The wall materials show differing degrees of brightness but are steeper than the crater-rim materials; their albedo can only be estimated by means of detailed photometric investigation of the photographs. The general outline of the classification scheme adopted is shown in the explanation to the map of Fig. 36.

In addition to grouping similar materials and separating those that are different, the classification scheme used on the map provides the dimension of time by indicating the order in which the materials have formed. Where two types of material are in contact, the principles of superposition and intersection should indicate their relative age. Most of the materials have essentially the same albedo, however, so that the overlap relations between many of the units are not well defined. Overlap relations between some of the materials are indicated on the map by the termination of the older unit against

the younger. In order to place all of the map units in a stratigraphic column, it is necessary to adopt a model of the structure of the mare at the map scale. The model used is essentially that of Shoemaker (Ref. 1, pp. 75–134), which postulates that most of the craters on the mare are due to impact, but also recognizes that some of the craters may be collapse features of internal origin, as suggested by Kuiper (Ref. 1, pp. 9–73). At the scale of this model, the mare surface has been covered with craters several times over, so that the original surface material is no longer present. As successive cratering wears down crater rims and fills crater bottoms, the degree to which a crater is subdued is an index of its age. The model also suggests that the material beneath the surface of the mare has, on the average, a higher albedo than the material at the surface because of the effects of ultraviolet radiation and solar-proton bombardment. Thus, the brightness of the ejecta around an impact crater is also an index of age, with the brightest materials being the youngest. The geologic relations found in the map area are all consistent with the model as outlined above. Additional mapping at small scales should eventually produce a self-consistent geology that will indicate the most likely model of the lunar surface.

In the following paragraphs, the geologic units on the map (Fig. 36) are discussed in order of ascending stratigraphic sequence, referred to the standard systems of the lunar stratigraphic column as defined by Shoemaker and Hackman (Ref. 22), and Shoemaker (Ref. 29).

Imbrian System. The geologic unit occupying the relatively featureless parts of the area between the mapped crater materials is referred to as mare material. The whole series of *Ranger* photographs indicates, of course, that this material is not featureless but is covered by small craters with diameters down to 1 m. The small craters cannot be mapped at the scale of Fig. 36, however. In previous geologic reports, which were based on telescopic photography and observation (Refs. 22 and 29), the material of the mare itself, as contrasted with its surface layer, has been assigned to the Procellarum Group of the Imbrian system. The smoothness of this material when viewed telescopically and its occurrence in depressions have led to its interpretation as a series of volcanic materials (Ref. 29). The depth to unaltered volcanic material probably varies widely over the map area.

Eratosthenian System

Material of indistinct craters. Some of the most abundant materials in the quadrangle occur in and around

very gentle depressions which have low rims and gently sloping interior walls. The walls of the depressions cast no shadow on the floors. The raised rims are distinguishable on the stereo model of the ER-55 plotter, but the gentle slopes of the rims could not be shown on the topographic map, as their relief is less than the contour interval. The albedo of the materials of indistinct craters is the same as that of the intercrater material mapped as mare material.

Because of the high degree of modification and the low albedo of their materials, the indistinct craters have been assigned to the Eratosthenian System. This system includes those materials formed after the maria but before the rayed craters (Ref. 22). The indistinct craters are interpreted as worn-down impact and volcanic craters. The original form of any given crater cannot be determined.

Chain-crater material. The material occupying rows of craters having similar morphology is mapped as chain-crater material. All gradations may be found between chains of craters with well-defined, raised rims and lines of very shallow, irregular, rimless depressions that are mapped as lineaments. Most of the chain craters are aligned parallel to a system of lineaments occurring in the same area.

All of the chain-crater material has been placed in the Eratosthenian System because of the subdued nature of most of the crater rims and the fact that many of the chains are overlapped by materials that are also assigned to the Eratosthenian System, although a few may be younger. The strict parallelism of many of the chains with the regional system of lineaments leaves little doubt that they are of internal origin. The raised rims are probably caused by the venting of ejected material around the margins of the craters.

Dark-crater materials. Materials of craters which have rims with the same albedo as the mare material and walls sufficiently steep to cast shadows are common in the map area and are shown as dark-crater materials. Most of the dark craters have subdued rims, but three of them have relatively sharp rims. One of the latter is the large crater that dominates the western side of the map area. Its outer rim is markedly concave upward and contains distinct radial ridges that resemble in pattern the radial ridges in the rim deposits of small experimental impact and explosion craters (Figs. 13 and 15). The topographic map shows that the rim of this crater is higher on the east side than it is on the north and

south. Unfortunately, the west rim is not covered by the stereo model, but in the photographs it appears to be lower than the rim on the east side.

The dark-crater materials are placed in the Eratosthenian System because of their low albedo and the fact that they are overlapped in places by brighter materials of younger age. The subdued dark craters are taken to be modified sharp craters, but their original form cannot now be determined. The large crater with a sharp rim in the western half of the area may be post-Eratosthenian in age. The asymmetry of its rim may indicate that it is a secondary-impact feature (Ref. 30).

Materials of Eratosthenian or Copernican age

Material of rimless pits and cratered cones. Rimless pits are circular depressions with steep walls and bowl-shaped floors; cratered cones are low, nearly conical mounds with summit craters. Both types of features are rare. Their albedo is the same as that of the mare material and the dark-crater materials.

These pits and cones are relatively sharp features, whose age is uncertain and whose original form and albedo are not known. Both features are unlike any known impact structures. The rimless pits apparently were formed by the drainage of material through a vent, while the cratered cones look like small terrestrial volcanoes with summit calderas.

Intermediate-crater materials. Craters with rims exhibiting an albedo intermediate between the albedo of the dark-rimmed craters and that of the bright-rimmed craters are moderately abundant. All the examples of such craters are small. They have rims that appear to be sharp and concave upward, with the exception of one crater in the northeast corner of the map, which has a moderately subdued rim. The materials of medium albedo extend beyond the areas occupied by the topographically raised rims and have a somewhat irregular outline.

Copernican System. Craters with bright rims are scattered over the map area, but are slightly less abundant than craters with rims of intermediate albedo. They are similar in all respects to the latter, except that none of the bright-rimmed craters have subdued relief. The materials of high albedo extend well beyond the observable raised rims and overlap the materials of some of the darker craters in places.

Both the overlap relations and the brightness of the crater rims indicate that the materials of the bright-rimmed craters are the youngest in the map area. They are accordingly assigned to the Copernican System. They are probably of impact origin.

Materials of craters with rims of medium and high albedo overlap darker materials at several places in the map area, indicating that the lighter materials are younger. This relation is consistent in all the *Ranger VIII* photographs. No examples of darker material overlapping brighter have been noted. There is also no evidence in any of the *Ranger* photographs that the bright-rimmed craters have been modified by the formation of later, relatively young collapse craters; most of the indistinct craters and subdued craters are probably old, eroded features. The young, bright craters have sharp rims and exterior profiles that are concave upward. The stratigraphic succession in the map area indicates that lunar-surface materials darken with time and that a concurrent process of erosion wears down sharp features such as crater rims.

c. Structure

Mare ridges and scarps. A few low ridges and broad, rounded scarps, mostly with a north–south orientation, are present in the map area. This orientation coincides with the dominant trend of more prominent nearby ridges and scarps on Mare Tranquillitatis. Relief of the prominent north–south scarp in the northwestern quarter of the area is shown on the topographic map. The gentle ridges have much less relief and are not revealed by the map. Their age cannot be determined by mapping in this one small area.

Lineaments. The remarkably widespread system of lineaments on the lunar surface is well represented in the map area, with the greatest concentration appearing in the southern half. The lineaments are subdued scarps, very shallow linear depressions, and lines of shallow linear depressions. The straight sides of some crater walls lie along lineaments or their extensions. An azimuth–frequency plot (Fig. 37) of the lineaments shown on the map reveals a marked preferred alignment in the north-west–southeast and northeast–southwest directions. As the stereo model on which the surface trends of the lineaments were measured is rectified, the azimuths are believed to be accurate to 1 deg.

The regularity of the lineaments indicates that they are of internal origin (Ref. 29) and are probably the reflection of a system of fractures or joints in the lunar
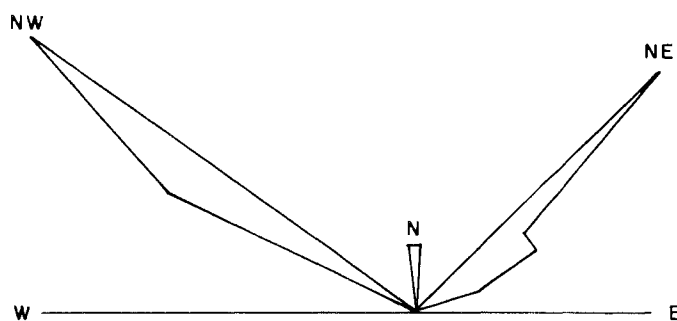
Fig. 37. Azimuth–frequency diagram of lineaments within map area of Fig. 36.

subsurface. It is worth noting that, on the Earth, fractures can propagate upward to the surface from bedrock through essentially unconsolidated material. In western Canada, lineaments are present in nearly unconsolidated glacial deposits ranging from a few feet to several hundred feet above bedrock (Ref. 31), and their orientations are generally similar to those of the fractures and joints in the nearby exposed bedrock. The presence of closely spaced lineaments on the lunar surface thus does not rule out the possibility that the lunar surface material is only weakly consolidated.

Irregular depressions. Very gentle, rimless depressions with irregular outlines have been mapped as irregular depressions. They are shown by a structural symbol and most likely were formed by collapse of the surface materials.

E. Utilization of High-Resolution Photographs in Manned Lunar Geologic Investigations

Harrison H. Schmitt

The primary goals of geologic investigation of the lunar surface are to determine the stratigraphy and structure of the outermost parts of the Moon and, from these data, to decipher the Moon's history. The ultimate purpose of such an investigation is to make an interpretive comparison of the Moon with the Earth and, eventually, with the other terrestrial planets. Both unmanned and manned exploration will be required to achieve these geologic goals. Man's active role on the lunar surface will be to obtain the observations, the samples, and the measurements of physical properties that cannot be obtained by remote sensing from the Earth or from space near the Moon. On the other hand, the geologic and engineering data that can be obtained from photographs similar to those taken during the flights of *Rangers VIII*

and *IX* will form the basis of plans for future manned exploration. The following discussion illustrates how the geology of areas portrayed by the *Ranger* photographs (or by similar photographs to be acquired from lunar orbit) can be of importance to the planning of geologic field work in early manned missions and indicates the nature of some of the scientific data that can be expected to accrue from geologic studies carried out on the lunar surface.

1. Geology of Mare Tranquillitatis as Shown in the High-Resolution *Ranger VIII* Photographs

The last few *Ranger VIII* frames confirmed that many small features on Mare Tranquillitatis are similar to those photographed on Mare Cognitum by *Ranger VII*. Features associated with ray material predominate in the largest-scale photographs of Mare Cognitum. Similar features are present locally on Mare Tranquillitatis; however, some of the features shown in *Ranger VIII* photographs, such as B-camera frame 90 (Fig. 38), may be more characteristic of mare material itself and may have been formed by processes connected with the deposition of the mare material or by tectonic processes that are currently active within the mare.

The resolution of the last *Ranger VIII* frames is sufficient to permit a preliminary morphological classification of mare craters and depressions and a determination of the stratigraphic relationships of materials associated with these craters. Figure 39 is a geologic map of materials present in the area covered by B-camera frame 90. Some additional data from the last A- and P-camera frames were used in the compilation of this map. The stratigraphic relations and possible origins of the features shown are discussed below; they will be used later to illustrate the planning of a manned geologic investigation of the area.

a. Stratigraphy

The many craters observed on the last frames of *Ranger VIII* can be assigned to six morphological categories: (1) sharp-rimmed craters, (2) convex-rim craters, (3) funnel craters, (4) dimple craters, (5) low-rim craters, and (6) indefinite-rim craters. The materials associated with these craters. Figure 39 is a geologic map of ma- of crater with which they occur. The smooth-appearing material between recognizable craters has been mapped as mare surface material; it undoubtedly contains many unresolved small craters. Although the relative ages of many of the crater materials are indicated by their over-

lap relations, their place in the standard lunar time scale of Shoemaker and Hackman (Ref. 22) is uncertain. Craters with bright-rim material are assumed to have formed during the Copernican Period. The mare material is classed as Imbrian; it is probably covered by a thin layer of surficial debris of younger age. The large, indefinite-rim craters are classed as Imbrian or Eratosthenian. All other materials are given an indeterminate Copernican or Eratosthenian age.

Imbrian System. The mare surface material is assigned to the Imbrian System. Any surficial deposits of impact-shattered debris that may be present are probably mostly derived from local lava flows or ash deposits of the Procellarum Group.

Materials of Imbrian or Eratosthenian age. Materials on the rims and walls of poorly defined craters and depressions in the mare material are mapped as indefinite-rim crater materials. The crater rims are gently convex upward but are very low. The walls have very low slopes. The shape and general alignment of the craters suggest that they may be degraded composite secondary craters (Ref. 1, p. 81). On the other hand, they may be structurally controlled subsidence features of the mare, as subsidence features with similar shapes are present on the surfaces of both lava flows and nuée ardente deposits on Earth. A strong northwest alignment of the large indefinite-rim craters is parallel with the alignment of rows of small depressions and lineaments in the southeast part of the map area; the craters and lineaments may be related. The origin of the indefinite-rim crater materials is uncertain, and they cannot be assigned an age more definite than the general one of Imbrian or Eratosthenian.

Materials of Eratosthenian or Copernican age

Materials of low-rim craters. Two craters in the map area are circular in outline, with well defined but very low rims (one is the large, nearly flat-floored crater appearing in the southeast corner of the map). The material of these craters is mapped as low-rim crater material. The slopes of the outer rims are all less than 5 deg; the steepest slopes on the walls are approximately 15 deg. Blocky crater-wall material in the large, low-rim crater appears to consist partly of relatively coherent, possibly solid blocks imbedded in the wall. These blocks may be fragments of the crater wall broken off by impact or fragments of an impacting body that have come to rest on the wall. From its subdued form, however, the crater appears to be of such an age that original irregularities of this type would have been worn down by
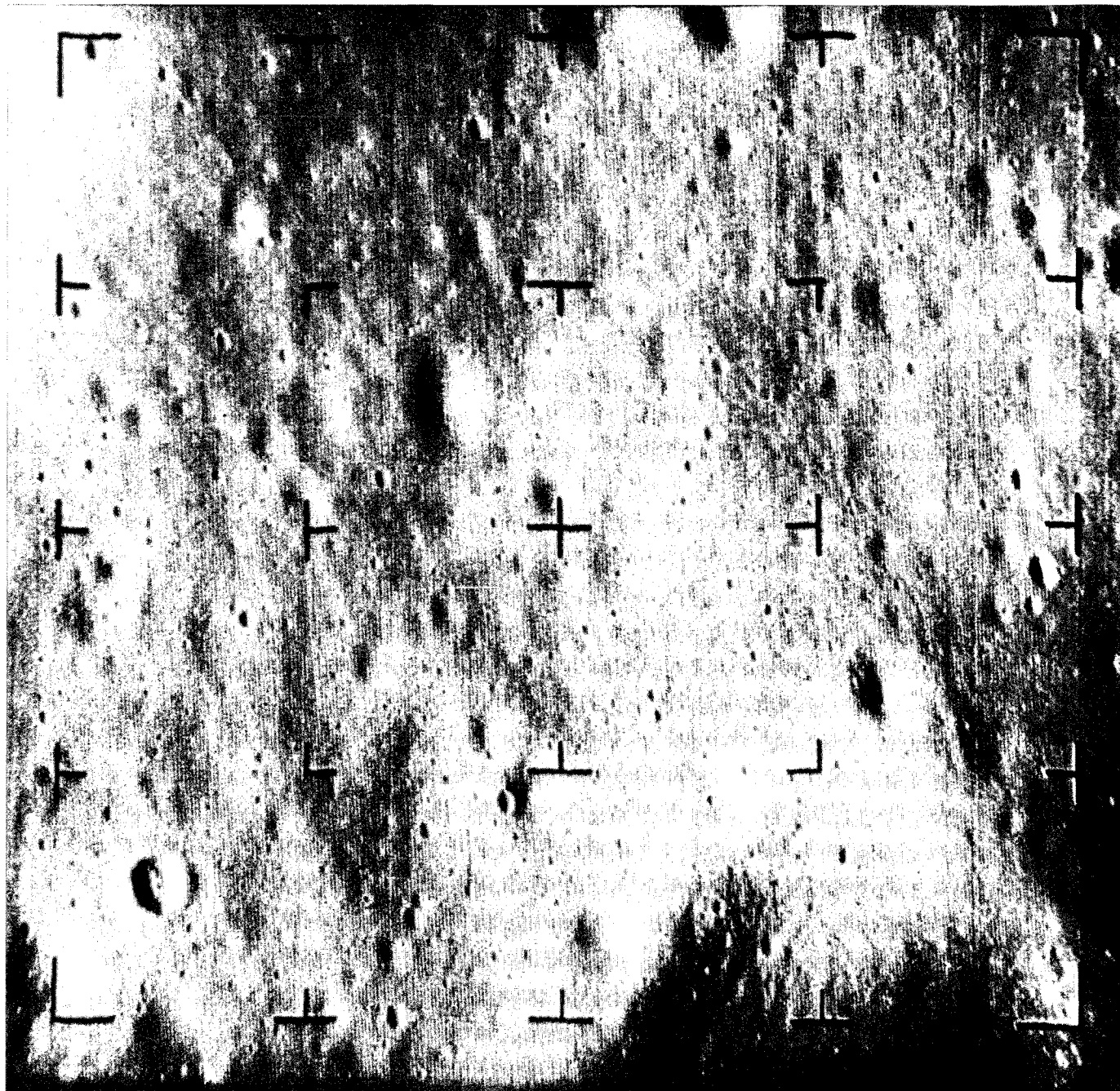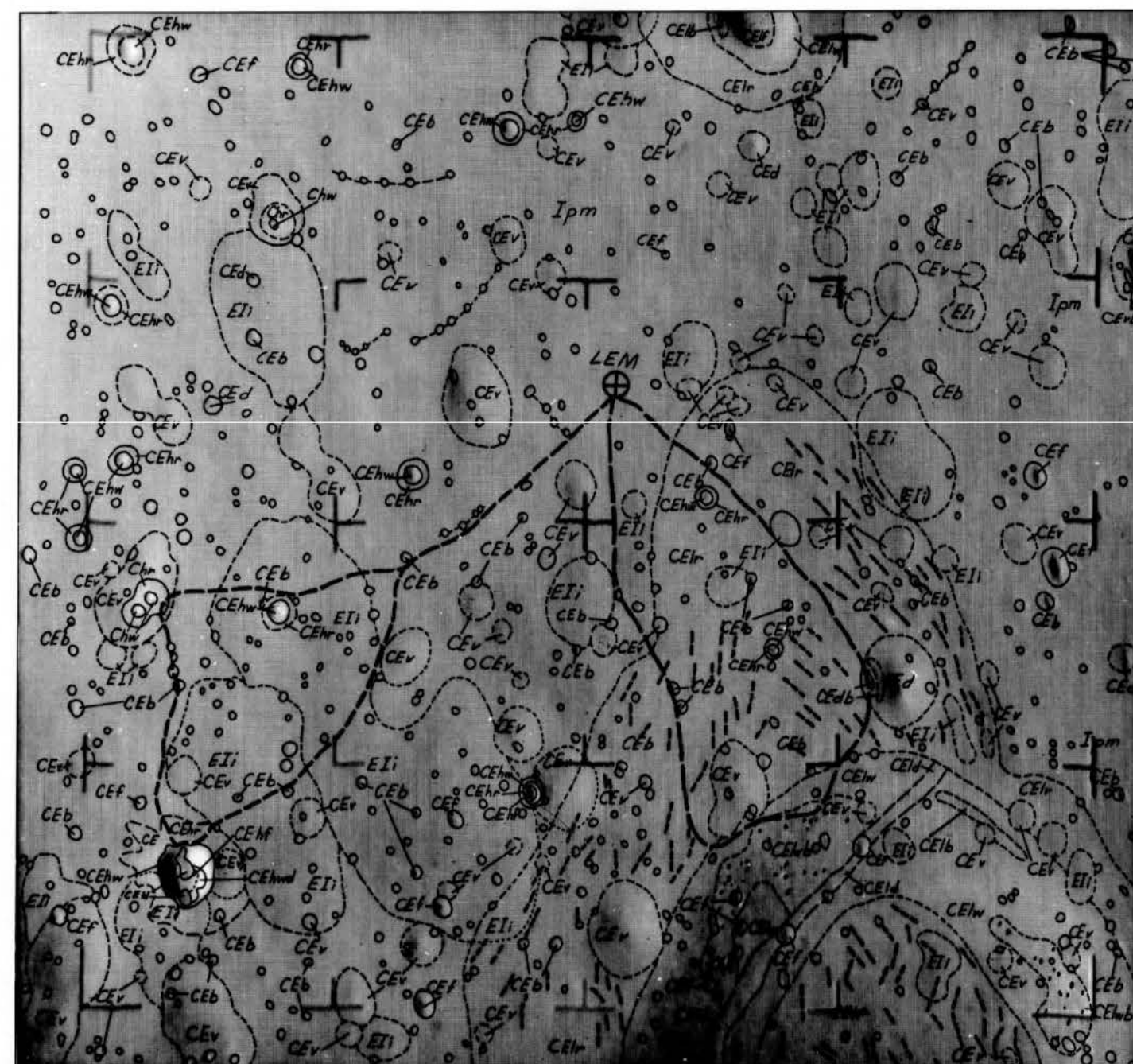
Fig. 38. *Ranger VIII* B-camera photograph 90, showing representative
potential landing area in Mare Tranquillitatis.

GEOLOGY BY H.H. SCHMITT

0   200 m
APPROXIMATE SCALE

↑ N

EXPLANATION

COPERNICAN SYSTEM

Chr — Crater rim material, sharp rim craters
Bright material on rims of sharp, generally circular craters. Outer rims are concave upward with steepest slopes greater than 15°. Rim crests are cusp-shaped in cross section. Craters probably formed by impact.

Chw — Crater wall material, sharp rim craters
Bright-appearing material on walls of sharp, generally circular craters with bright rims. Walls are concave upward with slopes greater than 15°.

CEhr — Crater rim material, sharp rim craters
Material on raised rims of sharp circular craters. Albedo is close to that of mare surface material. Morphology of craters is the same as that of Copernican craters. Craters are probably of impact origin.

CEhw — Crater wall material, sharp rim craters
Material on walls of sharp circular craters without bright rims.

CEhwd — Crater wall material, dark, sharp rim craters
Relatively dark material in walls of sharp circular craters without bright rims.

CEhf — Crater floor materials, sharp rim craters
Material with relatively flat topography in floors of sharp, circular craters without bright rims.

CEhl — Crater lobe material, sharp rim craters
Hummocky material occurring in lobate patches on the lower walls and floors of sharp circular craters without bright rims. Probably crater rim and wall material that has undergone mass movement down the crater wall.

CEf — Funnel crater material
Material of well-defined, circular craters that have no apparent raised rims and no rim deposits. Crater walls have conical shape with slopes greater than 15°. Craters may be small maar craters or drainage craters over large fractures.

CEd — Dimple crater material
Material of well-defined craters with walls that are convex upward. Slope of walls varies from less than 15° to more than 15° with depth. Outer rim is poorly defined. Craters may be drainage craters over narrow fractures or openings, or sharp-rim craters that have undergone extensive inward slumping of their rim and wall materials.

CEdb — Crater bench material, dimple craters
Material on relatively flat areas between steeper slopes on walls of dimple craters. Probably downfaulted crater rim or wall material.

CEld — Linear depression material
Material lying in narrow, roughly linear depressions. Depressions probably caused by subsidence or volcanic activity along fractures in mare surface material.

CEb — Bright crater wall material
Material of small, steep-walled craters. Wall materials cannot be resolved at the scale of the photographic base. Slope of walls is greater than 15° on upper part and less than 15° on lower part. Craters probably mostly sharp-rim craters with unresolvable rims or small low-rim craters caused by high-angle secondary impacts.

CEv — Crater materials, undifferentiated, convex rim craters
Materials in subdued craters with raised topographic rims; albedo of rims is the same as that of the mare surface material. Crater walls are concave inward with slopes of approximately 15° and less. Rim crests are poorly defined. Craters probably extensively eroded sharp rim, funnel and dimple craters.

CEvb — Crater bench material, convex rim craters
Same as CEdb.

ERATOSTHENIAN SYSTEM

CElr — Crater rim material, low rim craters
Material on wide, low rims of generally circular craters. Topographic rims are only slightly raised above surrounding mare material and outer limit of rim is poorly defined. Albedo is the same as that of mare surface material. Steepest slope on rim is less than 5°. Rim crests are well defined. Craters are probably secondary impact craters or partly-eroded sharp-rim craters.

CElw — Crater wall material, low rim craters
Material on walls of low-rim craters. Walls are concave inward with slopes of approximately 15° or less.

CElwb — Crater wall material, blocky, low rim craters
Low-rim crater wall material that is covered by blocks of apparently cohesive material less than 10 m average diameter. Black dots indicate position of individual blocks. May be allogenic breccia resulting from secondary impact.

CElf — Crater floor material, low rim craters
Same as CEhf

CElb — Crater bench material, low rim craters
Same as CEdb.

IMBRIAN SYSTEM

Eli — Crater material, undifferentiated, indistinct craters
Material of indefinite craters and depressions with low topographic rims of the same albedo as the mare surface material. Rims are convex upward. Walls are concave inward with slopes that are markedly less than 15°. Long axes of craters have a general northwest alignment that resembles the lineation of patterned ground. Craters may be eroded impact craters, eroded depressions on original mare surface or depressions caused by structurally controlled subsidence.

Ipm — Mare surface material
Material making up the bulk of the mare surface. Probably a heterogeneous layer of debris repeatedly stirred by formation of small unresolved craters and consisting of locally derived brecciated volcanic material, some extra-lunar fragments and fragments of material derived from distant impact events elsewhere on the moon.

— — — Contact, long-dashes where approximately located, short-dashes where gradational or indefinite.

------------- Concealed contact. Buried formation shown in parentheses.

—?—?— Contact uncertain.

━━━━ First two man traverse.

━ ━ ━ Second two man traverse.

- - - Lineament. Shallow linear depression.

∘∘∘∘ Craters that are too small to be classified. Joined by dashed line if several lie on smooth curve.

Fig. 39. Geologic map of area shown in *Ranger VIII* B-camera photograph 90, illustrating foot traverses from hypothetical landing point of *Apollo* Lunar Excursion Module: 2.66°N latitude, 24.75°E longitude at central reticle.

meteorite and secondary-particle bombardment. It therefore seems more likely that the blocks are the partially exposed fragments of a coarse, allogenic breccia in the crater-wall material. The exposure was probably caused by the slumping of material down the crater wall, which, in turn, could have been initiated by low-intensity seismic activity or by nearby impact. Crater-bench material in the low-rim craters may also have been formed by the downslope movements of weakly coherent wall material.

Materials of convex-rim craters. Materials of craters with low, poorly defined rims that are convex upward are classed as convex-rim crater materials. These craters, whose walls are as steep as 15 deg, are probably eroded or degraded forms of sharp-rim, funnel, and dimple craters. There is a continuous gradation in characteristics between the convex-rim and the small indefinite-rim craters; materials of the former, however, stratigraphically overlap and are younger than many of the larger indefinite-rim craters.

Funnel-crater material. The funnel craters in the map area are rimless, steep-walled, funnel-shaped depressions; the slopes of the walls are nearly uniform from the crater lips to the bottoms of the craters. Slopes of the crater-wall material are greater than 15 deg. The shape of the funnel craters and their local association with a shallow linear depression suggest an origin either by upward discharge or by downward drainage of weakly coherent fragmental material through fissures in the mare material.

Dimple-crater material. The dimple craters have walls that are convex upward and come nearly to a point at depth. They resemble the funnel craters and may have been formed by drainage through narrow orifices. Both funnel and dimple craters probably developed by the drainage of finely divided solids rather than fluids, as they are younger than the large, low-rim crater in the southeast corner of the map area, which was probably formed by impact into solid mare material. It is also possible that the dimple craters were formed from sharp-rim craters by mass movement on the crater walls.

Linear-depression material. This material is confined to the narrow, roughly linear depression in the large, low-rim crater in the southeast part of the map area. Several funnel craters appear to be related to this depression, and both the depression and the craters may have developed by subsidence along a fissure (although there is a possibility that they are small eruptive features related to outgassing of the cooling mare at depth) Inasmuch as the linear depression post-dates the large

crater, it is probably not directly related in origin to the emplacement of the mare material.

Bright crater-wall material. The many small craters in the area have been mapped as (1) bright-walled craters or (2) craters too small to be classified. (The latter are shown by a structural symbol.) The bright-walled craters have maximum diameters near the lower limit of size at which the shapes of the craters can be defined; were they larger, they could probably be placed in one of the other morphological groups. Although the sunlit walls of the craters are bright, it is not known to what extent this brightness is due to their relatively steep inclination toward the Sun. The circular shape and steep walls of these craters suggest that they are small impact craters.

Materials of sharp-rim craters. A variety of materials aassociated with well defined, generally circular craters are mapped as sharp-rim crater materials. The outer rims of these craters are concave outward, and the rim crests are cusp-shaped. The inner walls are concave upward, with slopes greater than 15 deg near the rim crests. Some of the craters have well defined floors. A lobe of hummocky material appearing on the floor of one sharp-rim crater has probably been derived from the crater wall by slumping. Most of these craters have rim materials of the same albedo as the surrounding mare surface material, and most are probably primary- or secondary-impact craters.

Copernican System. Sharp-rim craters of the Copernican System are identical to those assigned to a Copernican or Eratosthenian age, except that the crater-rim materials in the former are markedly brighter than the surrounding mare surface material.

b. Structure

Two types of structural features are recognizable in the map area: (1) a general, northwest-trending alignment of indefinite-rim craters and depressions and (2) lineaments in and on the rim of the large, low-rim crater in the southeast corner of the area. The latter are rows of very gentle, irregular linear depressions approximately 10 m wide. Both northwest-trending and northeast-trending sets of lineaments are present. Where the two sets intersect, the so-called "tree-bark" structure, or patterned ground, is produced. Irregularities in the trends of the fine lineaments suggest that the lineaments may be more closely related to the internal structure of the crater materials on which they occur than to regional structures within the mare. The mapping of larger areas

by means of orbital photographs should give a clearer picture of the regional relations of lineaments and patterned ground.

2. Early *Apollo* Explorations

Ranger VIII photograph B90 (Fig. 38) illustrates a part of Mare Tranquillitatis that is of a size accessible on foot from a landed *Apollo* Lunar Excursion Module or from any other stationary vehicle on the lunar surface. The geologic features and units in Fig. 39 are probably typical of this and other mare surfaces.

Early manned exploration of an area such as that shown in Fig. 39 will have as its major scientific goals: (1) the representative sampling of materials of the local geologic units on the mare surface and of exotic rock fragments, (2) the investigation of the physical properties and composition of the various surface units, (3) the sampling of materials derived from depth in the mare, (4) the investigation, sampling, and photography of details of the fine structure not identifiable from pre-mission photographs, and (5) the identification and measurement of subsurface structure.

The fundamental constraints on achieving the above goals during *Apollo* exploration are: (1) the limited number of man-hours available for scientific tasks, (2) the limited mobility of a man in a spacesuit, (3) the restricted weight and characteristics of scientific gear that can be transported to the Moon and during a traverse, and (4) the weight of samples that can be returned to Earth. Assumptions concerning these constraints that may be made for the purpose of planning the scientific phases of the missions are given below. Some of these assumptions are optimistic; they are based, however, on what the writer feels is a reasonable extrapolation from the current status of the development of *Apollo* systems.

a. Exploration Time and Astronaut Mobility

Current estimates of the time available for surface activities during early *Apollo* landings average about 15 man-hours divided among three excursions of no more than 3-hr duration each. These figures are largely a function of the capacities of the Lunar Excursion Module and astronaut life-support systems. Such a division of time could include one extravehicular excursion by one man and two excursions by two men working together.

The mobility of the astronaut outside the spacecraft will be governed by the mechanical properties of the surface, the characteristics of the spacesuit and the life-support system, and the nature of the scientific gear that must be transported. Although the distances that an astronaut can traverse under various conditions have not been determined with any degree of certainty, some estimates can be made. Allowing 0.5 hr for egress, equipment checkout, and ingress, the maximum useful time for surface exploration during an excursion would be about 2.5 hr. Tests conducted by the Manned Spacecraft Center of the National Aeronautics and Space Administration and by the U. S. Geological Survey suggest that average geologic traverse speeds (including time for descriptive and other activities) over rolling, loosely aggregated terrain may be approximately 10 m/min. Thus, maximum traverse lengths on the order of 1500 m can probably be anticipated during any given excursion, provided that sampling, photographic, and descriptive operations can be carried out efficiently.

b. Scientific Exploration Equipment

The following equipment can probably be available for early *Apollo* surface exploration:

(1) Television camera
   (a) Hand-held
   (b) Confined to use within 30 m of the Lunar Excursion Module by the camera cable
   (c) 0.625 frame/sec, 1280 lines/frame
   (d) Recording orientation system

(2) Exploration staff
   (a) Surveying, stereometric, spectrophotometric, and photometric film camera
   (b) Orientation system for recording camera orientation and the geometry of structural features
   (c) Detachable scraper–pick–hammer combination
   (d) Gamma-ray flux meter (visual readout)
   (e) Penetrometer (visual readout)
   (f) Stadia markings

(3) Instrument and sample carrier
   (a) Rack for field-sample containers
   (b) Rack for special-purpose-sample containers
   (c) Scoop–pick–hammer combination
   (d) Sample orientation device
   (e) Small, single-lens camera
   (f) Holder for television camera
   (g) Holder for photogeologic map, photograph, and traverse plan

(4) Active seismic gear

(5) Emplaced scientific station instruments

c. A Representative Scientific Mission Profile

The local geology; such as that shown in Fig. 39, is of prime importance to the detailed planning of a nominal scientific mission in the area to be explored. The observed distribution of craters, depressions, positive-relief features, and geologic units—together with previous inferences on the origin of the lunar features, based on terrestrial field and laboratory research—should govern the selection of geologic and geophysical traverse locations. However, traverse plans based on geologic analysis of photographs and other data acquired before the mission should not be so restrictive that they prevent the examination of the unexpected.

Figure 39 illustrates representative traverses that permit the systematic sampling, photography, and description of each major type of geologic unit or feature present within walking distance of an arbitrarily chosen landing point. In addition, it is expected that on each traverse, samples can be obtained of material derived from impact events in rocks far removed from the landing site. An analysis of the geology suggests several areas of interest for subsurface exploration by seismic-refraction methods to determine the thickness of surficial fragmental debris on the relatively level parts of the mare and across the shallow mare depressions. Seismic data could also be obtained on the thickness of crater-rim materials, such as the unit around the large southeast crater. The traverses shown are intended to illustrate how efficient exploration of a previously unknown area can be planned on the basis of a geologic map. A similar use of photographic data is made in terrestrial geologic field work. Deviations from the planned traverse are expected to occur where important new features are observed below the identifying resolution of the available photographic base.

First excursion. The first excursion (not shown in Fig. 39) of the hypothetical mission on Mare Tranquillitatis is planned for one man and is confined to an area within approximately 100 m of the landed Lunar Excursion Module. The principal geologic target for this excursion is a part of the mare surface that is relatively free of resolved craters. A detailed television and sampling survey of the landing site is to be carried out first, using the television camera mounted on the instrument and sample carrier. The television survey is directed toward obtaining photometric and photogrammetric data on the materials and features of the landing site in the immediate vicinity of the Lunar Excursion Module. The overall survey should provide data on the nature of any crater formed by the rocket effluent during landing of

the Module, samples taken from the bottom of this crater and progressing outward to the undisturbed material, and samples of apparently exotic materials in the vicinity of the Module. Large samples that are required for special purposes and can be found near the landing site should be obtained during the first excursion. Such samples might include material newly exposed by the rocket effluent; specially preserved samples of the mare surface, to be used for textural studies; and specimens for biological tests.

An active seismic experiment could be carried out during the first excursion to determine the mare subsurface structure and the properties of rocks found in the relatively uncratered part of the surface. Also of particular interest would be a seismic-refraction profile across the indefinite depression to the northeast of the landing site (Fig. 39), in order to determine whether depressions of this class are original shallow features of the mare or filled-in craters.

The emplaced scientific station should be set up during the first excursion on favorable ground near the Lunar Excursion Module, but at sufficient distance to be undisturbed by the later ascent of the upper stage.

Second excursion. In the second excursion (long-dashed traverse in Fig. 39), features to the south–southeast of the landing site will be sampled and examined. This is planned as a two-man excursion, with one astronaut performing most of the descriptive and photographic operations that utilize the exploration staff; using the instrument and sample carrier, the other astronaut will concentrate on the systematic sampling of materials described and photographed by the first astronaut.

The geologic targets for the second excursion include an average-size indefinite crater; the rim and wall materials of the large, low-rim crater southeast of the landing site; a large dimple crater and the bench units within it; a small, bright-walled crater; and the lineaments and patterned ground on the rim of the large, low-rim crater.

Verbal descriptions of the features and materials along the traverse should record data that will not be provided by the returned photographs and samples and, especially, relate the photographs and samples taken to the observed fine structure of the mare. Among other information that will probably not be recoverable entirely from the photographs or returned samples will be the stratigraphic relations of geologic units, such as the mare-surface material and various crater-rim materials. Descriptions of

variations with depth and the interrelations of the lunar surface materials exposed in the walls of small, sharp-rim craters will be important for an understanding of the radiation and micrometeoroid impact history of the mare surface. Observations of the presence or absence of patterned ground, small craters, and bright or dark streaks on crater walls will provide information on the effectiveness of the processes of mass wasting on the lunar surface and, in turn, may offer clues to lunar seismic activity. Careful observation and description will probably be required to decipher the nature and origin of the blocky crater-wall material in the large southeast crater.

Stereometric, photometric, and spectrophotometric photographs taken along the traverse should emphasize the near field, here defined as the range from about 10 cm to a distance equal to the identifying resolution of pre-mission photographs. In the early *Apollo* missions, the near field will probably extend to about 5 m.

Sufficient near-field photographs should be taken to permit quantitative characterization of the geologic units shown in Fig. 39 and the subunits within them, with respect to their textures and photometric and spectrophotometric properties. This will make possible post-mission correlation and interpretation of units and subunits which will augment the visual interpretations made during the traverse. The stereo photographs will play a major role in documenting the crater-wall and rim textures and will provide data on the crater-wall slopes and the size–frequency distribution of craters less than 5 m in diameter. Photographs taken at various phase angles will help to determine the photometric functions for surfaces such as the wall of the large southeast crater. Also, the long focal-length lens of the camera may be used to obtain high-resolution photographs which will provide information on features not actually reached on the traverse, such as the linear depression and associated funnel craters crossing the wall of the large southeast crater.

Other instruments on the exploration staff will provide supplementary information on the structure and physical properties of the geologic units. The staff orientation system gives the data necessary for the photogrammetric and photometric control of the film-camera photographs; with this control, quantitative information may be obtained on structural features such as layers and fractures exposed in crater walls. Systematic penetrability measurements on the various units may yield data that will assist in determining the relative age or stratigraphic sequence of these units, as the processes of micro-

meteoroid bombardment and solar radiation probably affect the cohesiveness and bearing strength of exposed materials and the thickness of finely pulverized material probably increases with time. Penetrability measurements also provide engineering data of importance to post-*Apollo* vehicular traverses. Determination of the flux of gamma rays from various units may help to distinguish relative differences in chemical composition as a guide to the delineation and sampling of subtle geologic units. The detection of exotic fragments of unusual composition may be facilitated by use of the gamma-ray flux meter, especially if finely pulverized material coats most of the surface.

The traverse sampling activities, for the most part, should be designed to provide as varied and complete a collection of representative, exotic, and textural samples as can be obtained along the traverse. General grab sampling, coupled with data on the spatial relations of the samples, should provide a representative suite of materials from the geologic units encountered. Most of the exotic samples collected will probably have been derived from areas far removed from the landing site by ejection from impact craters elsewhere on the Moon, and will provide preliminary data on the nature of lunar materials other than those of the mare.

Samples of the rim material around the large southeast crater may provide a profile of mare material to a depth approximately equal to the crater depth. Samples from the blocky crater-wall material may yield relatively fresh, coherent pieces of mare material. The blocky crater-wall material may also be partially mantled with material related to the linear depression and funnel craters farther down in the main crater.

The sampling of profiles in the surface fragmental layer, exposed either in the walls of the sharp-rim craters or by digging, will be of major importance in determining the radiation, micrometeoroid impact, and, possibly, the volcanic history of the mare. Ideally, each recognizable geologic unit should be sampled, so that the effects of events that have taken place over as broad a span of lunar history as possible can be studied.

The locations of data and sample points and of photographic stations along the traverse are obtained by photographing the unit coordinate system defined by the Lunar Excursion Module, using the long focal-length lens of the film camera. Each survey photograph should also be accompanied by a stereo photograph of the near field,

for continual expansion of the photogrammetric coverage of the area. A similar procedure can be followed for locating necessary data and sample points out of view of the Lunar Excursion Module by utilizing the single-lens film camera to photograph the exploration staff from a known point, or the staff film camera to photograph the instrument and sample carrier situated at some known point.

Third excursion. The third excursion (short-dashed traverse in Fig. 39) will be operationally similar to the second, except that a final seismic profile is shot across one of the large indefinite craters southwest of the landing point. Such a profile would yield comparative data for further evaluation of the origin(s) of this type of depression.

The geologic targets for this excursion include a string of very small craters, a convex-rim crater, two large indefinite craters, and the rim materials and surface features of relatively dark and bright sharp-rimmed craters.

Acknowledgments

REFERENCES

1. *Ranger VII, Experimenters' Analyses and Interpretations,* Technical Report No. 32-700, Pt. II, Jet Propulsion Laboratory, Pasadena, California, February 10, 1965.

2. Shoemaker, E. M., Hackman, R. J., and Eggleton, R. E., "Interplanetary Correlation of Geologic Time," *Advances in the Astronautical Sciences,* Vol. 8, New York: Plenum Press (1963), pp. 70–89.

3. Dodd, R. T., Salisbury, J. W., and Smalley, V. G., "Crater Frequency and the Interpretation of Lunar History," *Icarus,* Vol. 2 (1963), pp. 466–480.

4. McGillem, C. D., and Miller, B. P., "Lunar Surface Roughness from Crater Statistics," *Journal of Geophysical Research,* Vol. 67 (1962), pp. 4787–4794.

5. Milton, D. J., "Stratigraphy of the Terra Part of the Theophilus Quadrangle," *United States Geological Survey, Astrogeologic Studies Annual Progress Report, July 1, 1963, to July 1, 1964,* Pt. A (1964), pp. 17–27.

6. Morris, E. C., and Wilhelms, D. E., *Preliminary Geologic Map of the Julius Caesar Quadrangle,* United States Geological Survey (1965).

7. Moore, H. J., "Density of Small Craters on the Lunar Surface," *United States Geological Survey, Astrogeologic Studies Annual Progress Report, August 25, 1962, to July 1, 1963,* Pt. D (1964), pp. 34–51.

8. Kuiper, G. P., et al., *Photographic Lunar Atlas,* Chicago: University of Chicago Press (1960).

9. Young, J., "Preliminary Report of a Statistical Investigation of the Diameters of Lunar Craters," *Journal of the British Astronomical Association,* Vol. 43 (1933), pp. 201–209.

10. Baldwin, R. B., "Lunar Crater Counts," *Astronomical Journal,* Vol. 69 (1964), pp. 377–392.

11. Moore, H. J., Kachadoorian, R., and Wilshire, H. G., "A Preliminary Study of Craters Produced by Missile Impacts," *United States Geological Survey, Astrogeologic Studies Annual Progress Report, July 1, 1963, to July 1, 1964,* Pt. B (1964), pp. 58–92.

12. Vortman, L. J., Chabai, A. J., Perret, W. R., and Reed, J. W., *Buckboard,* Sandia Corporation Final Report SC-4675, 1960.

13. Murphy, B. F., *High Explosive Crater Studies: Desert Alluvium,* Sandia Corporation Research Report SC-4614, 1961.

14. Halajian, J. D., *Gravity Effects on Soil Behavior,* Grumman Aircraft Engineering Corporation, Bethpage, N. Y., 1963.

15. Strom, R. G., "Analysis of Lunar Lineaments, I: Tectonic Maps of the Moon," *Communications of the Lunar and Planetary Laboratory,* University of Arizona, Vol. 2, No. 39 (1964), pp. 205–221.

16. Minakami, T., "On Explosive Activities of Andesitic Volcanoes and Their Forerunning Phenomena," *Bulletin Volcanologique,* Vol. 10 (1950), p. 59.

REFERENCES (Cont'd)

17. *Manual of Photogrammetry,* 2nd Edition, American Society of Photogrammetry, Washington, D. C. (1952), pp. 44–45.

18. Harpe, R. W., Private communication.

19. "ER-55 Plotter Procedures," *Topographic Instructions,* Book 3, Chapter 3F6, United States Geological Survey, Washington, D. C.: Government Printing Office (1961).

20. Arthur, D. W. G., "Some Systematic Visual Lunar Observations," *Communications of the Lunar and Planetary Laboratory,* University of Arizona, Vol. 1, No. 3 (1962), pp. 23–26.

21. American Commission on Stratigraphic Nomenclature, "Code of Stratigraphic Nomenclature," *Bulletin of the American Association of Petroleum Geologists,* Vol. 45 (1964), pp. 645–665.

22. Shoemaker, E. M., and Hackman, R. J., "Stratigraphic Basis for a Lunar Time Scale," *The Moon — Symposium No. 14 of the International Astronomical Union,* ed. by Z. Kopal and Z. K. Mikhailov, London: Academic Press (1962), pp. 289–300.

23. Hartmann, W. K., and Kuiper, G. P., "Concentric Structures Surrounding Lunar Basins," *Communications of the Lunar and Planetary Laboratory,* University of Arizona, Vol. 1 (1962), pp. 51–72.

24. Gilbert, G. K., "The Moon's Face — A Study of the Origin of Its Features," *Philosophical Society of Washington Bulletin,* Vol. 12 (1893), pp. 241–292.

25. Eggleton, R. E., "Preliminary Geology of the Riphaeus Quadrangle of the Moon and Definition of the Fra Mauro Formation," *United States Geological Survey, Astrogeologic Studies Annual Progress Report, August 25, 1962, to July 1, 1963,* Pt. A (1964), pp. 46–63.

26. Masursky, H., *Preliminary Geologic Map of the Ptolemaeus Quadrangle,* United States Geological Survey (1965).

27. Hackman, R. J., *Geologic Map and Sections of the Kepler Region of the Moon,* United States Geological Survey Map I-355 (1962).

28. Marshall, C. H., *Geologic Map and Sections of the Letronne Region of the Moon,* United States Geological Survey Map I-385 (1963).

29. Shoemaker, E. M., "The Geology of the Moon," *Scientific American,* Vol. 211 (1964), pp. 38–47.

30. Moore, H. J., Private communication.

31. Blanchet, P. H., "Development of Fracture Analysis as Exploration Method," *Bulletin of the American Association of Petroleum Geologists,* Vol. 41 (1957), pp. 1748–1760.

V. OBSERVATIONS ON THE RANGER VIII AND IX PICTURES*

Harold C. Urey
University of California, San Diego
La Jolla, California

Pictures are a limited way of investigating a physical problem. On the other hand, in many ways they are a good beginning for the investigation of a subject which cannot otherwise be seen in detail, such as the Moon at a distance of 384,000 km from the Earth. However, the picture should be judged in relation to other physical evidence. It is the purpose of this introductory statement to outline some of the physical evidence secured by other methods which bear on the problem of interpreting the photographs of the lunar surface.

I have assumed that the Moon was captured by the Earth and that it is thus a more primitive object than the Earth and the planets. It is assumed to have accumulated from materials of solar composition and hence to contain less iron than typical meteorites and the terrestrial planets. It is also assumed to have had a molten layer on its surface at one time, with a layer of iron–nickel below. However, it moved about the Sun in the neighborhood of the Earth and accumulated a surficial layer of material of terrestrial composition. The thickness of the layer has

not been estimated, but a depth of kilometers or tens of kilometers of broken-up material is predicted on the basis of this model.

Some favor the view that the Moon escaped from the Earth, although most experts regard this theory as improbable or impossible. If the Moon is of terrestrial origin, then all evidence of the violent separation process has been covered up by subsequent collisional processes. In this case, the surface will be badly broken up for some depth and, in fact, may have the same sort of structure as that outlined for the previous model.

Another school assumes that the Earth and the Moon have the same chemical composition and that the core of the Earth consists of high-density silicates and not of iron–nickel. It is then assumed that the Moon was formed in the neighborhood of the Earth. I have rejected this model because of the fundamental hypothesis on which it is based. The density of Mars and Mercury and the composition of the meteorites do not agree with this postulate. There remains the difficulty of the differing compositions of the Sun and terrestrial planets. Some

believe that the solar composition is the primitive composition, that the Earth has this composition, and that its core is not iron–nickel. Others believe that the Earth and the meteorites have the primitive composition and that astronomers are in error in regard to the solar composition. I argue that the Sun and terrestrial planets have different compositions and, hence, that involved cosmic chemical engineering processes are needed to produce the differences in composition of the planets and the Moon. But if I had to select one or the other model, I would prefer the assumption that the solar values are incorrect. In this case, the Moon must have escaped from the Earth. Although I reject the assumption that the Moon accumulated near the Earth, the model may be accepted by others; again, this would require that the surface of the Moon consist of highly broken and fragmented material.

In any case, great crevasses and cavities probably existed beneath the surface and have been modified to some extent, though not removed completely, during the life of the Moon.

The Moon is a triaxial ellipsoid with three moments of inertia whose values are not consistent with the forces acting upon the Moon at the present time. These values have been reviewed by astronomers for many years, with little change resulting in the final values. When the moments of inertia are converted to radii, assuming uniform density of the Moon, it is found that there are projections toward and away from the Earth about 1 km in height as compared with the polar radius, and the radius is perpendicular to these two radii, whereas the equilibrium height should be in the neighborhood of 60 m. This implies one of two possibilities: a substantial stress of about 20 bars must exist at the center of the Moon if the Moon has strength throughout; or an outer shell of the Moon must have sufficient strength to support the nonequilibrium shape.

The suggestion that the Moon has sufficient strength throughout to support the difference in elevation seems unlikely when one considers the great length of time that is to be taken as a reasonable age of the Moon.

A second suggestion was made by Urey et al. (Ref. 1), namely, that there is a variation of density with angle in the body of the Moon, the least dense material being distributed along the axis pointing toward the Earth, the densest material in the polar direction, and a material of intermediate density along the axis perpendicular to these. This hypothesis requires much less strength than

the first, and it requires a mechanism for the origin of the Moon which would produce the difference in density distribution with angle.

A third explanation is that slow convection occurs on the interior of the Moon, with rising currents of matter toward and away from the Earth along the axis pointing toward the Earth, and falling currents in the regions of the limb of the Moon. This theory is favored by Runcorn (Ref. 2).

It would seem to this author that the first suggestion is unlikely but that the latter two are possibilities. In any case, all three of them require a relatively cold Moon to account for the triaxial ellipsoidal shape.

The differences in elevation on the lunar surface, with comparatively deep areas in the region of the maria and rather high mountainous areas in other regions, have been studied by Baldwin (Ref. 3), but there is some disagreement in regard to his results. Watts (Ref. 4) has found differences in elevation on the limb of the Moon, with one case on the eastern limb amounting to some 10 km. Rather simple calculations show that if the Moon had the rigidity of the Earth, such differences in elevation would have decreased considerably in comparatively short periods of time (say, a quarter of a billion to a billion years). This again speaks for a cold interior of the Moon.

These arguments have been revived recently by Urey and are considered pertinent to the problem of lava flows on the Moon. It is surprising that very little attention has been given to these considerations by other students of the *Ranger* pictures.

Proceeding on the basis of such observational facts, Urey (Refs. 5 and 6) and MacDonald (Ref. 7) have tried to construct thermal histories for the Moon that would be consistent with these observations. They assumed low temperatures for the Moon at origin (0°C for example), and found that only the deep interior of the Moon should have melted. Slightly different physical constants were used, but the results were in substantial agreement. Urey in particular concluded that if a thermal diffusivity of 0.005 in cgs units and calories were assumed, if the abundances of K, U, and Th in the chondritic meteorites were used, and if an initial temperature of 0° were postulated, then complete melting would occur only near the center of the Moon. MacDonald obtained similar values, starting with an initially cold Moon, and showed that the values would be considerably higher if some 600°C were assumed for the initial condition. There is no basis for

choice of the initial conditions except the evidence that the Moon has irregular shapes that favor a low temperature.

The Russian school has assumed a higher temperature for the interior of the Moon, and consequently, a highly melted core. This assumption seems quite unreasonable to the writer. Since silicate liquid is less dense than its solid, a melted interior would be unstable, and outer parts of the Moon should sink to the interior. Hence, enormous lava flows would be characteristic if this were the correct thermal history. Of course, convection in the Moon would probably transport heat more rapidly to the surface than thermal conductivity, in which case a colder Moon again would be expected. No more than slight melting seems likely in any case, which is the situation that exists in the mantle of the Earth. It seems most unlikely that the Moon would possess a higher temperature distribution than does the Earth and it seems equally unlikely that the silicate materials of the Moon can be melted more than to a slight extent.

In very general considerations, one should expect that small planetary objects will be colder than large ones because (1) the rate of heat generation is proportional to the volume, and the loss of heat is proportional in some way to the surface; and (2) the energy of accumulation per unit mass is less for the smaller objects, and hence, initial temperatures would probably be less. Thus, we would expect the Earth to have a high general temperature, Mars, for example, to have a lower temperature, and the Moon to be still cooler. It therefore seems reasonable to believe that the smaller planetary objects in the solar system are likely to have less volcanic activity than the larger ones. Also, it seems likely that lava flows and volcanic activity on the Moon have been substantially less than those on Mars and on the Earth. The recent *Mariner* photographs of Mars, though they supply us with only a small sampling of the surface, are nevertheless consistent with very limited volcanic activity over the areas explored, a result which was expected and is reasonable. Dr. H. Brown of CIT and I pointed out some 15 years ago that the Clairaut constant of Mars was consistent with a smaller core than that of the Earth or no core at all, in agreement with the *Mariner IV* conclusions. It therefore seems appropriate to suggest that *possibly* the smooth areas of the Moon are not due to lava flows, as has been traditionally assumed for many years. I believe that this assumption was based on completely inadequate evidence, and that the people who proposed it long ago did so because no other explanations of the extensive smooth areas occurred to them. Were they living today, they might agree with the reasoning presented above.

Difficulties in regard to the lava hypothesis have been recognized in the past. The lava flows, if such they are, have apparently traveled over great distances. If they resemble such phenomena on the Earth in any way, they must have been very fluid (Ref. 8). Also, it is indeed surprising that so many separate lava flows should have occurred in the mountainous areas of the Moon, since one must assume that a pipe extending down 100 km or so in the interior of the Moon would bring lava out in many small pools, within craters and between craters, in all of the land areas of the Moon. This is a point brought to our attention by T. Gold (Ref. 9).

We also owe to Gold the suggestion that dust, which he first ascribed to erosion processes on the mountainous areas of the Moon (a postulate which does not seem to have stood up with time), was responsible for the smooth filling of the older craters and the great maria. Urey (Ref. 10) suggested that highly fragmented material was created by the great collisions that produced the maria and the large craters. He also suggested that perhaps temporary rains washed the dust off the mountainous areas into the neighboring regions. A number of people have discussed the dust problem since it was introduced by Gold, and much detailed argument has been devoted to the method of transport of the dust. It does seem to the author that Gold's suggestion of dust and the extension by Urey to fragmented material from the great collisions might well be considered as an alternative explanation for the smooth areas on the Moon, or that such material contributes to the phenomena to some extent.

In recent years, Gold in particular has emphasized the possible importance of water in the subsurface regions of the maria and has suggested specifically that some of the phenomena of permafrost regions of the Earth are in evidence in the lunar mare areas. The question of the origin and composition of the maria is so complicated at the present time because of what I believe is good evidence for erosion by micrometeorites, possible proton bombardment, small and large macrometeorites, cometary collisions, possible evaporation of water from beneath the surface, probable lunar seismic activity, and other processes that it is too much to expect that pictures of the Moon, even those taken by the *Rangers*, would be able to provide a decisive answer.

There have been discussions of meteorites coming from the Moon, a suggestion which I believe goes back to the last century but which was reconsidered by the present author on what appear to be modern physical bases (Refs. 11 and 12). The stone meteorites have spent only

relatively short times in space (from some 25,000 up to perhaps 100 million years, with a rather large concentration of ages at 20 million years), whereas the iron meteorites are often hundreds of millions of years old, although some cosmic-ray ages are in a lower range. Therefore, it appeared possible that they were coming from two sources: the stones from the Moon and the irons from the asteroidal belt. Considerable study has been devoted to this subject in recent years, but the validity of the hypothesis is certainly not clear on the basis of meteorite studies, although a number of arguments are currently being presented which favor it. Because of the difference in composition of the meteorites and the nonvolatile fraction of the Sun, as reported by astronomers, it appears that the stone meteorites are some special sample of matter which probably originated in some specialized region such as the surface of the Moon or the surface of the larger asteroids, and that these materials do not represent a true average primordial composition. It is not unreasonable to consider the possibility that the stone meteorites do indeed come from the Moon, and it might even be that some of the irons also originated on this body. There are pros and cons to this problem (which will not be reviewed at this point) that will probably not be resolved until samples from the lunar surface are secured.

There have been persistent assumptions that tektites come from the Moon since the suggestion was made by Dr. Nininger some years ago which the present writer considered seriously on the occasion of an invitation to speak before the American Physical Society 10 years ago. However, the suggestion was rejected for reasons that still appear to be valid (Refs. 13 and 14). The tektites have a chemical composition which is very similar to that of certain granites or mixtures of sedimentary rocks or so-called ash flows on the Earth. They are high in silica and alumina, low in magnesium, and have other characteristics of this acid form of rock. Rocks of this composition are believed to be produced on the Earth mostly by remelting of sedimentary rocks that come from the water erosion of basalts, which in turn have been produced by extensive lava flows. It is difficult to conceive of a prominent fraction of the Moon's surface being of this composition. Furthermore, the tektites are observed only in limited areas of the Earth. One group arrived in southeast Asia and Australia 600,000 years ago; another group arrived in Europe about 15 million years ago, still another in North America some 30 million years ago, and a group in west Africa some 15 million years ago. In addition, there are fused silicas in the Libyan Desert and on the island of Tasmania that are very difficult to account for on the basis of melting processes on the Earth. It

seems highly unlikely that batches of material of this kind could have been thrown from the Moon to the Earth and could be located in these small patches only, and not spread uniformly all over the Earth. Also, some should have missed the Earth entirely and returned to collide with it again in a uniformly distributed pattern over the surface of the Earth. Experienced physical scientists will recognize the inherent probability of this type of collision, but although rather unusual and remarkable postulates have been made in regard to this problem, to the author's knowledge, no model of high probability has been devised. It seems likely that if material of approximately the composition of the tektites occurs on the Earth, it would be much more probable, and involve a much less energetic process, for such material to have been melted and scattered comparatively short distances over the Earth than to assume that similar collision and melting processes produced the objects on the Moon and distributed them only in localized areas 384,000 km away. I am rejecting the tektite hypothesis as I have rejected it in the past, but I believe that the meteorite hypothesis is not unreasonable. Incidentally, no one has suggested that the meteorites could not have come from the Moon because they fell uniformly over the Earth's surface and not in localized areas on a few distinct occasions.

The next item of consideration appears more doubtful, although during recent years considerable interest has been manifested in it. It has been reported that biological material exists in the carbonaceous chondrites. The possible existence of fossils in chondrites has been reported by reputable micropaleontologists, as has the existence of compounds characteristic of living things, such as the fatty acids, hydrocarbons, optically active compounds, and other materials of this sort. To me, possibly the most convincing evidence offered by micropaleontologists is their discovery of the residue of organisms that are very similar in many ways to well established microfossils on the Earth. If biological material is indigenous to these objects, the most reasonable postulate would be that they are coming from the Moon. If this should prove to be true, it seems very likely that the maria of the Moon consist partly of carbonaceous chondritic material, possibly mixed with water below the surface, and that the highlands consist of meteoritic material of the non-carbonaceous kind. I do not wish to present this possibility as a firmly established fact but only to say that I have been considering it for some years and have kept it in mind as I studied the *Ranger* pictures of the Moon.

In summary, there is considerable evidence that the lunar maria may not be the result of traditional lava flow

but may be filled with dust or fragmented material mixed with water. Also, the entire surface may consist of fragmented materials from many collisions for which evidence exists on the surface, as well as possibly many collisional layers below the visible one. It was with this background in mind that I approached the pictures taken by *Ranger VII*, as well as those obtained by *Rangers VIII* and *IX*. It is my firm conclusion in regard to the general problem that it is not possible, on the basis of pictures alone and what we can deduce from them, to decide firmly what the maria and the highland areas of the Moon consist of. They may be lava, or they may be fragmented material, and water may have played a part in the history of the Moon for a short period of time.*

A. Summary of the Ranger VII Observations

There are several very interesting features in the *Ranger VII* photographs which the author mentioned in the *Ranger VII* report (Ref. 16) and which have been discussed by others. During the past year, since the *Ranger VII* mission, the writer has had considerable occasion to think over his statements concerning these pictures.

It seems certain that considerable smoothing of the smaller craters has occurred, which seems to have very nearly obliterated craters as large as 300 to 400 m in some cases. This interpretation indicates that the fragmented material on the inside of these craters is some 30 to 40 m deep. Related to the interpretation of this smoothing effect is another observation, namely, that there appear to be crevasses in certain areas consisting of very smooth material covered only slightly with finely divided matter. It is difficult to understand how comparatively small features of this kind could have been preserved if a considerable transport of fragmented material occurred. As far as I know, no satisfactory explanation of this apparent contradiction has been advanced.

There is certainly considerable evidence for collapse features of various kinds, as was pointed out in the *Ranger VII* report (Ref. 16) by the present author. Upon further consideration, I am still of the opinion that at least some of these features are indeed due to collapse into crevasses below the surface.

---

*Gilvarry (Ref. 15) suggested that seas existed on the Moon for billions of years. In this case, extensive river systems should have been present, and extensive erosion should have occurred. Since no evidence exists for such effects, we must conclude that free water had no more than a very temporary existence on the Moon.

The explanation of the dimple craters as being the result of material draining through a hole at the bottom of the crater or of the scattering of material leaving a dimple-like depression seems reasonable, although L. Jaffe's alternative observation (Ref. 16) that finely divided material on a laboratory scale will in some cases settle down into an approximate dimple shape is worthy of serious consideration. It may be that the dimples, in some cases at least, were caused by the walls of a collision crater moving in slowly, that is, by a flow in the surface regions of the Moon. Gault has observed that dimple craters of small size sometimes are produced by high-velocity projectiles in loosely divided solid materials.

The "crater with the rocks," in which a fairly large object is suspended in the crater, was explained as possibly being due to the escape of water from the interior of the Moon or perhaps to some collisional effect. Since this hypothesis was put forward in the Experimenters' meeting last fall, my attention has been drawn to Gold's early discussions with his colleagues to the effect that this phenomenon was similar to the pingos of the frozen North of the Earth, and observations by Smalley and Ronca (Ref. 17), who also concluded that it might be due to water. I believe that water is the most reasonable explanation of the crater with the rocks.

The many secondary craters have attracted the attention of observers of the *Ranger* photographs. Clusters of craters appear to be definitely due to secondaries from large craters, though other small craters may, of course, also be secondaries. Certain of these secondaries appear to have come from Tycho, 1000 km away, or from Copernicus, some 600 km distant, the latter assumption having been made by Gault, Quaide and Overbeck (Ref. 18). In either case, this theory speaks for the projection of very large objects across the surface of the Moon for very substantial distances and suggests definitely that much smaller objects were probably thrown off the Moon when a crater such as Tycho was produced. Also, it may be that in the production of smaller craters, objects of the size of meteorites might indeed leave the Moon. The rows of craters that appeared in the *Ranger VII* photographs and the elongated gashes may be due to secondaries or they may, in some cases, be the collapse features previously suggested.

These *Ranger VII* photographs would indicate that friable material probably covers the Moon to depths of as much as 20 m and possibly even greater. There seems to be very little evidence supporting the view of extensive

lava flows in the photographs, although they do not exclude this possibility.

B. The Ranger VIII Pictures

The landing area of Mare Tranquillitatis was chosen to make possible comparison with another mare area, and because Mare Tranquillitatis looks more like a lava flow than many other parts of the Moon. The mare has an irregular area and is very dark, as though a liquid of some kind had flowed back into all the bays. It has been my contention for many years that the lava produced during the fall of the planetesimal that created Mare Serenitatis flowed out over the neighboring areas of Mare Tranquillitatis. This lava appeared to be of a very dark kind. I have not abandoned this suggestion, even though others have pointed out that collisions of objects of this kind do not in general produce much liquid. However, arguments against the production of lava are based upon the assumption that one pure crystalline solid collides with another. If, on the other hand, the objects which fell on the Moon were not pure but heterogeneous in density and perhaps not well compacted, then sufficient heat might well have been generated throughout the colliding bodies to produce the lava flows.

A-camera photographs 46 to 51 show areas which appear to be slightly elevated with respect to neighboring regions, and there seem to be terminal walls at the edges of the more elevated smooth areas (Fig. 1). At first glance, these appear to be lava flows, but on closer examination, it is difficult to decide where the lava flows originated and in what directions they flowed. It seems possible that they are not lava flows at all. Note that the rilles appear to be sunken areas which for some reason have collapsed below the general level of the mare; irregular areas may be phenomena of the same sort. As pointed out above, the idea of recent lava flows on the Moon does not seem reasonable on energetic grounds.

There are many collapse features in the area covered by the Ranger VIII pictures. There is a beautiful dimple on B-camera photograph 90 (Fig. 2), a "square brick" depression, and the irregular and complicated "bathtub" on B86 (Fig. 3), all of which may well be collapse features which were not produced by simple collisions alone. There are also several lines of craters and shallow linear depressions. Dr. Shoemaker argues that these are due to the effects of objects projected from neighboring craters; that is, they are secondary craters of a certain kind. I find it difficult to be sure that this is the case and believe that some of them may indeed be collapse features.

The Ranger VIII pictures show many secondaries of a kind similar to those observed in the Ranger VII photographs. Undoubtedly, these can be assigned to secondaries from various large craters in the neighborhood, and the assignment to any particular crater in many cases can hardly be expected to be unique. There is a very interesting group of secondaries in Delambre, on the outside of the western wall and on the inside of the eastern wall, which could well be due to objects thrown from Langrenus in a single swarm, for example. The individual small craters have an elongation that suggests that they may have been formed by ejecta from Theophilus; but if this were the case, there would have had to be two groups of objects. It is difficult to choose between these possibilities. However, throughout the region photographed by Ranger VIII there are many craters that can undoubtedly be assigned to secondaries, and they seem to have been produced by large objects similar to those that produced the craters recorded by Ranger VII. Thus, it appears that very large objects have been thrown from these craters to considerable distances, just as was the case in the regions observed by Ranger VII.

There are projections above the surface shown in the pictures taken by Ranger VIII. In the lower right-hand corner of B-camera photograph 90 (Fig. 2), one sees very definite projections on the wall of the very nearly obliterated crater that look as though they may have been eroded from the wall. One, however, seems to be perched on the side of a small crater, and it would be quite easy to assume that the projection is the result of the collision that produced the crater. No "rocks in craters" of the type seen in the Ranger VII photographs have been observed in the Ranger VIII pictures.

The rilles are quite prominent and seem to be linear depressed areas, possibly similar to graben on the Earth. There is some disagreement in regard to the origin of the terrestrial graben, some maintaining that it is the result of a block being depressed by pressure from the sides, and others that the depression is due to expansion of the sides. The rilles would indicate that there has been some very general and large-scale movement of the lunar surface. However, it is difficult to see any evidence for this kind of movement. The rilles, of course, were seen in terrestrial photographs, and the Ranger VIII pictures add only minor details and therefore raise no new problems.

There are many ridges in the region covered by the Ranger VIII pictures, radiating from the collision of Mare Imbrium, that were seen in less detail in terrestrial photographs.
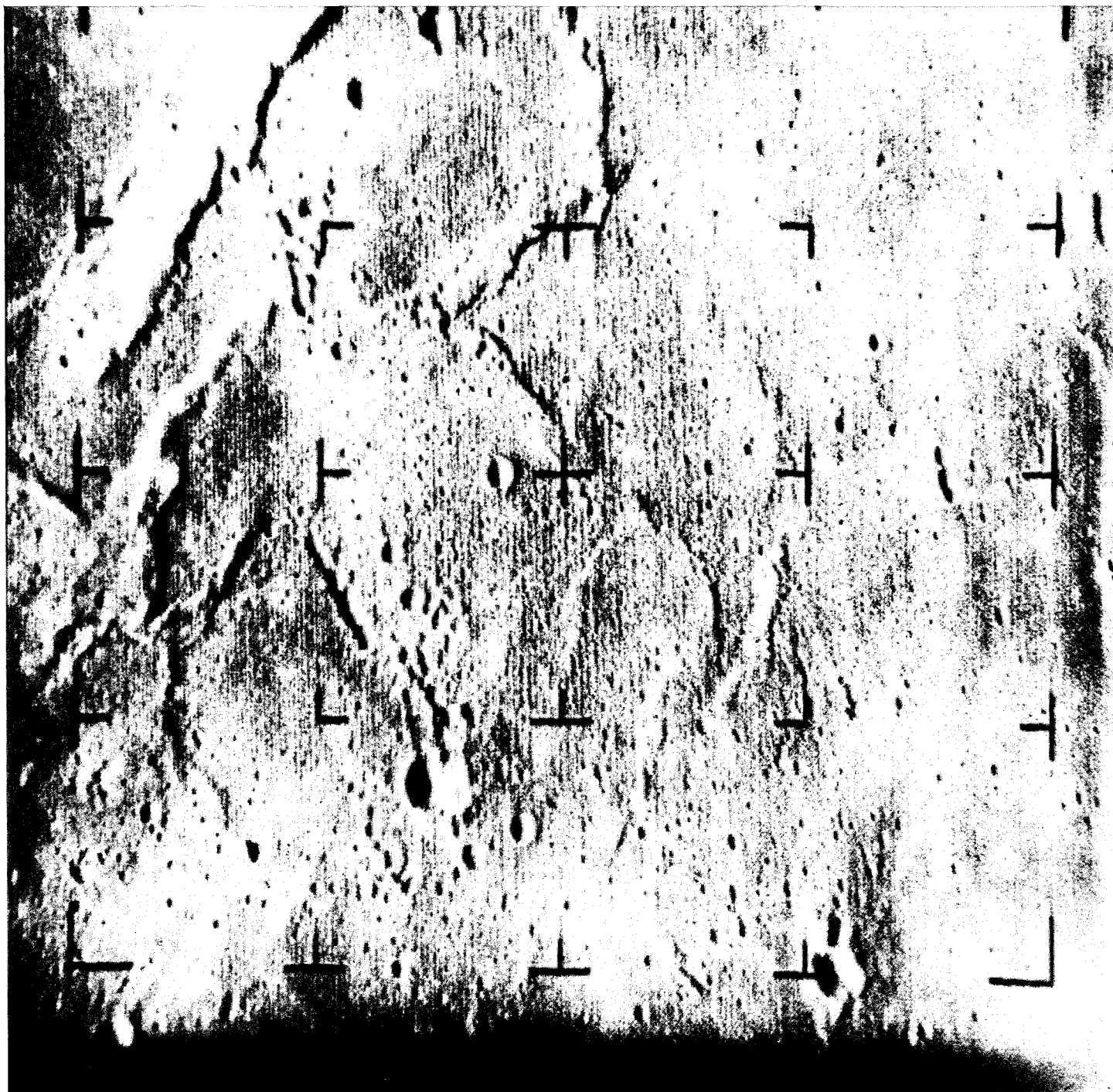
Fig. 1. *Ranger VIII* A-camera photograph 46, showing slightly elevated areas and apparent terminal walls at edges of more elevated, smooth regions.
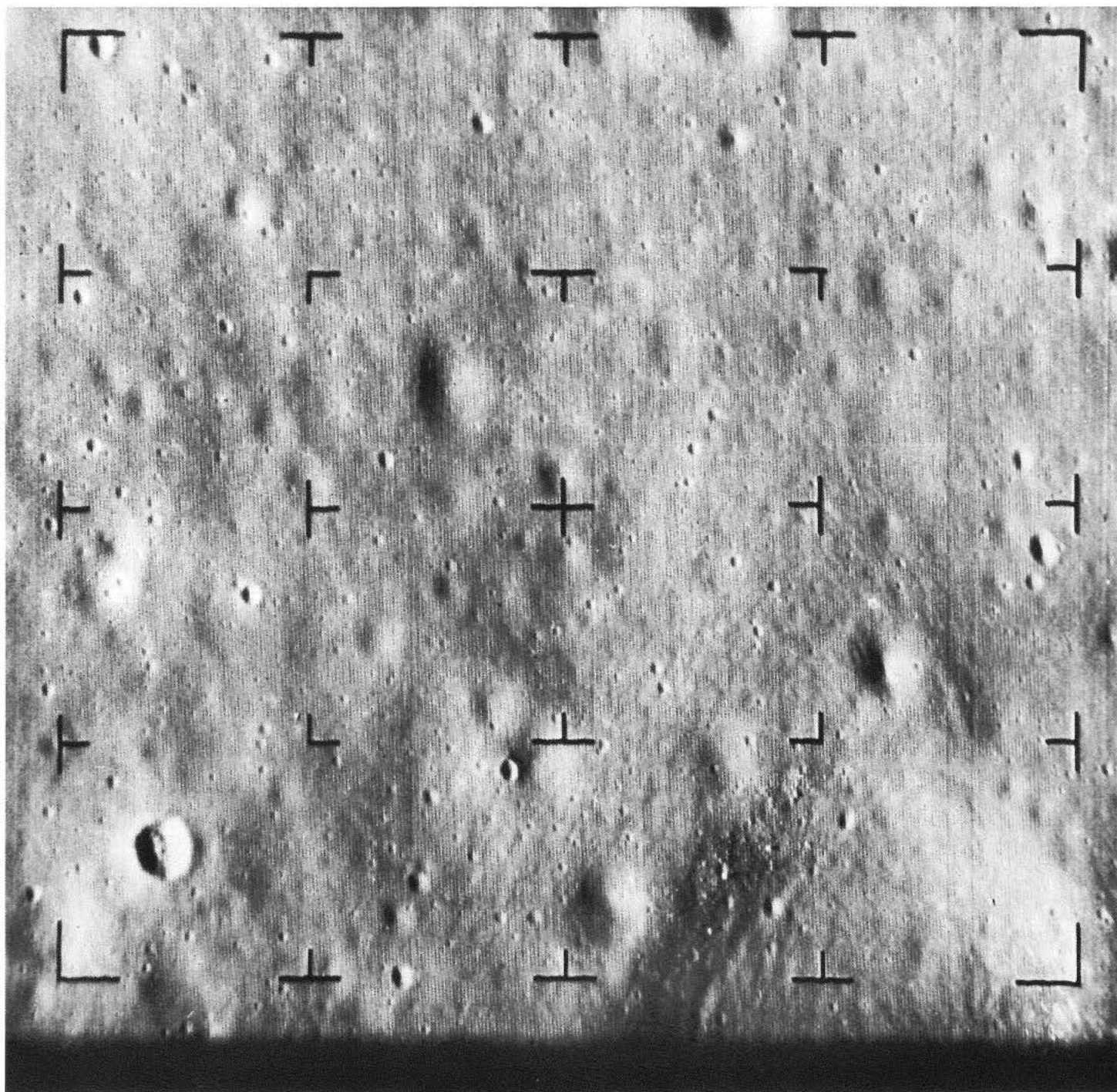
Fig. 2. *Ranger VIII* B-camera photograph 90, showing dimple crater as
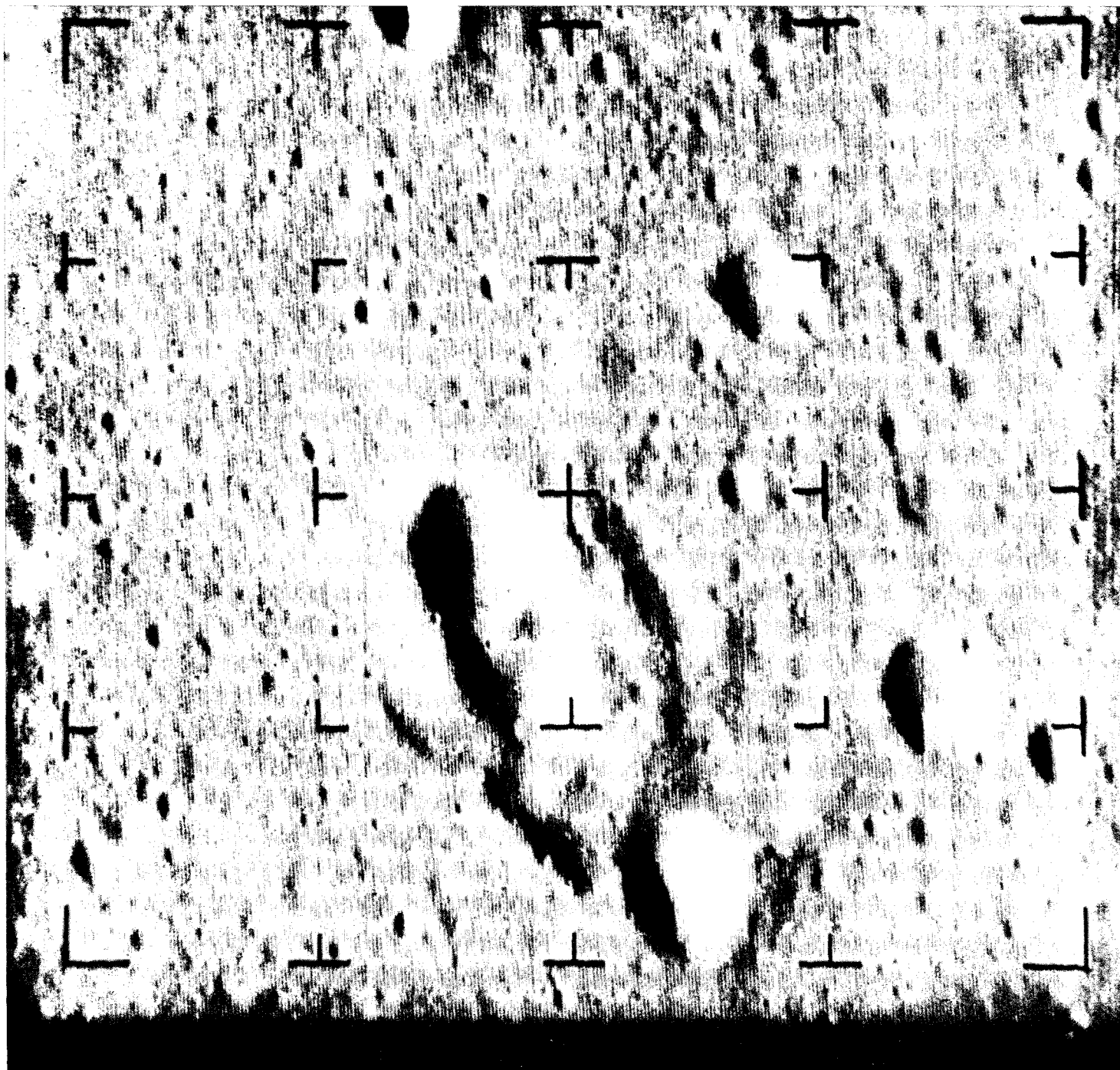an example of collapse features found in the area.

Fig. 3. *Ranger VIII* B-camera photograph 86, showing "square brick" depression and "bathtub."

Definite evidence for different types of collisional processes is found on these photographs, confirming similar evidence provided by terrestrial photographs. Thus, Delambre is known to be an older crater in the mountainous areas, with slump features in its walls and a rough floor and with no central peak. It is undoubtedly of collisional origin. On the other hand, Theon Junior and Theon Senior are two nearby collisional craters which have been formed in similar lunar material and have very smooth interiors. I suggest that Delambre was produced by a high-density object, and that the Theons were produced by low-density objects such as comet heads. (Photograph B22 [Fig. 4] shows these craters and features very well.) Other examples of both types are evident. A high-density object would penetrate into loosely conglomerated material and cause slumping, whereas a low-density object such as a comet head would produce a high-density, high-temperature mass of gas which could blow out smooth craters such as the Theons. These smooth craters are smaller than the craters with slumped walls, but I doubt that the difference can be ascribed entirely to size.

In general, little new information was obtained from the *Ranger VIII* pictures. They were unsatisfactory, in my opinion, because there was no nesting of the frames, so that the landing site was not present in any of the pictures. It was not possible, especially toward the end of the flight, to compare one picture with another in a satisfactory way. Comparison of the photographs is a feature I found particularly valuable in the *Ranger VII* series and very interesting in the case of *Ranger IX*.

C. The Ranger IX *Pictures*

The *Ranger IX* landing area in Alphonsus is in a region of the Moon believed for various reasons to be of volcanic origin. Kozyrev (Refs. 19 and 20) reported the escape of gases from the neighborhood of the central peak, and Earth-based photographs showed halo craters (craters surrounded by dark areas) in considerable numbers within the crater Alphonsus. It had been supposed for a long time that the halos of darker material in the neighborhood of these craters were an indication of the escape of gases from the interior of the Moon. Kozyrev claimed to have detected the spectrum of C_2, but band spectroscopists are very skeptical about this interpretation. On the basis of Kozyrev's suggestion, I made the proposal that the dark areas were due to graphite because of the deposit of C_2 on the surface. Of course, if Kozyrev's observation is not correct, this suggestion is not correct either. It has been pointed out that high-energy protons

would probably remove graphite in any case. The dark areas are quite similar in general appearance to dark areas on other parts of the Moon. This evidence for some sort of plutonic activity was an important reason for selecting Alphonsus for the *Ranger IX* landing site. It might be noted that Alphonsus is also a large crater filled with smooth material, and it was of interest to see whether this smooth material has characteristics similar to those of the mare areas. The B-camera took pictures to the east of Alphonsus, while the A-camera photographs covered the western areas predominantly; the landing area was to the north and east of the central peak.

Alphonsus is a very large crater, undoubtedly produced by the fall of a great object at some time in the past. The floor of the crater has been filled with smooth grey material, superimposed upon which are numerous craters and a central distribution of material oriented north and south, approximately in a direction toward the center of the Imbrian collision. This central region, which falls slightly to the west of the central peak, must have been produced during the formation of Mare Imbrium and consists either of material from the Imbrian collision itself or of material driven from the wall of Alphonsus by ejecta from the Imbrian collision. It will be noted, for example on photograph A55 (Fig. 5), that rather high cliffs occur on the western edge of this central mass, indicating that when it fell, it depressed the floor of the crater. This implies that the smooth material of the crater floor was in position before the Imbrian collision occurred; it also suggests that the smooth material of the crater floor was capable of considerable compaction, that is, that it is composed of unconsolidated material with ample pore space.

One of the marked general features which is immediately evident is that the number of craters per unit area within Alphonsus is greater than the number of craters on the Alphonsus crater walls. This indicates a very distinct difference between the kinds of materials which make up the walls and those of the crater floor. It is also true that the number of craters within Alphonsus is different from the number of craters in the neighboring smooth areas to the west of the crater, and even the western part of Alphonsus has a lower crater density than the eastern part. It is probable that several different explanations of these phenomena will be advanced.

It appears evident that there is some difference between the composition of the Alphonsus crater wall material and that of the smooth material of the interior. This might be explained as being due to a difference in the number of objects falling within the crater to produce
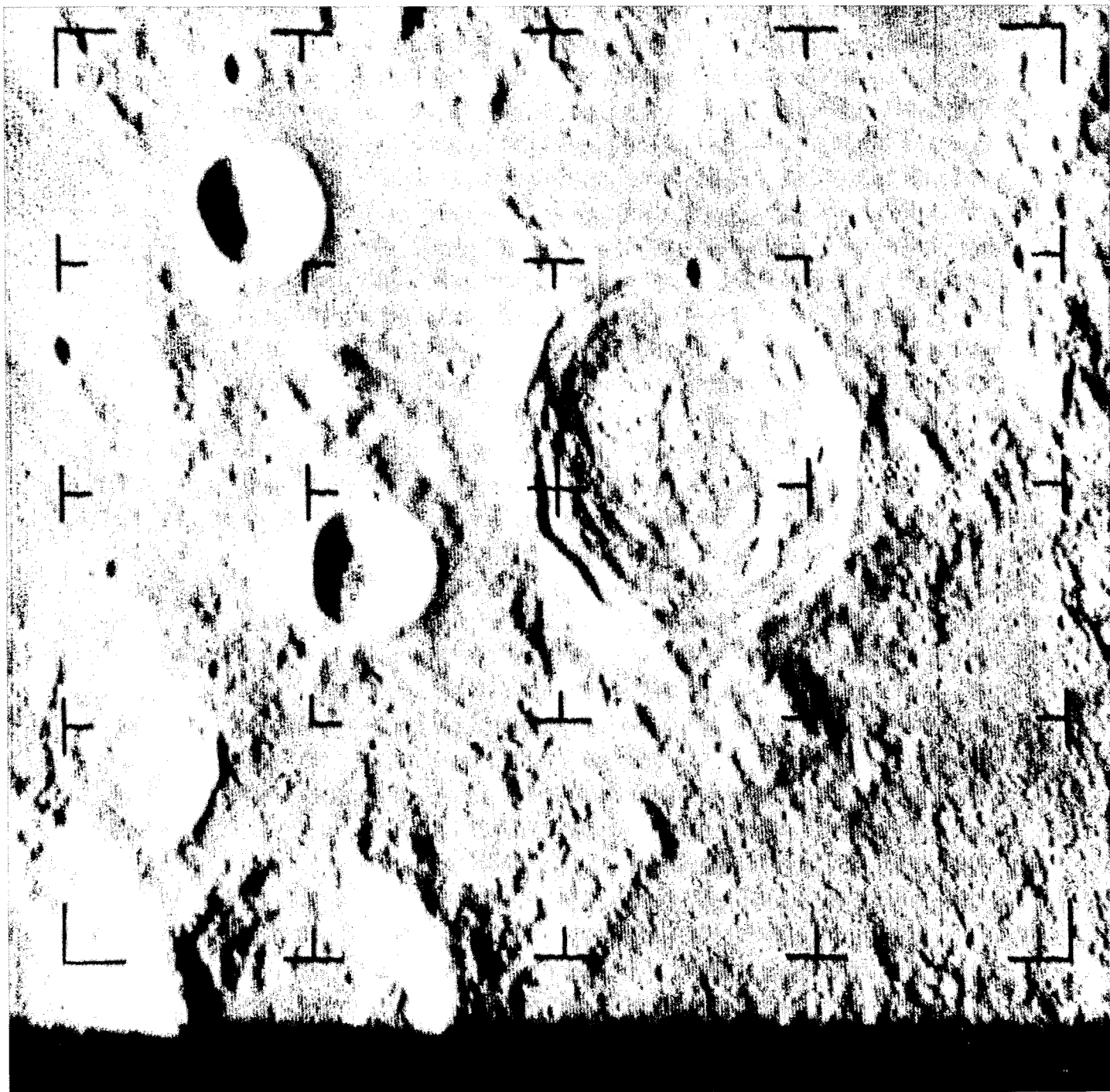
Fig. 4. *Ranger VIII* B-camera photograph 22, showing evidence for different types of collisional processes.
(Delambre has slump features in its walls, a rough floor, and no central
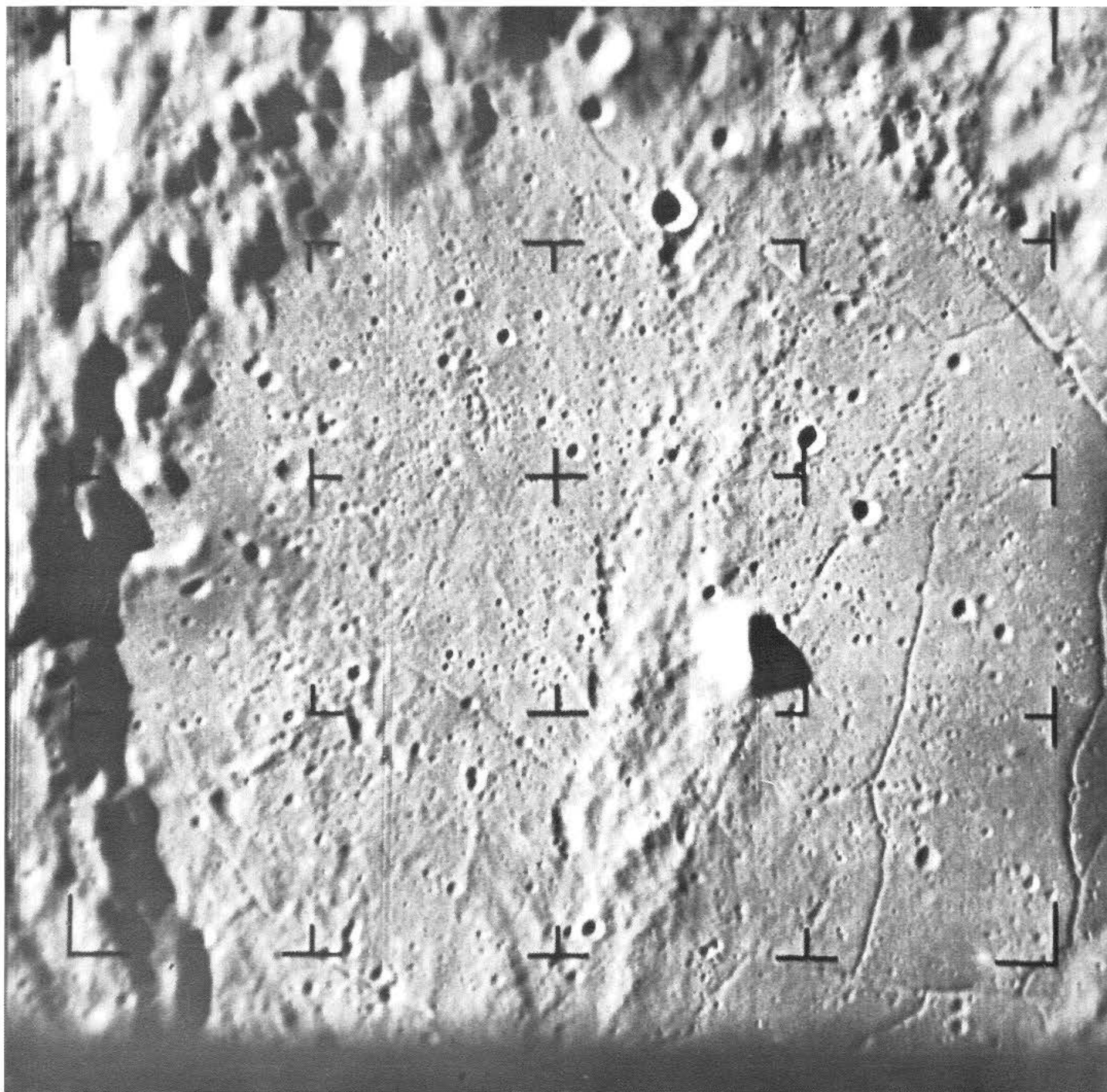peaks; Theon Junior and Theon Senior have smooth interiors.)

Fig. 5. *Ranger IX* A-camera photograph 55, showing high cliffs on W edge of central mass of Alphonsus. (Cliffs indicate that smooth crater-floor material was in position prior to Imbrian collision.)

small craters, in which case one would expect that most of them are secondaries and that for some reason an accidental variation occurred in the distribution of the falling objects. Another possible explanation is that the material within the crater was much more subject to the production of collapse craters than the material in the walls and outside. Undoubtedly, another explanation that will be offered is that more recent lava flows have occurred outside Alphonsus than within the crater. In regard to this last suggestion, it is curious that there is evidence for plutonic activity within Alphonsus, namely, the escape of gases from the interior of the Moon, whereas evidence of this kind outside the crater is far less obvious, if it exists at all. Some explanation for this apparent discrepancy can undoubtedly be given. It is difficult to arrive at a definite conclusion, except that there does seem to be evidence for a difference in physical properties of the crater walls and the floor regions.

Several kinds of craters are evident from the *Ranger IX* photographs. Many of the larger craters within Alphonsus are of the collisional type, and this type of crater also occurs to a considerable extent on the crater walls. Collisional craters appear to be approximately uniformly distributed between the interior of Alphonsus and the neighboring smooth areas, as well as in the mountainous regions. I believe that these craters are due to collisional effects that have been occurring since the general features were formed at some remote time.

Eruptive craters are characteristic of the Alphonsus floor and have been recognized on terrestrially obtained photographs for a good many years. They are in general surrounded with dark halos. Two in the west part of Alphonsus, beautifully shown on many A pictures (A46 [Fig. 1], for example) near the western wall, are quite obvious. One might think that these craters are primarily collisional in origin, but one of them is elliptical, lies on a crevasse, and is probably not collisional at all. Both craters are surrounded by the dark halos which are believed to consist of ash-like thrown-out material. This material obliterates some of the numerous craters in their neighborhood. Another eruptive crater lies just west of the central peak, again on a crevasse. These craters seem to be of a type that is quite distinct from most of the volcanic craters on Earth. Geologists whom I have consulted have confirmed this impression.

Other craters of the eruptive type can readily be seen on many other photographs. There are some eight, and possibly more, craters of this kind, most of which were detected on terrestrial photographs but are seen more clearly in the *Ranger IX* pictures. In general, they occur

on great crevasses. They appear to be due to the loss of gas from the interior of the Moon in an explosive or near-explosive type of eruption, and are surrounded by dark halos.

There appears to be no doubt but that many craters within the Alphonsus floor are collapse features. Great crevasses extend across the floor of the crater, in some cases terminating in rows of depressions which are probably craters of a collapse nature. For example, A46 (Fig. 1) gives a suggestion of this feature. It appears that many similar features in other areas of the Moon may indeed be due to collapse and not to secondary collisions. Other examples of features of this kind can be found in the *Ranger IX* photographs, as for instance in A26 (Fig. 6) near the northern part of the picture, just west of Davy. This particular depression might be interpreted as being due to a collision phenomenon, i.e., a group of objects having fallen in such a way as to produce the slightly curved linear feature, but because of the large size of the craters in the chain, it seems improbable that this is a correct explanation. The *Ranger IX* pictures have supplied a great deal of evidence for collapse features, which also seemed evident in *Ranger VII*. *Rangers VIII* and *IX* have reinforced my previous conclusion in this regard.

The paucity of craters on the mountainous areas and their mottled character have been mentioned previously. This is best seen on the B-camera photographs, ranging from about 45 down through 74 (Fig. 7). In the region shown in these pictures, the mountainous walls are covered with very poorly formed craters and with patches that reflect light more readily than the smooth crater floor. There are small craters in the relatively level mountainous regions, but craters on the walls are badly formed. This indicates that the crater walls consist of rather soft material, which slides down the hill in a collision. Gault and Quaide have made experiments on sloping loose material which suggest this explanation.

On the other hand, there are bright peaks in the crater walls, as seen in the east walls of Alphonsus, which extend above the surrounding areas as though they consisted of more durable material than the surroundings and therefore were able to maintain themselves on the top of the peak as other material was eroded to lower levels. It comes to mind immediately that this material may be iron–nickel or that it contains considerable amounts of iron–nickel. Material of the iron–nickel kind would be unlikely to retain its brightness under bombardment by protons from the Sun and by micrometeorites, but these brighter spots are actually only slightly brighter than their surroundings, though they do appear to be
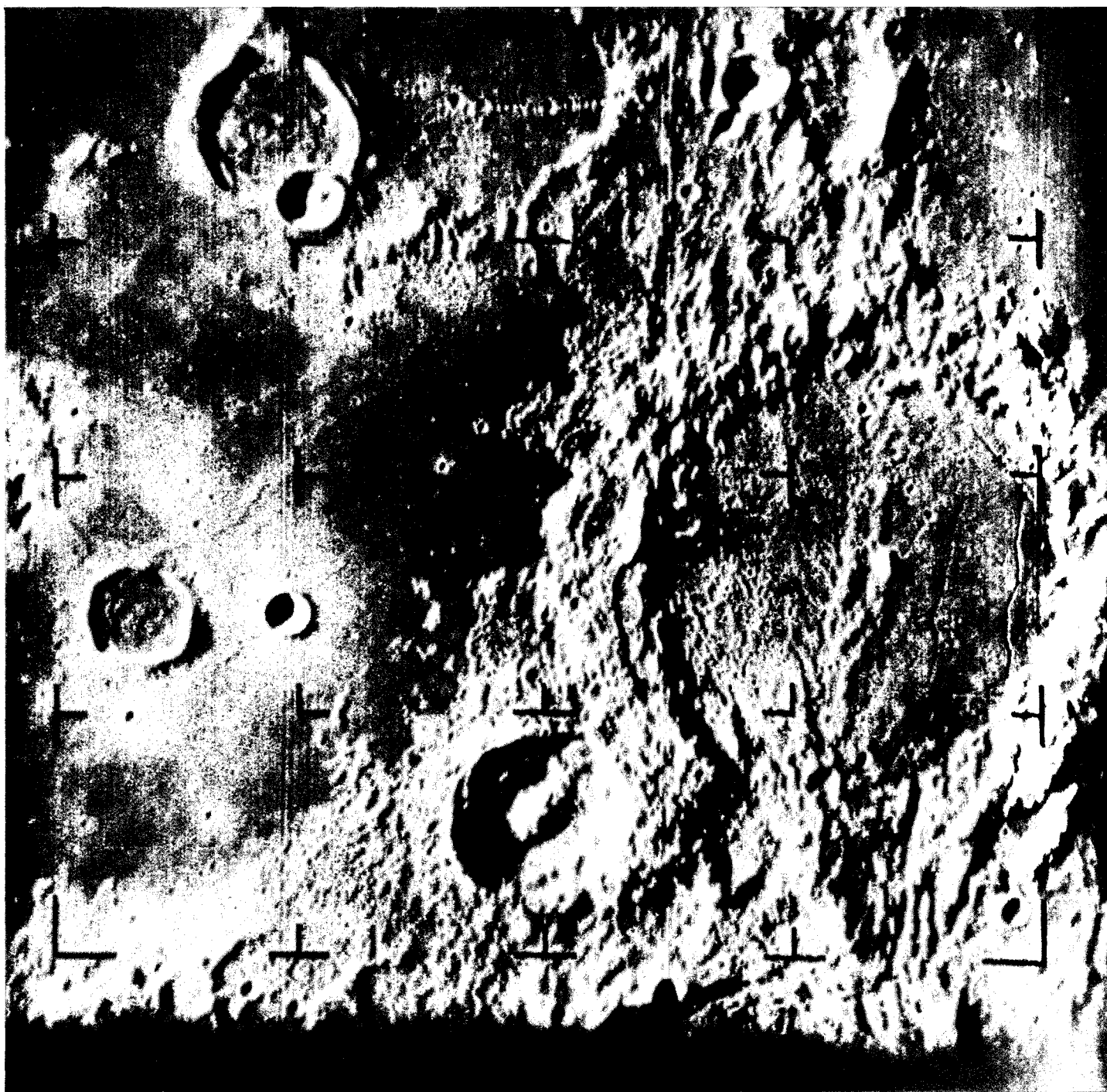
Fig. 6. *Ranger IX* A-camera photograph 26, showing example of collapse feature just W of Davy.
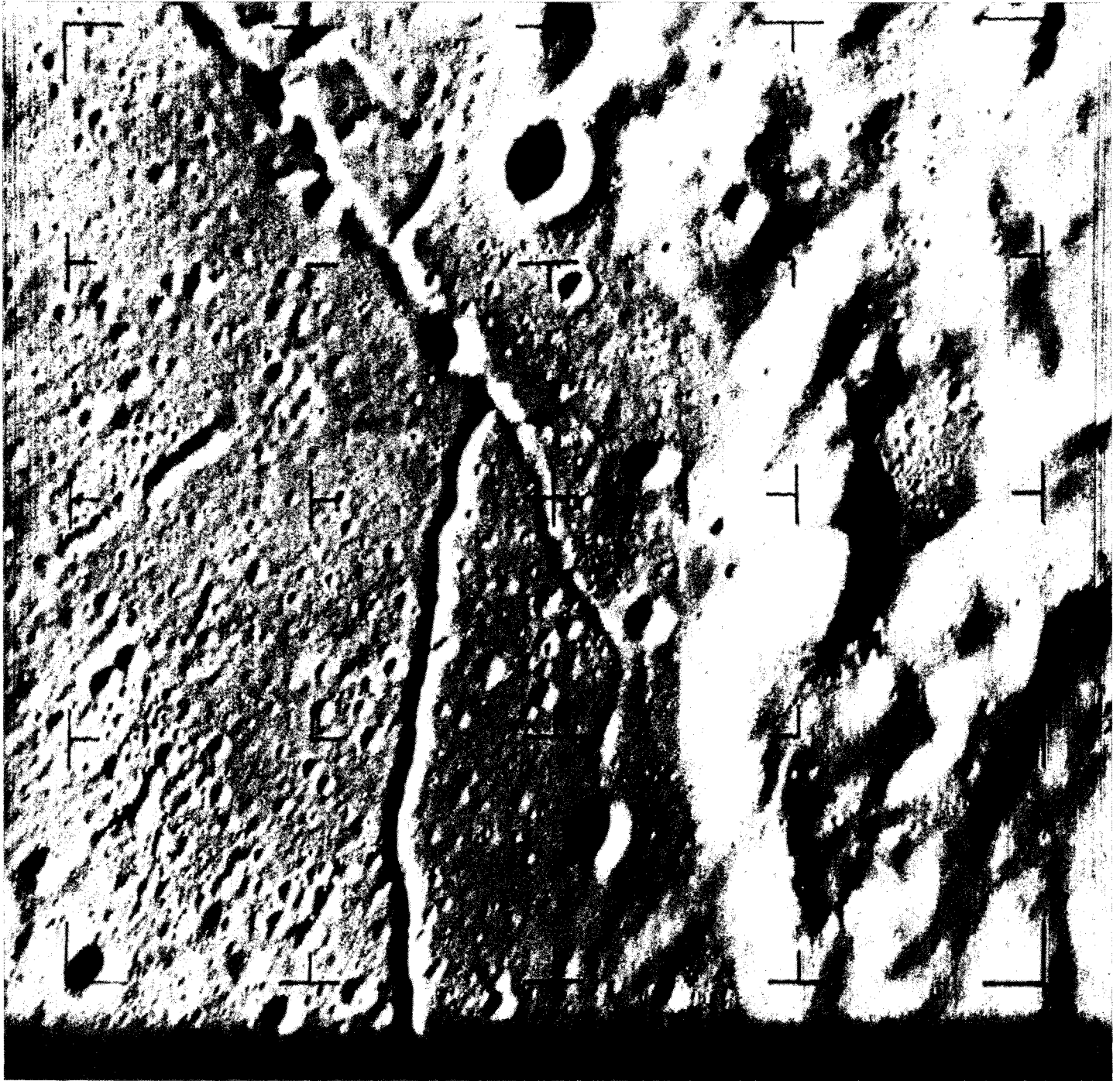
Fig. 7. *Ranger IX* B-camera photograph 74, illustrating paucity and mottled
character of craters in mountainous areas.

considerably stronger. One would certainly expect, on almost any grounds, that some iron–nickel would be present on the lunar surface because of the bombardment by meteorite type of material during geologic time and probably during the terminal stage of the formation of the Earth–Moon system. One might call to attention that Urey's model for the Moon, as a primary object which developed substantial masses of iron–nickel below its surface (Ref. 12), is of precisely the nature needed to produce substantial masses of iron–nickel in the walls of a large crater such as Alphonsus. If the primitive Moon had a layer of iron–nickel at some unknown but, let us assume, short distance below the surface, then a massive collision such as that required to produce Alphonsus could well have lifted metallic iron–nickel from beneath the surface and left some masses distributed on the high areas of the crater walls.

There is a question as to whether or not the smooth areas within Alphonsus and neighboring craters, in patches within the crater walls and in the neighborhood of the craters, are lava flows, as many undoubtedly believe. As Gold remarked some 10 years ago, and as mentioned earlier, it seems odd that lava flows should have come up through all of this region of the Moon within craters, between craters, and in small areas in crater walls and outside them, and have left smooth lava flows sometimes apparently with approximately the same level as the large crater floor and sometimes with markedly different levels in the smooth areas. This theory assumes a very substantial volcanic activity, which, as explained in the introduction to this Part, seems improbable on energetic grounds. There are other reasons for questioning this interpretation. For example, photograph B74 (Fig. 7) shows a smooth dark area in the crater wall region at the right and, as a matter of fact, at the south end, a line leaving this region and extending southward to the crater floor. When I first saw this picture as it was being transmitted during the flight, it occurred to me that the dark patch might be the bottom of a dried-up lake and that the line at the south was the path of the overflow. Almost immediately thereafter, however, this initial explanation did not seem very probable, one of the reasons being that lower overflow regions might have existed through other paths from the postulated lake-bed area. But after a number of months of consideration, I am convinced that the postulate that such smooth areas as the one in question are indeed the bottoms of dried-up lake beds is probably just as reasonable as the postulate of lava flows, if not more so. On B35 (Fig. 8), for example, there are other areas in this region that might be discussed on a similar basis.

The high flat area on the western wall of Alphonsus, which Mr. Whitaker facetiously labeled "Lake Titicaca" as the pictures were arriving, is shown in A61 (Fig. 9) and neighboring pictures. This elevated smooth area on the western wall seems to have a slight rim around it on the east side and a higher wall in the west, and possibly an overflow region in the shadow toward the north. The area is approximately 1½ km above the floor of the crater. Is it not astonishing that a lava flow would come up through the broken and fragmented materials of the walls to a high level and not find some crevasses, some openings through the material of the crater wall to a lower level? It strikes me that the explanation of "Lake Titicaca" as a lava flow is unreasonable and that the possibility that it is indeed the remains of a temporary lake area is worthy of consideration.

The great crevasses within the floor of Alphonsus are, of course, obvious and were indicated in terrestrial photographs, although they can be seen in much greater detail in the *Ranger IX* pictures (for example, A61 [Fig. 9]). There is a concentration of them near the walls, and most follow the walls of the crater to some extent. There are others that have general directions across the crater floor, with possibly some preferred directions, which, however, are not sufficiently consistent to make it possible to draw any important conclusions relative to them.

Because of the illumination, there is always a tendency to see north and south crevasses of this kind more readily than east and west ones, though I do find two such lines of craters on A61 (Fig. 9) in the southeast region, running almost due east and west. The crevasses are evidently collapse features of a marked kind, and they often terminate in rows of craters extending from the crevasse area. In some cases, they cross the central Imbrian deposit, indicating that they were formed after this deposit was laid down on the crater floor. Some, I am sure, will maintain that these crevasses are of the same character as crevasses due to lava flows found on the Earth; I am skeptical of this explanation for reasons explained in the introduction to this Part. The highly broken and fragmented outer layers of the Moon due to its terminal collisional history also provide an adequate explanation. Again, they might well be the result of the evaporation of subsurface water along the lines suggested by Gold, Kopal, and myself, especially if evaporation occurred from solid water. One argument against the water hypothesis is that some of these crevasses enter the mountainous regions, such as the line of craters in the northern crater walls seen in A61 (Fig. 9) and the prominent line of craters mentioned earlier, lying to the west of Davy. A line of craters
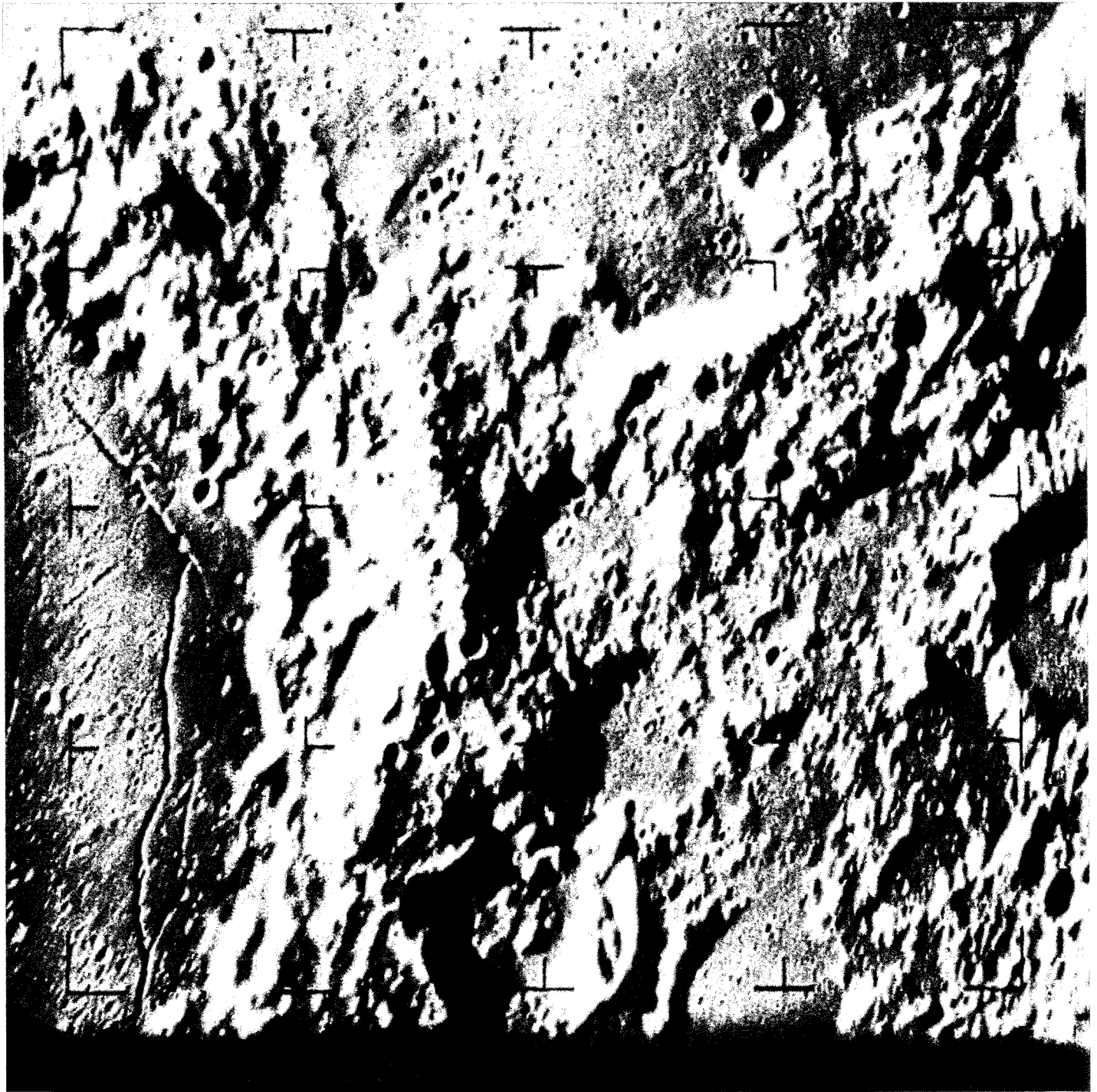
Fig. 8.   Smooth areas such as those in *Ranger IX* B-camera photograph 35 support the postulate
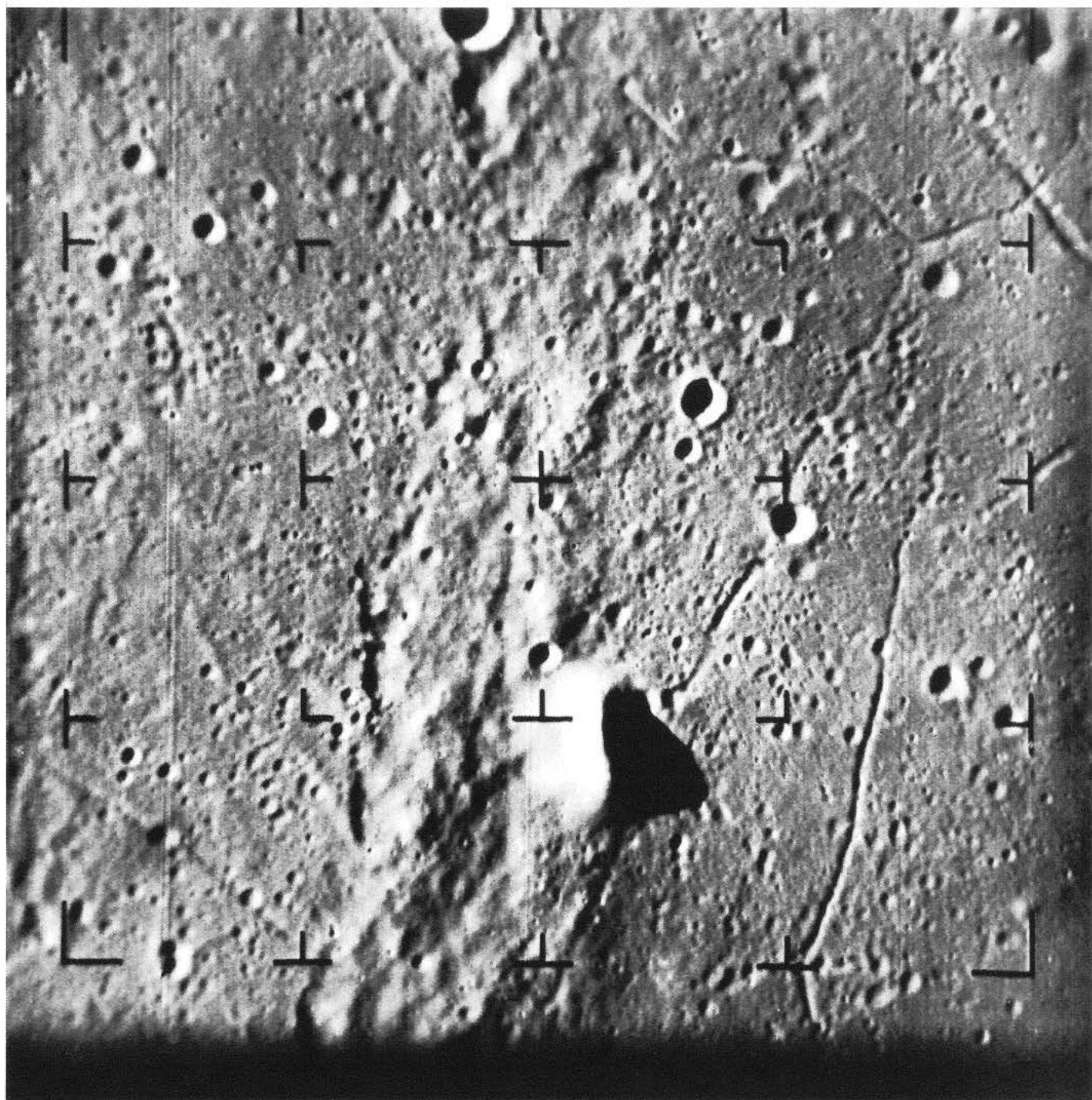that these regions may be the bottoms of dried-up lake beds.

Fig. 9. *Ranger IX A-camera photograph 61,* showing "Lake Titicaca" on W wall of Alphonsus.

such as that in A61 also indicates that the source of the crevasses is not entirely related to the smooth material within the crater floors regardless of its origin or character. It is very likely that no particular single explanation will account for all of these features, and possibly more than one suggested mechanism has contributed to the final result.

At this point, it is appropriate to note Alpetragius and its curious peak, which has puzzled people for a long time. Gold (Ref. 22) and MacRae (Ref. 23) have suggested that this peak is related to the pingo phenomenon in regions where permafrost exists on the Earth. Of course, it is much larger than the usual pingo formations, which resemble the whole structure — crater wall and central rounded peak—in many ways. More specifically, the explanation suggests that in the collision which produced Alpetragius, an opening to lower sources of water was produced through which water flowed to the surface and froze, creating the curious rounded mass in the middle of the crater. I am not convinced of the validity of this explanation, but as far as I am aware, no other suitable explanation of this unusual peak has been offered. It just may be that it is another rare modification of a central peak produced by the collision phenomena that produced the craters on the Moon and, incidentally, apparently the central peaks of some of the craters on Mars.

It should also be noted that there are ridges in the floor of Alphonsus to the west of the central line of Imbrian debris which have a predominantly northwest-southeast orientation. These may be related to the fall of the Imbrian debris, which came from the north and fell with a component of velocity toward the south, possibly producing this effect.

The P pictures and the last B and A pictures show regions where smooth, pillowy masses appear in crevasses of moderate size (i.e., meters to tens of meters in width). These features are found in all three of the *Ranger* series of photographs. They are interpreted by Dr. Kuiper as conclusive evidence for the lava-flow hypothesis and for lava flows so recent that little dust has accumulated on the surface. If such lava flows are very ancient, i.e., 4.5 billion years old, then no fragmentation of the surface has occurred in all geologic time. This is highly improbable, for there is good reason to believe that much fragmentation due to micro- and macrometeorite infall, atomic-ion bombardment, etc., has occurred. The assumption of recent lava flows meets also with many difficulties when one considers the entire history of the lunar surface,

with its superimposed craters, maria, more craters, mountainous masses, etc. I have no specific solution to this difficulty, but if the permafrost hypothesis emphasized by Gold should be correct, it may be that an explanation of the pillow structures will be found in some movement of the permafrost.

D. Summary

The *Ranger* pictures give considerable evidence supporting the view that the whole lunar surface—maria and terrae—consists of highly unconsolidated material. In the first place, because of the erosion caused by micrometeorites, small macrometeorites, bombardment with ionized atoms from the Sun, and heat and light and effects, we expect that some layer of fragmented material will be present. The fact that craters up to approximately 300 or 400 m appear to be smoothed over indicates that this erosion may be at least as deep as some 20 or 40 m in places.

The conclusions of Gault and Quaide, based upon their laboratory studies, are in accord with this general conclusion. There is, however, an element not consistent with this view, namely, the very smooth, rolling character of some of the crevasses in the lunar surface. No entirely satisfactory explanation of this inconsistency has occurred to the writer, but it is not certain at all that such features must be ascribed to lava flows upon which there had been no erosional effects of any kind since they were formed.

There is extensive evidence for slump features on the Moon. The dimple effect may indeed indicate that there is a hole at the bottom of the crater through which material drains, although I believe that this is not necessarily the only explanation for these objects. There are extensive crevasses in the maria and terrae. Large crevasses have been evident for years from Earth-based photographs, both in the smooth regions and in the mountainous regions. The *Ranger* pictures show many such features on a smaller scale. The slump features range from some tens of meters in size up to kilometers, with various sizes spanning the whole range almost continuously. These features are very similar in some ways to slump features on the Earth, mostly seen in connection with lava flows, although such slump features are rather small on the Earth, where they are due to the draining of lava from crusted-over channels. One of the major problems in ascribing the slump features on the Moon to similar phenomena is that it is difficult to see from what point the lava flowed and where it went, if it is actually lava.

There are extensive rows of slump features evident in the *Ranger VII, VIII,* and *IX* pictures. Sometimes it is difficult to distinguish between these and the elongated features that may have been produced by collisions.

Several sources for the crevasses below the surface can be postulated. (1) The cavities below the surface are the residue of such features produced by the original intense collisional processes that formed the surface of the Moon. (2) They may be due to the collapse of cavities left by lava flows (though I find it difficult to take this suggestion seriously). (3) If water was once present in the maria of the Moon below the surface, if it froze, and if it has evaporated over geologic time, it can be expected that great subsurface cavities and low-density material would exist. I feel sure that the first source of crevasses is present, and I am uncertain as to the others.

It has been evident that there are marked differences in nature as well as appearance between the maria and other smooth surfaces of the Moon and the mountainous areas. There is, for example, the difference in color. The mare areas in general are darker than the mountainous regions. Lava flows on the Earth are generally darker than the areas upon which they flow; but we must keep in mind that terrestrial areas are subject to the effects of water and oxygen in the air, which produce sediments and eroded material of lighter color than the lava flows. Such effects should not be present on the Moon. The mountainous areas can hardly be claimed to be light for the same reason that sedimentary and other rocks subjected to the action of water on the Earth have a light character. Studies made on the effect of proton bombardment on silicate materials indicate that all such materials turn dark under these conditions, some more so than others. Possibly Gold's suggestion of erosion from the mountainous masses to materials below has some merit in explaining the differences in color.

There are greater crater densities in Alphonsus than is generally true in the mountainous areas. The craters are mostly small and much more densely distributed than had been suspected from terrestrial photographs. The increased density of craters suggests to me that they are collapse features in many cases. In Alphonsus, at least, the greatly increased number of craters may be due in part to this effect.

The mottled character of the crater walls of Alphonsus indicates some inhomogeneity of composition, with some material having darkened less than other material. These are markedly brighter peaks than have been referred to,

which indicates that they erode less rapidly than neighboring material and have remained as rather definite projections on the tops of certain mountainous areas. Since, according to all suggested theories of the origin of the Moon, iron–nickel should be present on the lunar surface, it seems likely that these stronger masses consist of such material. Indeed, the mottled character of the mountainous crater walls may be due in part to this same composition.

The greatest source of controversy in regard to the surface of the Moon is, of course, the presence of lava in the maria and its origin, the possible presence of finely divided material, and the possible presence of water within this material as an explanation of the great smooth areas. Two sources of lava have been suggested. The first is internal, which postulates a high-temperature interior; for the various reasons outlined above, this appears to me to be quite improbable. But it would be reasonable to suppose that in the early history of the Moon, as it was accumulating and the intense bombardment of the surface took place, substantial temperatures existed below the surface even if it were not melted. Collisional effects of solid materials of a poorly consolidated character occurring at moderate temperatures could well have produced a considerable conversion of kinetic energy to heat energy and perhaps some melting. The origin of lava on the Moon was ascribed to the collisional processes by Gilbert some 72 years ago. In my early studies on this subject, I accepted Gilbert's conclusions. They have been criticized in subsequent years by people who maintain that collisional processes will not produce melting. There are difficulties with their arguments, in that collisional processes on the Moon of a sufficient magnitude to produce the maria probably did not involve materials of uniform composition and of highly consolidated character; hence, more heat may have been produced in such collisions than would be expected in collisions involving uniform and compact materials. There are also important difficulties with the origin of lava by melting deep in the lunar interior which, it seems to me, the proponents of the lava hypothesis have not tried to solve. However, I would not be willing to maintain that no lava flows of any kind have occurred on the Moon. I have thought that Mare Tranquillitatis looked like a large lava flow, and I still do; and there are a few terminal wall effects shown in the *Ranger VIII* pictures that would confirm this point of view.

That the maria of the Moon consist of dust or fragmented material is a hypothesis that goes back again to the early years of this century but which was brought forward in modern form by Gold some 10 years ago. It

seems to me that the processes postulated by him should be present to some extent. But I do believe that the great collisions that have produced the maria and the great craters of the Moon should have produced enormous quantities of fragmented material. Assuming temporary atmospheres during the enormous collisions that produced the maria, one would expect that substantial amounts of fragmented material would have fallen in localized areas of the lunar surface. Also, the larger collisions could well have penetrated below the outer surface of the Moon to regions where mixtures of gases, presumably mostly water, and solids similar to ignimbrite flows on the Earth could have been produced, accompanied by an outwelling of enormous masses of finely fragmented material. Such flows on the Earth are of a very acid character, consisting of the granitic type of material. To postulate that material of this kind exists on the Moon implies some way of producing such material by processes presumably similar to those that have produced them on Earth. It is very difficult to believe that granites, which are the result of active and complicated igneous processes on the Earth, should be present as a prominent feature on the surface of the Moon. But possibly finely divided material of nongranitic composition may have been produced by different processes, such as the great collisions penetrating deep below the surface.

It would be difficult to prove the existence of water in the surface regions of the Moon from the results of these studies. It would be equally difficult to maintain definitely that it is not present. Escape of the Moon from the Earth might well have been accomplished by some retention of water on its surface. We know so little about the processes by which water is captured on planets during their formation that the possible capture of water on planetary objects is not necessarily excluded.

The halo craters in Alphonsus and elsewhere on the Moon are most readily explained as being due to the escape of gases from the interior which carry with them dust and ash-like material; the most likely gas to be expected is water. In fact, it is a general belief that the surface water of the Earth has come largely from the interior as a result of volcanic action. The halo craters do not look to me like typical Earth volcanoes, and they indicate a much milder type of plutonic activity than that characteristic of the Earth. Otherwise, I can find no reliable evidence from the *Ranger* pictures for the escape of water from the interior of the Moon.

Gold's explanation of Alpetragius' peak being related to the terrestrial pingo phenomenon is interesting, but of course, the evidence was present before the *Ranger* pictures were taken. The "crater with the rocks" of the *Ranger VII* pictures may be due to a similar effect, and there is a second crater shown in the *Ranger VII* series, with two black dots in it, that may indicate another crater of this kind. However, this sort of effect is not evident in any of the craters of the *Ranger VIII* and *IX* series.

Much has been learned about the lunar surface as a result of the *Ranger* pictures, but the interpretations are very controversial in character. It is to be hoped that actual samples of the lunar surface will be returned to the Earth. When this occurs, many of the postulates that are made in this discussion and others will be subjected to serious re-evaluation. A few samples taken almost at random on the Moon will settle the questions of whether differentiation of the lunar surface has occurred, whether granites and basalts are present, and thus, whether lava flows of a terrestrial type exist, and whether free water has had any part in shaping the surface. It is to be hoped that such chemical tests will be made in the future.

REFERENCES

1. Urey, H. C., Elsasser, W. M., and Rochester, M. G., "Note on the Internal Structure of the Moon," *Astrophysical Journal*, Vol. 129 (1959), pp. 842–848.

2. Runcorn, S. K., "Convection in the Moon," *Nature*, Vol. 195 (1962), pp. 1150–1151.

3. Baldwin, R. B., *The Face of the Moon*, Chicago: University of Chicago Press (1949).

4. Watts, C. B., Private communication and address before AAAS meeting, Washington, D.C. (1958).

5. Urey, H. C., "Origin and History of the Moon," Chap. 13, *Physics and Astronomy of the Moon*, ed. by Z. Kopal, London: Academic Press (1962).

6. Urey, H. C., "Age of the Moon, Chemical Composition, Geological Aspects, Stress and Cooling History," *Proceedings of the Conference on Lunar Exploration*, Virginia Polytechnic Institute, Blacksburg, Va., August 1962 (1963), pp. III-1–III-31.

7. MacDonald, G. J. F., "Calculations on the Thermal History of the Earth," *Journal of Geophysical Research*, Vol. 64 (1959), pp. 1967–2000.

8. Dietz, R. S., "The Meteoritic Impact Origin of the Moon's Surface Features," *Journal of Geology*, Vol. 54 (1946), pp. 359–375.

9. Gold, T., "The Lunar Surface," *Monthly Notices of the Royal Society*, Vol. 115 (1955), pp. 585–604.

10. Urey, H. C., "The Origin of the Moon's Surface Features," *Sky and Telescope*, Vol. 15, Nos. 3 and 4 (1956), pp. 108–111 and 161–163.

11. Urey, H. C., "Primary and Secondary Objects," *Journal of Geophysical Research*, Vol. 64 (1959), pp. 1721–1737.

12. Urey, H. C., "Meteorites and the Moon," *Science*, Vol. 147 (1965), pp. 1262–1265.

13. Urey, H. C., "On the Origin of Tektites," *Proceedings of the National Academy of Sciences*, Vol. 41 (1955), pp. 27–31.

14. Urey, H. C., "Origin of Tektites," *Science*, Vol. 137 (1962), pp. 746–748.

15. Gilvarry, J. J., "The Nature of the Lunar Maria," *Astrophysical Journal*, Vol. 127 (1958), pp. 751–762.

16. *Ranger VII: Part II. Experimenters' Analyses and Interpretations*, Technical Report No. 32-700, Jet Propulsion Laboratory, Pasadena, California, February 10, 1965.

17. Smalley, V. G., and Ronca, L. B., Abstract, *Transactions of the American Geophysical Union*, Vol. 46 (1965), p. 138.

18. Gault, D. E., Quaide, W. L., and Overbeck, V. R., *Interpreting Ranger Photographs from Impact Cratering Studies*, Preprint, Goddard Space Flight Center, April 15–16, 1965.

REFERENCES (Cont'd)

19. Kozyrev, N. A., "Observation of a Volcanic Process on the Moon," *Sky and Telescope,* Vol. 18 (1959), pp. 184–186.

20. Kozyrev, N. A., *The Moon,* ed. by Z. Kopal and Z. Mikhailov, New York: Academic Press (1959), p. 263.

21. Urey, H. C., "The Early History of the Solar System as Indicated by the Meteorites," *Proceedings of the Chemical Society,* London (March 1958), pp. 67–78.

22. Gold, T., Private communication (1965).

23. MacRae, D. A., paper presented at the American Astronomical Society Meeting, Montreal, Dec. 28–30, 1965.

ACKNOWLEDGMENT

I wish to thank Dr. Alexander R. McBirney for interesting conversations in regard to this report. Following are some general comments made by him.

"I find no unequivocal evidence for lava flows. There is a scarcity or total lack of such features as broad lava shields with summit craters, fissure vents with lines of spatter cones, contrasting textures resulting from slight differences of vesiculation and oxidation, and fumarolic alteration in possible vent areas. Depressions thought by some workers to be collapsed lava tubes are too large to be compared with terrestrial lava tubes. There are few if any pressure ridges, flow lines, kipukas, and many other features that are also ubiquitous in lavas.

"On the other hand, there is certainly evidence for mantle bedding by aerially deposited fragmental debris. It is difficult to state whether the debris results from collision or has been carried to the surface in gaseous eruptions. One would expect that if the cones were actually volcanic pyroclastic cones formed by gaseous eruptions, there would be a few recognizable lava flows coming from the same vents. These cones could possibly be formed by gas discharges through a thick dust layer without any magmatic activity.

"In view of the present popularity of the theory that ignimbrites fill the maria, I have tried to find evidence for this, either pro or con. If magmatic activity has resulted in volcanism on the Moon, it would seem that ignimbrites of rhyolitic composition would be easier to produce than lavas of basaltic composition, provided the appropriate composition is available to be melted. Ignimbrites tend to produce very flat surfaces lacking the textural features of lava flows, and many of the maria fillings could well be composed of fragmental debris transported and deposited by 'nuées ardentes' or 'ash flows.' I do not believe that this question can be decided on the basis of the photographs alone, however.

"Many craters seem to be caused by subsidence or collapse. They are identical to collapse pits in volcanic regions or over large mine cavings. These are quite distinct in form from the more common bowl-shaped craters which are presumably impact scars."

VI. PRODUCTION OF THE RANGER BLOCK III PHOTOGRAPHIC RECORDS*

Ewen A. Whitaker

Lunar and Planetary Laboratory
University of Arizona
Tucson, Arizona

An important phase of the *Ranger* program is the production and publication of photographic prints which have been prepared from the original magnetic tape and 35-mm film records. Clearly, the aim is to produce prints which retain as much of the original information content as possible, and which have not been degraded by the introduction of spurious details or density gradients in the intermediate stages. The writer has been closely associated with the various phases of this program.

The following Sections have been included in this Report in order to supply information concerning the procedures adopted in the production of the photographic editions of the *Ranger VII, VIII,* and *IX* atlases.

A. Original Records

In all three missions, the output of the receiving equipment at the Goldstone station of the Deep Space Instrumentation Facility was recorded simultaneously on magnetic tapes and on 35-mm film via two kinescopes, one each for Channels F and P. The kinescope recorders

possessed the added facility of being able to produce 10-sec Polaroid prints of selected frames without interfering with the exposure of the 35-mm film.

After the completion of each of the three missions, the exposed but undeveloped 35-mm films were placed in cans and sealed. The tape recordings were immediately played back through the recording apparatus without any change being made to the various dial settings, since further 35-mm films were being recorded. In the remainder of this Part, the films produced during the actual missions are referred to as "prime" data, while those made subsequently by replaying tapes are termed "secondary" data. Eastman Kodak television recording film, type 5374, was used in the production of both prime and secondary films.

The completed secondary films were flown from Goldstone to the Los Angeles area, where they were processed at a large commercial processing house and delivered to JPL for examination. Since the procedures from this point were slightly different for the three missions, each is described separately.

B. Ranger VII

Examination of the secondary negative films by the Experimenter team and JPL staff showed immediately that the quality of the photographs was excellent; not only were all densities within the optimum dynamic range of the film, but also the amount of electronic "noise" present was very small. The only apparent degradation introduced by the tape recorder was due to "jitter" caused by slight fluctuations in tape speed; this, in turn, caused a slight lengthwise displacement of consecutive TV scan lines, which are manifested as small ripples in the images of the fiducial marks (Fig. 1a). The same marks as recorded on the prime film are, of course, undistorted (Fig. 1b).

The spatially variable sensitivities of the vidicon targets over their exposed areas caused considerable shading in the photographic images; this effect may be seen in Fig. 2, which illustrates the appearance of typical portions of both F- and P-channel films at natural scale. The considerable difference in density between the A-, P_3-, and P_4-camera frames on the one hand, and the B-, P_1-, and P_2-camera frames on the other is due to widely differing camera sensitivities. These differences in sensitivity were deliberately introduced in order to minimize the possibility of gross under- or overexposure.

For the preparation of press-release photographs, ten representative frames were chosen from the secondary films, and prints were made by direct enlargement. Considerable "hand-dodging" was required in this process in order to remove as much as possible of the density gradients. The prints were then photographed at natural scale, and the 8 × 10-in. negatives so produced were used to prepare, by contact printing, the large number of press kits required.

On the strength of the good photographic quality of the secondary films, the two prime films were processed in a similar manner (to a gamma of 1.4). Next, two positive films were made from each of the prime negative films, using Kodak type 5235 fine-grain panchromatic film in a continuous-motion contact printer. In this case, the films were developed to a gamma of 1.0. A pair (one for the F and one for the P channel) of these master positive prime films was then used to prepare a number of duplicate negative prime films, which were later distributed to the Experimenters and certain collaborating establishments.

Comparison of the prime positive film with one of the duplicate negatives prepared from it revealed a very small reduction in image quality, due to the nature of the process. A small number of frames showed a slightly
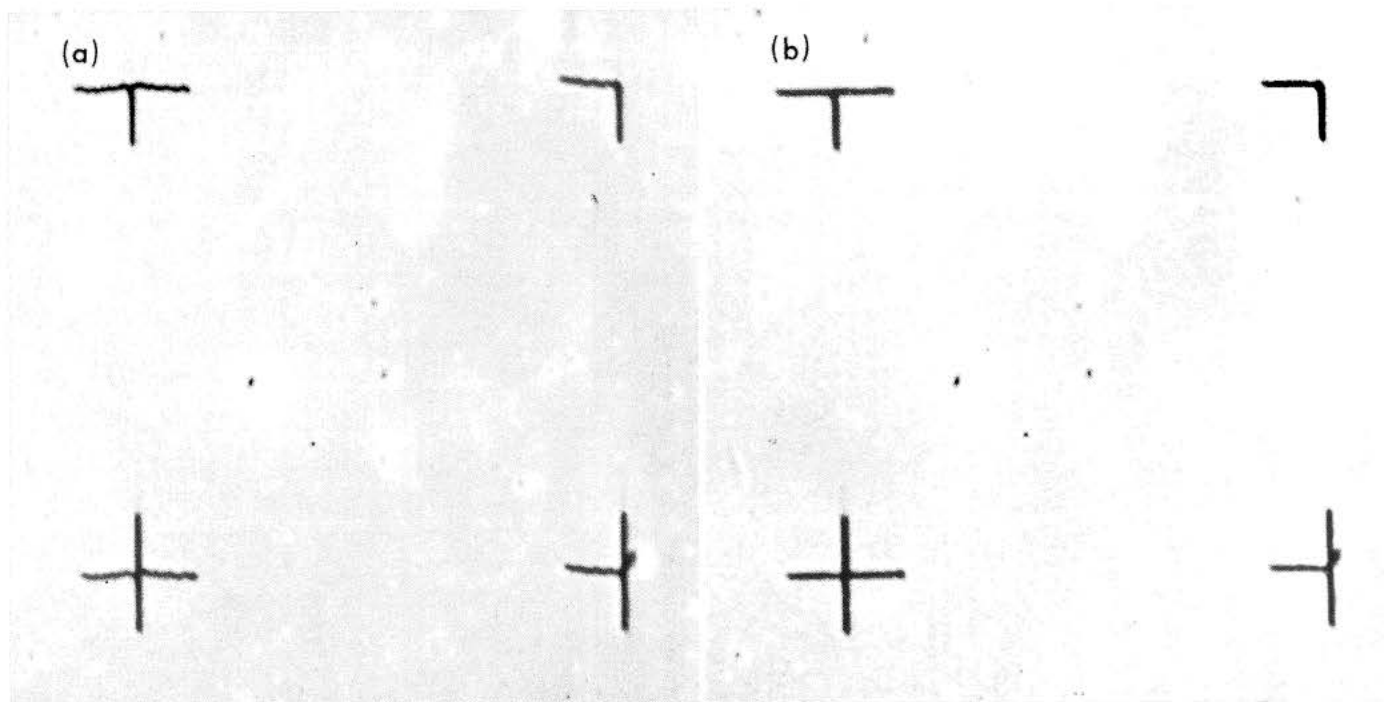

Fig. 1. Portion of a *Ranger VII* A-camera frame, illustrating (a) the small distortions due to recording on magnetic tape as compared with (b) the prime film data.
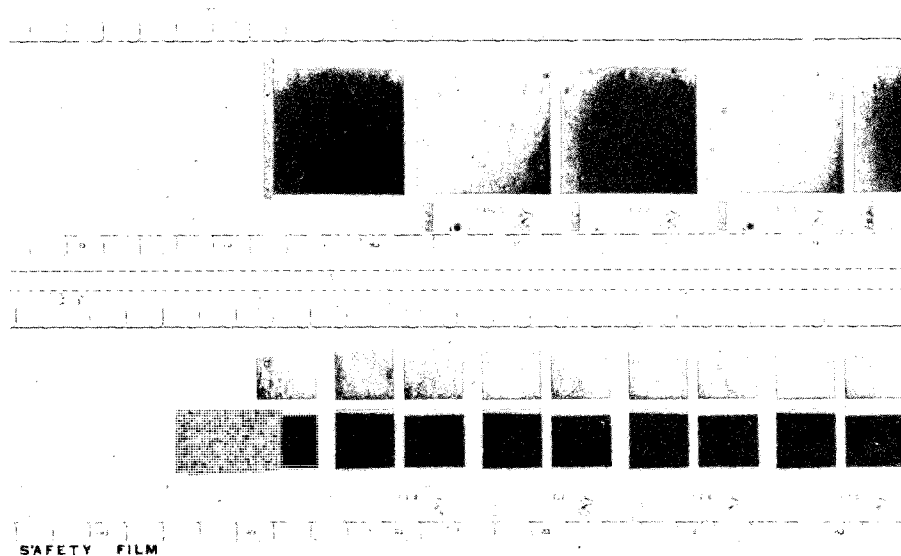
Fig. 2. Last few frames of *Ranger VII* duplicate negative prime films, shown at natural scale. (Top, F-channel images; bottom, P-channel images.)

greater degradation, apparently due to imperfect contact, but these were considered acceptable. Image jitter in the secondary negatives was considered more objectionable than this slight degradation; therefore, the decision was made to use the prime material, preferably the master positive film, to produce the photographic atlases.

1. Size and Form of the Atlases

Because of the consistently high quality of the *Ranger VII* photographs, Dr. Kuiper recommended that all the F-channel data be published, with the P-channel data to be reviewed at a later date. This recommendation was accepted. It was also deemed desirable to have a number of complete A-camera atlases prepared in time for the XII General Assembly of the International Astronomical Union, to be held in Hamburg from August 25 to September 3, 1964.

It was agreed that for these atlases, an image size slightly smaller than 8 in. (20 cm) square, similar to that used for the press kits, would be optimum. In order to avoid getting fingerprints on the image area during normal handling, it was decided to use 11 × 14-in. photographic paper. For durability, each print would be mounted on a linen backing, and each atlas, consisting of approximately 200 unbound prints and an accompanying explanatory text, would be housed in a strong cardboard box provided with a side-opening flap secured with snap fasteners.

2. Production of the A-Camera Atlas

Because roughly 100 to 200 atlases would be required, production by direct enlargement was excluded. Therefore, a set of 8 × 10-in. negatives had to be prepared from which contact prints could be made. This involved one or two intermediate steps, for which several alternative methods were available. Removal of the vidicon-produced density gradient from each frame presented the most difficult problem. Since a Log-E-Tronics automatic dodging enlarger was available at JPL, it was decided to use this instrument to deal with the shading problem. Accordingly, the film holder was modified to accommodate 35-mm film and supplied with a piece of anti-Newton-ring glass to prevent buckling of the film.

One of the prime master positive films was used, and enlargements of each A-camera frame were made on 8 × 10-in. sheets of Kodak Plus X film. The full dodging capability of the enlarger had to be used in order to remove the shading; this entailed exposure times of the order of 80 sec for each of the 199 frames.

Contact prints were made from these negatives using a Morse contact printer, which permitted further shading control by means of lamps that could be switched off selectively. The photographs were printed on Du Pont Varigam paper because it was readily available and had the correct contrast characteristics for use with the

argon lamps of the printer. Fifty sets of prints were produced at JPL under the partial supervision of Lunar and Planetary Laboratory staff.

After the decision had been reached to make 150 atlases in all, the production of the remaining 100 copies was undertaken by a commercial photography house situated close to the University of Arizona in Tucson. This permitted close supervision of the production of the prints.

3. Production of the B-Camera Atlas

Because the automatic dodging of the Log-E-Tronics enlarger had reduced the visibility of lunar rays in many A-atlas frames, it was decided to use a somewhat different technique in the case of the B-camera frames. Experimentation showed that the shading could be almost entirely nullified by the penumbral effects of two small, opaque screens placed below the lens of the enlarger. As before, the prime master positive film was used, but enlargements were made on 8 × 10-in. sheets of Estar-base Kodak Commercial film through a good-quality Leitz enlarger. The films were developed to a gamma compatible with that of the Morse printer and Varigam paper setup used before.

The 150 sets of 200 prints each were made at the same commercial photography house in Tucson and under the same close supervision as the A-camera prints.

4. Production of the P-Camera Atlas

The P cameras recorded a total of about 970 usable frames, each containing four images. Because of the large number of pictures recorded in a relatively short time, there was considerable redundancy of information, especially in the earlier stages, in which the apparent image motion is virtually undetectable from frame to frame. The fact that the P-camera fields of view fell close to the overlap of the A- and B-camera fields meant even further redundancy. However, an examination of the material showed that the P frames provided valuable confirmatory evidence of several lunar-surface formations, and that certain formations were shown better or more completely by these cameras. Since not less than 150 prints would be required for good coverage without excessive redundancy, it was again decided to make a 200-print atlas; 190 of these would be selected from the prime film, with the remaining 10 being prints of the last 10 frames prepared by a digitized technique by which distortions, reticle marks, and coherent and noncoherent noise could be removed.

Examination of the master positive film revealed a systematic loss of definition in the P_3- and P_4-camera photographs of each alternate frame; this was clearly caused by slow movement, in one direction only, of the exposing shutters. Choice of frames was therefore limited to those with the best definition, up to the point at which every frame was included.

It was found that by selecting the frames on the basis of an increase in scale of approximately 2.5%, it was possible to represent the entire P-camera series by about 180 frames. A preliminary choice was therefore made using this criterion. Careful examination of the film showed that the quality of the P_1- and P_2-camera images varied from frame to frame due to the effects of coherent noise (caused by extraneous radio frequencies) and random noise (caused by the mechanical jarring occasioned by the operation of the shutters of other cameras). Figure 3 illustrates the maximum (a,c) and minimum (b,d) effects of this interference. The preliminary choice was therefore modified to include frames in which the interference was small and the P_3- and P_4-camera images were optimum. An additional slight modification was made to provide better coverage of the crater Bonpland H.

After the decision was made to use the same format for the P-camera atlas as for the A- and B-camera atlases, and also to preserve the image order as it appeared on the original film, the production of the 190 contact negative films was undertaken at the Lunar and Planetary Laboratory. Enlargements were made on 8 × 10-in. sheets of Kodak Commercial film as before, using the prime master positive film in the same Leitz 35-mm enlarger. Because of the differences in the densities of the P_1- and P_2-camera images from those of the P_3 and P_4 cameras, considerably different exposure times were required for these pairs to produce comparable densities in the negatives. A limited degree of hand dodging was applied to the P_1 and P_2 images in order to reduce the small amount of shading present.

Negatives of the last ten frames were also prepared by the JPL staff, but in this instance, their digital-computer technique was used to remove fiducial marks, noise, and

Fig. 3. Representative *Ranger VII* P-camera frames, illustrating image degradation: (a) P_1 frame with electronic interference, (b) P_1 frame with minimum electronic interference, (c) P_2 frame with mechanical interference, (d) P_2 frame with minimum mechanical but some electronic interference.
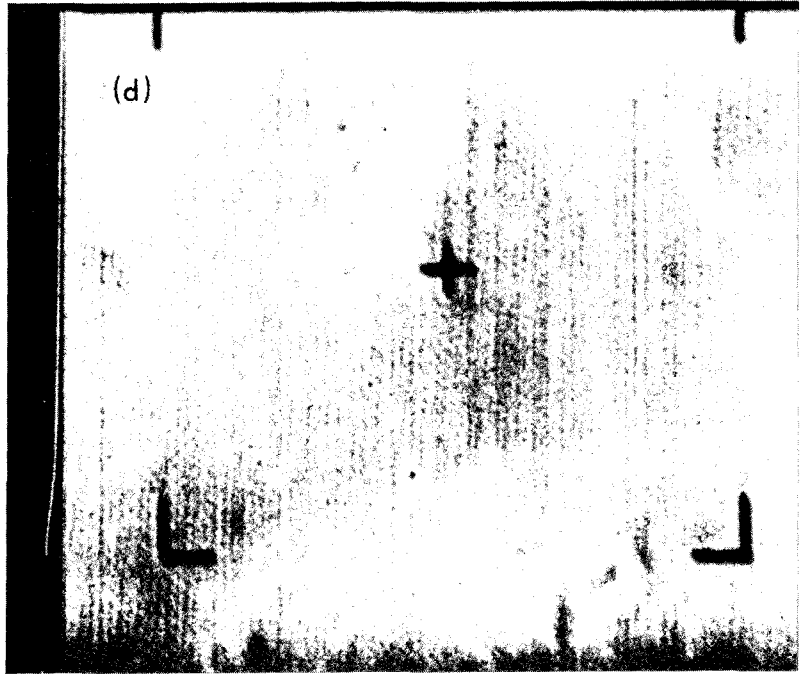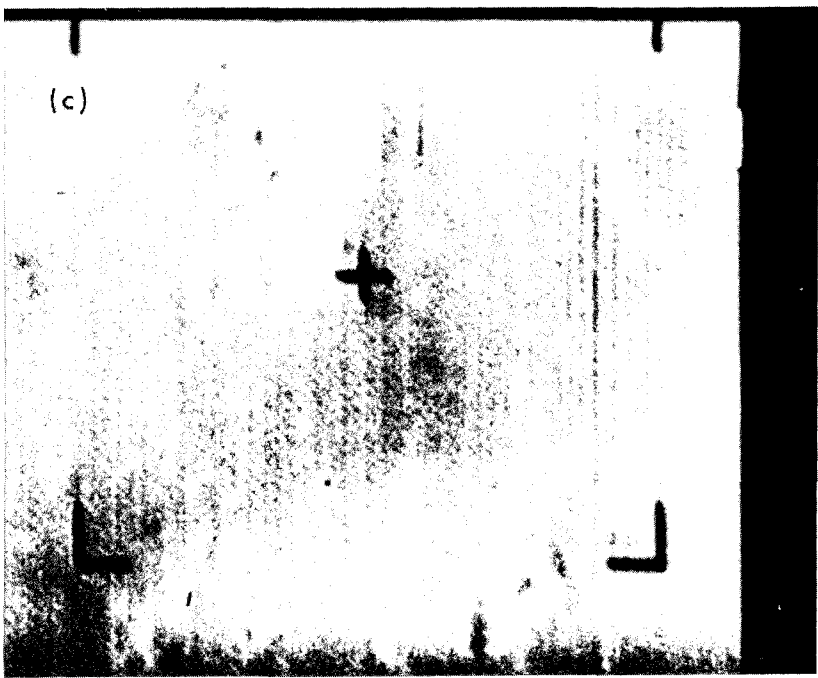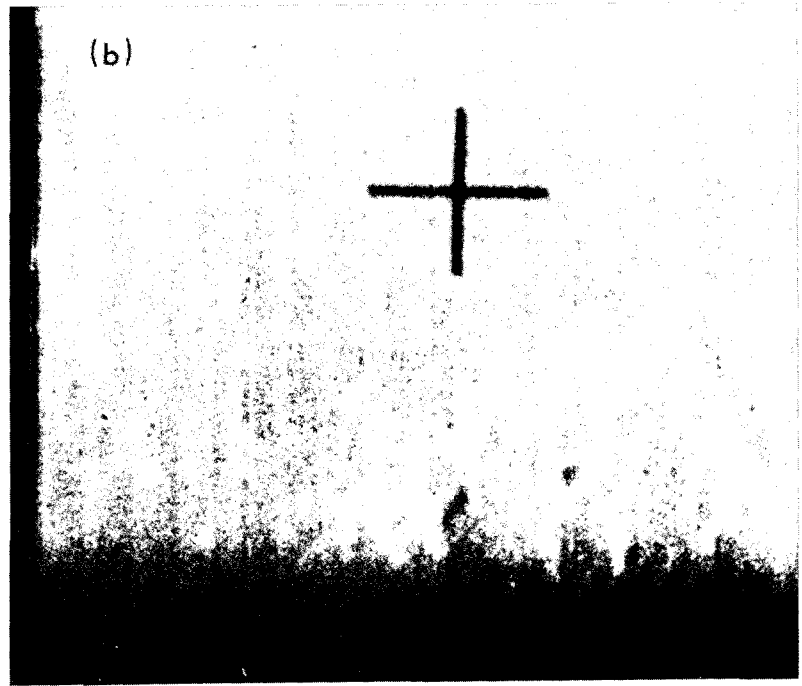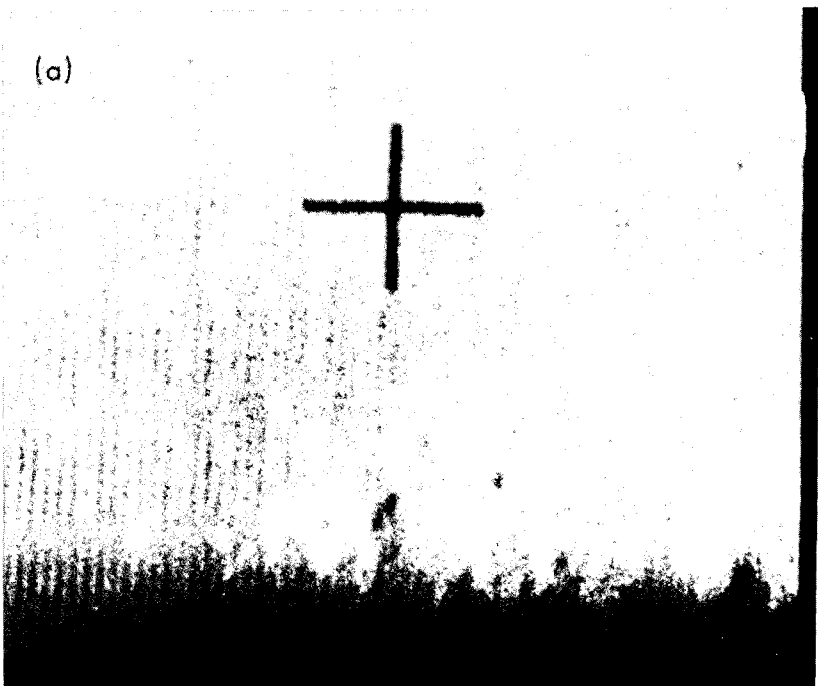
distortions. The 150 sets of contact prints were prepared from these 200 negatives by the same commercial photographers who made the A and B prints, under the usual LPL supervision.

5. Discussion of the Atlases

As mentioned earlier, the attempt was made to present as much pictorial detail as possible in the photographs. Since photographic paper does not possess the dynamic range of films, photometric distortion was introduced in some of the prints which had large density variations from the mean. Clearly, some photometric distortion had to be introduced into those frames in order to retain detail. For example, on sheet 1 of the A atlas, the density of the formation Deslandres, situated at the terminator in the lower right corner, is little different from that of Mare Humorum in the lower left corner. At the time the photograph was taken, however, the former was considerably darker than the latter. Users of the atlases should therefore not make brightness comparisons from the prints. In addition, as has already been pointed out, the contrast between the lunar ray elements in A-atlas frames 160–199 was reduced by the Log-E-Tronics automatic-dodging enlarger. (Persons wishing to make a study of these rays should obtain a film copy of the F-channel data and prepare their own enlargements.)

Although it was possible to equalize densities over large areas, it was impossible to do so over small areas. Thus, in B-atlas frame 85, for instance, the right inner walls of at least ten craters are completely white, whereas in the original master positive film, these brightly illuminated walls actually display detail. In B frames 179–193, the images of the four bright craters passing through the field were sufficiently large to allow longer exposure through a hole in a piece of cardboard during the production of the printing negatives. Despite this, the appearance of these craters in the atlas sheets is still not considered optimum. Similar conditions prevail in certain P-atlas sheets.

Since all photographic paper stretches considerably more in one direction than the other during the drying process, and the paper manufacturers cut the paper in either direction, all atlas prints suffer from an elongation in either the horizontal or the vertical direction. (Users making measurements should bear this in mind, and should also remember that the photographs represent electronic, not optical, images, and suffer slight distortions in small areas, from frame to frame.)
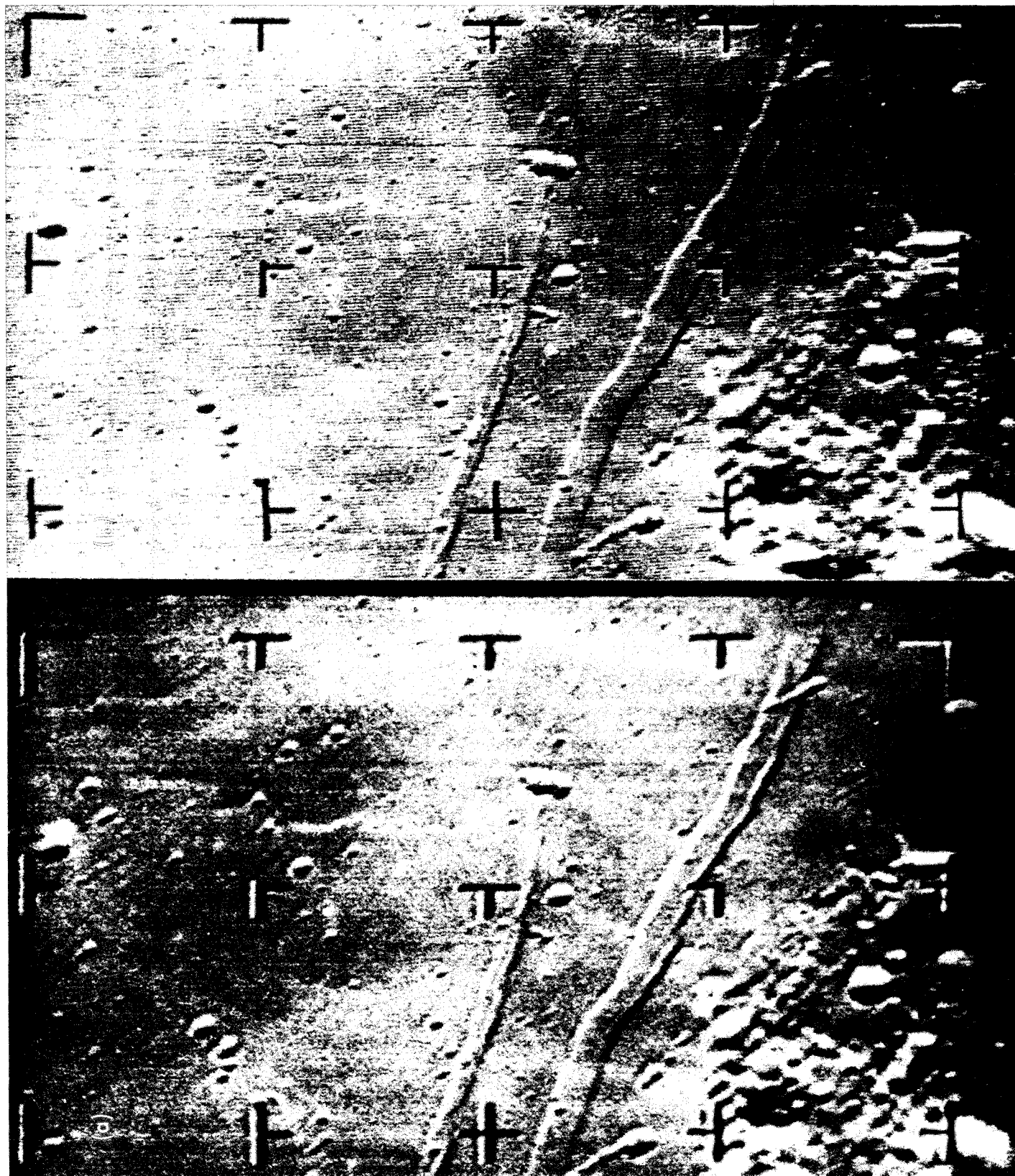
C. Ranger VIII

The plan for data recording on this mission was basically the same as for the previous one. However, in the case of *Ranger VIII*, the Pioneer site at Goldstone was also made available for the preparation of magnetic tapes, and the brightness and contrast settings of the film recorder were different from those used for the previous mission.

For the purposes of quick examination and the production of press-release sets, the magnetic tapes were played back through a link recorder at the Space Flight Operations Facility at JPL in Pasadena. Although this method produced quick results, it was known that some of the finer detail would be lost, and that spurious bright edges would be produced on one side of all dark regions (e.g., reticle marks and crater shadows). Eight representative frames were chosen for the press kits and prepared as before. Unfortunately, the photographs, intended only for immediate and temporary use, have been reproduced in the literature. Figure 4a illustrates a portion of one of these prints, while 4b was prepared directly from a secondary negative film made on the Goldstone film recorder.

Because of the higher contrast settings for this mission, and also because of the early camera turn-on, the initial frames of both the secondary film and the prime negative film were considerably overexposed. Additional secondary films were prepared with a lower gain setting; this removed the overexposure, but the finer detail was lost.

At the time of writing, a firm decision has not been reached on which films to use to prepare the 8 × 10-in. printing negatives. The overexposure of much of the prime film precluded the use of the prime master positive, which was prepared from it for this purpose. It was therefore decided to use two secondary negative films to produce the printing negatives, the one with the high-gain setting for the later frames and the other for the earlier frames; the actual point of changeover has not yet been determined. The printing negatives will be made by the JPL Photography Section, using a Durst enlarger. Dodging will be accomplished by means of the two-opaque-screens technique already described. The positive transparencies so produced will be used to prepare the contact printing negatives in a normal contact printer.

Fig. 4. Portion of *Ranger VIII* B-camera frame, illustrating (a) poorer quality of press-release photograph as compared with (b) photograph prepared from tape playback film.

Printing of the atlas sheets will be undertaken by the same commercial photographers in Tucson that prepared the *Ranger VII* atlases, under close supervision by the LPL staff.

As noted already, the decision to reproduce the entire *Ranger VII* F-channel as well as much of the P-channel material was made because of the consistently excellent quality of the data and the fact that this was the first successful mission of the *Ranger* Program. However, it was never intended that the entire material from *Rangers VIII* and *IX* would be published in atlas form, but rather that a representative selection should be made. An examination of both the *Ranger VIII* and *IX* films indicated that a total of between 150 and 200 frames from all three series (i.e., A, B, and P) would be adequate for each mission. It was decided that the boxes should be of the same size as those used for the *Ranger VII* atlases but that, to facilitate the handling of the prints, each atlas would be divided into several sections, and the sections placed in individual folders. In order that the boxes could accommodate the extra thickness of the folder, the atlases were limited to 170 prints.

The *Ranger VIII* mission produced about 270 each A- and B-camera frames and 1650 P frames. Because no terminal maneuver was performed, no nesting sequences were taken by any of the cameras, although, of course, there was considerable overlap of all frames except for the last three P images. Thus, the areas covered by the photographs were long and wedge-shaped. (See Figs. 10 and 11.)

The earlier A frames were taken under moderately high solar illumination, and (as was anticipated) were poorer in definition than good Earth-based photographs. The changeover occurred at about the 190th frame, the last 80 being better in definition than good Earth-based photographs. Almost the entire B series was superior in definition to Earth-based photographs, while only the last 15 P frames equalled or exceeded the last A and B frames. The final choice of frames was therefore made as follows:

A camera:

> Frames 1–190, 5 frames chosen at about 33% scale increase between frames.
>
> Frames 191–220, 5 frames chosen at about 10% scale increase between frames.
>
> Frames 221–270, every frame.
>
> TOTAL, 60 frames.

B camera:

> Frames 1–220, 40 frames chosen at about 7.5% scale increase between frames.
>
> Frames 221–270, every frame.
>
> TOTAL, 90 frames.

P cameras:

> Last 15 frames, plus 5 others selected because of useful coverage of interesting lunar formations.
>
> TOTAL, 20 frames.

GRAND TOTAL for all cameras, 170 frames.

D. Ranger IX

The processes for recording the *Ranger IX* photographic data were similar to those employed for the *Ranger VIII* mission, with the additional facility of prime data recording on film and in Polaroid prints at the Pioneer site at Goldstone. Furthermore, a microwave link established between Goldstone and Pasadena permitted both tape recording and real-time viewing of the F-channel frames as they were received. The slow scans of the A and B cameras were converted into stationary kinescope pictures by means of a special scan converter, and the images were relayed live over the national commercial television networks.

The magnetic tapes recorded at JPL in Pasadena via the microwave link from Goldstone were played back through the link recorder, whose performance had been considerably improved since the previous mission, and preliminary prints were prepared for examination by the Experimenters and release to the press. Eight representative frames were selected for the press-release kits and reproduced in the usual manner.

Contact copies of the prime negative films were made as before, but a step process was used on this occasion to eliminate relative motion during exposure of the frames. Duplicate negative films were subsequently prepared from these positives by the same process and distributed to the Experimenters and other concerned members of the *Ranger* team, and secondary negative films were again made by replaying the magnetic tapes. Examination of the prime duplicate negative films and the secondary negative films showed the latter to be slightly better in quality than the former, although the difference was very small. It was decided to use the secondary films to prepare

the atlas prints in order to avoid possible degradation of some of the frames by the two extra photographic processes involved in producing the prime duplicate negative films. The JPL Photography Section prepared 8 × 10-in. film positives and made enlargements of selected frames onto 8 × 10-in. sheets of Du Pont Commercial film ("Cronar" base) by means of a Durst enlarger. As before, the two-screen dodging technique was used for the F-channel frames, and differential exposure times were employed for the P_1–P_2 and P_3–P_4 image pairs. Printing negatives were made from the positives by direct contact printing, and contact prints are being prepared in Tucson under the supervision of the writer.

The *Ranger IX* mission produced about 220 each A- and B-camera frames and 1340 P frames. The terminal maneuver aligned the nominal average camera axis with the terminal velocity vector, ensuring complete nesting of the A frames, partial nesting of the B frames, and nesting of the last P frames. Coverage of the lunar surface was therefore more restricted than in either of the previous missions.

Comparison of the *Ranger IX* material with the well-known, high-quality lunar photographs taken with the Mt. Wilson 100-in. telescope in September 1919 under similar illumination conditions showed that comparable definition occurred at about the 130th frame for the A camera, the remaining 90 being superior. All except the first few B-camera frames were of superior definition. Comparison of the P frames with the last two or three F frames showed that only the last 12 P frames were equal to, or better than, the F frames. None of the earlier P frames contained better detail than the F-channel frames, because the larger fields of view of the F cameras permitted any given lunar surface features to be photographed from a viewpoint closer than that of the

P cameras. The final choice of frames was therefore made as follows:

A camera:

> Frames 1–168, 18 frames chosen at 7.6% scale increase between frames.
>
> Frames 169–220, every frame.
>
> TOTAL, 70 frames.

B camera:

> Frames 1–165, 33 frames chosen at 3.8% scale increase between frames.
>
> Frames 166–220, every frame.
>
> TOTAL, 88 frames.

P cameras:

> Last 12 frames.

GRAND TOTAL for all cameras, 170 frames.

E. Discussion of the Ranger VIII and IX Atlases

Since, at the time of writing, only the *Ranger IX* A-camera atlas has been prepared, it is not possible to present a specific discussion of the material. However, the same general remarks concerning density equalization, lack of detail in bright highlights, differential paper stretching, etc., apply to these atlases as to the *Ranger VII* atlases.

The areas of the lunar surface covered by the *Ranger VII, VIII,* and *IX* atlas prints are shown in Figs. 5–15. Figures 9, 12, and 15 indicate the relationship between the last F and P frames for each mission.

Fig. 5. Earth-based lunar photograph, illustrating coverage by *Ranger VII* A-camera frames 1 and 150 and impact point. (Curved lines in this and in Figs. 6–8, 10, 11, 13, and 14 are loci of corners outlining total area photographed.)
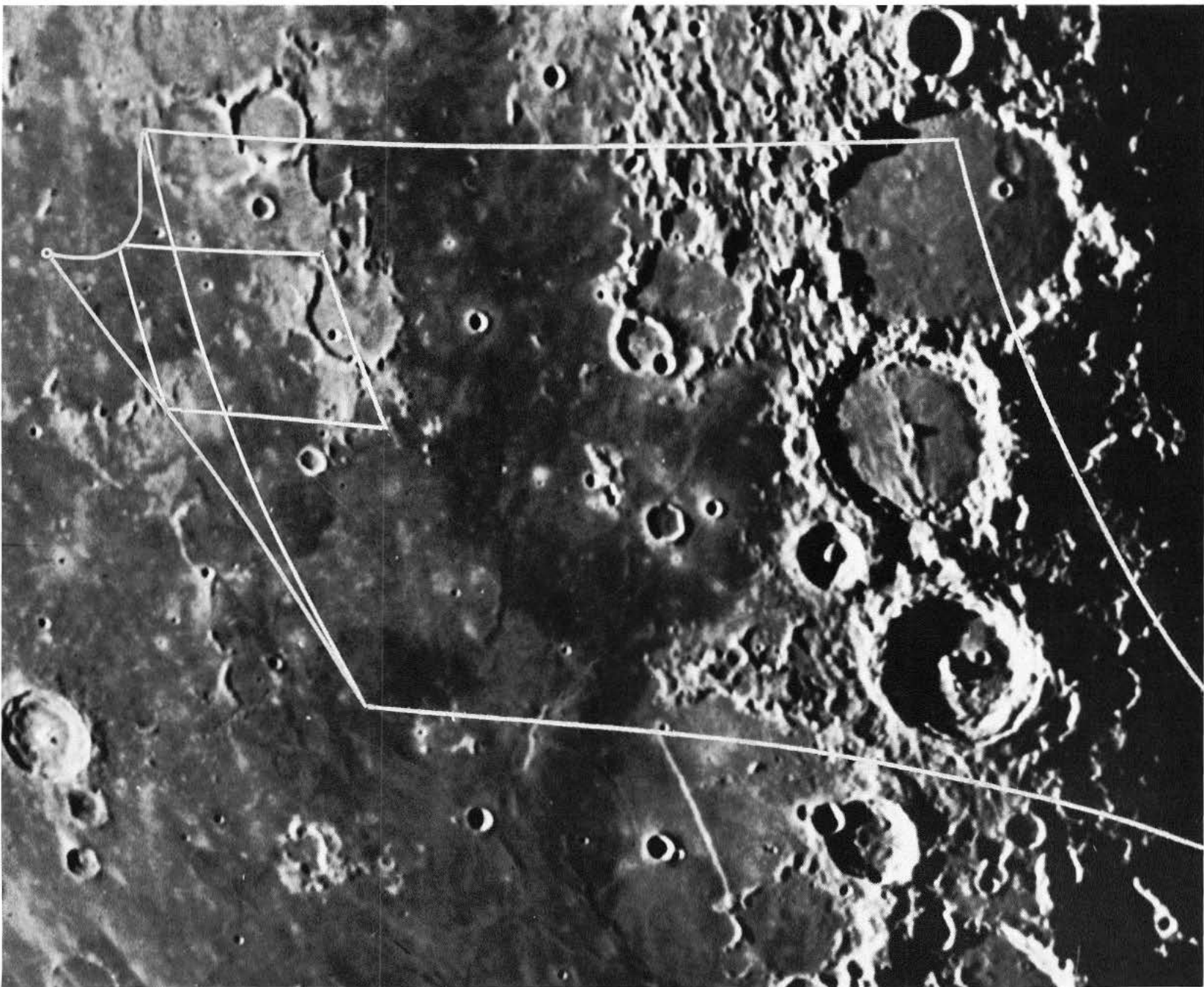
$\longrightarrow$
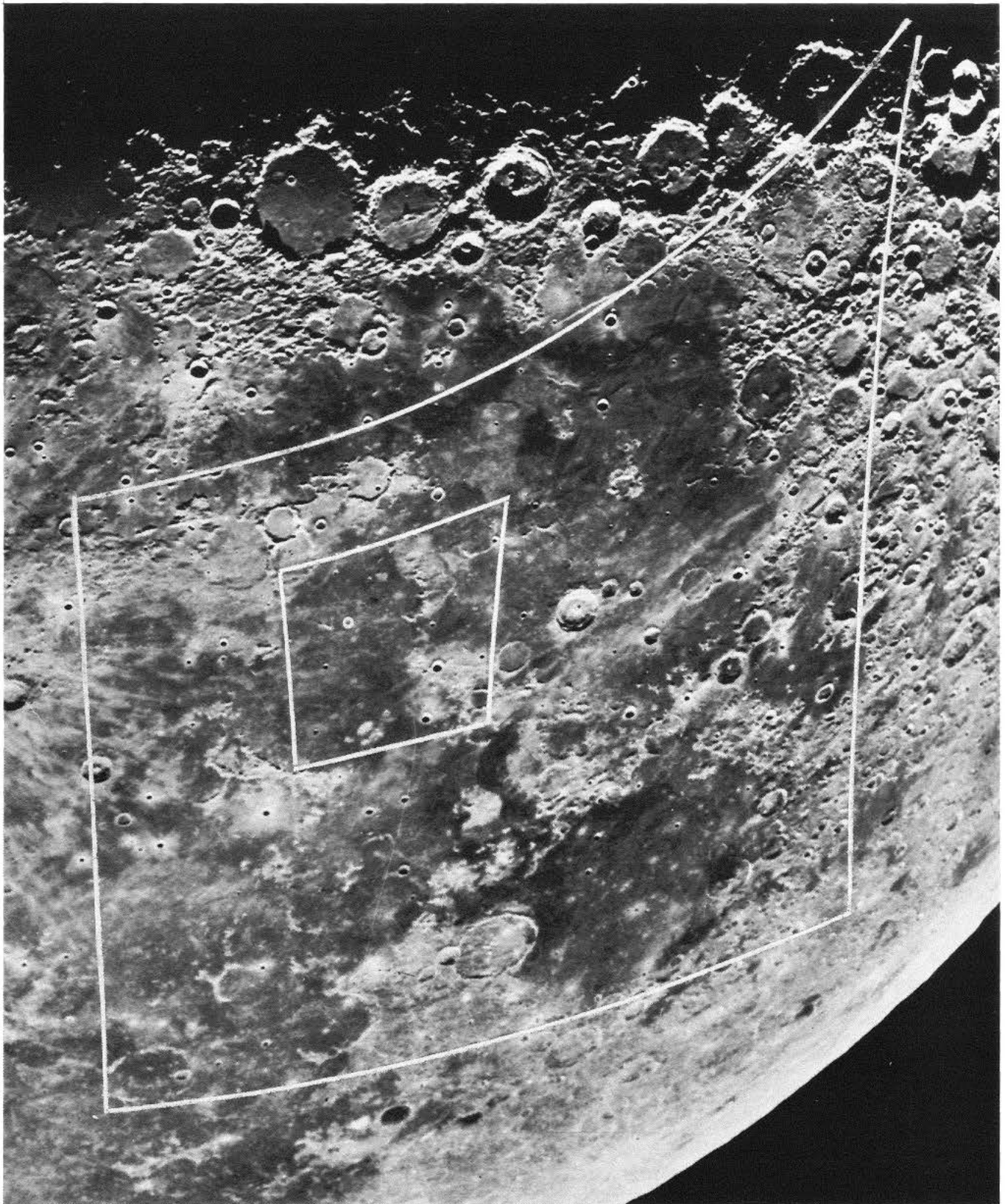
Fig. 6. Earth-based lunar photograph, illustrating coverage by *Ranger VII* B-camera frames 1 and 150.
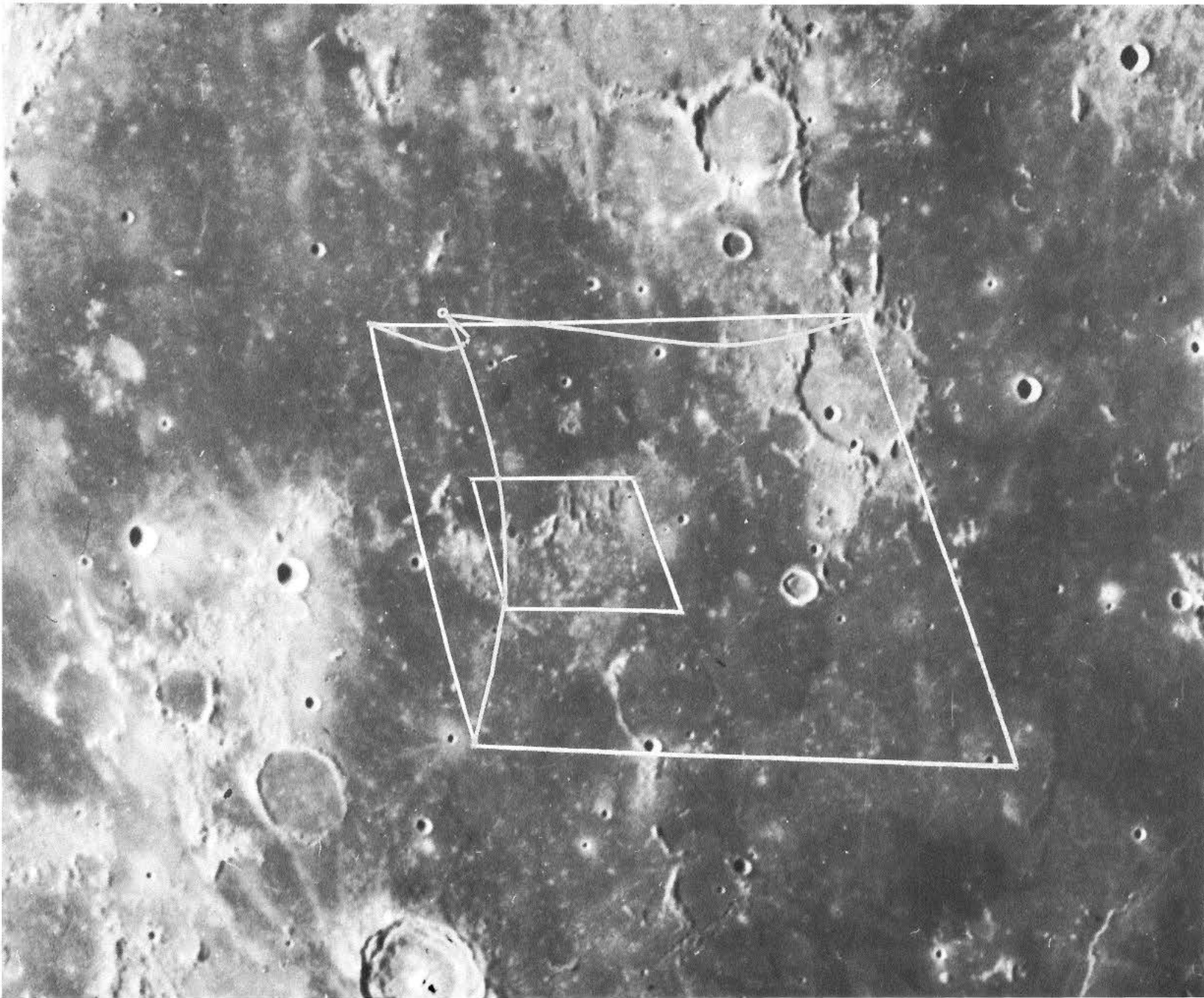
Fig. 7. Earth-based lunar photograph, illustrating coverage by *Ranger VII* P₁- (smaller area) and P₃-camera frame 1.
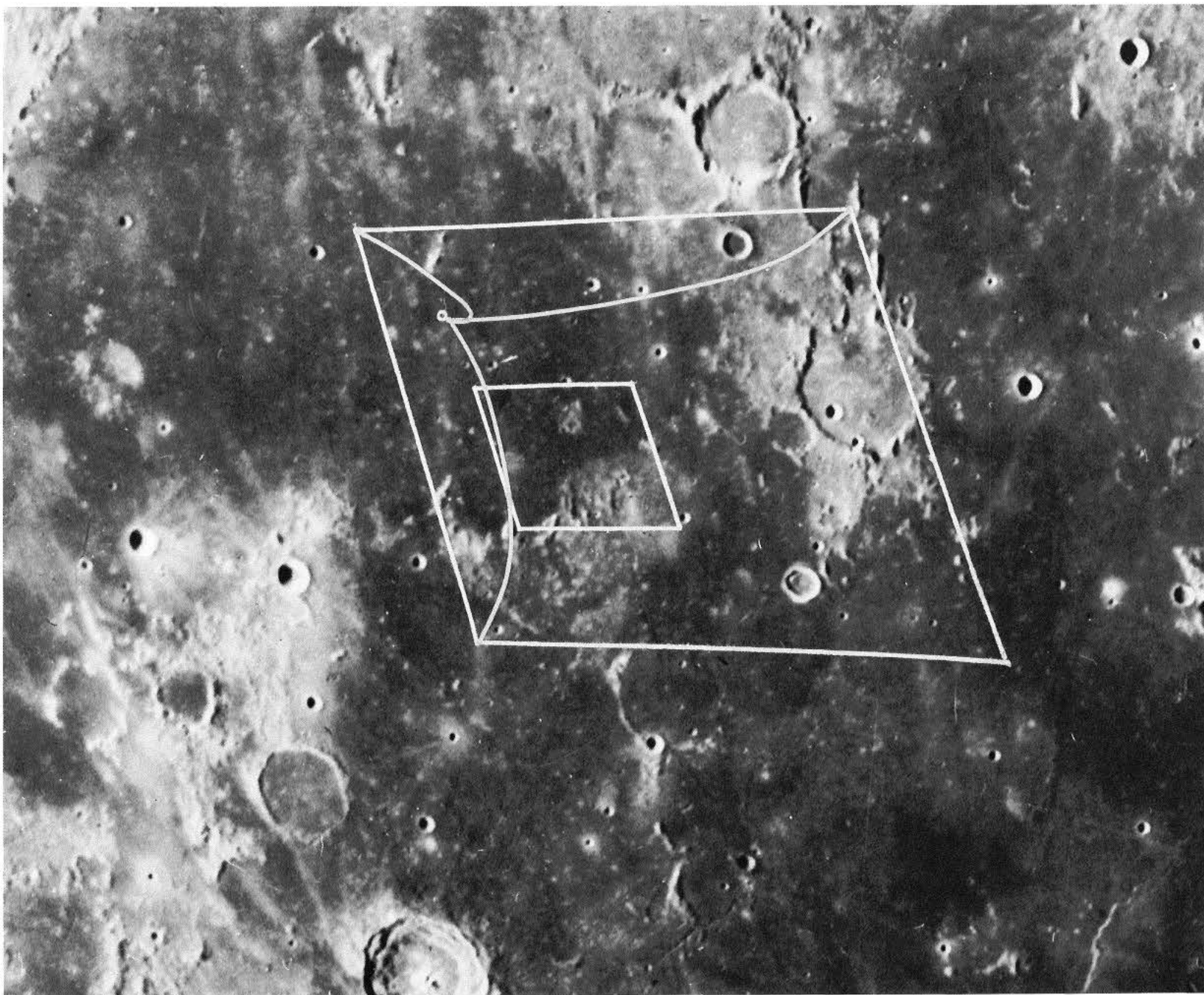
Fig. 8. Earth-based lunar photograph, illustrating coverage by *Ranger VII* P$_2$- (smaller area) and P$_4$-camera frame 1.
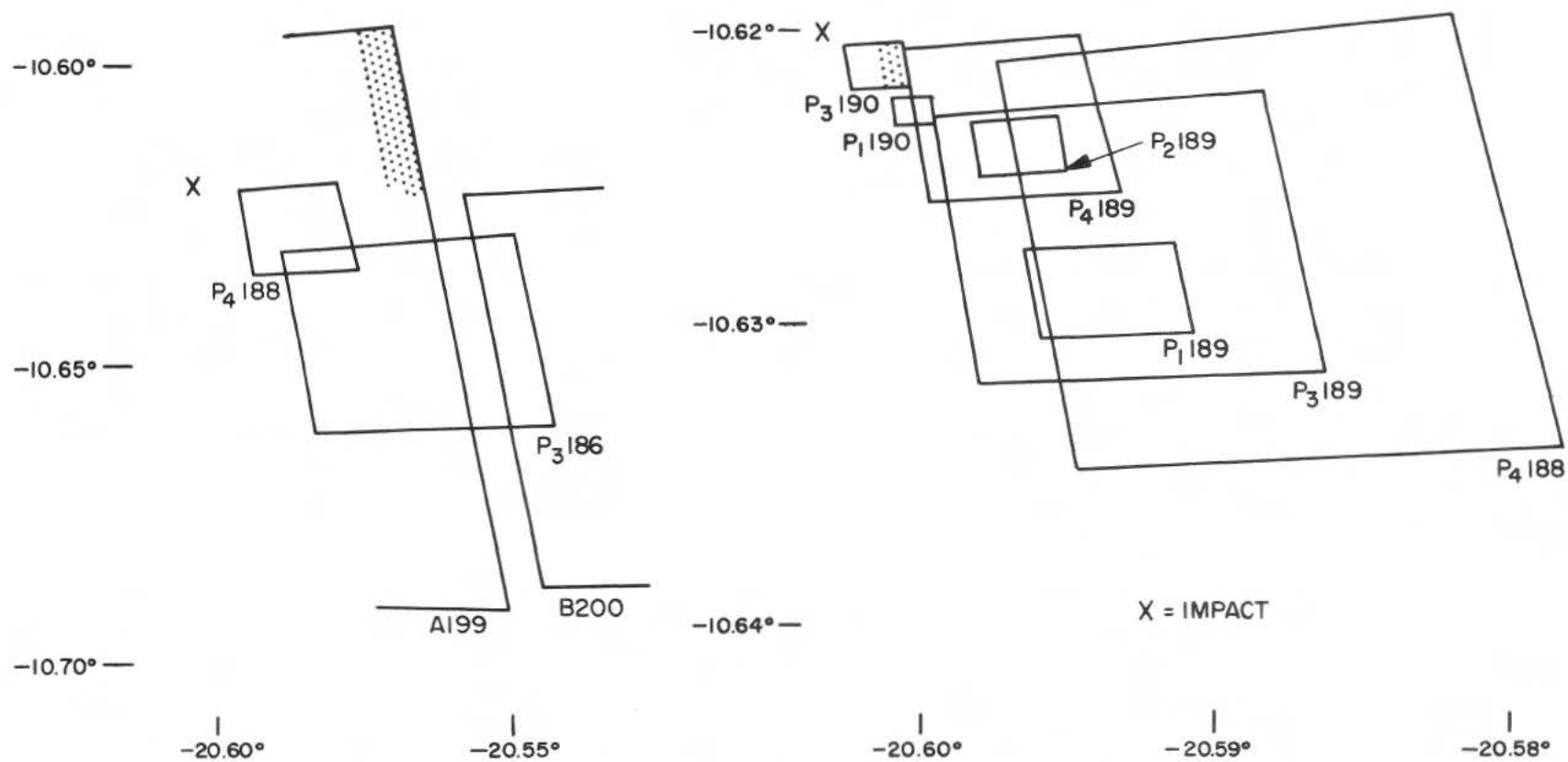
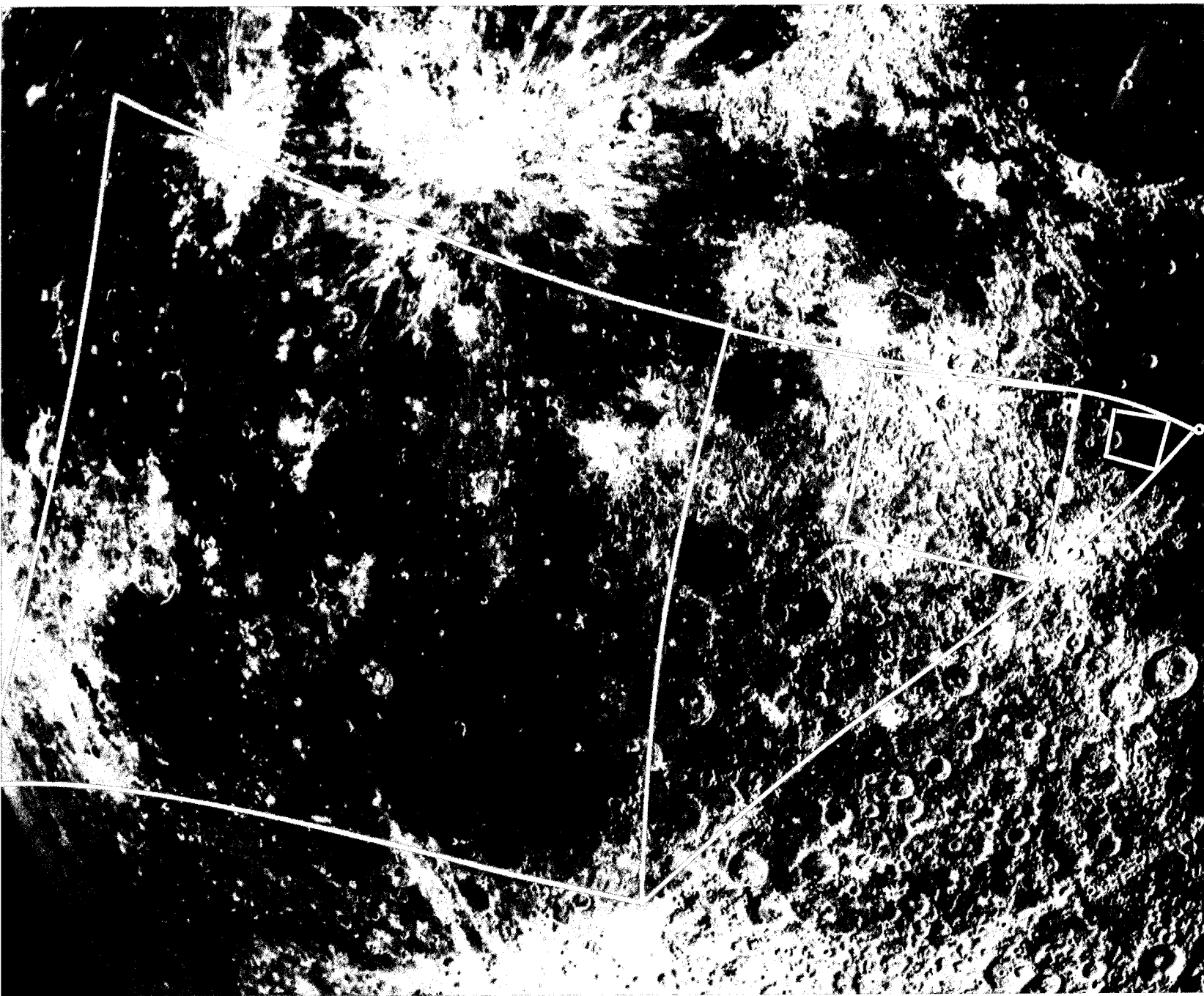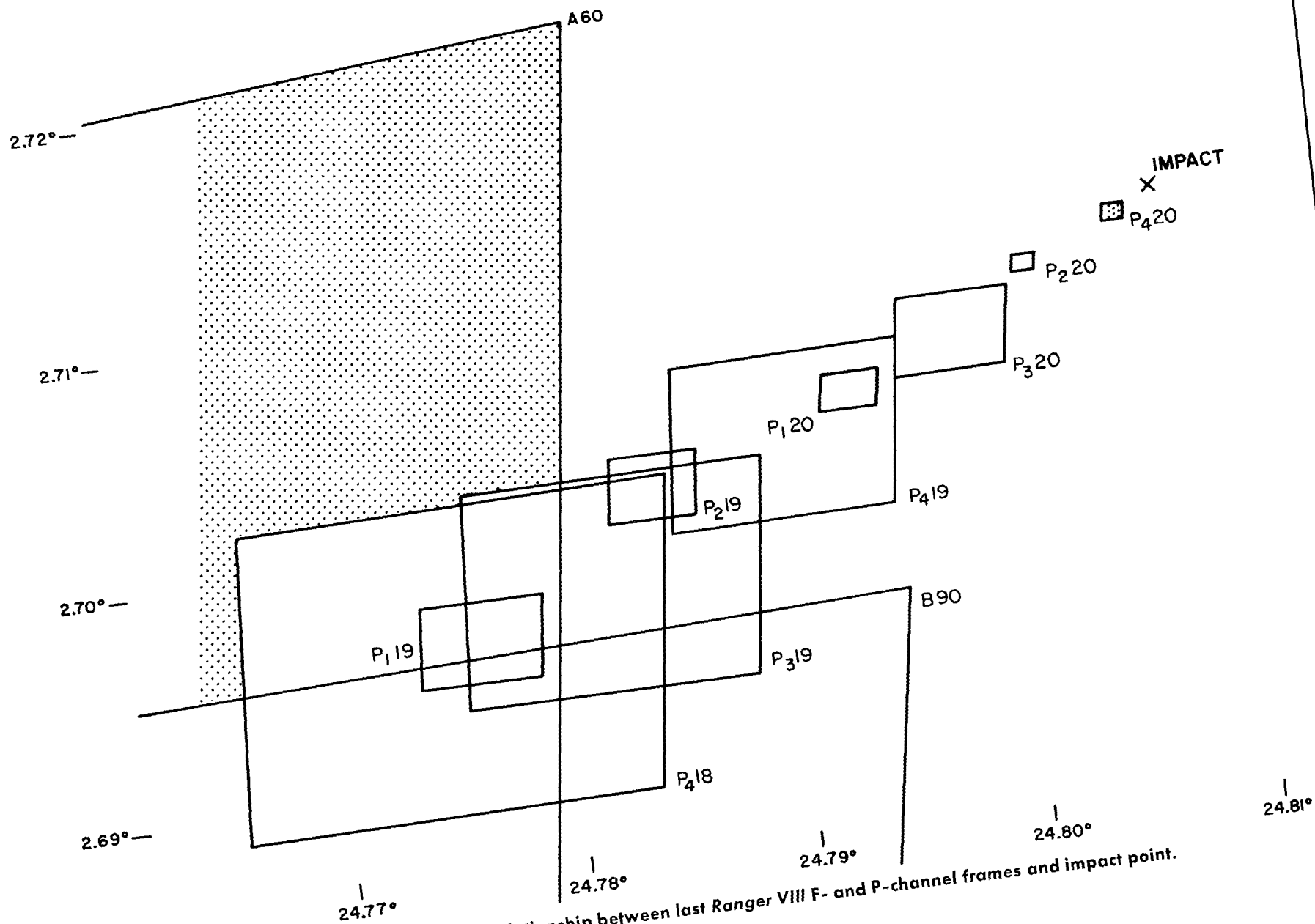Fig. 9. Diagram illustrating relationship between last *Ranger VII* F- and P-channel frames and impact point.

Fig. 10. Earth-based lunar photograph, illustrating coverage by *Ranger VIII* A-camera frames 1, 5, and 40.
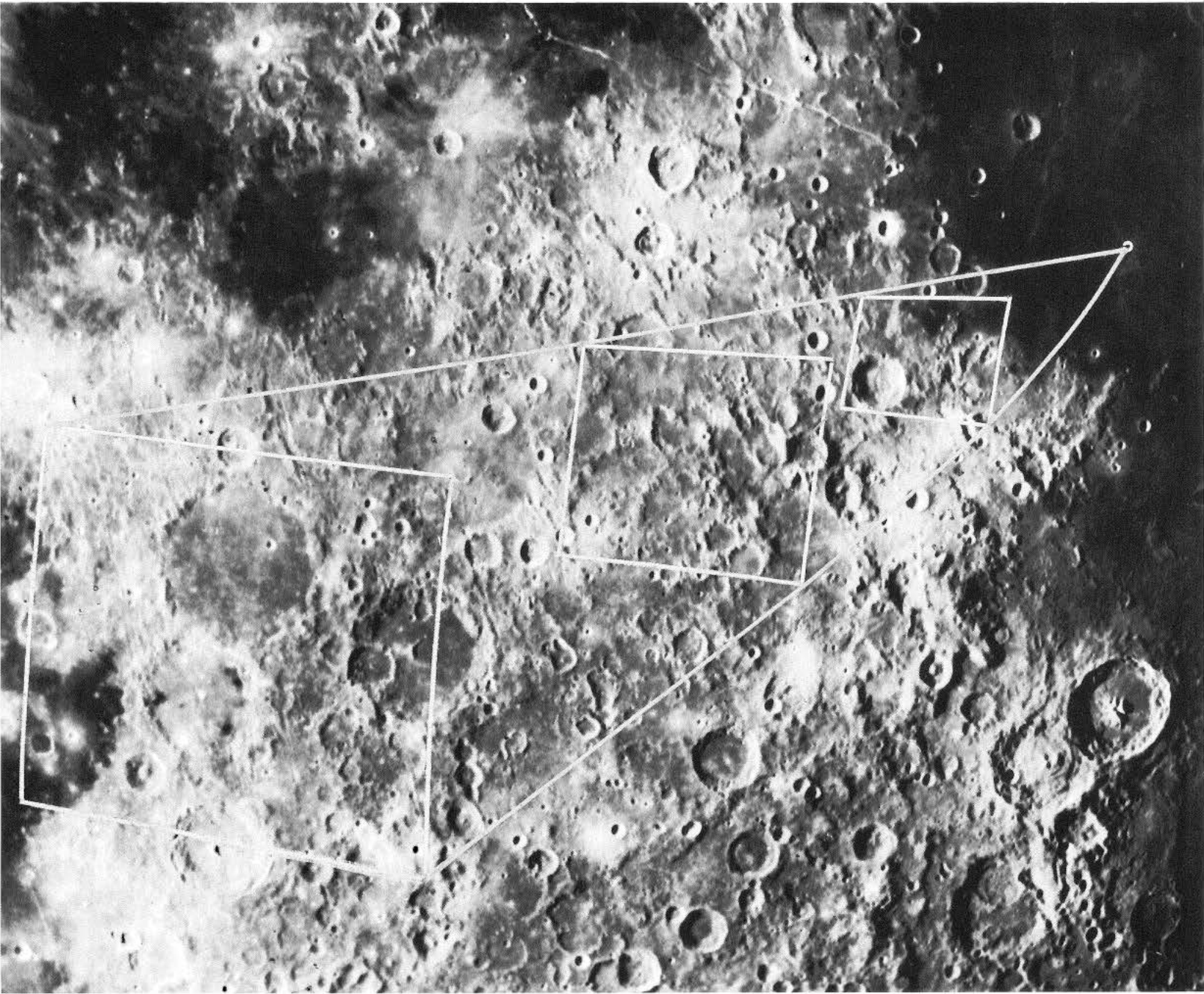
Fig. 11. Earth-based lunar photograph, illustrating coverage by *Ranger VIII* B-camera frames 1, 10, and 30.

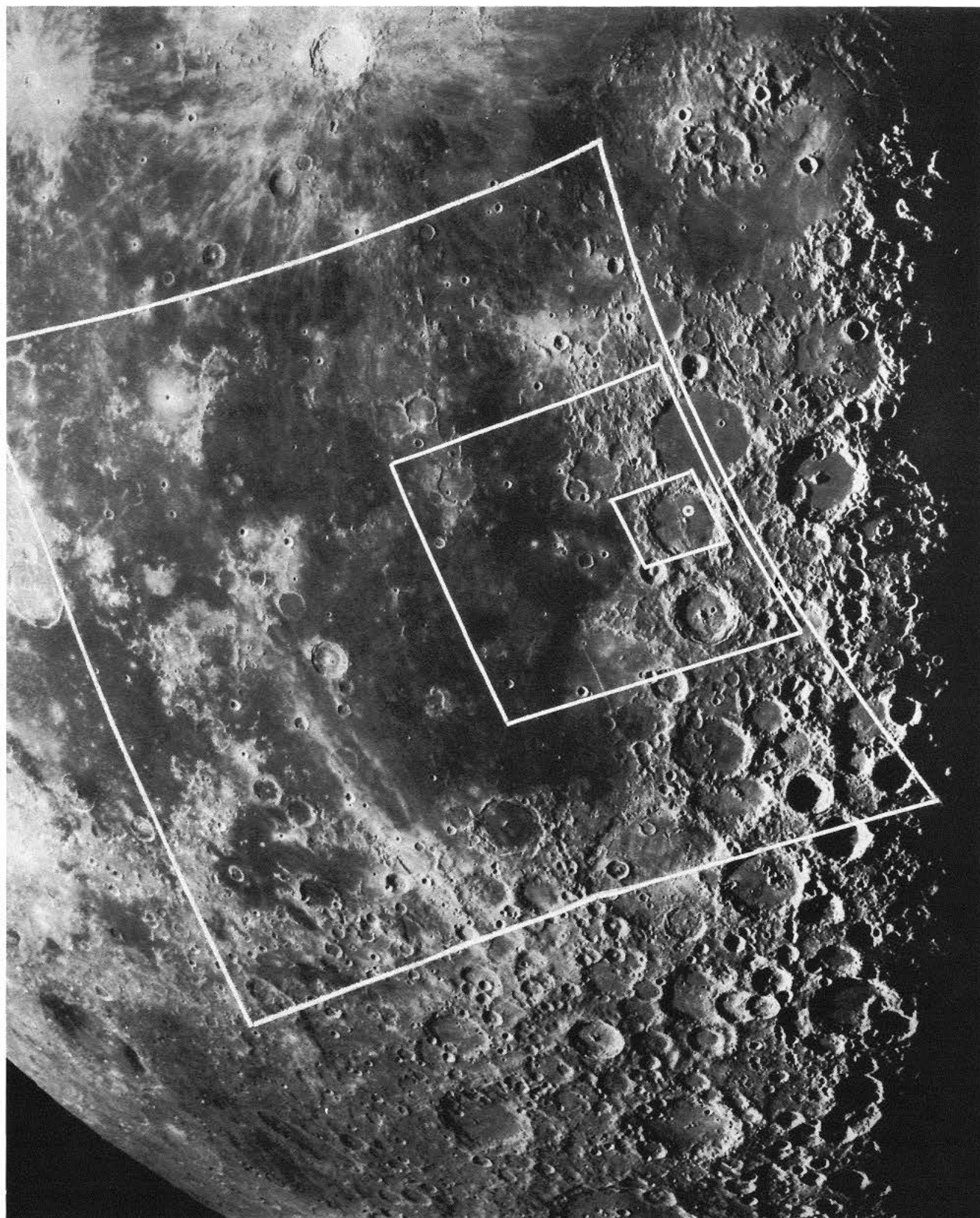Fig. 12. Diagram illustrating relationship between last *Ranger VIII* F- and P-channel frames and impact point.

Fig. 13. Earth-based lunar photograph, illustrating coverage by *Ranger IX* A-camera frames 1, 12, and 50.
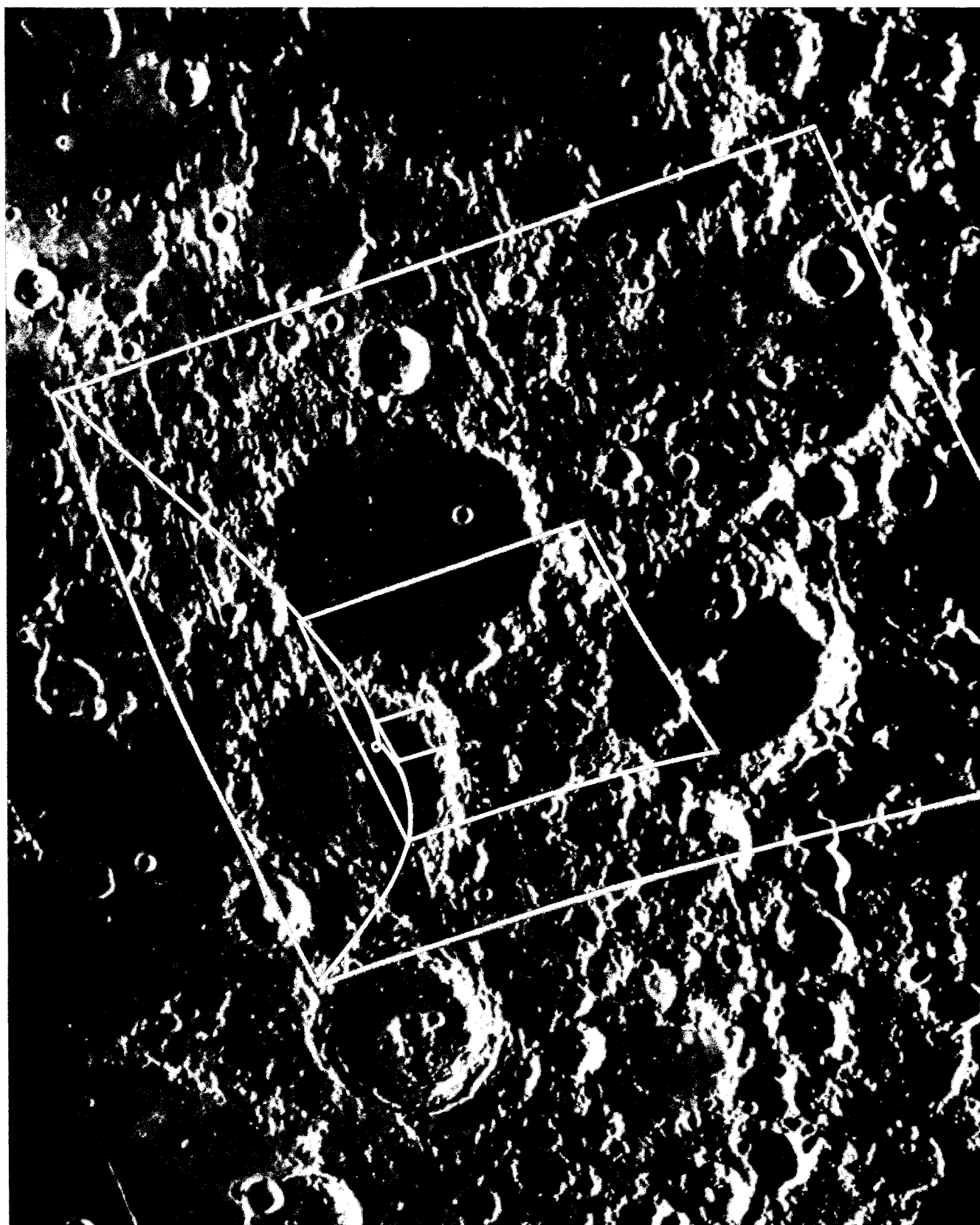
Fig. 14. Earth-based lunar photograph, illustrating coverage by *Ranger IX* B-camera frames 1, 25, and 75.
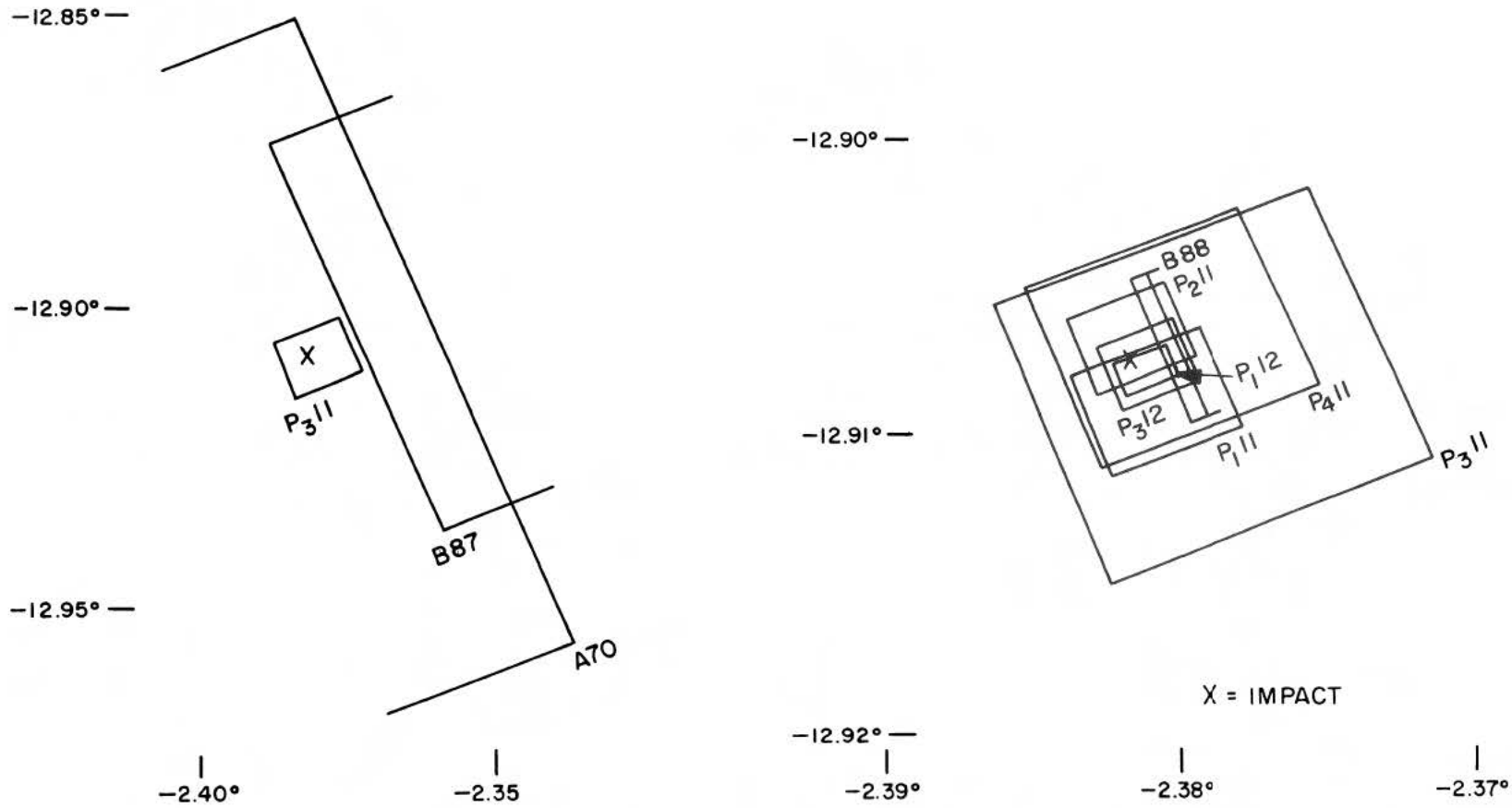
Fig. 15. Diagram illustrating relationship between last *Ranger IX* F- and P-channel frames and impact point.